Thermosphere Dynamics Workshop II

Proceedings of a Workshop held at
Beltsville/Calverton, Maryland
October 3-5, 1984

NASA

Thermosphere Dynamics Workshop II

Hans G. Mayr and Nathan J. Miller, *Editors*
Goddard Space Flight Center
Greenbelt, Maryland

Proceedings of a Workshop held at
Beltsville/Calverton, Maryland
October 3-5, 1984

THERMOSPHERE DYNAMICS WORKSHOP II

Preface

The second Goddard workshop on thermosphere dynamics was held at the Ramada Inn in nearby Calverton, Maryland during October 3-5, 1984. Much of the discussion at the workshop involved the measurements from the Dynamics Explorer spacecraft (DE-1 and DE-2) and ground based measurements at radar facilities and optical observatories. Theoretical models were presented which amply attest to our maturing understanding of the processes that govern the structure and dynamics of the Earth's thermosphere. The phenomenology ranged from auroral meteorology to equatorial tides and gravity waves. Some of the discussion was devoted to the thermosphere of Venus. The papers, abstracts, and extended abstracts included in this volume are in alphabetical order by author and cover most of the material that was presented.

We express our thanks to the individuals who chaired the sessions and to the speakers of the invited and contributed papers for the high quality of their presentations. Our special gratitude is due to Dianna Gemma from Birch and Davis and Aleta Johnson (GSFC, Code 610) for coordinating the meeting.

Organizing Committee:

H. G. Mayr, Chairman (GSFC)
F. A. Herrero, Co-Chairman (GSFC)
N. J. Miller (GSFC)
N. W. Spencer (GSFC)
H. C. Carlson (AFGL)
J. M. Forbes (Boston University)
W. B. Hanson (University of Texas)
T. L. Killeen (University of Michigan)
R. G. Roble (NCAR)
J. T. Lynch (NASA Headquarters)
R. L. Waltersheid (Aerospace Corporation)

NOTICE TO WORKSHOP PARTICIPANTS

The following page numbers contain black and white figures that are reproduced in color among the Addendum Figures: 287-290, 317-322, 332-339, 350-351, 356-360, 437-438.

THERMOSPHERE DYNAMICS WORKSHOP II

PROGRAM

Beltsville/Calverton, Maryland

Wednesday October 3, 1984

MORNING

9:00 *Welcome*   H. G. Mayr

9:15 *Invited Reviews I*   E. R. Schmerling, Chairman

Implications of in situ temperature and wind
    measurements   N. W. Spencer
A brief history of the measurements of
    thermospheric winds   P. B. Hays

COFFEE BREAK

Satellite measurements of NO in the lower
    atmosphere   C. A. Barth
Particle precipitations   P. H. Reiff

LUNCH

AFTERNOON

1:30 *Invited Reviews II*   C. O. Hines, Chairman

Magnetosphere-ionosphere coupling modes
    involving field aligned currents: A key question
    concerning the joule heating   M. Sugiura
Convection pattern morphology and variations   R. A. Heelis
Thermosphere dynamics   R. E. Dickinson

COFFEE BREAK

Modelling the ionospheric wind dynamo   A. D. Richmond
Tidal coupling with the lower atmosphere   J. M. Forbes
Interactions between dynamics and chemistry
    in the mesosphere and lower thermosphere   R. R. Garcia

MORNING

8:30 PARALLEL SESSIONS

Global Dynamics I., J. T. Lynch, Chairman

Evidence for momentum source winds at low latitudes
   N. J. Miller and N. W. Spencer

Observations of the equatorial midnight temperature anomaly
   F. A. Herrero

Medium and large-scale variations of dynamo-induced electric fields from AE and DE ion drift measurements
   W. R. Coley and J. P. McClure

Bubble dynamics
   W. B. Hanson

COFFEE BREAK

Dynamics of the thermosphere from inco-herent scatter measurements at Arecibo
   R. G. Burnside, J. C. G. Walker and C. A. Tepley

Initial results from the global thermo-spheric mapping study
   W. L. Oliver, Jr. and J. E. Salah

Millstone Hill measurements and TGCM simulation for the 30 May 1984 annular solar eclipse
   J. E. Salah, W. L. Oliver, B. A. Emery, R. G. Roble, E. C. Ridley and H. C. Carlson

A method for extracting meridional winds from ionosonde measurements by using ionospheric models
   P. G. Richards and D. G. Torr

Polar Processes I., R. A. Hoffman, Chairman

Ion-neutral coupling in the high latitude thermosphere
   T. L. Killeen

Magnetic meridian component of the dayside neutral winds at Sondrestrom between 200 and 300 km altitude
   V. B. Wickwar

EISCAT velocity patterns for theoretical convection models
   H. Rishbeth and J. J. Sojka

COFFEE BREAK

Thermal and dynamic perturbations associated with auroral disturbances
   M. H. Rees and R. G. Roble

Polar cap observations of thermospheric winds and temperatures
   J. W. Meriwether, Jr. and P. Shih

Geostrophic adjustment in the high-latitude thermosphere: Numerical solutions at large Rossby numbers
   M. F. Larsen

A numerical nonlinear spectral thermosphere model
   I. S. Mikkelsen

LUNCH

Thursday October 4, 1984

AFTERNOON

1:00 PARALLEL SESSIONS

Global Dynamics II., M. A. Geller, Chairman

Simulation of the thermospheric tides by use
of the NCAR thermospheric general
circulation model
    C. G. Fesen, R. E. Dickinson and
    R. G. Roble

Global thermospheric NO
    J. Gerard

Equatorial observations of thermospheric
winds and temperatures
    J. W. Meriwether, Jr. and M. A. Biondi

Global large scale structures in the F region
    S. H. Gross

COFFEE BREAK

A dynamo theory prediction for solar cycle 22
    K. H. Schatten and A. E. Hedin

Observations of composition from Pioneer
Venus
    H. A. Taylor, Jr.

Applications of a Venus thermospheric
circulation model
    S. W. Bougher, R. E. Dickinson
    E. C. Ridley and R. G. Roble

Spectral model of the Venusian thermosphere
    D. Stevens-Rayburn, H. G. Mayr, and
    I. Harris

Polar Processes II., H. Rishbeth, Chairman

UT/longitudinal variations of composition in
DE data
    A. E. Hedin

Atomic nitrogen densities near the polar cusp
    M. J. Engebretson

Satellite accelerometer measurements of
neutral density and winds during geomagnetic
storms
    F. A. Marcos and J. M. Forbes

Measurements of thermospheric response to
auroral activities
    S. Okano and J. S. Kim

COFFEE BREAK

Observations of the origin of thermospheric
gravity waves launched by auroral substorms
and westward travelling surges
    D. Rees

The time-dependent dynamical response of the
upper thermosphere to major geomagnetic
disturbances
    D. Rees, T. Killeen, P. Hays,
    N. Spencer, and L. Wharton

WAMDII observations of an auroral
atmospheric wave event
    R. H. Wiens, G. G. Shepherd,
    and K. V. Paulson

The transient response of the neutral
atmosphere near narrow auroral features
    R. L. Walterscheid

Transfer function analysis of thermospheric
perturbations
    H. G. Mayr, I. Harris, F. Varosi and
    F. A. Herrero

Friday October 5, 1984

MORNING

8:30 *Polar Processes III*   W. Hanson, Chairman

    Current results from mapping of the earth's   L. A. Frank and J. D. Craven
        atmosphere with DE-1 (*invited*)

    Self-consistent modelling of the polar thermo-   D. Rees, J. Quegan, and
        sphere and ionosphere to magnetospheric   T. Fuller-Rowell
        convection and precipitation (*invited*)

    Modelling of thermospheric composition changes   H. Rishbeth, D. Rees, and
        produced by geomagnetic substorms   R. Gordon

COFFEE BREAK

    Modelling the thermosphere dynamics (*invited*)   R. G. Roble

    The quadrupole ionosphere   H. Rishbeth

12:00 *Banquet luncheon* Dixon Butler, NASA Headquarters, guest speaker

TABLE OF CONTENTS

PROGRAM

Abstracts and Figures

APPLICATIONS OF A VENUS THERMOSPHERIC CIRCULATION MODEL

S. W. Bougher, R. E. Dickinson, E. C. Ridley, and R. G. Roble
National Center for Atmospheric Research
Boulder, CO 80307

A variety of Pioneer Venus observations suggest a global scale, day-to-night Venus thermospheric circulation. The two-dimensional hydrodynamic model of Dickinson and Ridley (1977) correctly predicted the gross characteristics of this largely symmetric circulation. However, it failed to calculate the observed cold nightside temperatures, and the exact phases and densities of the neutral constituents. This paper presents model studies of the dynamics and energetics of the Venus thermosphere, in order to address new driving, mixing and cooling mechanisms for an improved model simulation.

The adopted approach has been to re-examine the circulation by first using the previous two-dimensional code to quantify those physical processes which can be inferred from the Pioneer Venus observations. Specifically, the model was used to perform sensitivity studies to determine the degree to which eddy cooling, eddy or wave drag, eddy diffusion and 15 μm radiational cooling are necessary to bring the model temperature and composition fields into agreement with observations. Three EUV heating cases were isolated for study.

Global temperature and composition fields in good agreement with Pioneer data were obtained. Large scale horizontal winds ≤ 220 m/s were found to be consistent with the observed cold nightside temperatures and dayside bulges of O, CO and CO_2. Fine tuning required that an eddy coefficient $\leq 20\%$ of previous one-dimensional models be used for nightside diffusion ($K = 7.5 \times 10^6$ cm^2/s). Very little eddy diffusion was required for the dayside ($K \leq 4 \times 10^6$ cm^2/s). Observed dayside temperatures were obtained by using a 7-19% EUV heating efficiency profile. The enhanced 15 μm cooling needed for thermal balance is obtained using the best rate coefficient ($K_{CO_2-O} = 5 \times 10^{-13}$ cm^3/s) available for atomic O collisional excitation of $CO_2(0, 1, 0)$. Eddy conduction was not found to be a viable cooling mechanism due to the weakened global circulation. The strong 15 μm damping and low EUV efficiency imply a very weak dependence of the general circulation to solar cycle variability. Finally, the NCAR terrestrial thermospheric general circulation model (TGCM) was adapted for Venus inputs using the above two-dimensional model parameters, to give a three-dimensional benchmark for future Venus modelling work.

1
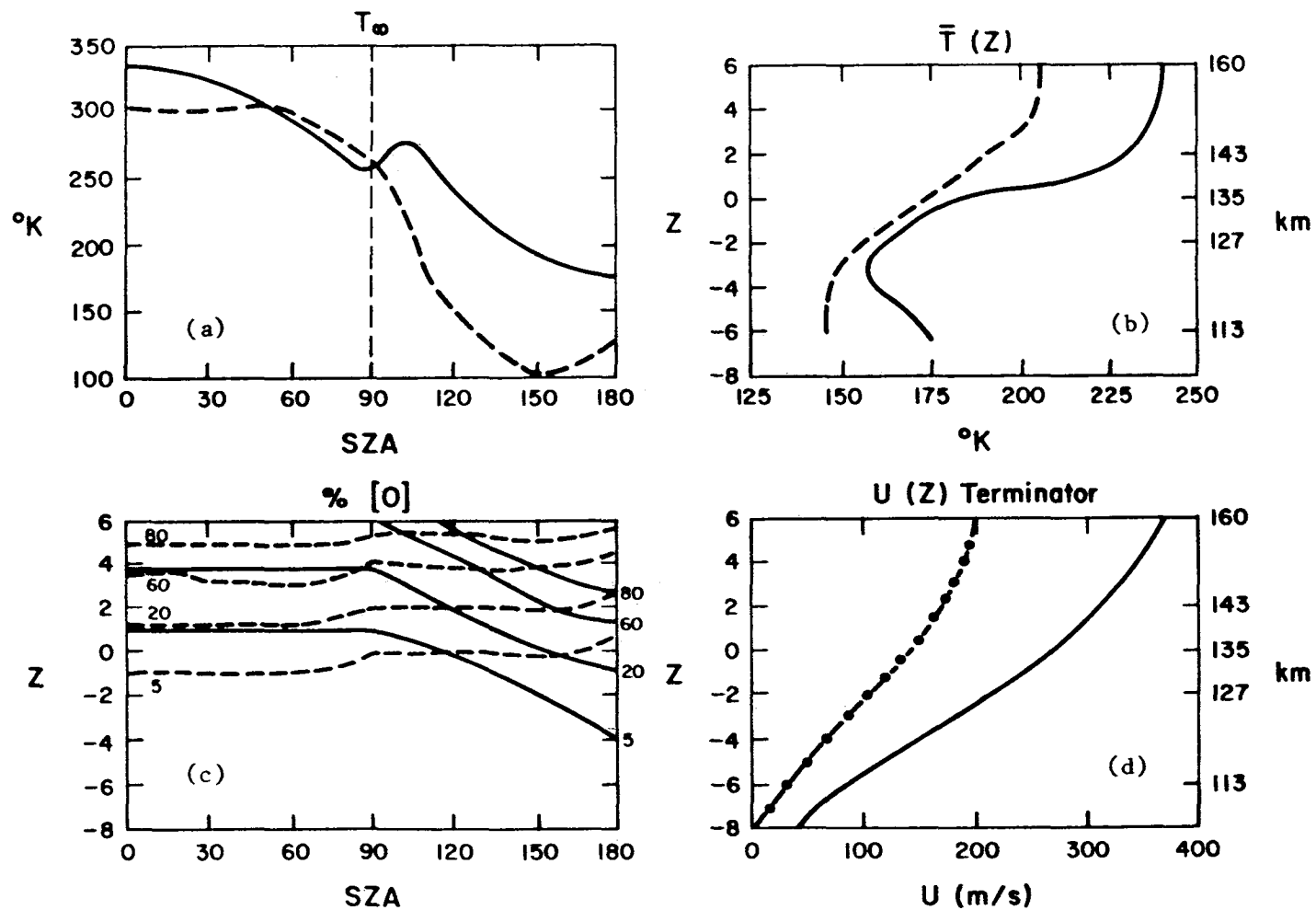
Figure 1. Comparisons of Dickinson and Ridley (1977) (DRM2) predictions and Pioneer Venus (PV) observations (_____DRM2; ------PV; .-.-. Mayr et al., 1980) where z = log (5x10^{-3} μbar/p).
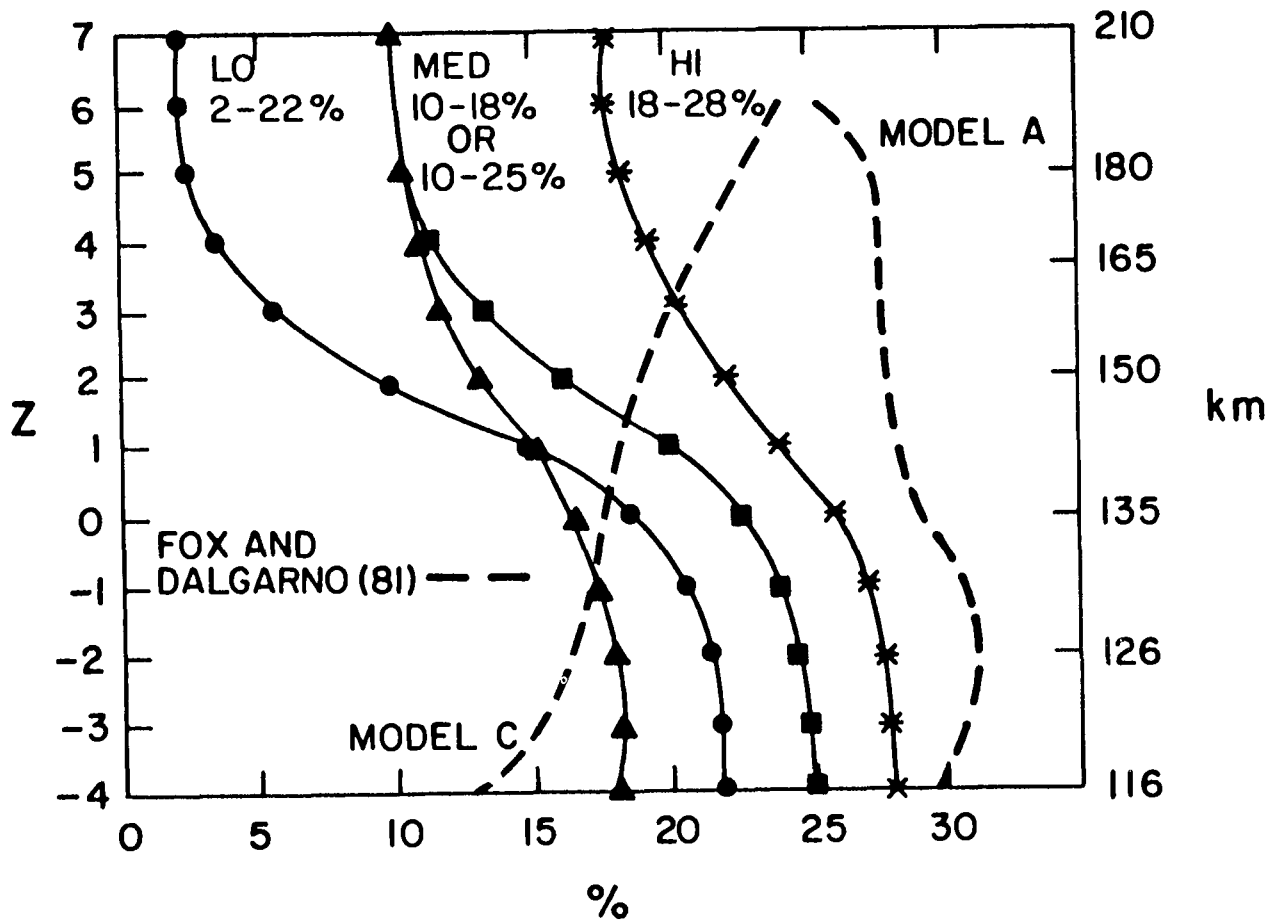
Figure 2. EUV heating efficiency profiles.
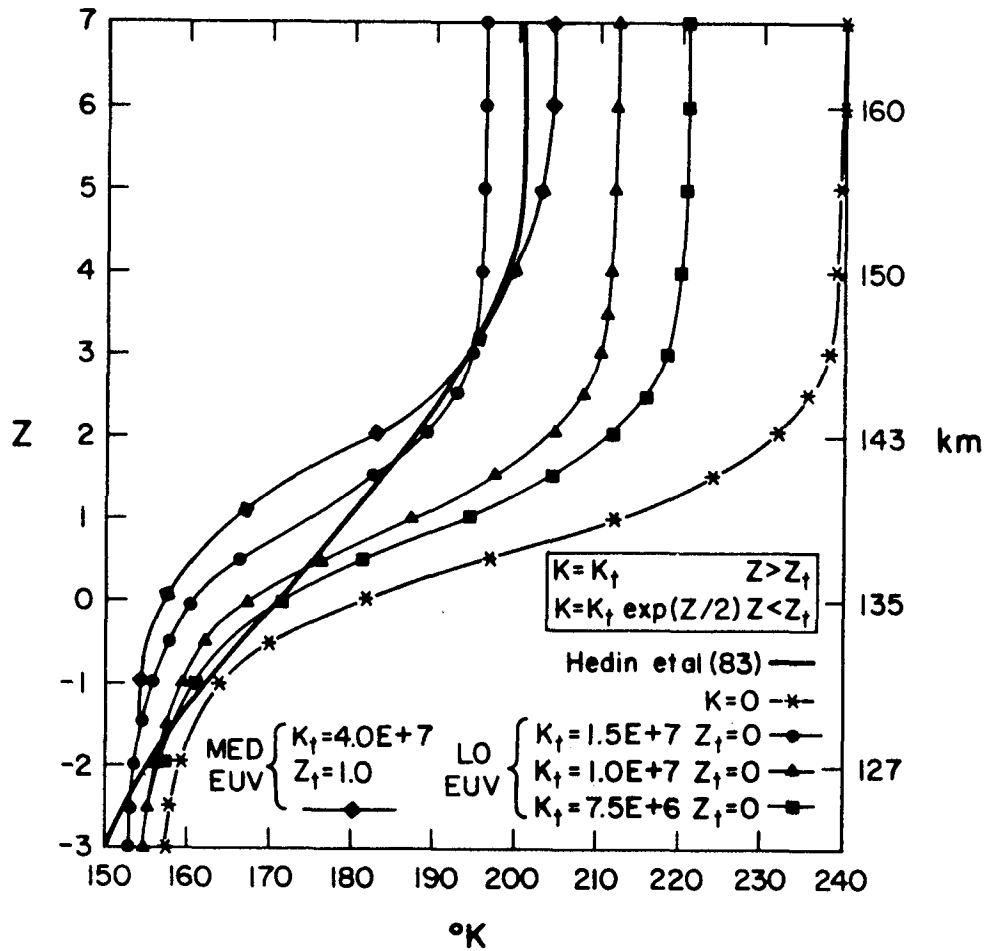
Figure 3. Global mean Venus one-dimensional thermospheric temperature profiles: eddy cooling tests. Here K_t is the turbopause value of the eddy coefficient and Z_t corresponds to the turbopause level.
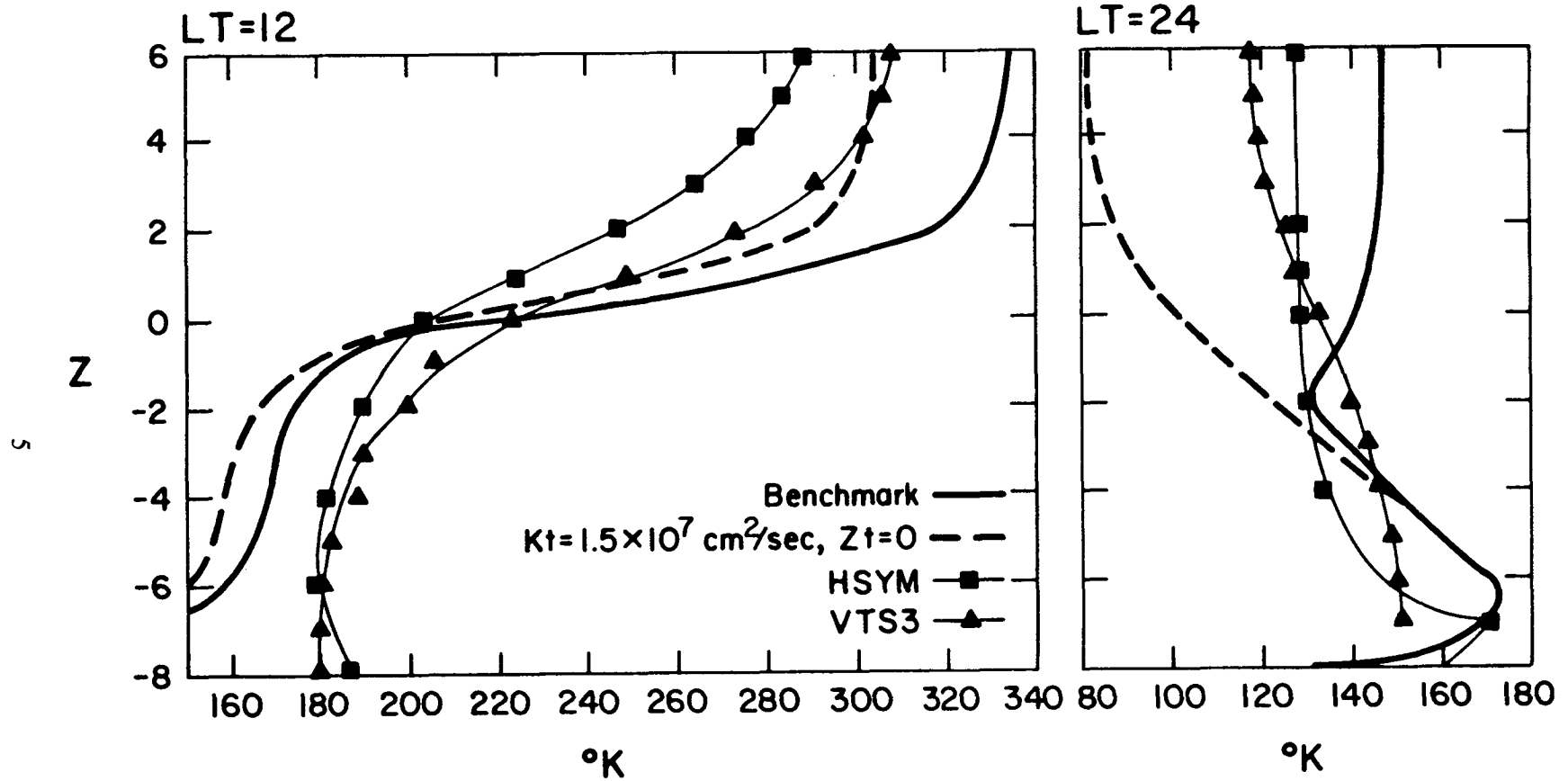
Figure 4. Venus two-dimensional model temperature response to eddy cooling. HSYM corresponds to the Keating et al. (1984) model atmosphere, and VTS3 to the Hedin et al. (1983) empirical model.
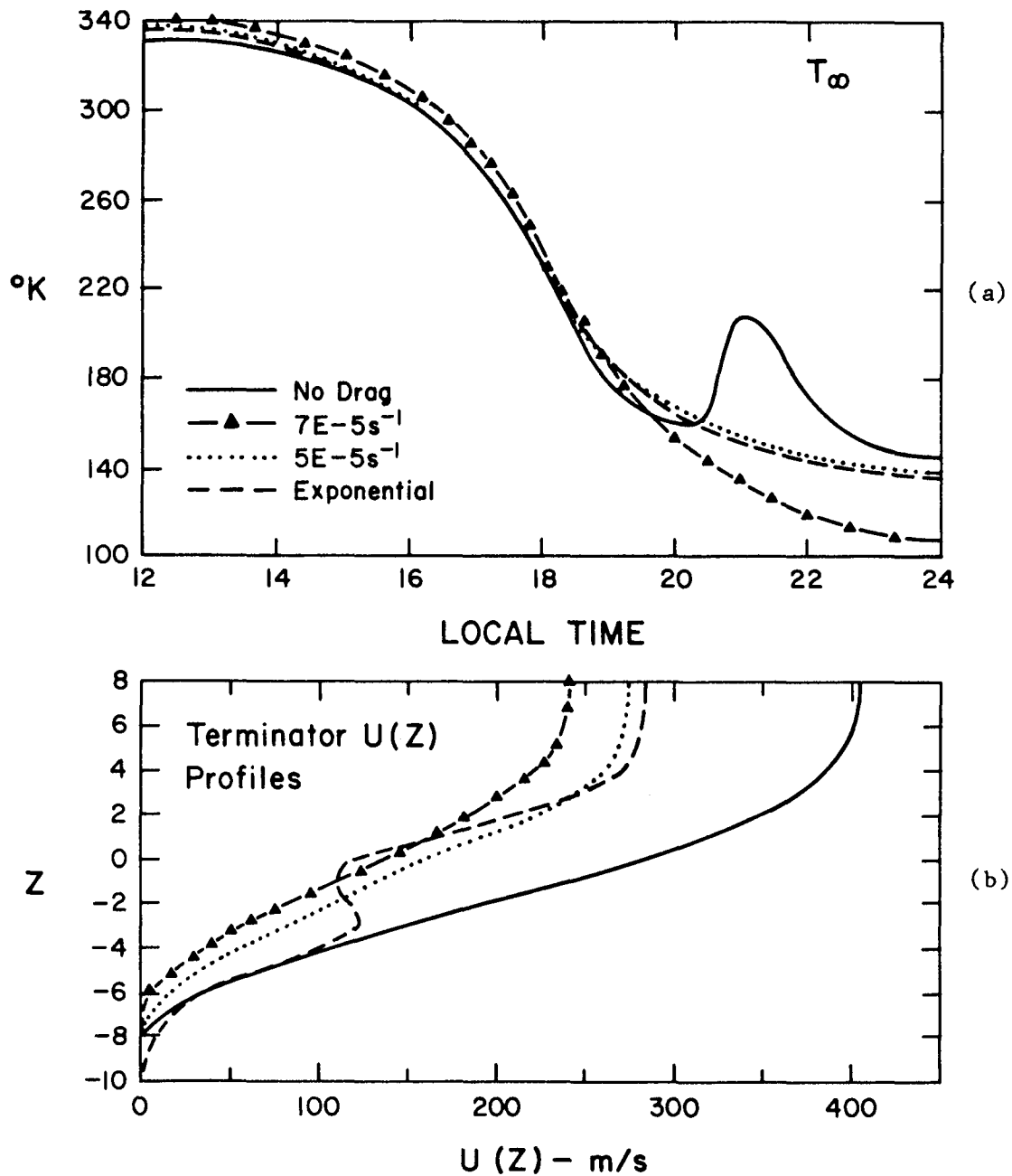
Figure 5. Venus two-dimensional model response to viscous drag tests. The effects are shown for various adjustments of a Rayleigh friction coefficient (K_{RA}) (a) T∞, (b) terminator u(z) profiles.
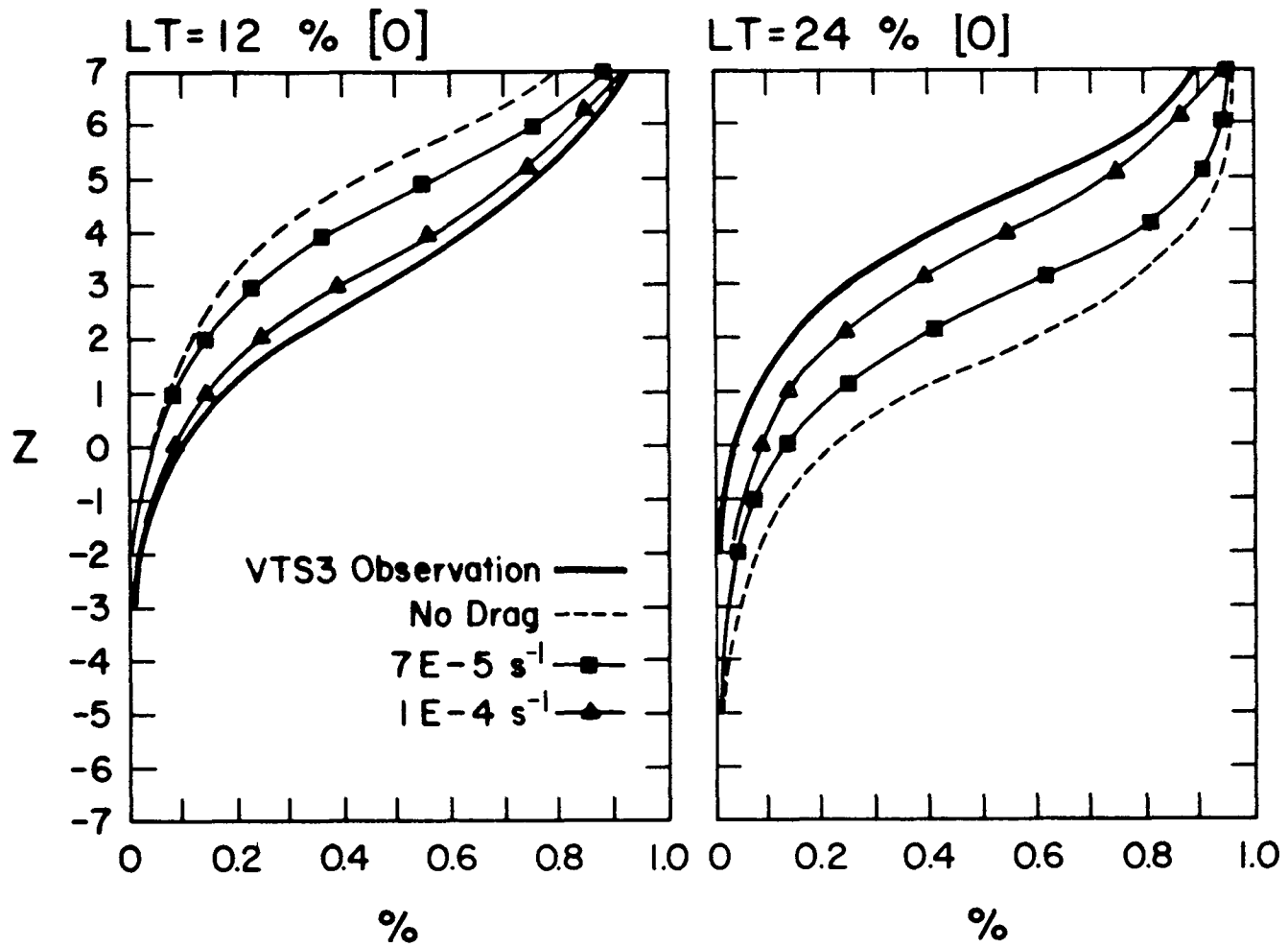
Figure 6. Venus two-dimensional model response to viscous drag tests (c) composition.
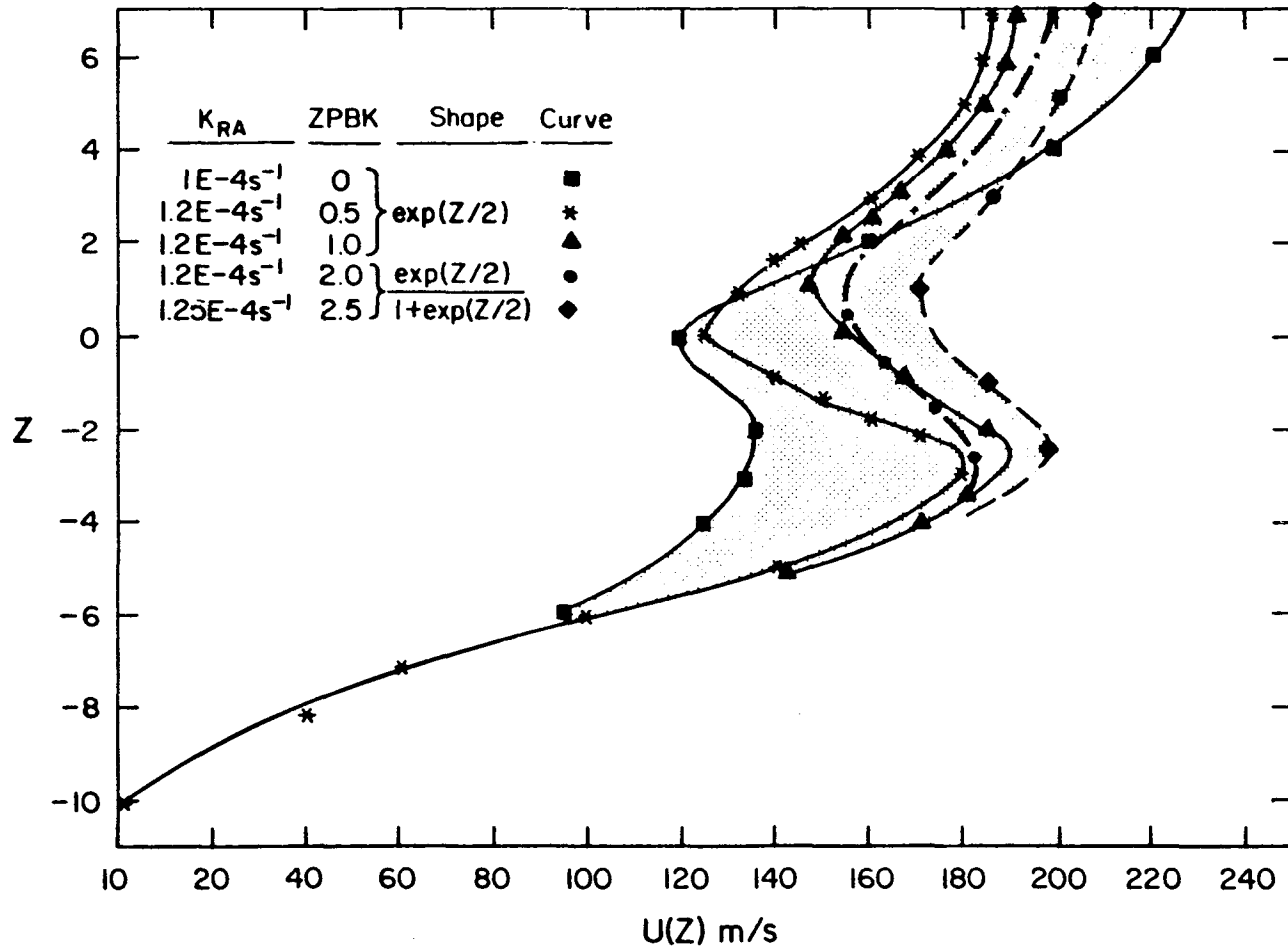
Figure 7. Family of terminator horizontal wind profiles. Various drag profile shapes and K_{RA} magnitudes were examined to obtain the best day-night distribution of model composition and temperature fields.
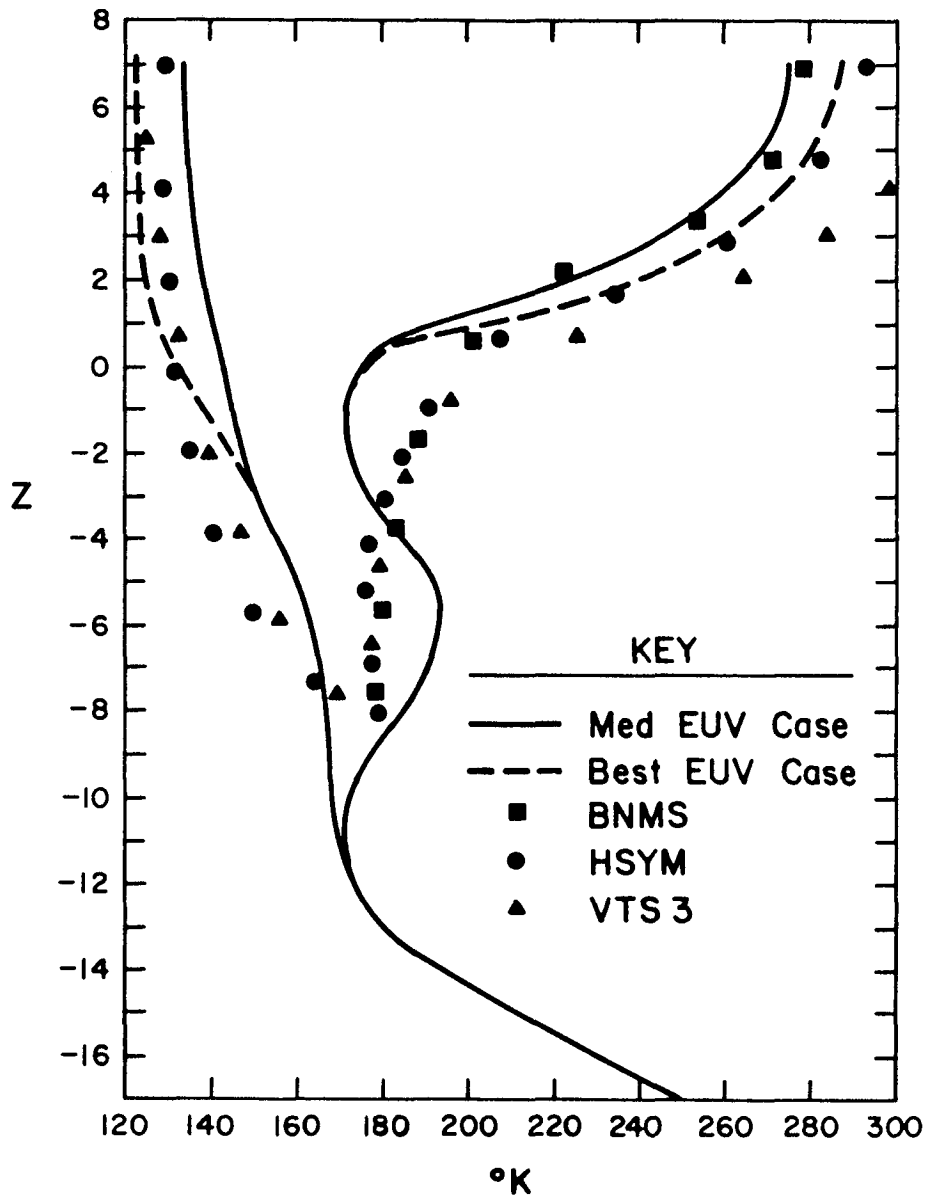
Figure 8. One-dimensional radiative transfer model reference
temperatures: dayside and nightside mean profiles. These were
calculated using the enhanced 15 μm cooling (K_{CO_2-O} = 5x10^{-13} cm^3/s)
possible via atomic O collisional excitation of CO_2 (0, 1, 0). Results are
given for the BEST EUV case (7-19% profile) heating.

Best Parameter Adjustments for Each EUV Efficiency Case

Parameter	Low (2-22%)	Medium (10-25%)	High (18-28%)	Best (7-19%)
Eddy Cooling				
DY: Kmax/ZPBK	$1.0\times10^7/0$ (NG)	$4\times10^7/0$ (NG)	–	none
15 μm Cooling				
$k(CO_2\text{-}O)$	2×10^{-13}	7.5×10^{-13}	1.75×10^{-12}	5×10^{-13}
Eddy Drag				
K_{RA}	$1\text{-}1.25\times10^{-4}s^{-1}$	$1\text{-}1.2\times10^{-4}s^{-1}$	–	$1.2\times10^{-4}s^{-1}$
ZPBK	0	0→1	–	2.0
Eddy Diffusion				
DY: K_{max}/ZPBK	$<5\times10^6/0$	none	–	none
NT: K_{max}/ZPBK	$1\text{-}1.5\times10^7/0$	$7\times10^6/0$	–	$7.5\times10^6/\phi$
SZAF	2.0	≥2.0	–	≥2.0
Efficiency Profile Shape				
$\varepsilon(z)$	$0.02+0.4*f(p)$	$0.10+0.3*f(p)$	$0.18+0.2*f(p)$	$0.07+0.24*f(p)$
$f(p)$	$0.5/\left(1.+\dfrac{1.05\times10^{-3}}{p}\right)$	$0.5/\left(1.+\dfrac{1.05\times10^{-3}}{p}\right)$	$0.5/\left(1.+\dfrac{1.05\times10^{-3}}{p}\right)$	$0.5/\left(1.+\dfrac{4.73\times10^{-4}}{p}\left(\dfrac{T}{200}\right)^{0.55}\right)$
ε_{Top}	2%	10%	18%	7%
ε_{Bot}	22%	25%	28%	19%

Figure 9. Best parameter adjustments for each EUV efficiency case. The 7-19% case was isolated for further study since the 15μm cooling K_{CO_2-O} rate adopted is comparable to that inferred by Sharma and Nadile (1981) from a terrestrial rocket measurement of CO_2 emission limb radiance above 100 km.

10
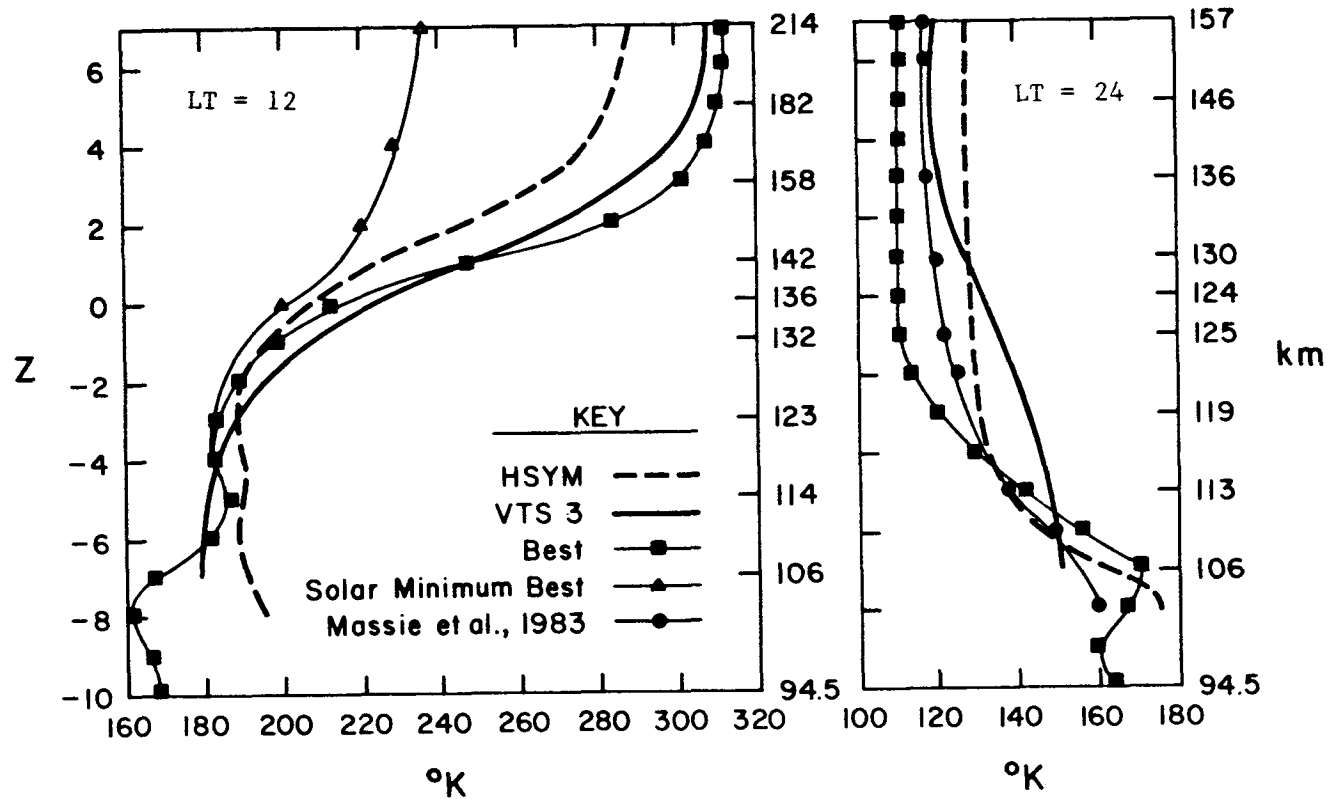
Figure 10. Venus two-dimensional model temperature: BEST EUV case. Comparisons are made with Pioneer Venus model atmospheres (HSYM and VTS3) as well as with the adopted nightside temperature profile of Massie et al. (1983). Solar minimum fluxes of Heroux and Hinteregger (1978) (F10.7 = 80x10^{-22} Wm^{-2} Hz^{-1}) are used to derive a new noon temperature profile. Exospheric temperatures are seen to vary by nearly 70°K from solar minimum to solar maximum conditions.
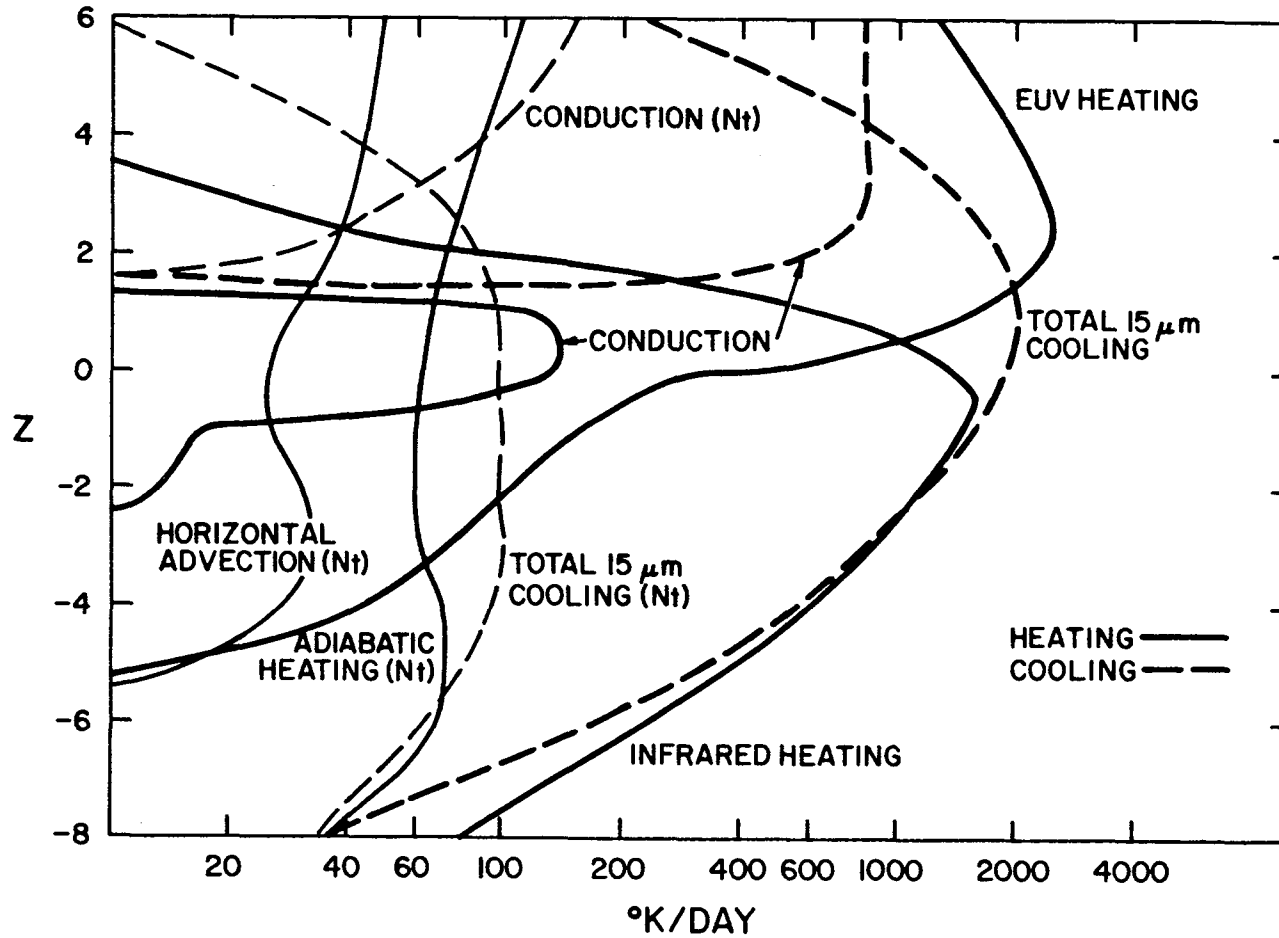
Figure 11. Heating and cooling rates at 60° and 120° SZA: BEST EUV case. Weakened adiabatic heating and horizontal advection on the nightside (plus improved 15 μm cooling) combine to give cooler nightside temperatures than Dickinson and Ridley (1977).

Model and Empirical Data Set Comparisons at 150 km

Averages Over Dayside (LT = 12-16 hr)

	Hedin et al. (1983) H	H/2D	Keating et al. (1984) K	K/2D	H/K	2-D Model 6/84
n_T	1.39(10)	1.01	1.36(10)	0.99	1.02	1.38(10)
n_O	4.70(9)	1.74	3.56(9)	1.32	1.32	2.70(9)
n_{CO}	2.32(9)	1.05	1.80(9)	0.82	1.29	2.20(9)
n_{CO_2}	5.82(9)	0.77	7.13(9)	0.95	0.82	7.52(9)
n_{N_2}	1.01(9)	1.11	1.04(9)	1.15	0.97	9.06(8)
n_{He}	6.39(6)	1.73	4.57(6)	1.24	1.40	3.70(6)
T	271.3	0.97	252.5	0.90	1.07	280

Averages Over Nightside (LT = 19-24 hr)

	Hedin et al. (1983) H	H/2D	Keating et al. (1984) K	K/2D	H/K	2-D Model 6/84
n_T	1.43(9)	1.15	1.39(9)	1.12	1.03	1.24(9)
n_O	1.12(9)	1.14	1.03(9)	1.05	1.09	9.80(8)
n_{CO}	1.10(8)	1.26	1.09(8)	1.25	1.01	8.73(7)
n_{CO_2}	9.70(7)	0.89	9.90(7)	0.91	0.98	1.09(8)
n_{N_2}	7.63(7)	1.17	9.74(7)	1.50	0.78	6.51(7)
n_{He}	1.49(7)	0.14	3.11(7)	0.29	0.48	1.08(8)
T	119.3	0.98	129.8	1.06	0.92	122.1

Figure 12. Model and empirical data set comparisons at 150 km.

TOTAL TEMPERATURE IN DEG. K

HORIZONTAL VELOCITY IN CM/SEC
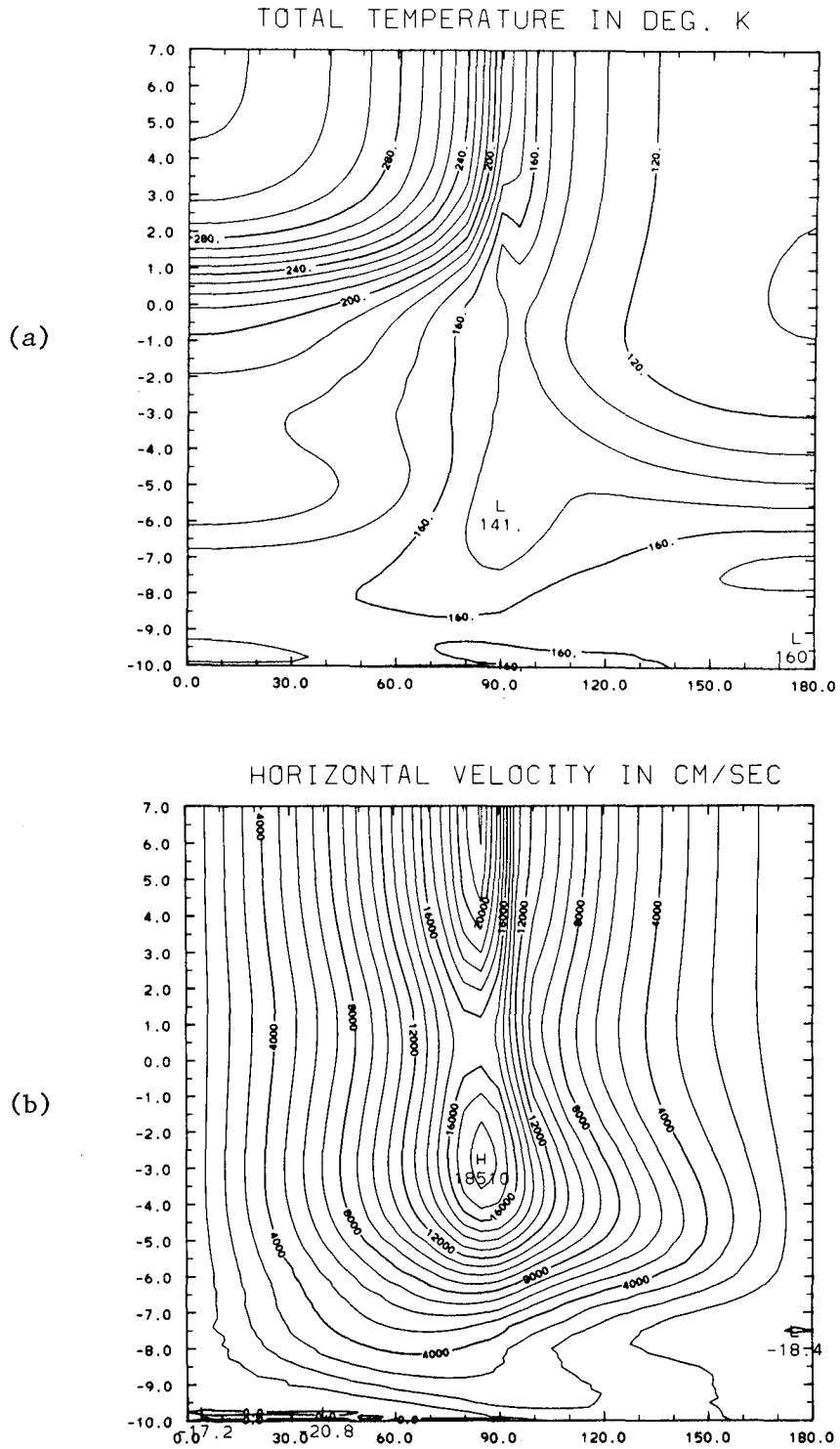
Figure 13. Best EUV case contour plots (SZA vs Z):
(a) Total temperature in deg K.
(b) Horizontal velocity in cm/sec.

14

VERTICAL VELOCITY IN CM/SEC

(c)

FRACTIONAL NUMBER DENSITY FOR O

(d)
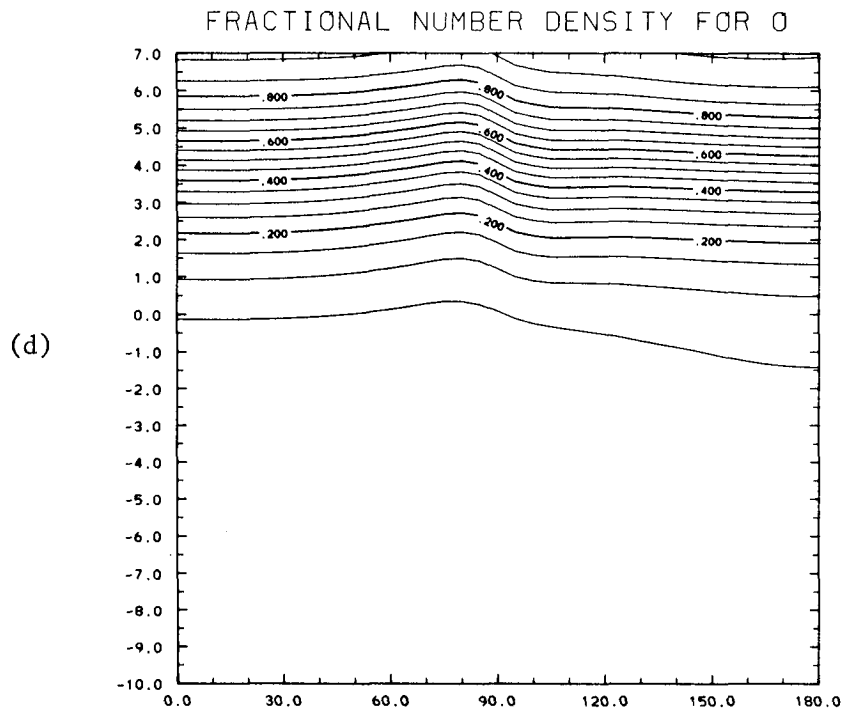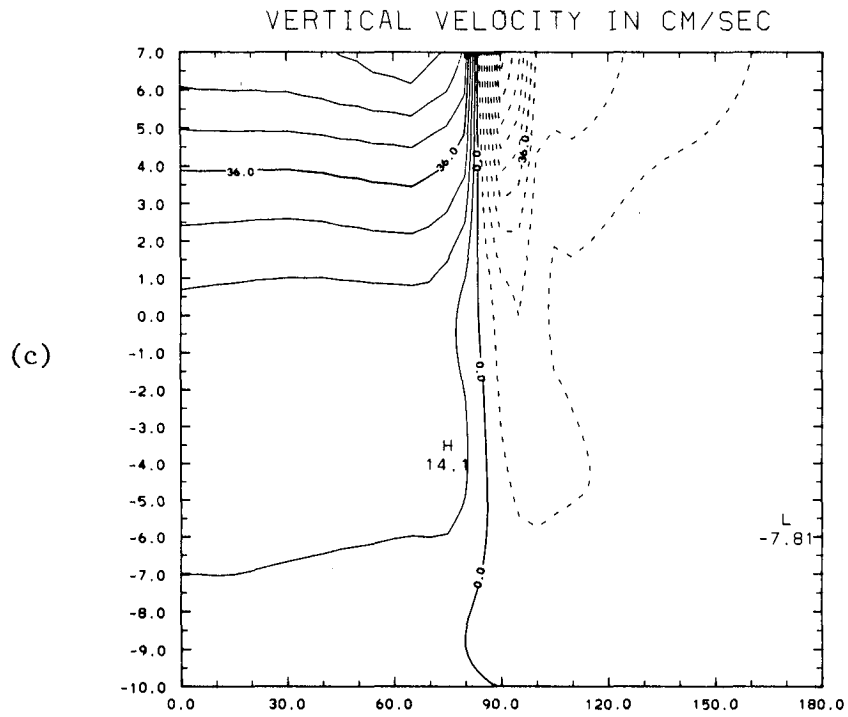
Figure 13 (continued)
(c) Vertical velocity in cm/sec.
(d) Fractional number density for O.

15
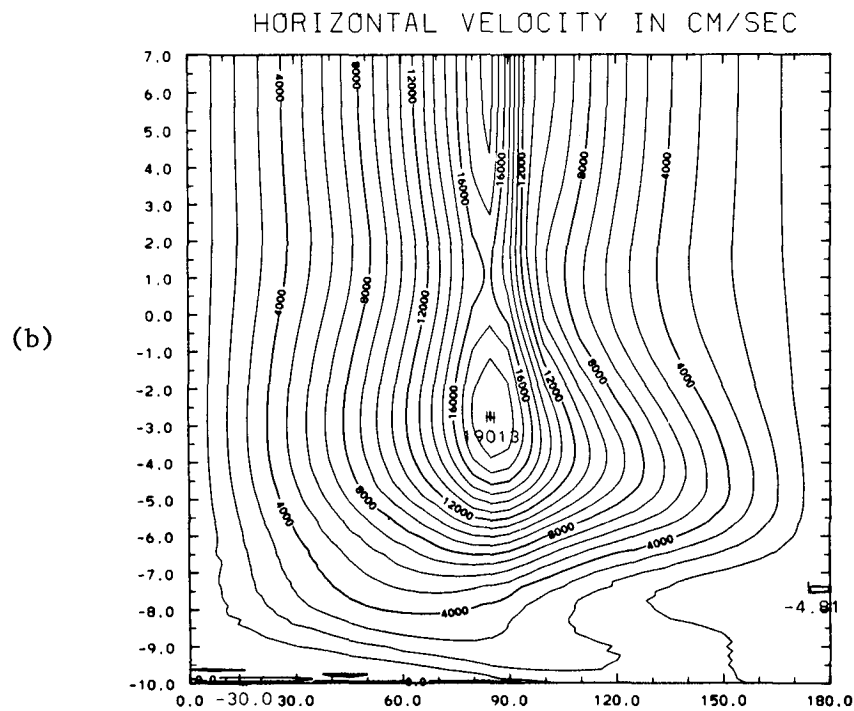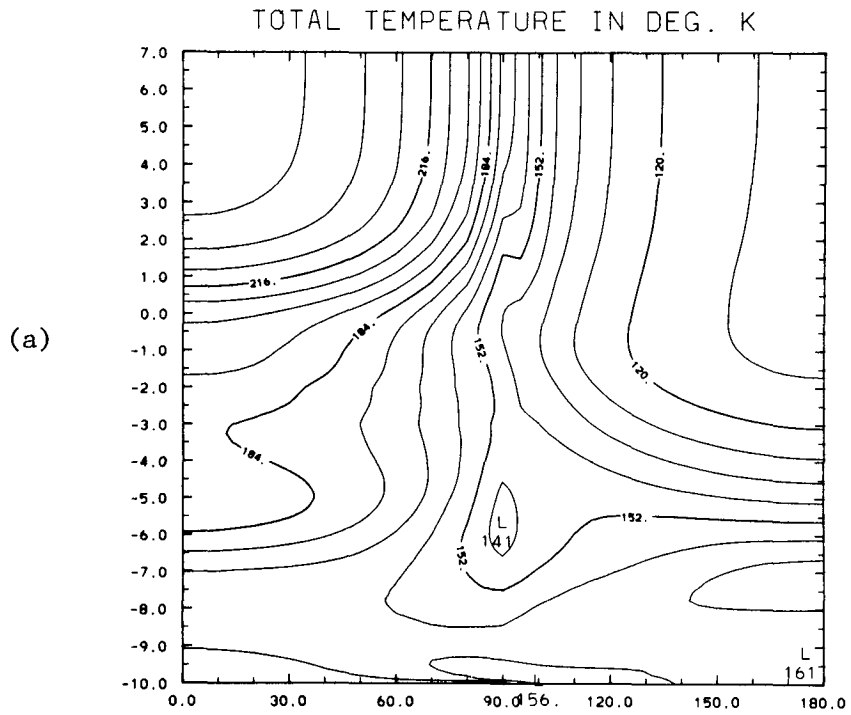
Figure 14. Solar minimum case contour plots (SZA vs Z):
(a) Total temperature in deg K.
(b) Horizontal velocity in cm/sec.
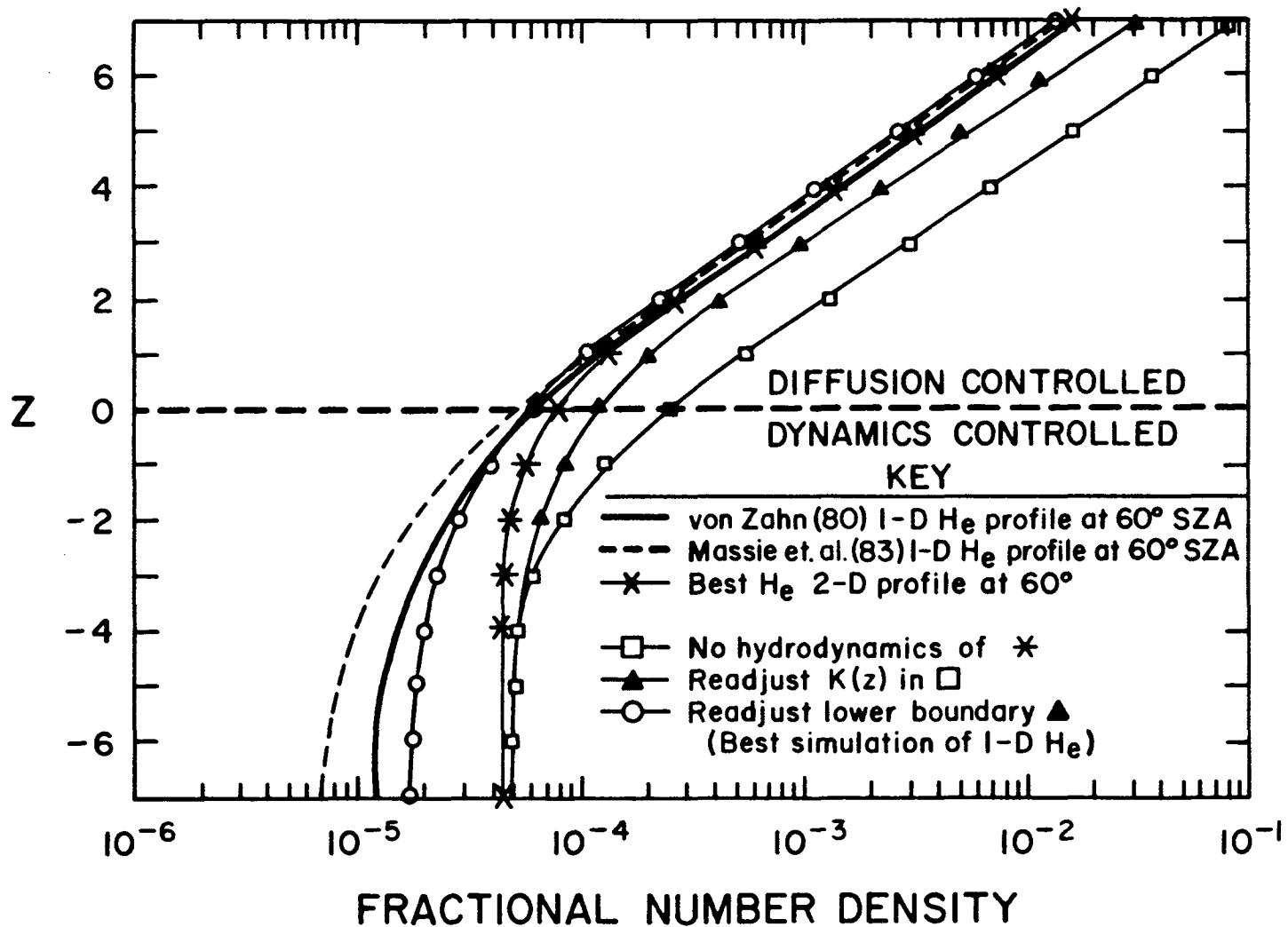
Figure 15. 60° SZA model helium (He) calculations. It is apparent from comparison of the one-dimensional and hydrodynamic model predictions for He at 100 km ($Z \approx -8$) that the self-consistent large-scale dynamics is crucial to a proper calculation of composition. One-dimensional models are insufficient.
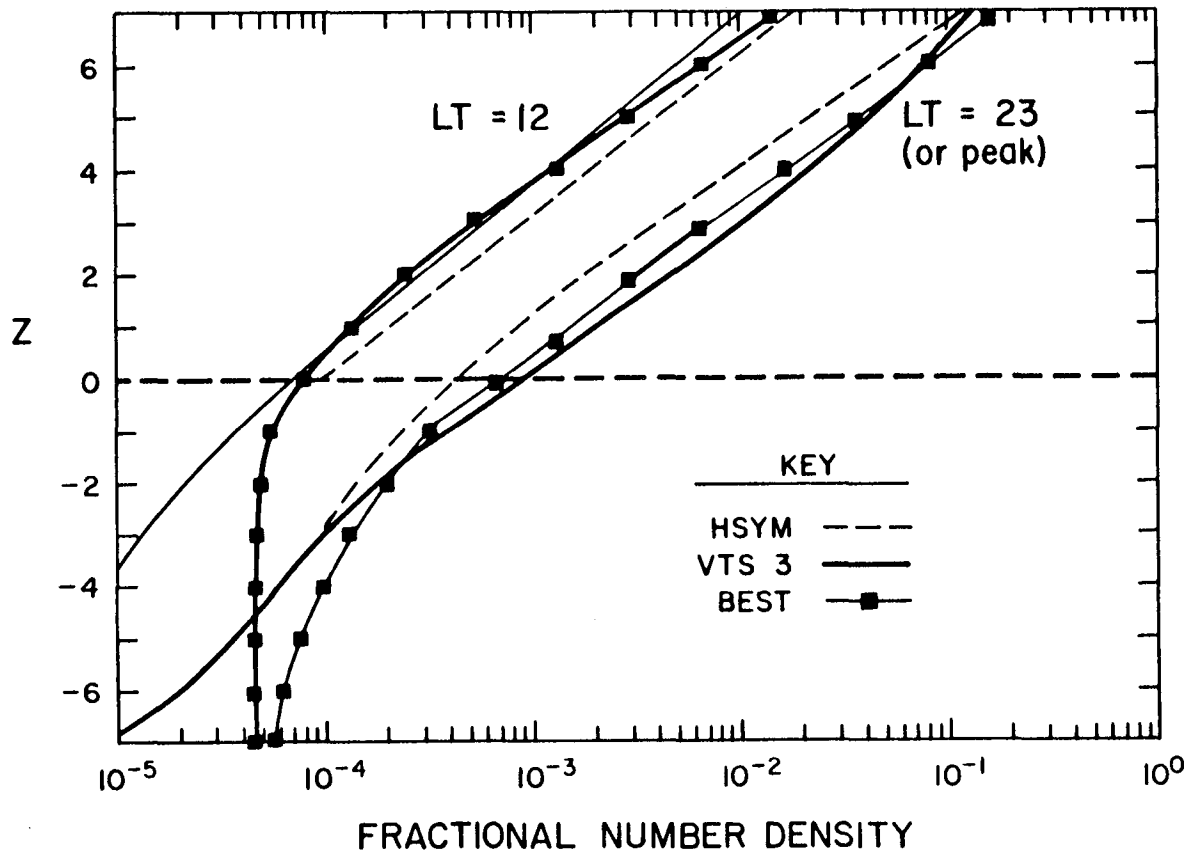
Figure 16. Venus two-dimensional model composition, helium: BEST EUV case. Noon and "nightside peak" profiles of helium are shown. The two-dimensional symmetric model approximately simulates dynamical conditions for the observed 3-4 AM helium peak near LT = 23.

(a)

UTIME=12. 0   T+(U,V)   Z= 5.0

(maximum vector ≡ 206 m/s)

(b)

UTIME=12. 0   T+(U,V)   Z= 0.0

(maximum vector ≡ 169 m/s)

(c)

UTIME=12. 0   T+(U,V)   Z=-4.0

(maximum vector ≡ 140 m/s)
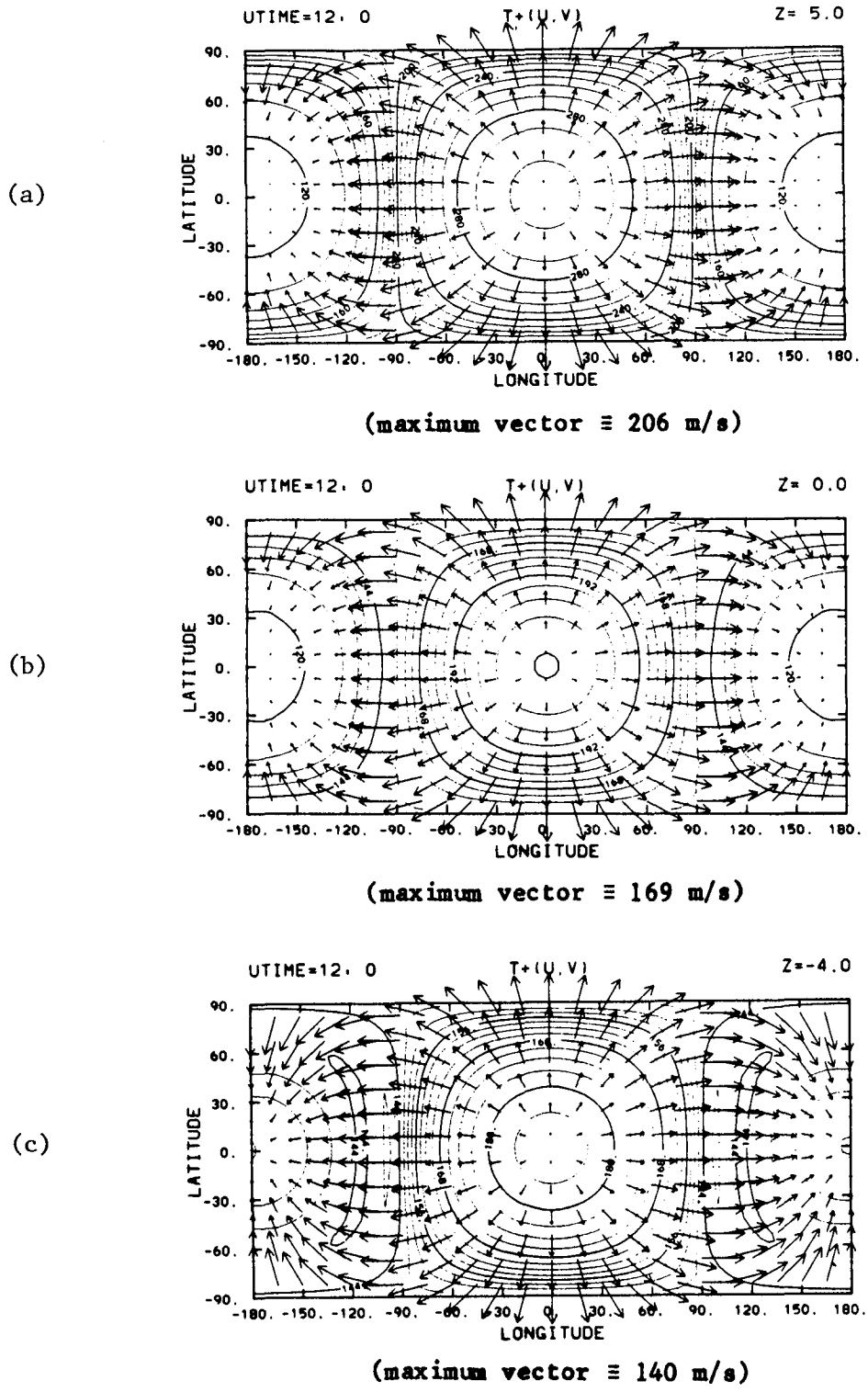
Figure 17. T + (u, v) contours on a pressure level slice for the Venus three-dimensional model adaptation of the terrestrial TGCM (a) Z = 5, (b) Z = 0, (c) Z = -4. Temperature contours are superimposed upon horizontal wind vectors.

19
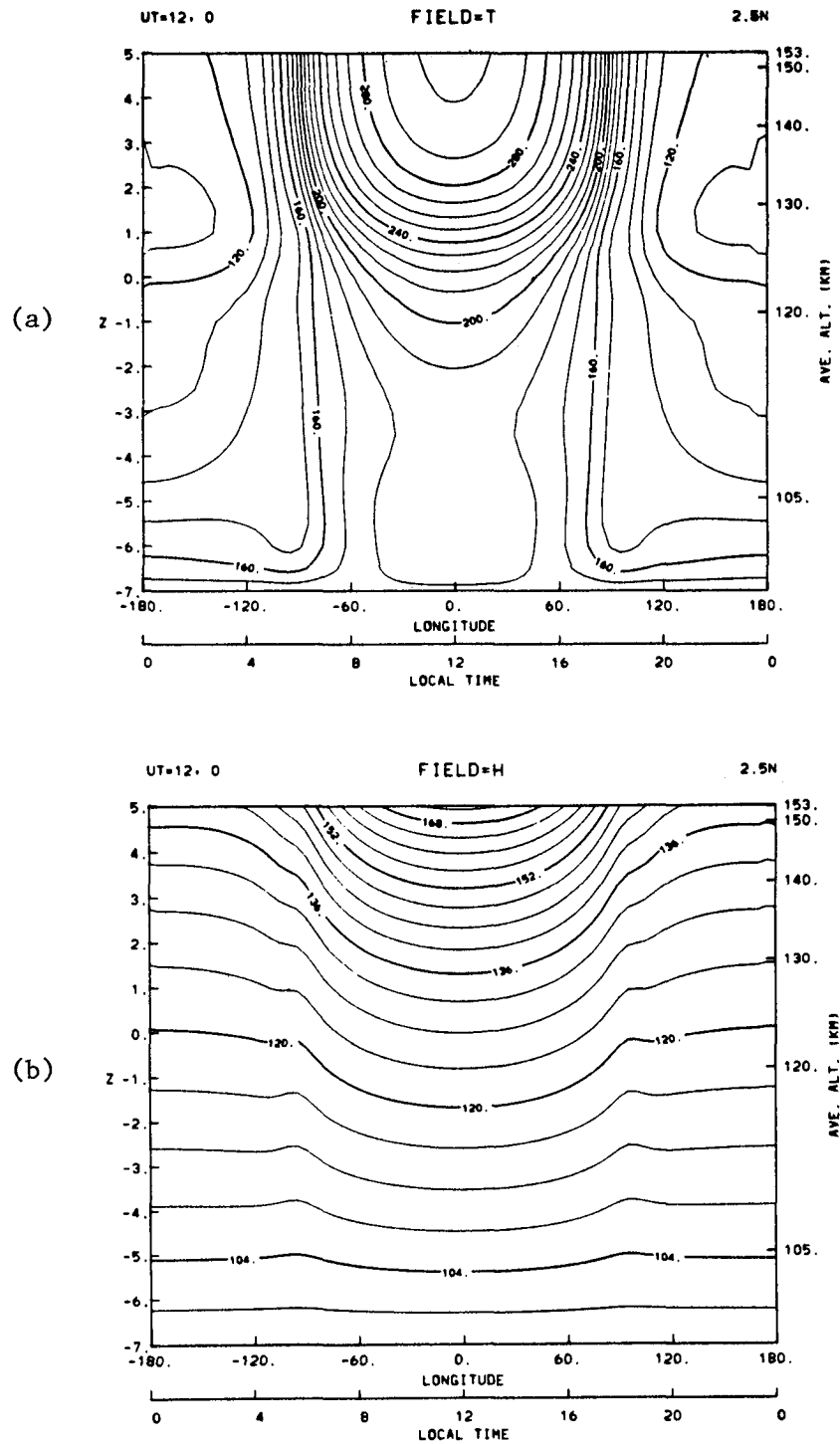
Figure 18. Equatorial slices (SZA vs Z) for the Venus three-dimensional adaptation of the terrestrial TGCM:
(a) T (total temperatures)
(b) h (height field in km)
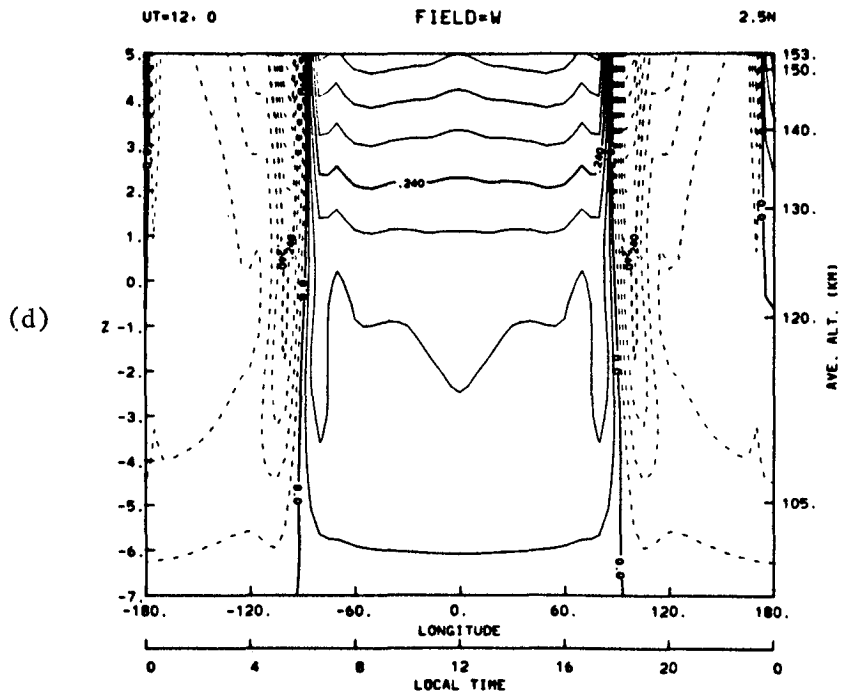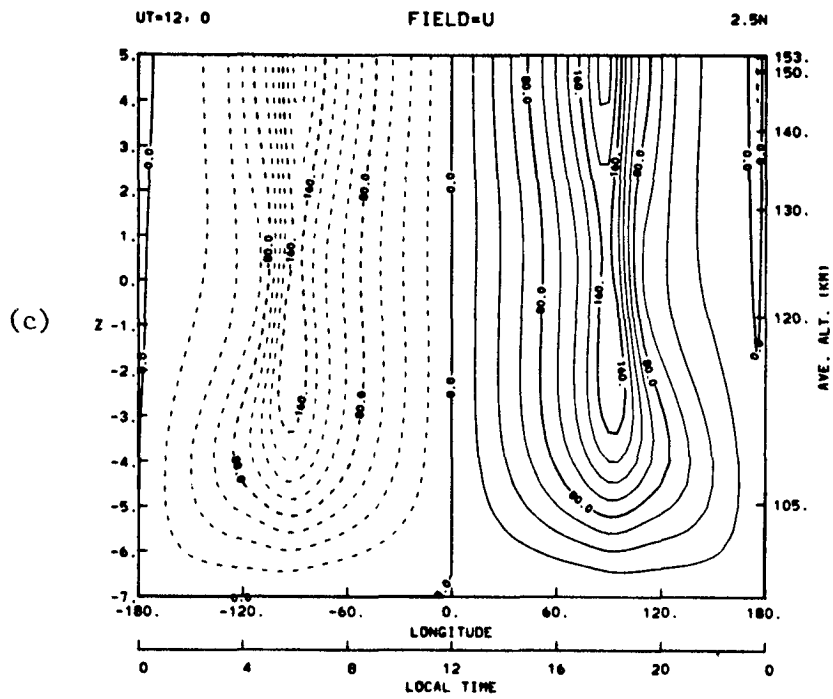
Figure 18 (continued)
(c) u (horizontal winds in m/sec)
(d) w (vertical winds in m/sec)

21

DYNAMICS OF THE NIGHTTIME THERMOSPHERE AT ARECIBO

R. G. Burnside and J. C. G. Walker
Space Physics Research Laboratory
Department of Atmospheric and Oceanic Science
University of Michigan
Ann Arbor, Michigan 48109

C. A. Tepley
Arecibo Observatory
P.O. Box 995
Arecibo, Puerto Rico 00613

Incoherent scatter radar observations of the nighttime F layer at Arecibo, Puerto Rico, are used to determine the O^+ diffusion velocity at different altitudes. Further analysis allows evaluation of the neutral wind and the ion-drag force in the direction of the magnetic meridian. The local acceleration of the meridional neutral wind is also determined. The possibility of evaluating the viscous force using incoherent scatter radar data has also been investigated. Preliminary results indicate that, at certain times and at altitudes above about 350 km, viscous drag may be a significant term in the neutral equation of motion. Combining these results allows height profiles of the meridional pressure gradient to be deduced. The pressure gradient thus derived is compared with that determined from measurements of the horizontal temperature gradient and that given by the MSIS model atmosphere.

Geophysical parameters that may be measured or
derived from incoherent scatter (radar) or
optical (FPI) observations at Arecibo

parameter	symbol	vertical variation	horizontal variation
electron density	N	radar	radar
ion temperature	T_i	radar	radar
electron temperature	T_e	radar	radar
neutral temperature	T_n	MSIS	FPI
meridional ion velocity	v_x	radar	radar†
zonal ion velocity	v_y	radar	–
meridional neutral velocity	u_x	radar†	FPI
zonal neutral velocity	u_y	–	FPI

† The diffusion velocity, which may be derived from the
observed slope of the electron density profile and the
MSIS model atmosphere, is also required to evaluate
these parameters.
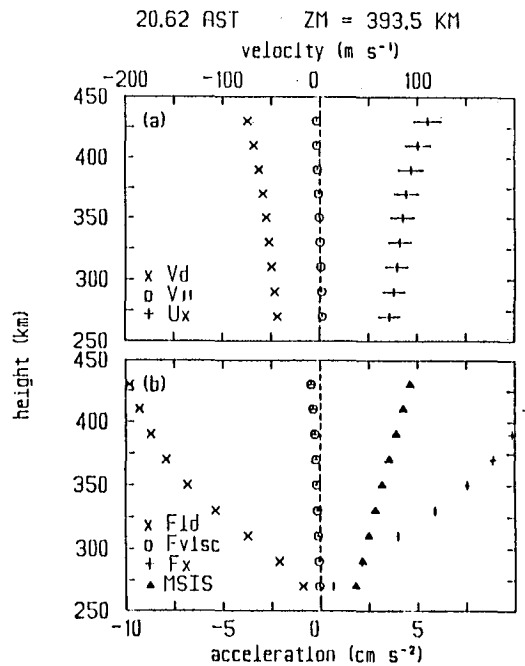
Figure 1. (a) Parallel ion velocity (v_{11}), diffusion velocity
(v_d), and inferred southward neutral wind (u_x) on 17-18
August 1982. (b) Derived ion and viscous drag
accelerations, and the net southward pressure gradient.

Arecibo   Meridional ion and viscous drag

16-17 August 1982.   17-18 August 1982

Arecibo   Meridional ion. and viscous drag at 350 km

7-8 October 1983   9-10 October 1983
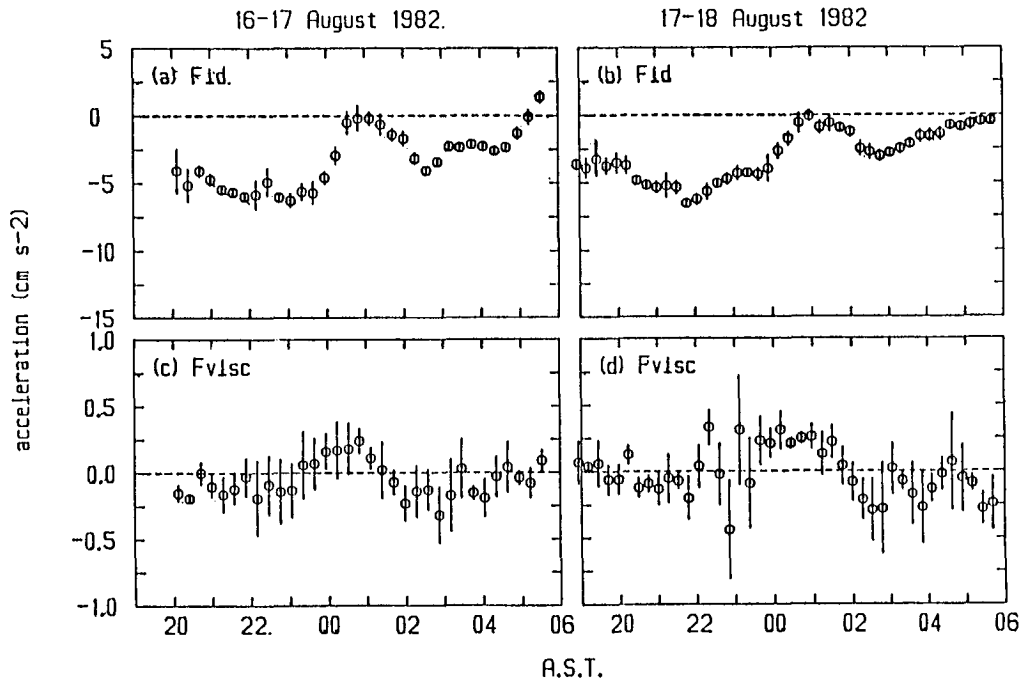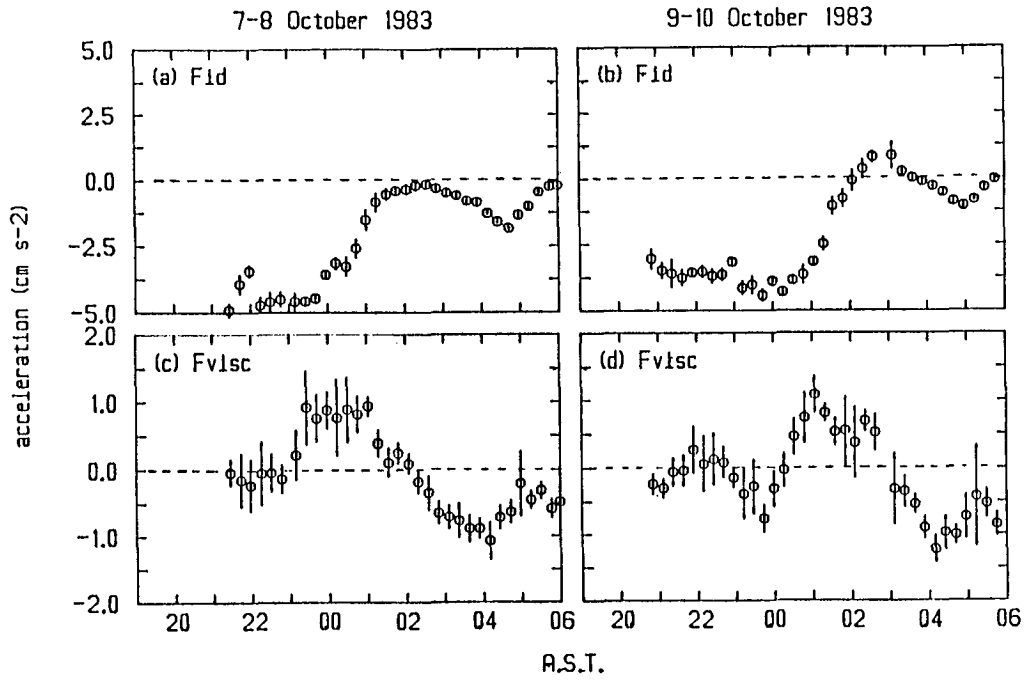
Figures 2 and 3. Examples of meridional ion and viscous drag at 350km above Arecibo.
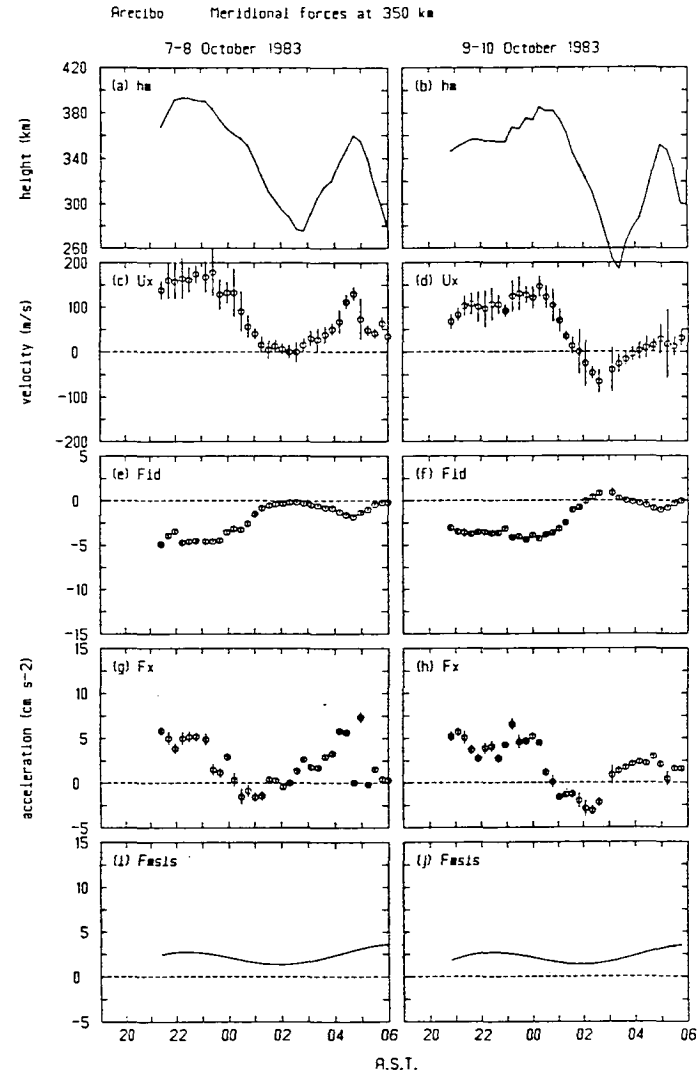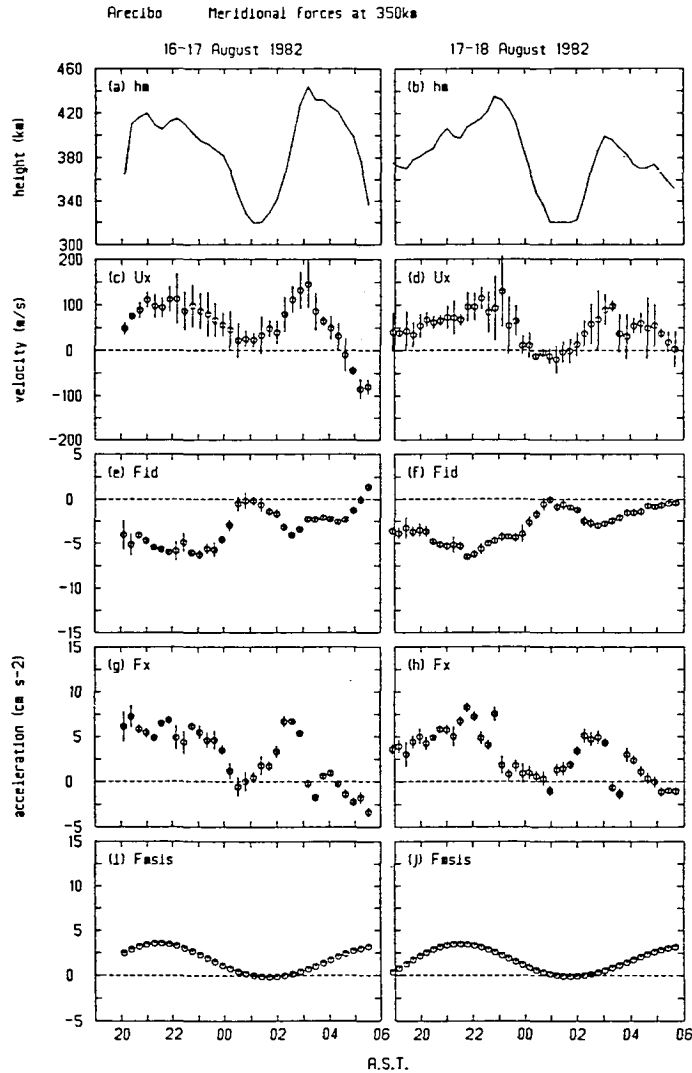
Figures 4 and 5. h_m = height of F layer peak. u_x = southward neutral wind velocity. F_{id} = inferred ion drag. F_{visc} = viscous drag. F_x = inferred net southward pressure gradient. F_{msis} = pressure gradient predicted by MSIS-83 model atmosphere.
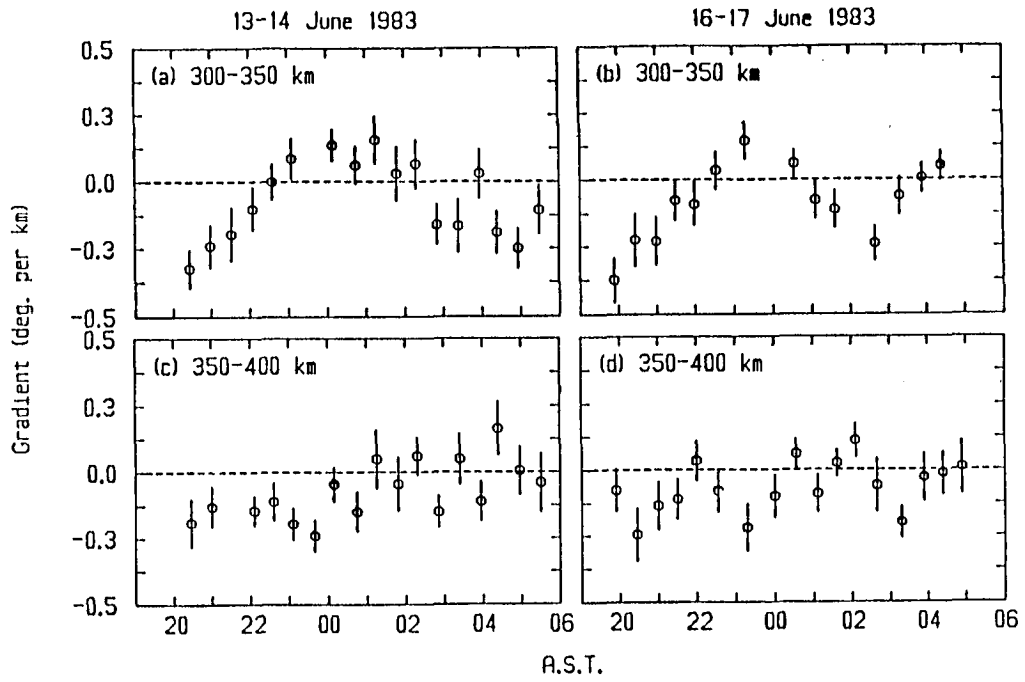
Figure 6. Observed meridional gradients in ion temperature from incoherent
scatter measurements at Arecibo.
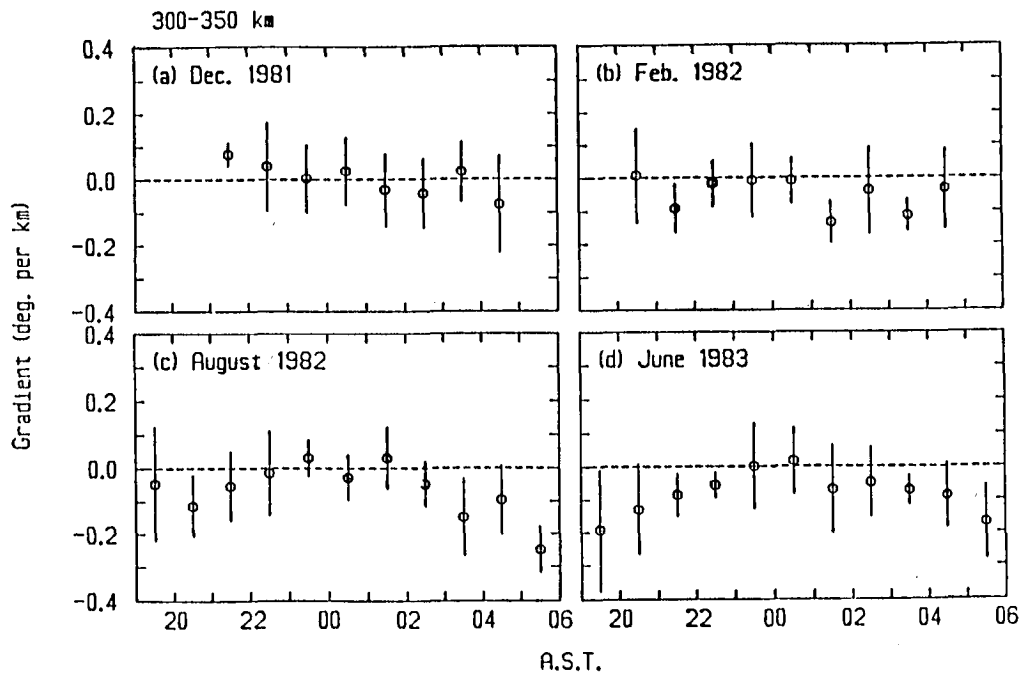
Figure 7. Monthly mean values of meridional ion temperature gradient for four
different seasons.

Temperature and density gradients from MSIS-83
F10.7 (June) = 130   F10.7 (October) = 120   z = 350km
June 1983   October 1983

Meridional temperature and density gradients from MSIS-83   350 km
F10.7 (August) = 155   F10.7 (December) = 180
August 1982   December 1981

(a) Tn   (b) Tn   (a) Tn   (b) Tn

(c) rho   (d) rho   (c) rho   (d) rho

(e) 1/T dT/dx   (f) 1/T dT/dx   (e) 1/T dT/dx   (f) 1/T dT/dx

(g) 1/rho d rho/dx   (h) 1/rho d rho/dx   (g) 1/rho d rho/dx   (h) 1/rho d rho/dx

(i) -Fx   (j) Fx   (i) Fx   (j) Fx

temperature (deg. K)
density (x10**14 cm-3)
gradient (cm-e-2) 1000 km -1
acceleration (cm s-2)
gradient per 1000 km

A.S.T.

Figures 8 and 9. Examples of meridional temperature and density gradients at Arecibo, and the net southward pressure gradient predicted by the MSIS-83 model atmosphere.

MEDIUM AND LARGE-SCALE VARIATIONS OF DYNAMO-INDUCED ELECTRIC FIELDS FROM AE ION DRIFT MEASUREMENTS

W. R. Coley and J. P. McClure
Center for Space Sciences, Physics Program
The University of Texas at Dallas
Richardson, Texas 75083

Current models of the low latitude electric field are largely based on data from incoherent scatter radars. We are extending these observations through the addition of the rather extensive high quality electric field measurements from the Ion Drift Meter (IDM) aboard the Atmosphere Explorer (AE) spacecraft. We present here some preliminary results obtained from the Unified Abstract files of satellite AE-E. This satellite was active from the end of 1975 through June 1981 in various elliptical and circular orbits having an inclination near 20°. The resulting data can be examined for the variation of ion drift with latitude, longitude, season, solar cycle, altitude, and magnetic activity. The results presented here will deal primarily with latitudinal variations of the drift features.

Figure 1 shows data from a single AE-E orbit. Of particular interest is the upward ion drift enhancement at 2:38 UT. This corresponds to 18:30 solar local time (SLT). This enhancement of the upward drift after sunset prior to reversal is a classic pattern that is often seen both by ground-based radar and satellite. However, on many occasions this prereversal enhancement (PRE) is absent. In order to investigate the reasons for these and other variations of the observed drift features it is of course necessary to deal with large quantities of data.

Figures 2a and 2b show the type of data presentation used in this study. Figure 2a is a "mass plot" of vertical drift data from AE-E obtained from the 15-second average values of the Unified Abstract files. All vertical drifts in the file between −20° and 20° dip latitude (DLAT) for the August-September 1978 time period are plotted versus SLT. In all there are some 6987 points. Figure 2b shows the same data averaged into 30-minute bins. The dotted line represents the 24-hr average vertical drift. For comparison, Figure 3 shows some incoherent scatter radar results from Jicamarca for the July-August 1968-1971 time period (Fejer et al., 1979). In both cases we see the same general features: downward flow at night reversing at 0600 SLT, a daytime peak followed by a decline to a prereversal enhancement between 19 and 20 SLT, and a reversal to downward flow at night.

Figures 4a and 4b cover May-July 1979 from −20° to 20° DLAT. The satellite was in a near-circular orbit during this period within altitudes of 450-475 km. There are some 17,000 points plotted on Figure 4a, most falling in a band some 75 m/s wide. The exception is the large spread in velocity in the post-sunset time period.

The next four figures take the data set of Figure 4 and break it up into 10 degree wide bins of dip latitude. Figures 5 through 8 cover the ranges 10° to 20° DLAT, 0° to 10° DLAT, −10° to 0° DLAT, and −20° to 10° DLAT, respectively. The raw data plots indicate generally a much smaller spread in the vertical ion velocity at any given local time. The averaged plots indicate a systematic variation of the average velocity with latitude. The largest average upward velocity is

found in the most northerly latitude bin (summer hemisphere). The most southerly bin (winter hemisphere) has a net downward velocity. Other features also show latitude dependence; the evening prereversal enhancement is strong in the summer hemisphere and weak or nonexistent in the winter hemisphere.

Figures 9 and 10 show a similar pattern for the Nov 77 – Jan 78 time period. Figure 9 shows the 10° to 20° DLAT bin (winter hemisphere). Figure 10 shows the −20° to −10° DLAT bin (summer hemisphere). As before there is a generally upward bias of the drift in the summer hemisphere and a downward bias in the winter hemisphere.

One possible interpretation of this pattern is that the dynamo induced ion velocities are being modified by neutral wind flow, the meridional component of which flows generally from the summer to winter hemisphere under solstice conditions. Dachev and Walker, 1982, calculated the vertical ion drift velocity imposed by dynamo electric fields and the zonal and meridional winds in the 19-22 SLT range (Figure 11). These calculated patterns give good qualitative agreement with the data presented. This model also predicts longitudinal variations in the ion drift. This has not yet been tested for in the AE-E data set. Such tests should provide a useful check on this proposed mechanism. The preliminary results presented here indicate that IDM data from the AE and the more recent Dynamics Explorer B spacecraft should continue to disclose some interesting and previously unobserved dynamical features of the low-latitude F-region.

REFERENCES

Fejer, B. G., D. T. Farley, and C. A. Gonzales, F Region east-west drifts at Jicamarca, J. Geophys. Res., *86,* 215, 1981

Dachev, T. P. and J. C. G. Walker, Seasonal dependence of the distribution of large-scale plasma depletions in the low-latitude F-region, J. Geophys. Res., *87,* 7625, 1982

DAY=78112 ORBIT= E 13406

CROSS
DRIFT
M/S

200
100
0
-100
-200

VERT
DRIFT
M/S

50
30
0
-30
-60

LOG
ION
CONC

6
5
4
3

UT (HR:MIN)   2:30   2:35   2:40   2:45   2:50   2:55   3:0
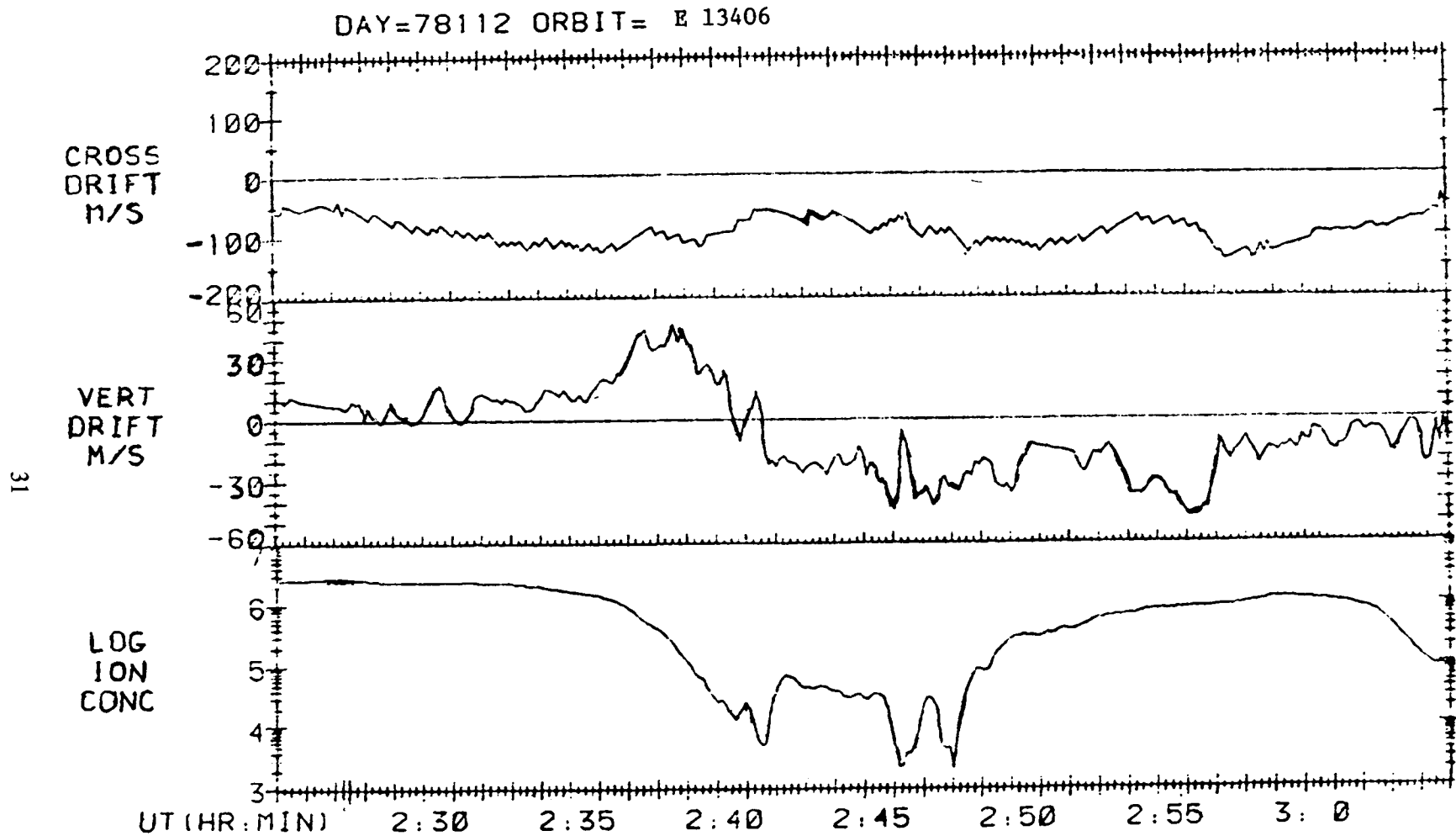
Figure 1. Data from AE-E orbit 13406 showing the sunset behavior of N_i and V_v at low dip latitudes at 315 km altitude in the Atlantic longitude sector on 22 April 1978. The post-sunset enhancement and reversal of V_y is clearly visible in this example of our routinely processed data.

32

VERTICAL ION VELOCITY (M/S)

SOLAR LOCAL TIME

UTD SPACE SCIENCES
W.R. COLEY

Figure 2a. Aug - Sept 1978
−20° to 20° DLAT

AE-E

78213 - 78273

ALT RANGE 200.   500.
LAT RANGE -90.   90.
LONG RANGE -180.   180.
ILAT RANGE   0.   90.
DLAT RANGE -20.   20.
VEL RANGE -125.   125.
MINIMUM NI   3000.

RUN NUMBER   813

33

VERTICAL
ION
VELOCITY
(M/S)

SOLAR LOCAL TIME

UTD SPACE SCIENCES
W.R. COLEY

Figure 2b.   Aug - Sept 1978 $-20°$ to $20°$ DLAT

Figure 3

Figure 4a.   May - July 1979   − 20° to 20° DLAT
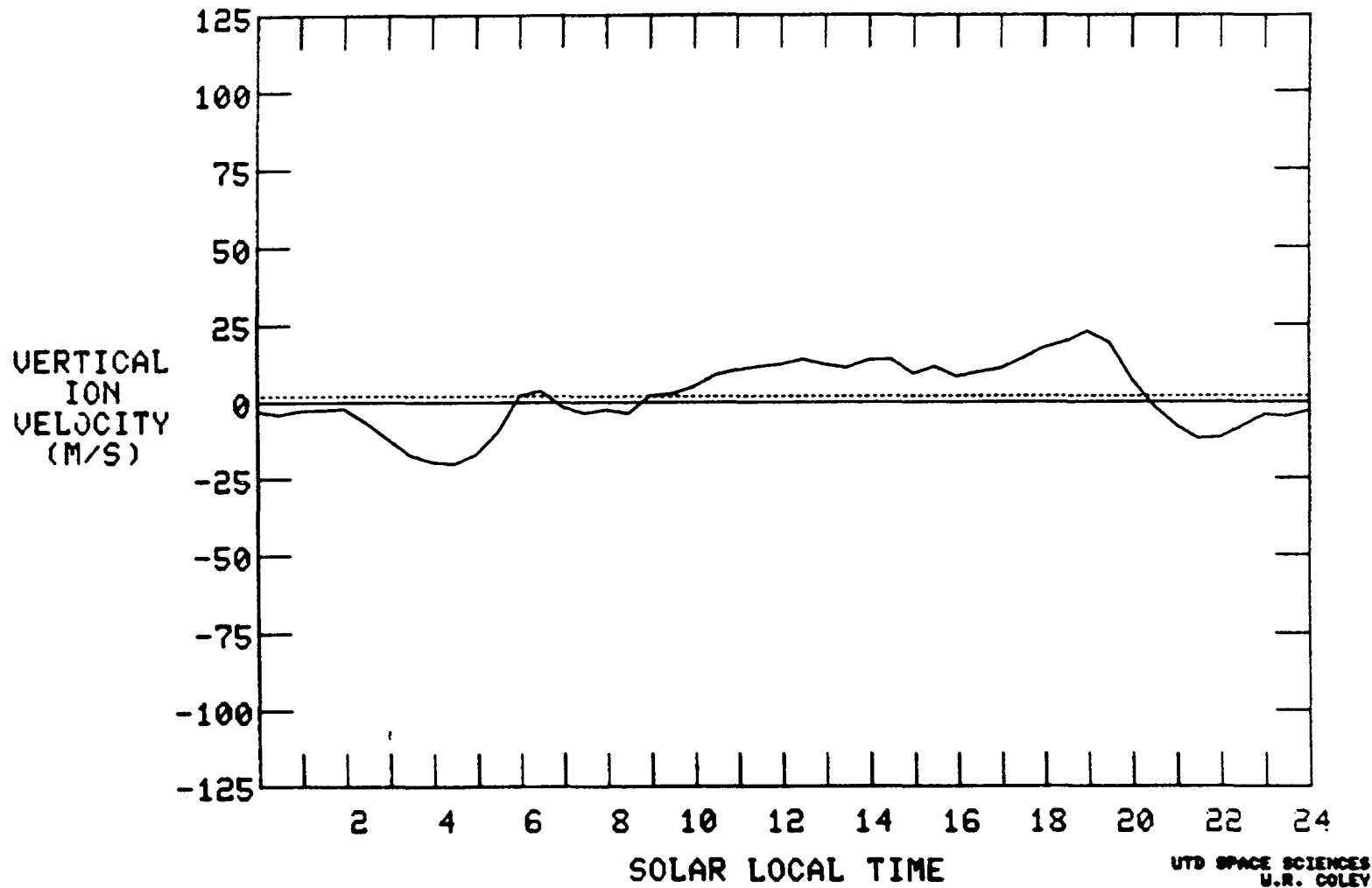
Figure 4b.   May - July 1979   − 20° to 20° DLAT

Figure 5a.   May - July 1979   10° to 20° DLAT

Figure 5b.   May - June 1979   10° to 20° DLAT

AE-E

79181 - 79212

ALT RANGE   200.   500.
LAT RANGE   -90.   90.
LONG RANGE -180.   180.
ILAT RANGE   0.   90.
DLAT RANGE   0.   10.
VEL RANGE -100.   100.
MINIMUM NI   3000.

RUN NUMBER   135

39

VERTICAL
ION
VELOCITY
(M/S)

SOLAR LOCAL TIME

UTD SPACE SCIENCES
U.R. COLEY
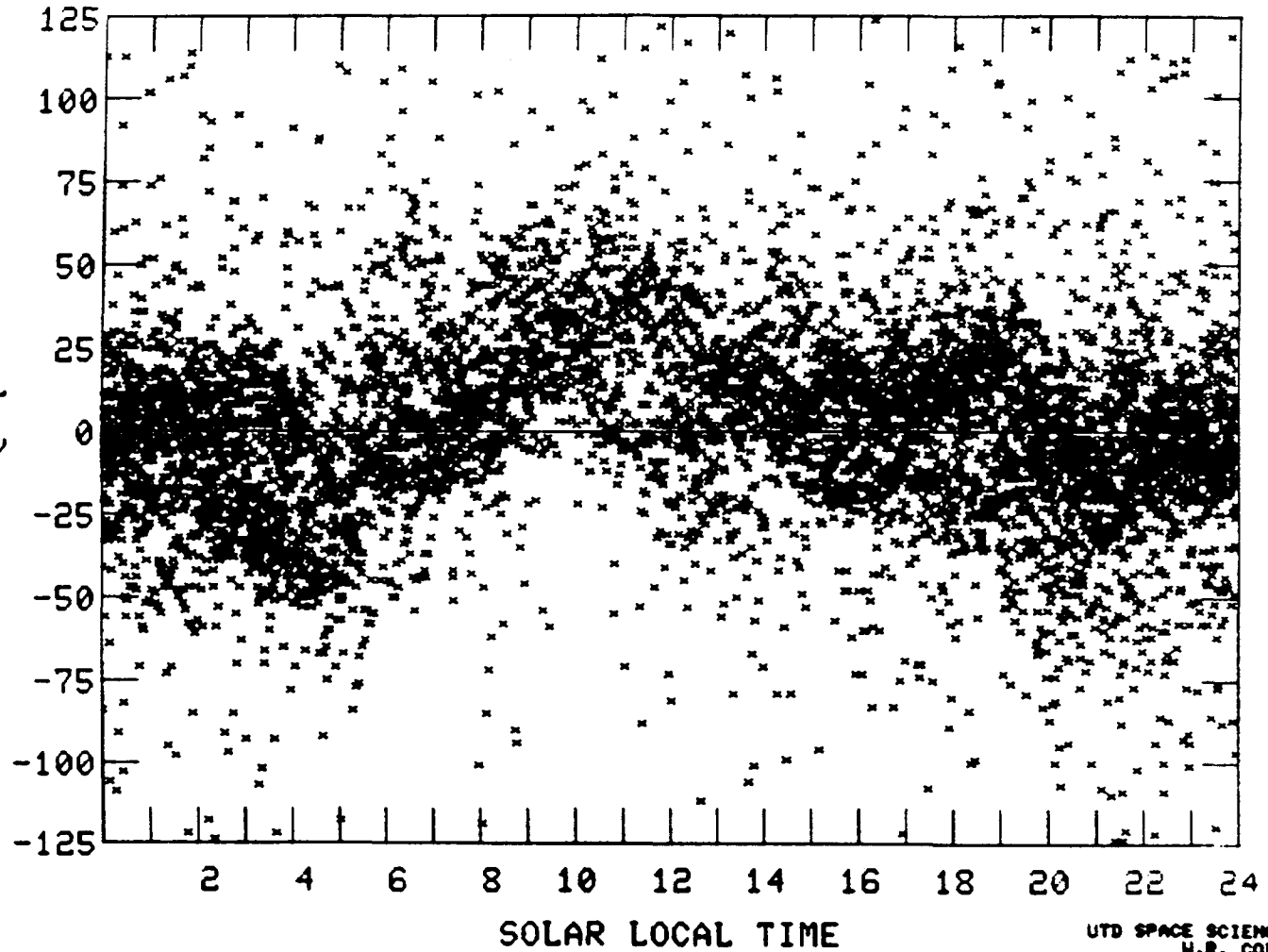
Figure 6a.   May - July 1979   0° to 10° DLAT

AE-E

79121 - 79212

ALT RANGE 200. 500.
LAT RANGE -90. 90.
LONG RANGE -180. 180.
ILAT RANGE 0. 90.
DLAT RANGE 0. 10.
VEL RANGE -100. 100.
MINIMUM NI 3000.

RUN NUMBER 135

VERTICAL
ION
VELOCITY
(M/S)

SOLAR LOCAL TIME

UTD SPACE SCIENCES
W.R. COLEY

Figure 6b. May - July 1979   0° to 10° DLAT
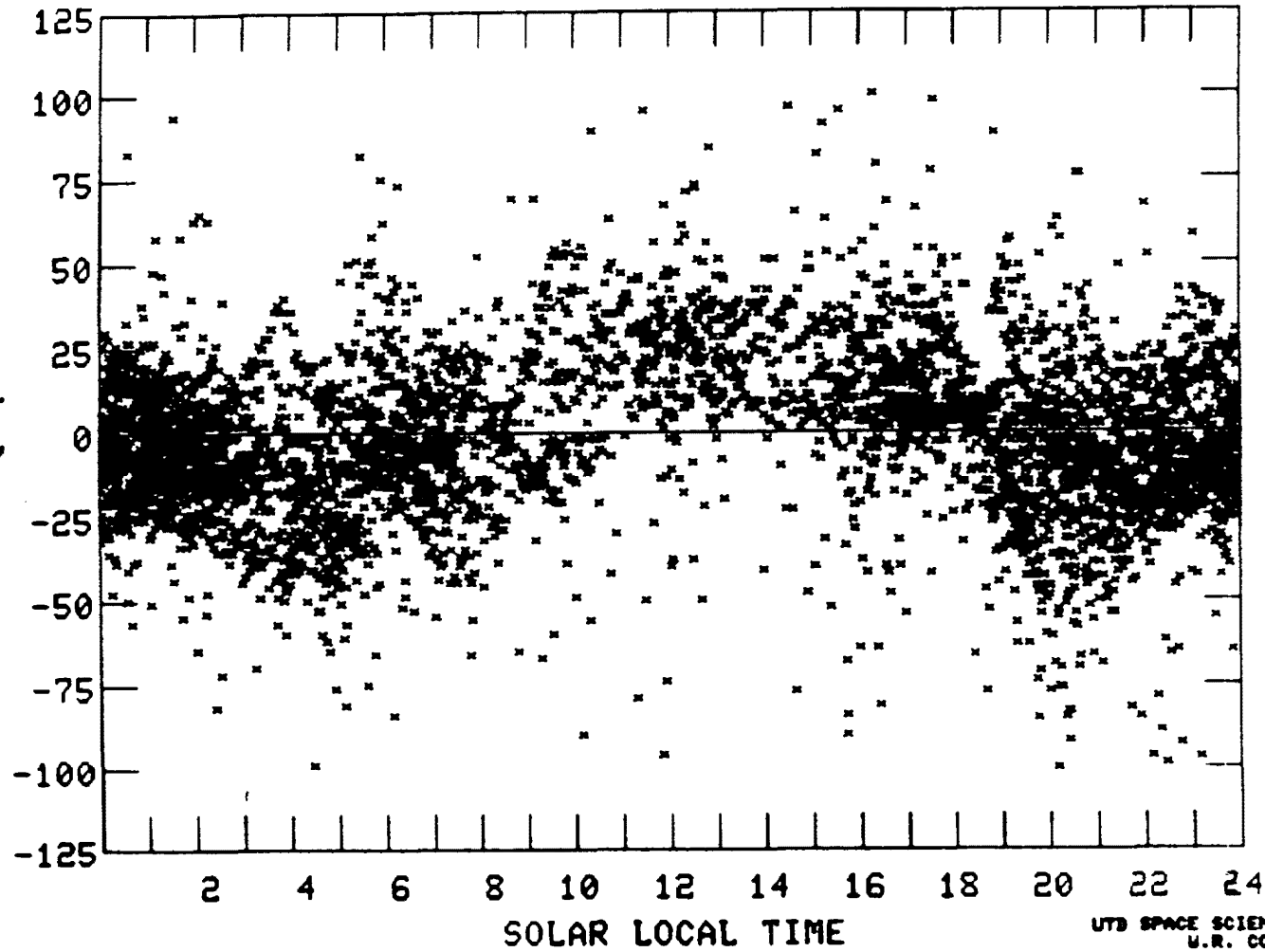
Figure 7a. May - July 1979 −10° to 0° DLAT
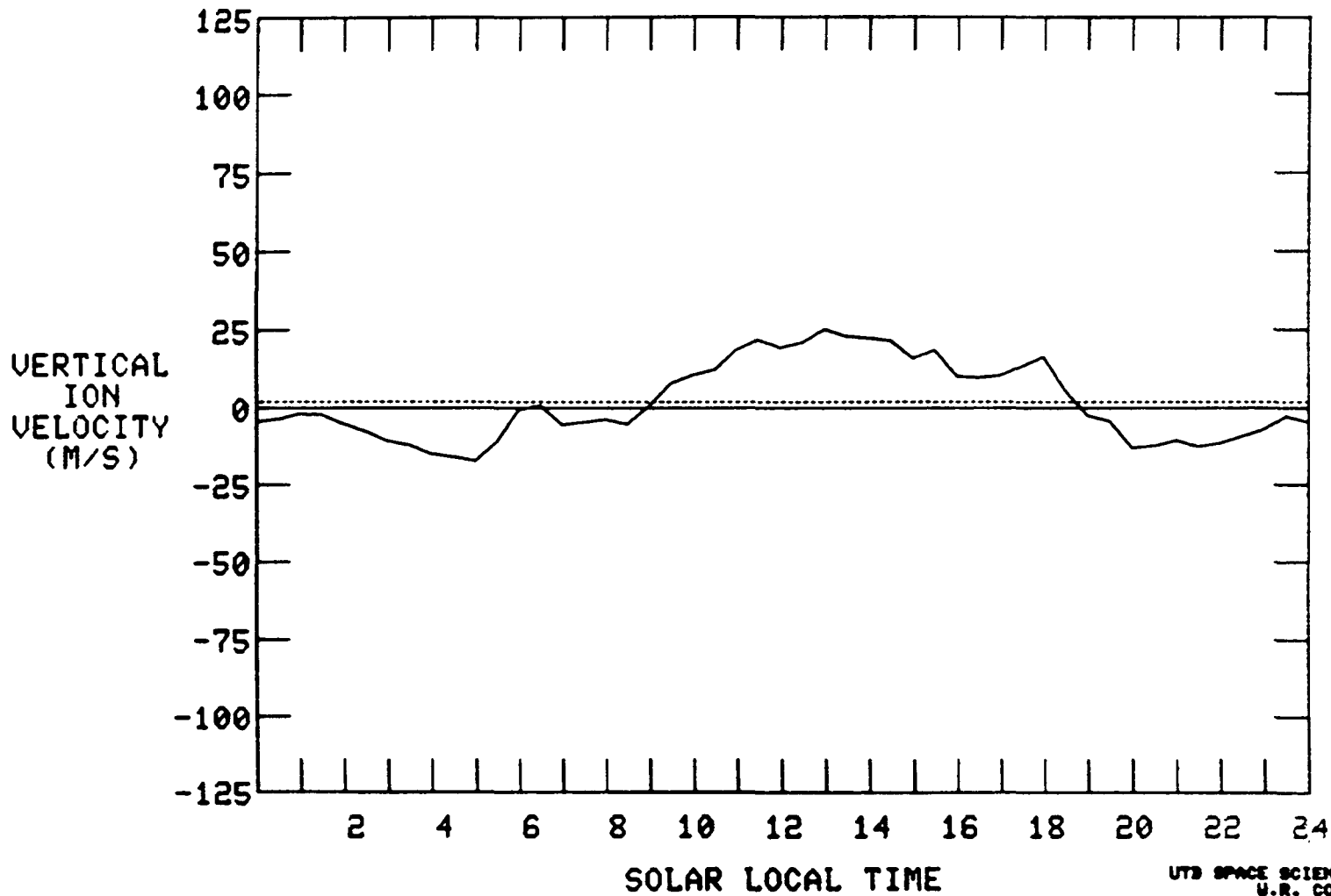
Figure 7b. May - July 1979 $-10°$ to $0°$ DLAT

Figure 8a. May - July 1979   − 20° to 10° DLAT
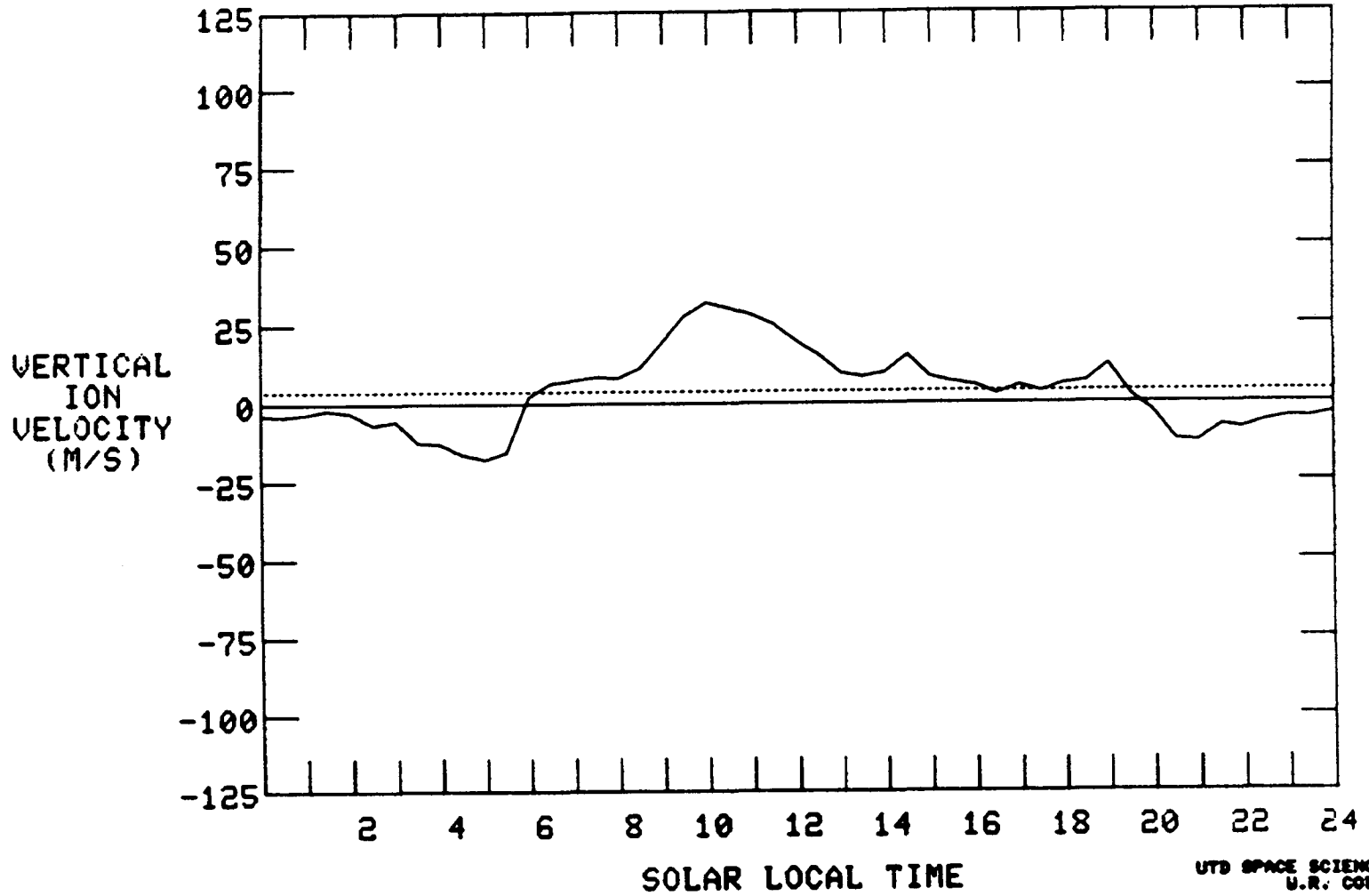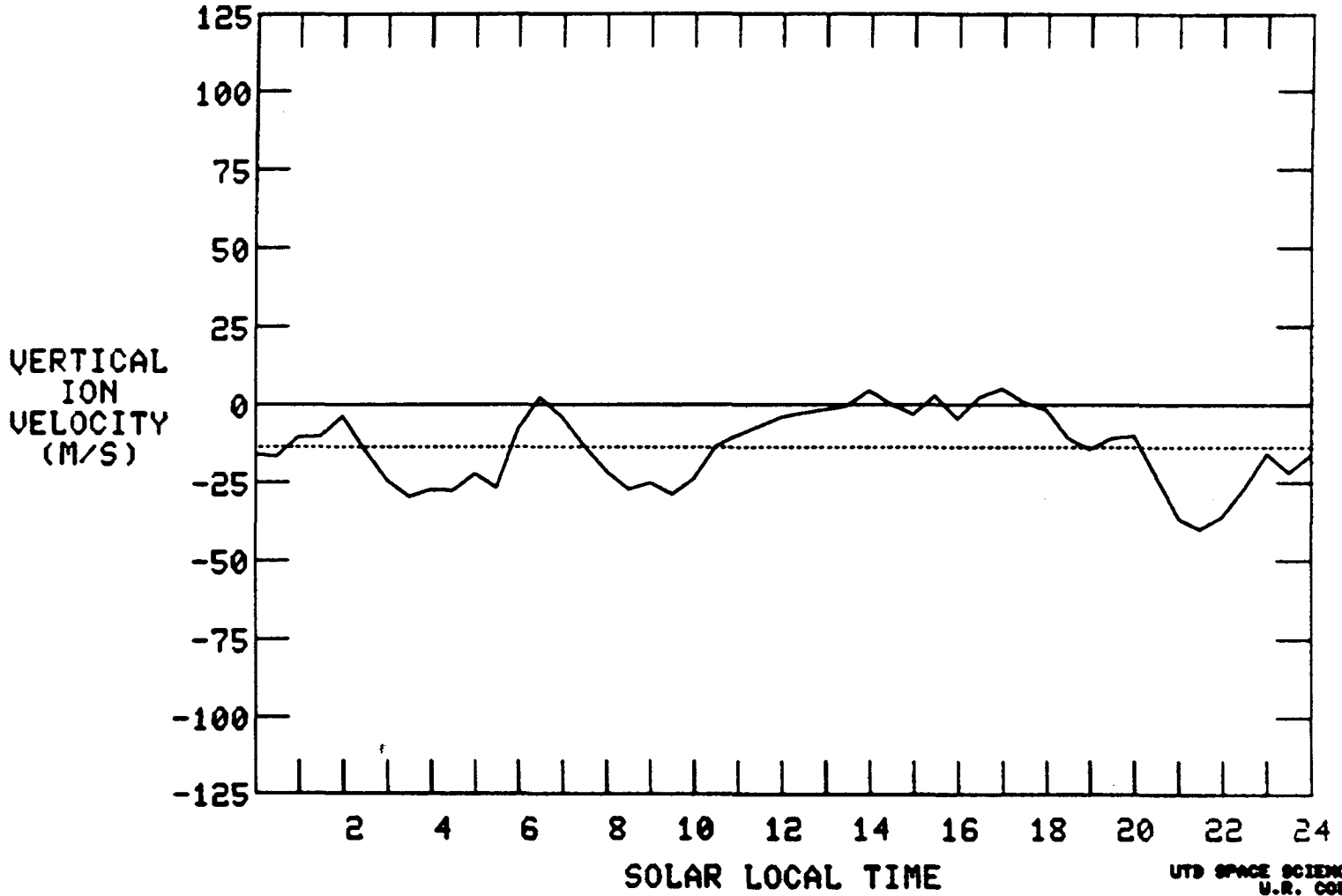
Figure 8b.   May - July 1979 $-20°$ to $-10°$ DLAT

AE-E

77305 - 78031

ALT RANGE 200.   500.
LAT RANGE -90.   90.
LONG RANGE -180. 180.
ILAT RANGE   0.   90.
DLAT RANGE   10.   20.
VEL RANGE -100. 100.
MINIMUM NI   3000.

RUN NUMBER   186

VERTICAL ION VELOCITY (M/S)

SOLAR LOCAL TIME
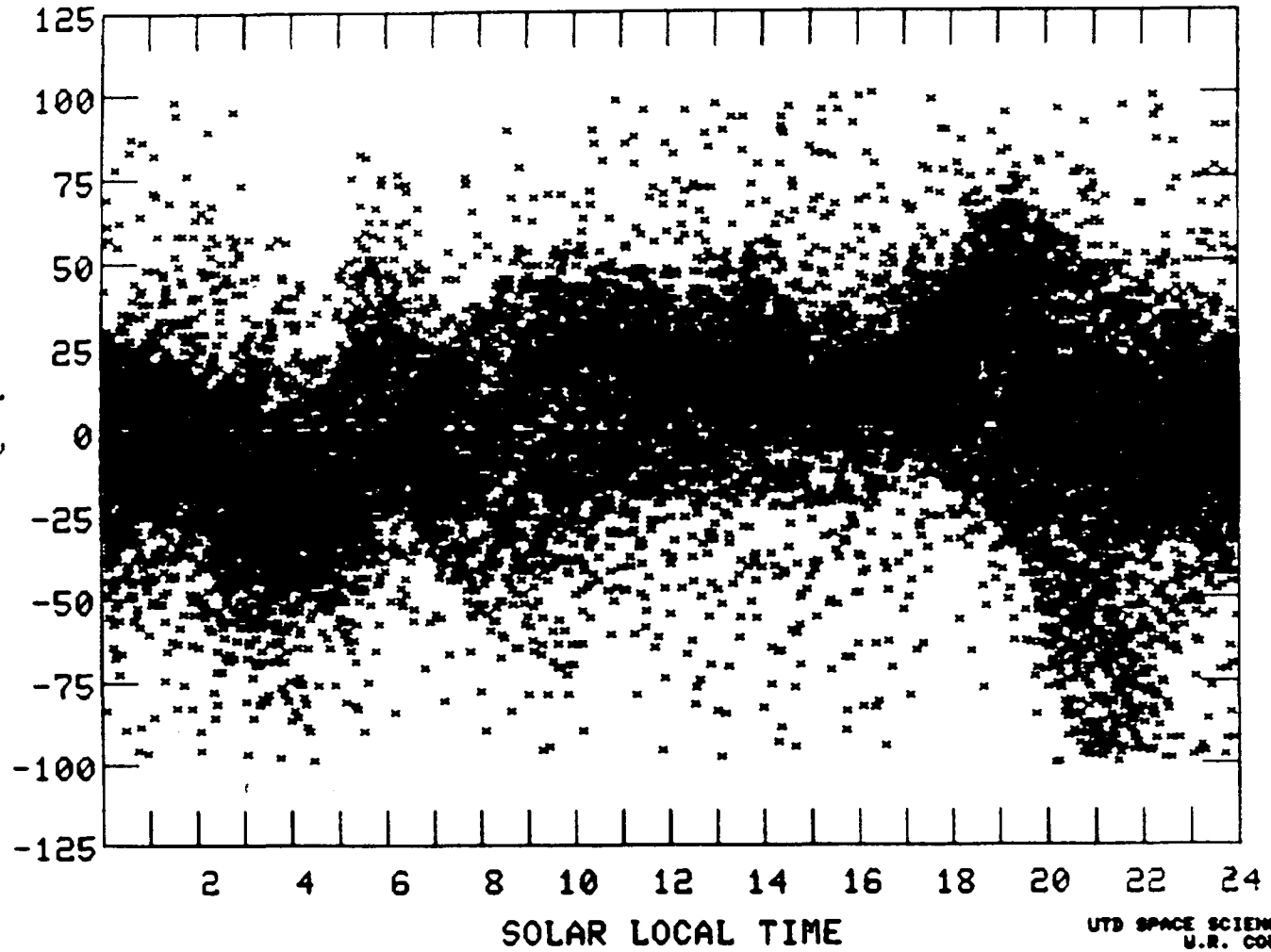
UTD SPACE SCIENCES
W.R. COLEY
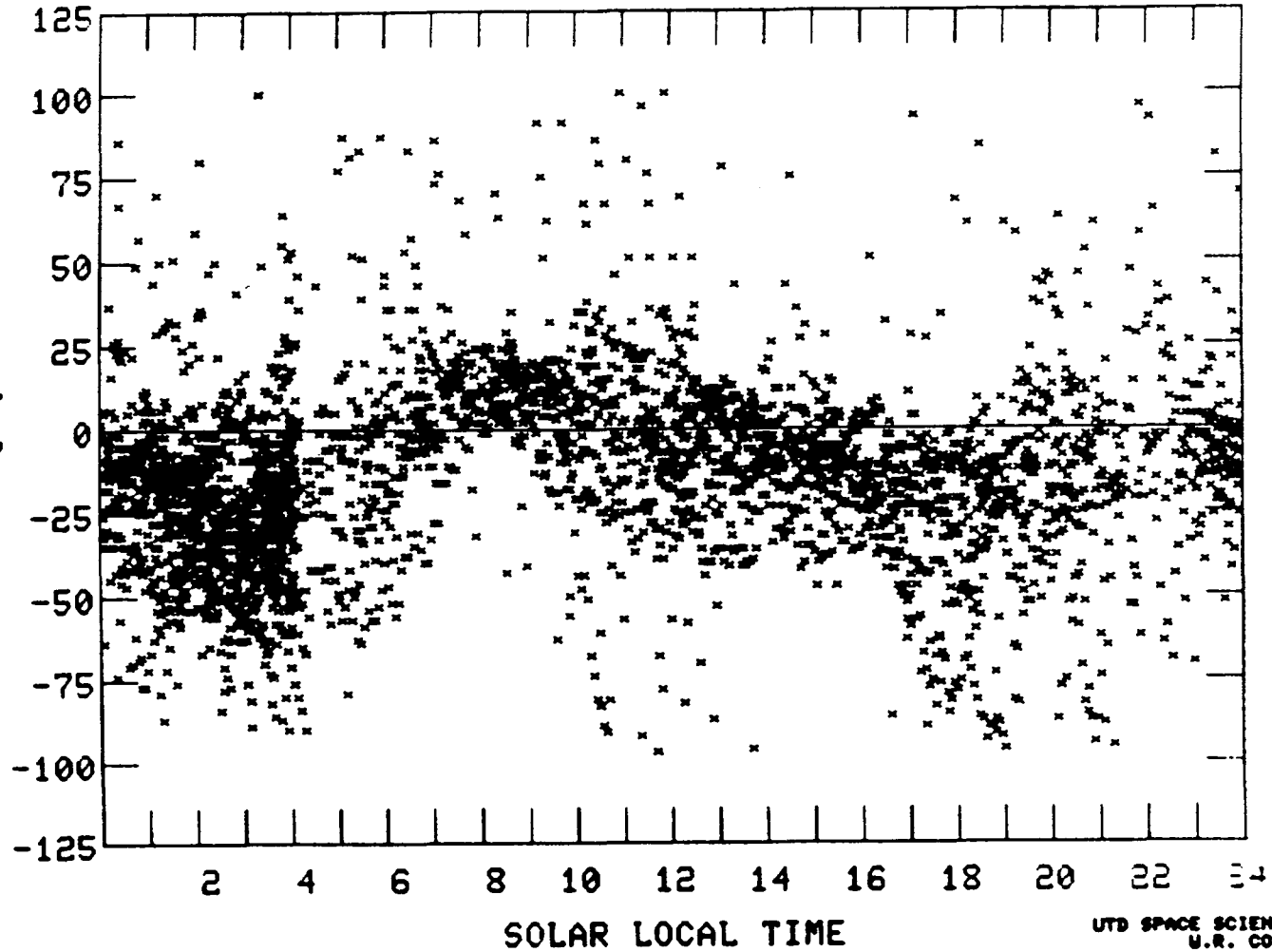
Figure 9a. Nov 1977 - Jan 1978
10° to 20° DLAT

45
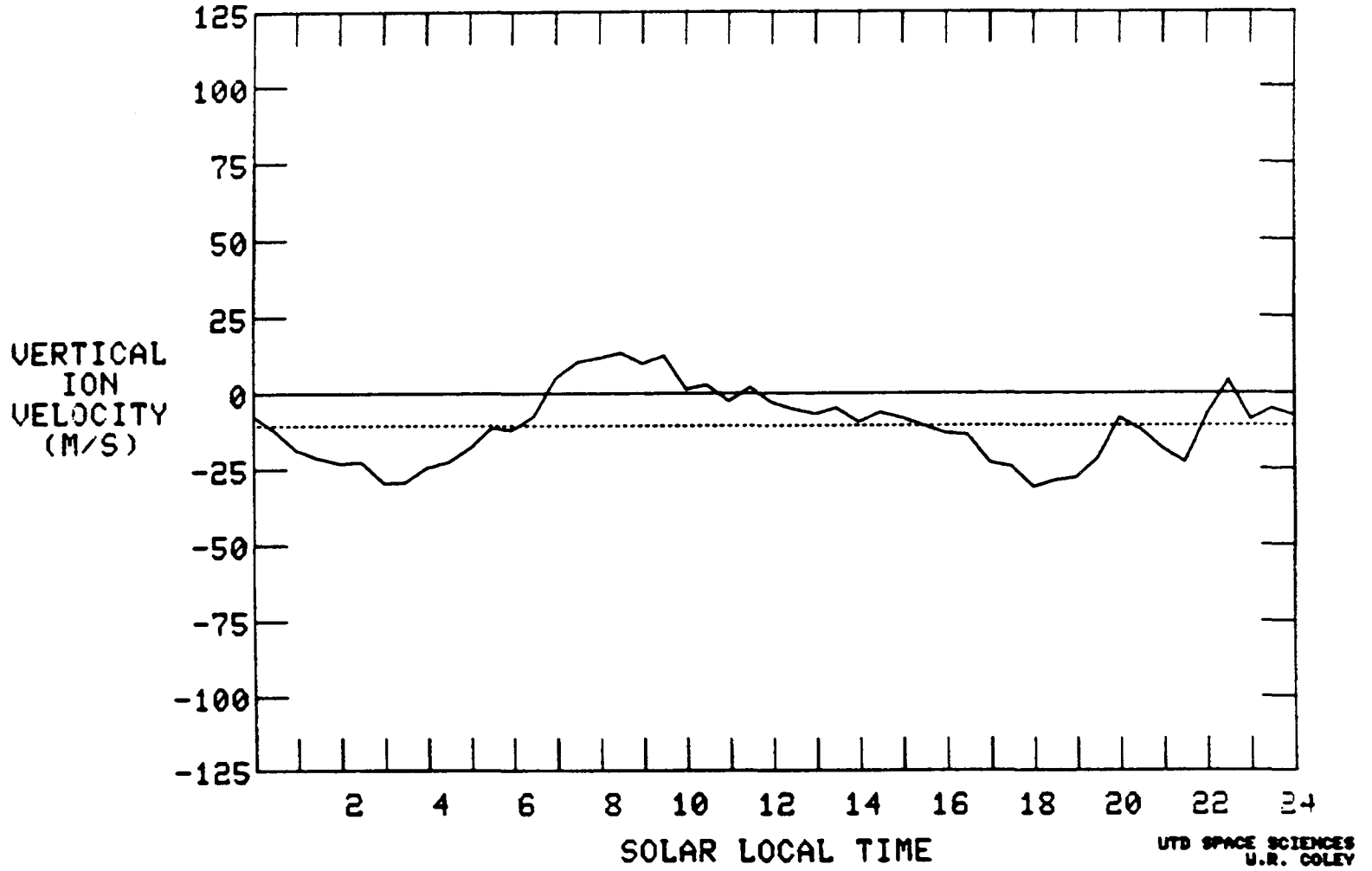
Figure 9b. Nov 1977 - Jan 1978   10° to 20° DLAT
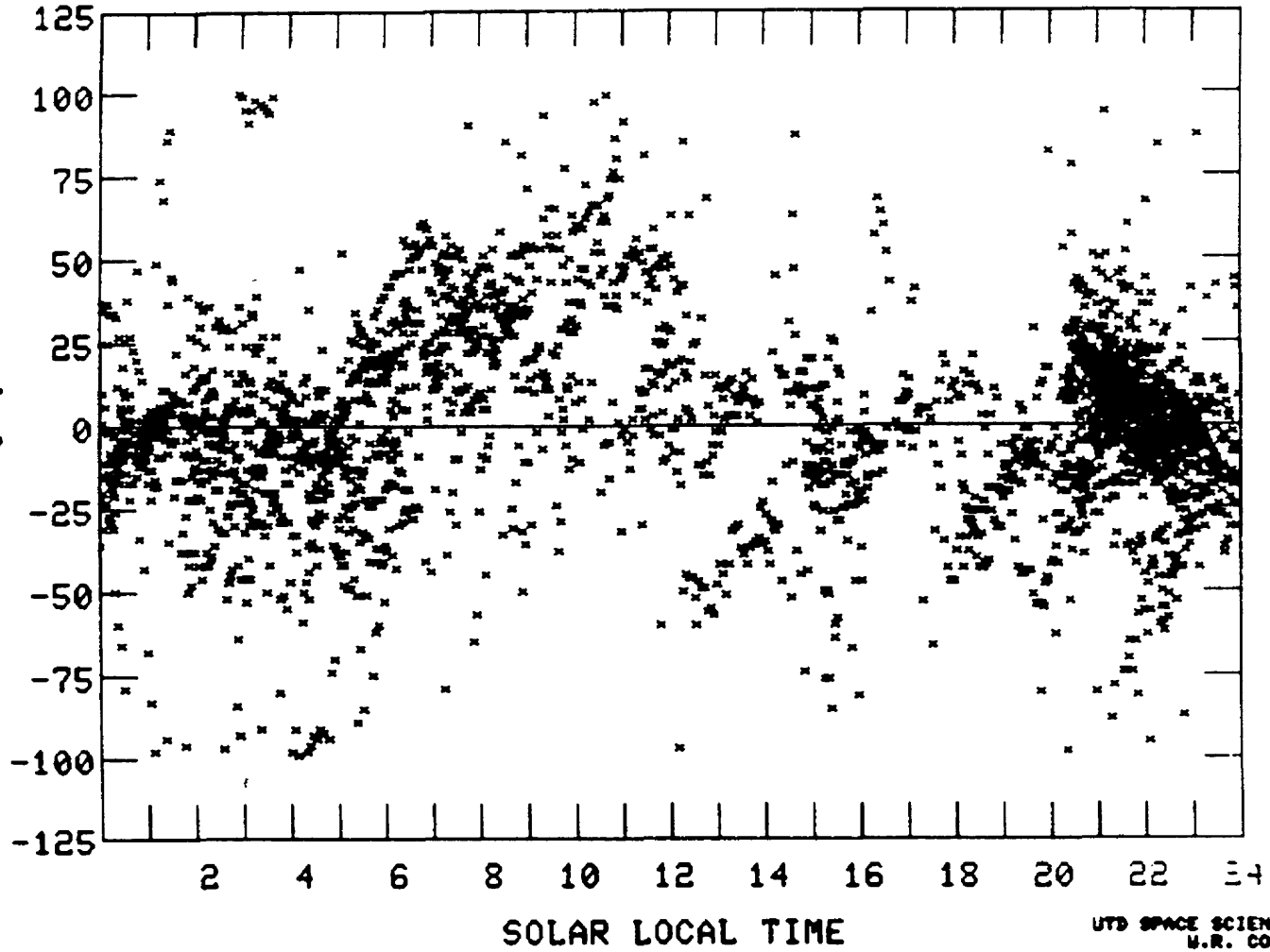
Figure 10a. Nov 1977 - Jan 1978
−20° to −10° DLAT
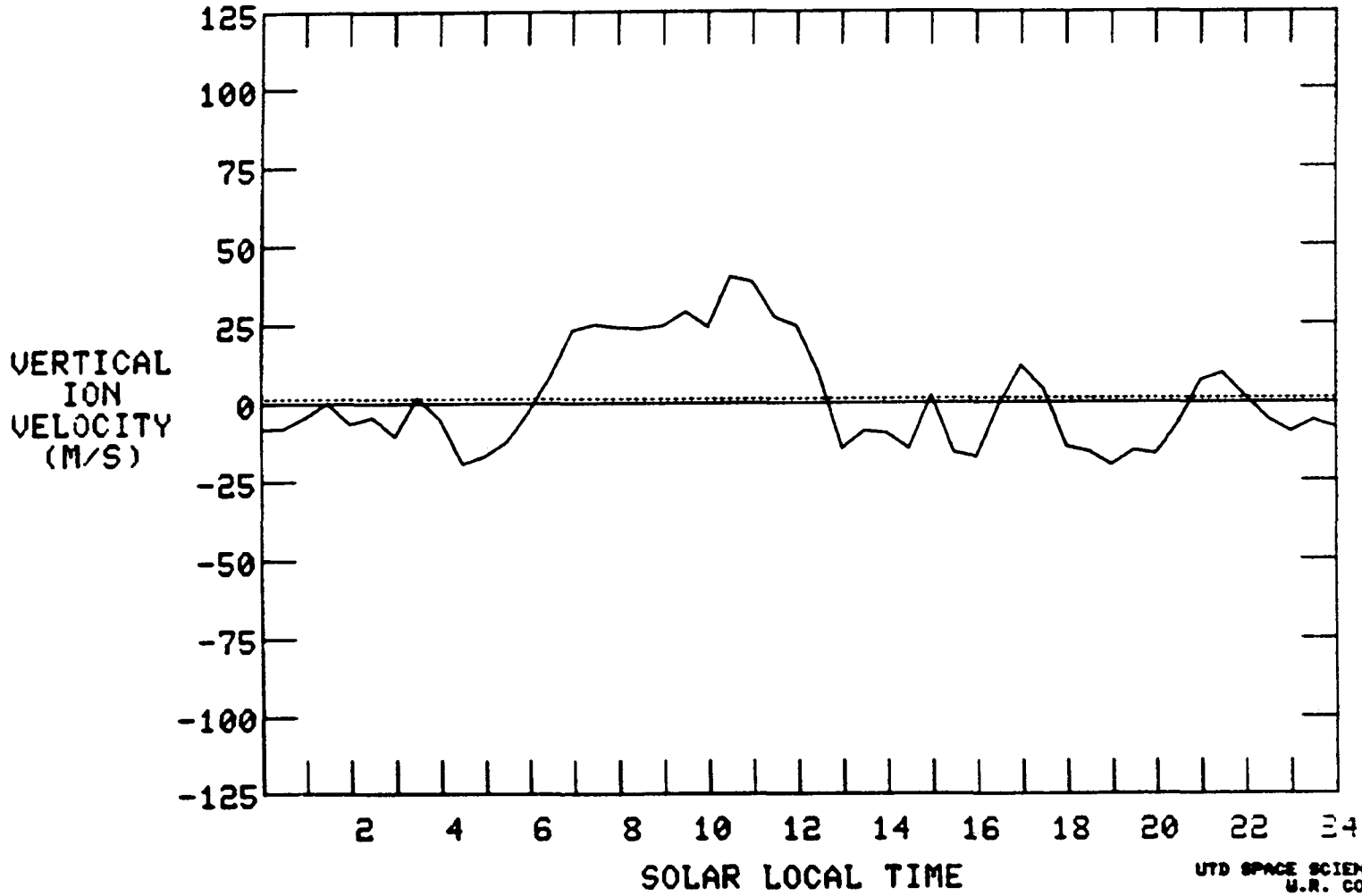
Figure 10b.   Nov 1977 - Jan 1978   −20° to −10° DLAT
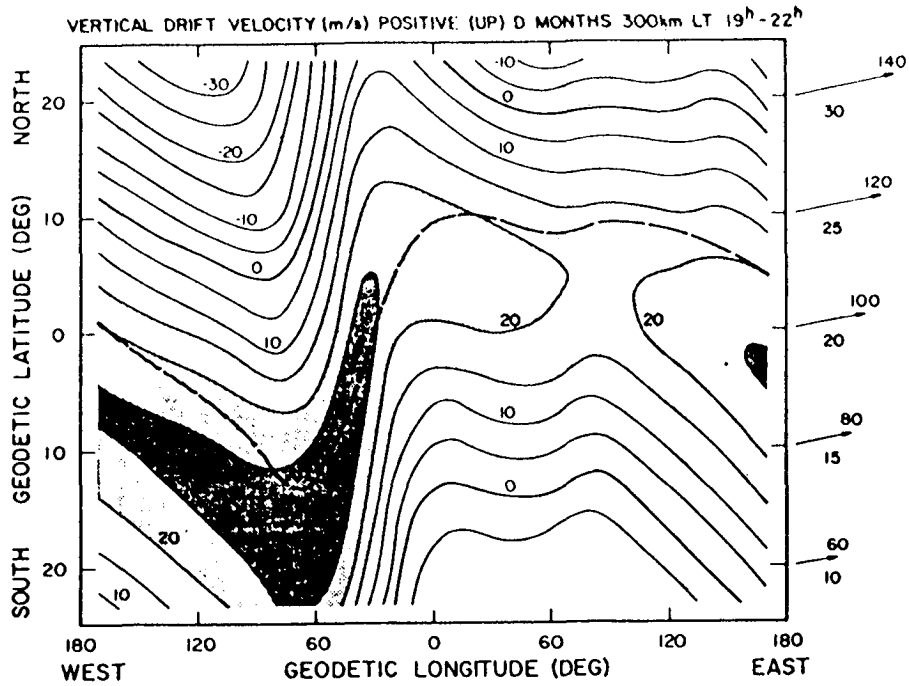
Figure 11. Contours of vertical ion drift velocity calculated for D months (northern hemisphere winter). A realistic model of the magnetic field at 300-km altitude is used for magnitude, inclination, and declination. The electric field is assumed to be constant and eastward at a value of 0.6 mV m^{-1}. The wind field varies linearly with geodetic latitude as indicated on the right-hand side of the figure. The dashed line denotes the geomagnetic equator, and the letter J refers to the Jicamarca Observatory. Regions of maximum upward drift velocity are shaded. Their locations correspond to the distribution of depleted plasma regions observed at winter solstice and shown in Figure 6.

VERTICAL DRIFT VELOCITY (m/s) POSITIVE (UP) J MONTHS 300km LT 19^h-22^h
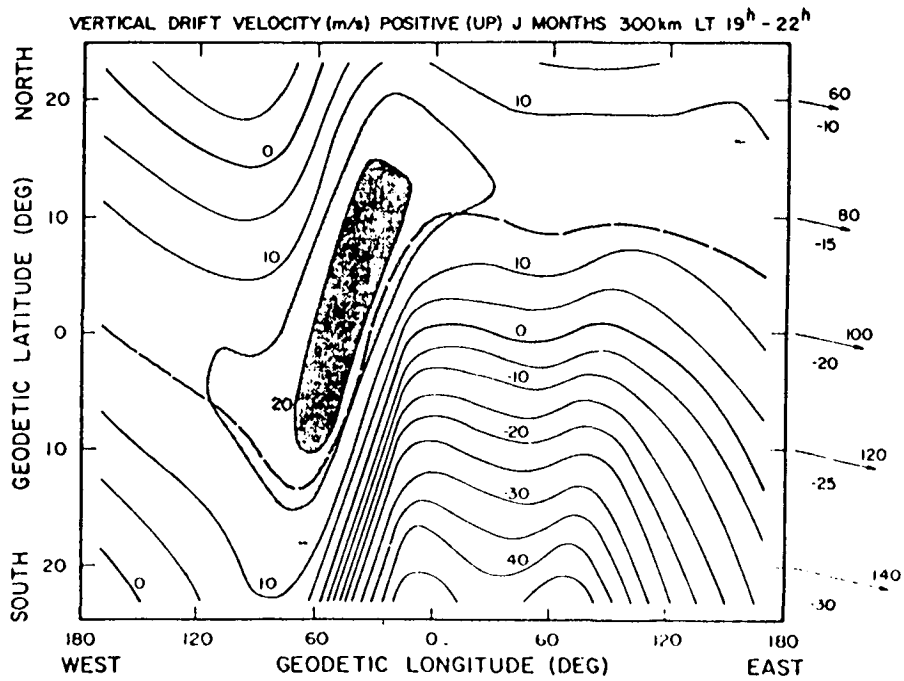
Figure 12. Vertical ion drift velocity calculated for northern hemisphere summer (J months). The wind field is the same as that used in Figure 11, with appropriate seasonal changes. Regions of maximum upward drift are shaded; their distribution corresponds closely to the observations of depleted plasma regions shown in Figure 7.

ATOMIC NITROGEN DENSITIES NEAR THE POLAR CUSP

M. J. Engebretson and J. T. Nelson
Department of Physics
Augsburg College
Minneapolis, MN 55454

The Neutral Atmosphere Composition Spectrometer (NACS) on board the Dynamics Explorer-2 spacecraft sampled several major and minor thermospheric gases including atomic nitrogen. We present here a selection of passes over the polar cusp that provide a quantitative measure of the increase of N densities due to soft particle precipitation occurring in this region. Increases in N densities are frequently observed, but are smaller than accompanying increases in N_2 densities. Our observations support earlier studies suggesting that 1) N densities increase more rapidly than O densities during periods of high solar EUV flux and 2) N densities are larger in the summer hemisphere than in the winter hemisphere. A series of passes in February 1983, late in the lifetime of DE-2, indicated N densities at 2000 km altitude which were a factor of $\approx$ 2 larger near the southern cusp than near the northern cusp.

TABLE I

Atomic nitrogen densities in or near the polar cusp late in the lifetime of DE-2.

ORBIT	DATE	$F_{10.7}$	Kp	CUSP	ALTITUDE (km)	DENSITY (cm^{-3})
		Northern Hemisphere				
8543	83047	91.9	4	Y	236	6.4×10^6
8553	83048	94.2	3	Y	238	6×10^6
8562	83048	94.2	3	N	186	1.1×10^7
		Southern Hemisphere				
8436	83040	125.3	3+	Y	236	1.4×10^7
8514	83045	94.1	3	N	230	1×10^7
8551	83048	94.2	4-	Y	205	2.4×10^7
8574	83049	99	3	N	199	2.8×10^7
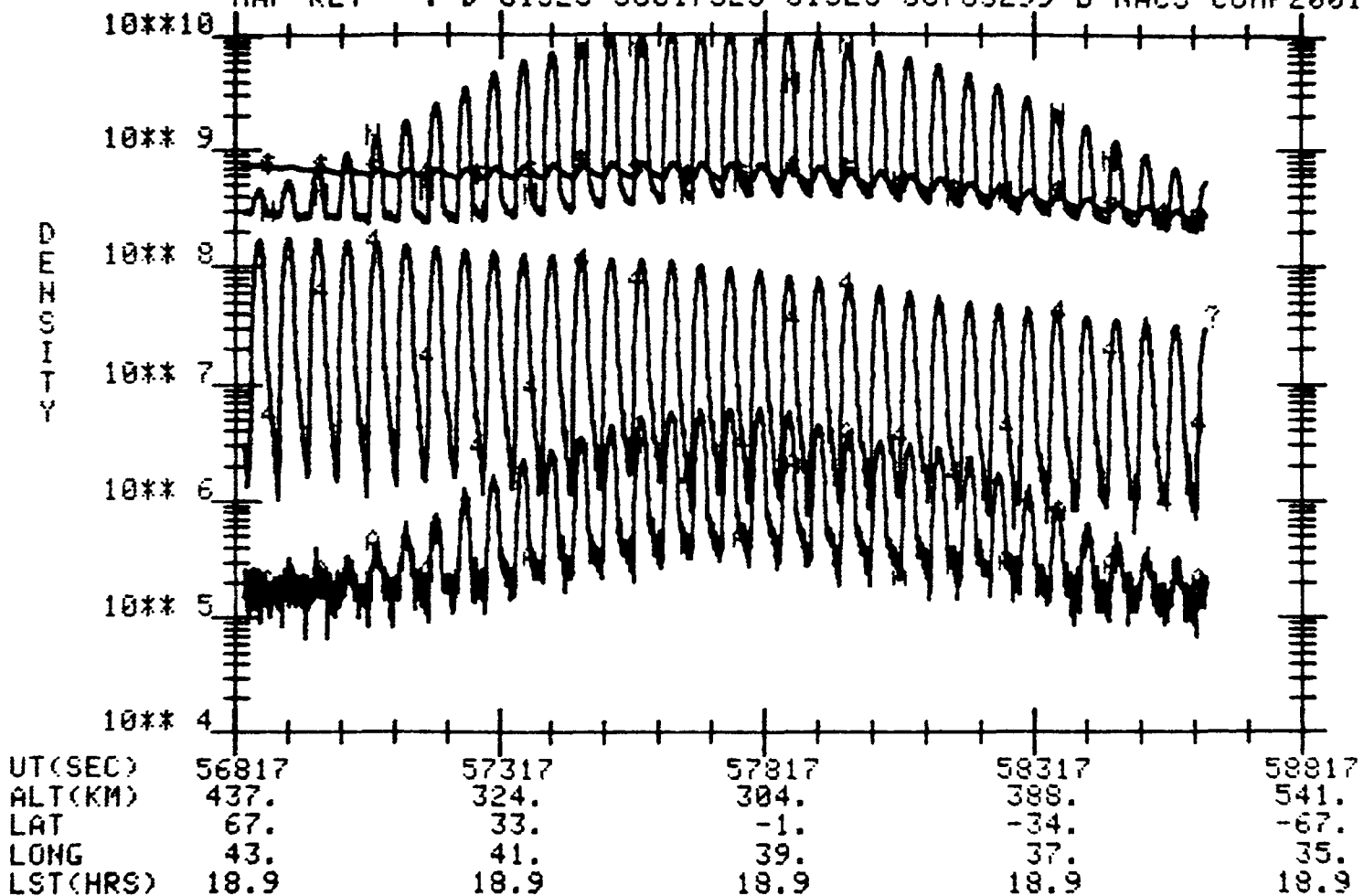
Figure 1. Ion source number densities of NO, Ar, N_2 and He measured by the Neutral Atmospheric Composition Spectrometer (NACS) of the Dynamics Explorer-2 satellite on orbit 1630, November 21, 1981. Number densities are plotted on a logarithmic scale as a function of universal time (UT). Also shown on the abscissa are satellite altitude, geographic latitude and longitude, and local solar time.

10/ 2/84

UT(SEC)	68433	68933	69433	69933	70433
ALT(KM)	434.	323.	304.	390.	544.
LAT	66.	33.	-1.	-35.	-67.
LONG	-5.	-7.	-9.	-11.	-14.
LST(HRS)	18.9	18.9	18.9	18.9	18.9
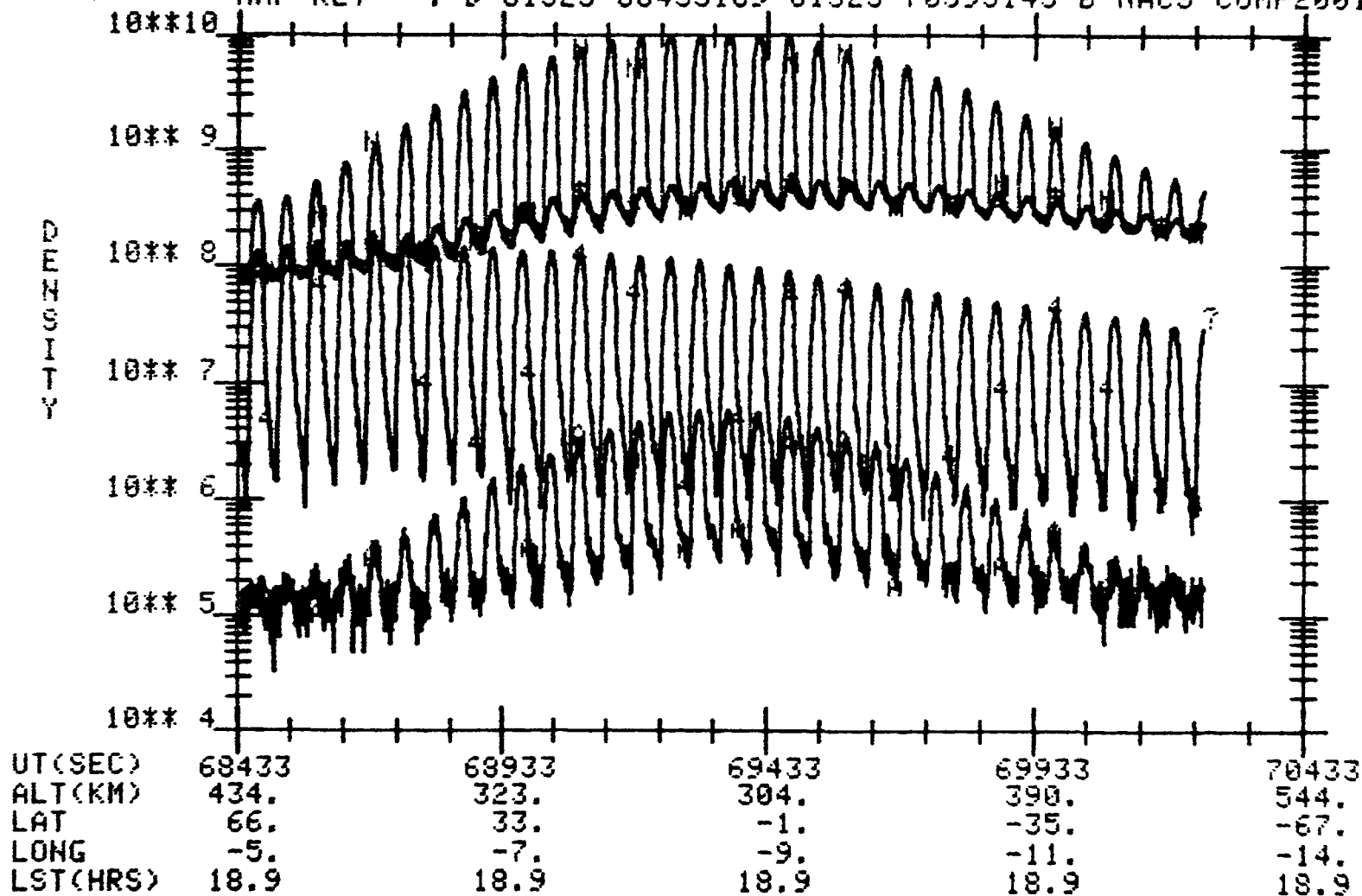
Figure 2. Ion source densities of NO, Ar, N_2, and He for orbit 1632 of DE-2, run on November 21, 1981, as in Figure 1.

Figure 3. Ambient number densities of N, O, N_2, and He determined from DE-2 NACS data for orbit 1630, November 21, 1981. Number densities are plotted on a normalized logarithmic scale as a function of universal time. The densities shown in the graph are to be multiplied by the appropriate scale factor shown at the top of the figure to give the correct ambient densities.
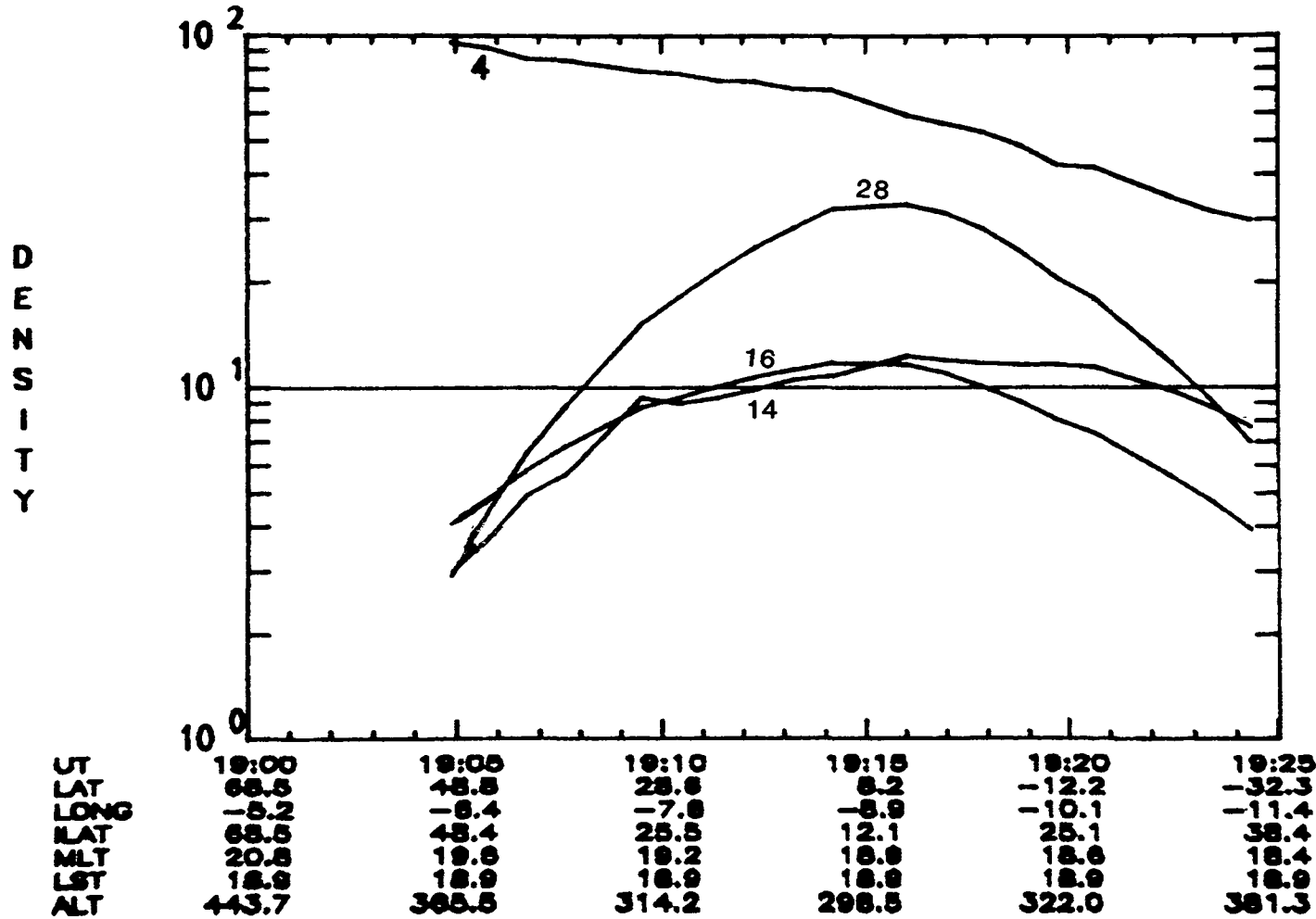
Figure 4. Ambient number densities of N, O, N_2, and He determined from DE-2 NACS data for orbit 1632, November 21, 1981, as in Figure 3.

DE—B NACS	N	O	N2	HE	DATA DATE:
AMBIENT	14	16	28	4	82212
DENSITIES					ORBIT NO.:
SCALE FACTORS	10^5	0^7	10^7	10^5	5426
					NET

UT	9:15	9:20	9:25	9:30	9:35	9:40
LAT	-66.4	-65.4	-45.2	-25.0	-4.9	14.9
LONG	71.6	70.8	69.6	68.4	67.1	65.9
ILAT	76.6	71.5	56.5	36.2	13.8	7.5
MLT	8.7	12.1	13.1	13.4	13.7	13.8
LST	13.8	14.0	14.0	14.0	14.0	14.0
ALT	336.4	306.9	301.3	316.8	351.8	406.6
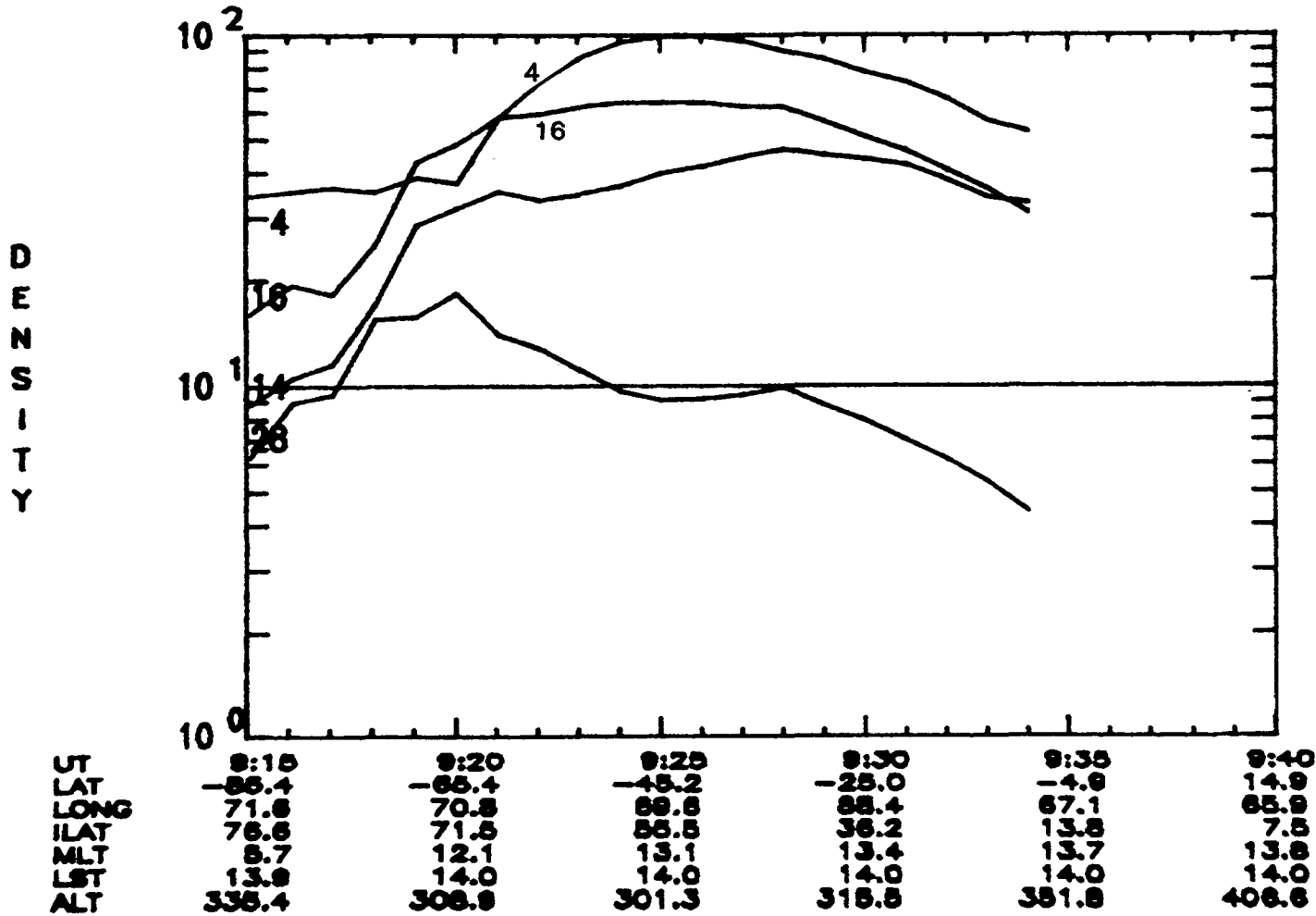
Figure 5. Ambient number densities of N, O, N_2, and He determined from DE-2 NACS data for orbit 5426, July 31, 1982, and in Figure 3.

DE-8 NACS	N	O	N2	HE	DATA DATE:
AMBIENT	14	16	28	4	81254
DENSITIES					ORBIT NO.:
SCALE FACTORS	10^8	10^8	10^7	10^5	574
					NET

UT	10:20	10:25	10:30	10:35	10:40	10:45
LAT	2.1	21.7	41.8	62.0	82.3	77.8
LONG	18.4	14.1	12.9	11.8	10.4	170.9
ILAT	16.0	17.3	36.8	60.2	78.9	74.2
MLT	11.4	11.7	12.1	12.8	15.8	20.9
LST	11.4	11.4	11.4	11.4	11.4	23.4
ALT	490.8	389.2	337.3	311.0	321.8	366.7
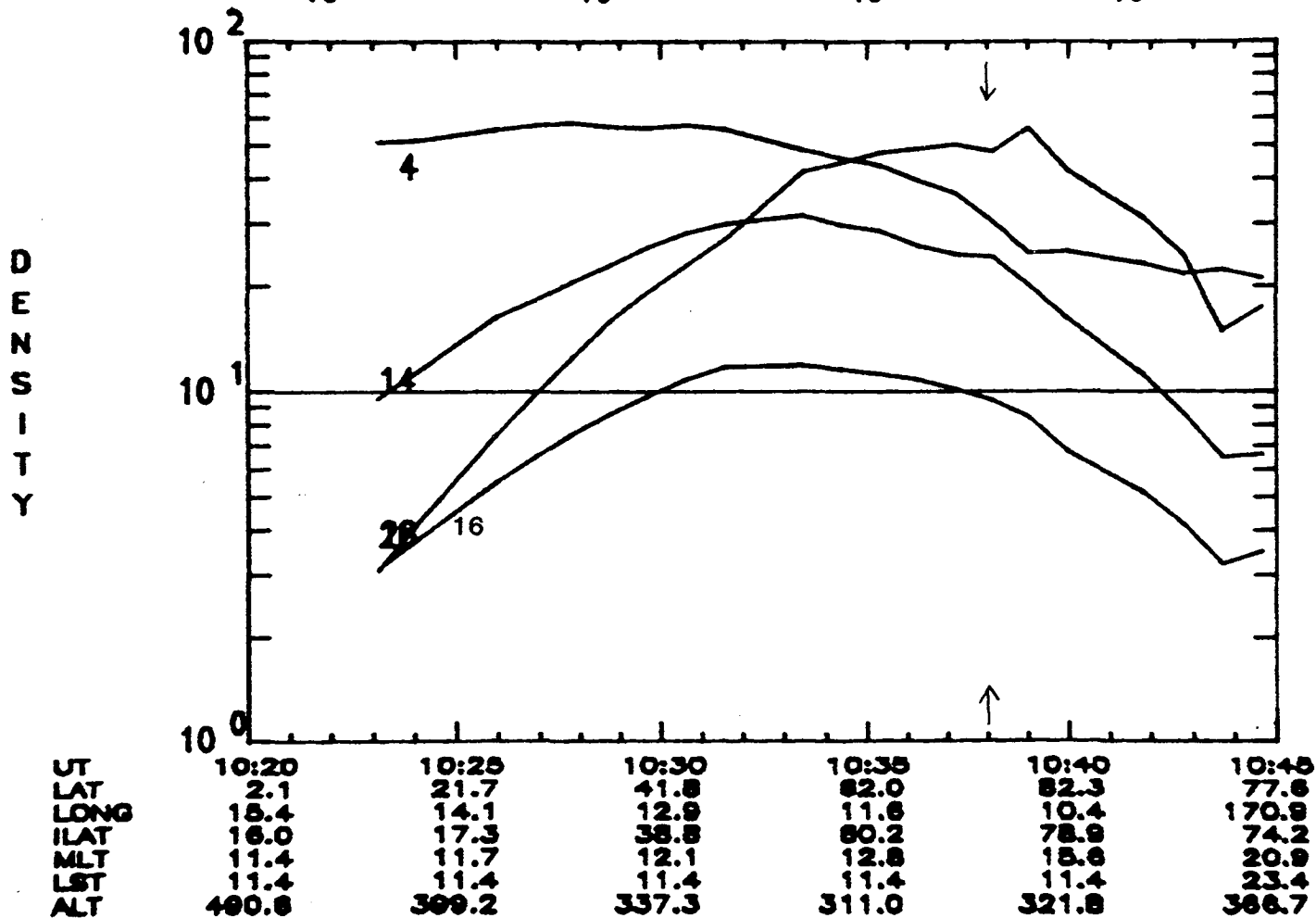
Figure 6. Ambient number densities of N, O, N_2, and He determined from DE-2 NACS data for orbit 574, September 11, 1981, as in Figure 3.

DE-B NACS   N   O   N2   HE   DATA DATE:
AMBIENT   14   16   28   4   83040
DENSITIES   ORBIT NO.:
SCALE FACTORS 10^6 10^8 10^8 10^6 8436
NET

UT	23:36	23:40	23:46	23:60	23:55	24:00
LAT	−30.9	−60.2	−60.4	−79.4	−59.3	−59.3
LONG	156.1	156.3	157.2	20.7	19.7	19.7
ILAT	40.6	59.9	73.9	69.9	66.2	66.2
MLT	13.4	14.1	16.1	21.6	23.6	23.6
LST	13.0	13.0	13.0	1.0	1.0	1.0
ALT	226.7	232.0	236.2	246.2	262.1	262.1
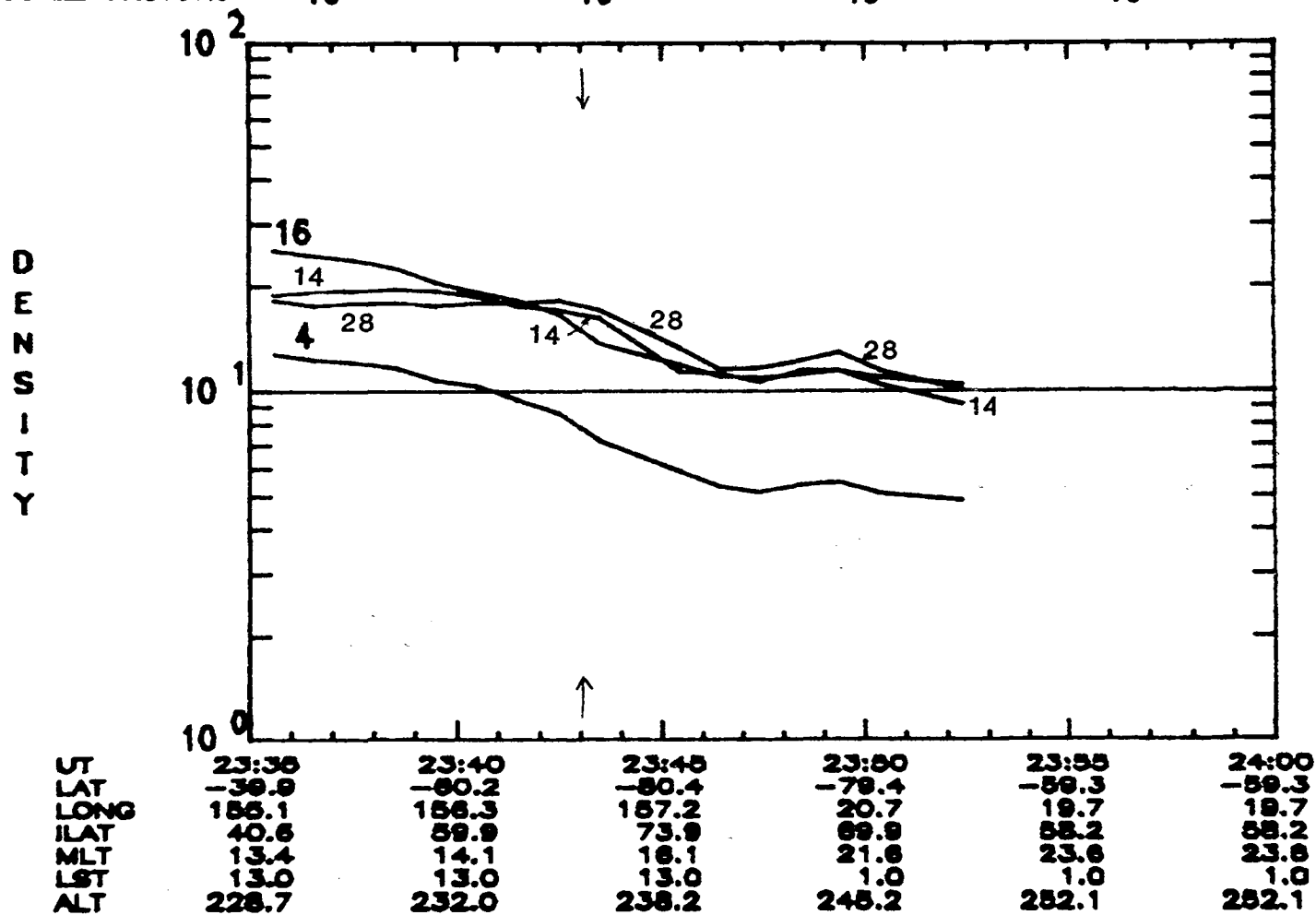
Figure 7. Ambient number densities of N, O, N_2, and He determined from DE-2 NACS data for orbit 8436, February 9, 1983, as in Figure 3.
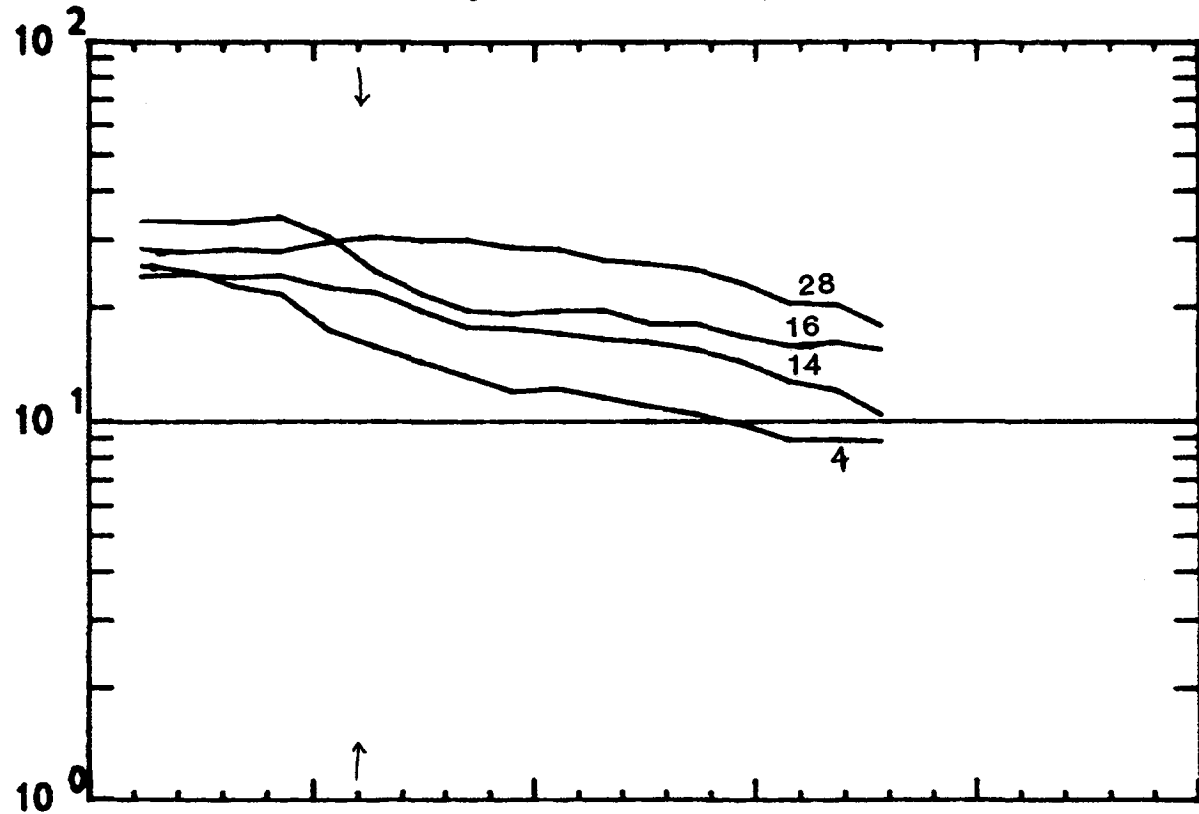
Figure 8. Ambient number densities of N, O, N_2, and He determined from DE-2 NACS data for orbit 8551, February 17, 1983, as in Figure 3.
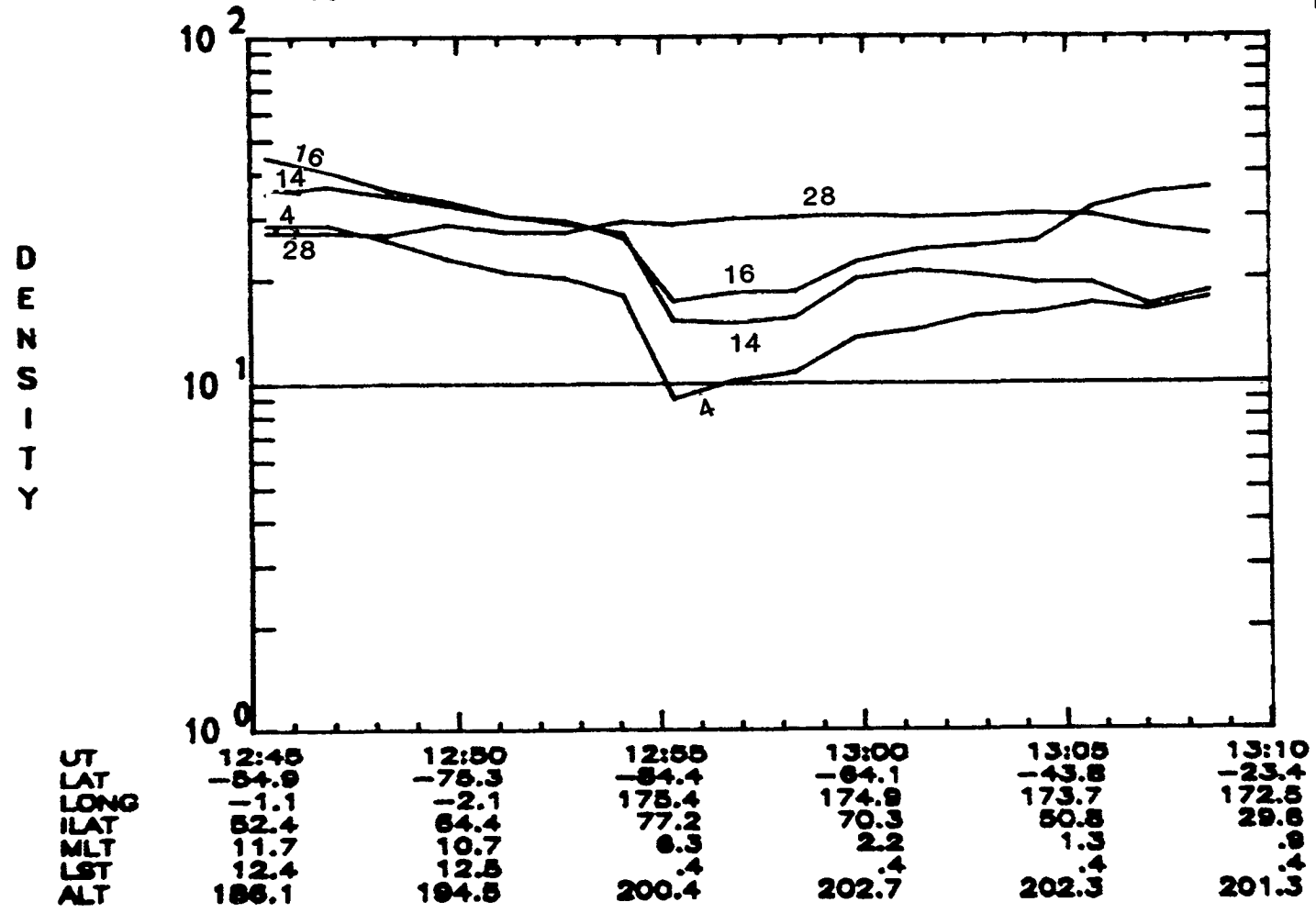
Figure 9. Ambient number densities of N, O, N$_2$, and He determined from DE-2 NACS data for orbit 8574, February 18, 1983, as in Figure 3.

SIMULATION OF THE THERMOSPHERIC TIDES BY USE OF THE NCAR THERMOSPHERIC GENERAL CIRCULATION MODEL

C. G. Fesen, R. E. Dickinson, and R. G. Roble
National Center for Atmospheric Research
P.O. Box 3000
Boulder, CO 80307

Numerical calculations of the thermospheric tidal winds and temperatures were produced by use of the NCAR Thermospheric General Circulation Model (TGCM). The present calculations were restricted to solar minimum equinox conditions. The effects of viscosity, conductivity, diffusion, ion drag, winds, and temperature gradients were included. The semidiurnal propagating waves excited by heating in the lower atmosphere were modelled by use of the classical tidal perturbations as lower boundary conditions. The TGCM was tuned by adjusting the tidal forcing term until calculated semidiurnal winds and temperatures matched incoherent scatter observations. The tidal TGCM results are consistent with previous theoretical work and successfully reproduce high altitude temperature and velocity data, but give somewhat lower magnitudes for velocities and temperatures near 160 km than are seen observationally. Future plans call for similar studies being done for solar maximum equinox conditions, and then the solstice cases. These studies would benefit enormously from additional data, particularly if higher order modes are to be accurately included.

SEMIDIURNAL HOUGH FUNCTIONS
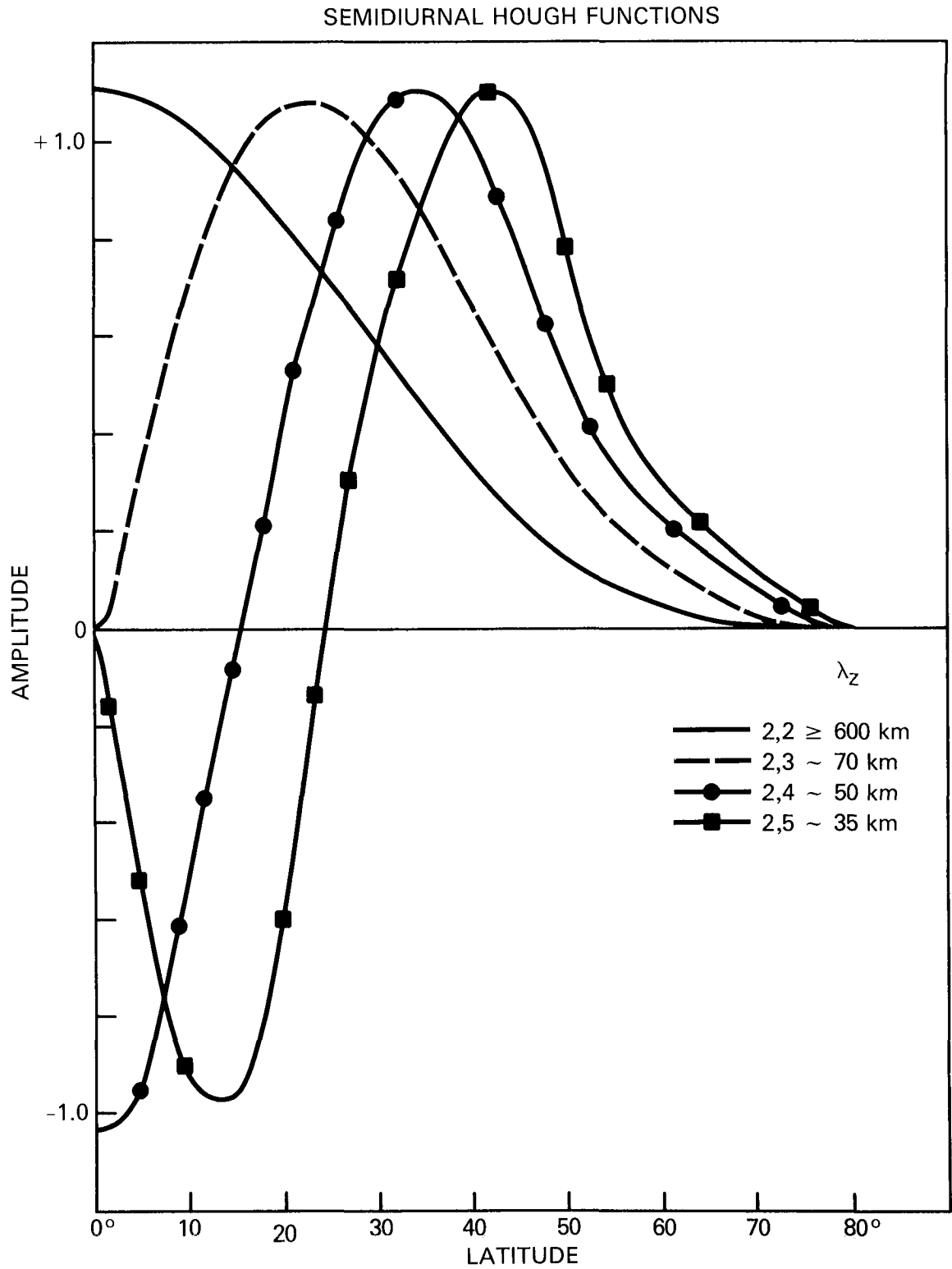
Figure 1. Classical Hough functions for the semidiurnal tides. Note increasing latitude structure for higher order modes.

$$G\ (Z,\ \Theta,\ t)\ =\ \sum_n\ L_n\ (Z)\ \Theta_n\ (\Theta)\ e^{i\ (\sigma t\ +\ s\lambda)}$$

FOR SEMIDIURNAL TIDES

$$\sigma\ =\ \frac{2\pi}{Y_2}$$

$$S\ =\ 2$$

$$\Phi_{97}\ =\ \Big\{\ \Phi_{2,\ 2_{97}}\ \Theta_{2,\ 2}\ e^{ik_{2,\ 2}\ Z_{97}}\ +$$

$$\Phi_{2,\ 4_{97}}\ \Theta_{2,\ 4}\ e^{i\ k_{2,\ 4}\ Z_{97}}\ \Big\}\ \bullet\ e^{i\ (4\pi t\ +\ 2\lambda\ )}$$

Figure 2. Classical solutions for any tidal variable as a function of altitude, latitude, and time can be written as shown in the top line of the figure. The geopotential Φ at 97 km can be written as shown.

1. SPECIFY THE GEOPHYSICAL CONDITIONS;

2. START WITH EQUILIBRIUM SOLUTIONS OF THE TGCM FOR
   SOLAR HEATING ALONE FOR THE APPROPRIATE CONDITIONS;

3. GUESS THE AMPLITUDE AND PHASE FOR THE 2,2 AND 2,4
   GEOPOTENTIAL AT 97 KM, AND CALCULATE THE TOTAL TIDAL
   GEOPOTENTIAL AT 97 KM;

4. CALCULATE U, V, T AT 97 KM FROM THE GEOPOTENTIAL AT 97 KM
   USING FORMULAE FROM CHAPMAN AND LINDZEN AND USE THESE AS
   LOWER BOUNDARY CONDITIONS;

5. INTEGRATE THE MODEL EQUATIONS UNTIL EQUILIBRIUM IS
   ACHIEVED. THIS TYPICALLY TAKES 10½ MIN CRAY CPU;

6. FOURIER DECOMPOSE THE U, V, AND T FIELDS INTO ZONAL
   WAVENUMBERS 1 AND 2;

7. COMPARE THE TGCM U, V, AND T AMPLITUDES AND PHASES AT
   18° AND 45° WITH OBSERVATIONS FROM ARECIBO, MILLSTONE
   HILL, AND SAINT SANTIN;

8. MODIFY THE INITIAL GUESSES FOR THE 2,2 AND 2,4 AMPLITUDES
   AND PHASES OF THE GEOPOTENTIAL AND REPEAT FROM STEP 4
   UNTIL REASONABLE AGREEMENT IS OBTAINED BETWEEN THE MODEL
   AND OBSERVATIONS.

Figure 3. Steps in the calculation of the thermospheric winds and temperatures including the effect of tidal excitation.
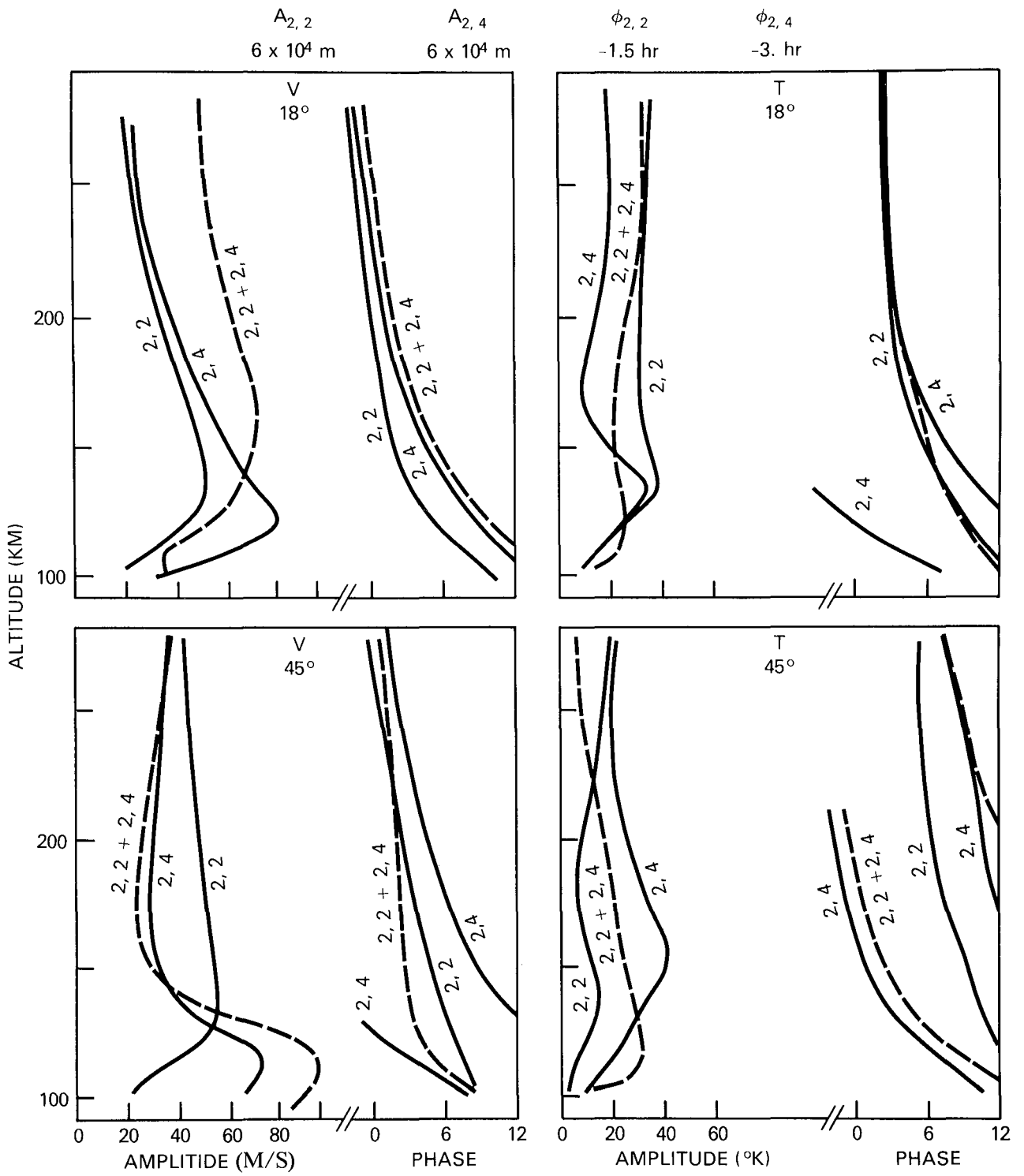
Figure 4. Results for a particular guess for the 2, 2 and 2, 4 components of the geopotential at 97 km.
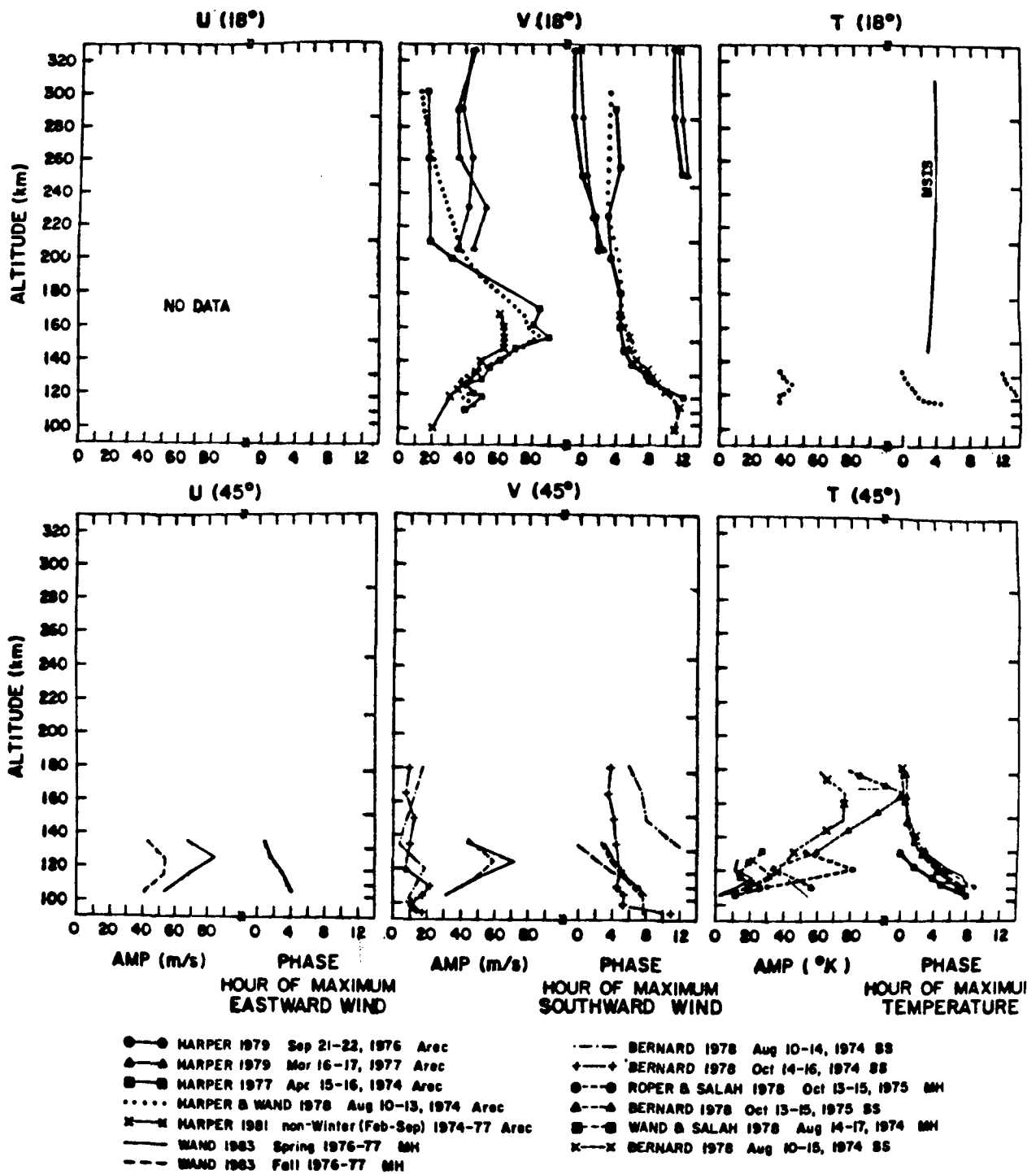
Figure 5. The incoherent scatter radar observations to which the TGCM winds and temperatures were compared.

BEST FIT TO OBSERVATIONS FOR
2, 2 AND 2, 4 GEOPOTENTIAL AT 97 KM:

$A_{2, 2} = 4 \times 10^4$ m

$A_{2, 4} = 3 \times 10^4$ m

$\phi_{2, 2} = -0.5$ hr

$\phi_{2, 4} = -2.5$ hr

Figure 6. The amplitudes and phases for the
2, 2 and 2, 4 geopotential at 97 km which
best fit the observations shown in Figure 5.
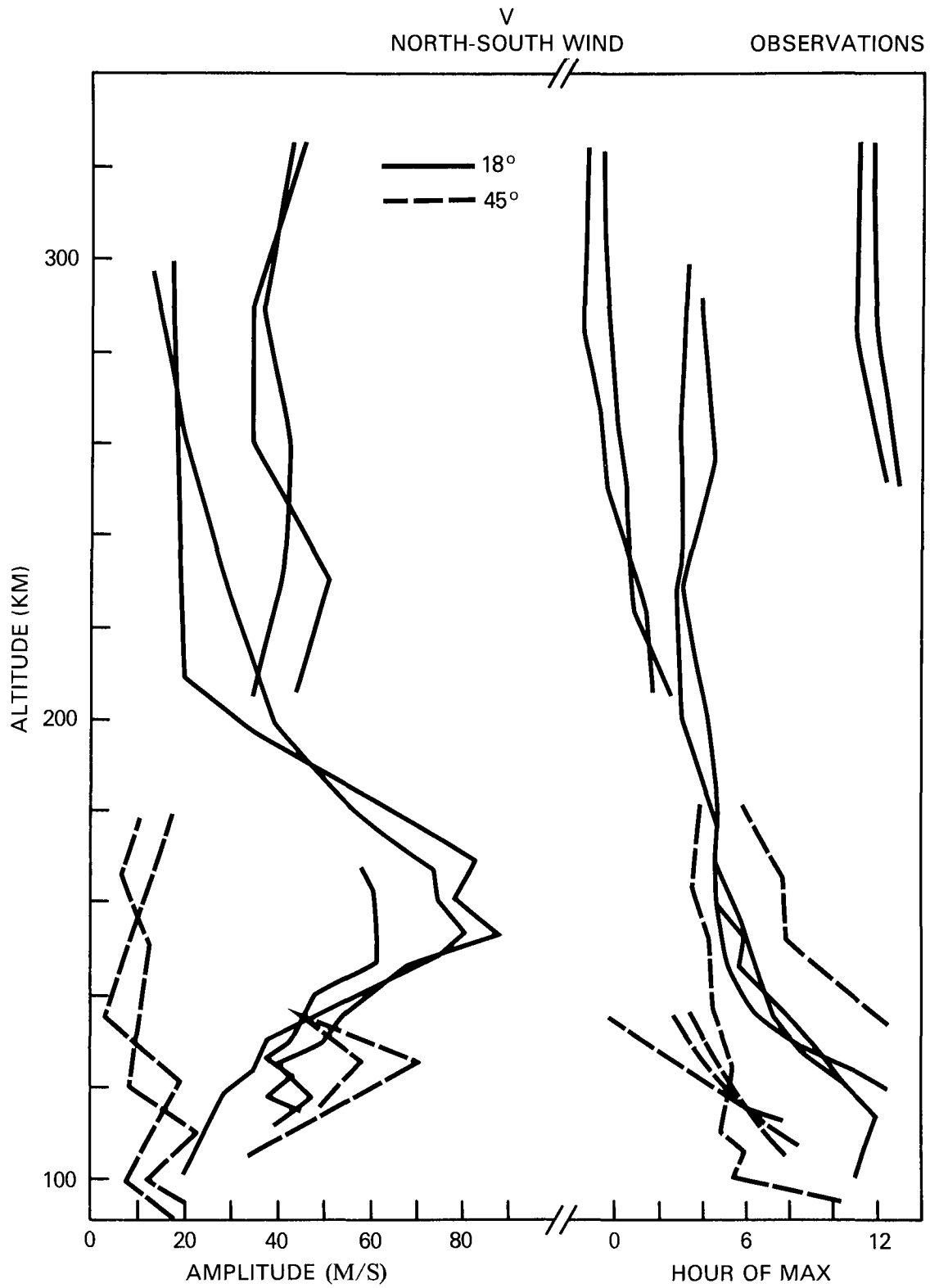
Figure 7. The north-south velocity observations at 18° and 45°.
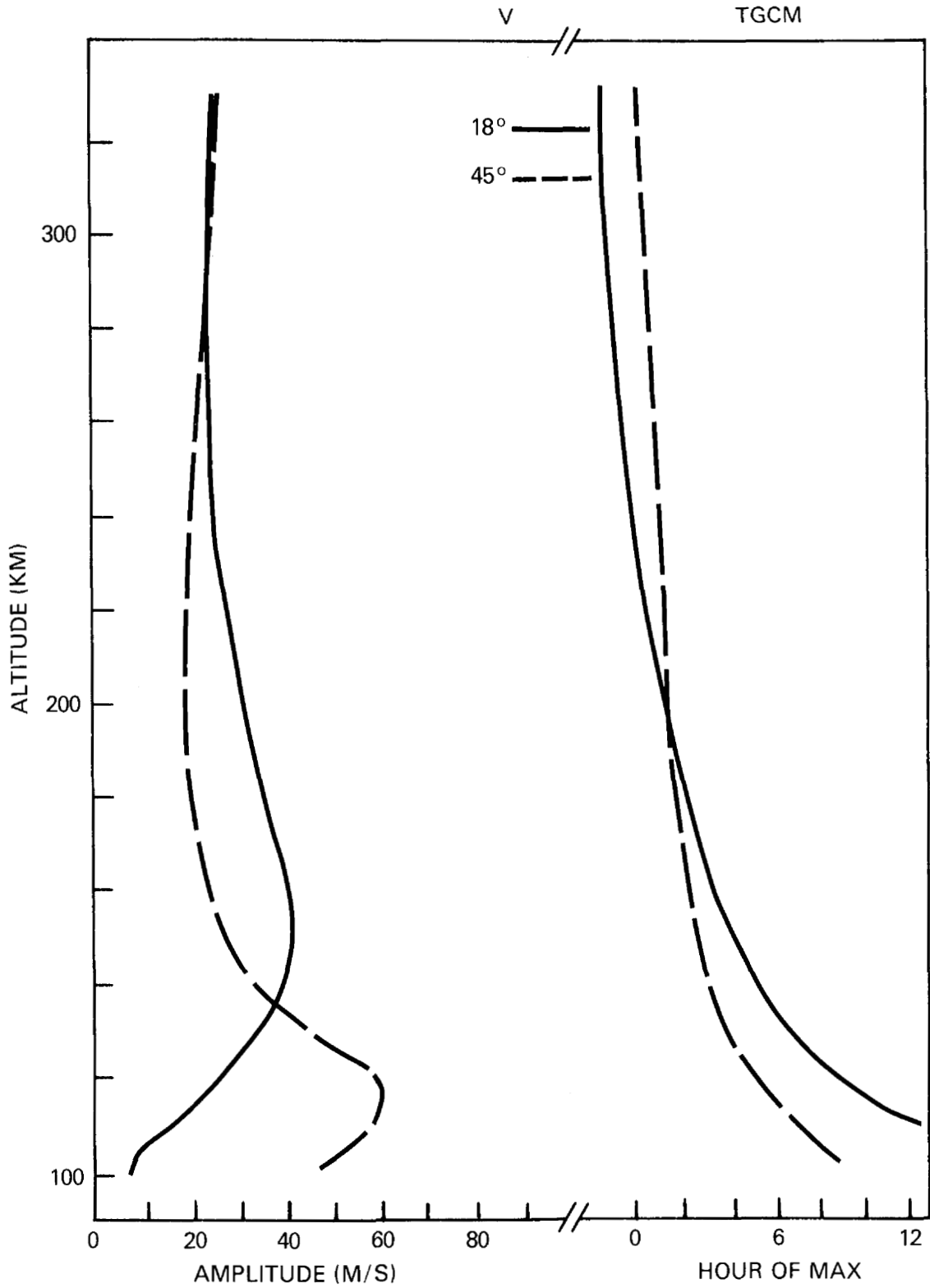
Figure 8. The TGCM north-south velocity at 18° and 45°.
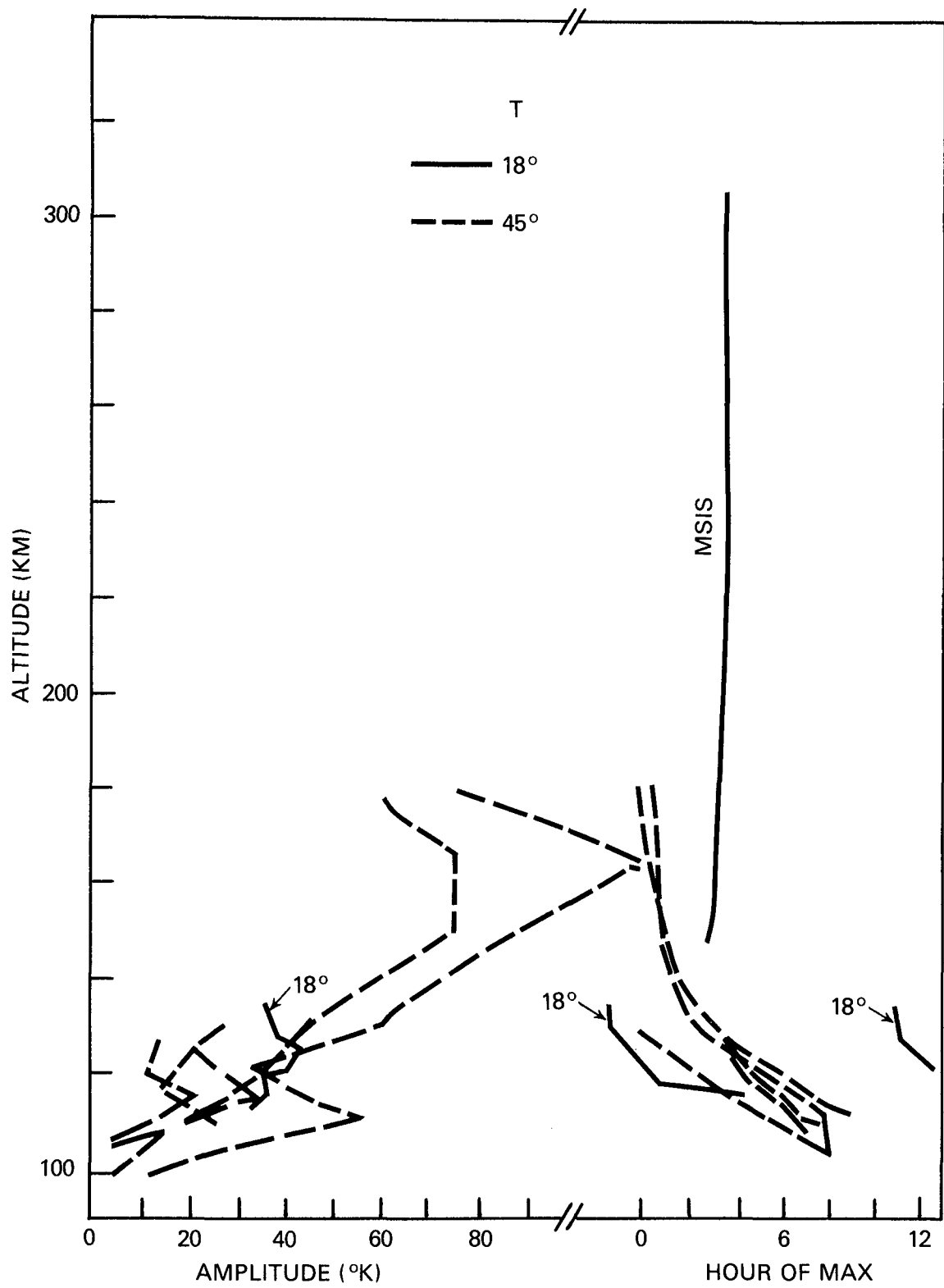
Figure 9. The temperature observations at 18° and 45°.
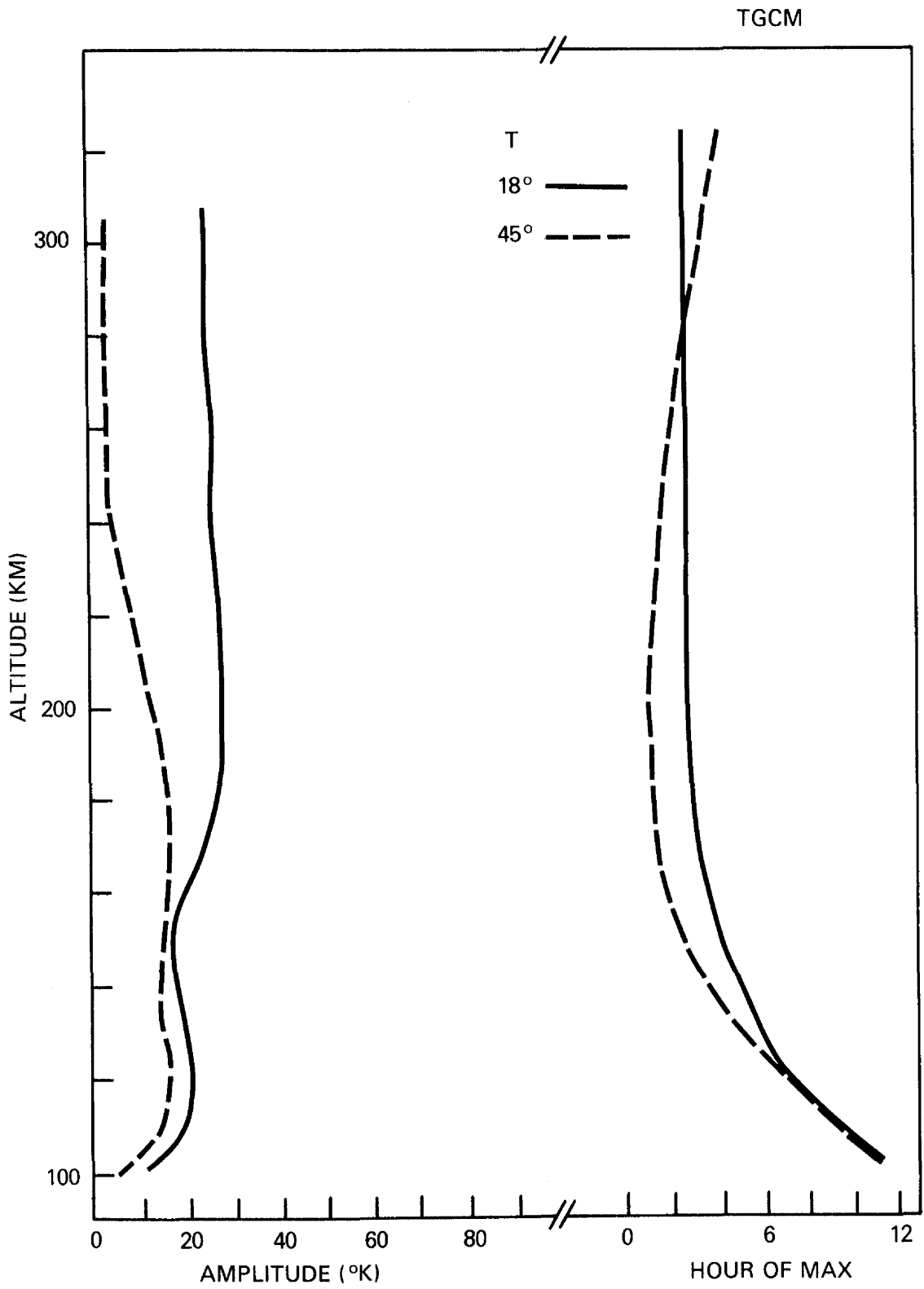
Figure 10. The TGCM temperatures at 18° and 45°.
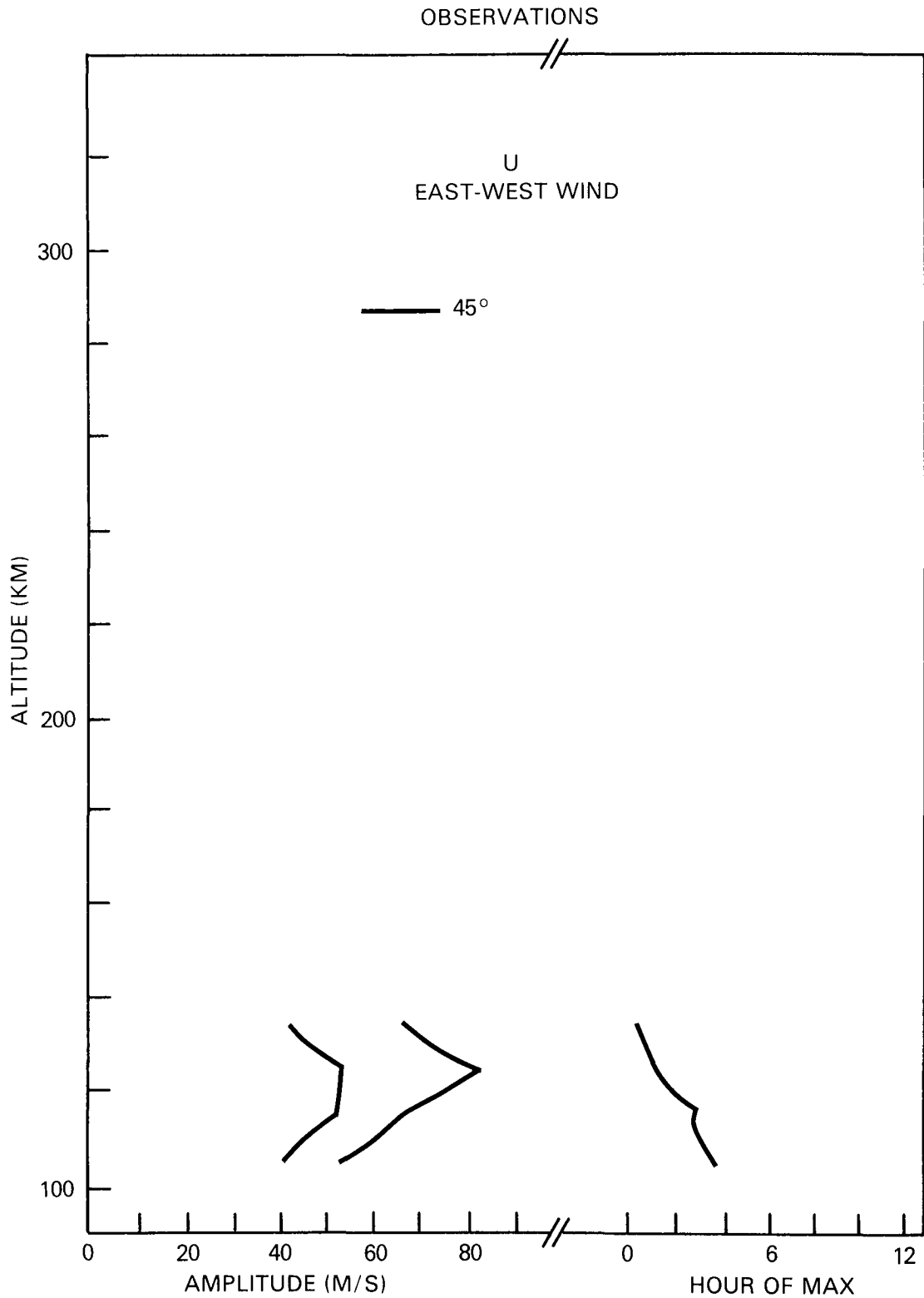
Figure 11. The east-west velocity observations at 45°.

74
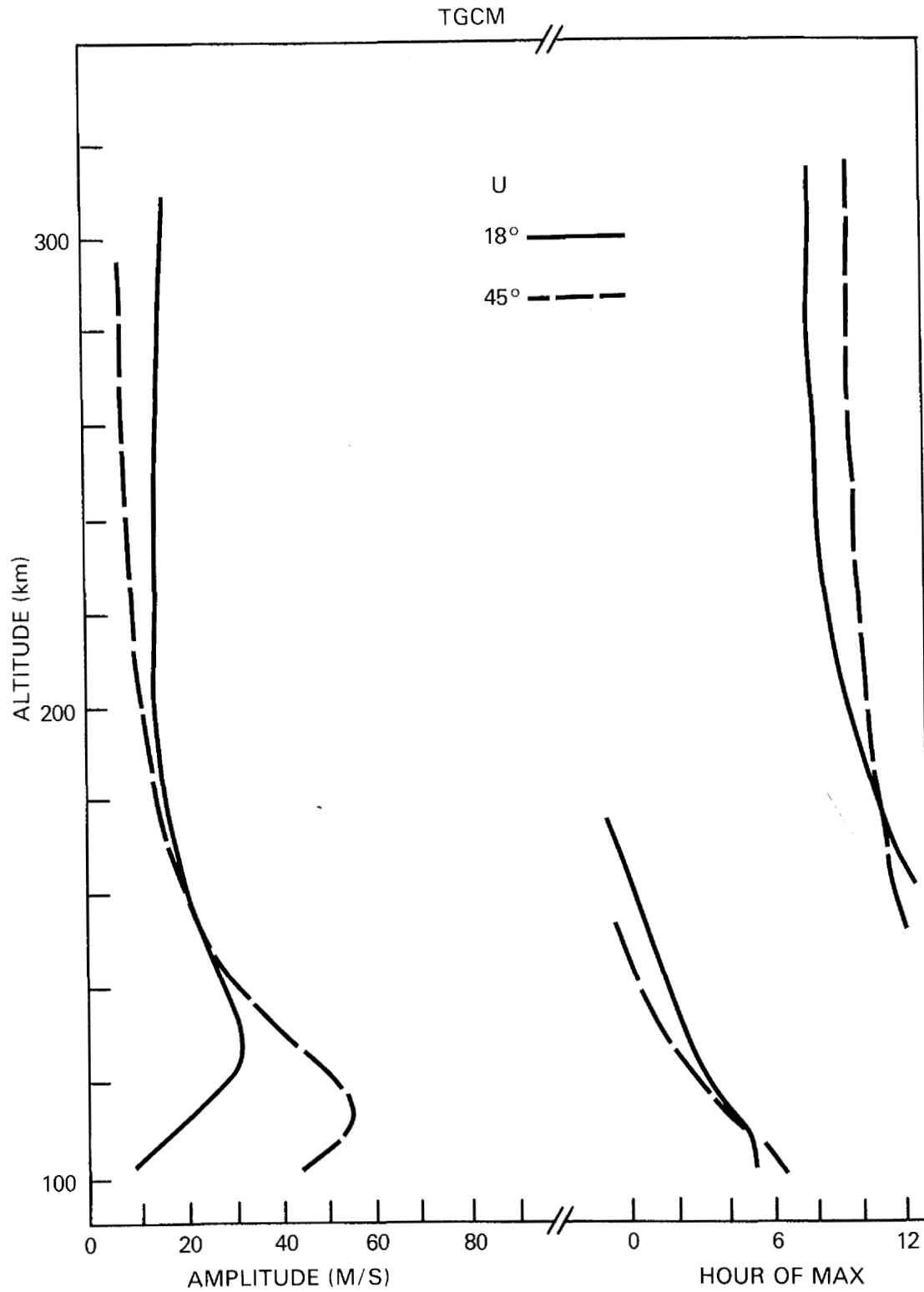
Figure 12. The TGCM east-west velocities at 18° and 45°.
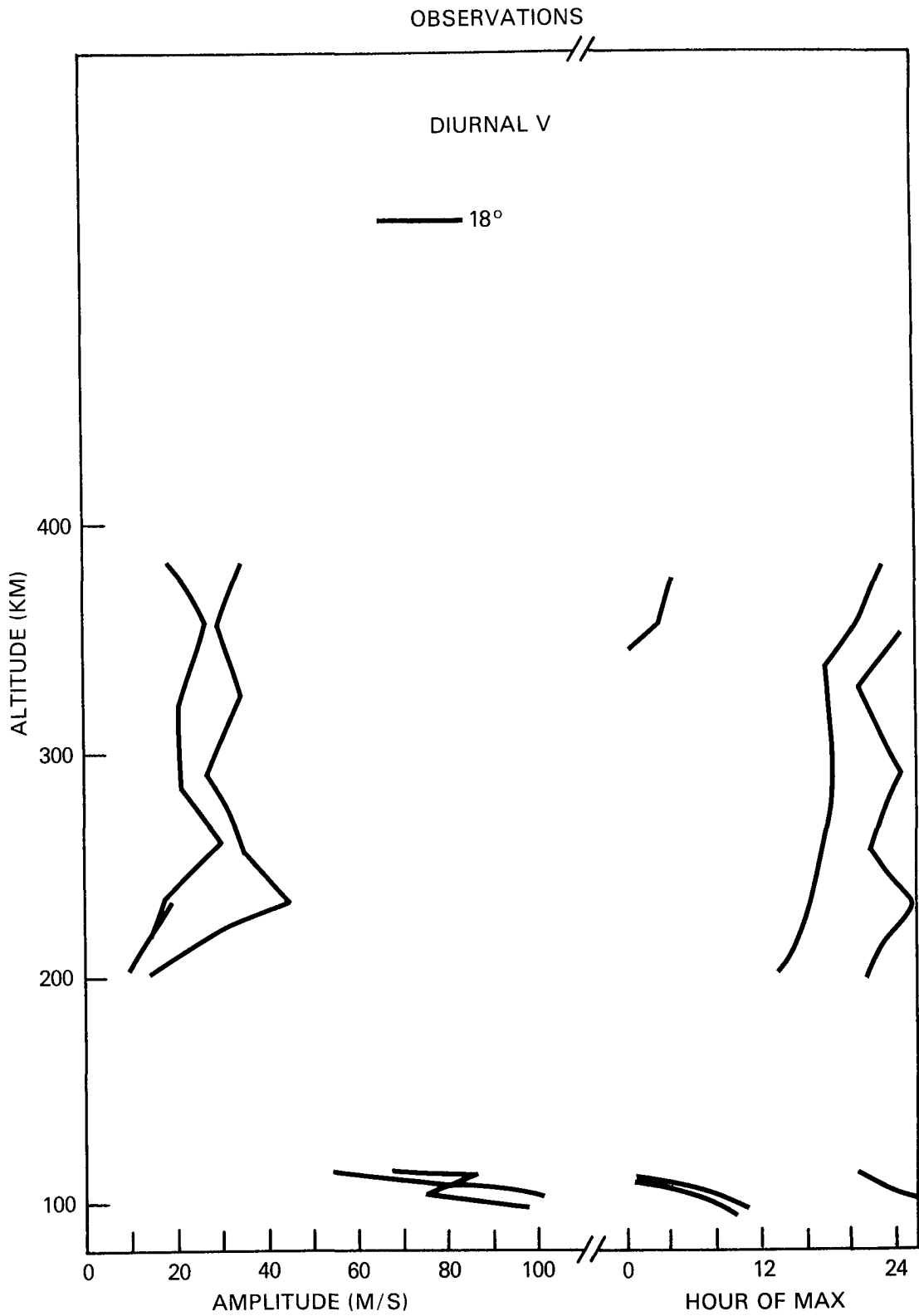
Figure 13. The diurnal north-south velocity observations at 45°.
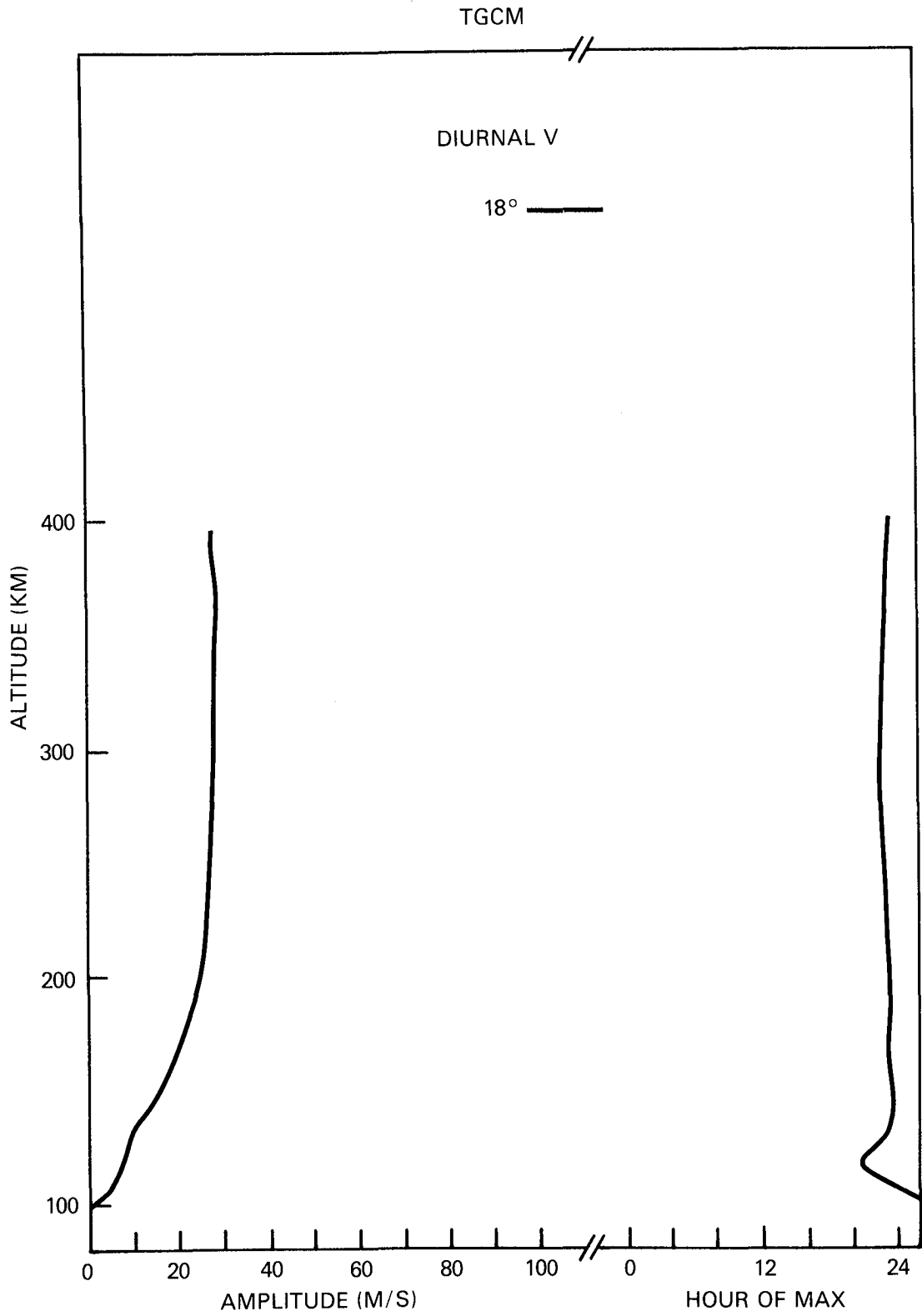
Figure 14. The TGCM diurnal north-south velocity results at 45°.

TIDAL COUPLING WITH THE LOWER ATMOSPHERE
(Invited Review)

Jeffrey M. Forbes
Department of Electrical, Computer, and Systems Engineering
Boston University, Boston, MA 02215

1. INTRODUCTION

The purpose of this paper is to review the various ways in which propagating tidal components excited in the mesophere and below affect the structure of the thermosphere and ionosphere above 100 km. Dynamo effects are not treated here, as they will be addressed separately in the paper by A. D. Richmond.

We begin by examining the physical processes affecting the propagation of upward propagating tides, and how they are interrelated in the context of a numerical model. Propagating diurnal and semidiurnal tides which reach thermospheric heights are excited *primarily* by insolation absorption by tropospheric water vapor (0-15 km) and stratospheric/mesospheric ozone (40-60 km), respectively. Simulation of these oscillations requires consideration of mean zonal winds and meridional temperature gradients, and the damping effects of turbulent and molecular dissipation, radiative cooling, and ion drag. These effects must be considered on a spherical rotating atmosphere extending from the ground to above 300 km, as they are in the model developed by Forbes (1982 a, b) depicted schematically in Figure 1.

2. WINDS AND TEMPERATURES

Figure 2 illustrates amplitudes and phase vertical structures at $0°$, $18°$, $42°$, and $60°$ latitude for the solar diurnal westerly wind at equinox from the Forbes model. In-situ EUV excitation above 90 km is included in these simulations. The following features are worth noting:

(1) Below 100 km at low latitudes the exponential amplitude growth and phase progression ($\lambda_z \approx 30$ km) with height are characteristic of the (1, 1) diurnal propagating tide. The (1, 1) mode attains its peak amplitudes near 110 km and decays rapidly above this height due to molecular dissipation.

(2) Below 100 km at high latitudes the relative absence of amplitude growth and phase progression with height is indicative of the (1, -2) trapped mode. Superposition of the (1, 1) and (1, -2) modes accounts for the illustrated changes in vertical structure of the diurnal tidal winds and temperatures.

(3) Amplitudes and phases of u, v, and δT are asymptotic to constant values above 200 km. This behavior is consistent with the dominance of diffusion in the upper thermosphere, and with the condition that there be no sources of heat or momentum in the upper thermosphere.

(4) Diurnal tidal oscillations in the 90-150 km region receive about equal contributions from upward propagating and in situ excited components.

Item (4) is examined in detail in Figure 3 where the *northerly velocity* at 18° latitude is separated into relative contributions due to the (1, 1) propagating tide (predominant below 150 km) and that excited in-situ by EUV and UV solar radiation absorption (predominant above 150 km). Note the transition from a 30-km vertical wavelength phase progression with height below 150 km indicative of the (1, 1) mode to phase and amplitude constancy with height indicative of fast molecular diffusion and in situ excitation.

Figures 4 and 5 illustrate amplitude and phase vertical structures at 0°, 18°, 42°, and 60° latitude for the solar and lunar semidiurnal westerly winds at equinox from the Forbes model. For the solar component the transition to shorter vertical wavelengths between 80 and 100 km, the effects of dissipation on the upward propagating components between 110 and 150 km, and the asymptotic behavior characteristic of the upper thermosphere are clearly illustrated. The upper thermosphere velocity and temperature fields, which typically range between 10-50 m sec^{-1} and 20-40 K with the larger values at low latitudes, originate with about equal weighting from three excitation sources: (1) in situ EUV excitation, (2) ion-drag momentum coupling with the diurnal tidal winds, and (3) upward propagating modes excited below 100 km. Although the lunar gravitational excitation consists of some (2, 4) in addition to the predominant (2, 2) forcing, the excitation of the higher-order (2, 4) and (2, 5) modes are due almost exclusively to mode coupling due to mesospheric mean winds and meridional temperature gradients. Winds (temperatures), in fact, reach amplitudes of order 10-15 m sec^{-1} (10-15 K) in the lower thermosphere, and 5-10 m sec^{-1} (5-10 K) in the upper thermosphere, and may thus account for a significant portion of day-to-day variability reported in measurements of the solar semidiurnal tide.

The joint presence of molecular viscosity, thermal conductivity, anisotropic ion drag, and rotation on a sphere renders the viscid tidal equations inseparable with respect to height and latitude, whereas in an inviscid atmosphere where the background temperature is independent of latitude the equations are separable, and classical tidal theory applies. In classical tidal theory the eigensolutions (Hough functions) of Laplace's tidal equation define the horizontal structures of each mode, and the eigenvalues (equivalent depths) fix each mode's vertical structure. Thus, besides alteration of the vertical tidal structures from exponential growth (for propagating tides) or decay (for trapped tides) to asymptotically constant solutions in the upper thermosphere, the region where χ, the ratio of the wave period to the dissipative time scale, approaches unity is also characterized by a transition from tidal solutions that are separable with respect to height and latitude to one in which vertical structures for a particular 'modal extension' into the thermosphere vary with height. This behavior is illustrated in Figures 7 and 8, which depict the horizontal shapes of the (2, 2) and (2, 4) Hough mode extensions (HME) of the semidiurnal temperature oscillation at various heights. Note that the node at 15° latitude for (2, 4) disappears and the (2, 2) horizontal shape broadens considerably at progressively greater heights in the thermosphere.

An illustration of how upward-propagating tides affect the local-time structure of the thermosphere is illustrated in Figure 9, taken from Garrett and Forbes (1978). These authors superimposed in-situ diurnal simulations with theoretical semidiurnal 'Hough mode extensions' calibrated to observational data. Note the high degree of structure exhibited below 200 km. The hour of maximum amplitude shifts to earlier times with increasing altitude, indicating the presence of upward propagation waves. A 12-hour period is particularly evident below 150 km.

At solar minimum, the upward propagating components can be expected to exert a greater influence on thermospheric structure, due to the relatively smaller contribution from in-situ EUV sources. An example of how this influence can be reflected in midlatitude exospheric temperatures is illustrated in Figures 10 and 11, where temperatures measured at Millstone Hill during 1974 (SSMIN) and 1980 (SSMAX) are depicted. Note the predominance of a diurnal component at SSMAX whereas the SSMIN curve exhibits structure containing semidiurnal and terdiurnal components.

Another manifestation of upward propagating tides occurs via the nonlinear coupling between the semidiurnal thermospheric oscillation (which originates via in-situ as well as lower atmosphere contributions) and the diurnal variation of ion drag to produce a terdiurnal component to the thermospheric temperature and density, particularly at low latitudes where the coupling is strong. The nonlinear coupling between tidal winds and ion drag has been invoked by Mayr et al (1974) to explain spurious anamalous increases in the equatorial neutral temperature around midnight observed by the NATE experiment on AE-E, as illustrated in Figure 12. The semidiurnal component receives strong contributions from (a) diurnal winds interacting with the diurnal ion drag and (b) upward propagating modes excited by O_3 insolation absorption. The semidiurnal fields interacting with the diurnal component of ion drag, in turn, generate a substantial terdiurnal component. The synthesis of all contributions can yield the signature of a midnight temperature maximum in the upper thermosphere as illustrated in Figure 12.

3. ACCELERATION AND HEATING OF THE LOWER THERMOSPHERE DUE TO DISSIPATING TIDAL WAVES.

In the zonal mean, the atmosphere can be accelerated and heated by the deposition of momentum and thermal energy by the so-called 'eddy' or 'perturbation' motions of the atmosphere. Since gravity wave and tidal amplitudes grow exponentially with height, it has often been suggested that these motions might contribute significantly to the mean momentum and energy budget of the lower thermosphere. These effects enter in the zonal mean momentum equation as a divergence of the eastward eddy momentum flux:

$$\overline{F}_u = \frac{1}{a\cos^2\phi} \frac{\partial}{\partial\phi} (\overline{u'v'}\cos^2\phi) - \frac{1}{p} \frac{\partial}{\partial z} p\overline{u'w'}$$

and in the thermal energy equation as a divergence of the thermal eddy momentum flux:

$$\overline{F}_T = -\frac{1}{a\cos\phi} \frac{\partial}{\partial\phi} (\overline{v'\Phi'_z}\cos\phi) - \frac{1}{p} \frac{\partial}{\partial z} p\overline{w'\Phi'_z},$$

where

a = radius of the earth
ϕ = latitude
z = altitude
p = pressure
u' = perturbation westerly velocity
v' = perturbation northerly velocity
w' = perturbation vertical velocity
Φ'_z = perturbation geopotential

Miyahara (1978) has investigated the deposition of mean momentum and heat in the lower thermosphere connected with the dissipating (1, 1) and (2, 4) tidal modes using the above equations. In Figure 13 Miyahara's calculation of F_u and the resulting mean zonal wind are illustrated.

The (1, 1) mode is apparently capable of producing an easterly jet (~ 60 m sec^{-1}) in the equatorial lower thermosphere, and a westerly flow of order 30 m sec^{-1} at midlatitudes. Results for the (2, 4) mode in Figure 14 indicate mean zonal winds of order 10-15 m sec^{-1}, which are smaller but not negligible compared with the (1, 1) mode. The zonal flow generated by the dissipating tidal modes is comparable to the flow generated by direct solar heating in this altitude regime as computed by Dickinson *et al* (1975).

Recent calculations by Groves and Forbes (1984) indicate that the effects of tidal heating on thermospheric temperature structure appear secondary to the influence of tidal accelerations on the zonal mean wind field of the 90-150 km region.

4. TIDAL EFFECTS ON COMPOSITION

Mayr and Harris (1977) and Forbes (1978) have investigated tidal variations in thermospheric O, O_2, N_2, Ar, He and H using models that take into account the effects of tidal temperatures, horizontal and vertical tidal winds, photo- and ion-chemistry, exospheric transport, and thermal diffussion. Hydrogen tidal variations are dominated by vertical flow due to lateral transport in the exosphere, but wind induced diffusion is the single most important process for causing deviations from diffusive equilibrium (temperature-dominated) solutions of tidal variations in O, O_2, N_2, Ar, and He in the thermosphere. The effects of ion- and photo-chemistry on the variations of O and O_2, and exospheric transport on He, are found to be of secondary or negligible importance above 120 km. Measurements of neutral composition and temperature aboard the AE-E satellite have been analyzed to determine the semidiurnal and terdiurnal variations of O, N_2, He and Ar from 145-295 km (Hedin *et al,* 1980). The semidiurnal variations of O and N_2 are illustrated in Figures 15 and 16, respectively, along with predictions from the MSIS model, the Forbes model, and the Mayr *et al* (1979) model. For O variations, the Forbes and Mayr et al models predict the overall phase and ampltitude structures quite well, with some overestimate of amplitude. Surprisingly, the empirical MSIS does not fit the measurements as well as the theoretical models. On the other hand, the MSIS model provides a much better fit to the semidiurnal amplitude of N_2 whereas the other models overestimate its amplitude. The semidiurnal phases for N_2 are adequately reproduced by Forbes and MSIS models, but the Mayr *et al* model yield phases about 2 h too late above 200 km.

It is well known that winds exert an important influence on the height and density of the F-layer peak. A pronounced example is the dynamic behavior of the nighttime Arecibo ionosphere, particularly the so-called 'midnight collapse' phenomenon, which receives its primary drive from the semidiurnal tide propagating upward from the lower atmosphere. A simulation of the Arecibo ionosphere from the model of Crary and Forbes (1984) is shown in Figure 17. The post-midnight descent (or 'collapse') of the F-layer peak is shown by these authors to be precipitated by a sudden abatement of southward winds determined by a reinforcement of the in-situ excited diurnal component, an upward propagating semidiurnal component, and a terdiurnal component which these authors conjecture to arise from ion-drag coupling between the semidiurnal wind and the diurnal component of ion drag. In addition, the bunching of contours in the bottomside F-region as illustrated in Figure 17 is due to the vertical shear of the semidiurnal wind field, and may produce electron density gradients sufficient to excite the ExB gradient drift instability.

REFERENCES

Crary, D. J. and J. M. Forbes (1984), The Dynamic Ionosphere over Arecibo, A Theoretical Investigation, submitted to *J. Geophys. Res.*

Dickinson, R. E., Ridley, E. C., and Roble, R. G. (1975), Meridional Circulation in the Thermosphere, *J. Atmos. Sci. 32,* 1737-1735.

Forbes, J. M. (1979), Tidal variations in Thermospheric O, O_2, N_2, Ar, He and H, *J. Geophys. Res. 83,* 3691-3698.

Forbes, J. M. (1982), Atmospheric Tides. I, Model Description and Results for the Solar Diurnal Component. *J. Geophys. Res. 37,* 5222-5240.

Forbes, J. M. (1982), Atmospheric Tides. II. The Solar and Lunar Semidiurnal Components, *J. Geophys. Res. 37,* 5241-5252.

Garrett, H. B., and J. M. Forbes (1978), Tidal Structure of the Thermosphere at Equinox, *J. Atmos. Terr. Phys. 40,* 657-668.

Groves, G. V., and J. M. Forbes (1984), Equinox Tidal Heating of the Upper Atmosphere, *Plant. Space. Sci. 32,* 447-456.

Hedin, A. E., Spencer, N. W., and Mayr, H. G. (1980), The Semidiurnal and Terdiurnal Tides in the Equatorial Thermosphere from AE-E Measurements, *J. Geophys. Res. 85,* 1787-1791.

Mayr, H. G., Harris, I. (1977), Diurnal Variations in the Thermosphere -2. Temperature, Composition, Winds, *J. Geophys. Res. 82,* 2628-1640.

Mayr, H. G., Harris, I., Spencer, N. W., Hedin, A. E., Wharton, L. E., Porter, H. S., Walker, J. C. G., and Carlson, H. C. (1979), Atmospheric Tides and the Midnight Temperature Anomaly, *Geophys. Res. Lett. 6,* 447-450.

Miyahara, S. (1978), Zonal Mean Winds induced by Vertically Propagating Atmospheric Tidal Waves in the Lower Thermosphere, *J. Meteor. Soc. Japan 56,* 36-98.
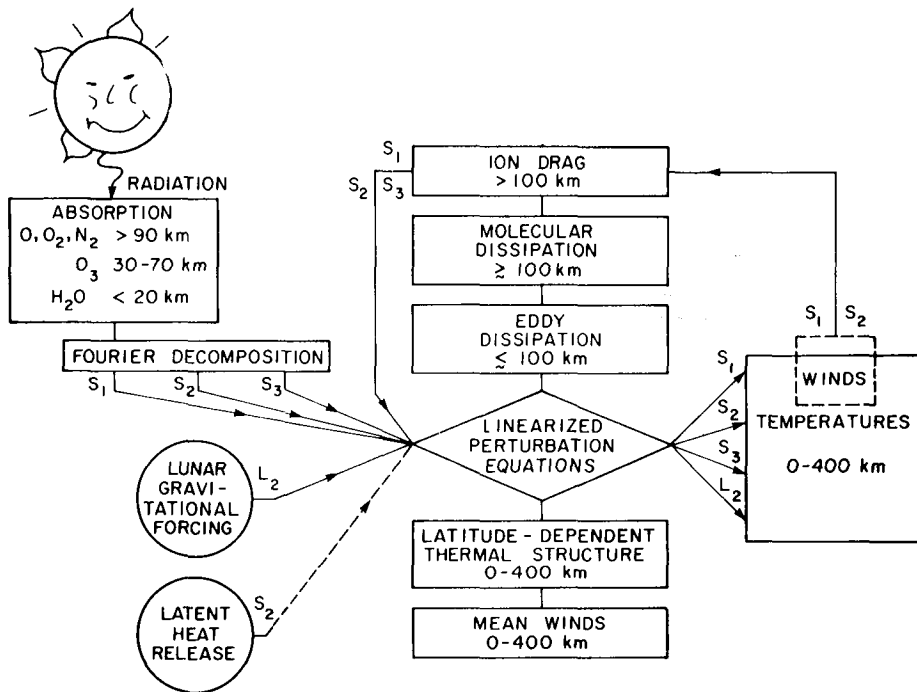
Figure 1. Schematic describing the numerical model of atmospheric tides developed by Forbes (1982 a, b).
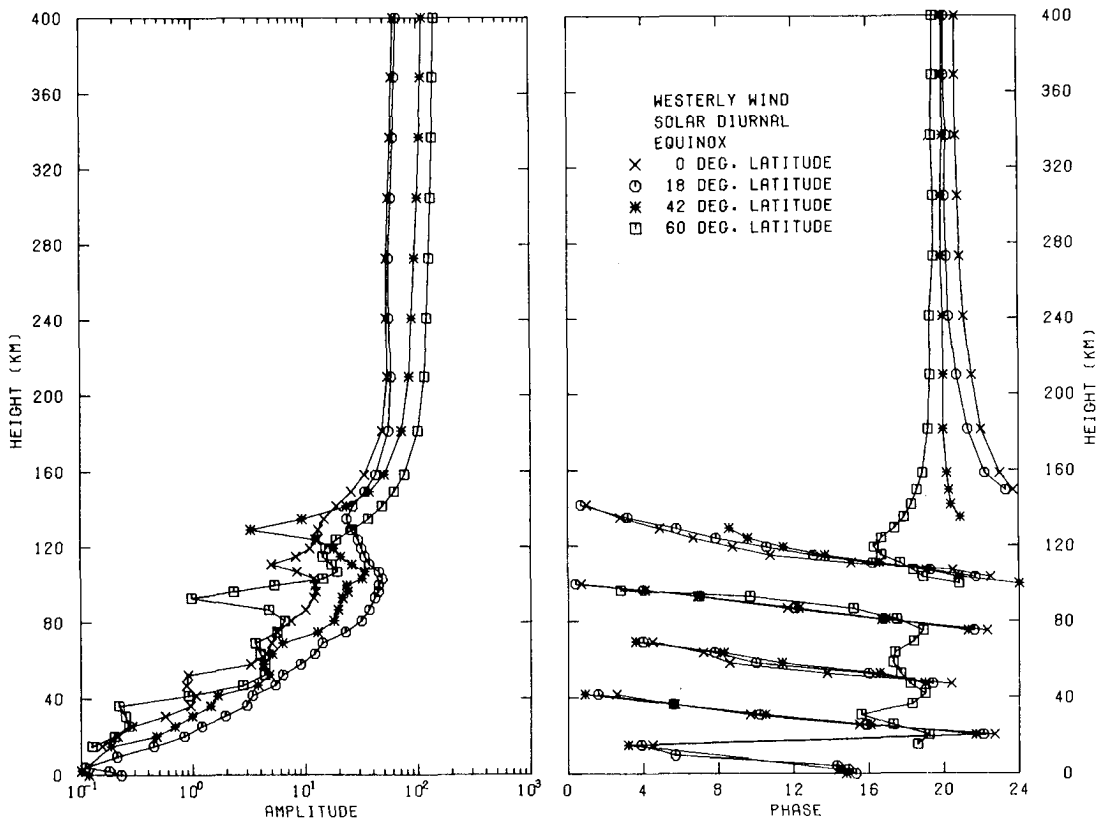
Figure 2. Diurnal westerly winds from the Forbes (1982 a, b) model.
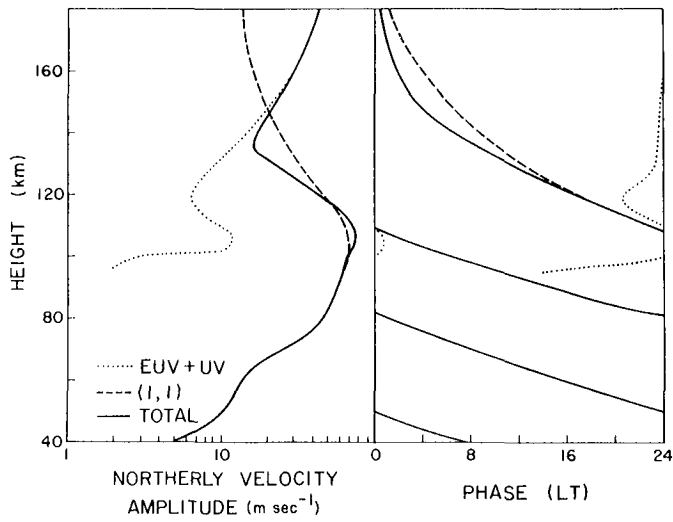
Figure 3. Northerly velocity at 18° latitude due to in situ excitation, the propagating (1, 1) Mode, and the sum of these components.
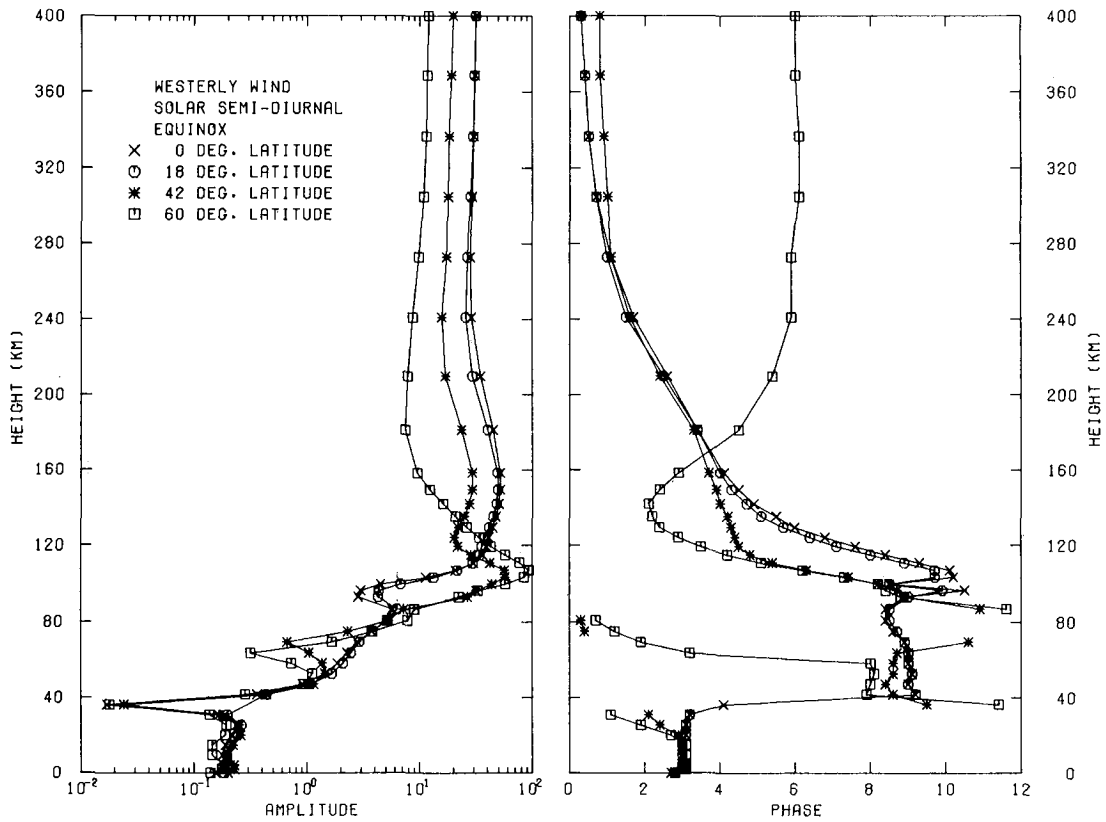
Figure 4. Solar semidiurnal westerly winds from the Forbes (1982 a, b) model.
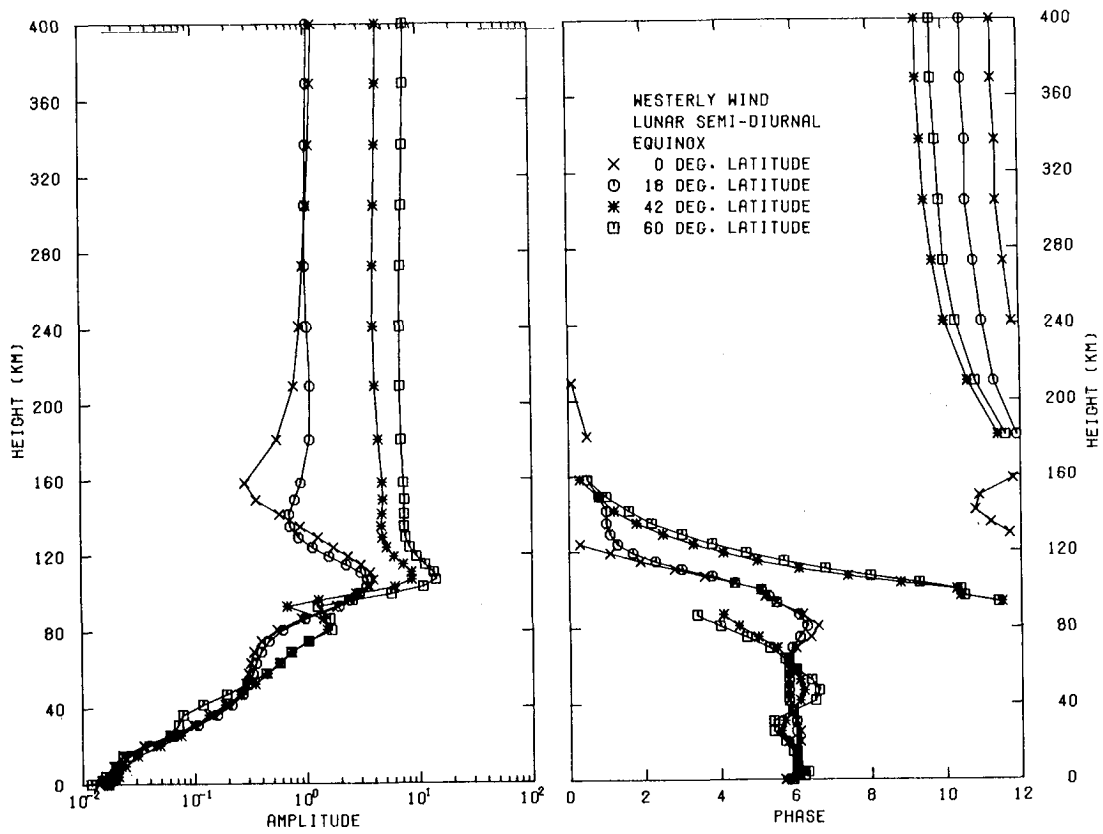
Figure 5. Lunar semidiurnal westerly winds from the Forbes (1982 a, b) model.

87
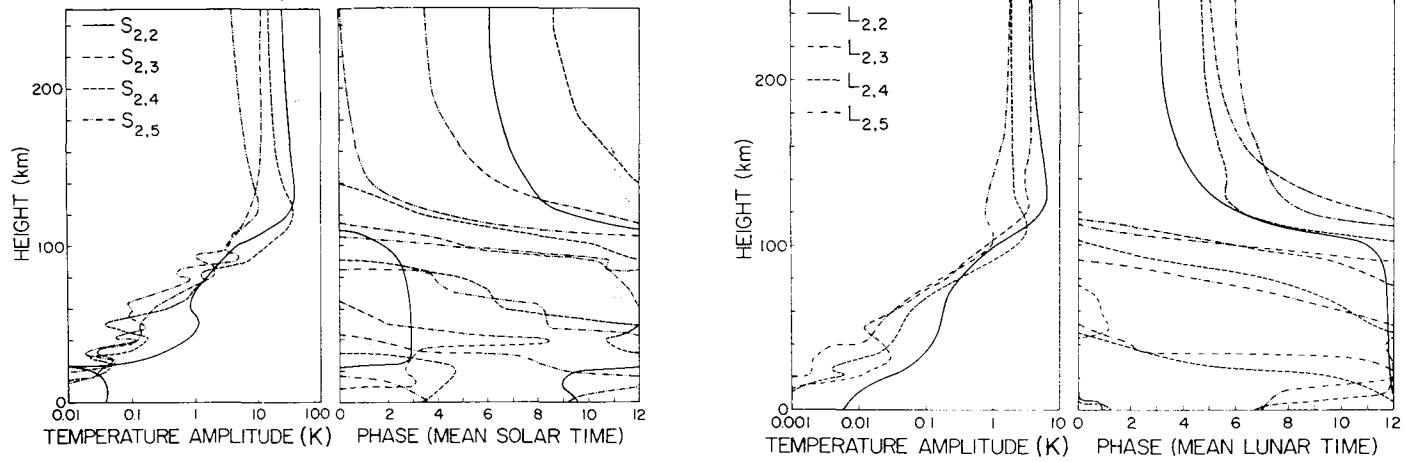
Figure 6. Hough mode decompositions of solar and lunar semidiurnal temperatures excited in the lower thermosphere.
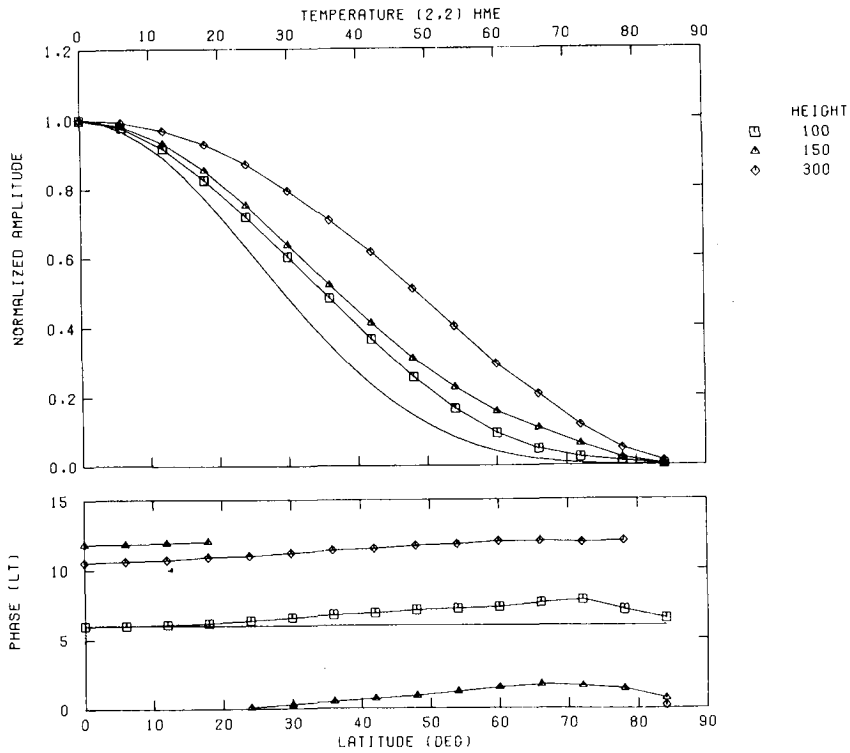
Figure 7. Normalized temperature oscillation amplitude and phase
vertical structures of the (2, 2) Hough Mode Extension at 100,
150, and 300 km for T_o = 1000 K with normalizing factors equal to
1.00, 7.00, and 4.87, respectively.
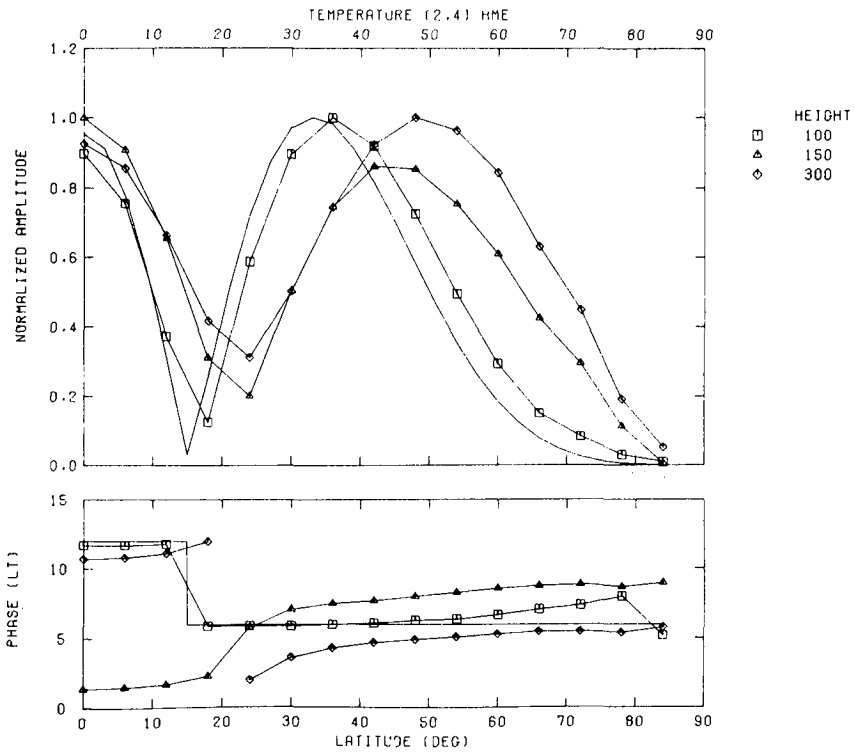
Figure 8. Normalized temperature oscillation amplitude and phase vertical structures of the (2, 4) Hough Mode Extension at 100, 150, and 300 km, for T_o = 1000 K with normalizing factors equal to 1.00, 2.91 and 1.88, respectively.

90
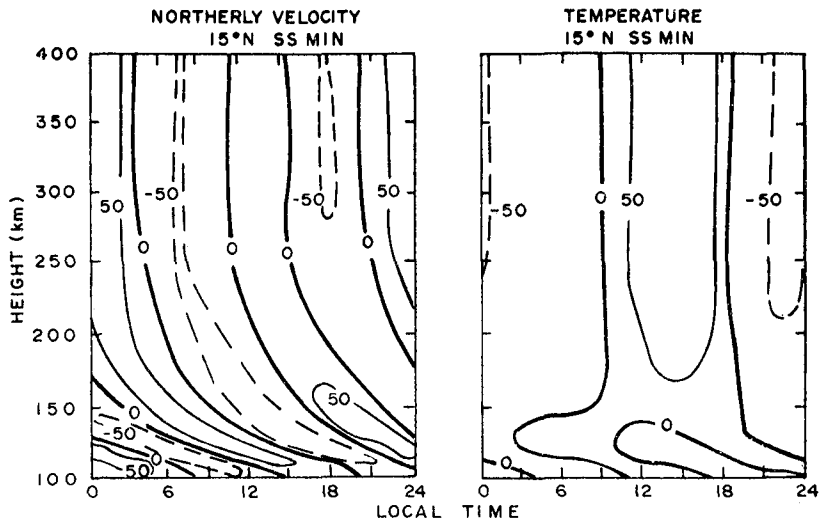
Figure 9. Wind and temperature contours from the model of
Garrett and Forbes (1978).
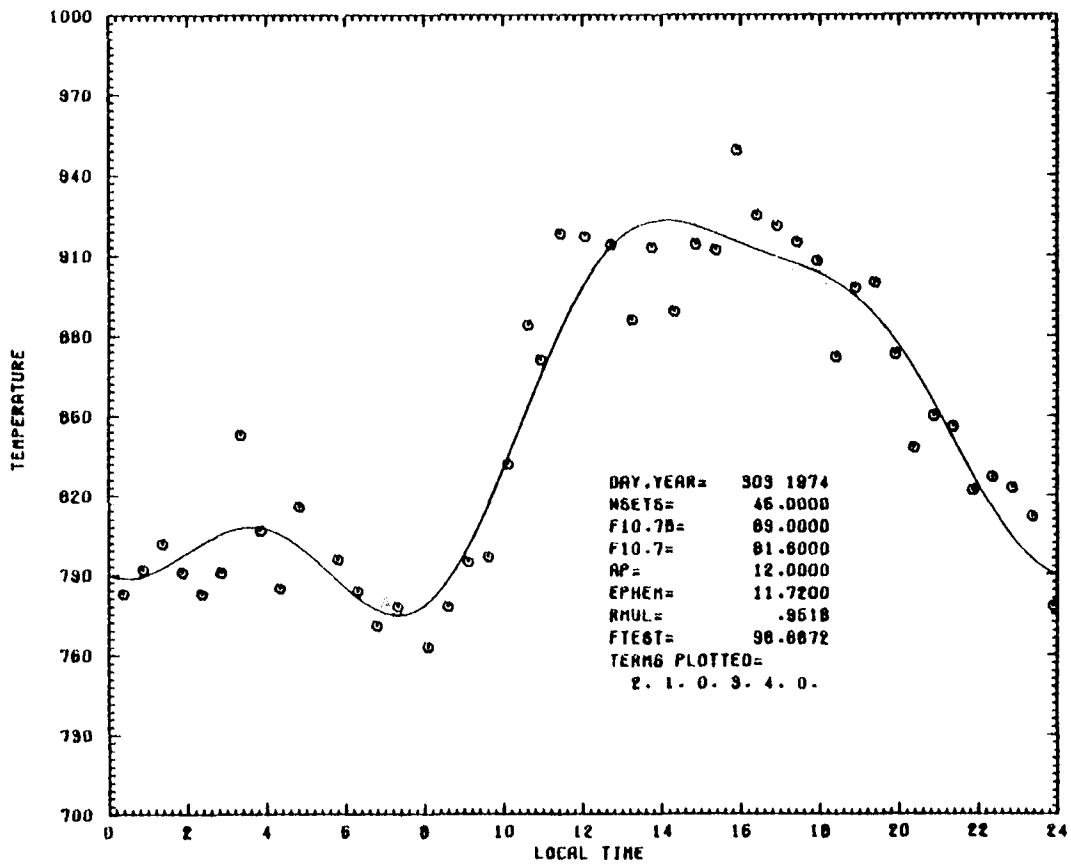
Figure 10. Example of Millstone Hill neutral exospheric temperature data during a
magnetically quiet day at solar minimum.
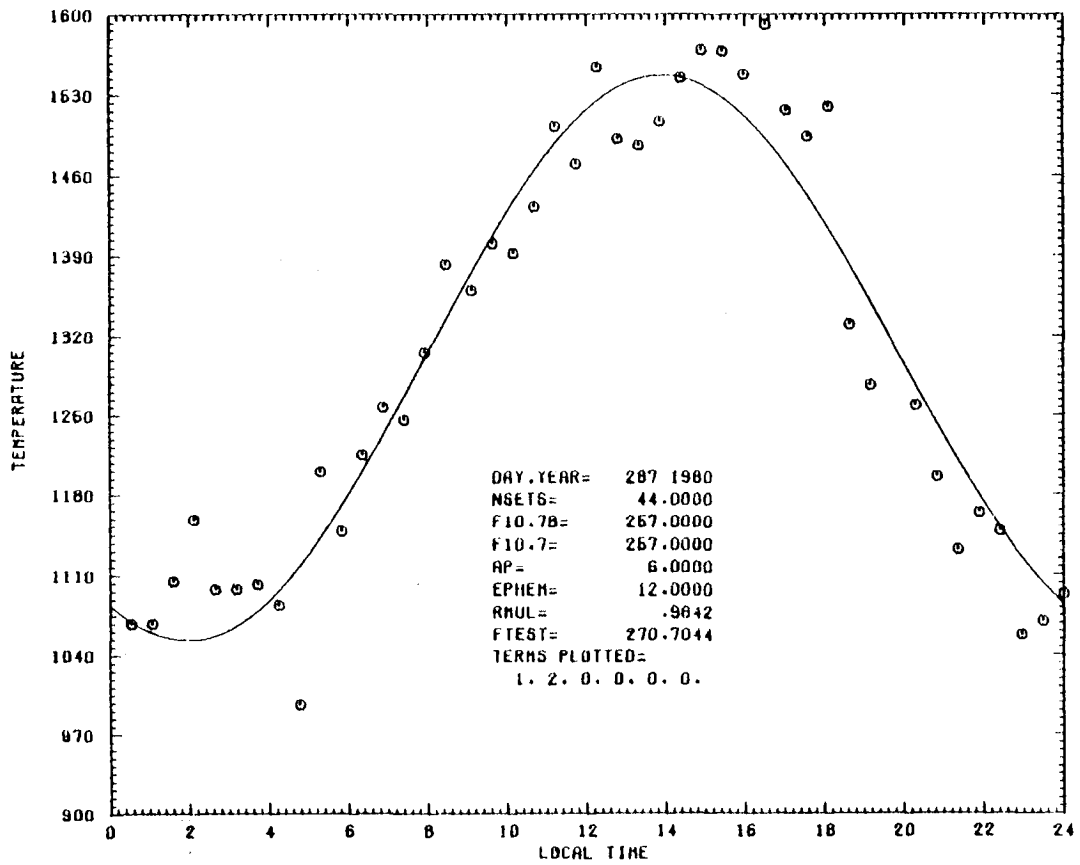
Figure 11. Example of Millstone Hill Neutral Exospheric Temperature Data During a Magnetically Quiet Day at Solar Maximum.
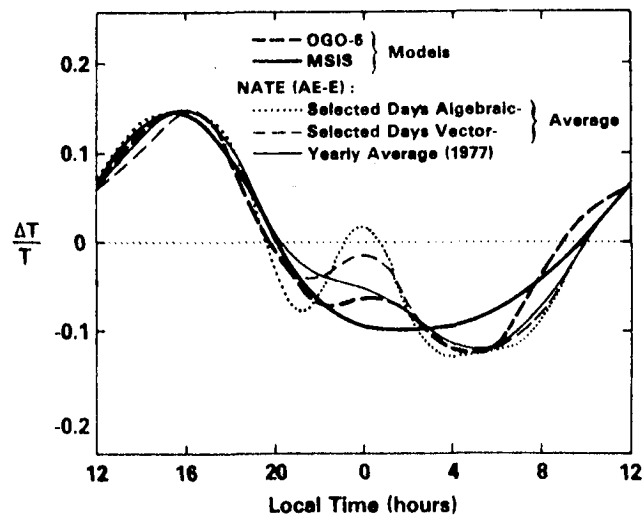
Figure 12. Comparisons between OGO-6 and
MSIS models at 250 km and fourier analyzed in-
Situ T_g measurements from the NATE
experiment on AE-E (Mayr, et al., 1979).
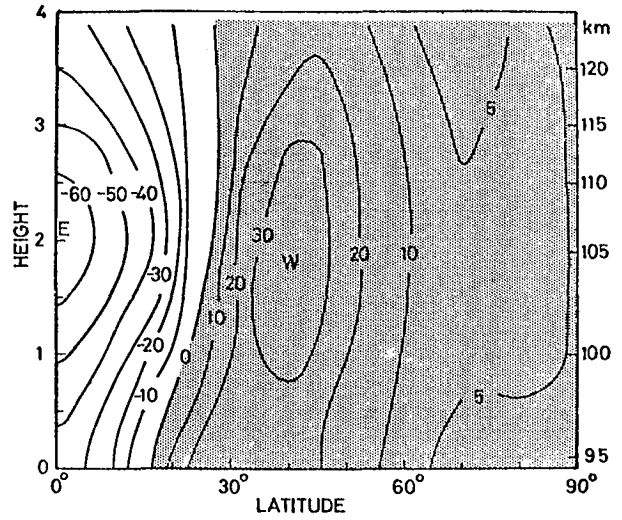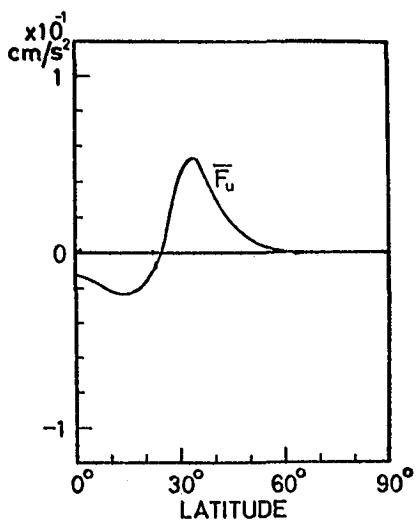
Figure 13. Divergence of eddy momentum flux (F_u) and zonal mean wind due to (1, 1) tidal mode (Miyahara, 1978).
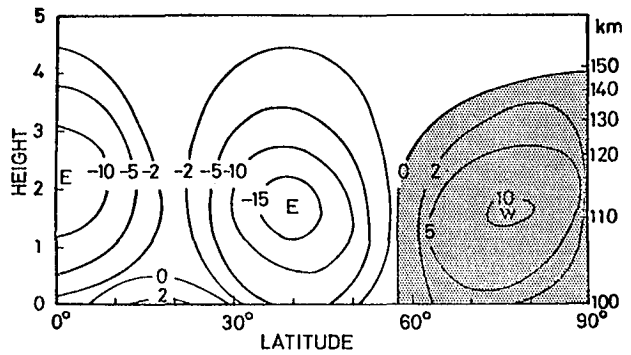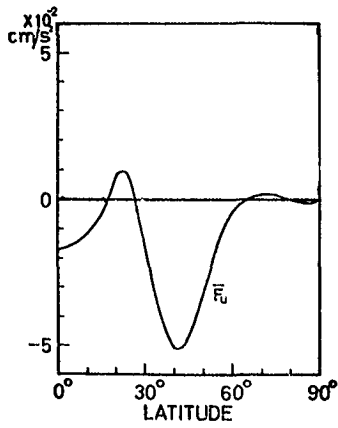
Figure 14. Divergence of eddy momentum flux (F_u) and zonal mean wind due to (2, 4) Mode. (Miyahara, 1978).

94
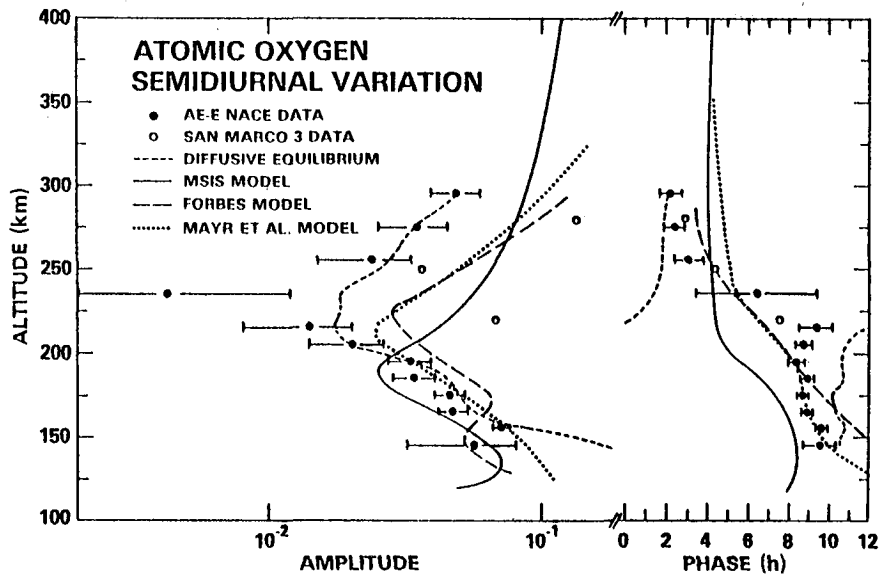
Figure 15. Atomic oxygen semidiurnal variations (Hedin, et al., 1980)
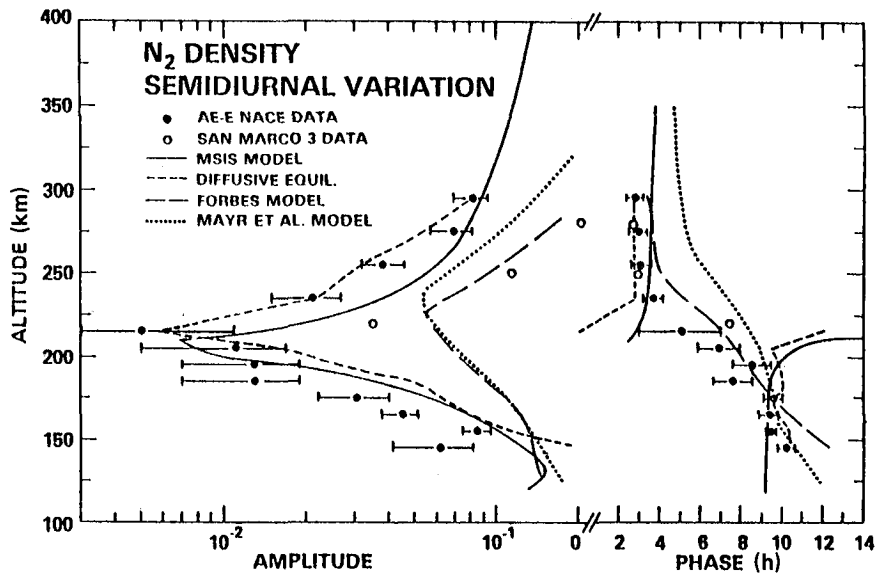
Figure 16. Molecular nitrogen semidiurnal variations (Hedin, et al., 1980).
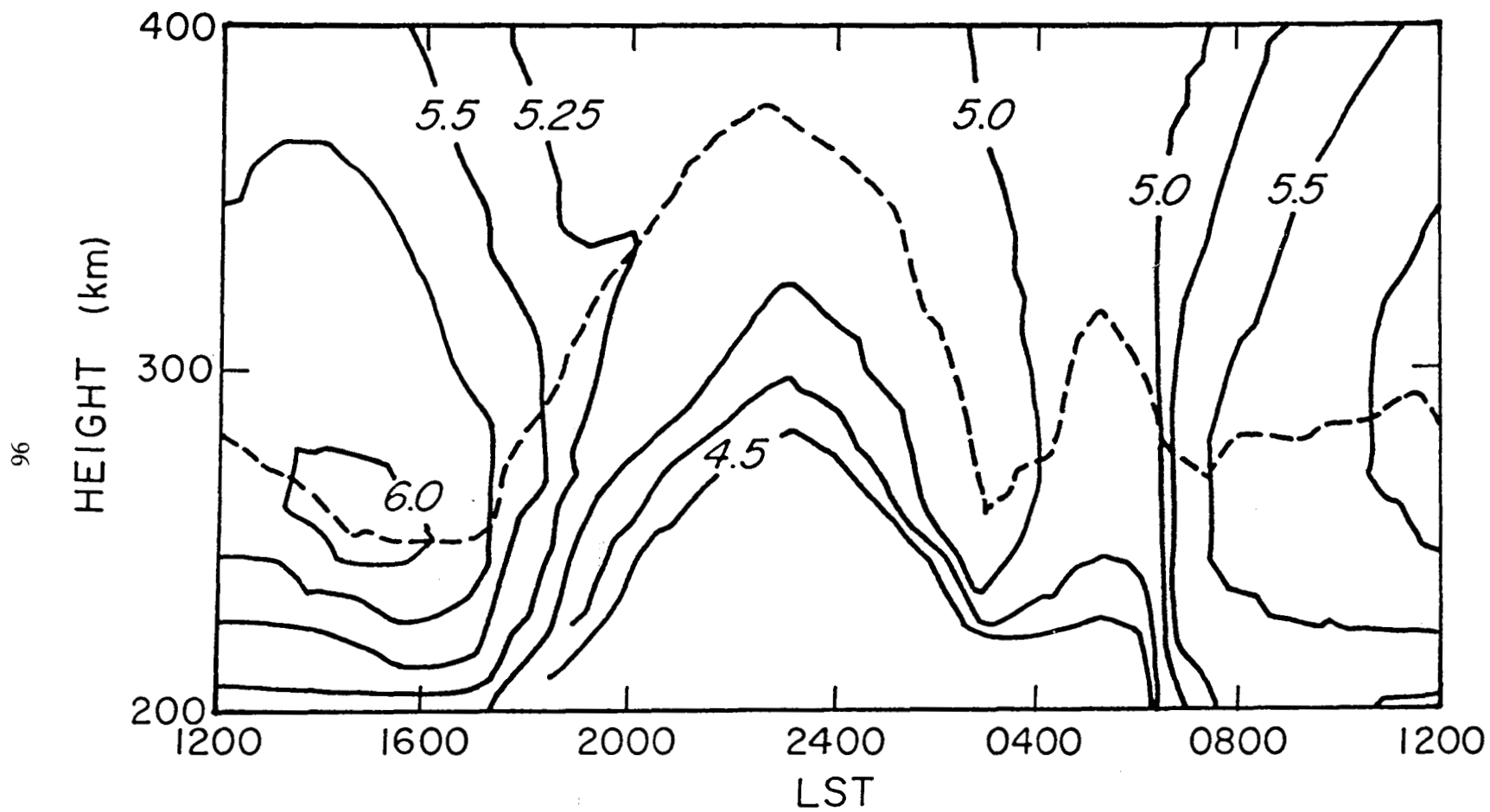
Figure 17. Log electron density contours and height of F-layer maximum density (dashed line) simulated for equinox conditions over Arecibo using the model of Crary and Forbes (1984).

THE EFFECT OF BREAKING GRAVITY WAVES ON THE DYNAMICS AND CHEMISTRY OF THE MESOSPHERE AND LOWER THERMOSPHERE
(Invited Review)

Rolando R. Garcia
National Center for Atmospheric Research*
P.O. Box 3000
Boulder, Colorado 80307

The influence of breaking gravity waves on the dynamics and chemical composition of the 60-110 km region is investigated with a two-dimensional model that includes a parameterization of gravity wave momentum deposition and diffusion.

The dynamical model is that described by Garcia and Solomon (1983) and Solomon and Garcia (1983) and includes a complete chemical scheme for the mesosphere and lower thermosphere. The paramaterization of Lindzen (1981) is used to calculate the momentum deposited and the turbulent diffusion produced by the gravity waves.

It is found that wave momentum deposition drives a very vigorous mean meridional circulation, produces a very cold summer mesopause and reverses the zonal wind jets above about 85 km (Fig. 1). The momentum deposition and turbulent diffusion are much weaker at equinox than at solstice (Fig. 2). In Figure 3 the seasonal variation of the turbulent diffusion coefficient is consistent with the behavior of mesospheric turbulence inferred from MST radar echoes (Balsley *et al.,* 1983; see Fig. 3 a, b).

The large decreases in turbulent diffusion at the equinoxes have profound effects on the distribution of certain chemical trace species. In particular, atomic oxygen in the lower thermosphere increases at the equinoxes because loss through diffusion into the sink region below $\simeq 90$ km is reduced. This increase in atomic oxygen is reflected in the greater intensity of the 5577Å green line airglow emission. The model reproduces very well the observed seasonal variation of the green line airglow (Fig. 4).

Ozone in the upper mesosphere is destroyed efficiently by HO_x ($H + OH + HO_2$) catalysis. HO_x abundance at the 80 km level depends sensitively on the concentration of water vapor, which in turn is determined by upward diffusion from the lower mesosphere. At equinox, the diffusive flux of H_2O is reduced, HO_x abundances decrease and O_3 increases in the upper mesosphere. The 1.27 μm O_2 airglow is a proxy for O_3 abundances at 80 km. Fig. 5 shows that the model reproduces the major features of the seasonal variation of 1.27 μm airglow observed by the SME satellite (Thomas *et al.,* 1984).

In conclusion, the large degree of consistency between model results and various types of dynamical and chemical data supports very strongly the hypothesis that breaking gravity waves play a major role in determining the zonally-averaged dynamical and chemical structure of the 60-110 km region of the atmosphere. A detailed account of this work is given in Garcia and Solomon (1984).

REFERENCES

Balsley, B. B., W. L. Ecklund, and D. C. Fritts, 1983: VHF echoes from the high-latitude mesosphere and lower thermosphere: Observations and interpretations, *J. Atmos. Sci.,* *40,* 2451-2466.

Cogger, L. L., R. D. Elphinstone, and J. S. Murphree, 1981: Temporal and latitudinal 5577Å airglow variations. *Can. J. Phys., 59,* 1296-1307.

Garcia, R. R., and S. Solomon, 1983: A numerical model of the zonally-averaged dynamical and chemical structure of the middle atmosphere. *J. Geophys. Res., 88,* 1379-1400.

Garcia, R. R., and S. Solomon, 1984: The effect of breaking gravity waves on the dynamics and chemical composition of the mesosphere and lower thermosphere, *J. Geophys. Res.* (submitted).

Lindzen, R. S., 1981: Turbulence and stress owing to gravity wave and tidal breakdown. *J. Geophys. Res., 86,* 9707-9714.

Solomon, S., and R. R. Garcia, 1983: On the distribution of nitrogen dioxide in the high latitude stratosphere. *J. Geophys. Res., 88,* 5229-5239.

Thomas, R. J., C. A. Barth, and S. Solomon, 1984: Seasonal variations of ozone in the upper mesosphere and gravity waves. *Geophys. Res. Lett.,* (in press).
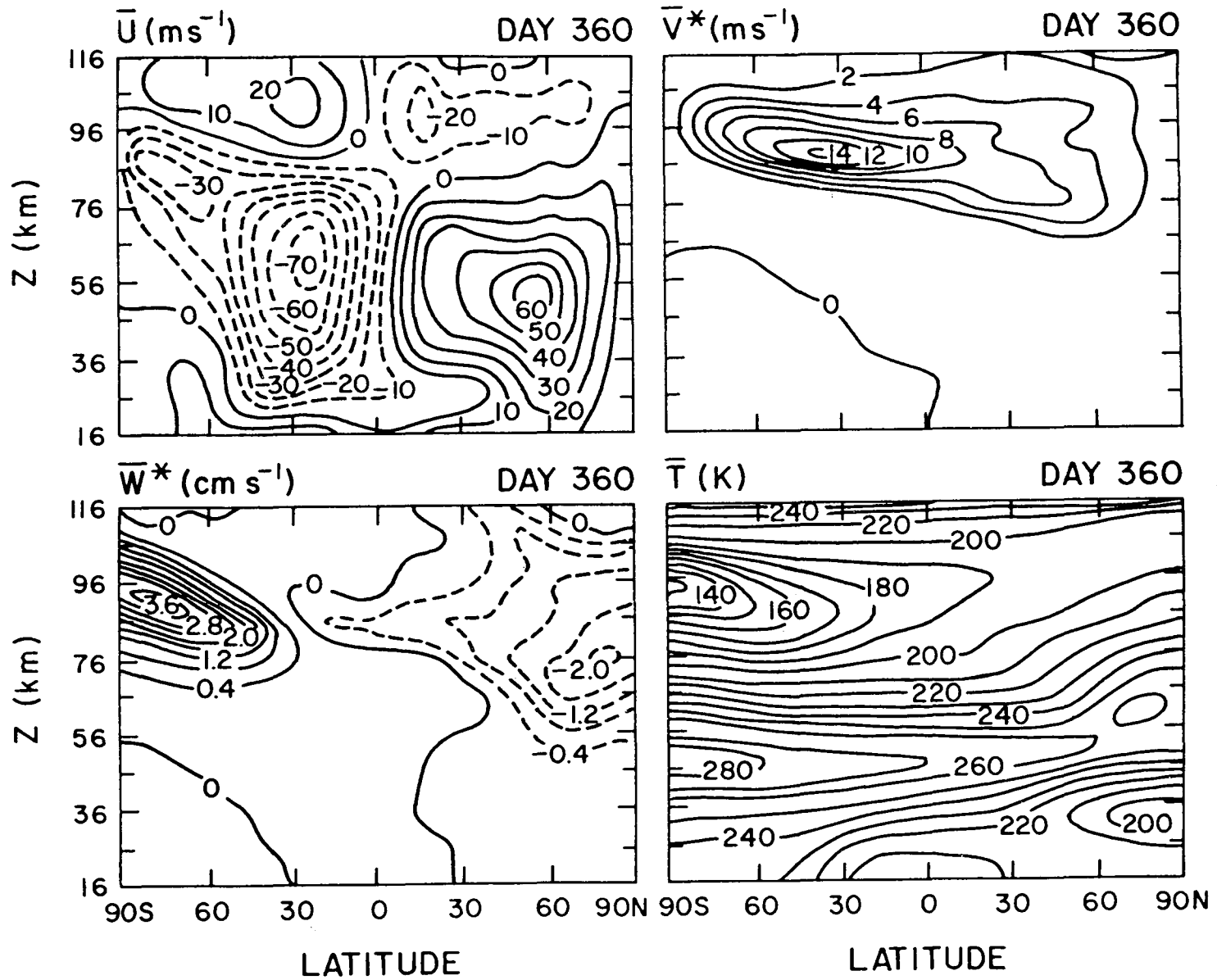
Figure 1. Zonally averaged circulation and temperature for model northern hemisphere winter solstice.
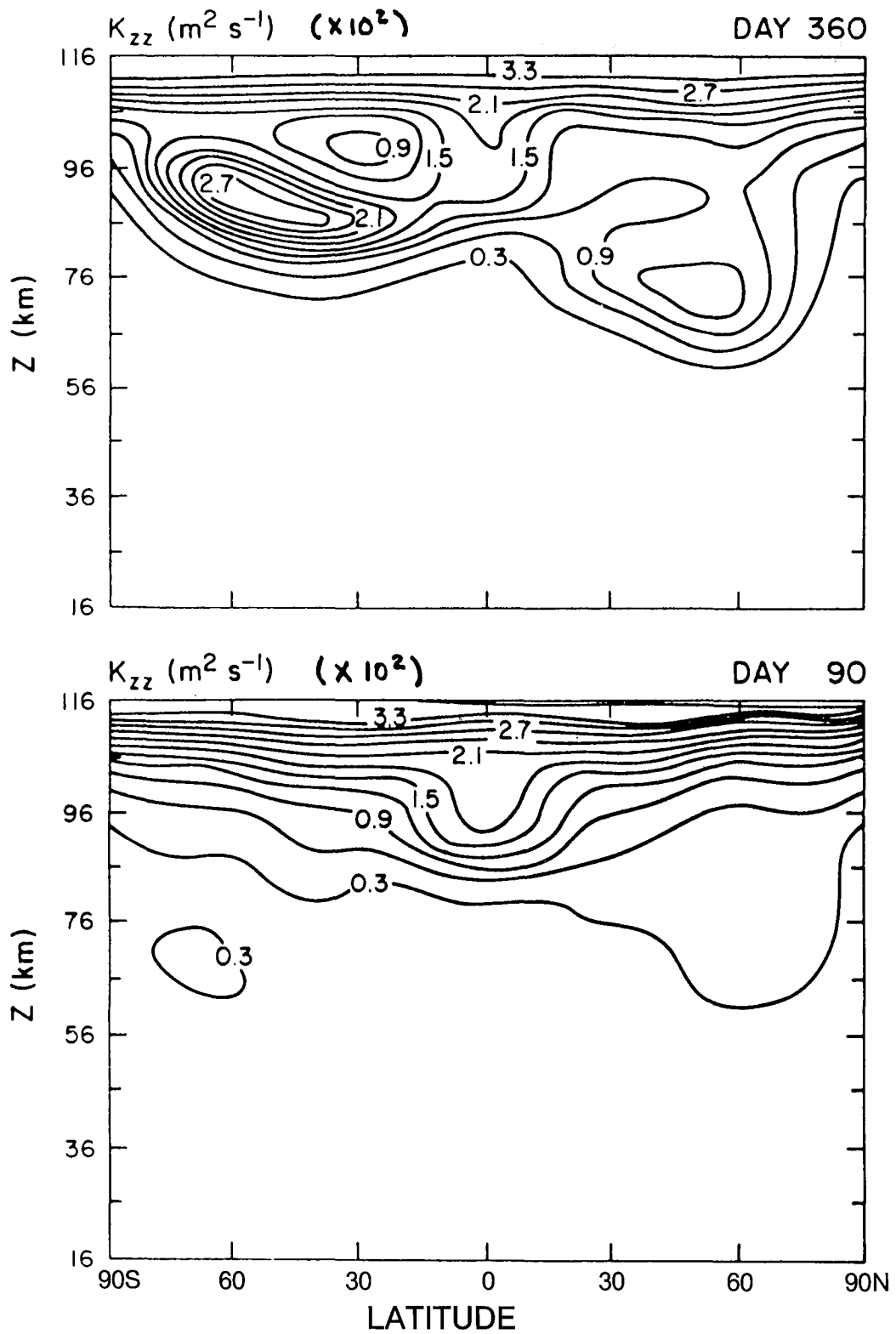
Figure 2. Vertical eddy diffusion coefficient due to breaking gravity waves for solstice and equinox.
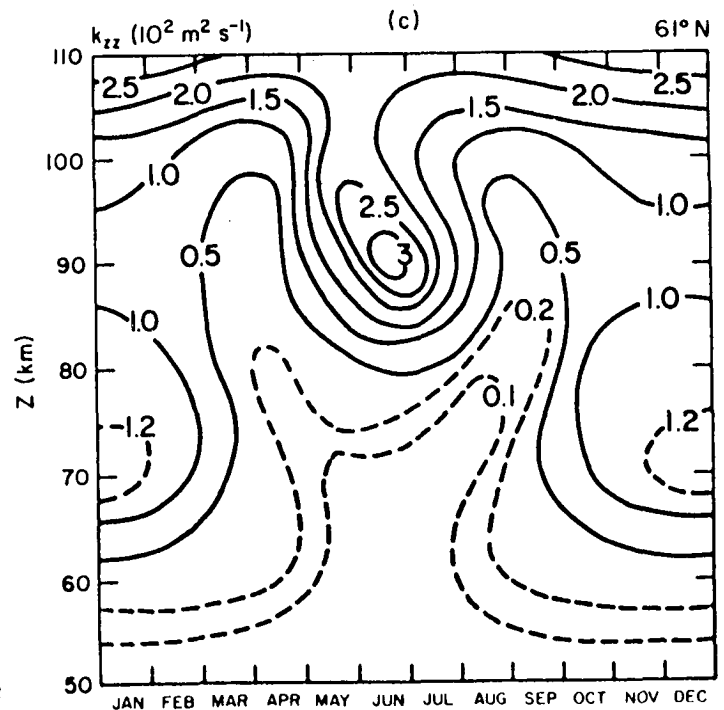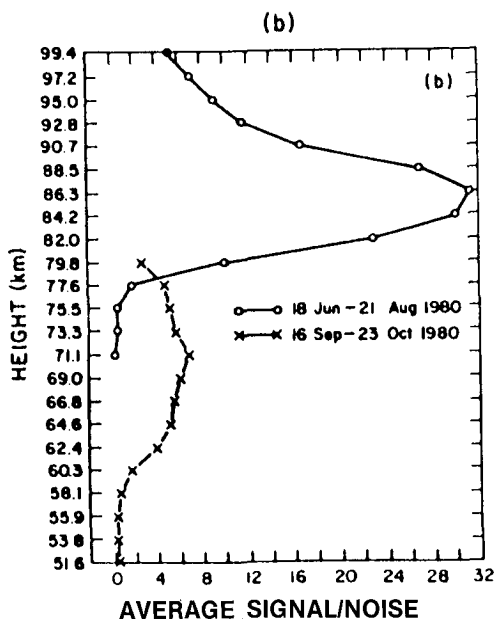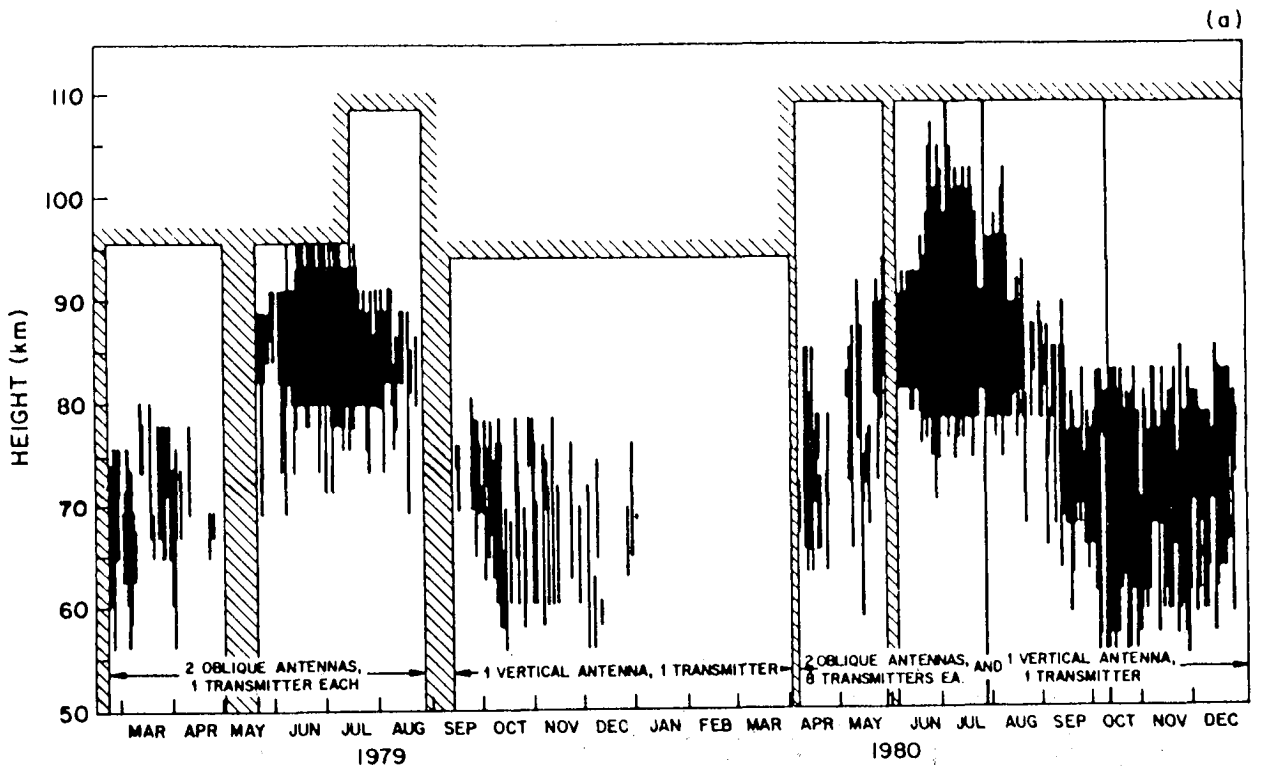
Figure 3. (a) Height distribution of MST radar echoes at Poker Flat (65 °N) as a function of season. Cross-hatched areas denote periods and altitudes for which no data are available. (From Balsley et al., 1983). (b) Vertical profiles of radar echo signal-to-noise ratio for summer (June 18-August 21, 1980 average) and fall (September 16-October 23, 1980). (Balsley et al., 1983). (c) Seasonal variation of the turbulent diffusion coefficient at 61 ° north latitude.

101
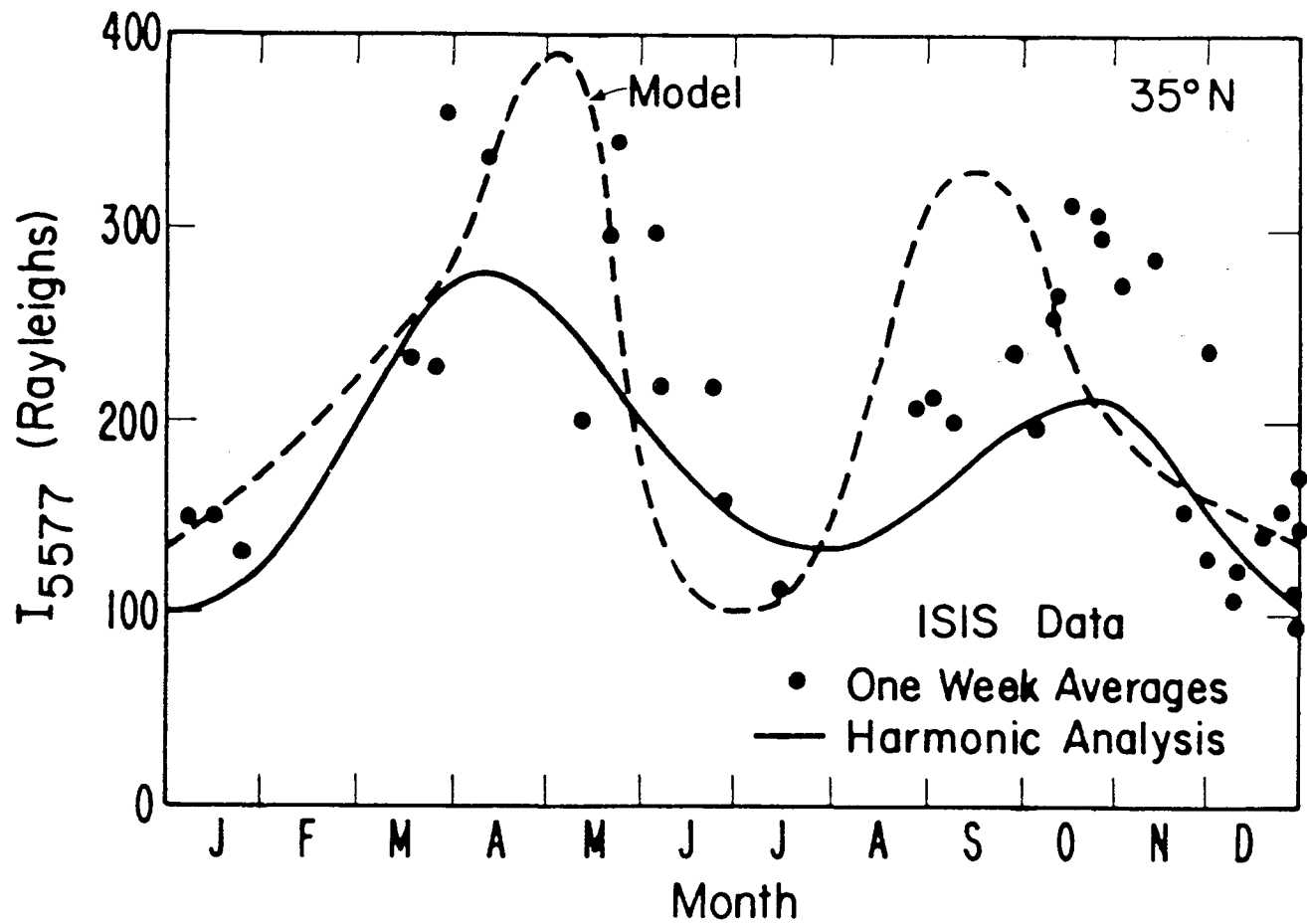
Figure 4. Seasonal variation of the atomic oxygen green line (5577 Å) emission intensities observed by the ISIS satellite at 35°N adapted from (Cogger et al., 1981) compared with model calculations.

EQUINOX/SOLSTICE O₃ COMPARISON
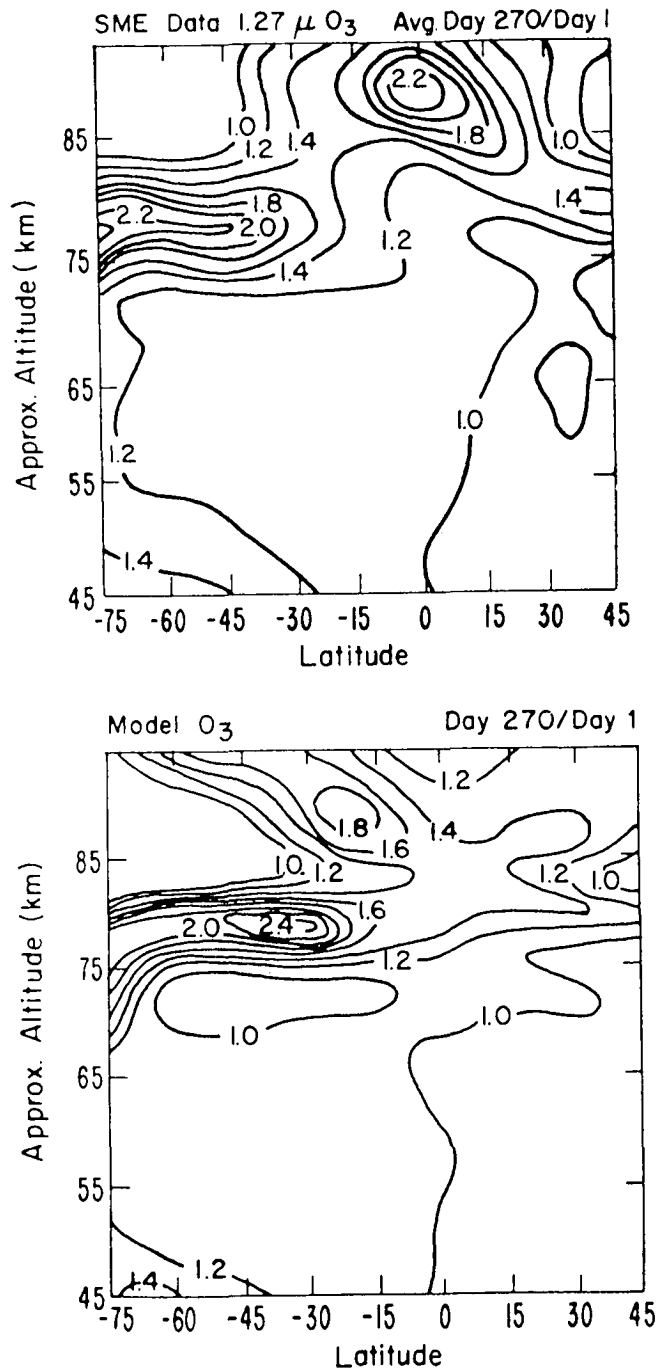
Figure 5. Top panel: Ratio of O_3 observations by the Solar Mesosphere Explorer satellite (Thomas *et al.*, 1984) for one week averages about day 270 to day 1 (southern hemisphere spring/summer; northern hemisphere fall/winter). Bottom panel: Same, as computed by the model.

THERMOSPHERIC NITRIC OXIDE AND ITS ROLE IN
THERMOSPHERIC DYNAMICS AND COMPOSITION

J-Cl. Gerard

Institut d'Astrophysique, Universite de Liége - B4200 Cointe-Liége Belgium
and
R. G. Roble
National Center for Atmospheric Research - P.O. Box 3000 - Boulder Colorado 80307

The global distribution of thermospheric nitric oxide has been measured under different geophysical conditions by the Atmosphere Explorer (AE) and Solar Mesosphere Explorer (SME) satellites. These observations show a great variability in the NO concentration but the existence of a latitudinal gradient is clearly evidenced by statistical maps of the NO meridional distribution. A two-dimensional zonally averaged chemical-dynamical model has been used to investigate the importance of nitric oxide 5.3 μm cooling and its role on thermospheric temperature, dynamics and major gas composition.

For this purpose, a 2-D background atmosphere code and an odd nitrogen code have been coupled and run to steady state. The NO distribution obtained is in good agreement with the AE-D global picture calculated at solstice for solar minimum activity. The importance of each term in the thermodynamic equation has been studied spatially. It is found that the NO I.R. cooling term competes with conduction in the upper thermosphere and reaches its maximum value near 200km at high summer latitudes.

The primary effect of including the NO cooling term is to increase the temperature in the upper winter thermosphere and decrease it in the other hemisphere, if the global average temperature is fixed. In general, the strength of the circulation is decreased and the thermal gradient is smoother. As a consequence of these changes in the wind and temperature fields, the O_2, N_2 and O densities also react to the effect of the NO cooling. The importance of this process depends on the level of solar activity which controls the NO distribution.
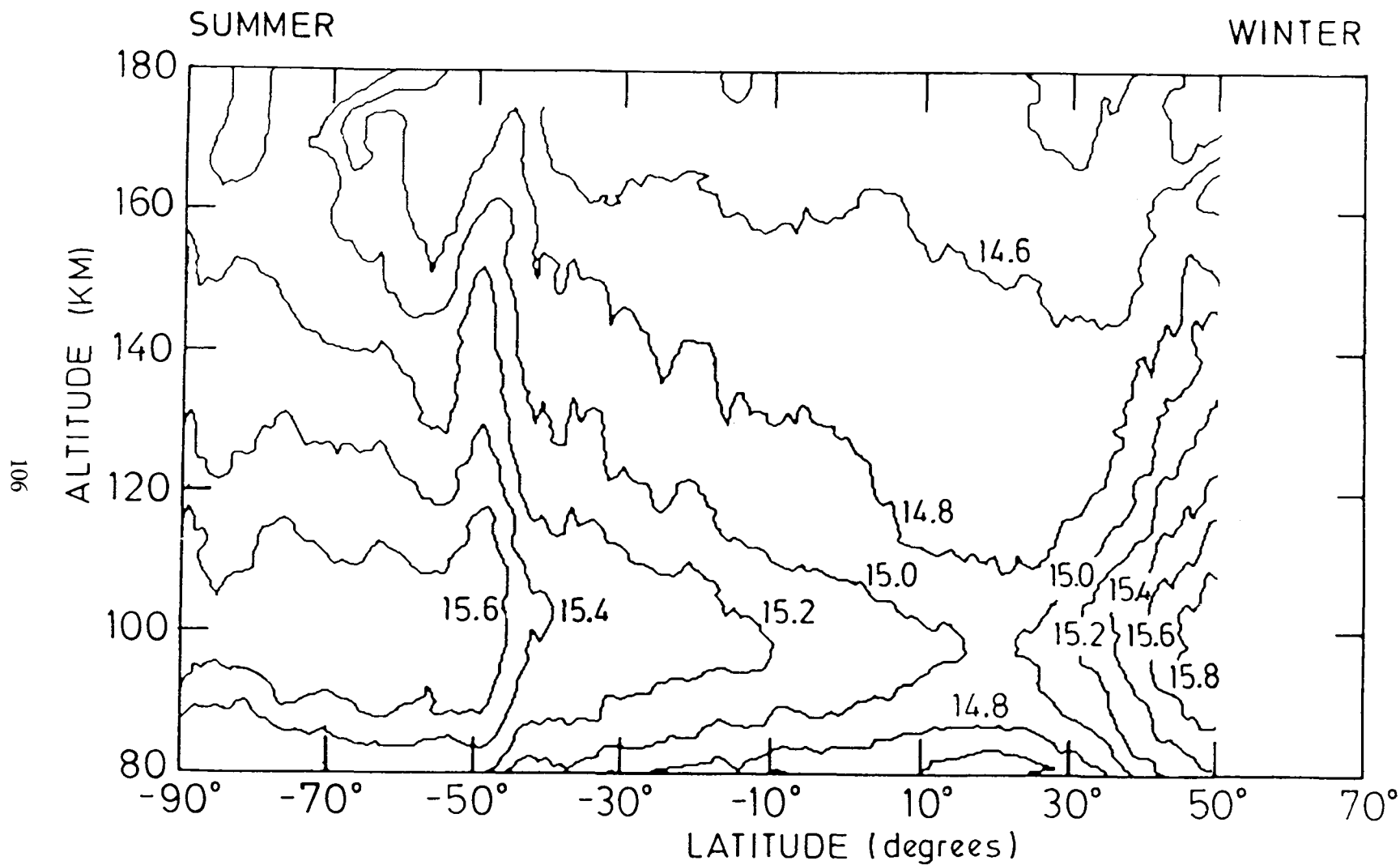
Figure 1. Log$_{10}$ of horizontal column densities (cm^{-2}) of NO observed with the UVNO experiment on the Atmosphere Explorer-D (AE-D) satellite.
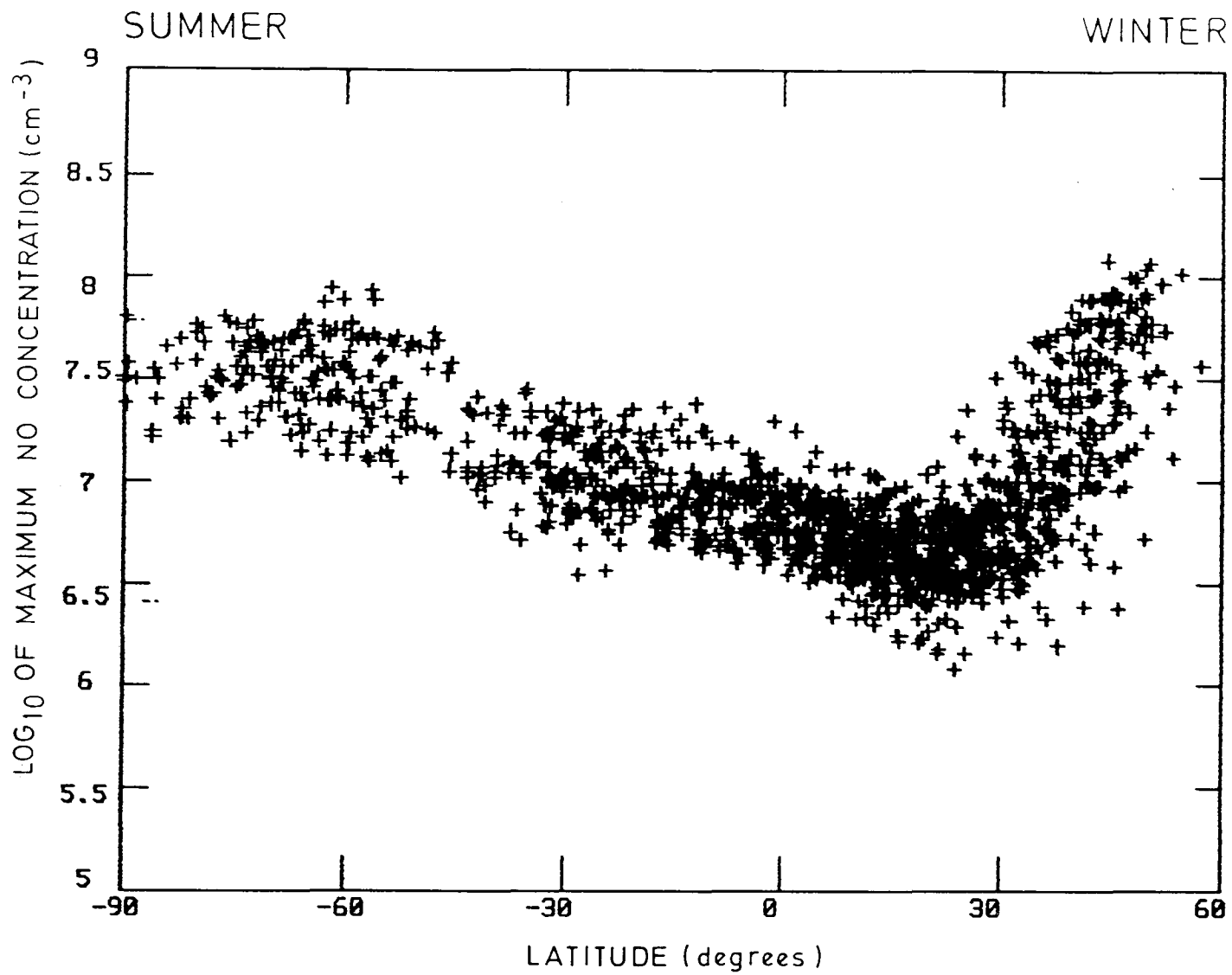
Figure 2. Latitudinal distribution of $\log_{10}$ of the NO peak concentration measured from AE-D ("spinning orbits").
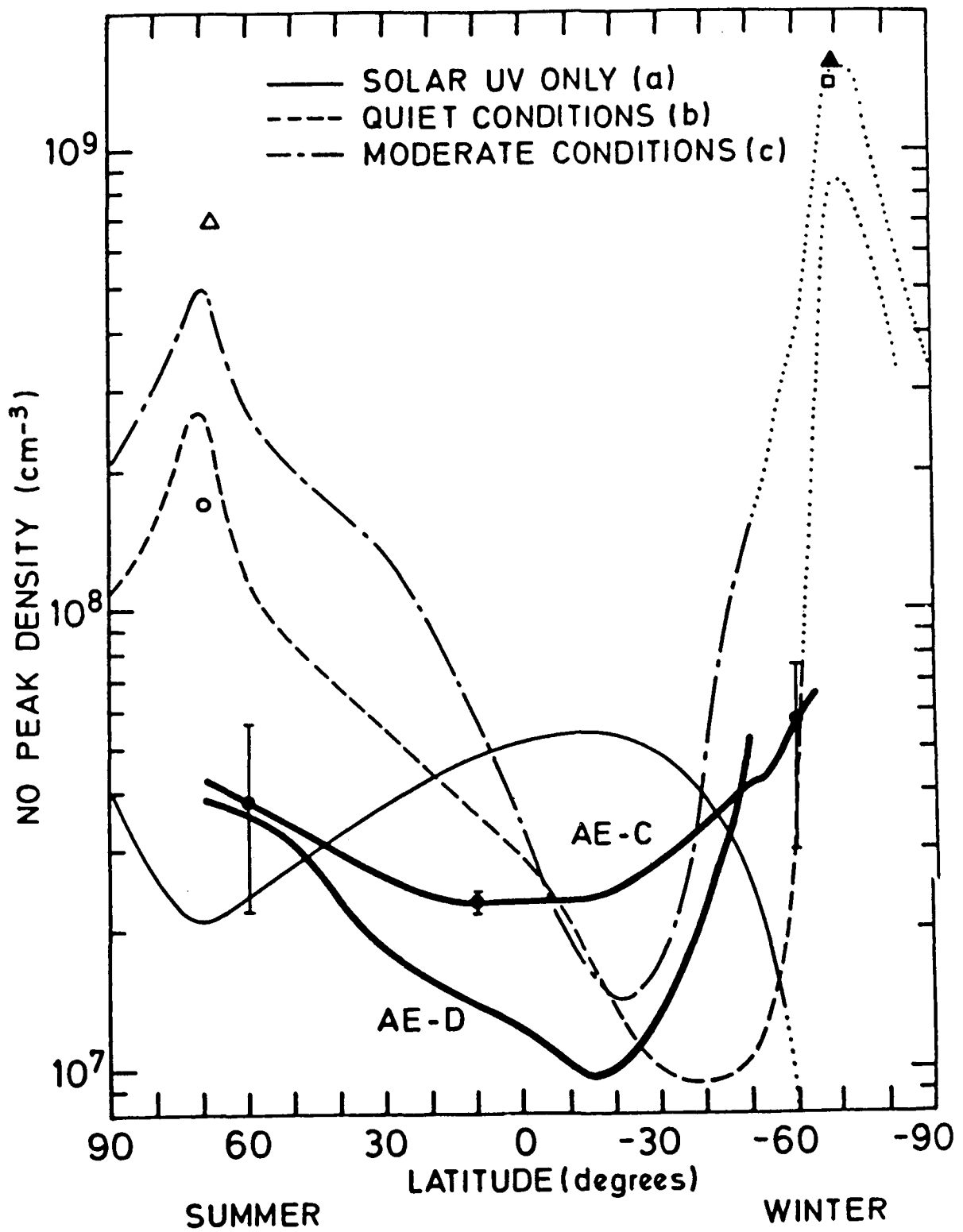
Figure 3. Comparison between NO peak densities obtained with the 2-D odd nitrogen model and AE-C, AE-D and high latitude rocket measurements.
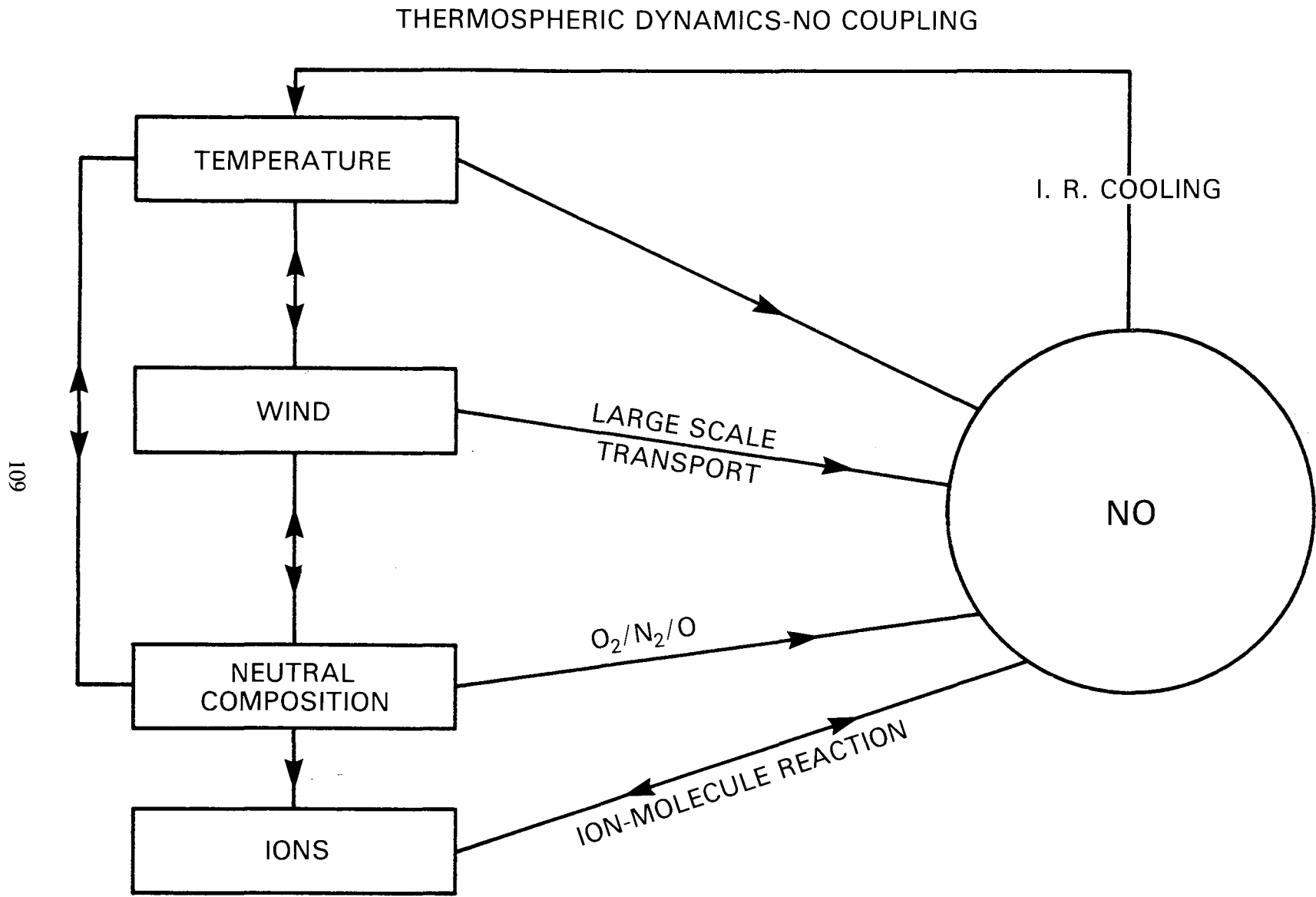
Figure 4. Block diagram of the coupling between the thermospheric structure and the nitric oxide concentration.

MODEL EQUATIONS

CONTINUITY:

$$\frac{d\rho}{dt} + \rho \, \text{div} \, \vec{v} = 0$$

THERMODYNAMIC:

$$\rho c_v \frac{dT}{dt} = - \, \text{div} \, \vec{\phi}_h - P \, \text{div} \, \vec{v} + Q$$

MOMENTUM:

$$\frac{d\vec{v}}{dt} = -2\vec{\Omega} \times \vec{v} - \frac{1}{\rho} \, \text{grad} \, P + \vec{g} + \nu \nabla^2 \vec{v} - \lambda \vec{v}$$

HYDROSTATIC:

$$\frac{\partial P}{\partial z} = - \frac{P}{H}$$

PERFECT GAS LAW:

$$P = \rho \, k \, T/\overline{m}$$

CHEMICAL:

$$\frac{\partial \, (n_i \, m_i \, \rho)}{\partial t} = p_i - l_i \, (n_i \, m_i \, \rho) - \text{div} \, \vec{\phi}_i$$

$$\vec{\phi}_i = n_i \, m_i \, \rho \, \vec{v} + \vec{\phi}_{\text{diff}}$$

Figure 5. Equations of the 2-D model of the
thermospheric structure.

NITRIC OXIDE I. R. COOLING

$$L_{NO} = h\nu \, [NO]_{v=1} \, A_{1,0}$$

$$= h\nu \, A_{1,0} \, \omega \, [NO]_{v=0} \, e^{-\frac{h\nu}{kT}}$$

WITH:

$$\omega = \frac{k_{1,0} \, [O]}{k_{1,0} \, [O] + A_{1,0}}$$

$k_{1,0}$: QUENCHING COEFFICIENT OF NO $(v=1)$ BY O $\simeq 6.5 \times 10^{-11}$ cm^{3}s^{-1}

$A_{1,0} = 13.3$ s^{-1}

Figure 6. Expression for the heat loss by NO $(v = 1 \to 0)$ infrared transition.

THERMODYNAMIC EQUATION

$$\frac{\partial T}{\partial t} = Q_c + Q_a + Q_{ad} + Q_{ch} + Q_s + Q_m + Q_{CO_2} + Q_{NO}$$

$$Q_c = \frac{1}{\rho c_v H_0} \frac{\partial}{\partial z}\left(\frac{K_e}{H_0} \frac{\partial T}{\partial z}\right): \text{CONDUCTION}$$

$$Q_a = \frac{\upsilon}{r} \frac{\partial T}{\partial \theta} - \frac{w}{H_0} \frac{\partial T}{\partial z} : \text{HORIZONTAL AND VERTICAL ADVECTION}$$

$$Q_{ad} = \frac{kT}{\overline{m}\rho c_v r} \frac{\upsilon}{\partial \theta} \frac{\partial \rho}{\partial \theta} + \frac{kT}{\overline{m}\rho c_v} \frac{w}{H_0} \frac{\partial \rho}{\partial z} : \text{ADIABATIC HEATING}$$

Q_{ch}: CHEMICAL HEATING

Q_s: SOLAR HEATING

$Q_m = Q_{particle} + Q_{JOULE} + Q_{CAP}$: MAGNETOSPHERIC HEATING

Q_{CO_2} : I. R. CO_2 RADIATION

Q_{NO} : I. R. NO RADIATION (5.3 μm)

Figure 7. Terms of the thermodynamic equation.

112

SOLAR ACTIVITY CONTROL
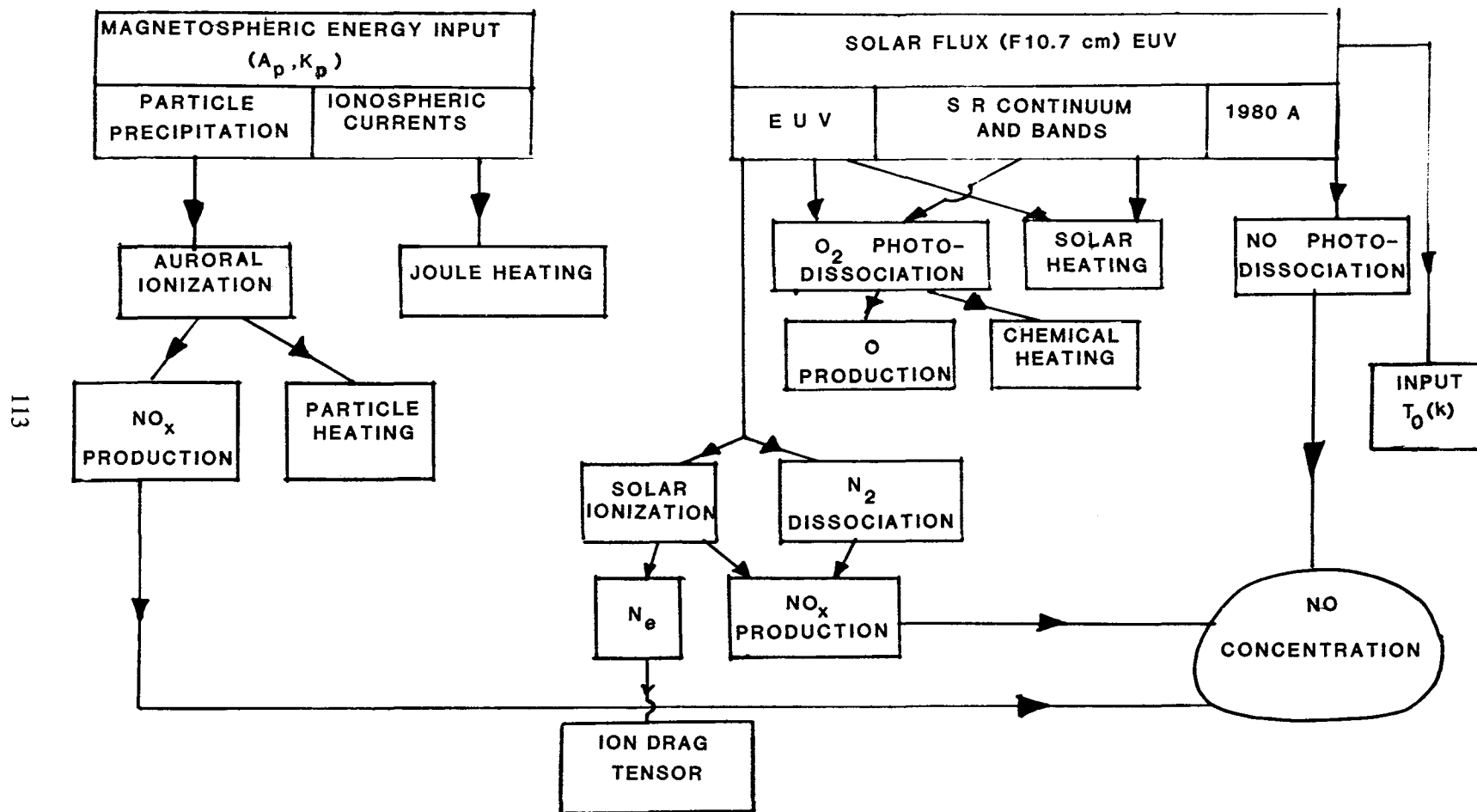
Figure 8. Block diagram showing the response of various processes in the model to solar activity.

113
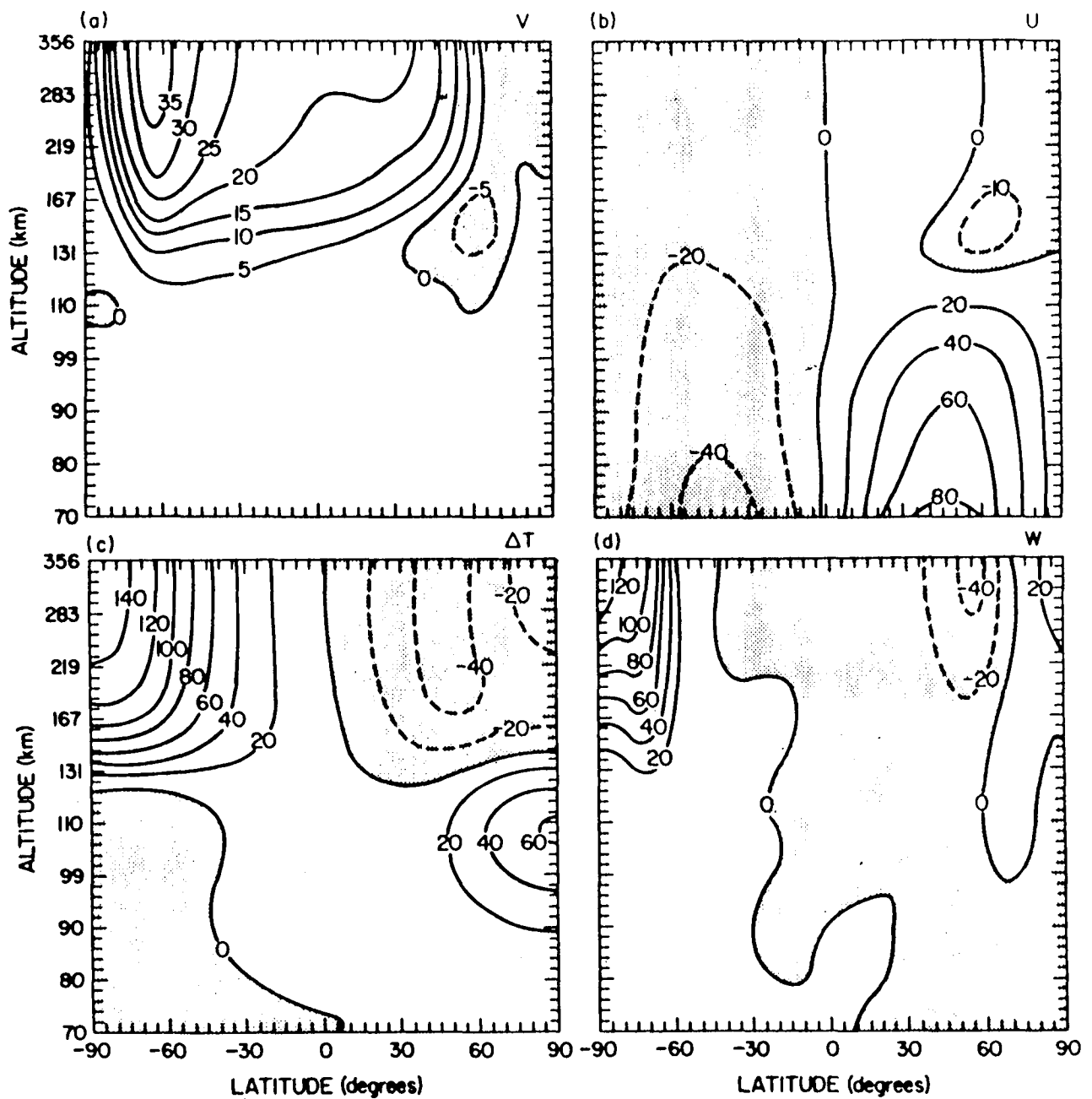
Figure 9. Contour plots of (a) the meridional wind (m.s^{-1}), (b) zonal wind (m.s^{-1}), (c) perturbation temperature (K), (d) vertical wind (cm s^{-1}) from the 2-D chemical-dynamical model.
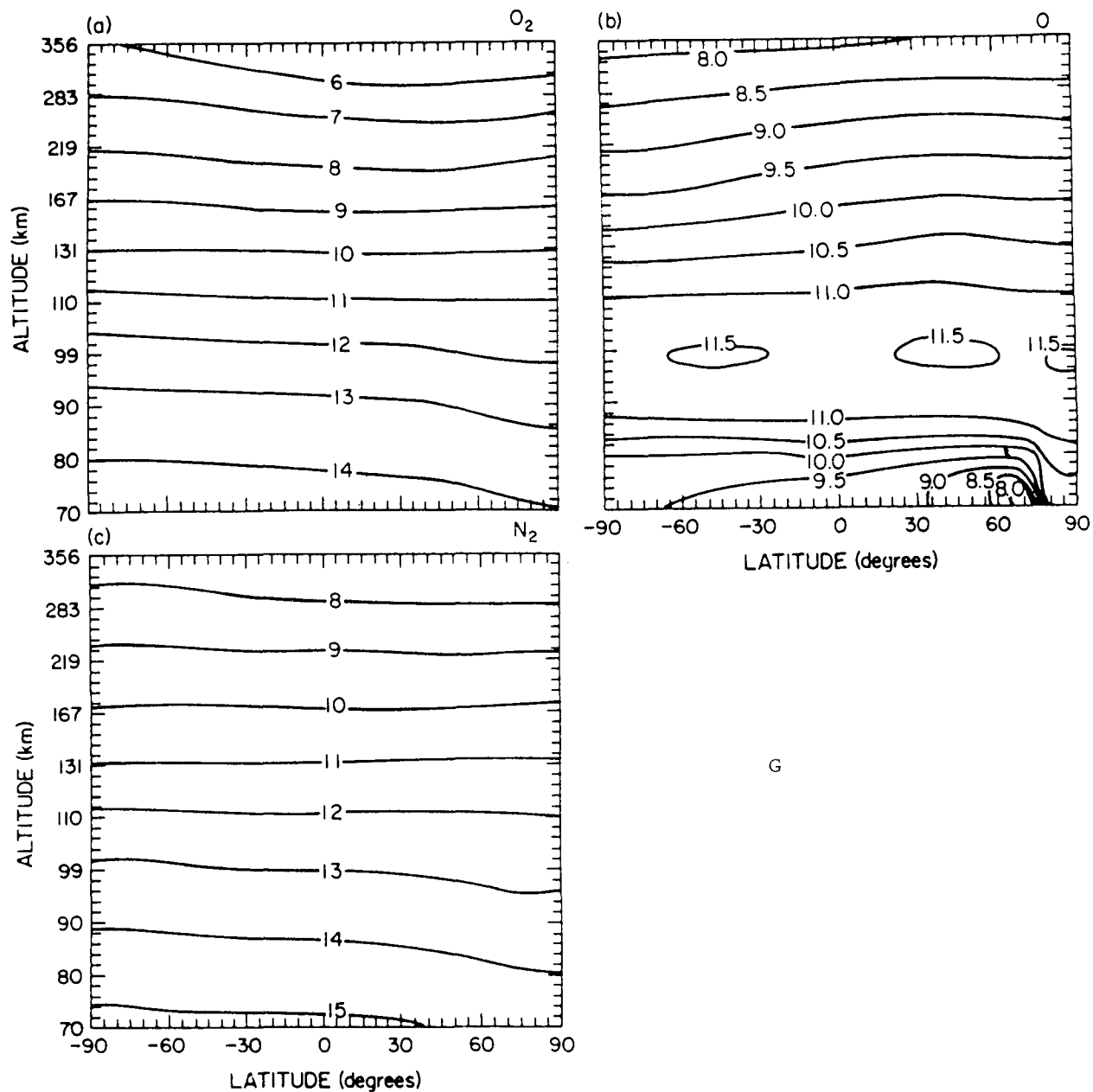
Figure 10. Contour plots of log of (a) O_2, (b) O and (c) N_2 from the 2-D dynamical-chemical model, all in cm^{-3}.
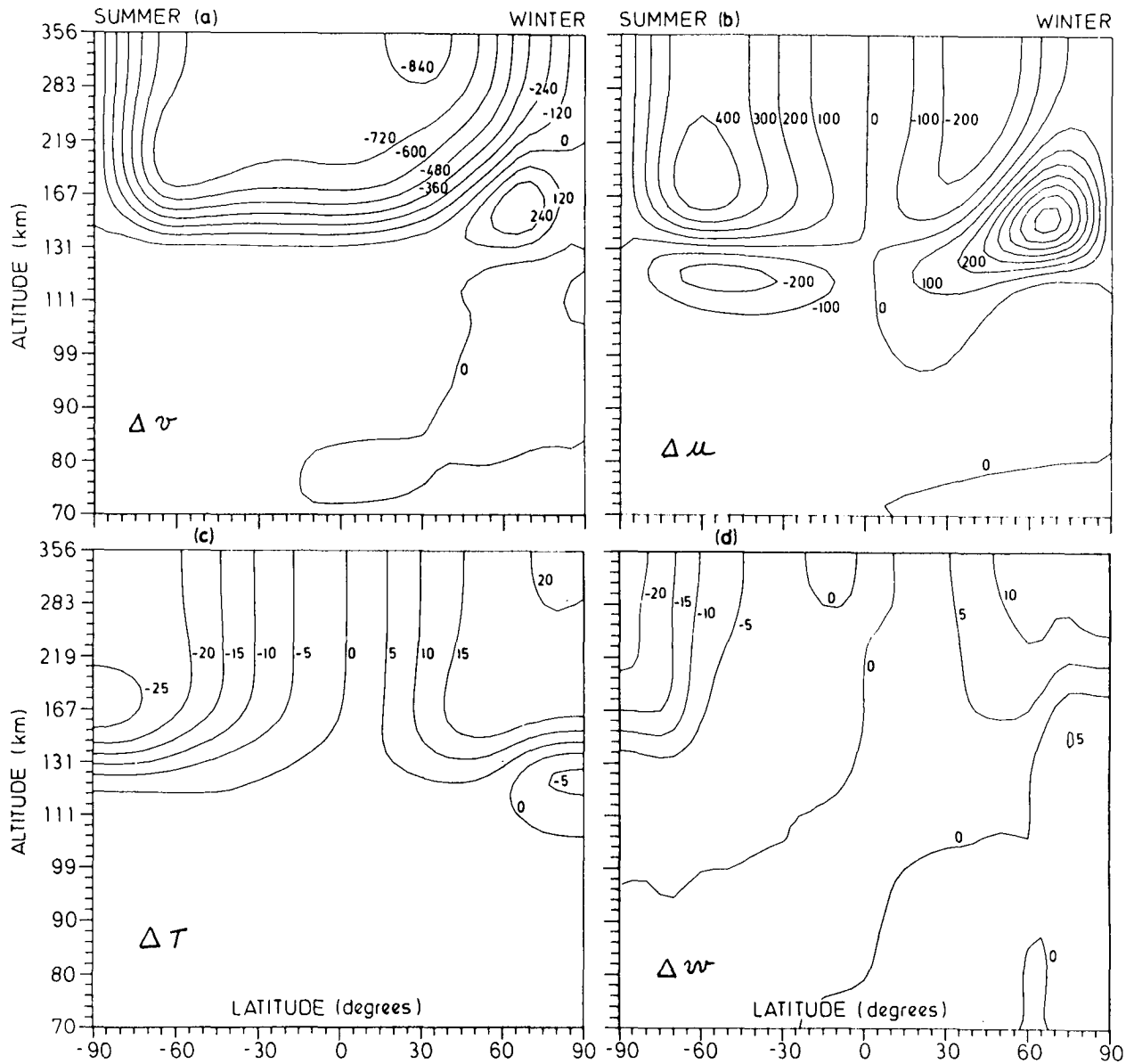
Figure 11. Contour plots of values with and without NO IR cooling for (a) meridional wind, (b) zonal wind, (c) temperature (K), (d) vertical wind. Winds are expressed in cm.s^{-1}.
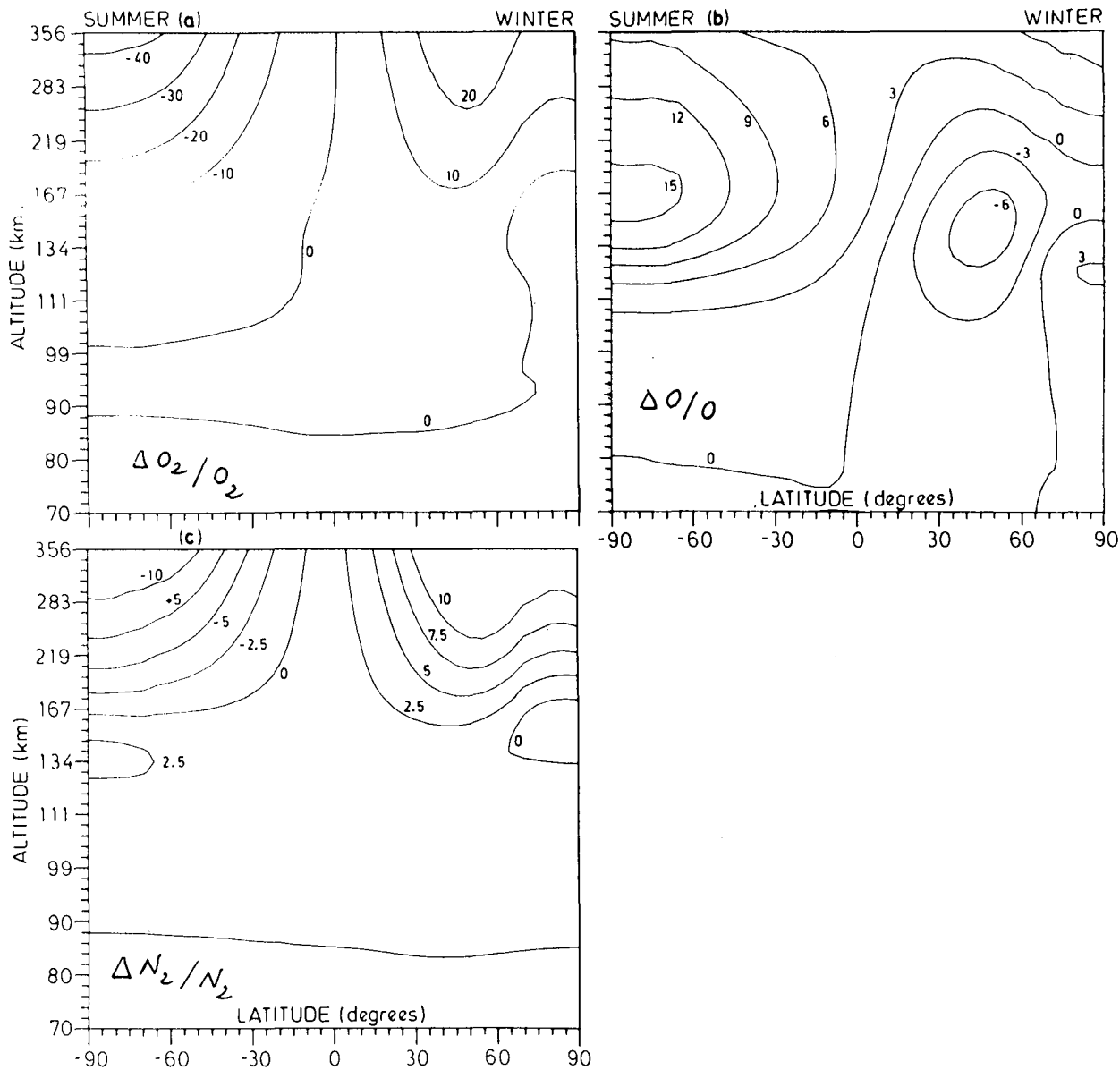
Figure 12. Contour plots displaying percentage variations of (a) O_2, (b) O and (c) N_2 when model calculations including NO IR cooling are compared to those without NO IR cooling.

117

GLOBAL LARGE SCALE STRUCTURES IN THE F REGION

S. H. Gross

Polytechnic Institute of New York

Farmingdale, NY 11735

Measurements of neutral densities, temperatures and ion density and temperature by the Atmosphere Explorer C and E satellites exhibit fluctuations made up of coherent waves of scale size from hundreds to thousands of kilometers. The fluctuations in the AE-C data are found at times of low magnetic activity to extend from the auroral region in one hemisphere across the equator to the corresponding region in the other hemisphere with little change in apparent wavelength. The fluctuations in the AE-E data similarly exhibit at times of low magnetic activity nearly uniform wave structure encircling the equatorial belt. Typical examples of waves of more than 1000 km apparent wavelength in both the AE-C and AE-E data will be presented. These observations during quiet times may be explained by a system of quasi-stationary waves excited by the auroral belts that are distributed about the earth possibly with tidal or sub-tidal periods and scale lengths determined by the structure of the belts. According to this interpretation, TID's are manifestations of transient wave systems moving past a ground observatory that result from changes in magnetic activity with periods and scale sizes associated with the regions of enhanced auroral activity. Some evidence suggesting tidal-like stationary waves from the Millstone Hill incoherent scatter radar is presented.

The first eight figures that follow are for AE-C. The next four are for AE-E and the last is for Millstone Hill incoherent scatter radar measurements. It will be seen for the fluctuations in the data measured by AE-C that there is little variation in the scale size of the structures while the satellite is moving from one hemisphere to the other. Since the orbit is inclined 68°, there are portions of the orbit when the satellite is at high latitudes moving almost west to east. There is no reason why the behavior of the wave structure for these parts of the orbit should be the same as the parts in which the satellite is moving mostly from north to south or from south to north. Furthermore, as one might expect with fixed wavelength waves, there is no evidence of exponential attenuation with distance as might occur due to loss processes. The mode of propagation, if these are propagating waves, must be such as to incur low losses.

Figure 1 is a plot of AE-C measured data on January 20, 1975. The orbit was nearly circular, inclined 68° and the satellite was at an altitude of about 250 km. Densities of atomic oxygen, nitrogen, helium and the electron density (Ne in the figure) are plotted in the upper graph. The lower graph contains the electron temperature (dotted line) and the ion temperature (heavy line). These are 15 seconds, United Abstract file data. (All the AE examples shown here are from these files, including AE-E). Magnetic activity was quite moderate on this day.

Figure 2 is a plot of fluctuations obtained for the data of Figure 1. The data are normalized, detrended and passed through a high pass filter that passes all waves with wavelengths less than 2600 km. 2000 km waves are evident in the figure. Three pairs of fluctuations are shown. The solid

line in each is for oxygen for comparison, the other in each, shown dotted, is as indicated. The three nearly even peaks in the oxygen fluctuations near the start from just before 29760.0 seconds UT to about 29760.0 seconds are for the part of the orbit where the satellite is at high latitudes moving west to east. From 29760.0 seconds to about mid-way between 30585.0 and 31410.0 seconds there are five nearly even spaces between peaks in the oxygen fluctuations. Similar behavior is evident in the nitrogen fluctuations and the phase shifted ion temperature fluctuations. During this time the satellite was moving southward from just below 60°N to -30°S. Beyond, there is evidence of nearly equal spacing, but the magnitude is diminished. At 31410.0 seconds the satellite is again traversing mostly from west to east in the southern hemisphere. Exponential damping is not evident.

Figure 3 contains nitrogen fluctuations for AE-C measurements on January 19, 1975, a day of moderate magnetic activity in which k_p, did not exceed 3_o. The same filter as for Figure 2 is employed. The satellite is at high latitudes moving mostly from west to east until just before 62481.0 seconds UT when it starts moving southward. There are roughly evenly spaced waves of 2000 km scale size until a time midway between 64173.0 and 65019.0 seconds UT. At this point the satellite has reached southern high latitudes and is moving mostly from west to east before reversing its path and returning to the nothern hemisphere.

Figure 4 is for the same orbit as Figure 3, but the data were passed through a high pass filter that passes only waves with wavelengths less than 1300 km. Waves of the order of 900 km are evident. The north to south region is again from about 62481.0 seconds to midway between 64173.0 and 65019 seconds. More uniformity appears in the region from this midpoint (roughly -60°S) to earlier times, a point somewhat to the left of 63327.0 seconds (at about 30°N).

Figure 5 is for another day of AE-C data, February 17, 1975. The densities of nitrogen (top curve), helium (second highest), argon (heavy line) and electron density (thin curve varying about the argon curve after 36232.5 seconds) are plotted. Two auroral zone heating signatures are evident, one very distinct on the left at high northern latitudes, centered somewhat to the left of 34856.3 seconds, and a second, less distinct, at high southern latitudes centered to the left of 37608.8 seconds. The heating in both regions may act as wave sources. The k_p for this day did not exceed 3_+.

Figure 6 is a plot for the fluctuations of nitrogen (solid line) and argon (dotted line) for the data in Figure 5. It was obtained by passing the data through a bandpass filter allowing only waves in the range 1100 to 2600 km to pass. Strong waves to the left of 34971.0 seconds are for the northern auroral region. Similar strong waves are observed in the southern auroral region to the left of 37509.0 seconds. The equator is crossed at about 35817.0 seconds. The pattern looks like that of two interfering wave systems. High latitude west to east traversal in the northern hemisphere is for the time interval 34125.0 to 34971.0 seconds, and somewhat to the right of 36663.0 to somewhat past 37509.8 seconds for the southern hemisphere.

Figure 7 contains the cross correlation function for the fluctuations of Figure 6. The large negative peak of -.8 shows that argon and nitrogen are well correlated and that a coherent wave system exists.

Figure 8 contains fluctuations for the data of Figure 5 but for a bandpass filter passing waves in the range 800 to 1300 km. These are roughly 1000 km waves of nitrogen fluctuations. The southern region at about 36663.0 seconds is stronger by a factor of about 2. The fluctuations resemble that of two interfering waves, perhaps from two sources. Fairly evenly spaced waves are evident between 34971.0 and 36663.0 seconds.

Figure 9 is a plot similar to that of Figure 1, but is for AE-E measurements on August 1, 1977. AE-E was in a nearly circular orbit inclined 20° at an altitude of about 260-270 km. The upper graph contains densities of oxygen (upper curve), nitrogen (second highest), helium (third curve)

and the electron density (lowest). The lower graph contains ion temperature (dotted line) and neutral gas temperature (heavy line). Magnetic activity was moderate; k_p did not exceed 3 . The satellite was mainly moving from west to east in an equatorial belt between $\pm 20°$.

Figure 10 contains plots of four pairs of fluctuations for the data of Figure 9 as obtained from a high-pass filter passing only waves with wavelengths less than 2600 km. The scale size of the waves is about 1800 km. The solid line in all four graphs is for oxygen, the others (dotted) as indicated. The time shown is for about 3/4 of an entire orbit, limited due to the absence of data prior to and after the orbit. Nearly uniform waves are evident girdling this much of the equatorial belt.

Figure 11 is for AE-E for November 23, 1977. The satellite was in the same orbit as in Figure 9. Neutral and ion winds are shown as well. Magnetic activity was low for this day, k_p did not exceed 1_o.

Figure 12 is a plot of fluctuations for the data of Figure 11. Here the data were passed through a bandpass filter allowing only waves in the range 2600 to 5200 km to pass. The waves in the figure are roughly of 2800 km in scale size. The upper graph is for neutral temperature and nitrogen density fluctuations. Its cross correlation function is to its right and shows a negative peak of about -.85. Fluctuations of horizontal (roughly north-south) neutral winds and nitrogen density are shown in the lower graph. Its cross correlation function is to its right and contains a negative peak of about -.68. The time period covers about one half of an orbit, the limitation being the extent of the measurements.

Figure 13 is for the data of Figure 11, but the fluctuations are obtained from a high-pass filter that passes all wavelengths less than 1300 km. These waves are about 1000 km in scale size and the plot covers about half the equatorial belt. The uniformity of these waves is quite remarkable. The solid line is for nitrogen and the dotted for the neutral temperature.

Figure 14 is a plot of data obtained from a series of Millstone Hill incoherent scatter radar measurements while in an elevation scan mode from due south to due north. The scan is completed in about 20 minutes, but the scan to scan period is 45 minutes. Shown here are the so-called raw fluctuations for individual scans plotted with separations so that they can be seen relative to each other. Not all scans are shown. The plots are to a scale which is not shown. The abscissa is the geomagnetic latitude. The Millstone Hill station is at 54°. The curves shown are constant altitude electron densities at 350 km. The day and beginning time of each scan is shown on the left of each curve. The nature of the variation appears to change from flat to concave to flat to convex, etc., with a period that may relate to the diurnal or semi-diurnal period and for a half wavelength of about 1000 km, much like the behavior of a stationary wave. There is an unfortunate four hours 45 minutes gap between th 03:11 and 07:55 curves due to a radar malfunction. The change in shape for these two times is quite interesting. Whether these variations can be interpreted as evidence of tidal like, stationary variations is highly speculative at this time. Measurements on other days are also somewhat like these curves.
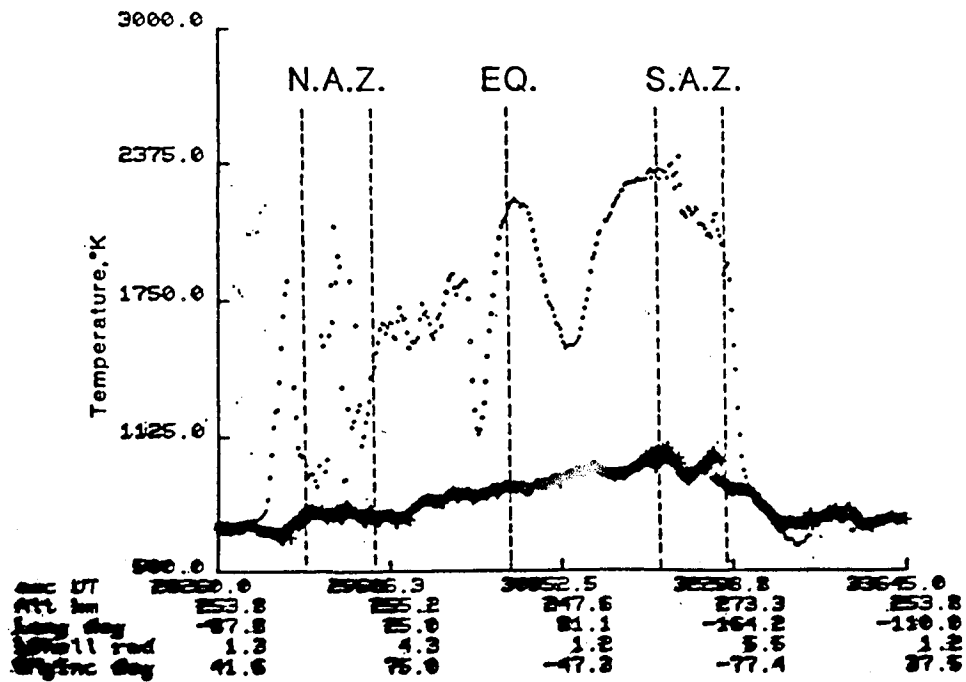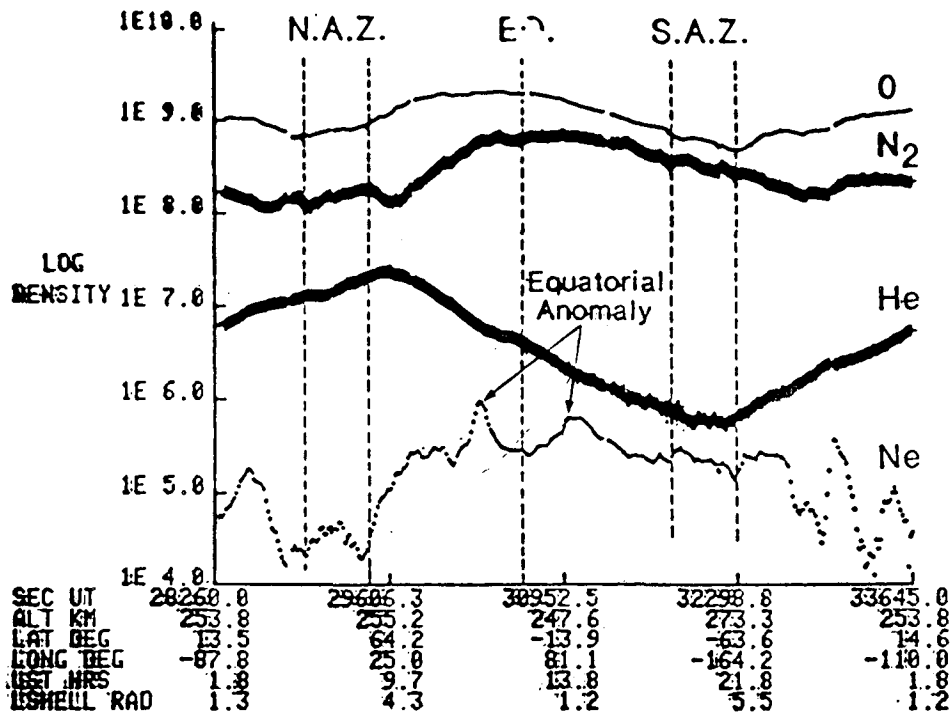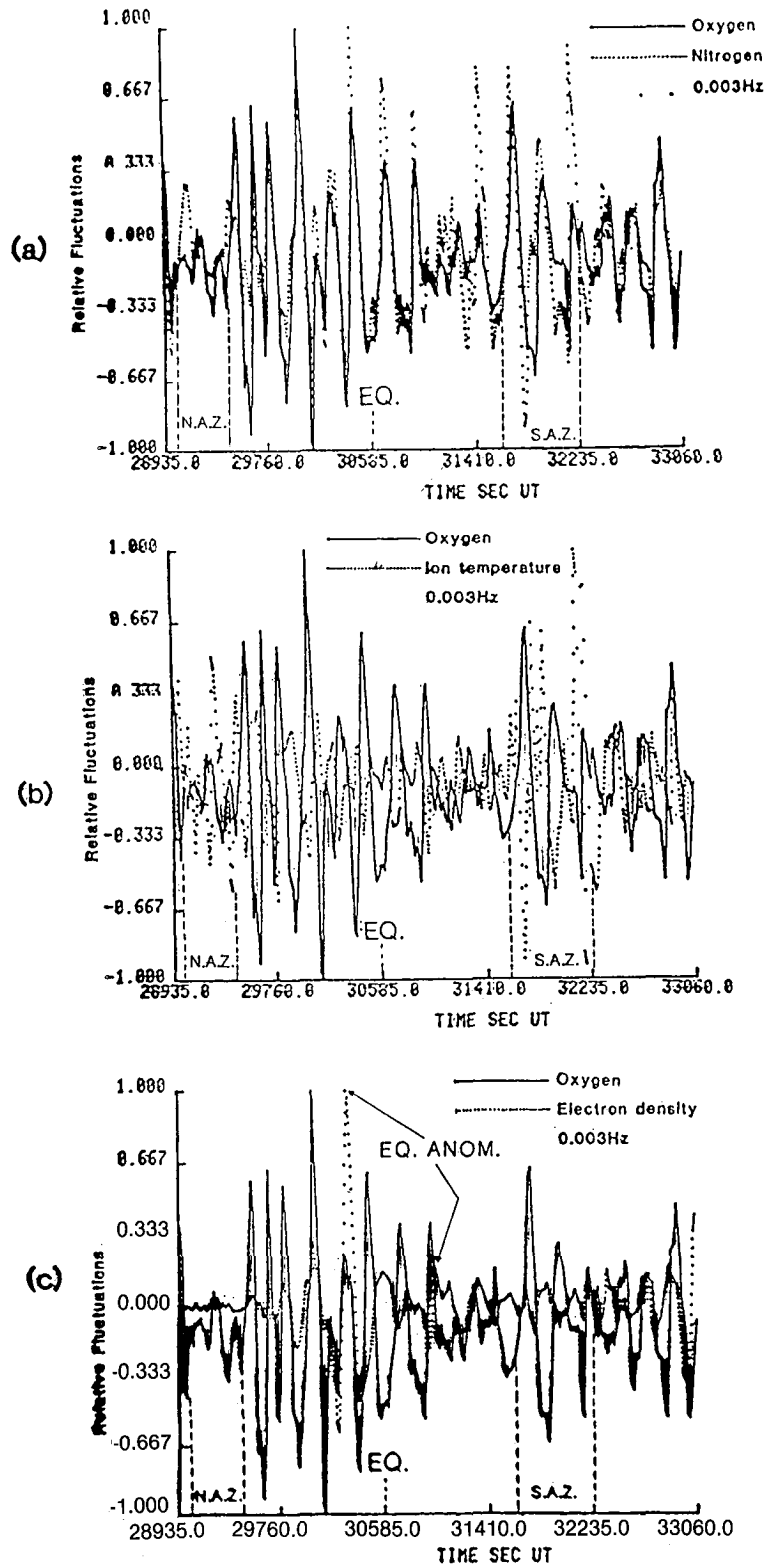
121

Figure 1.

Figure 2.

Figure 3.

Atmosphere Explorer C year,day 75019.   iav=1
parameter 42   order of filter 40   cutoff freq. 0.0060
             ymx=   0.52919e-01   average= -0.11628e-03
             ymn= -0.51506e-01   mean sq.dev.=   0.15422e-01
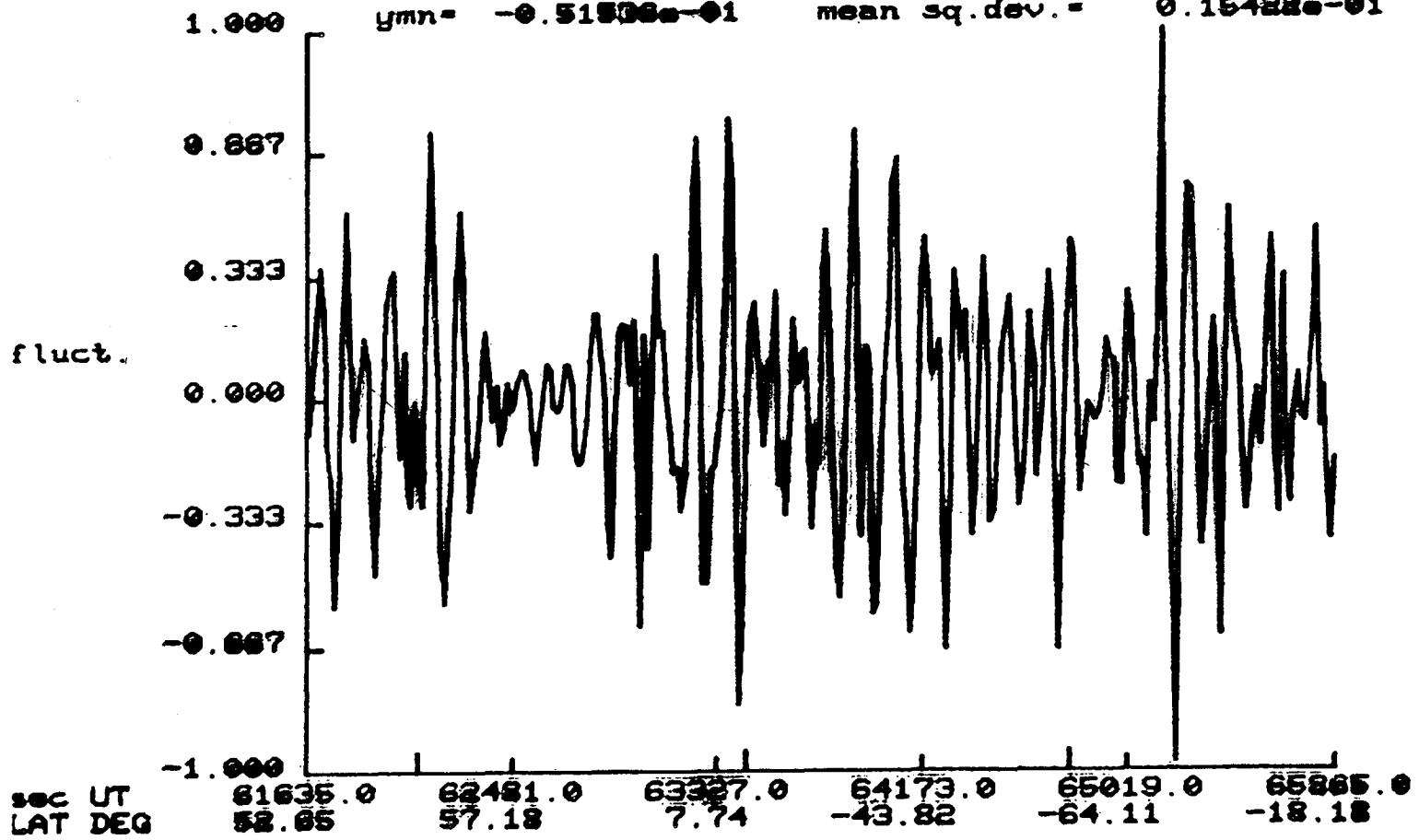
Figure 4.

ATMOSPHERE EXPLORER C UA DATA
75048. ORBIT 5596
CEP NP . NATE N2 - NATE HE . NATE A +

LOG DENSITY

SEC UT	33480.0	34856.3	36232.5	37609.8	38985.0
ALT KM	238.2	248.7	237.1	247.8	240.1
LAT DEG	18.5	59.7	-22.8	-55.6	28.0
LONG DEG	132.7	-104.1	-56.8	71.8	114.1
LST HRS	17.9	2.5	6.0	15.0	18.2
LSHELL RAD	1.0	8.1	1.1	5.4	1.1

Figure 5.

126
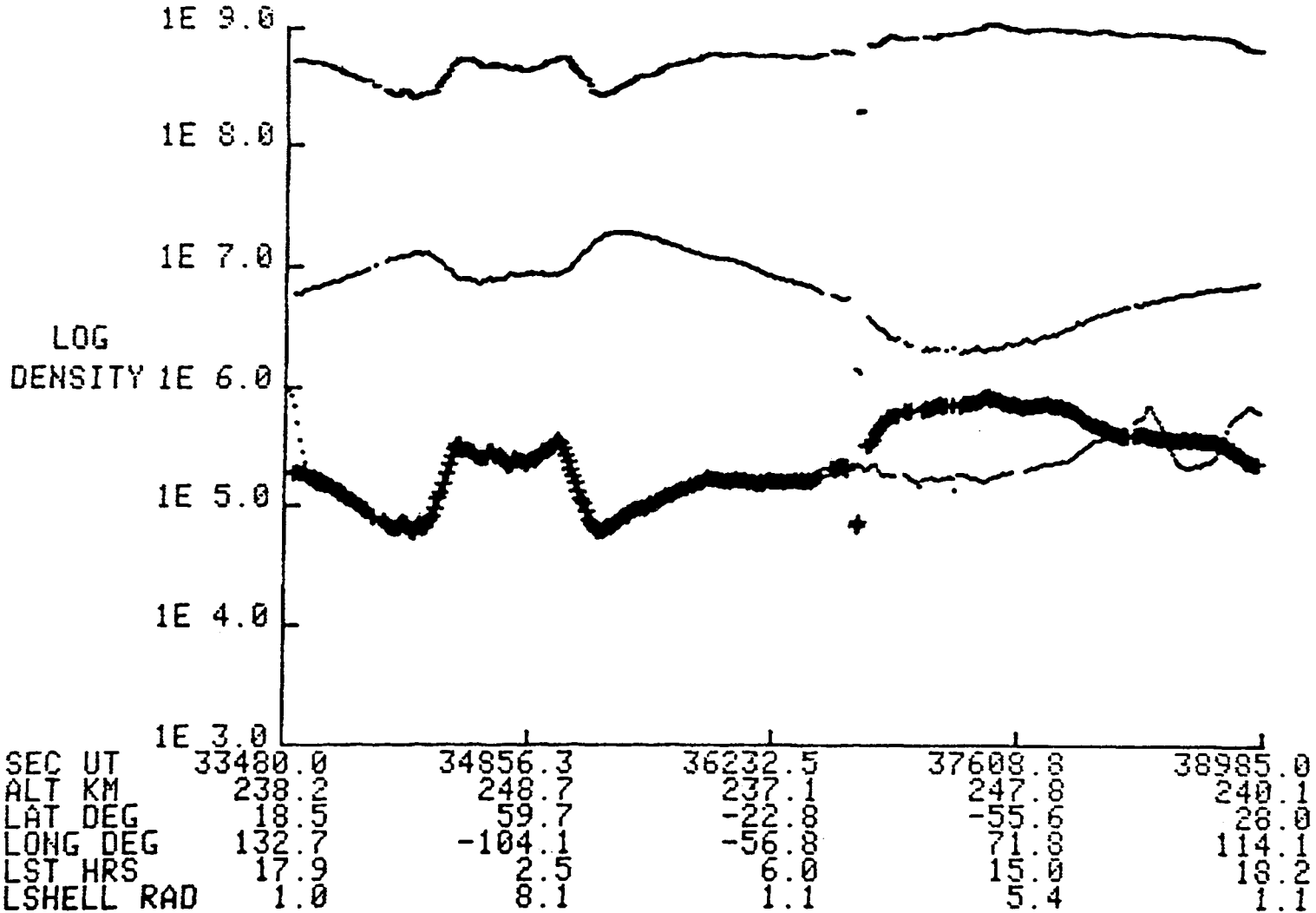
ATMOSPHERE EXPLORER C   YEAR.DAY 75048.0 IAU=1   PAR1=42   PAR2=45
ORDER OF FILTER 40   CUTOFF FREQ.0.0030-   0.0070   DT= 15.0
YMX1= 0.60574E-01   YMX2=   0.15201   DEV1= 0.2278E-01
YMN1= -0.52883E-01   YMN2= -0.12630   DEV2= 0.4617E-01
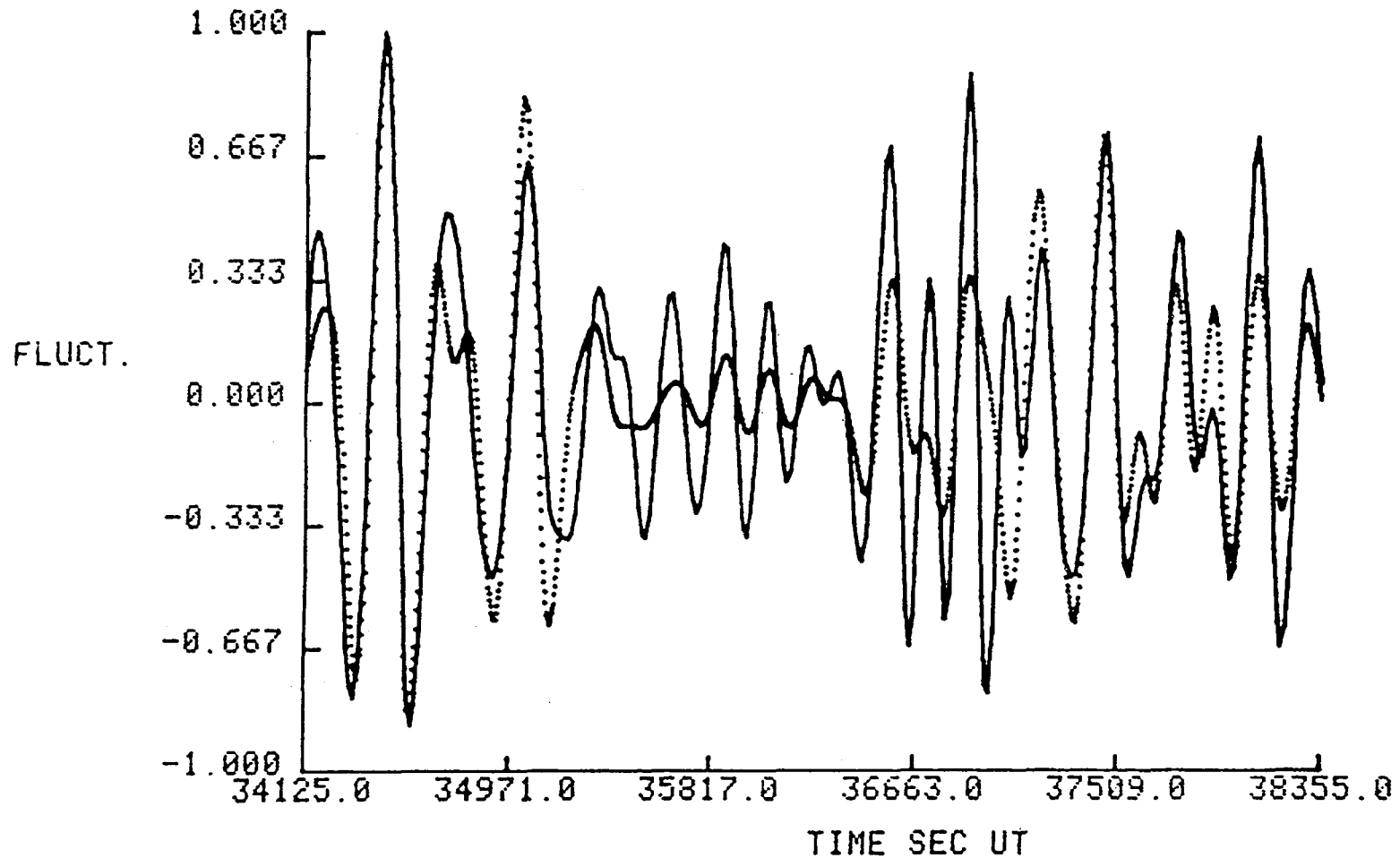
Figure 6.

ATMOSPHERE EXPLORER C YEAR, DAY 75048.0   34125.0- 38355.0
PAR1   42 PAR2   45   AV1= 0.2738E-03   34125.0- 38355.0
ORDER OF FILTER 40   AV2= 0.3652E-03   DEV1=   0.2278E-01
CUTOFF FREQ. 0.0030-   0.0070   DEV2=   0.4617E-01
IAV= 1   DT=   15.000
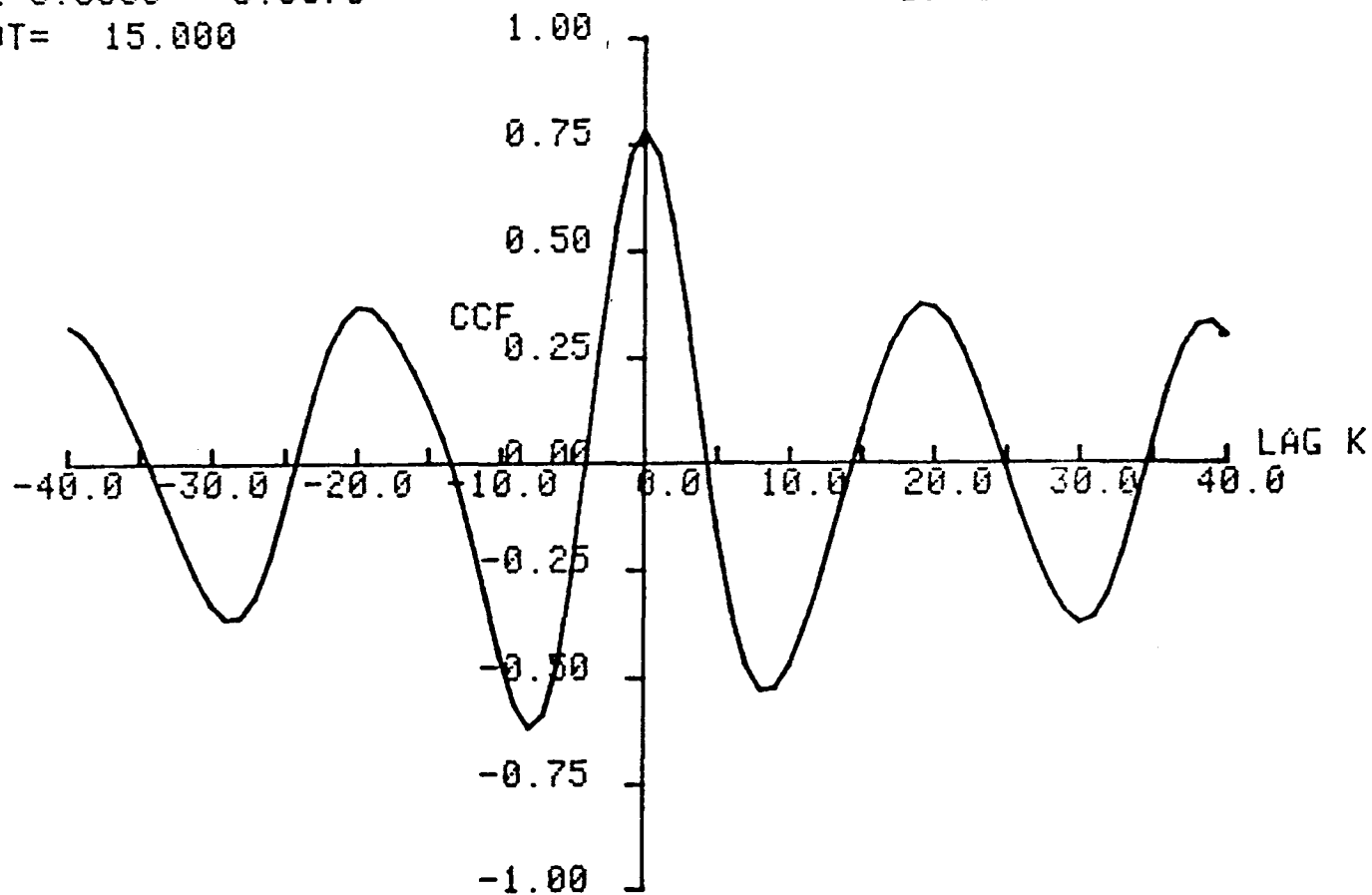
Figure 7.

ATMOSPHERE EXPLORER C YEAR,DAY 75048.   IAV=1
PARAMETER 42   ORDER OF FILTER 40   CUTOFF FREQ. 0.0060, 0.0100
YMX=   0.46793E-01   AVERAGE=   0.80775E-04
YMN= -0.46793E-01   MEAN SQ.DEV.=   0.13056E-01

SEC UT	34125.0	34971.0	35817.0	36663.0	37509.0	38355.0
GMGINC DEG	2.4	5.7	1.2	1.6	6.2	1.2
LST HRS.	19.8	3.2	5.3	7.1	14.3	17.0
LONG. DEG.	158.9	-94.5	-66.2	-42.0	61.2	99.2
LAT. DEG.	56.1	53.8	3.5	-47.8	-61.2	-13.2

Figure 8.

129
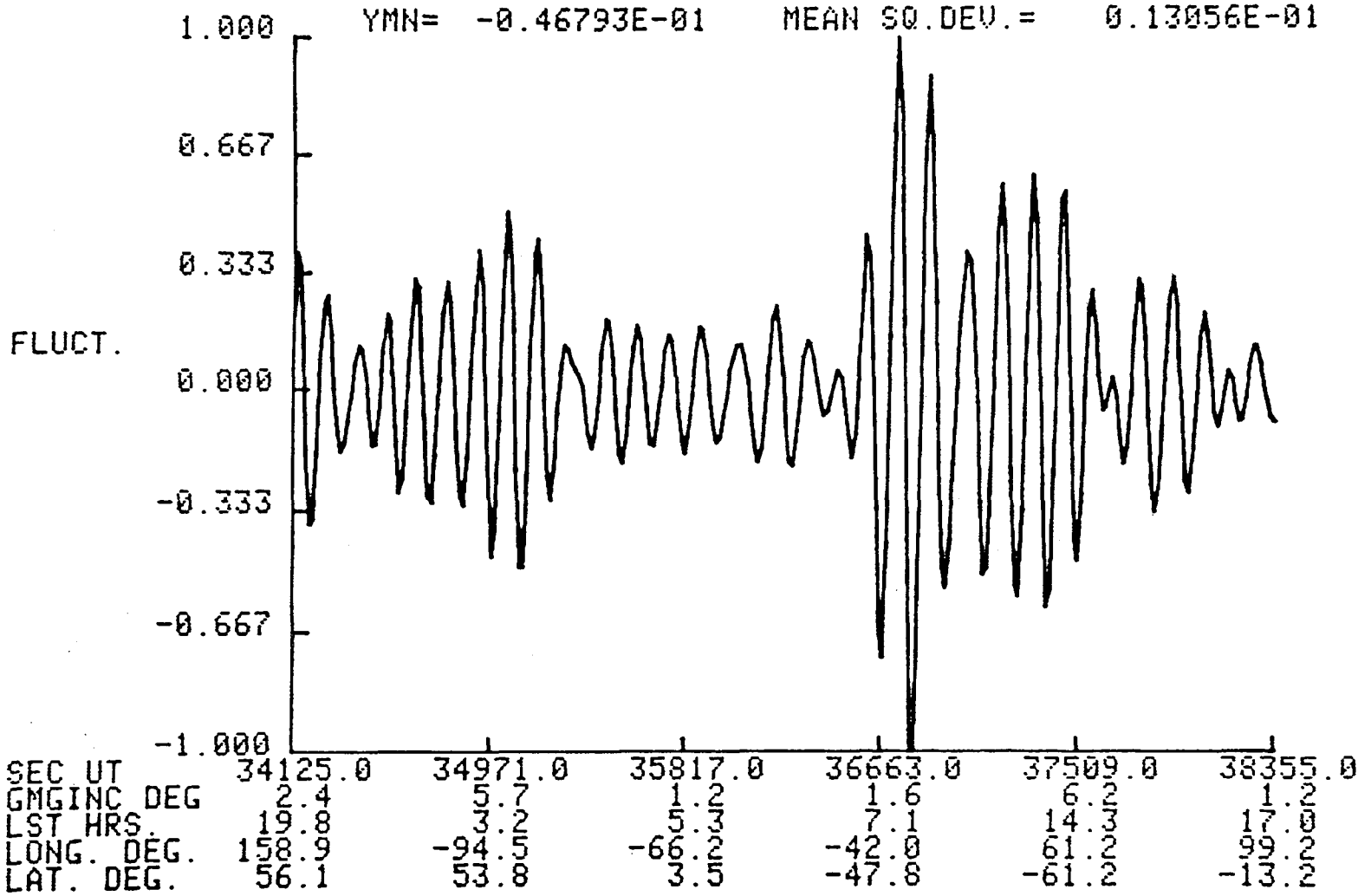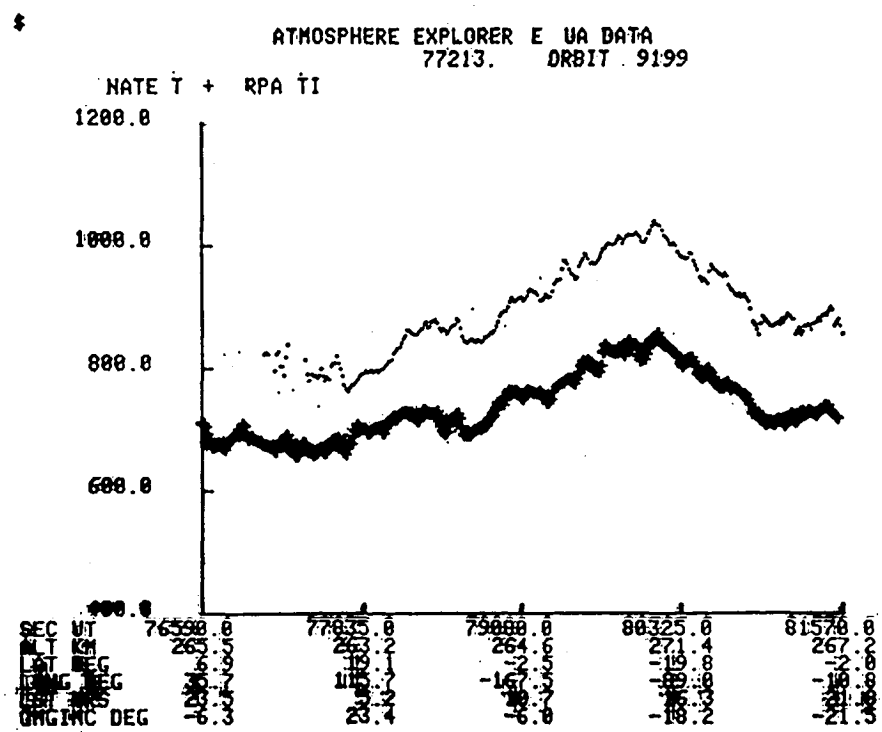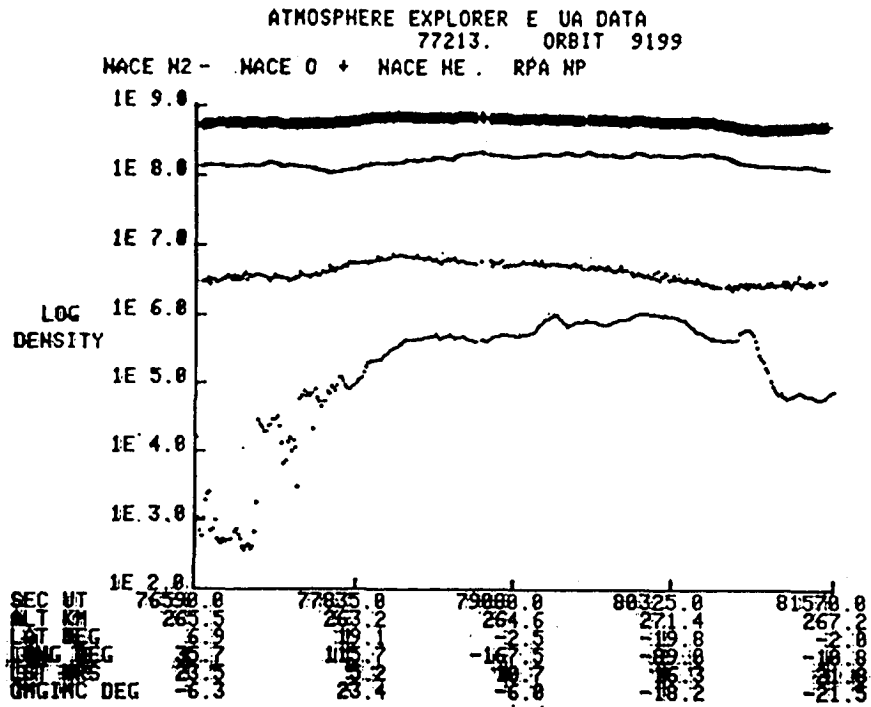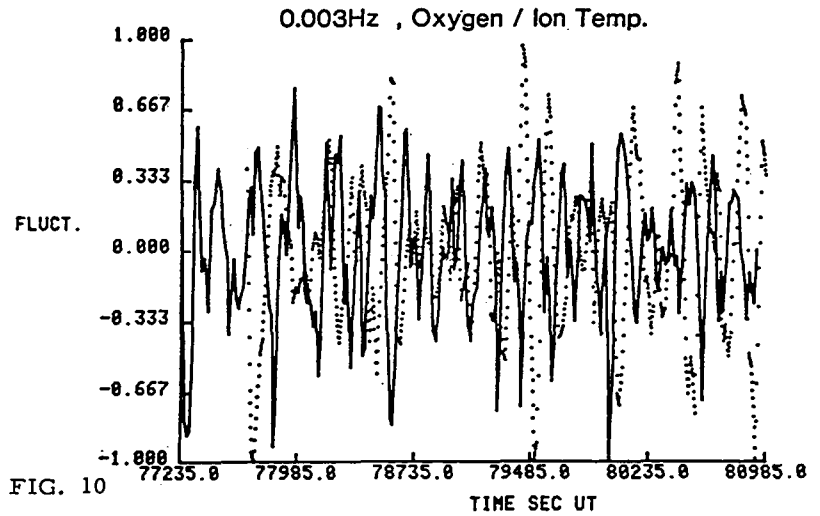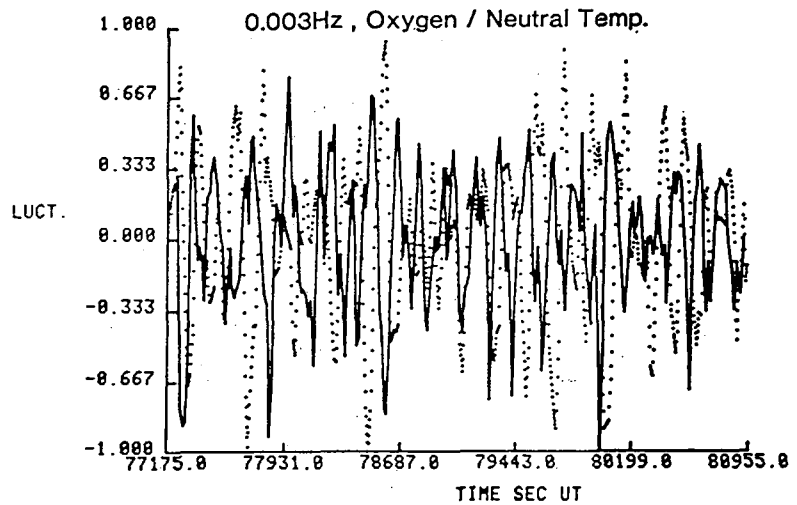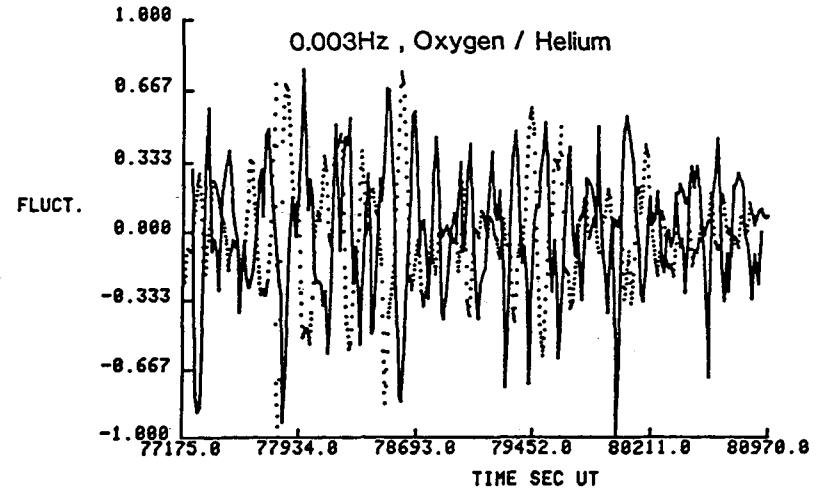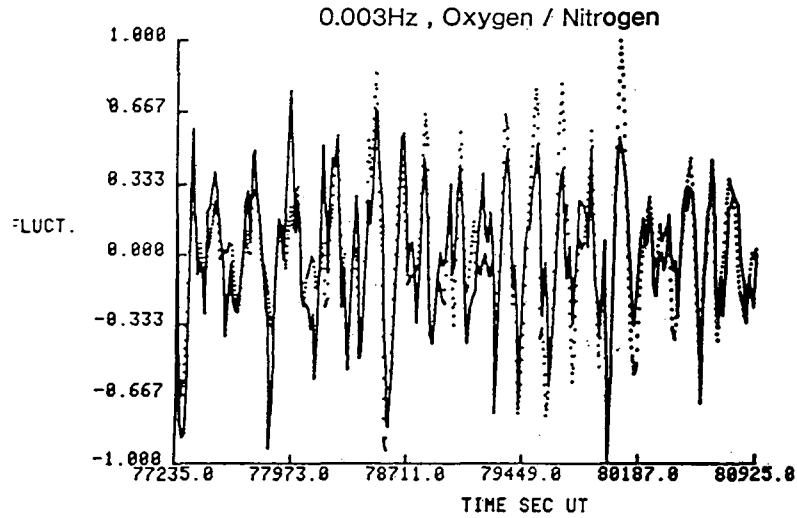
Figure 9.

Figure 10.

131
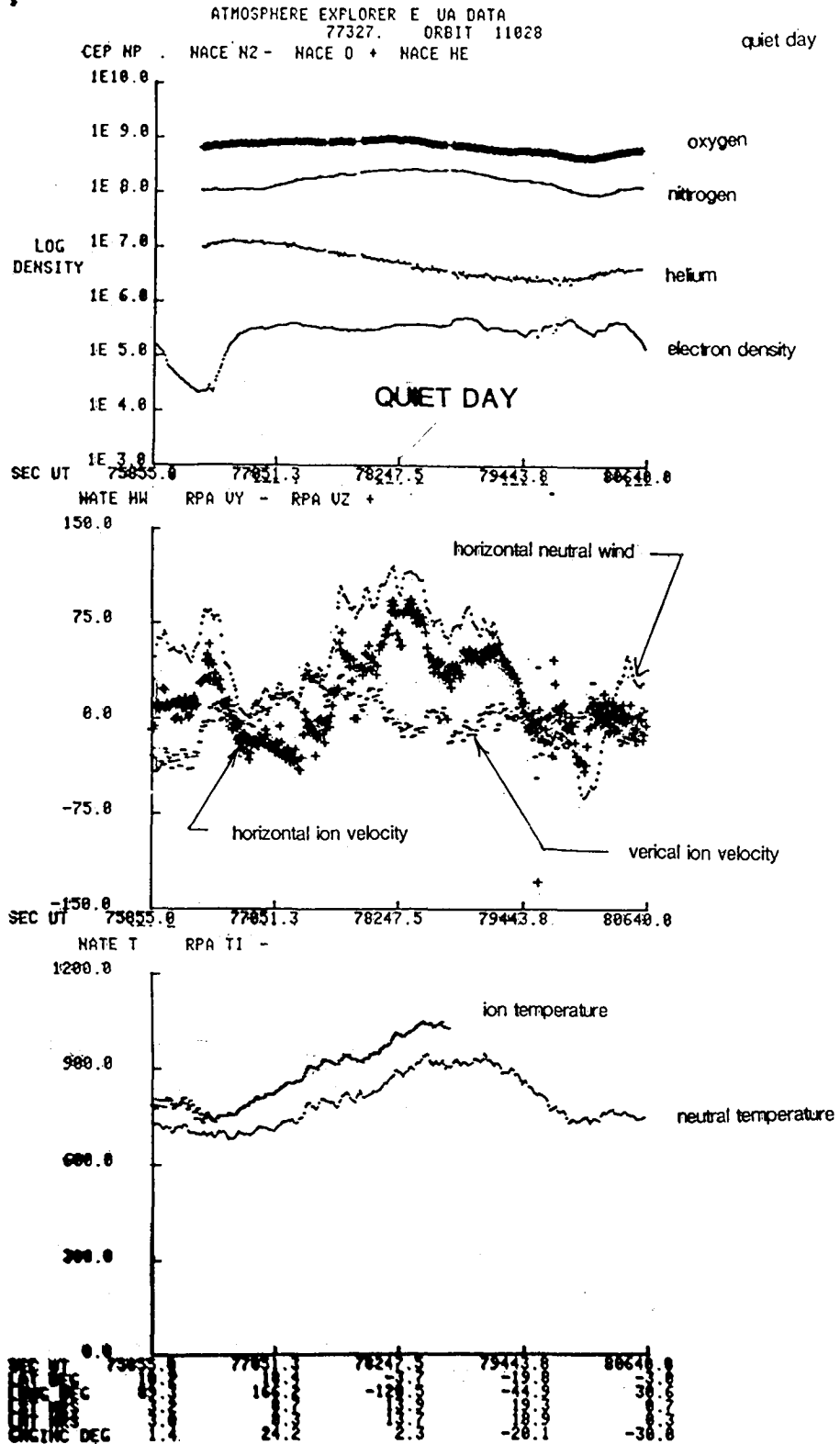
Figure 11.

NEUTRAL-NEUTRAL CORRELATION (3)

ATMOSPHERE EXPLORER E   YEAR,DAY 77327.0 IAV=1 PAR1=35   PAR2=41
ORDER OF FILTER 40   CUTOFF FREQ.0.0015- 0.0030   DT= 15.0
YMX1= 0.27842E-01   YMX2= 0.11131E-01   DEV1= 0.1376E-01
YMN1= -0.28692E-01   YMN2= -0.10251E-01   DEV2= 0.5631E-02

CCF

QUIET DAY   cross correlation function

FLUCT.

neutral temperature

nitrogen density

1.00
0.75
0.50
CCF 0.25
0.00
0.25
0.50
0.75
-1.00

LAG K
-40.0 -30.0 -20.0 -10.0 0.0 10.0 20.0 30.0 40.0

1.000
0.667
0.333
0.000
-0.333
-0.667

76985.0 77319.0 77733.0 78147.0 78561.0 78975.0
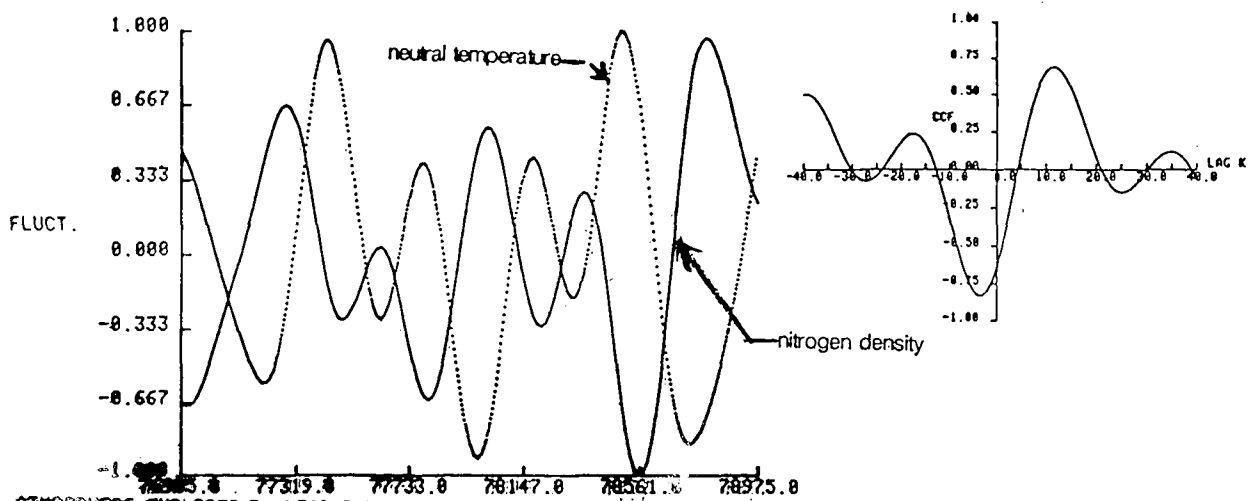
ATMOSPHERE EXPLORER E   YEAR,DAY 77327.0 IAV=1 PAR1=35   PAR2=46
ORDER OF FILTER 40   CUTOFF FREQ.0.0015- 0.0030   DT= 15.0
YMX1= 0.27842E-01   YMX2= 11.687   DEV1= 0.1376E-01
YMN1= -0.28692E-01   YMN2= -10.207   DEV2= 5.344

CCF

horizontal neutral wind

nitrogen density

1.00
0.75
0.50
CCF 0.25
0.00
-0.25
-0.50
-0.75
-1.00

LAG K
-40.0 -30.0 -20.0 -10.0 0.0 10.0 20.0 30.0 40.0

FLUCT.

1.000
0.667
0.333
0.000
-0.333
-0.667
-1.000

76985.0 77319.0 77733.0 78147.0 78561.0 78975.0

TIME SEC UT
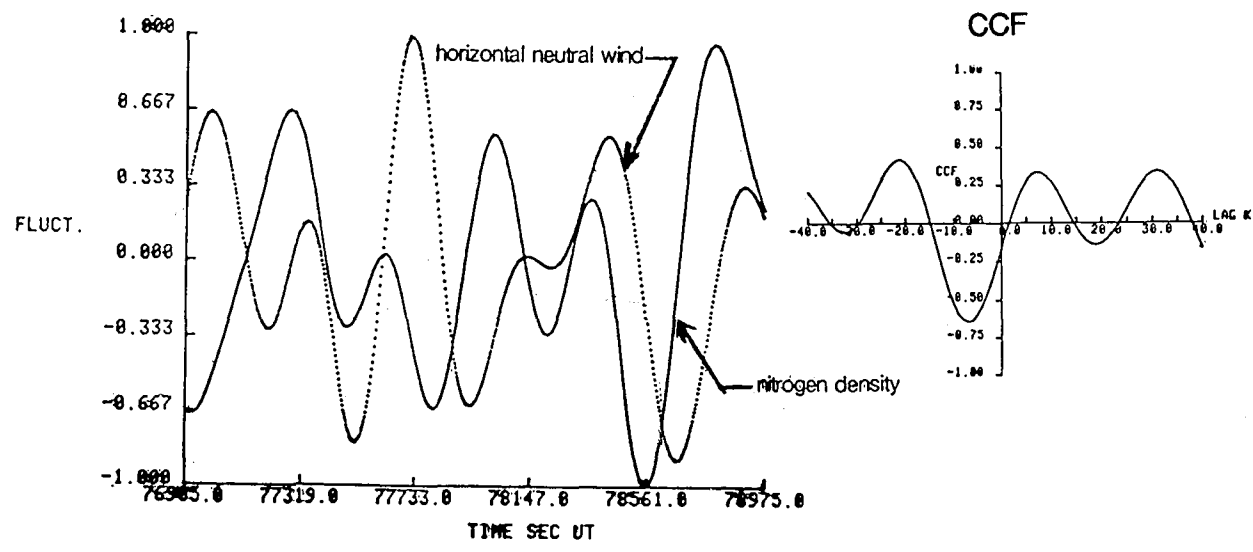
2800km

Figure 12.

ATMOSPHERE EXPLORER E   YEAR,DAY 77327.0 IAV=1   PAR1=35   PAR2=41
ORDER OF FILTER 40   CUTOFF FREQ.0.0060   DT= 15.0
YMX1= 0.24831E-01   YMX2= 0.13097E-01   DEV1= 0.1030E-01
YMN1= -0.25775E-01   YMN2= -0.12704E-01   DEV2= 0.5626E-02

Figure 13.

Figure 14.

135
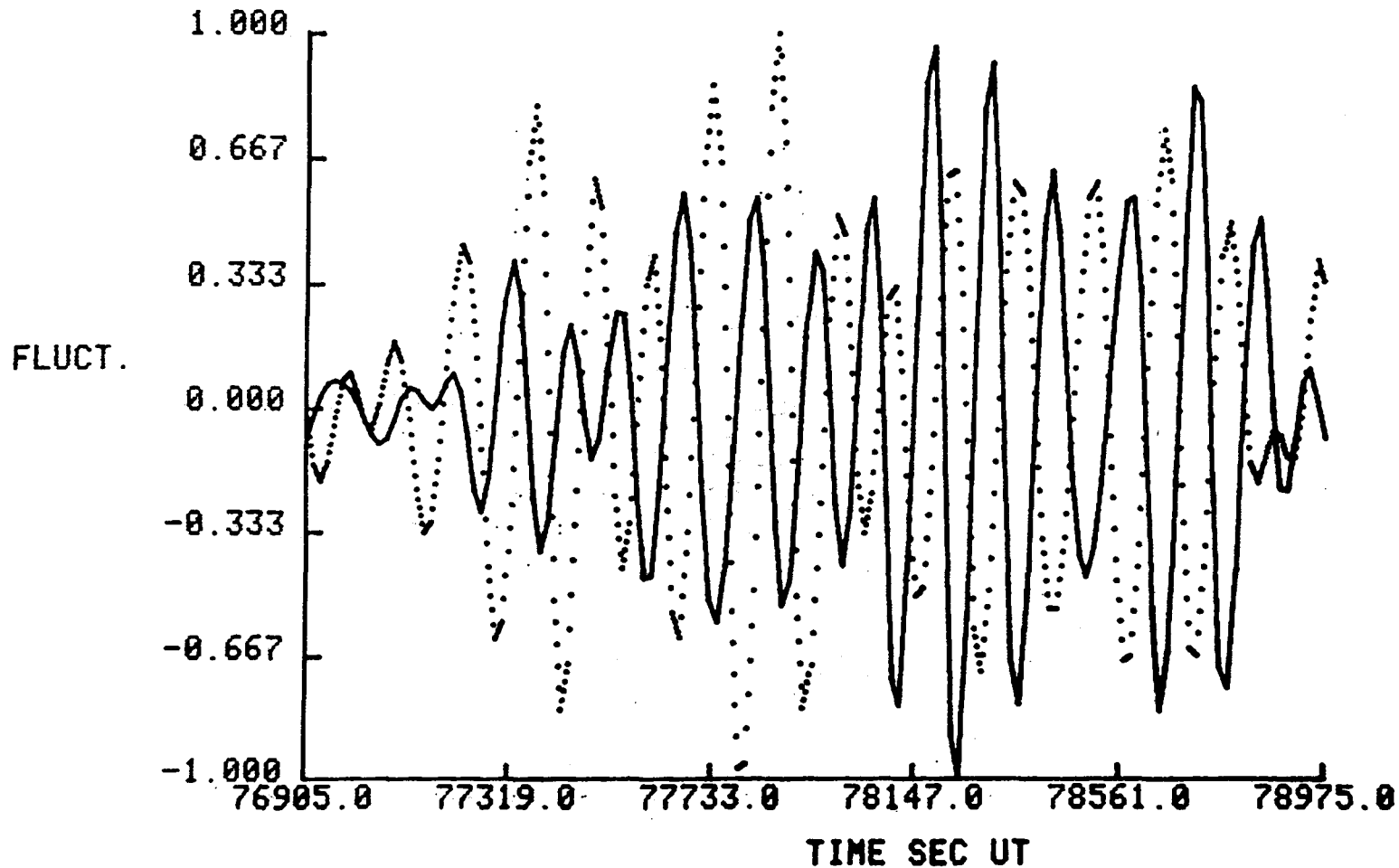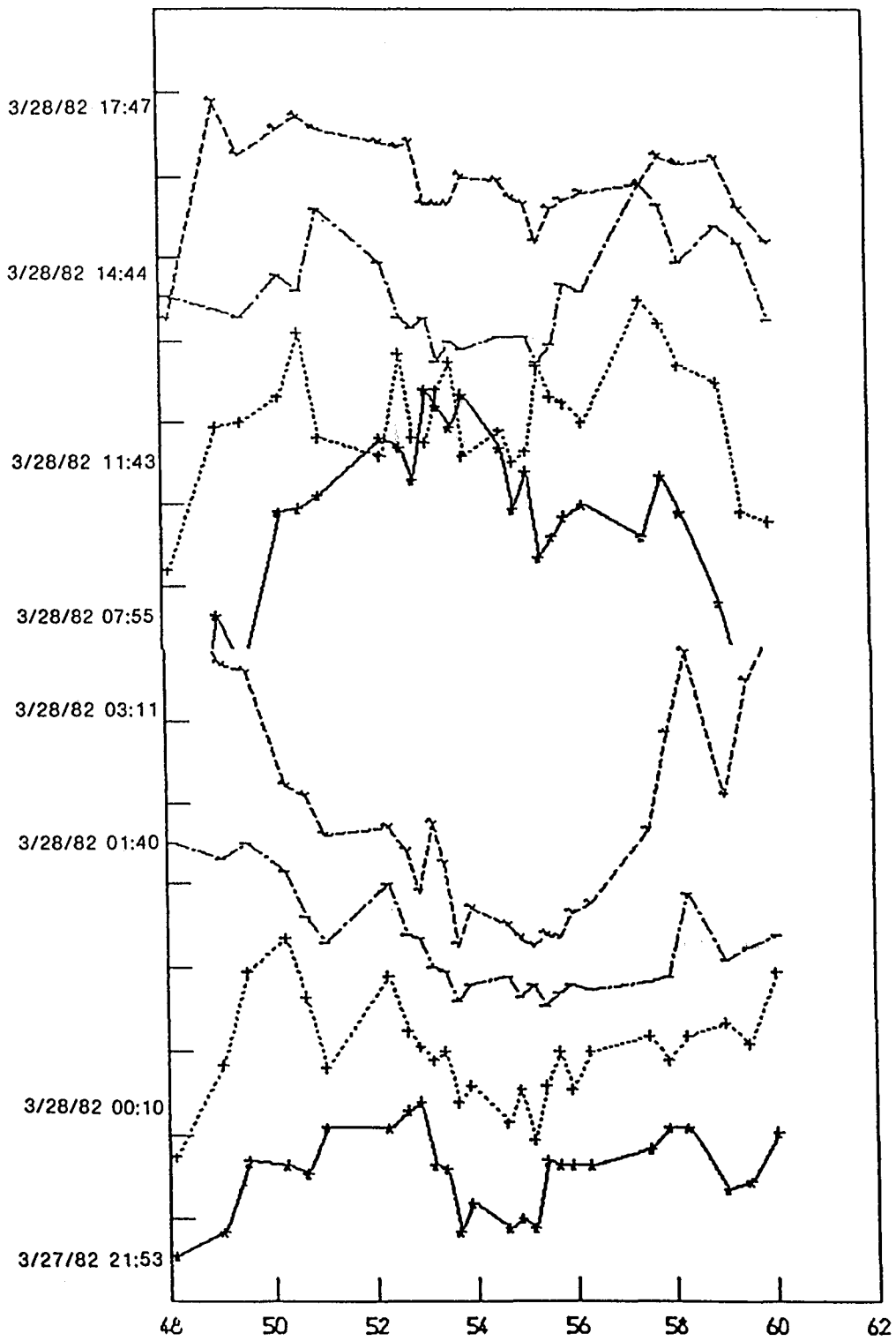
THE MEASURED MOTIONS INSIDE EQUATORIAL PLASMA BUBBLES

W. B. Hanson
Center for Space Sciences
P.O. Box 688
The University of Texas at Dallas
Richardson, TX 75080

D. K. Bamgboye
Physics Department
University of Ilorin
Ilorin, Nigeria

A preliminary study of the vertical and north-south horizontal ion motions in plasma bubbles in the near-equatorial ionosphere utilizing drift meter data from Atmosphere Explorer E is presented. High-resolution data show that the vertical ion velocity in some bubbles increases approximately linearly with $(N_0-N)/N$, where N_0 is the background ion concentration and N is the bubble ion concentration. At sufficiently large N_0/N the vertical ion velocity saturates, but often at a value substantially larger than the ratio of the gravitational acceleration to the ion neutral collision frequency (g/v_{in}), which is the nominal collision-dominated velocity limit for cylindrical bubbles. These larger than nominal velocities may result from background eastward electric fields and/or from a vertically elongated bubble cross section. The unanticipated observation that large poleward horizontal drifts accompany these vertical drifts seems to follow naturally from a redistribution of plasma along flux tubes as the plasma convects from the bottomside of the F region to high altitudes.
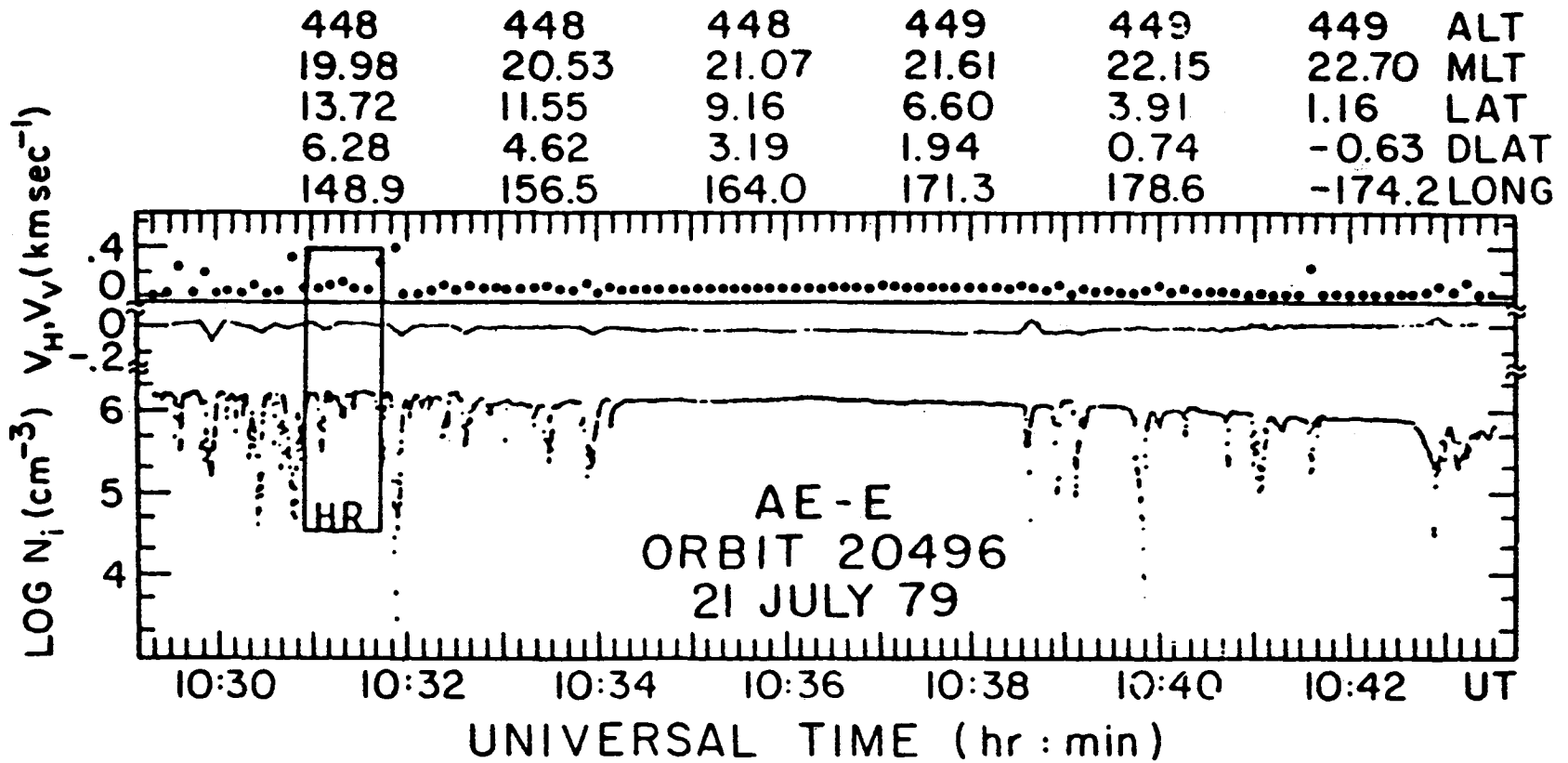
Figure 1. Ion number density and drift data (absolute points only) from the ion drift meter showing (in the lower trace) the density depletions (bubbles) and their horizontal (middle trace) and vertical (solid dots) velocities. The horizontal velocities are in a direction normal to the satellite velocity vector. The data are from AE-E orbit 20496 on July 21, 1979, when Ap = 7, Kp = 2, and $F_{10.7}$ = 144.
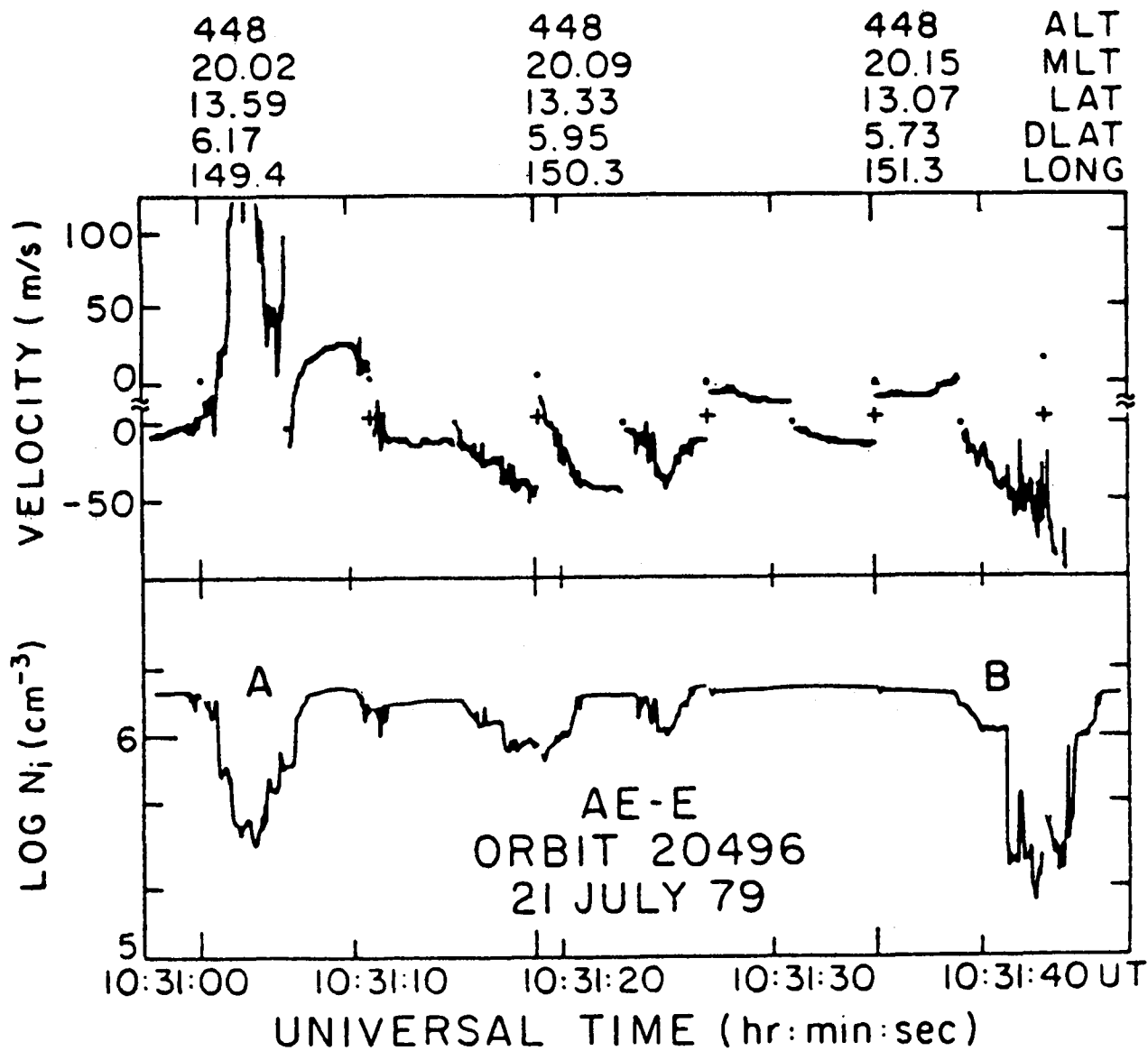
Figure 2. High-resolution version of the portion of Figure 1 marked HR. Note how depletions and velocities that are barely visible in Figure 1 can be quite clearly identified and measured in this format. Alternate 4-s segments of pitch (vertical) and yaw (horizontally) velocity data are shown in the upper trace.
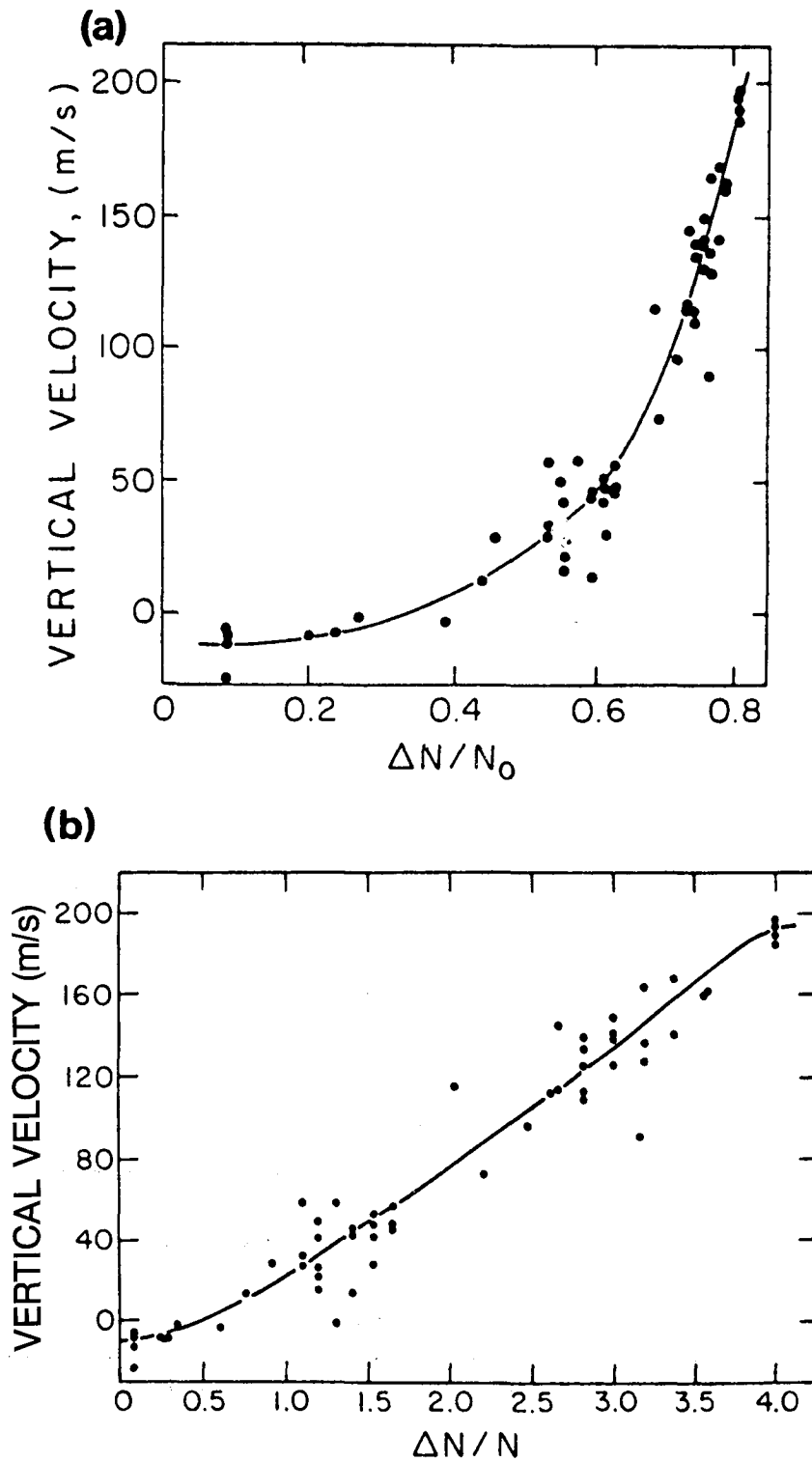
Figure 3. Vertical ion velocity data from the bubble labeled A in Figure 2 (a) plotted versus $(N_o-N)/N_o$ and (b) plotted versus $(N_o-N)/N$.
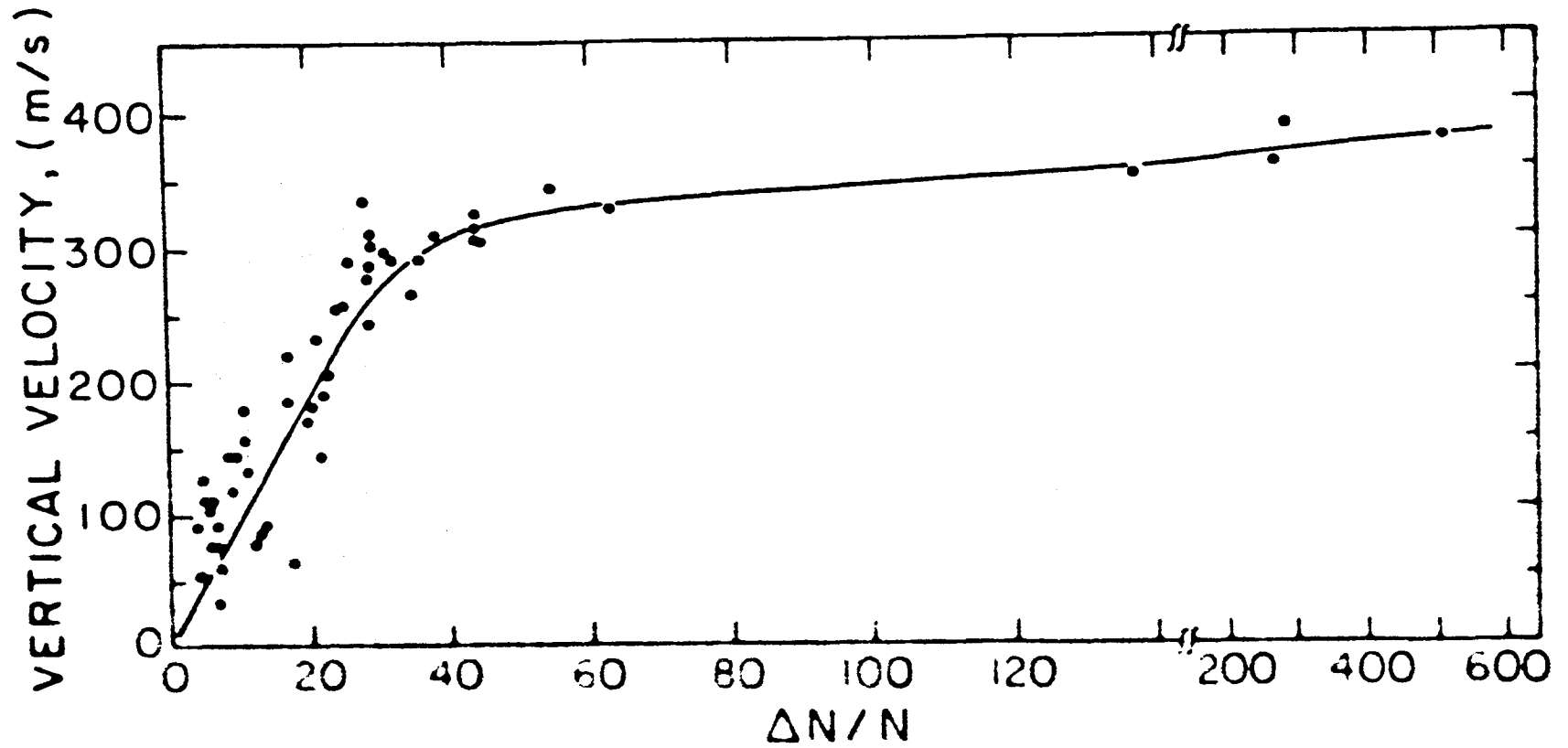
Figure 4. A plot of V_V versus $(N_o-N)/N$ for one of the very low concentration bubbles of Figure 1. Note the broken scale for $\Delta N/N$.
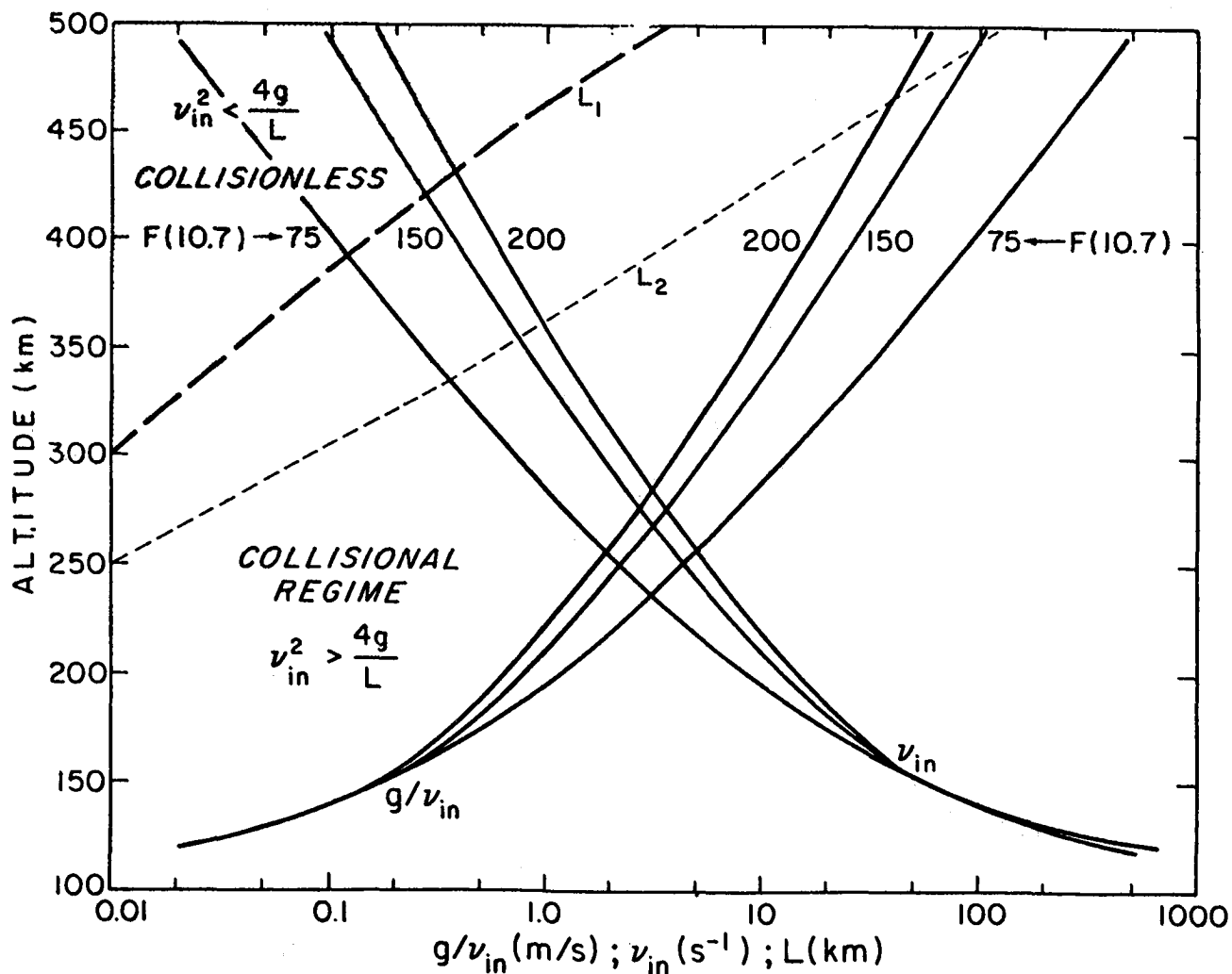
Figure 5. Plots versus altitude of the ion-neutral collision frequency (ν_{in}), the ratio of gravitational acceleration to ν_{in}, and the scale, L, that divides the collisional and collisionless regimes of the Rayleigh-Taylor gravitational instability. ν_{in} and g/ν_{in} are plotted for three different levels of solar activity, the MSIS model (Hedin, 1983) and collision cross sections from Banks and Kockarts (1973) were used to evaluate ν_{in}. The heavy dashed line (L$_1$) defines $\nu^2_{in} = 4g/L$ for F(10.7) = 175, and the light dashed line (L$_2$) does the same for F(10.7) = 75.
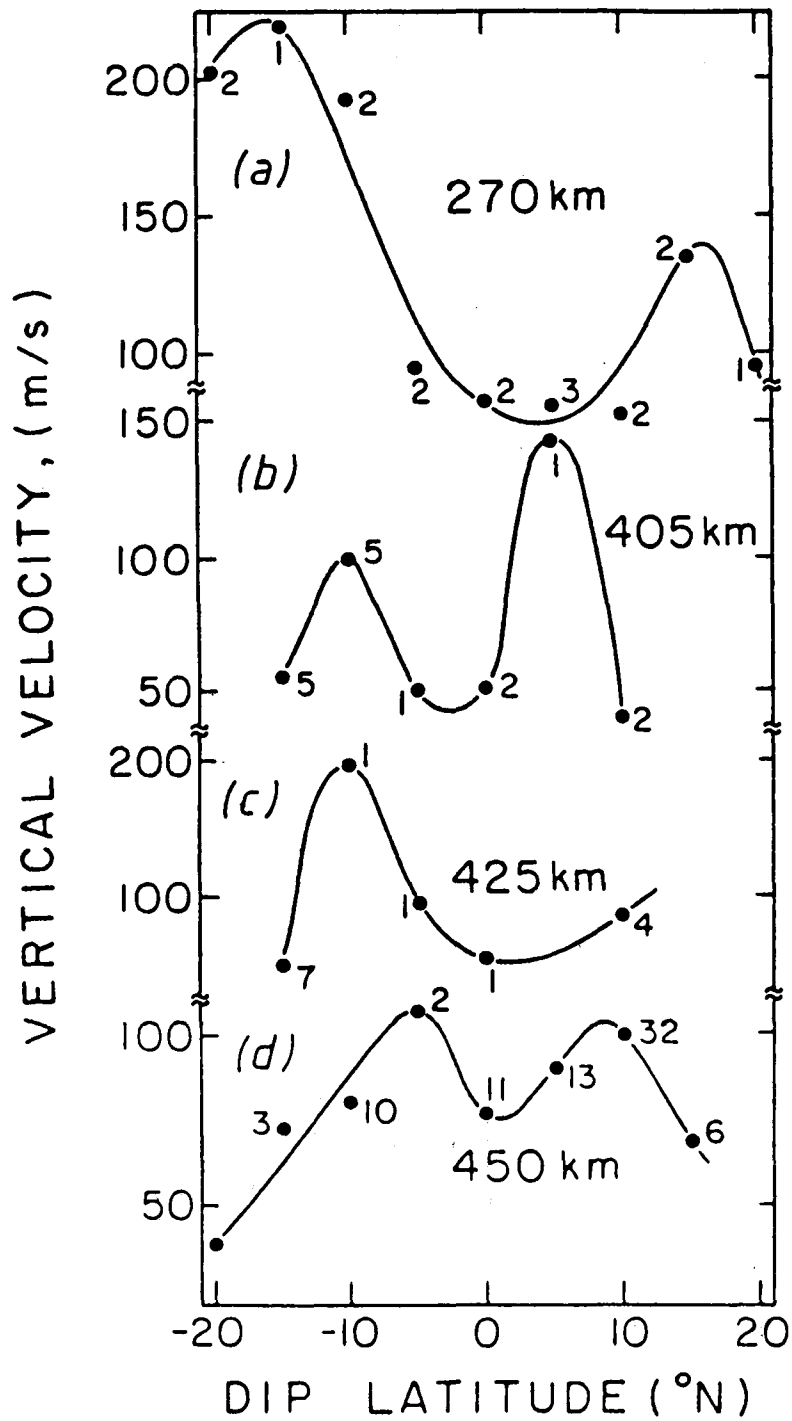
Figure 6. Vertical velocity variations with dip latitude for maximum depletions at fixed heights of 270, 405, 425, and 450 km. The number by each data point refers to the number of bubbles having that point as their mean maximum depletion velocity (low-resolution data).
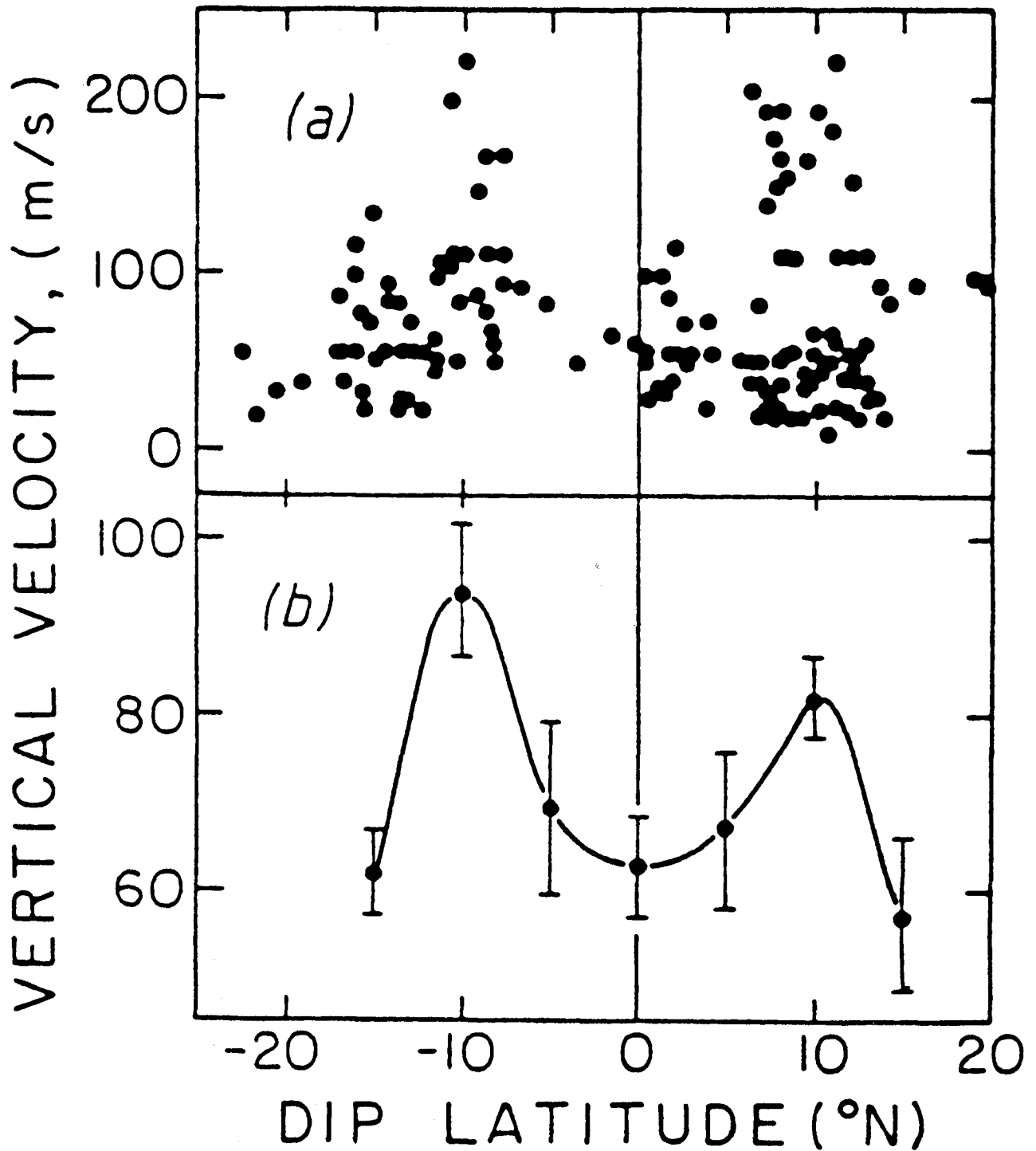
Figure 7. (a) The scatter plot and (b) the mean variation of the vertical velocity at maximum depletion as functions of dip latitude. In Figure 7b the standard error of each point is shown by a vertical bar. The data refer to bubbles with depletions of two orders of magnitude or less.
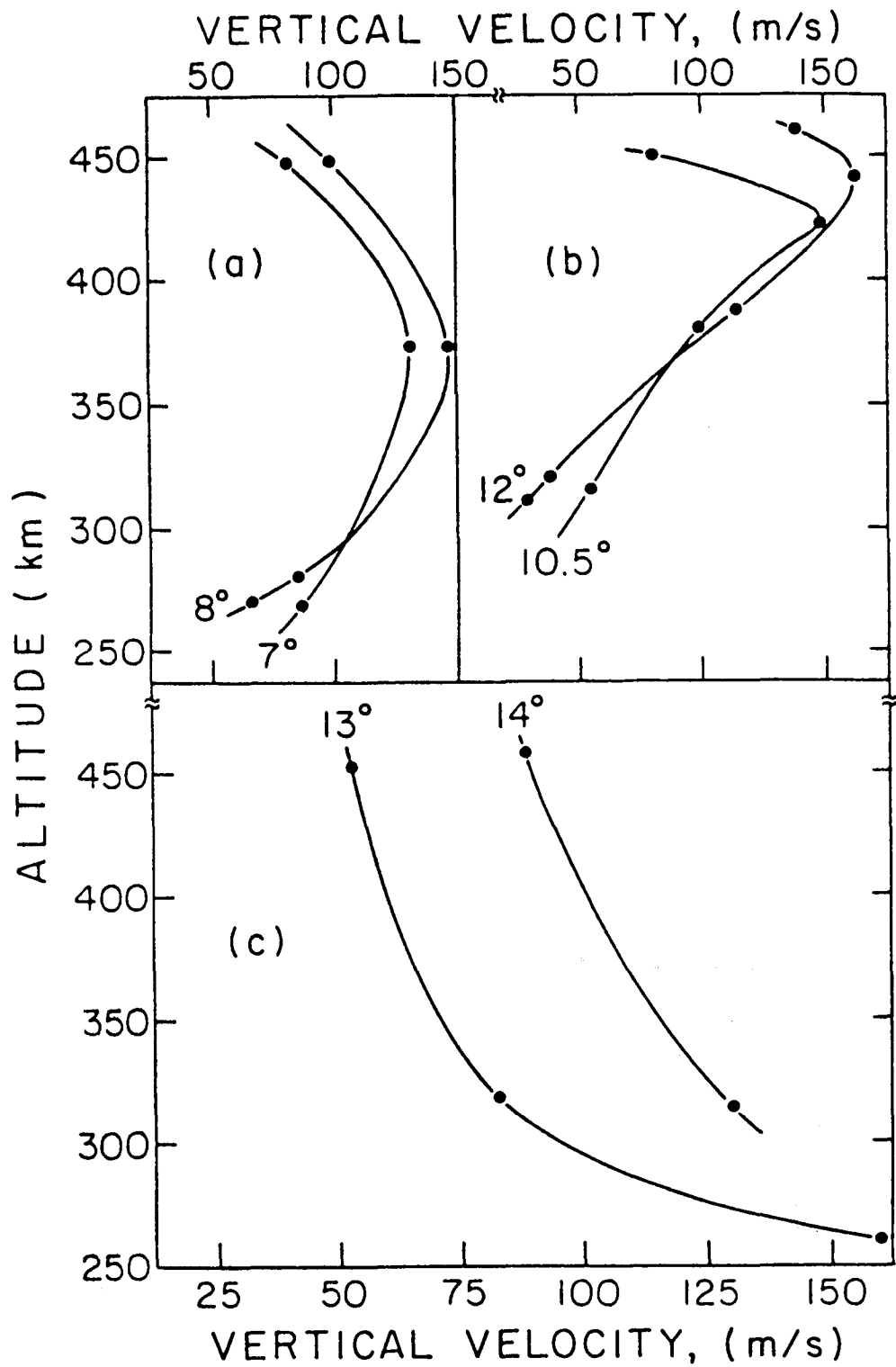
Figure 8. Variation of vertical velocity (at maximum depletion) with altitude at dip latitudes 7°, 8°, 10.5°, 12°, 13°, and 14°.
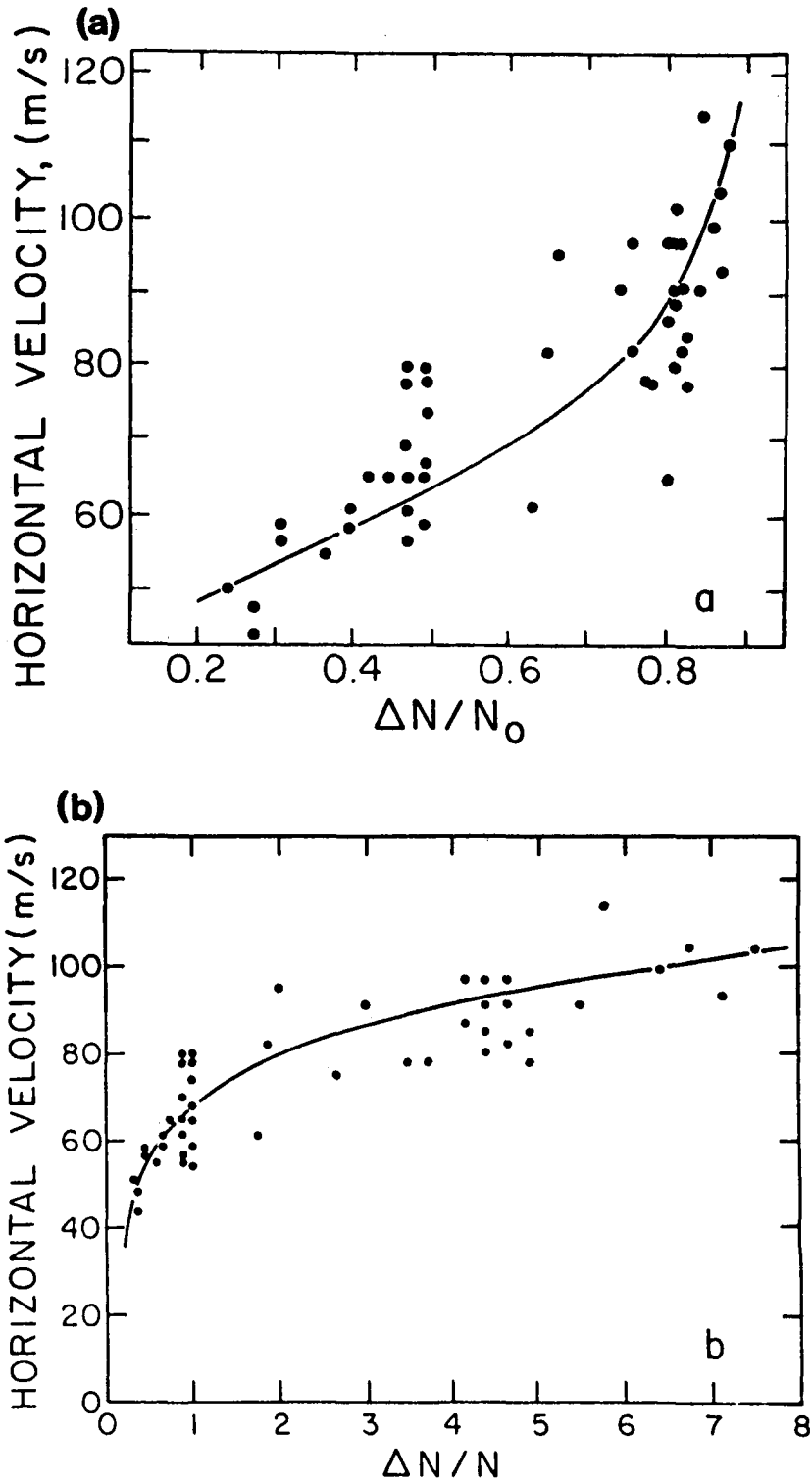
Figure 9. Plots of the horizontal ion velocity, V_H, versus depletion amplitude for the bubble labeled B in Figure 2. Figure 9a uses $\Delta N/N_o$ and Figure 9b uses $\Delta N/N$ for the abscissa.

146
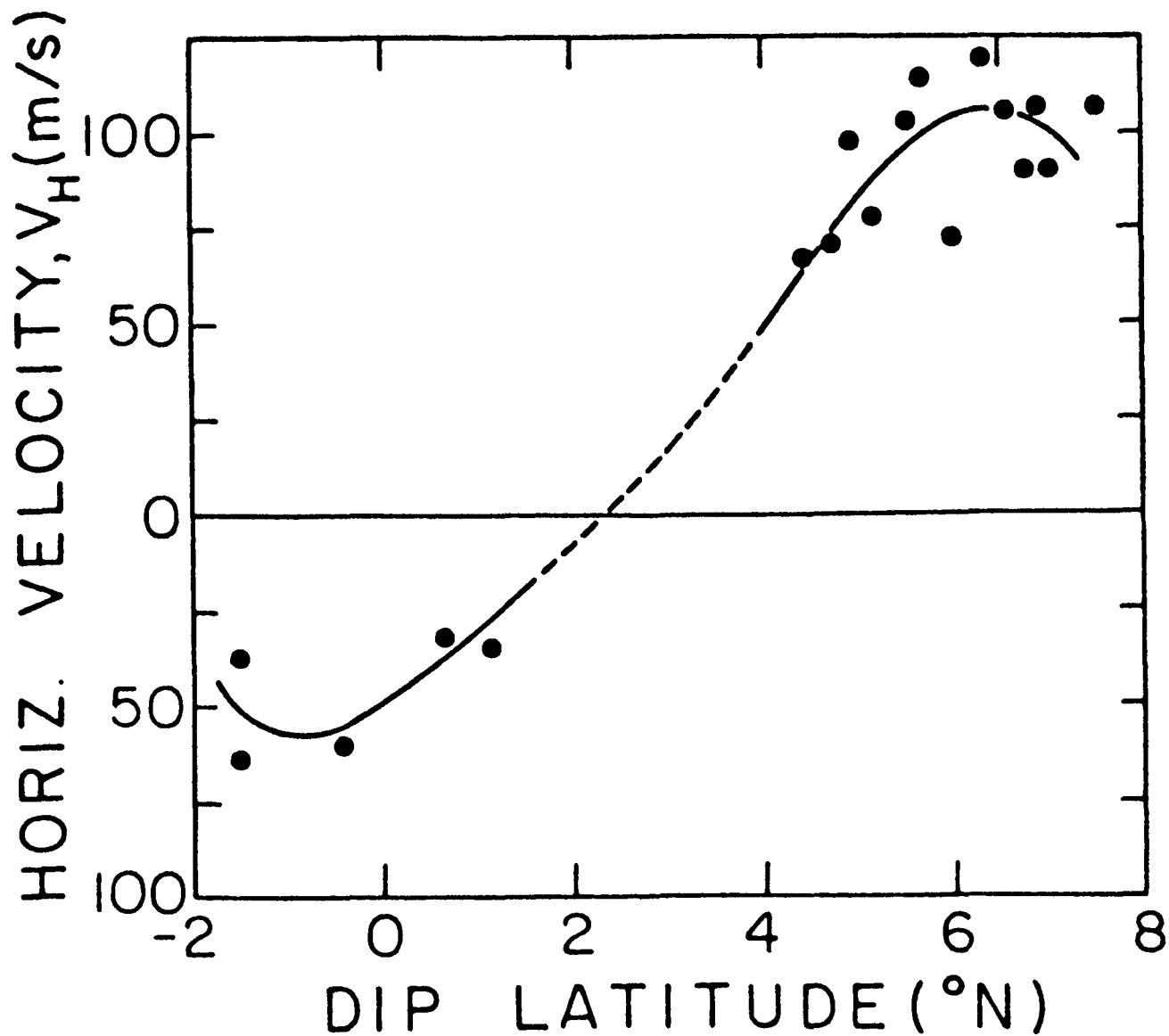
Figure 10. Plot of the maximum depletion horizontal velocity observed from the high-resolution data of AE-E orbit 20496 of July 21, 1979, as functions of dip latitude.
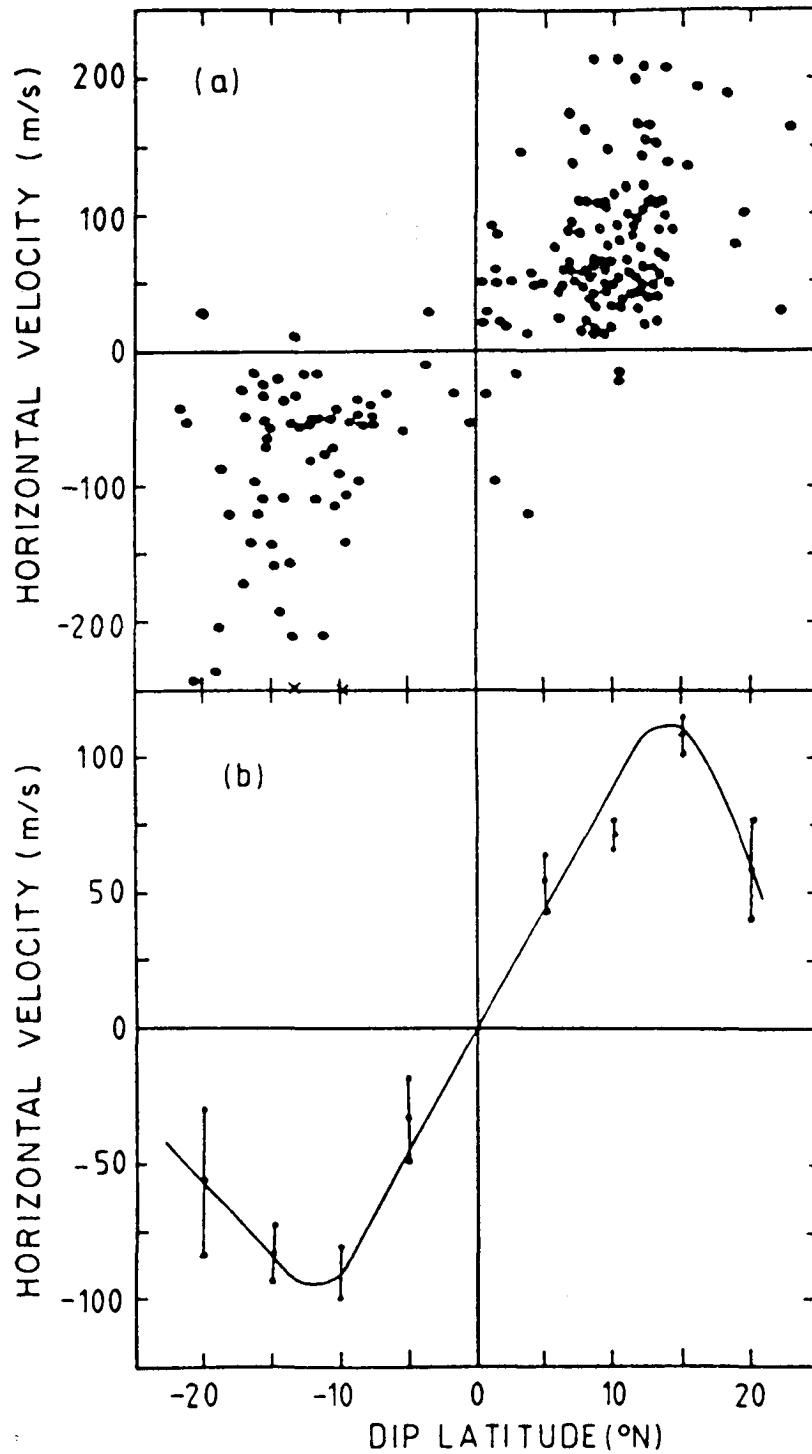
Figure 11. (a) Values of the north-south horizontal velocity at maximum depletion and (b) their mean variation, plotted as functions of dip latitude for bubbles with depletions of two orders of magnitude or less. In Figure 11b the standard error of each mean point is shown as a vertical bar.

148
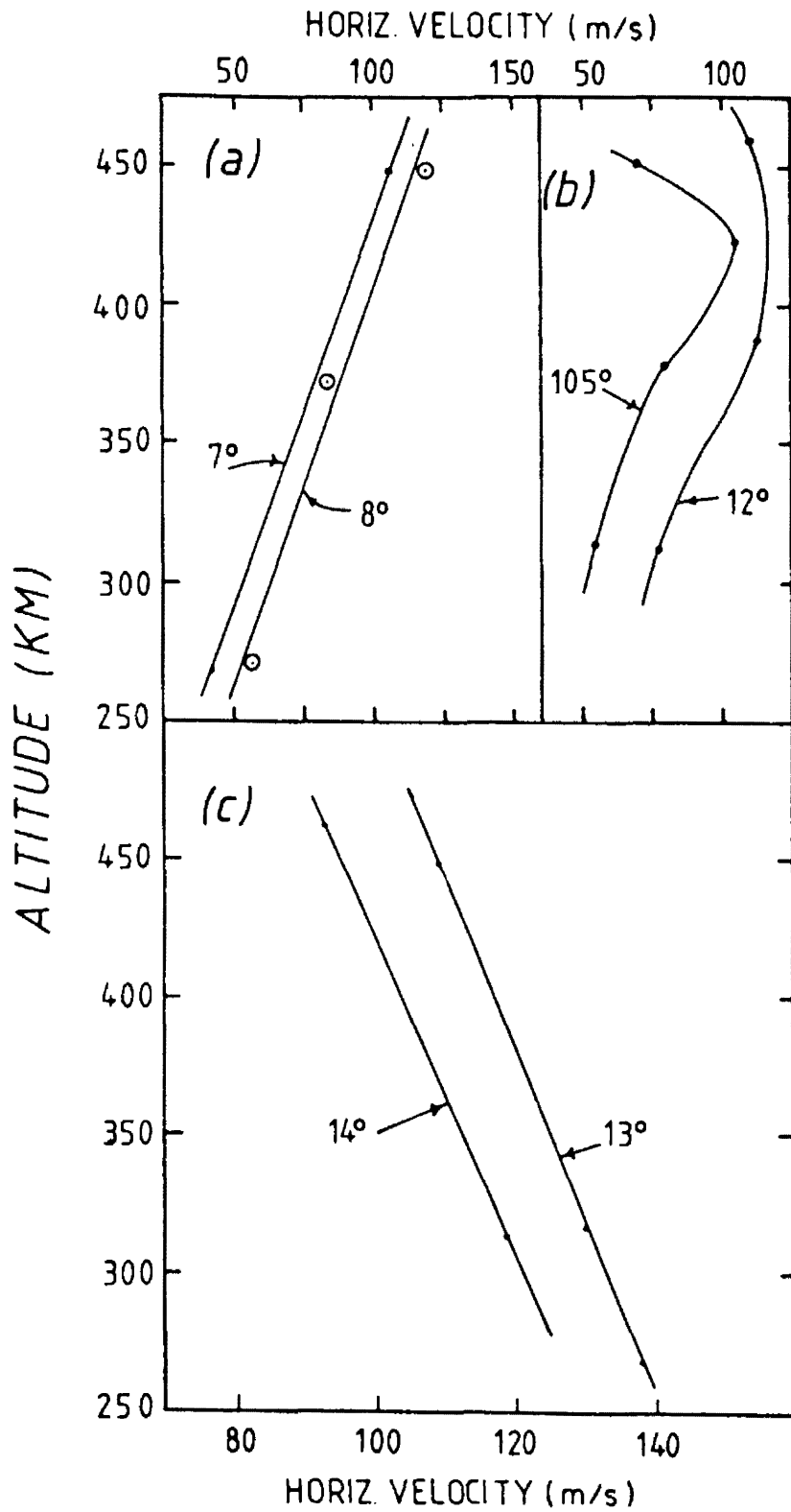
Figure 12. Same as Figure 8, but for horizontal velocity.
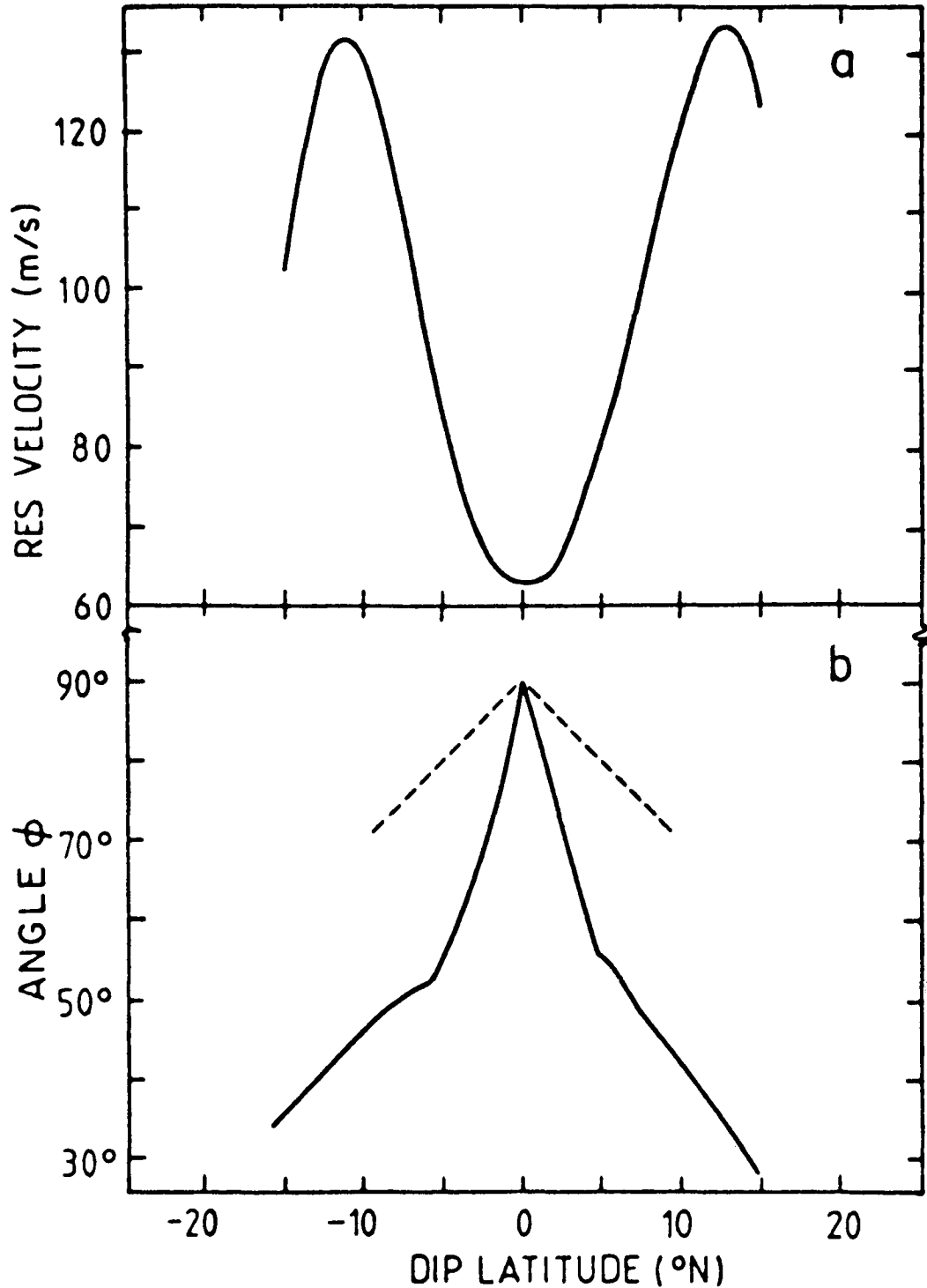
Figure 13. (a) The mean resultant ion velocity at maximum depletion as a function of dip latitude for bubbles from all the data with two-decade depletion or less. (b) The variation of the angle ϕ between the resultant velocity and the horizontal. The dashed lines give ϕ if there were no field-aligned motion.
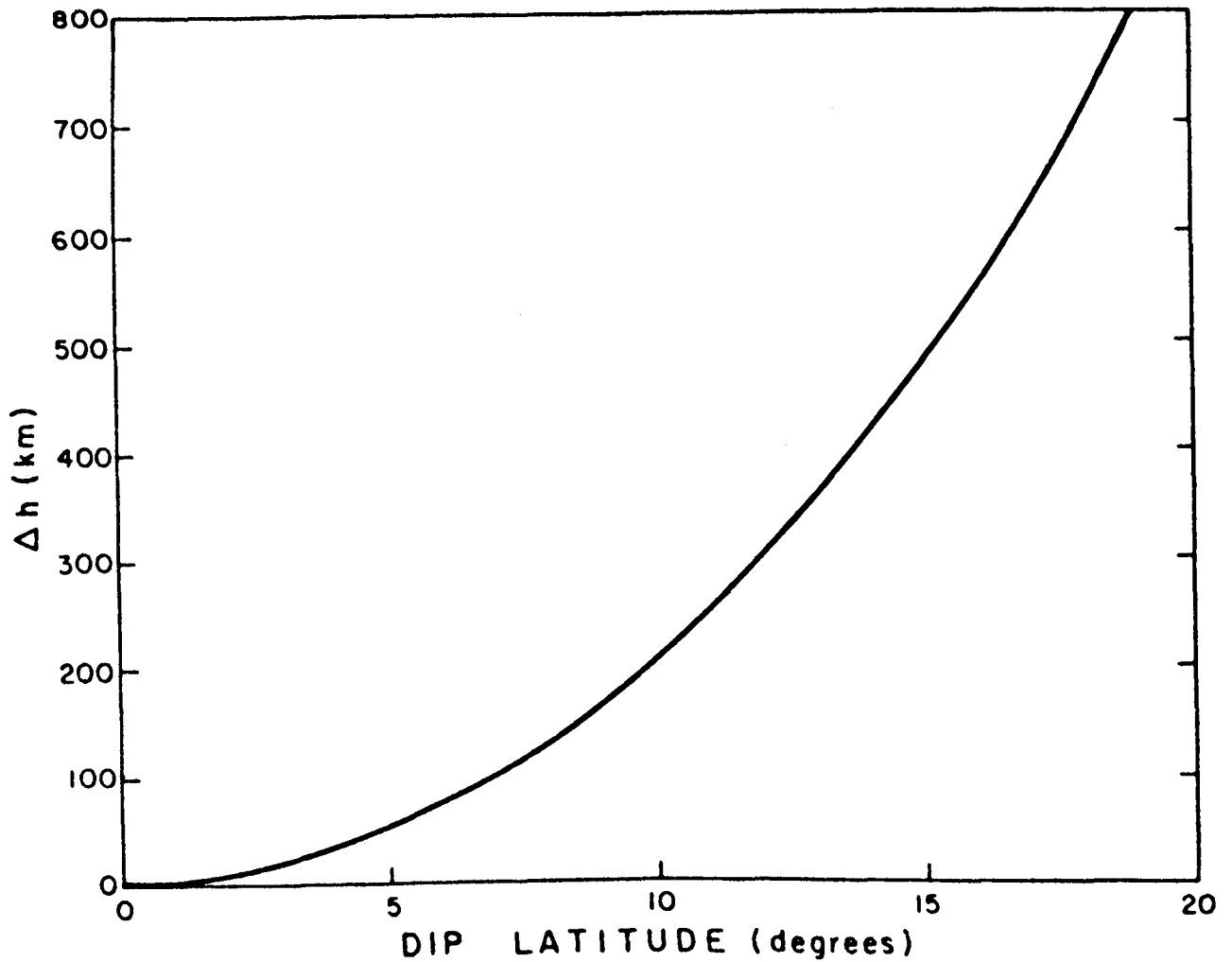
Figure 14. A plot of the altitude difference, Δh, between a satellite at radial distance r_o (6700 km) and a given dip latitude to the equatorial crossing point of its dipole field line, $\Delta h = r_o \tan^2 \lambda = r_{eq} \sin^2 \lambda$.

UT/LONGITUDINAL VARIATIONS OF COMPOSITION IN DE DATA

A. E. Hedin
Code 614
NASA/Goddard Spaceflight Center
Greenbelt, MD 20771

Composition data obtained by the quadrupole mass spectrometer (NACS) carried aboard the DE-B satellite have been examined for variations in the polar regions during magnetically quiet conditions. The corresponding predictions of the MSIS-83 model are often used for comparison. The MSIS-83 model is used to emphasize the variations of interest by suppressing all other variations. A persistent enhancement of N_2 density and a depletion of He density are present in the vicinity of the magnetic poles with maximum density response in the morning hours (magnetic) on average. A universal time (UT) variation in average density levels is evident near both the geographic and magnetic poles. There are systematic morphology changes with UT and between summer and winter which are qualitatively consistent with the simple concept that thermospheric heating effects are shifted or spread in the downwind direction of the global circulation systems driven by EUV and magnetospheric sources. The magnitude of the UT variations is larger in the southern hemisphere and is larger in local winter than summer.
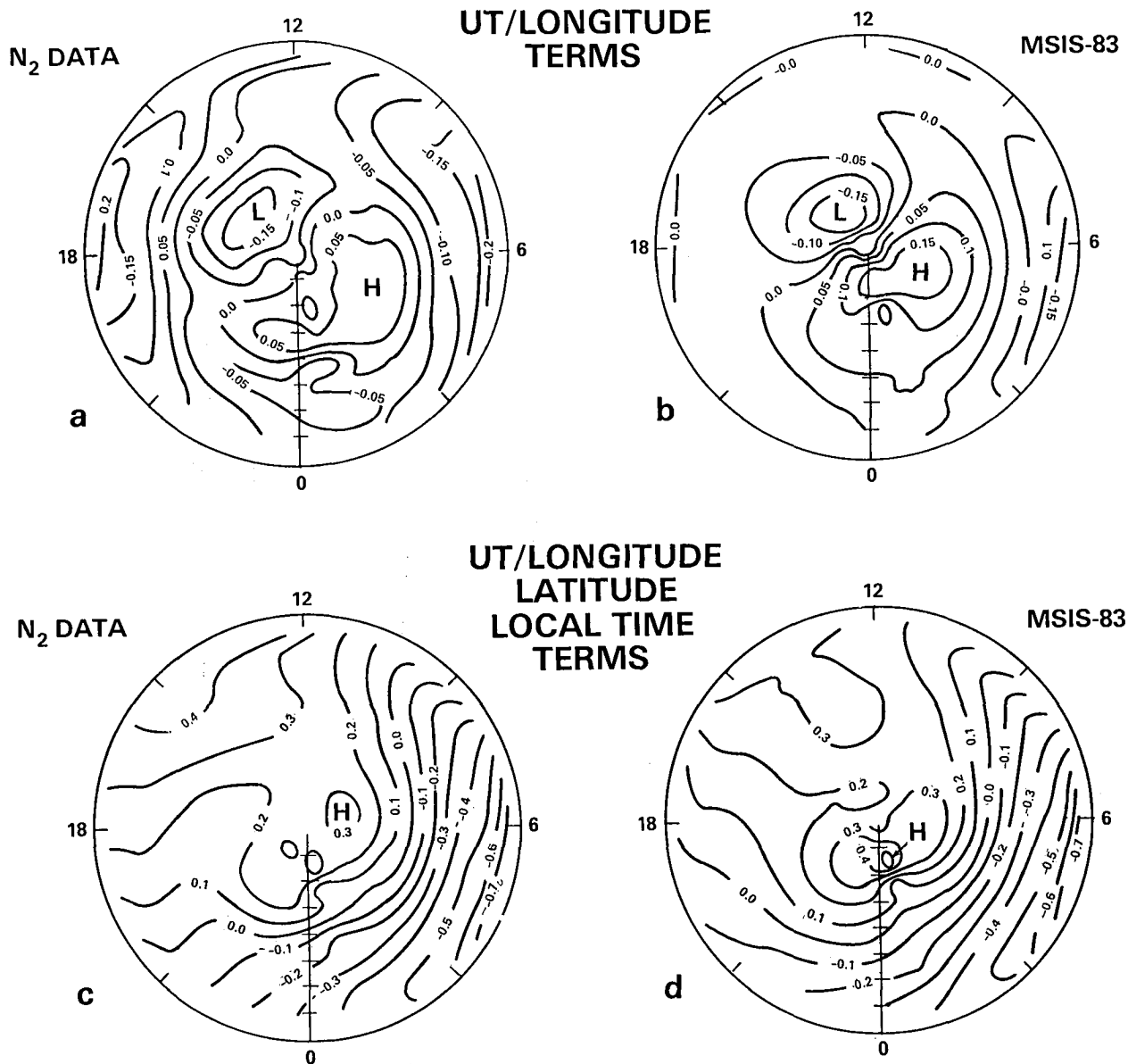
Figure 1. Contour plot in geomagnetic latitude (–90 to –30 degrees) and magnetic local time coordinates of southern hemisphere N_2 data and corresponding MSIS model results for the same data distribution: (a) logarithm of N_2 data divided by the MSIS model omitting the UT/longitude terms of the model; (b) same as panel (a) using full MSIS model N_2 densities in place of data; (c) and (d) same as panels (a) and (b) but dividing by MSIS model omitting the UT/longitude, local time, and time independent latitude terms.

154
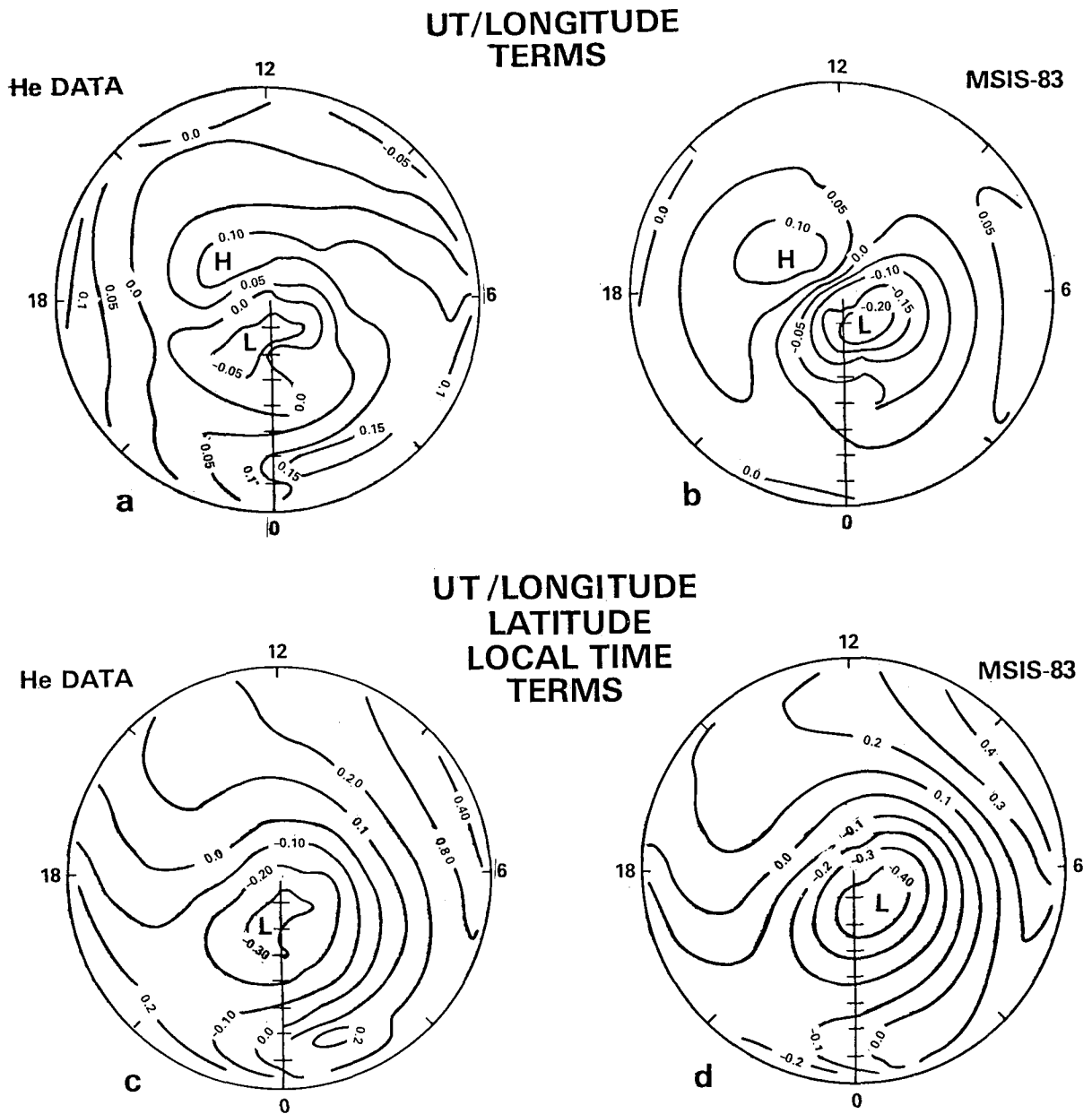
Figure 2. Contour plot in geomagnetic latitude (–90 to –30 degrees) and magnetic local time coordinates of southern hemisphere He data and corresponding MSIS model results for the same data distribution: (a) logarithm of He data divided by the MSIS model omitting the UT/longitude terms of the model; (b) same as panel (a) using full MSIS model He densities in place of data; (c) and (d) same as panels (a) and (b) but dividing by MSIS model omitting the UT/longitude, local time, and time independent latitude terms.

LONGITUDE
TERMS

He DATA

MSIS-83

a

b

LONGITUDE
LATITUDE
TERMS

He DATA

MSIS-83

c

d
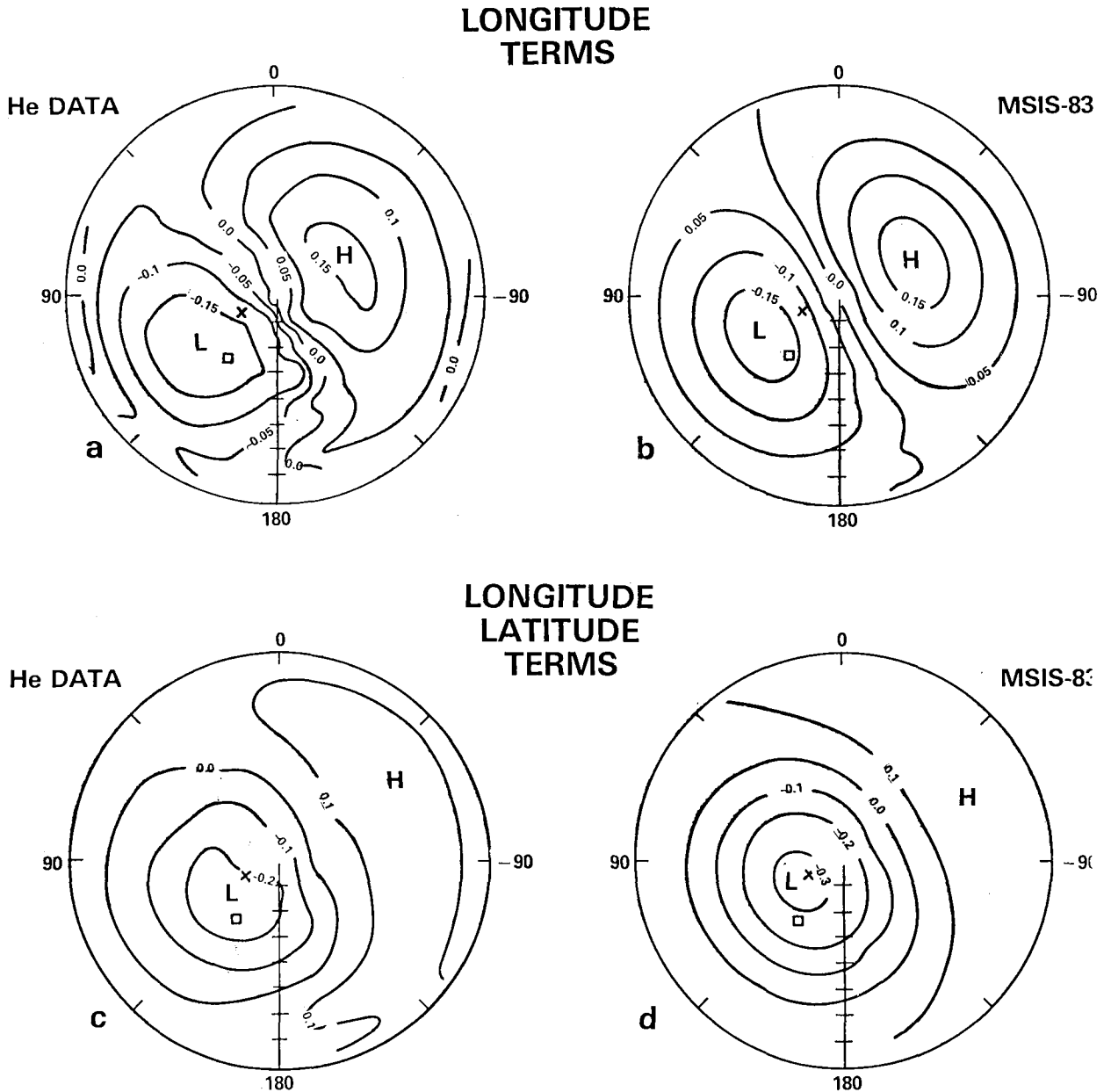
Figure 3. Contour plot in geographic latitude (-90 to -30 degrees) and longitude coordinates of southern hemisphere He data and corresponding MSIS model results for the same data distribution: (a) logarithm of He data divided by the MSIS model omitting the longitude terms of the model; (b) same as panel (a) using full MSIS model He densities in place of data; (c) and (d) same as panels (a) and (b) but dividing by MSIS model omitting the longitude and time independent latitude terms. The x indicates the geomagnetic pole and square the dip pole.

156

UT/LONGITUDE
TERMS
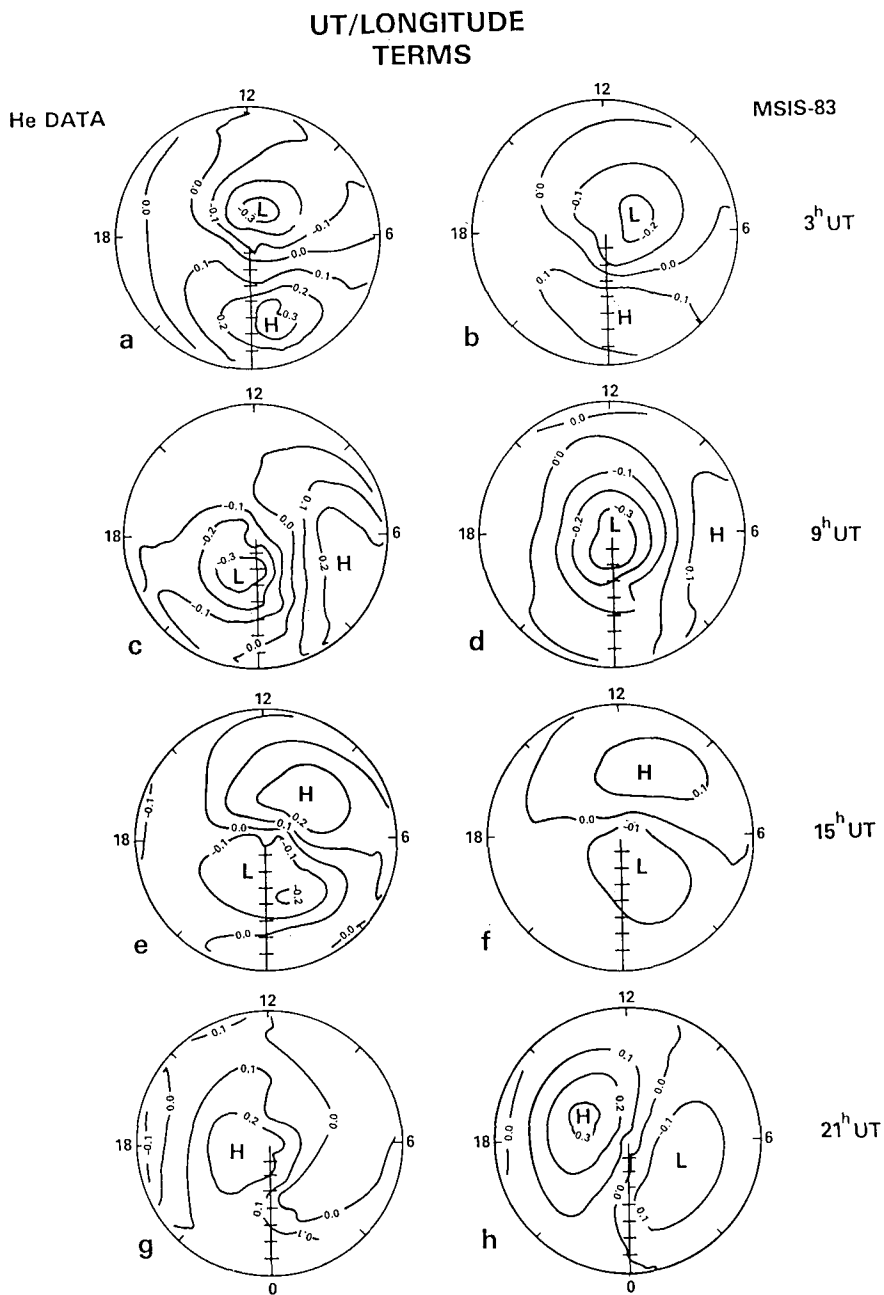
Figure 4. Contour plot in geomagnetic latitude (-90 to -30 degrees) and magnetic local time coordinates of southern hemisphere He data for six hour UT intervals and corresponding MSIS model results for the same data distribution: (a) logarithm of He data divided by the MSIS model omitting the UT/longitude terms of the model for 0 to 6 hrs UT; (b) same as panel (a) using full MSIS model He densities in place of data; (c) and (d) same as panels (a) and (b) for 6 to 12 hours UT; (e) and (f) for 12 to 18 hrs UT; (g) and (h) for 18 to 24 hrs UT.

UT/LONGITUDE
TERMS

He DATA   MSIS-83
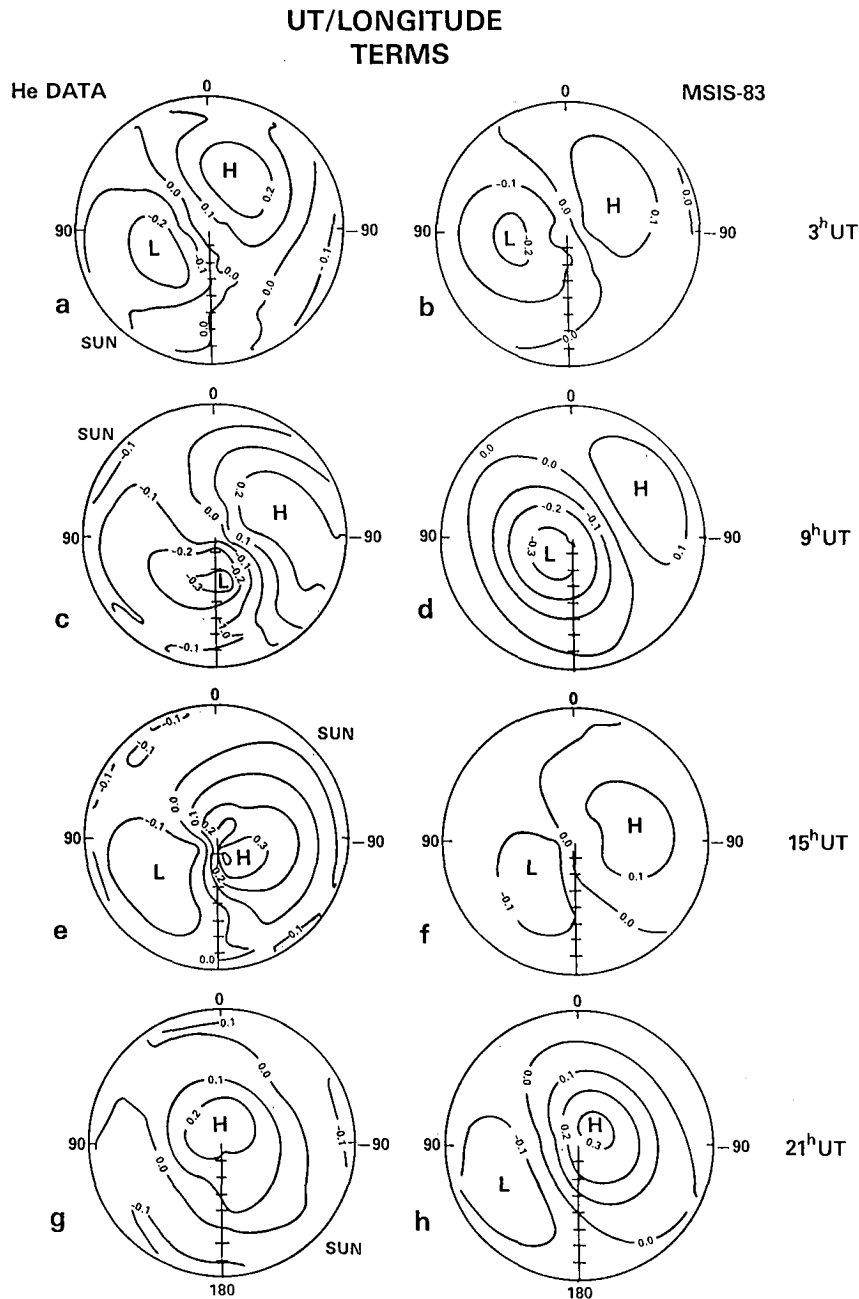
Figure 5. Contour plot in geographic latitude (-90 to -30 degrees) and longitude coordinates of southern hemisphere He data for six hour UT intervals and corresponding MSIS model results for the same data distribution: (a) logarithm of He data divided by the MSIS model omitting the UT/longitude terms of the model for 0 to 6 hours UT; (b) same as panel (a) using full MSIS model He densities in place of data; (c) and (d) same as panels (a) and (b) for 6 to 12 hours UT; (e) and (f) for 12 to 18 hrs UT; (g) and (h) for 18 to 24 hrs UT.

158
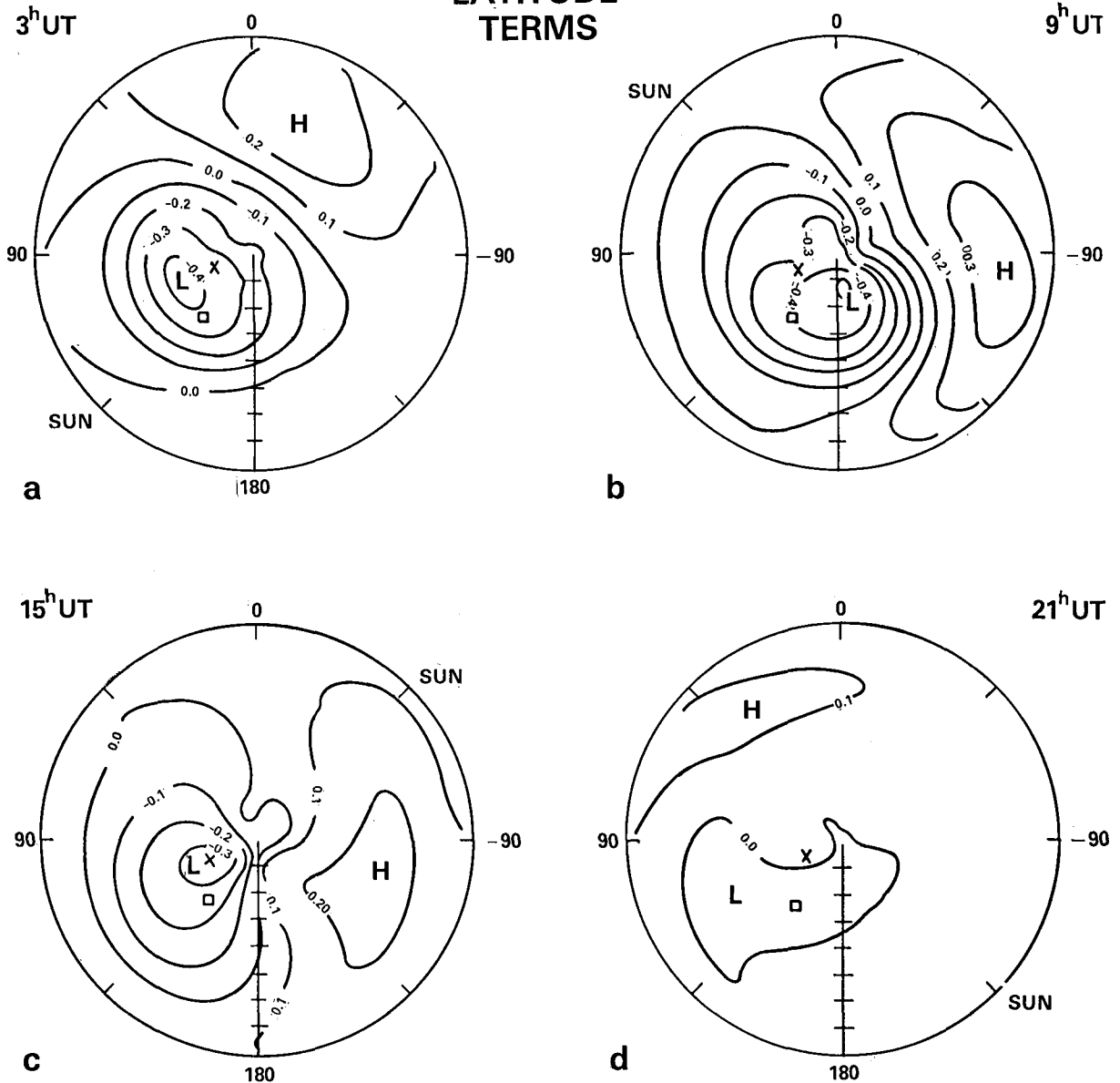
Figure 6. Contour plot in geographic latitude (-90 to -30 degrees) and longitude coordinates of southern hemisphere He data for six hour UT intervals. Contours indicate the logarithm of He data divided by the MSIS model omitting the UT/longitude and time independent latitude terms of the model for (a) 0 to 6 hrs UT; (b) 6 to 12 hrs UT; (c) 12 to 18 hrs UT; and (d) for 18 to 24 hrs UT.

159
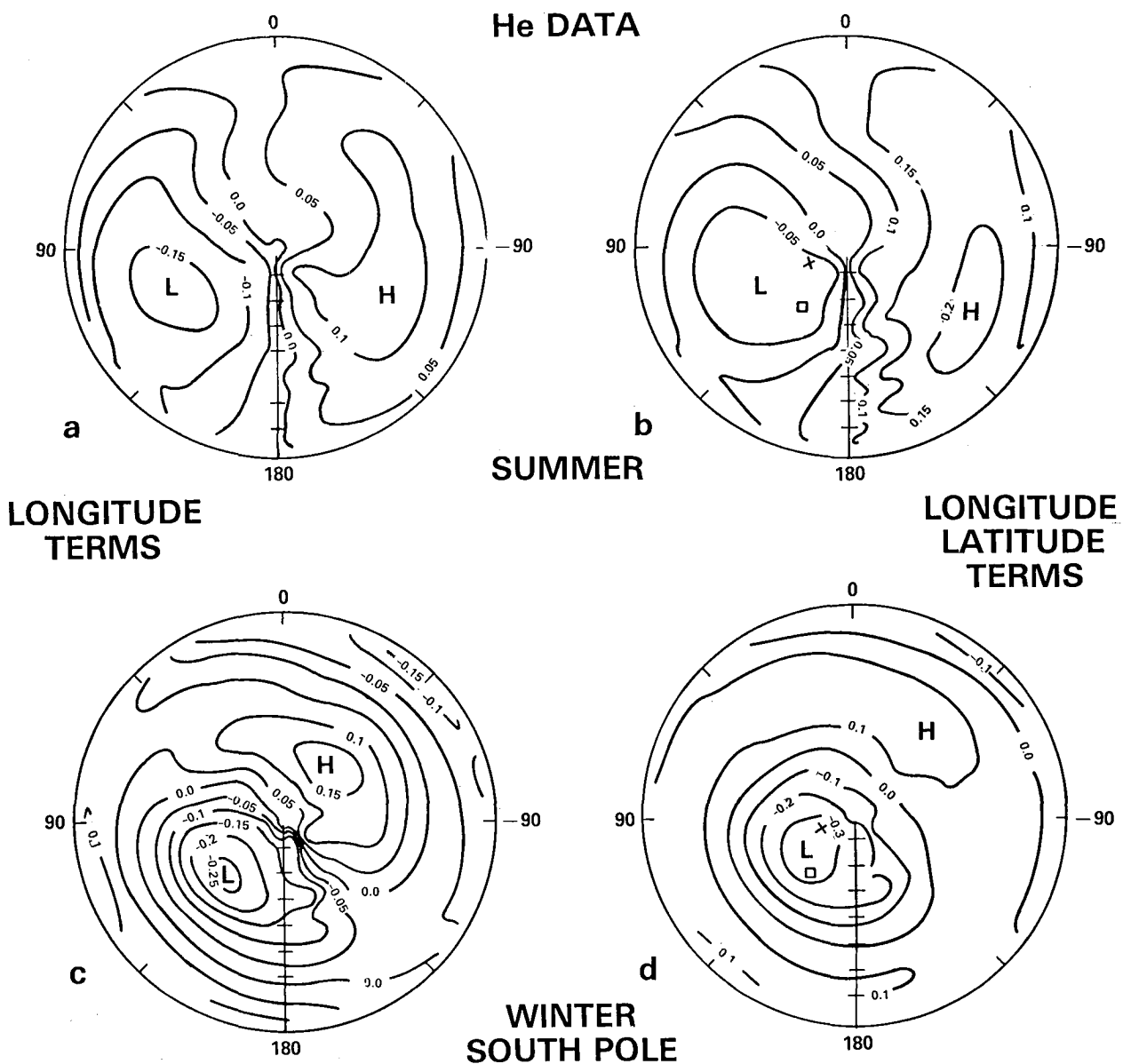
Figure 7. Contour plot in geographic latitude (−90 to −30 degrees) and longitude coordinates of southern hemisphere He data: (a) logarithm of He data divided by the MSIS model omitting the longitude terms of the model for summer data; (b) same as panel (a) but dividing by MSIS model omitting the longitude and time independent latitude terms; (c) and (d) same as (a) and (b) but for winter data.

He DATA

SUMMER

LONGITUDE TERMS

LONGITUDE LATITUDE TERMS

WINTER NORTH POLE
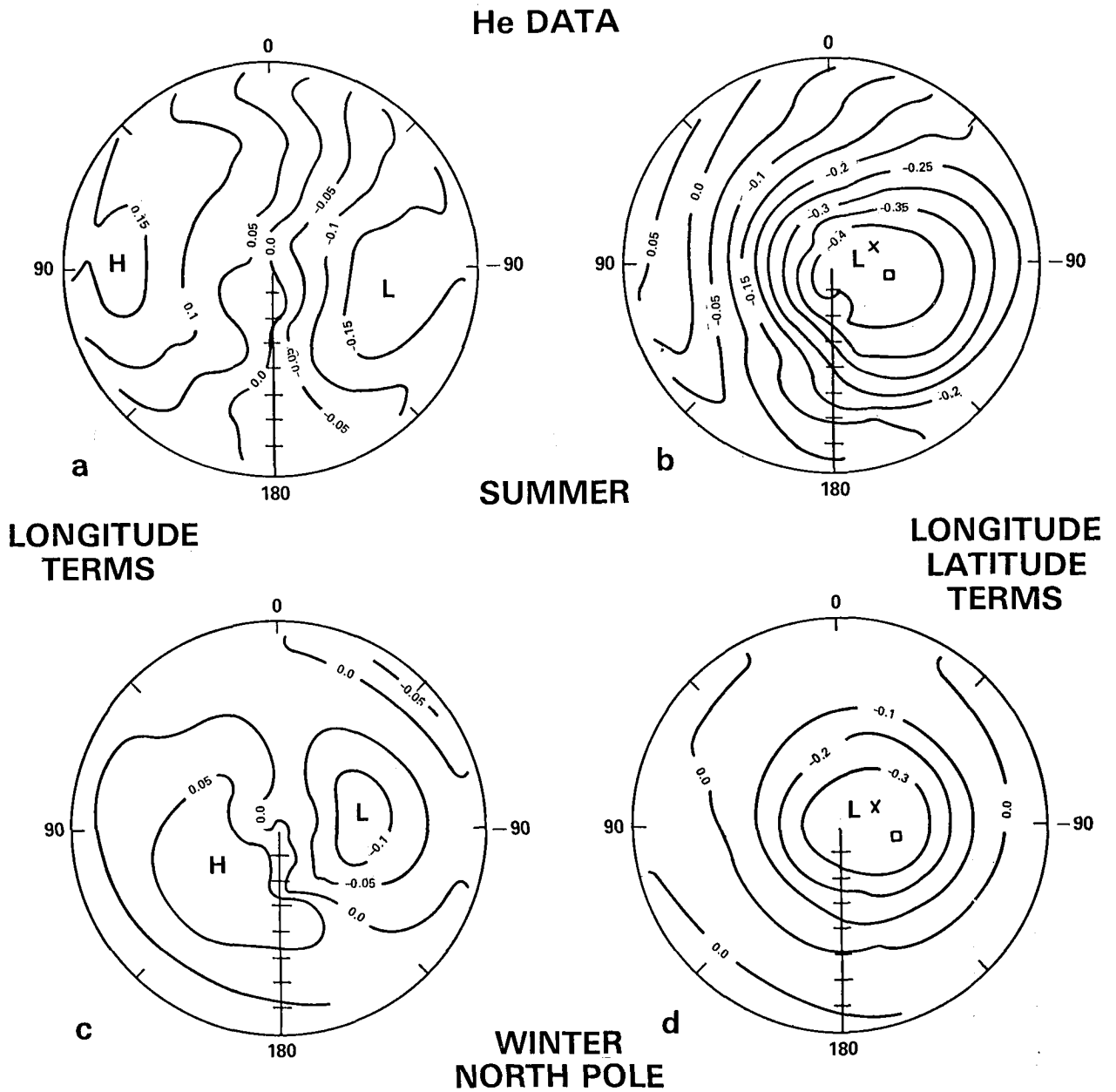
Figure 8. Contour plot in geographic latitude (-90 to -30 degrees) and longitude coordinates of northern hemisphere He data: (a) logarithm of He data divided by the MSIS model omitting the longitude terms of the model for summer data; (b) same as panel (a) but dividing by MSIS model omitting the longitude and time independent latitude terms; (c) and (d) same as (a) and (b) but for winter data.

N₂

He
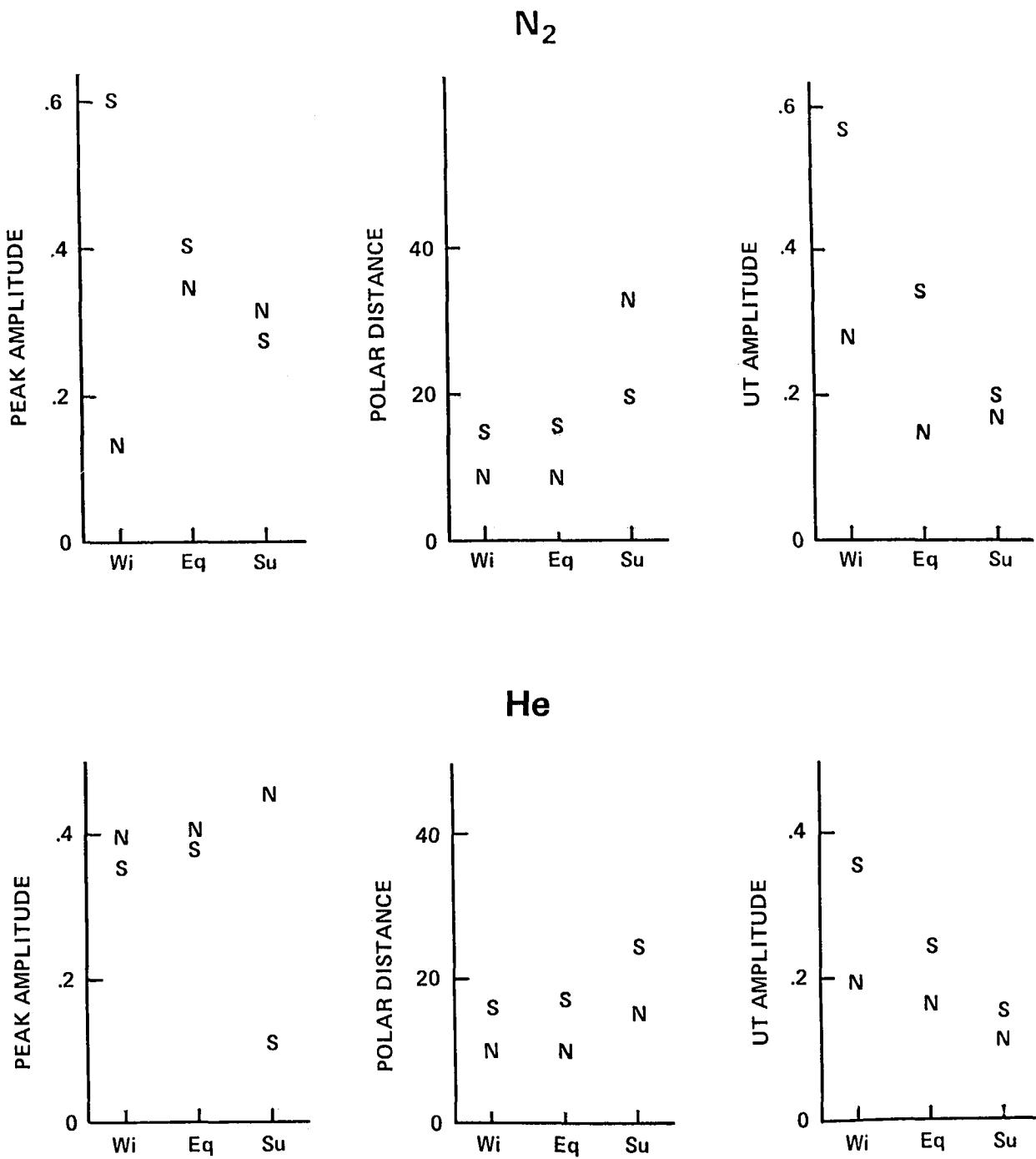
Figure 9. Magnitude of the polar peak, angular distance from the geographic pole, and amplitude of the UT variation at the geographic pole as a function of season for He and N₂ data. N indicates northern hemisphere and S indicates southern hemisphere.

CONVECTION PATTERN MORPHOLOGY AND VARIATIONS
(Invited Review)

R. A. Heelis
Center for Space Science
P.O. Box 688
The University of Texas at Dallas
Richardson, TX 75080

A fairly straightforward consideration of the interaction between a southward interplanetary magnetic field and the earth's magnetic field will result in the prediction of a two-cell convection pattern in the high latitude ionosphere. This is shown schematically in Figure 1 where the antisunward flow at high latitudes results from the application of the solar wind electric field to the ionoshpere and the return sunward flow results from an electric field generated in the plasma sheet to ensure continuity.

This convection pattern can be quite easily characterized in terms of the radius of the approximately circular region containing the anti-sunward flow, called the polar cap and the maximum potential difference applied across this region. The polar cap potential difference can be shown to be a sensitive function of the orientation of the interplanetary magnetic field and consideration of magnetic flux conservation can predict a dependence of the polar cap radius on the polar cap potential (Siscoe, 1982). The size of the polar cap is predicted to vary as the 3/16 power of the potential difference. This dependence is not strong enough to be unequivocably demonstrated by the data. However, Figure 2 shows the dependence of the polar cap potential drop on the ratio of electric fields inside and outside the merging region (Reiff et al., 1981). Merging theory simply expresses this ratio as the cosine of the angle between the IMF and a plane perpendicular to the sun-earth line (i.e. Bz/Bx) (Hill, 1974).

It can be seen from Figure 2 that the polar cap potential increases as the IMF becomes more southward and that a relatively large potential drop remains even when the IMF turns northward. This residual potential drop has been attributed to a 'viscous interaction' process at the flanks of the magnetosphere that exists in addition to the dayside merging process that operates when the IMF has a southward component. A more detailed analysis of the behavior of the potential difference when the IMF turns northward is shown in Figure 3 (Wygant et al., 1983). It displays an almost exponential decay, requiring some 2-4 hours to reach a residual value near 15 Kv.

In addition to a variation in the polar cap potential drop as a function of the IMF orientation examination of the signatures of ionospheric convection from satellites show that the cell geometry or cell shape is also dependent on the IMF. First observations of the flow geometry near local noon showed that substantial east-west flows could occur in this region. An arbitrary inspection of the data also showed that this flow could be predominantly to the east or predominantly to the west. Examples of these differing flow signatures are shown for almost identical orbital conditions in Figures 4 and 5. A compilation of such data without strict consideration of the IMF orientation leads to the concept of a restricted region of sunward flow near local noon sometimes called the 'throat'. Figure 6 shows a schematic of such a flow geometry generated from a mathematical model. Studies of the electric field near the dawn and dusk convection reversals had

already revealed a dependence of electric field magnitude on the IMF (Heppner, 1972). It was known that the antisunward flow on the poleward side of the convection reversal was larger on the dusk (dawn) side than on dawn (dusk) side if the IMF By component was negative (positive).

A rotation of the throat region was postulated to account for the previously known dependence of the dawn/dusk flow speeds on the IMF but it was recognized that the data base of convection signatures should be examined for different IMF orientations and that even then the single cuts available from satellites like AE and DE could not define the entire high latitude convection geometry. Examination of the AE data base shows that reproducible signatures of the convection pattern can be obtained if we restrict our attention to times when the IMF has a southward component (Bz < 0) and a normal garden hose orientation (BxBy <0). Under these conditions the pattern can be generally characterized by dividing it into signatures seen when By is positive and when By is negative.

Figure 7 shows examples of the signature seen in the northern high latitude ionosphere when By is positive (and Bx is negative). The most reproducible feature is that the flow near local noon is directed toward dawn at all invariant latitudes between 70 and 80 degrees. If we trace the position of the zero potential line that separates cells in which the flow is either clockwise around the dawn side or anti-clockwise around the dusk side, we note that it shows a tendency to be displaced slightly to the dawn side of local noon. This results in the dusk convection cell being relatively large and almost circular in shape while the dawn cell is apparently more cresent shaped and abuts the dusk cell. A more detailed description of the convection geometry for this orientation of the IMF has been obtained by using simultaneous data from the DE satellite and ground based radars at Chatanika and Millstone Hill. This data set provides multiple data points around the high latitude region at which the electrostatic potential and flow direction are specified. The results of an examination of this data set are shown in Figure 8 and confirm our expectations.

Figure 9 shows examples of the northern hemisphere high latitude convection signature seen when the IMF By is negative (and Bx is positive). Contrasting these signatures with those shown in the previous two figures it can be seen that the flow with an anti-sunward component near local noon is directed toward dusk rather than toward dawn. In extreme cases when the magnitude of By greatly exceeds Bx the flow may be directed eastward as shown in the last two examples. In all cases however the flow signature is consistent with a more circular perimeter to the dawn cell with a cresent shaped dusk cell that surrounds it. To my knowledge a study of multipoint measurements to confirm such a flow geometry has not yet been completed. Figure 10 shows schematically the dayside high latitude flow geometry that exists in the northern hemisphere for different configurations of a southward IMF.

When the IMF has a northward component (Bz > 0) the observed convection velocities are usually much more structured both in the summer and in the winter hemispheres. Nevertheless large scale convection signatures can often be recognized and reproducible features emerge with a dependence on the IMF orientation. Figure 11 shows the most easily identified feature from S3-2 electric field data (Burke et al., 1982). Here sunward convection exists at the very highest magnetic latitudes where anti-sunward convection would normally be expected if the IMF had a southward component. Figure 12 shows the ion convection signature observed by DE-B during times of northward IMF. Similar regions of sunward convection are seen in this data base but additional features dependent on By can also be identified. Regions of anti-sunward convection on one or both sides of this high latitude sunward convection allow the identification of one and sometimes two convection cells within a region that can be associated with open field lines. These convection cells are labelled I and II in the figure. In addition to the convection cells within the polar cap there usually exists additional convection cells at lower latitudes that circulate in the same sense as the cells existing during times of southward IMF. These cells are labelled III and IV in the figure.

Examination of a large data base shows a dependence of the number of convection cells and their sense of circulation on the By component of the IMF. Figure 13 shows schematically these dependences for the high latitude northern hemisphere. When By is close to zero two convection cells apparently exist within the polar cap. They occupy the dawn and dusk sides and circulate anti-clockwise and clockwise respectively to produce sunward flow at the highest latitudes. At lower latitudes cresent shaped cells form about each of the polar cap cells and circulate in the manner expected for a southward IMF. When By is negative the dawn-side polar cap convection cell tends to disappear giving way to a slightly larger dusk-side cell and more turbulent flow on its dawn side. The two lower latitude convection cells remain. When By is positive the polar cap dawn-side cell remains and perhaps expands and more turbulent flow exists on its dusk side. Again the lower latitude convection cells remain. The completeness of the convection cells is extremely difficult to observe since the nightside high latitude convection is extremely turbulent during times of northward IMF. The convection pattern I have described is at least understandable in terms of solar-wind/magnetosphere interaction in which open field lines are recirculated in the polar cap and a viscous interaction process exists near the flanks of the magnetosphere's equatorial plane giving rise to the lower latitude convection cells.
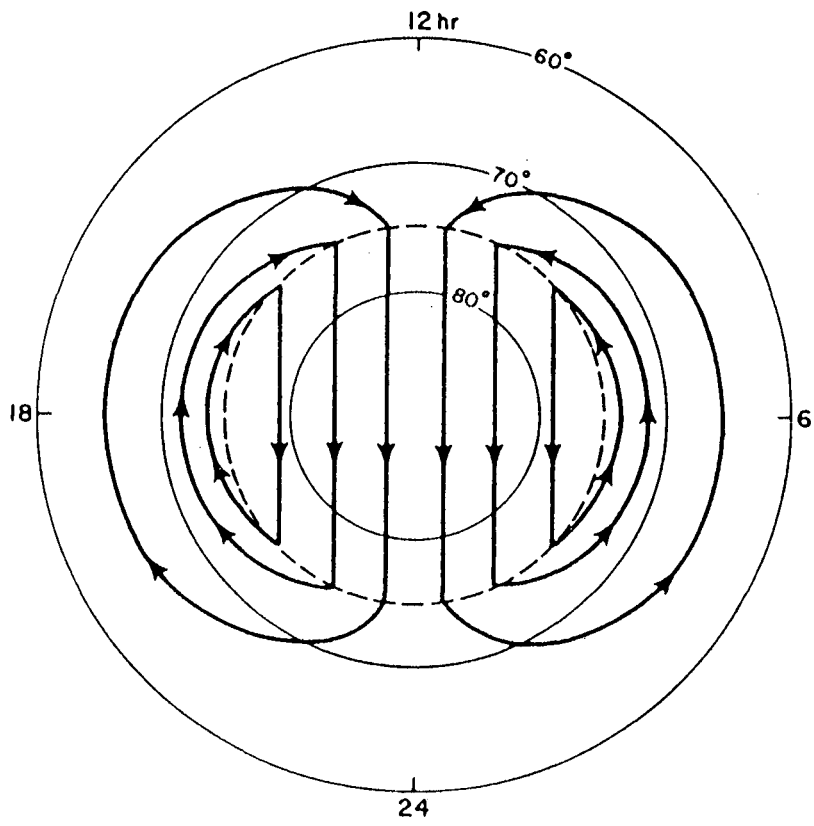
Figure 1.
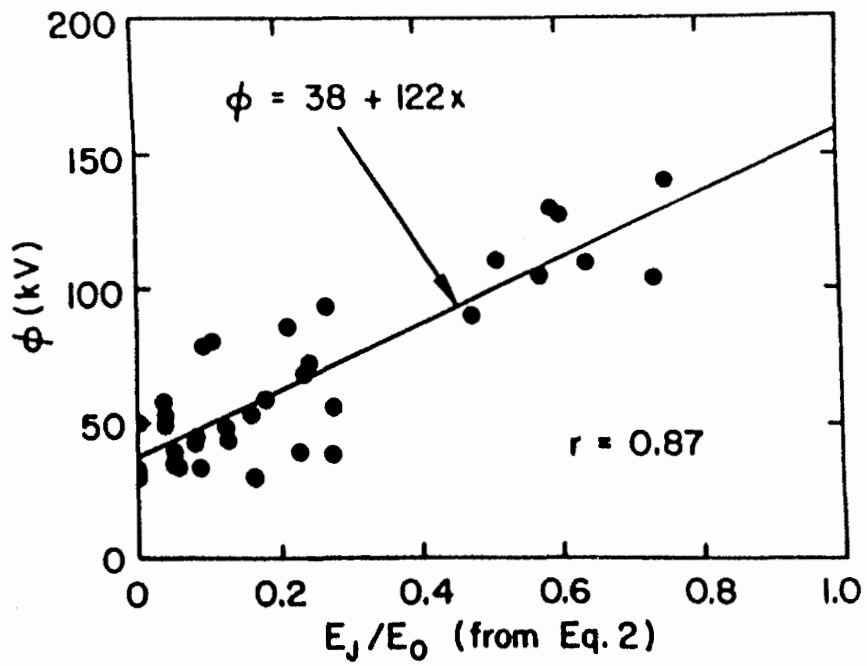
Figure 2.
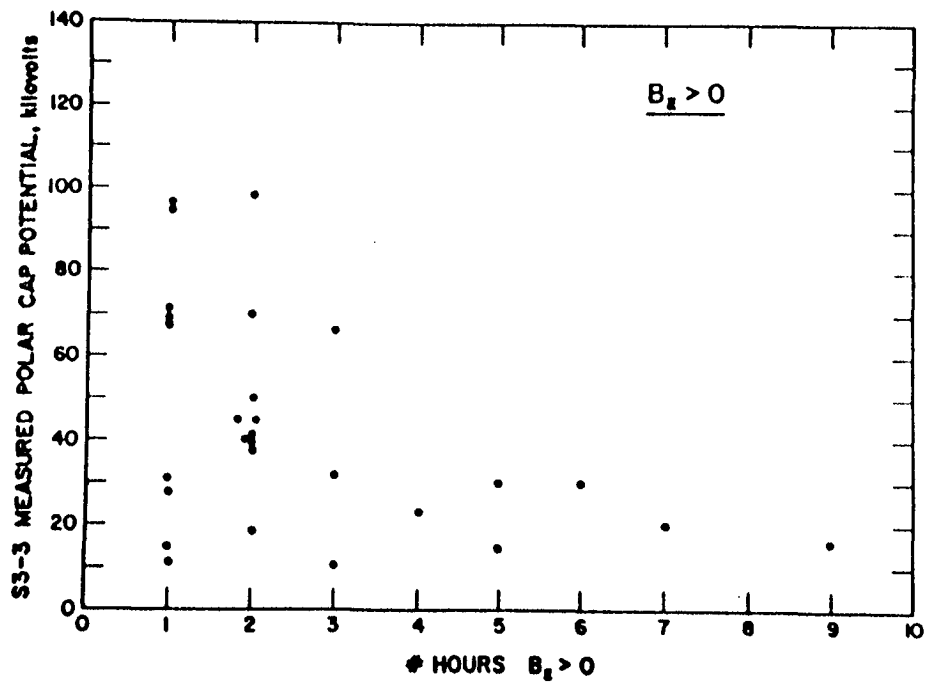
Figure 3.

DE-B ION DRIFT VELOCITIES
MLT V ILAT   NORTHERN HEMISPHERE
DAY 81298   UT 10:50   ORBIT 1226
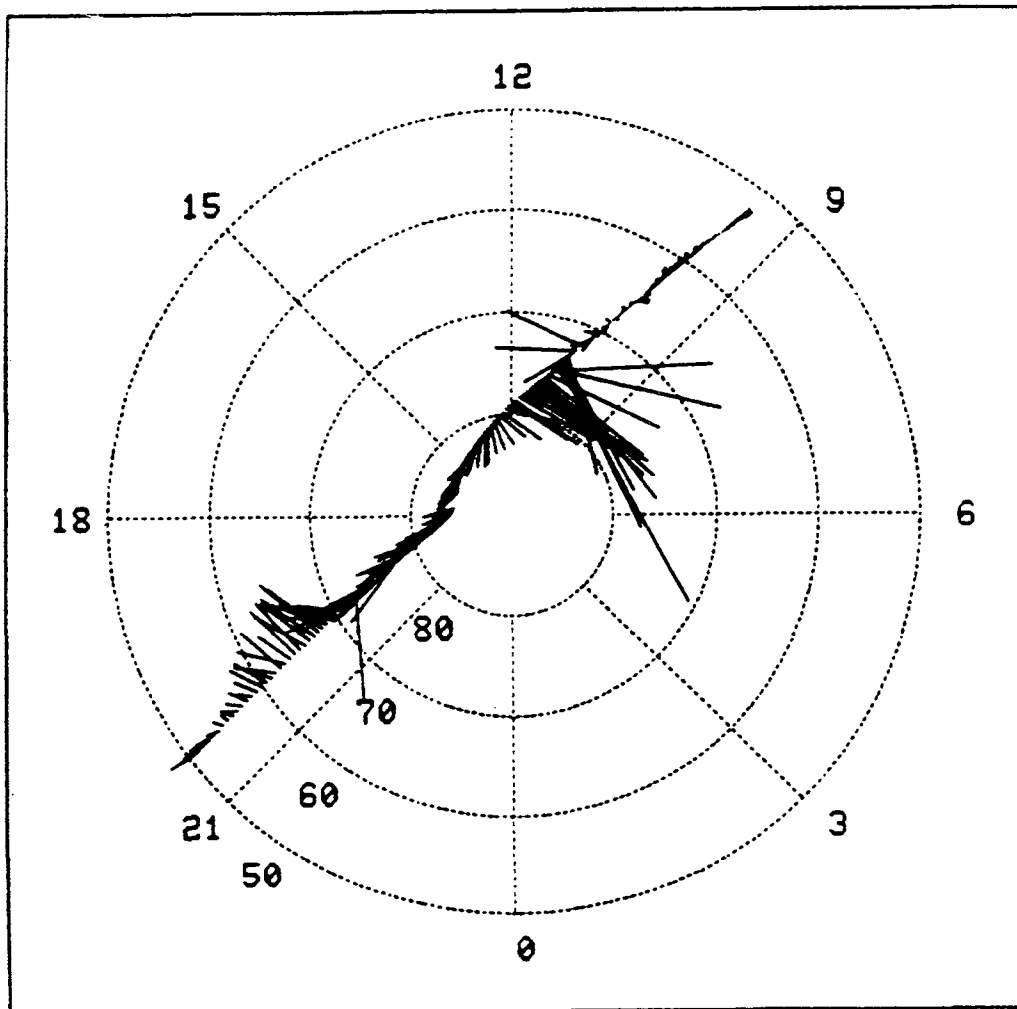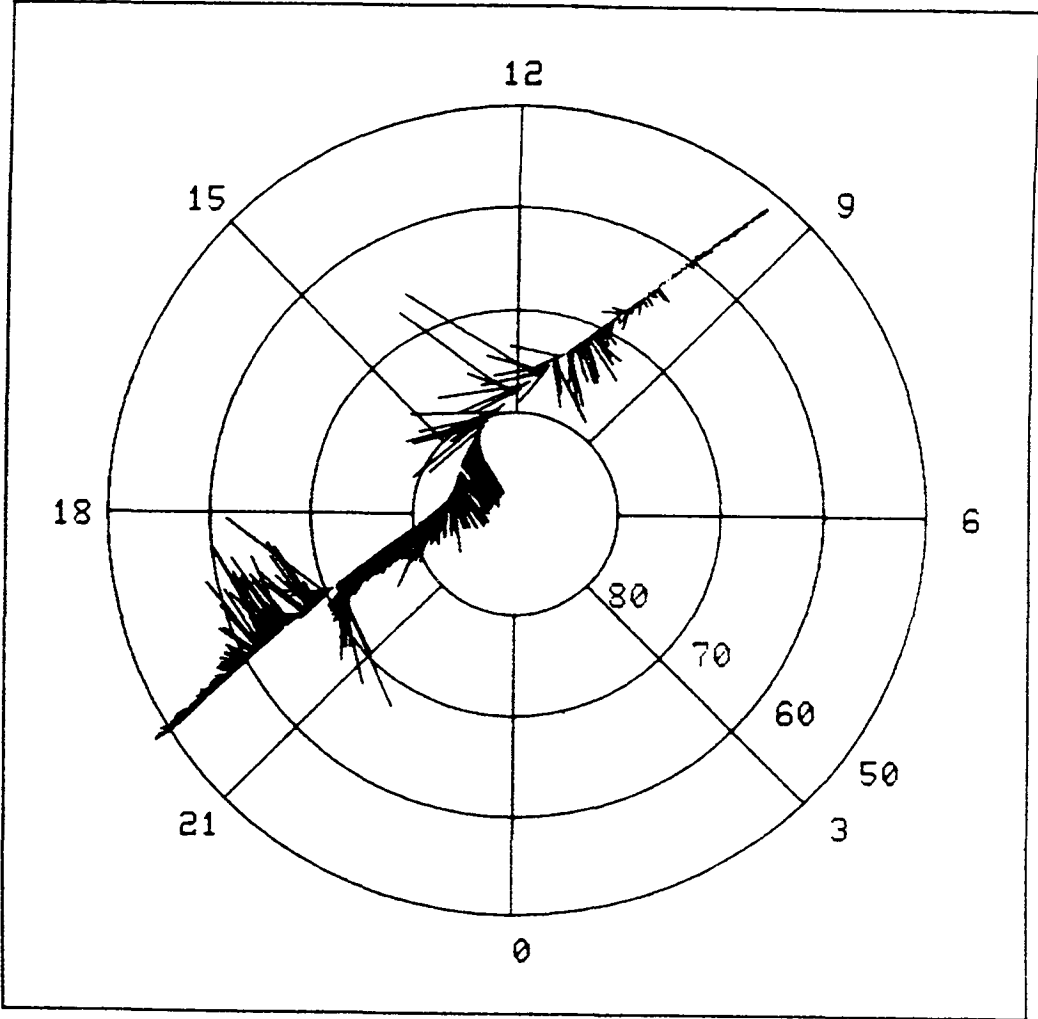
UTD SPACE SCIENCES.   1 KM/SEC

Figure 4.

169

Figure 5.

Figure 6.

171

Figure 7.

10:50 UT

14:00 UT

Figure 8.

Figure 9.

174

TOWARD

$B_Y < 0$

$B_Y << 0$

$B_Y \approx 0$

AWAY

$B_Y > 0$

$B_Y >> 0$

Figure 10.

175
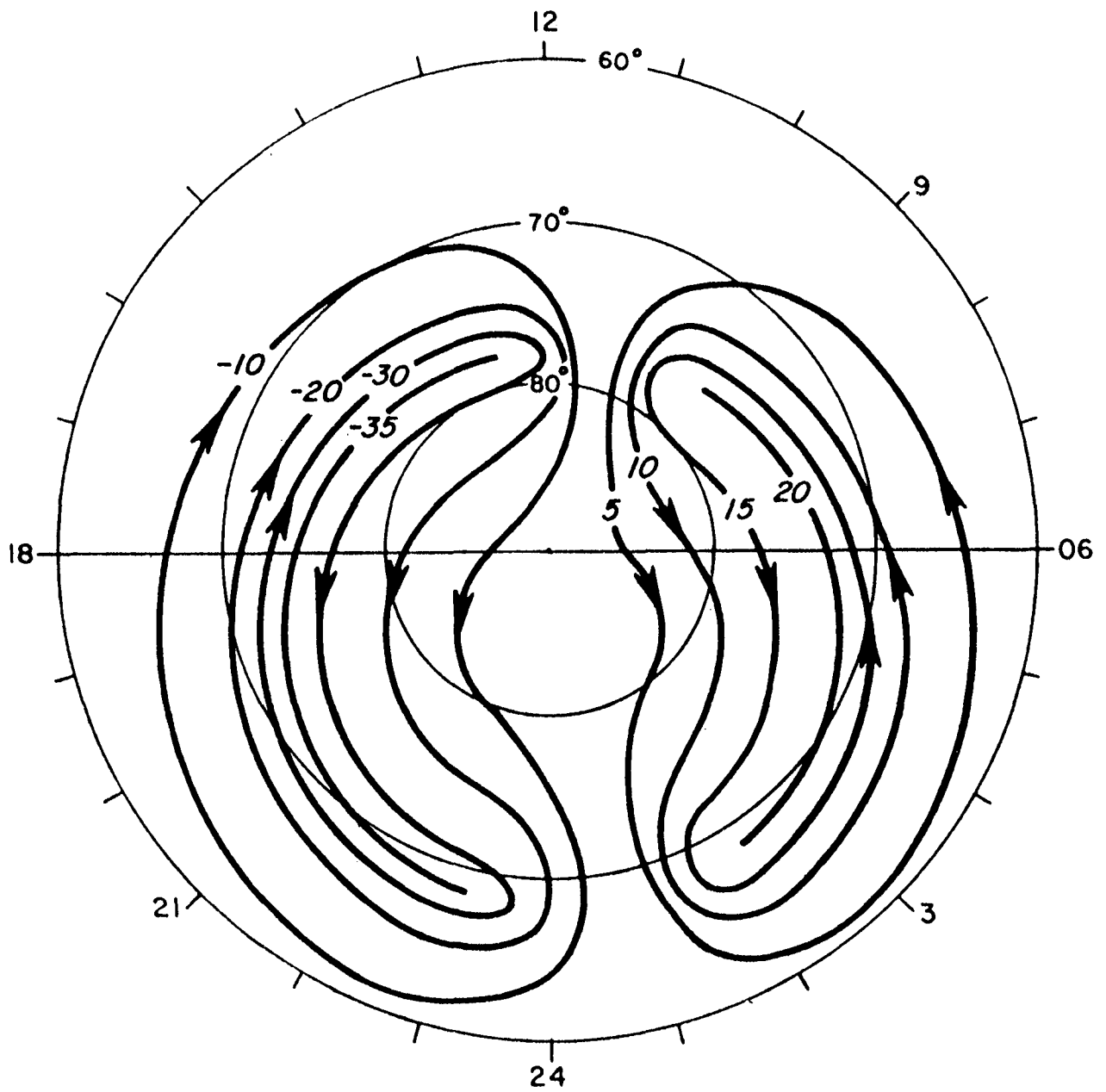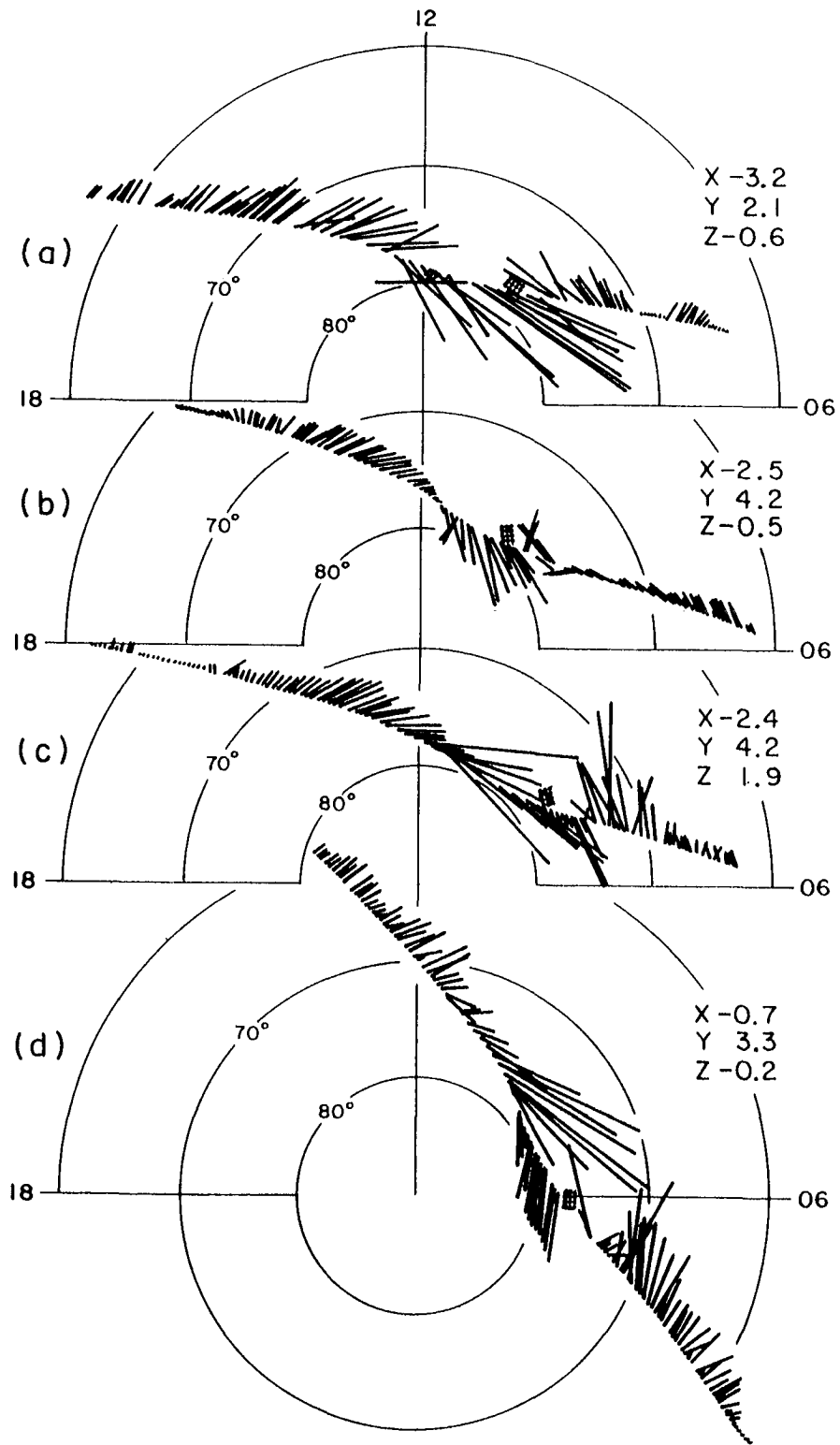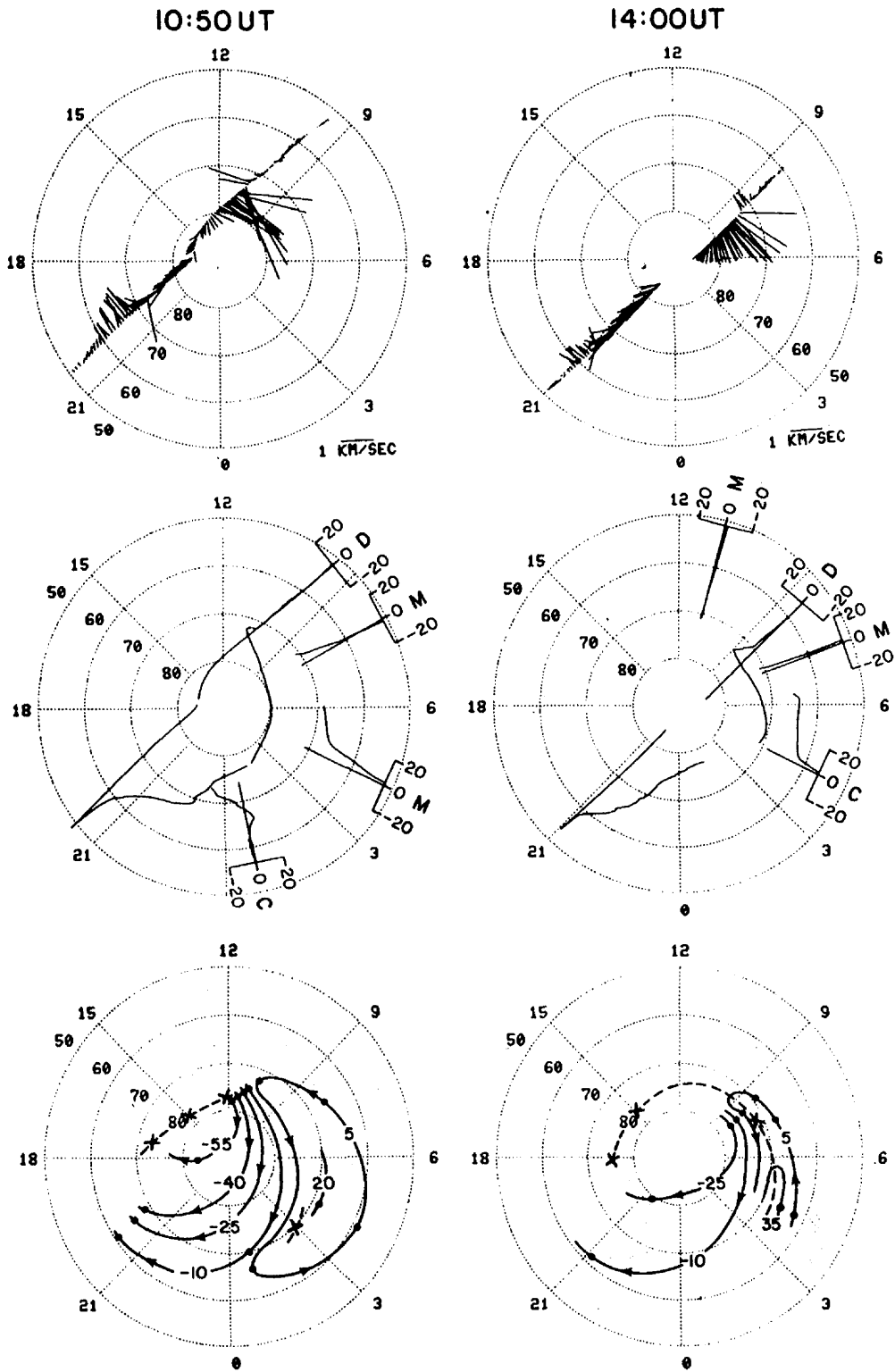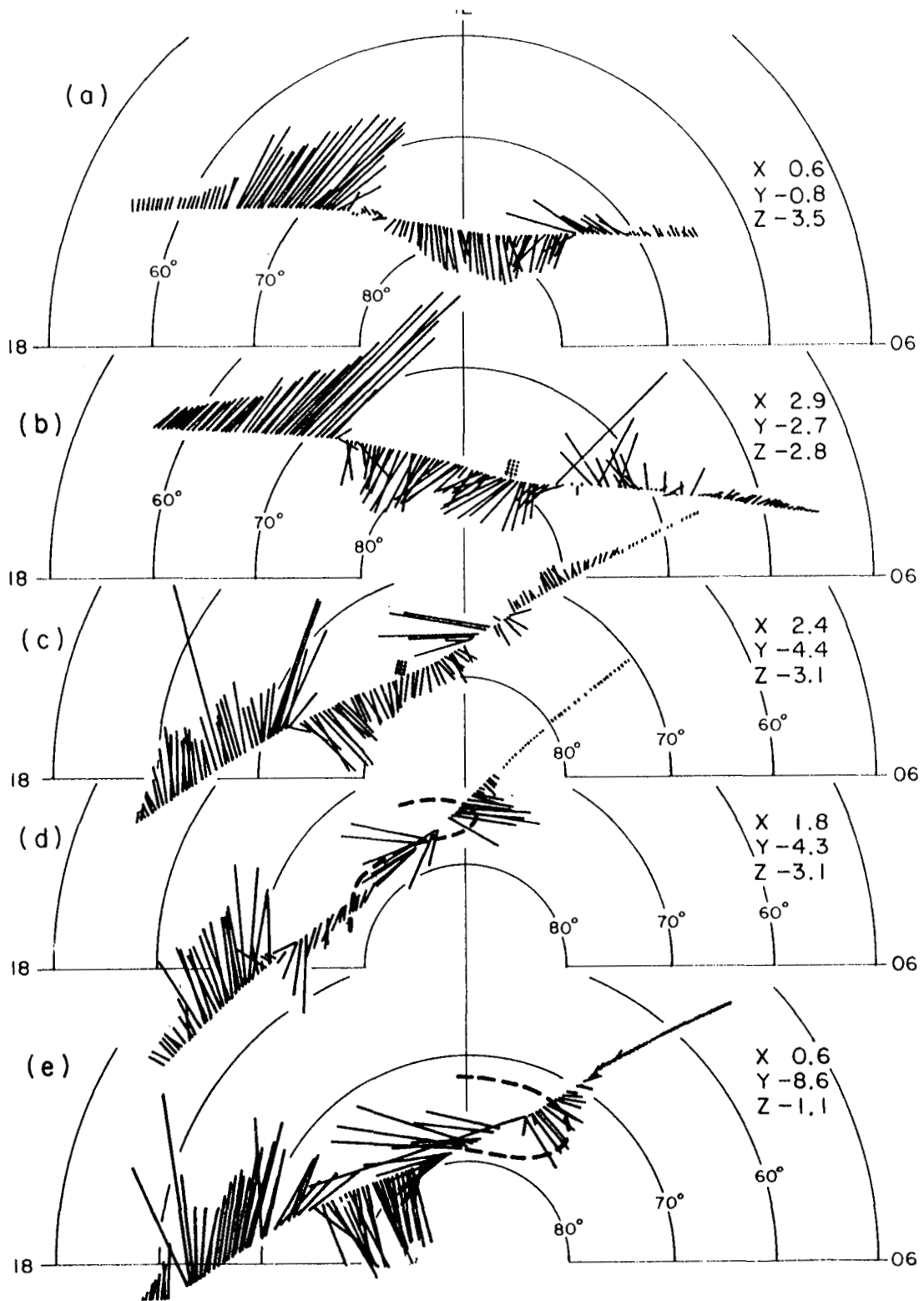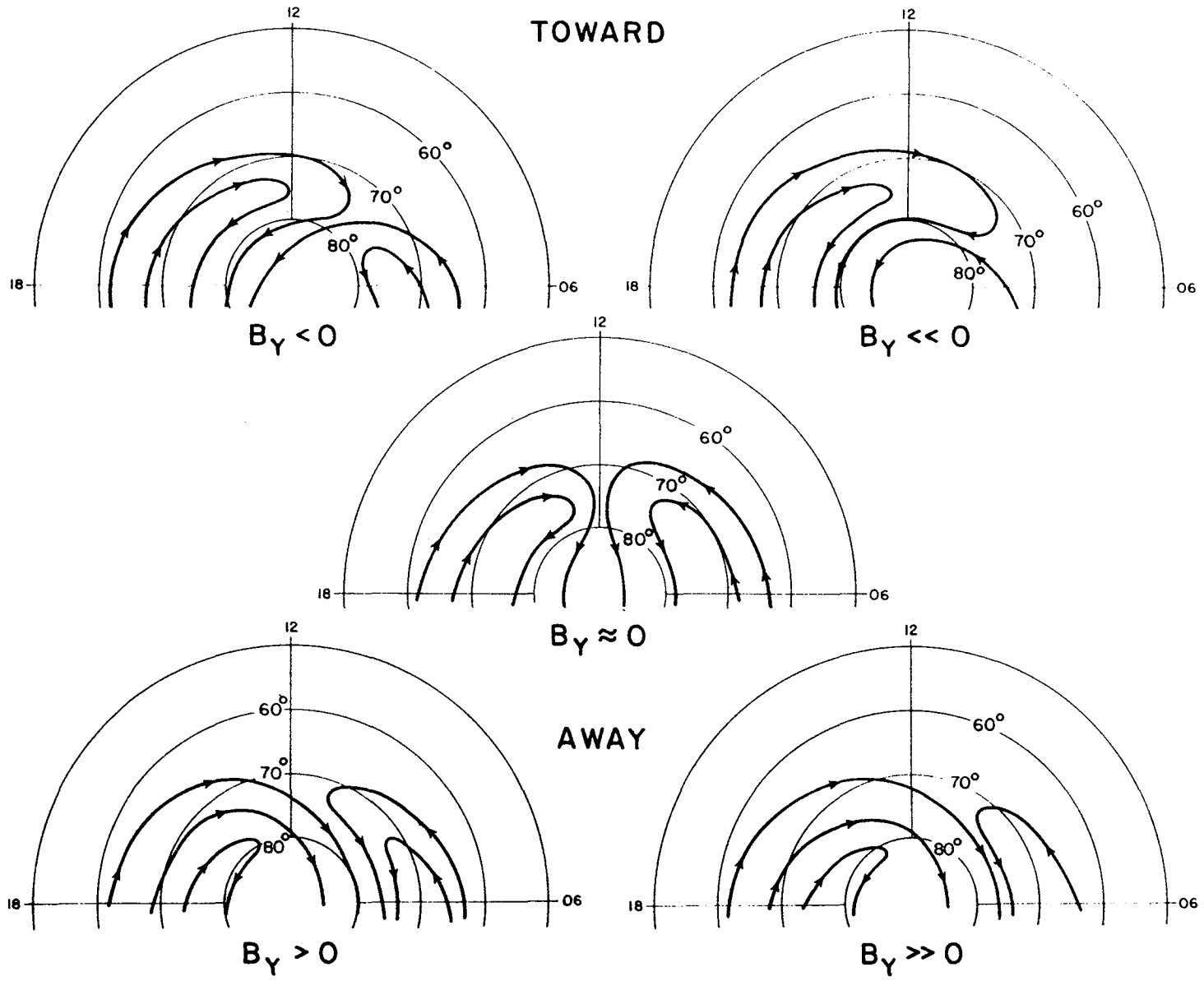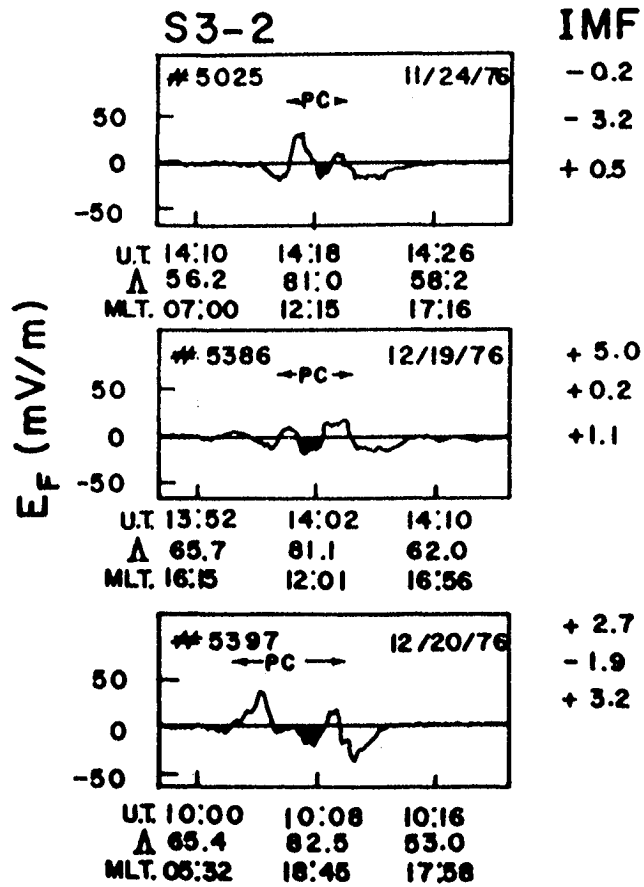
Figure 11.

DE-B ION DRIFT VELOCITIES
MLT v ILAT

DAY 81289 UT 13:09 ORBIT 1094   DAY 81289 UT 14:46 ORBIT 1095   DAY 81289 UT 3:26 ORBIT 1088

$B_y \approx 0$ $B_y < 0$ $B_y > 0$

Figure 12.

177
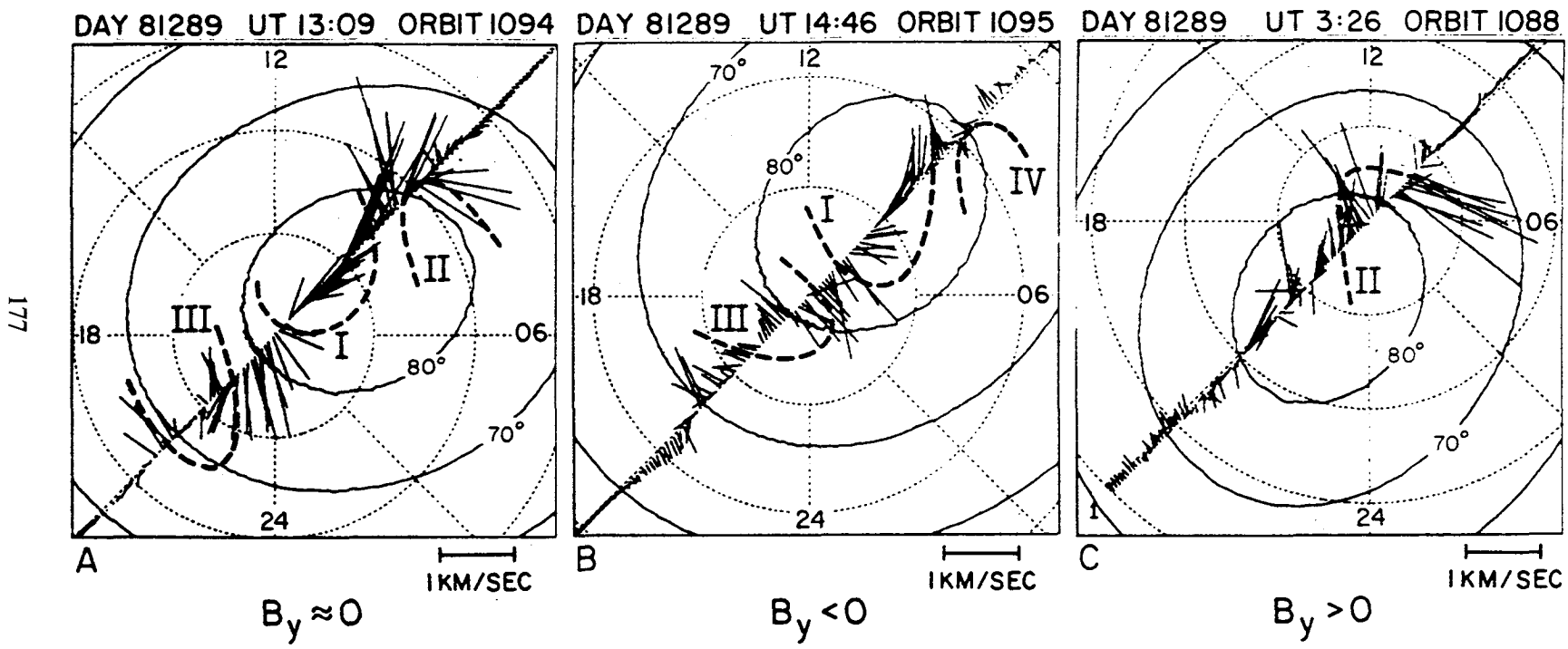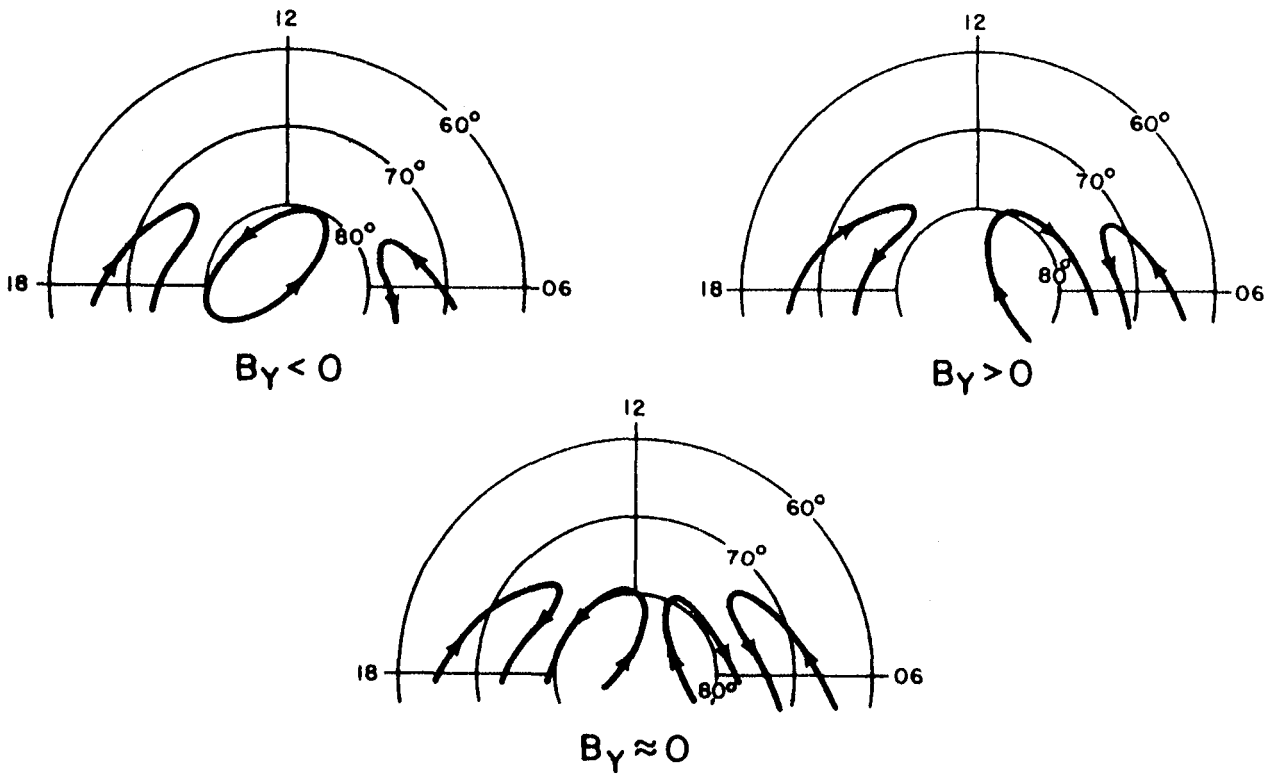
Figure 13.

INTERACTION OF THE EQUATORIAL MIDNIGHT PRESSURE BULGE AND THERMOSPHERIC ZONAL WINDS

F. A. Herrero
Code 614
NASA/Goddard Space Flight Center
Greenbelt, Maryland 20771

The zonal component of the thermospheric neutral wind in the equatorial region is found to flow eastward all night, having a minimum near midnight. The data, obtained by Spencer et al. (1981) on the Dynamics Explorer-2 (DE-2) satellite, and reported more recently by Wharton et al. (1984), indicate that the minimum feature is significant. The minimum is illustrated in Figure 1 which shows a 4th order Fourier series fit to the data points reported by Wharton et al. (1984). The table below the plot gives the amplitudes and phases of the four harmonic components used with the estimated errors for each amplitude. One asks whether this behavior is due to the local passage of the equatorial midnight pressure bulge associated with the midnight temperature anomaly. If so, it is to be exptected that other data characterizing the midnight temperature anomaly should show consistency with this observation, especially in view of the large changes observed in the zonal velocity in the midnight sector. Consistency in momentum conservation may be checked using available data from previous independent experiments. Such data, taken under similar conditions of solar activity, has been substituted into the momentum equation and found to be consistent using a priori estimates of the effect of viscosity.

The DE-2 data provide the zonal wind Ux, and its local time derivative $\partial U_x/\partial t$. The pressure gradient is obtained from the average equatorial nighttime neutral temperatures measured on AE-E (Herrero and Spencer, 1982) and the MSIS neutral density (Hedin, 1983), and this is shown in Figure 2. Specifying the ion-drag requires in addition the eastward ion-drift V_{ix} and the ion density n_i at the altitude of interest, 350 km in this case. The eastward ion-drift is well known near the equator from the Jicamarca measurements of 1970-71 (Woodman, 1972; Fejer et al., 1981; see Figure 3). Solar activity for that period was comparable to solar activity during the DE-2 measurements of 1981-82, essentially one solar cycle apart. The average ion density variation may be represented by Chiu's empirical model (Chiu, 1975), and this is plotted in Figure 4. Basically, zonal momentum is balanced as the pressure gradient dp/dx of the neutral gas is opposed by ion-drag and viscosity with the difference appearing as a local rate of change dUx/dt. That is,

$$\frac{\partial U_x}{\partial t} = -\frac{1}{\rho}\frac{\partial p}{\partial x} + \frac{\mu}{\rho}\frac{\partial^2 U_x}{\partial z^2} - \nu_{in}(U_x - V_{ix})$$

where the ion-drag term is characterized by the ion frequency ν_{in} and the difference in velocities $U_x - V_{ix}$. μ is the coefficient of viscosity and ρ the neutral mass density (see, for example, Rishbeth and Garriott, 1971). The similarity between the nighttime zonal winds and the eastward ion-drift is worth noting as it is responsible for a drastic reduction in the ion-drag term. U_x and V_{ix} both reach their highest maxima togehter at 2100 hours LT, and pass through a minimum

shortly after midnight and a secondary maximum between 0300 and 0400 hrs LT. This similarity makes it possible to approximate V_{ix} in terms of U_x. From Figures 1 and 2, $V_{ix} \sim 0.8U_x$. Thus, the ion-drag term may be written as U_x/τ_i where $\tau_i = 1/0.2 \, \nu_{in}$, where ν_{in} is proportional to n_i. The viscosity term is the only component of the equation that cannot be characterized by actual data. Therefore, it can be determined in terms of the others, and its magnitude checked for consistency against estimated values. The table below gives the magnitudes of the terms entering the momentum equation for the four time regions shown in Figure 2. The values of U_x, $\partial U_x/\partial t$, Ni and $-1/\rho \, (\partial p/\partial x)$ used correspond to the times near the middle of each region. The viscosity is found from the net effect of the terms in the Table and compared to the a priori estimates. In regions I, II, and III the net effect gives a viscosity value varying between $-.005$ and $+.005$ m/s^2. This amounts to 30% or less of the dominant term in each case, and perhaps is not indicative of the average behavior. However, in the early morning hours (section IV) the viscosity term should account for .01 m/s^2, and the fact that it is positive here may be significant and consistent with the simultaneous reversal in the pressure gradient shown in Figure 2.

A priori estimates of the viscosity term follow from approximating this term using a "viscosity" scale height H_v. This gives a viscosity decay time $\tau_v \approx \rho H^2/\mu$. Previous H_v estimates (Rishbeth, 1972) indicate values of the order of 100 km which are consistent with the numbers obtained here.

Table 1

	I (1930 LT)	II (2230 LT)	III (0130 LT)	IV (0430 LT)
τ_i (hrs)	0.81	2.1	6.2	7.2
U_x/τ_i (m/s^2)	0.035	0.014	0.004	0.002
$\partial U_x/\partial t$ (m/s^2)	0.020	-0.015	0.010	-0.025
$-1/\rho \, (\partial p/\partial x)$ (m/s^2)	0.050	0.004	0.015	-0.012

REFERENCES

Chiu, Y. T., An improved phenomenological model of ionospheric density, *J. Atmos. Terr. Phys., 37,* 1563-1570, 1975.

Fejer, B. G., D. T. Farley, C. A. Gonzales, R. F. Woodman, and C. Calderon, F-region east-west drifts at Jicamarca, *J. Geophys. Res., 86,* 215-218, 1981.

Herrero, F. A., and N. W. Spencer, On the horizontal distribution of the equatorial thermospheric midnight temperature maximum and its seasonal variation, *Geophys. Res. Lett., 9,* 1179-1182, 1982.

Rishbeth, H., Thermospheric winds and the F-region: A review, *J. Atm. Terr. Phys., 34,* 1-47, 1972.

Spencer, N. W., L. E. Wharton, H. B. Niemann, A. E. Hedin, G. R. Carignan, and J. C. Maurer, The Dynamics Explorer Wind and Temperature Spectrometer, *Space Sci. Instrumentation, 5,* 417, 1981.

Wharton, L. E., N. W. Spencer, and H. G. Mayr, The Earth's thermospheric superrotation from Dynamics Explorer 2, *Geophys. Res. Lett., 11,* 531-533, 1984.

Woodman, R. F., East-west ionospheric drifts at the magnetic equator, *Space Res. XII,* 969-974, 1972.

DE-2 ZONAL WINDS

Average altitude 350 km
Latitude: -10 to 10 degrees
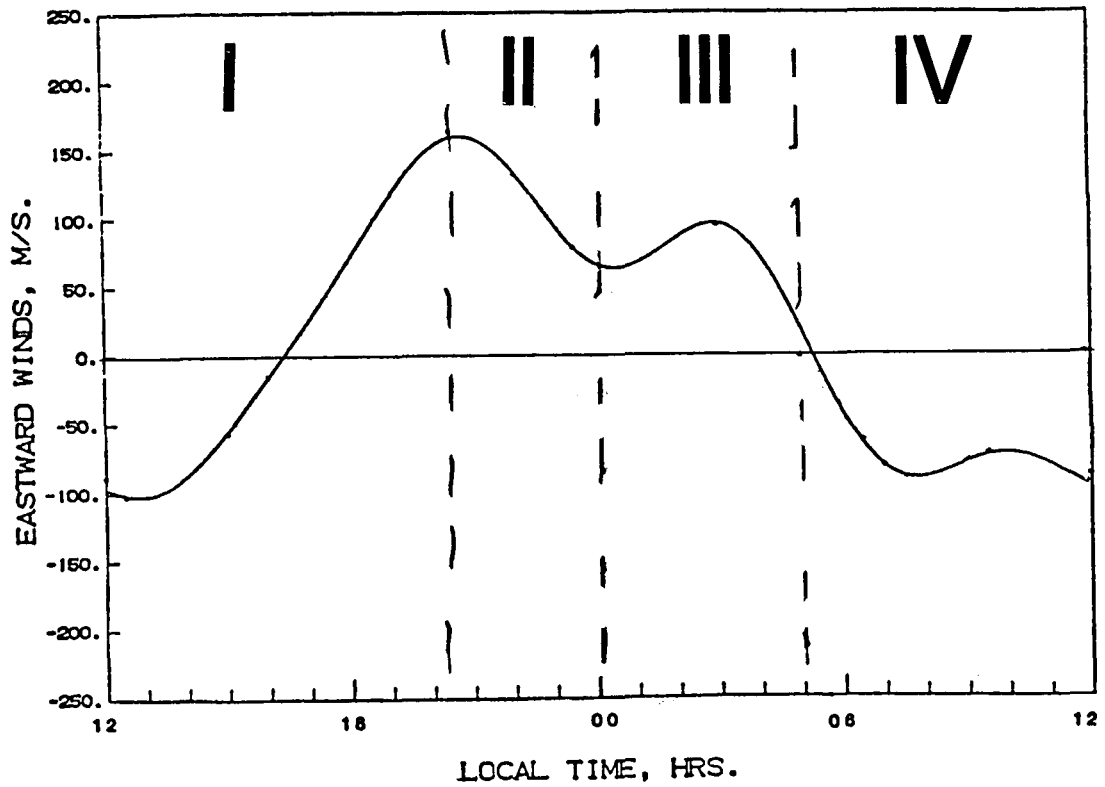
AMPLITUDES AND PHASES

ORDER	AMP(m/s)	PHASE(hrs)
1	117±7	-1.5
2	21±7	-9.9
3	34±7	10.3
4	19±7	-10.8

Figure 1

Figure 2

Figure 3

Figure 4

ION NEUTRAL COUPLING IN THE HIGH LATITUDE THERMOSPHERE: PART I

T. L. Killeen
Space Physics Research Laboratory
The University of Michigan
Ann Arbor, MI 48109

Measurements of the neutral wind in the polar F-region from Dynamics Explorer-2 (DE-2) have been used to illustrate asymmetries in the neutral circulation that are dependent on the sign of the B_y component of the interplanetary magnetic field (IMF). Individual DE-2 orbits and averaged data sets from different Universal times are presented. The data are categorized according to the sign of the hourly averaged IMF B_y component measured by ISEE-3 for the hour preceding the DE-2 measurement. The major features observed are: 1) an asymmetry in the polar cap neutral flow velocity with the region of most rapid anti-sunward flow shifting from the dawn-side to the dusk-side of the polar cap as B_y changes from positive to negative; 2) a shift in magnetic local time of the region of entry of neutral gas into the polar cap from a location on the dawn-side of the noon-midnight meridian for B_y positive to one more biased towards the dusk-side for B_y negative; 3) an enhancement in the velocities associated with the dawn, anti-clockwise neutral vortex for B_y negative relative to those observed for B_y positive. The B_y neutral wind asymmetries can be explained by similar asymmetries, previously observed, in the polar ion convection pattern. They imply a direct causal relationship between solar wind/magnetosphere coupling and neutral thermospheric dynamics.

ORBITS AVERAGED
FOR UNIVERSAL TIMES:

(A) 2:00-4:00
(B) 16:00-18:00
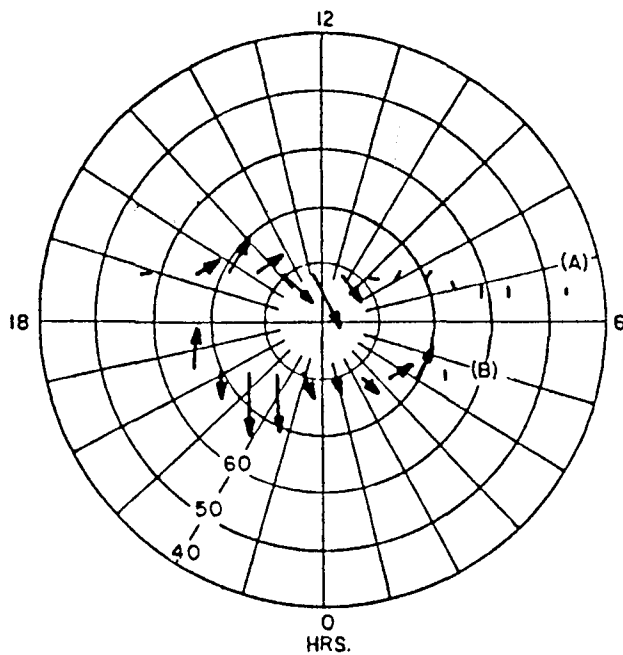
By NEGATIVE

ORBITS AVERAGED
FOR UNIVERSAL TIMES:

(A) 2:00-4:00
(B) 12:00-14:00
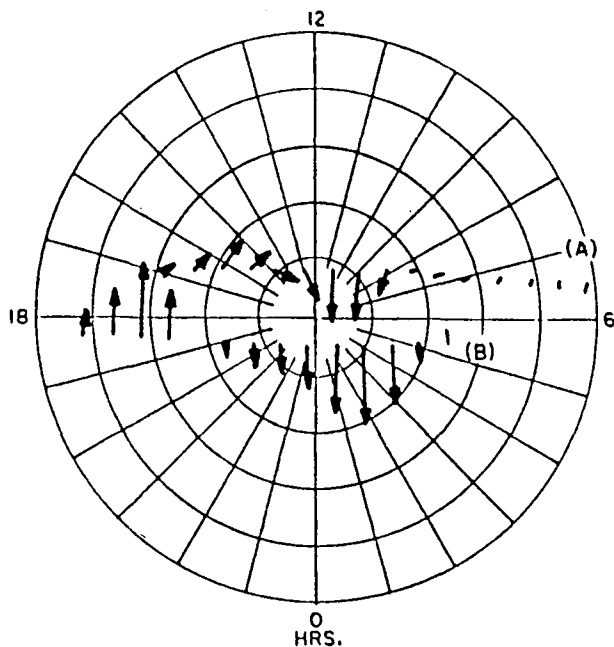
By POSITIVE

500 M/SEC.

Figure 1. Average neutral wind vectors for December 1981 plotted in geomagnetic polar coordinates (magnetic latitude and local time) obtained for the specified UT intervals with a) B_y negative and b) B_y positive.

DE - FPI/WATS NEUTRAL WIND VECTORS
12

ORBIT 1861

GEOMAGNETIC
COORDINATES

IMF   nT

Bx: -3.7
By: +3.2
Bz: -1.0

Kp   Ap

0+   3

18   6

60
50
40

2a

DATE 81341 UT 3:59   0 HRS   500 M/SEC.

DE - FPI/WATS NEUTRAL WIND VECTORS
12

ORBIT 1755

GEOMAGNETIC
COORDINATES

IMF   nT

Bx: +2.0
By: -5.0
Bz: +1.5

Kp   Ap

0   1

18   6

60
50
40

2b

DATE 81334 UT 1:18   0 HRS   500 M/SEC.

DE - FPI/WATS NEUTRAL WIND VECTORS
12

ORBIT 1853

GEOMAGNETIC
COORDINATES

IMF   nT

Bx: -2.9
By: +3.4
Bz: +0.6

Kp   Ap

1o   4

18   6

60
50
40

2c

DATE 81340 UT 15:02   0 HRS   500 M/SEC.

DE - FPI/WATS NEUTRAL WIND VECTORS
12

ORBIT 1749

GEOMAGNETIC
COORDINATES

IMF   nT

Bx: -0.8
By: -5.3
Bz: -0.8

Kp   Ap

0+   4

18   6

60
50
40

2d

DATE 81333 UT 15:34   0 HRS   500 M/SEC.

Figure 2. Vector neutral wind measurements for individual orbits of DE-2; a) orbit 1861, b) orbit 1755, c) orbit 1853 and d) orbit 1749. The winds are plotted in geomagnetic polar coordinates. The solar terminator is indicated by the curved hatched line. Where no FPI data are available, the WATS measurements are indicated by the bars plotted at right angles to the track of the satellite. The hourly averaged IMF values from ISEE-3 taken for the hour preceding the pass are shown at left with the Kp and Ap indices. The wind scale is given at bottom right.
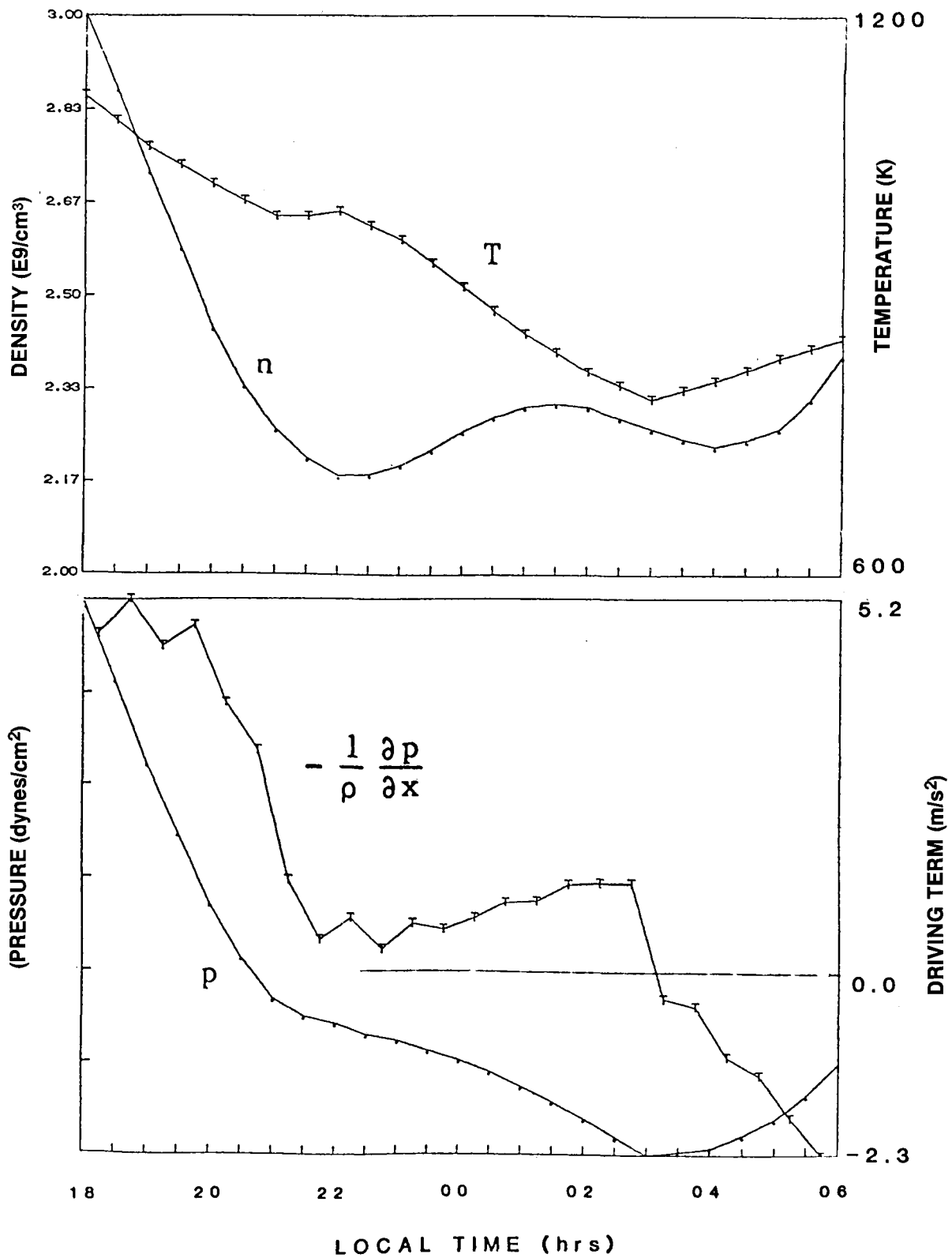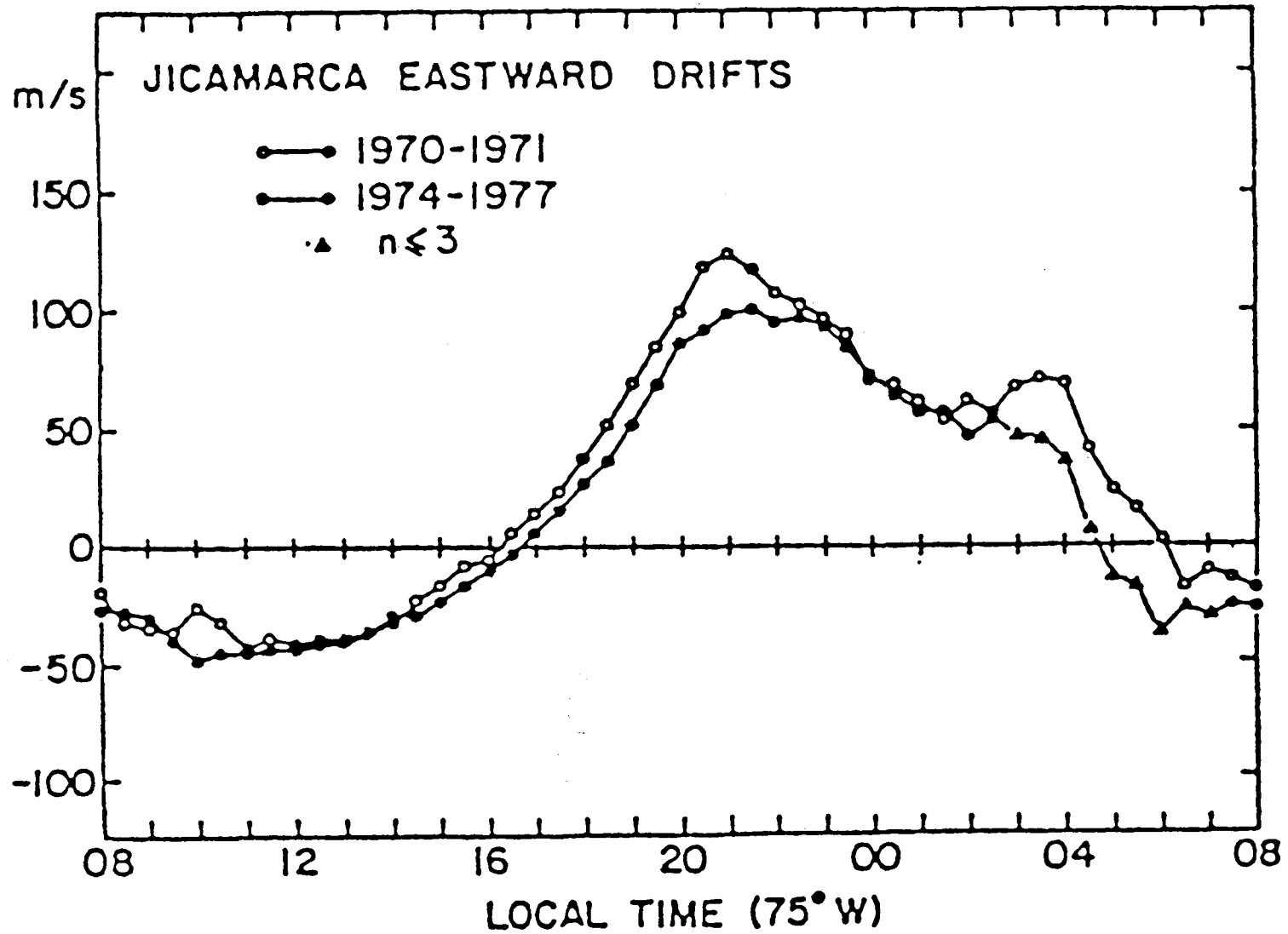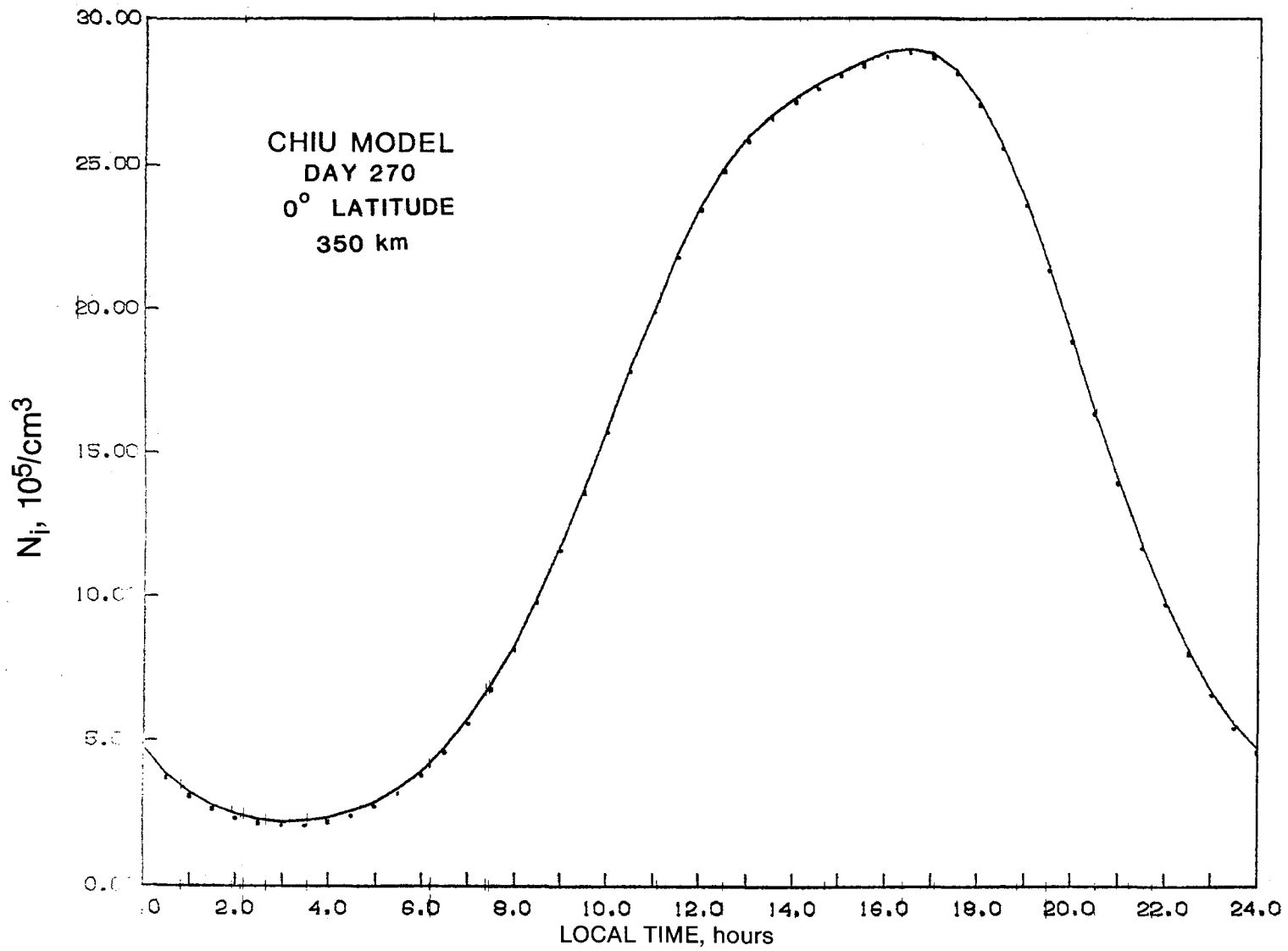
187

ION-NEUTRAL COUPLING IN THE HIGH LATITUDE THERMOSPHERE: PART II

T. L. Killeen
Space Physics Research Laboratory
The University of Michigan
Ann Arbor, MI 48109

On 24th November, 1982, The North-South (B_z) component of the Interplanetary Magnetic Field (IMF) became positive for a period of about 11 hours reaching a relatively large and steady value of ~ 25 nT. During this rare occurrence, the Dynamics Explorer-2 (DE-2) spacecraft was in a configuration that enabled the dynamics of both ionic and neutral species of the high-latitude F-region to be mesaured simultaneously along the track of the polar-orbiting satellite. Results from two Northern (winter) polar passes of DE-2, extracted from a larger data set, are shown to illustrate the response of the neutral F-region to ion drag forcing arising from a configuration of ion convection characteristic of strongly northward IMF. The measured neutral winds differ appreciably from those more commonly observed for periods of southward IMF. The multi-cellular ion drift pattern associated with positive B_z is observed to drive a similar but less structured and weaker neutral wind configuration in the winter polar cap. Major features of the ion drift pattern are mimicked by the neutral circulation but smaller-scale and more irregular structures of ion flow are not. This is ascribed to the relatively long time constant (few hours) for momentum exchange between the ion and neutral gases. The results demonstrate that sunward flow of neutral gas can be established and maintained by ion drag in the central polar cap for positive B_z.

GSM COORDINATES

ISEE-3 IMF   DAY 82328
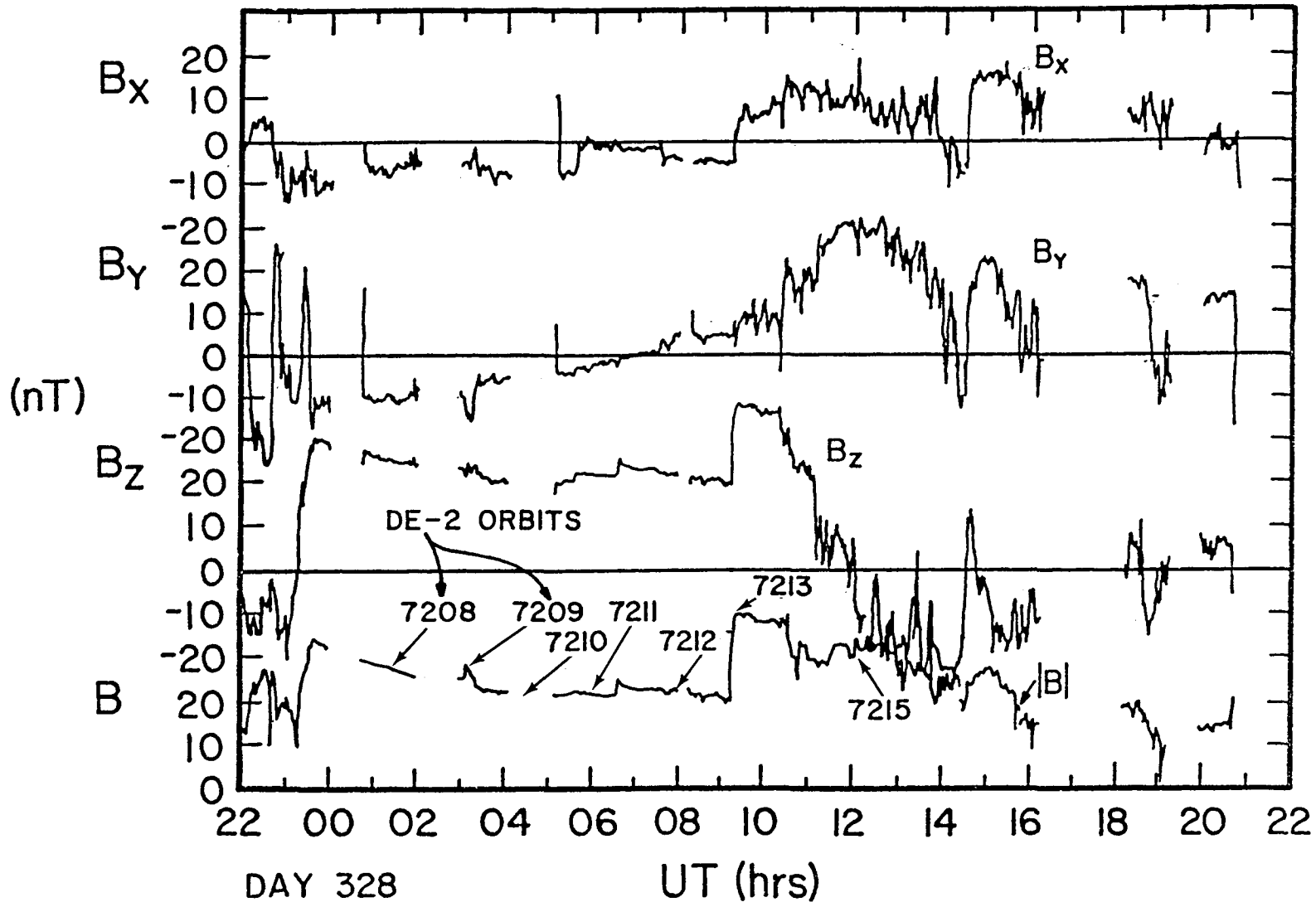
Figure 1. Variation of the Interplanetary Magnetic Field as measured by ISEE-3 during 24th November, 1982. The times corresponding to the orbits studied are indicated.

Figure 2. Neutral wind and ion drift vectors for orbit 7210 plotted in geographic polar coordinates (latitude, pole to 40°N; local solar time). The neutral winds are coded by the yellow (white) arrows, and the ion drifts are coded by the red (gray) bars. The curved line represents the solar terminator (90% solar zenith angle). The symbol N refers to the location of the invariant pole at the UT of the pass. Note the scale difference of a factor of 2 indicated at lower right.
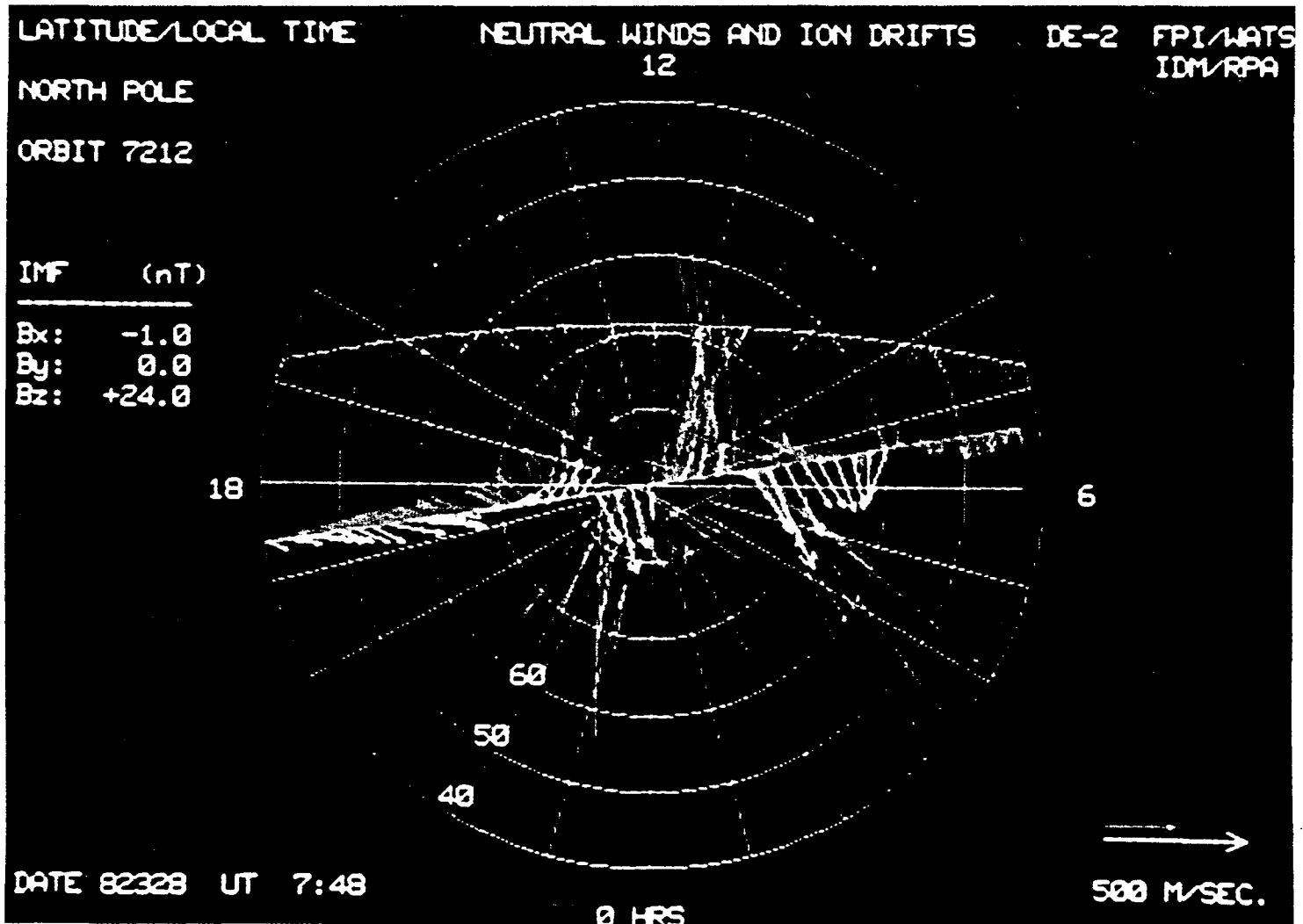
Figure 3. Neutral wind and ion drift vectors for orbit 7212 plotted in geographic polar coordinates (latitude, pole to 40°N; local solar time). The neutral winds are coded by the yellow (white) arrows, and the ion drifts are coded by the red (gray) bars. The curved line represents the solar terminator (90% solar zenith angle). The symbol N refers to the location of the invariant pole at the UT of the pass. Note the scale difference of a factor of 2 indicated at lower right.
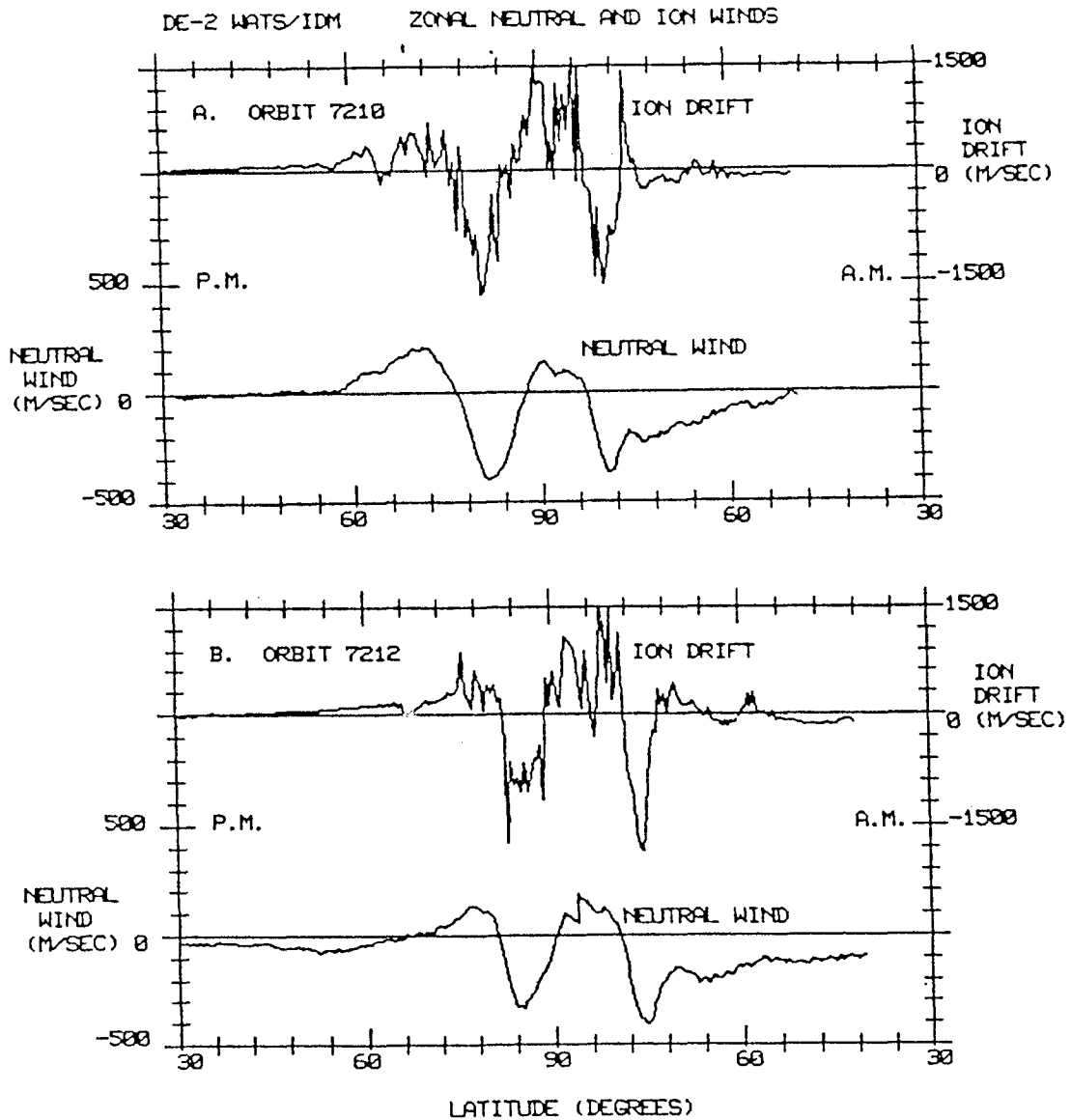
Figure 4. Zonal neutral winds and ion drifts measured on DE-2 for a) orbit 7210 and b) orbit 7212 plotted as a function of latitude along the track of the satellite. Neutral zonal winds are plotted according to the scale shown on the left, ion zonal drifts according to the scale on the right.

193

GEOSTROPHIC ADJUSTMENT IN A SHALLOW-WATER NUMERICAL MODEL AS IT RELATES TO THERMOSPHERIC DYNAMICS

M. F. Larsen[1] and I. S. Mikkelsen[2]

[1]Dept. of Physics and Astronomy
Clemson University
Clemson, SC 29631

[2]Geophysical Division
Meteorological Institute
Copenhagen, Denmark

The theory of geostrophic adjustment and its application to the dynamics of the high-latitude thermosphere have been discussed by ourselves (Larsen and Mikkelsen, JGR, 1983; Mikkelsen and Larsen, JGR, 1983) and Walterscheid and Boucher (JAS, 1984) in previous papers based on a linearized treatment of the fluid dynamical equations. However, a linearized treatment is only valid for small Rossby numbers given by $Ro = V/fL$, where V is the wind speed, f is the local value of the Coriolis parameter, and L is a characteristic horizontal scale for the flow. For typical values in the auroral zone, the approximation is not reasonable for wind speeds greater than 25 m/s or so. We have developed a shallow-water (one layer) model that includes the spherical geometry and full nonlinear dynamics in the momentum equations in order to isolate the effects of the nonlinearities on the adjustment process. A belt of accelerated winds between 60° and 70° latitude was used as the initial condition. We found that the adjustment process proceeds as expected from the linear formulation, but that an asymmetry between the response for an eastward and westward flow results from the nonlinear curvature (centrifugal) terms. In general, the amplitude of an eastward flowing wind will be less after adjustment than a westward wind. For instance, if the initial wind velocity is 300 m/s, the linearized theory predicts a final wind speed of 240 m/s, regardless of the flow direction. However, the nonlinear curvature terms modify the response and produce a final wind speed of only 200 m/s for an initial eastward wind and a final wind speed of almost 300 m/s for an initial westward flow direction. Also, less gravity wave energy is produced by the adjustment of the westward flow than by the adjustment of the eastward flow. The implications are that the response of the thermosphere should be significantly different on the dawn and dusk sides of the auroral oval. Larger flow velocities would be expected on the dusk side since the plasma will accelerate the flow in a westward direction in that sector.

REFERENCES

Larsen, M. F., and I. S. Mikkelsen, The dynamic response of the high latitude thermosphere and geostrophic adjustment, *J. Geophys. Res., 88,* 3158-3168, 1983.

Mihaljan, J. M., The exact solution of the Rossby adjustment problem, *Tellus, 15,* 150-154, 1963.

Mikkelsen, I. S., and M. F. Larsen, An analytic solution for the response of the neutral atmosphere to the high-latitude convection pattern, *J. Geophys. Res., 88,* 8073-8080, 1983.

Walterscheid, R. L., and D. S. Boucher, Jr., A simple model of the transient response of the thermosphere to impulsive forcing, *J. Atmos. Sci., 41,* 1062-1072, 1984.
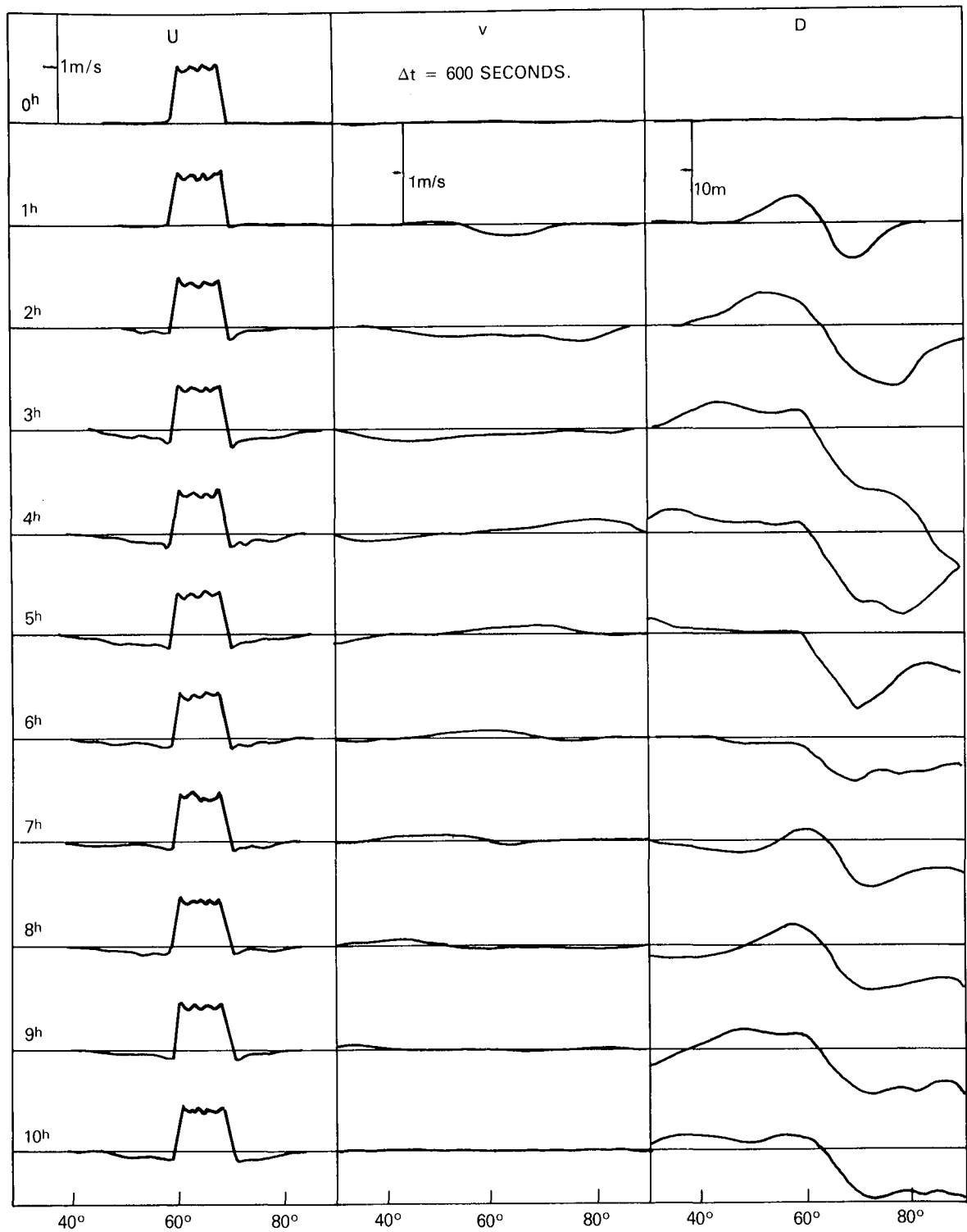
Figure 1. The zonal wind (left), meridional wind (middle), and height of the fluid surface (right) at 1 hr intervals. The initial condition at 0 hr is a 1 m/s eastward wind in the latitude band between 60° to 70°. The height of the fluid is directly related to the pressure. All subsequent figures will be presented in the same format.

197

MIHALJAN'S SOLUTION

100m/s

50

500m

50°   70°

50°   70°
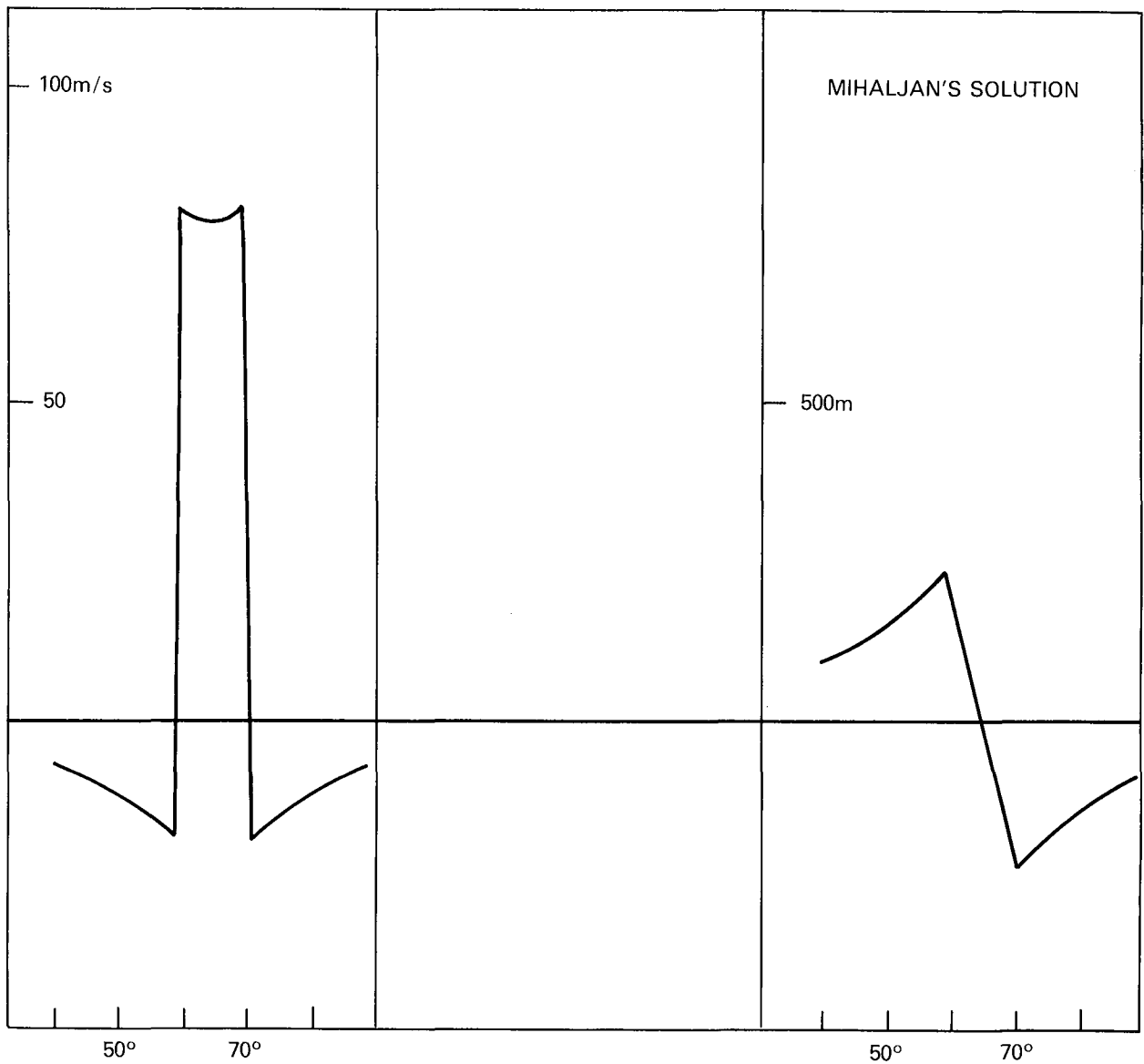
Figure 2. Analytic solution for the adjusted flow based on a linearized set of equations in a Cartesian coordinate system. The initial wind was 100 m/s, and the final wind is 80 m/s. The initial and final flow velocity will scale linearly together. Thus, an initial wind of 1 m/s will produce an adjusted wind of 0.8 m/s. This figure can be compared directly with the solutions shown in Figure 1.
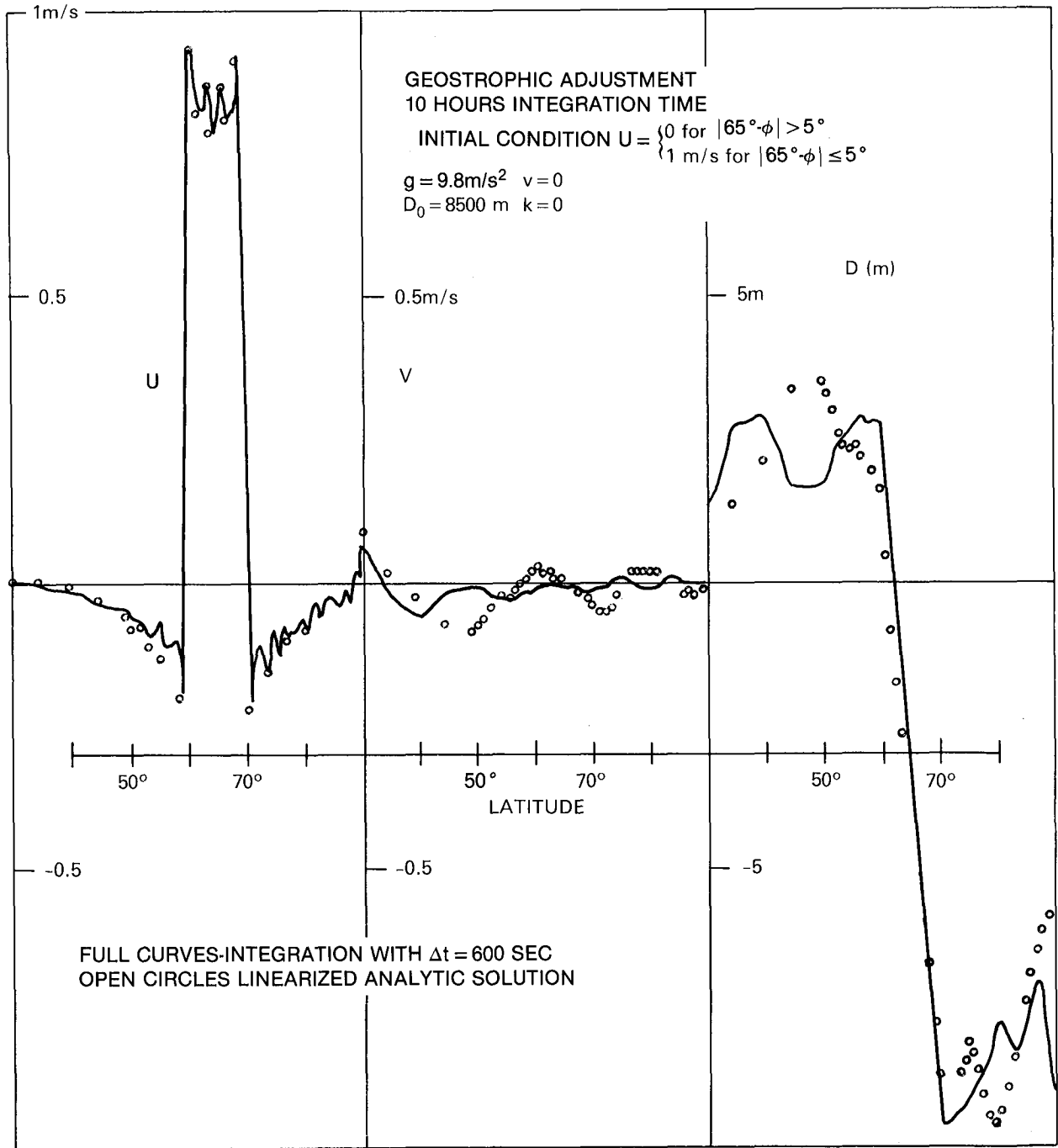
Figure 3. An enlarged graph showing the adjusted state after 10 hr. The initial wind is eastward at 1 m/s between 60° and 70°N. The final zonal velocity agrees closely with the zonal velocity given by the linearized analytic solution. The meridional wind is negligible. The height of the free surface, which is directly related to the pressure, shows an asymmetry across the channel. The spherical geometry causes a focusing at the pole. As a result, the heights are higher on the southern side of the belt and lower on the northern side.

100 m/s

GEOSTROPHIC ADJUSTMENT
10 HOURS INTEGRATION TIME
INITIAL CONDITION

$$U = \begin{cases} 0 \text{ for } |65°\text{-}\phi| > 5° \\ 100 \text{ m/s for } |65°\text{-}\phi| \leq 5° \end{cases}$$

50 m/s

50

500m

$g = 9.8$ m/s
$D_0 = 8800$ m
$f = 1.32 \times 10^{-4}$
$\lambda = 2228$ km

U (m/s)

V (m/s)

D (m)

50°   70°

50°   70°

50°   70°

-50 m/s

-50 m/s

-500

1000 m
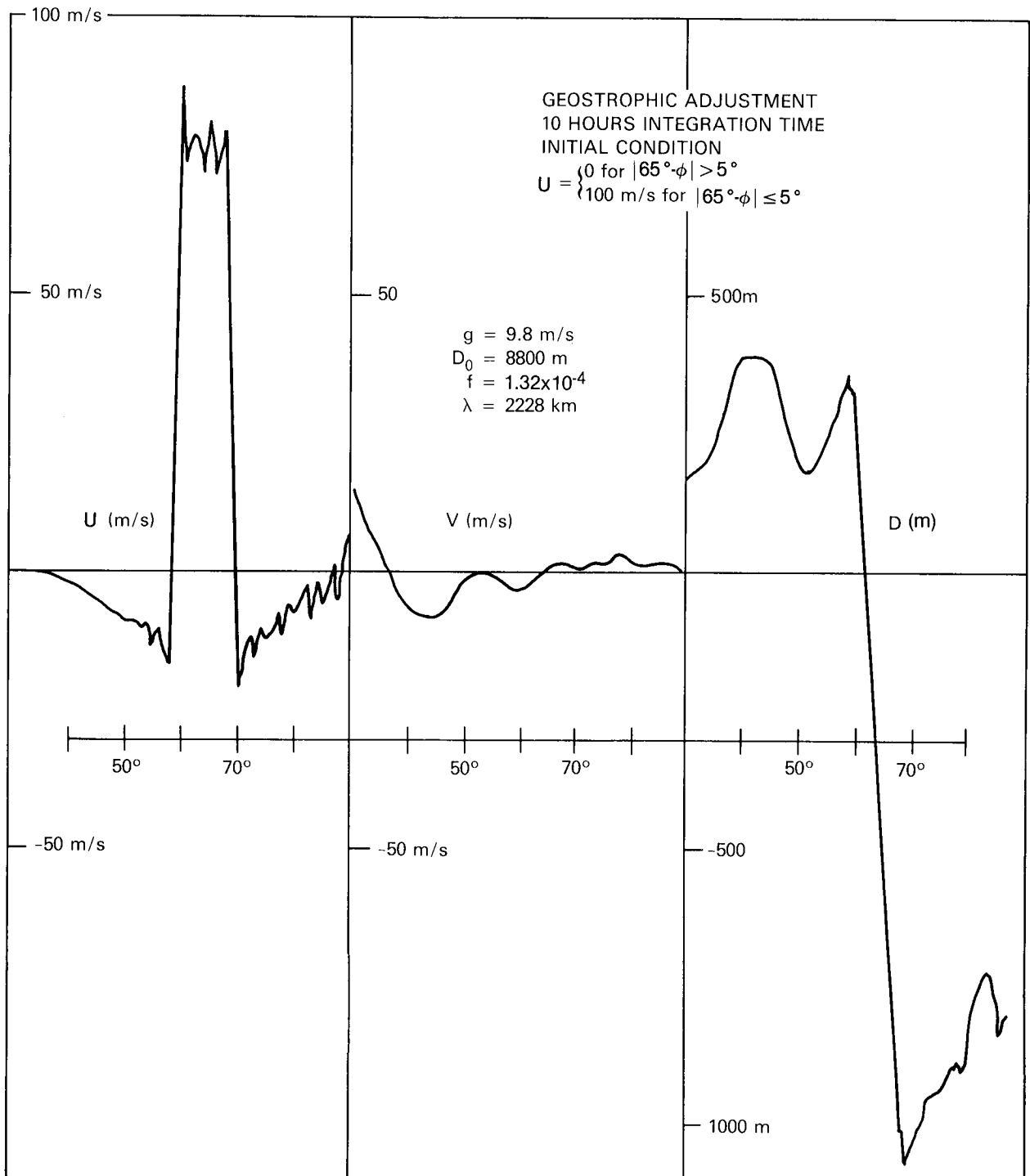
Figure 4. Adjusted state in the shallow-water model after 10 hr for an initial eastward wind of 100 m/s. The final zonal wind is approximately 75 m/s which is less than the final value of 80 m/s based on the solution of the linearized set of equations.

GEOSTROPHIC ADJUSTMENT
8 HOURS INTEGRATION TIME

$$U = \begin{cases} 0 \text{ for } |65°\text{-}\phi| > 5° \\ 300 \text{ m/s for } |65°\text{-}\phi| \leq 5° \end{cases}$$

THE SOLUTION IS GETTING UNSTABLE BETWEEN 65° AND 90°

300 m/s

200 m/s

100 m/s

U

-100

50°   70°

100 m/s

V

-100

50°   70°

50°   70°

1000 m

D

-1000

-2000

-3000
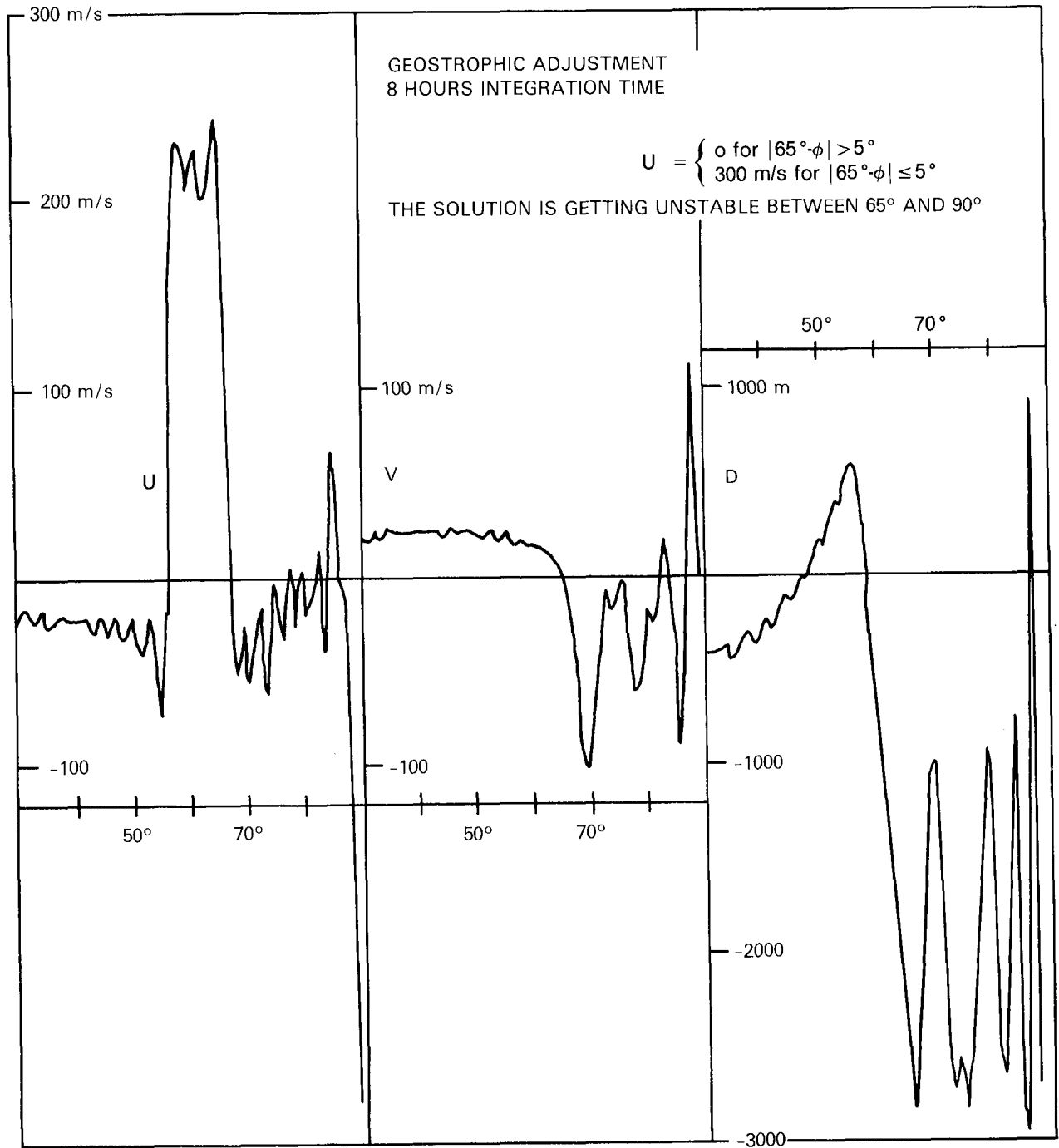
Figure 5. The adjusted state for an initial 300 m/s eastward wind after 8 hr. The final zonal wind is close to 210 m/s which is nearly 30 m/s less than the predicted value based on a linear analysis. The oscillations which are evident in all three fields are due to gravity waves generated by the adjustment process. The waves propagate north and are reflected by the boundary condition at the pole. Therefore, the 300 m/s case is near the limit of validity of the numerical solution.

201
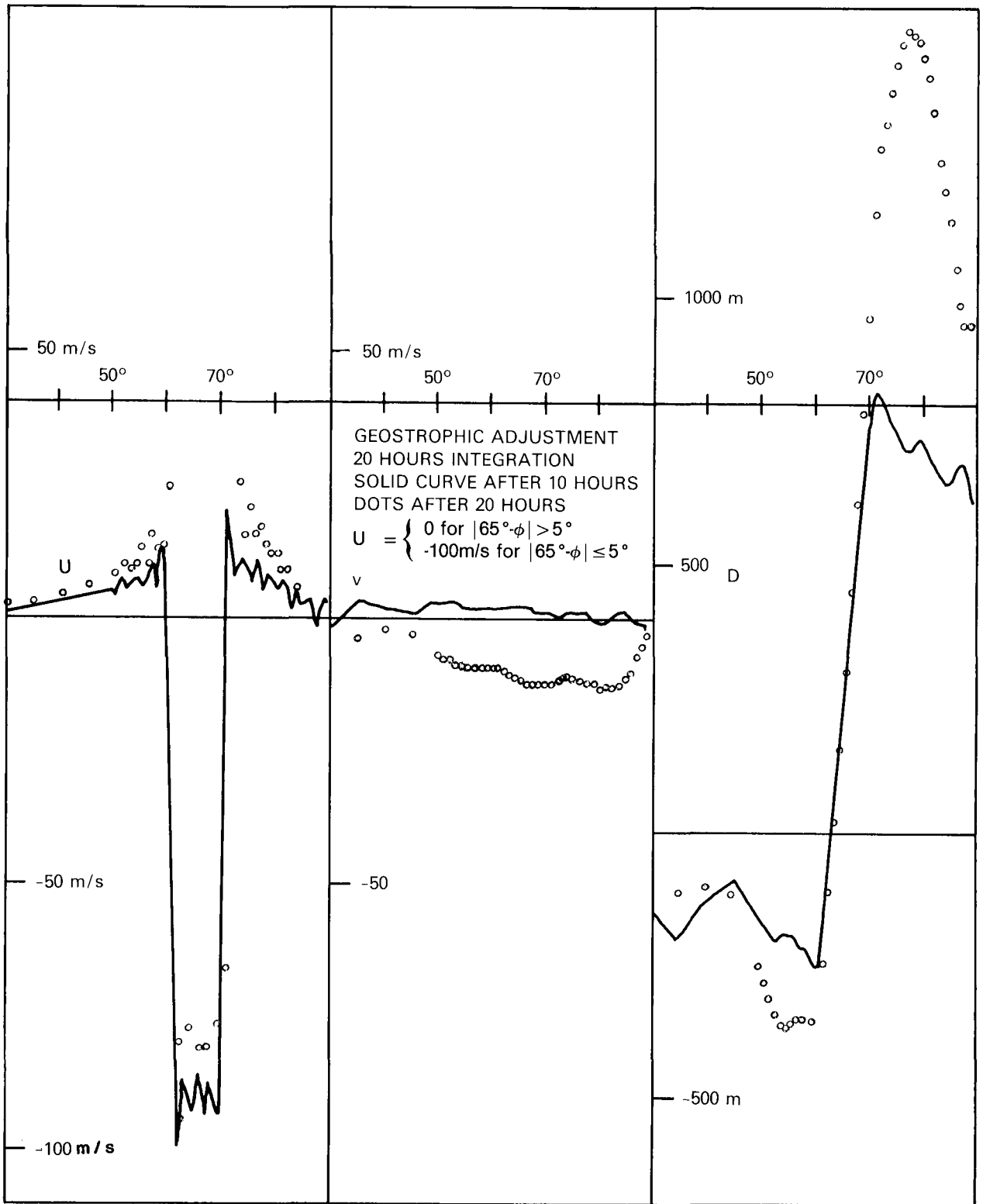
Figure 6. The adjusted state for an initial westward wind of 100 m/s is shown. The amplitude of the final zonal wind is approximately 90 m/s, or 10 m/s greater than expected based on a linear treatment.

202
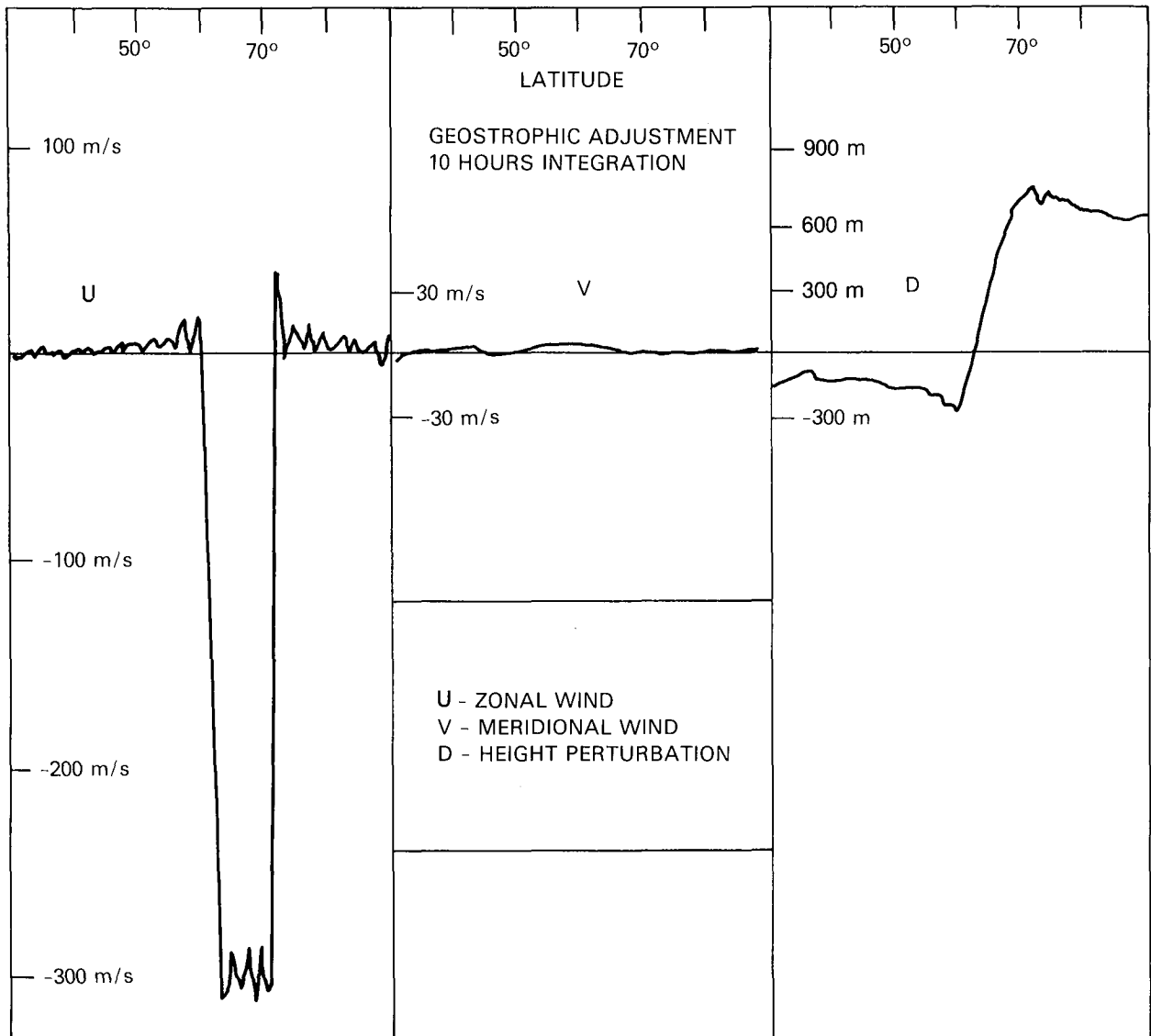
Figure 7. Here the adjusted state for an initial westward wind of 300 m/s is shown. The final state also has a zonal wind of 300 m/s. The pressure gradient is very small compared to the cases shown in the previous figures, and there is almost no gravity wave energy generated, as can be seen in the smoothness and low values of the meridional wind. Thus, a significant asymmetry between the dusk and dawn sides of the auroral oval would be expected. We expect that on the dusk side, where the winds produced by the Lorentz acceleration are westward, less gravity wave energy will be produced by the adjustment process, and the pressure gradients will be smaller.

INITIAL WIND	LINEAR	NONLINEAR
EASTWARD		
100 m/s	80 m/s	80 m/s
200 m/s	160 m/s	140 m/s
300 m/s	240 m/s	200 m/s
WESTWARD		
-100 m/s	-80 m/s	-90 m/s
-200 m/s	-160 m/s	-200 m/s
-300 m/s	-240 m/s	-300 m/s

Figure 8. Table comparing the initial wind speed, the wind speed after adjustment in a linearized formulation, and the wind speed after adjustment when the nonlinear terms in the momentum equation are included.

SATELLITE ACCELEROMETER MEASUREMENTS OF NEUTRAL
DENSITY AND WINDS DURING GEOMAGNETIC STORMS

Frank A. Marcos
Air Force Geophysics Laboratory
Hanscom Air Force Base
Bedford, MA 01731
and
Jeffrey M. Forbes
Department of Electrical, Computer, and Systems Engineering
Boston University
Boston, MA 02215

A new thermospheric wind measurement technique is reported which is based on a Satellite Electrostatic Triaxial Accelerometer (SETA) system capable of accurately measuring accelerations in the satellite's in-track, cross-track and radial directions. Data obtained during two time periods are presented. The first data set describes cross-track winds measured between 170 and 210 km during a 5-day period (25-29 March 1979) of mostly high geomagnetic activity. In the second data set, cross-track winds and neutral densities from SETA and exospheric temperatures from the Millstone Hill incoherent scatter radar are examined during an isolated magnetic substorm occurring on 21 March 1979.

A polar thermospheric wind circulation consisting of a two-cell horizontal convection pattern is reflected in both sets of cross-track acceleration measurements. Winds are generally trans-polar and parallel to the 1600h/0400 MLT meridian with return flows in the morning and evening sectors near 57° and 70° geomagnetic latitude, respectively. Winds are of order 100-200 ms⁻¹ during quiet periods, and attain maximum speeds of order 300-600 ms⁻¹ during storm conditions. The two-cell pattern is distinctively more well-ordered in geomagnetic rather than geographic coordinates. The substorm circulation pattern persists almost unattenuated for about 6 hours after the magnetic disturbance has returned to quiet levels.

The density response is highly asymmetric with respect to its day/night behavior. At high geomagnetic latitudes (>60°) the daytime density variation, about a 40% increase from quiet levels, distinctively reflects the response to an increase in magnetic activity with a time delay of less than 3 hours. At lower latitudes the response is smaller (20%) and less well-defined, occurring with a time delay of about 6 ± 2 hours near 10-20° latitude. The nighttime density response, on the other hand, is not so well defined poleward as it is equatorward of 60° latitude. The time delay increases from about 2 ± 2 hours to 6 ± 2 hours from high to low latitudes. An exospheric temperature response occurs at Millstone Hill (42°N) with an amplitude of 210°K and time delay of between 0 and 2.5 hours.

Latitude structures of the density response at successive times following the substorm peak suggest the equatorward propagation of a disturbance with a phase speed of between 300 and 600 ms⁻¹. A deep depression in the density at high latitudes (>70°) is evident in conjunction with this phenomenon. The more efficient propagation of the disturbance to lower latitudes during the night is probably due to the "midnight surge" effect.

205
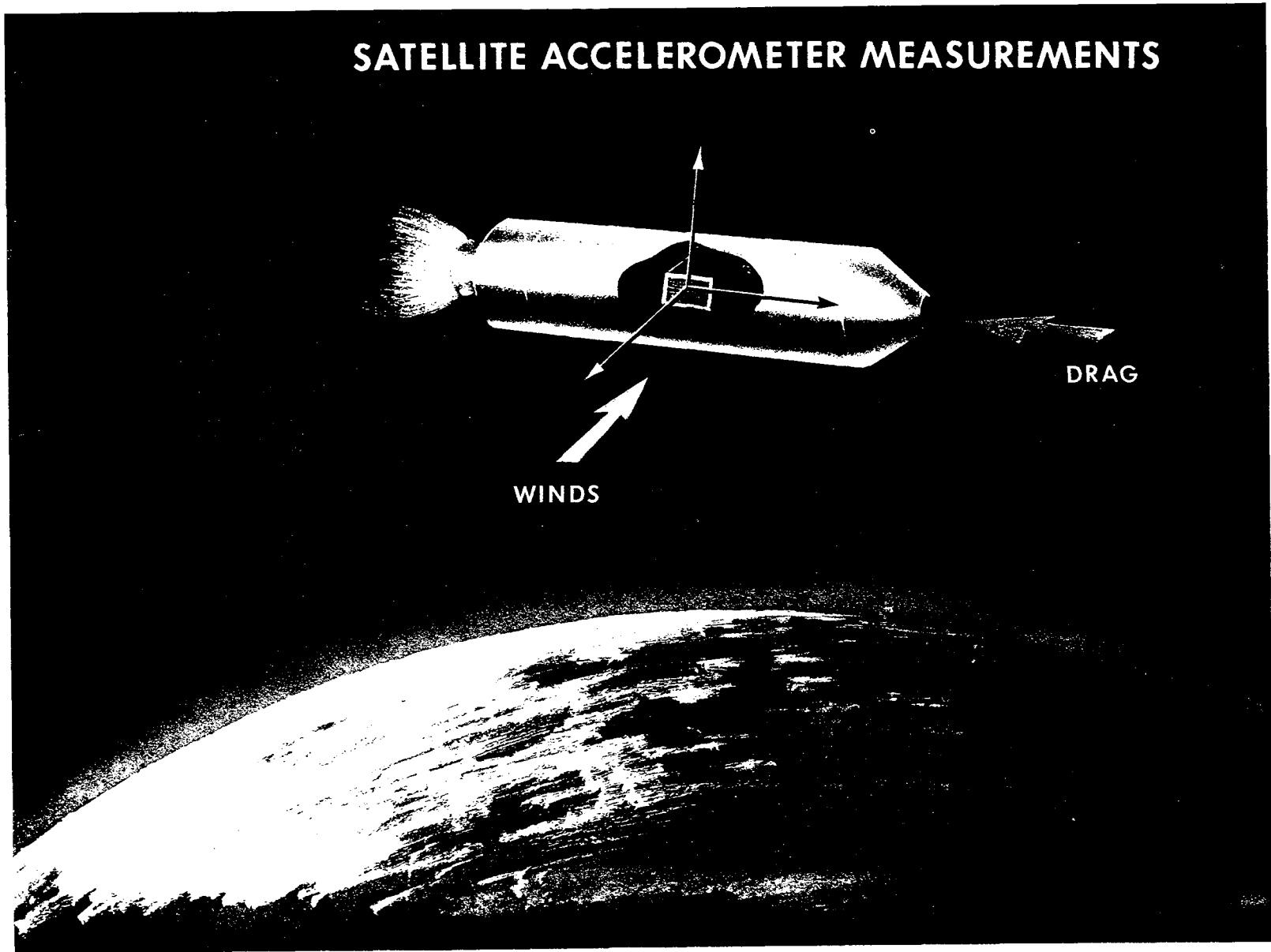
Figure 1. Cartoon showing orientation of accelerometer axes with respect to aerodynamic drag and cross-track wind vectors.
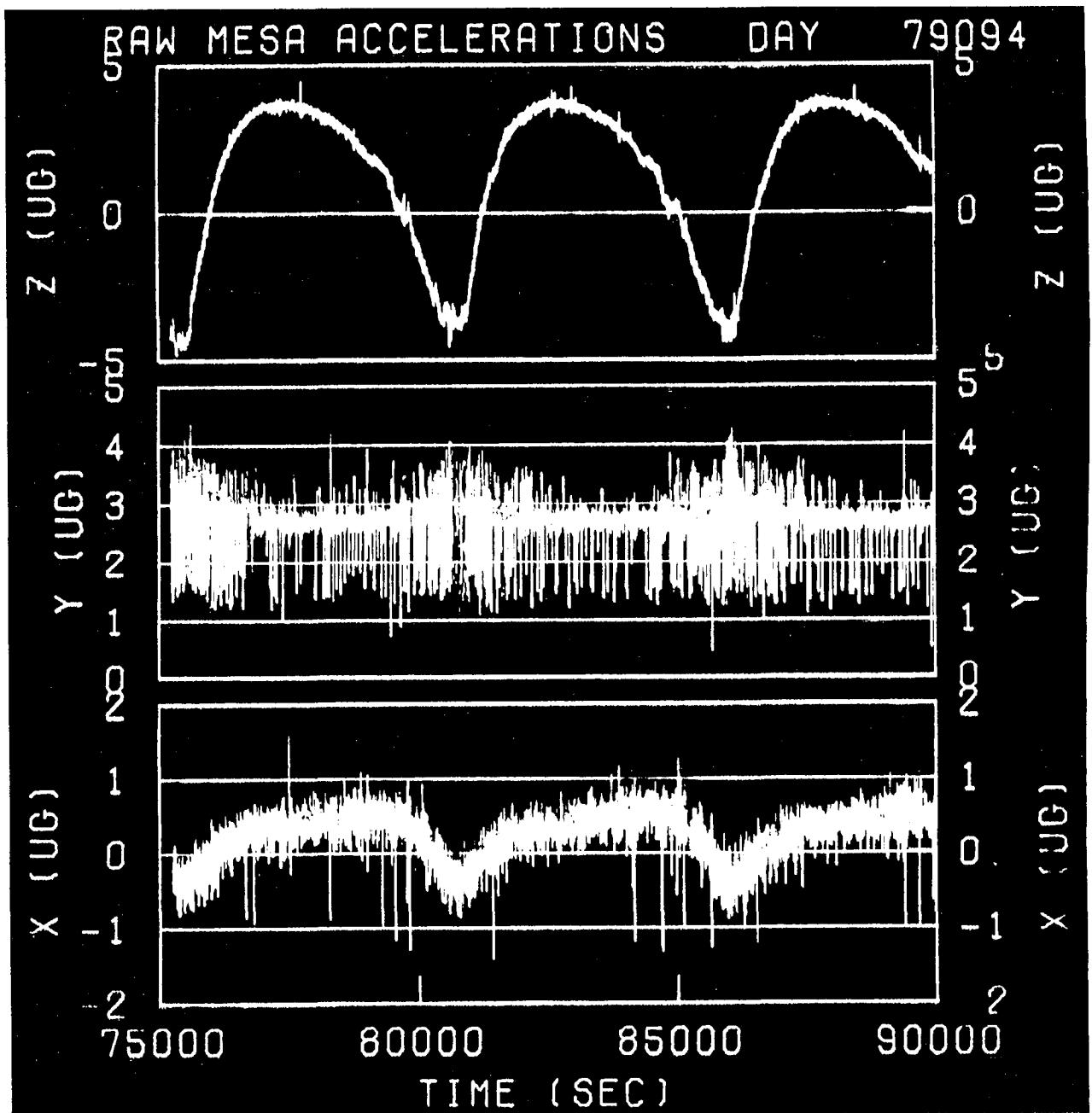
Figure 2. Raw acceleration data from each accelerometer axis plotted as a function of time. Period covered is almost three full orbits. The top frame shows accelerations measured in the along-track (Z) direction. Larger accelerations are indicated by larger negative values. Thus satellite minimum altitudes (and maximum drags) occur near 80500 and 85900 seconds.

First Data Set: period
of mostly high geomagnetic activity

DAY (1979)
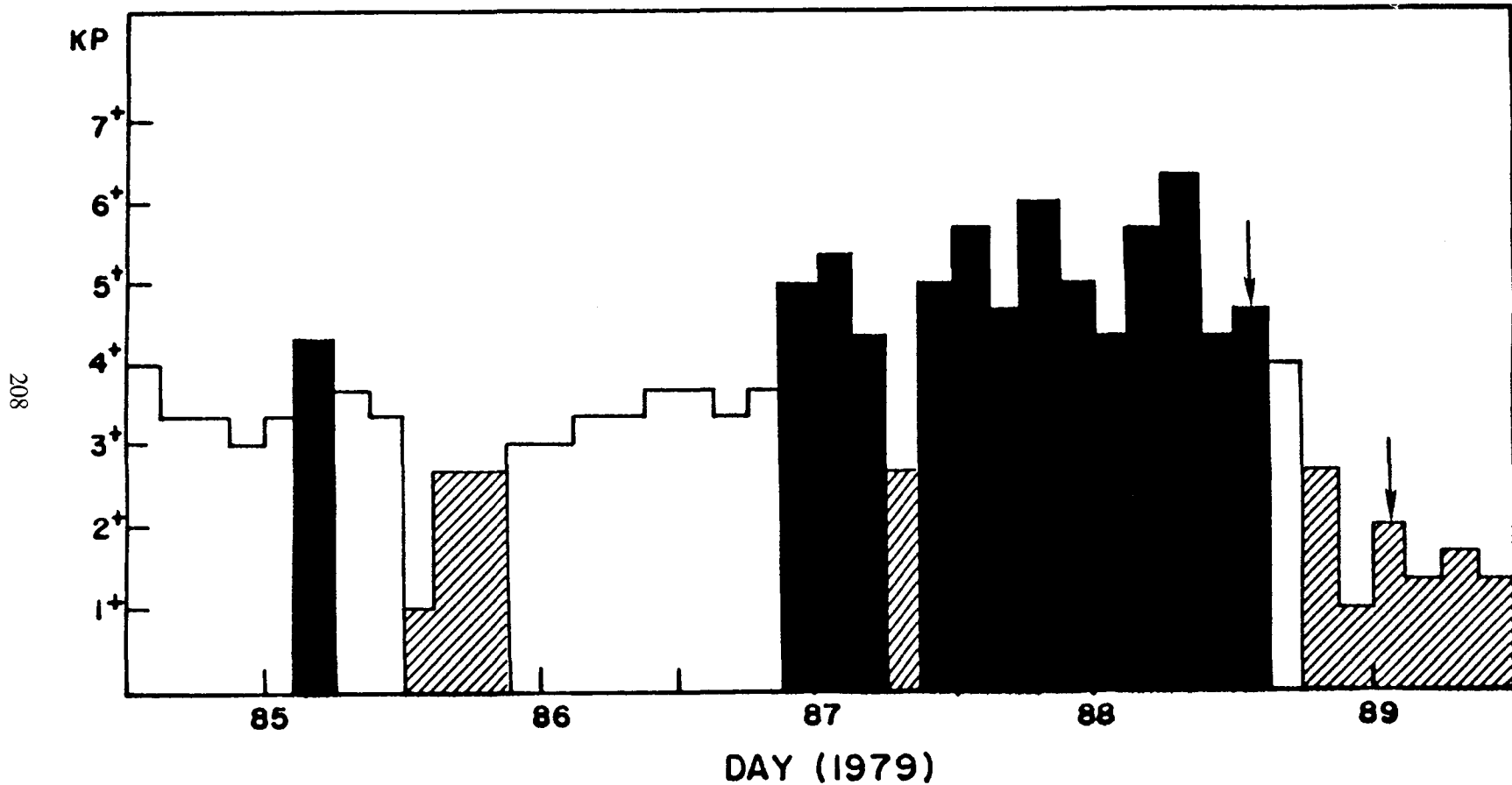
Figure 3. Kp variation during a 5-day period during 1979. Cross-hatched and solid areas represent Quiet (Kp ≤ 3°) and Active (Kp ≥ 5-) periods, respectively. Vertical arrows denote periods of the first data set analyzed.
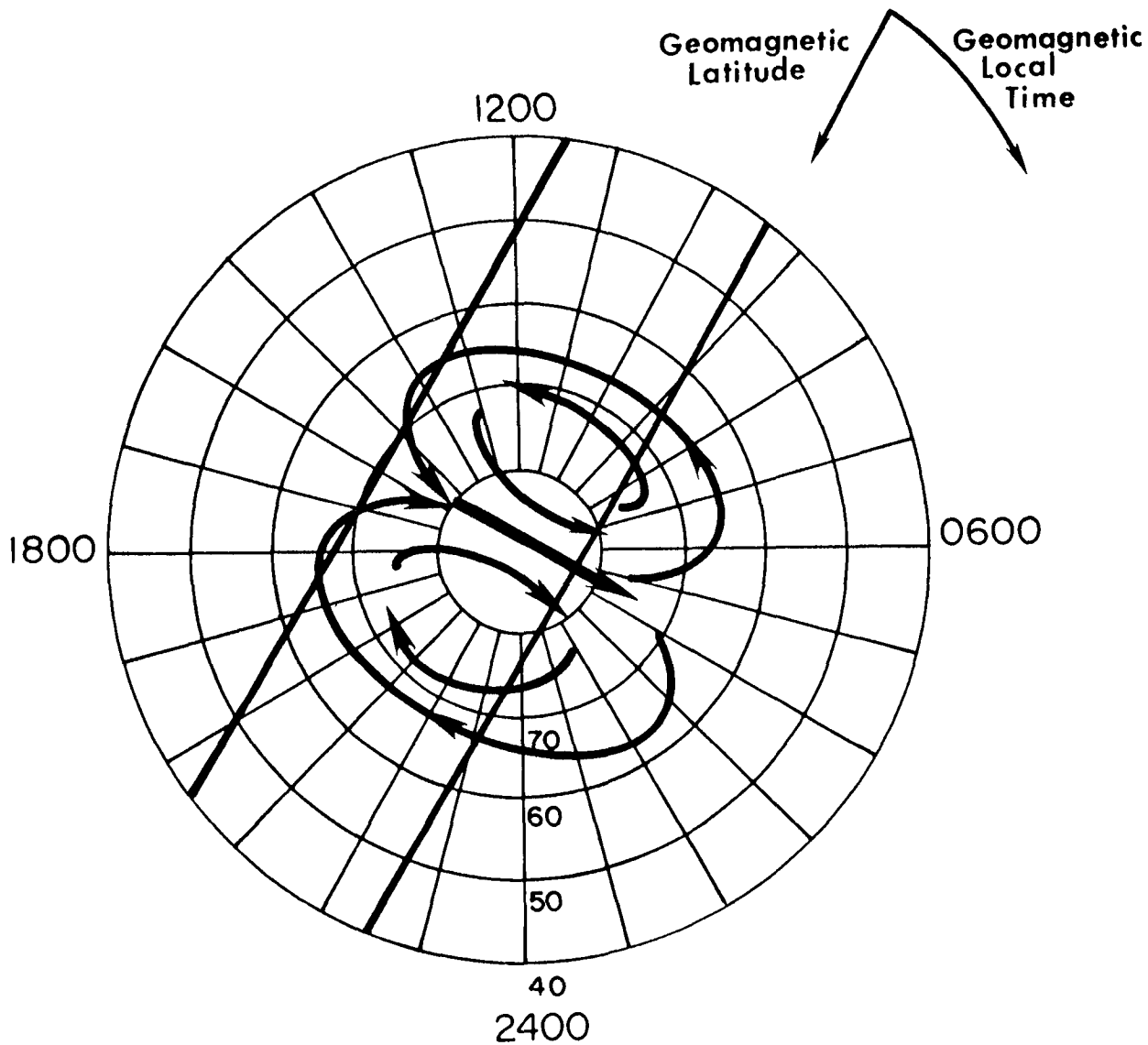
Figure 4. Schematic of 2-cell polar lower thermospheric circulation pattern in geomagnetic latitude and local time coordinates. Parallel lines represent bands of satellite tracks during 5-day period under study.

DAY 79088

NIGHT CELL   MORNING CELL

CROSS -TRACK WINDS

210

N

E   W

W

E

1000
800
600
400
200
0
-200
-400
-600
-800
-1000
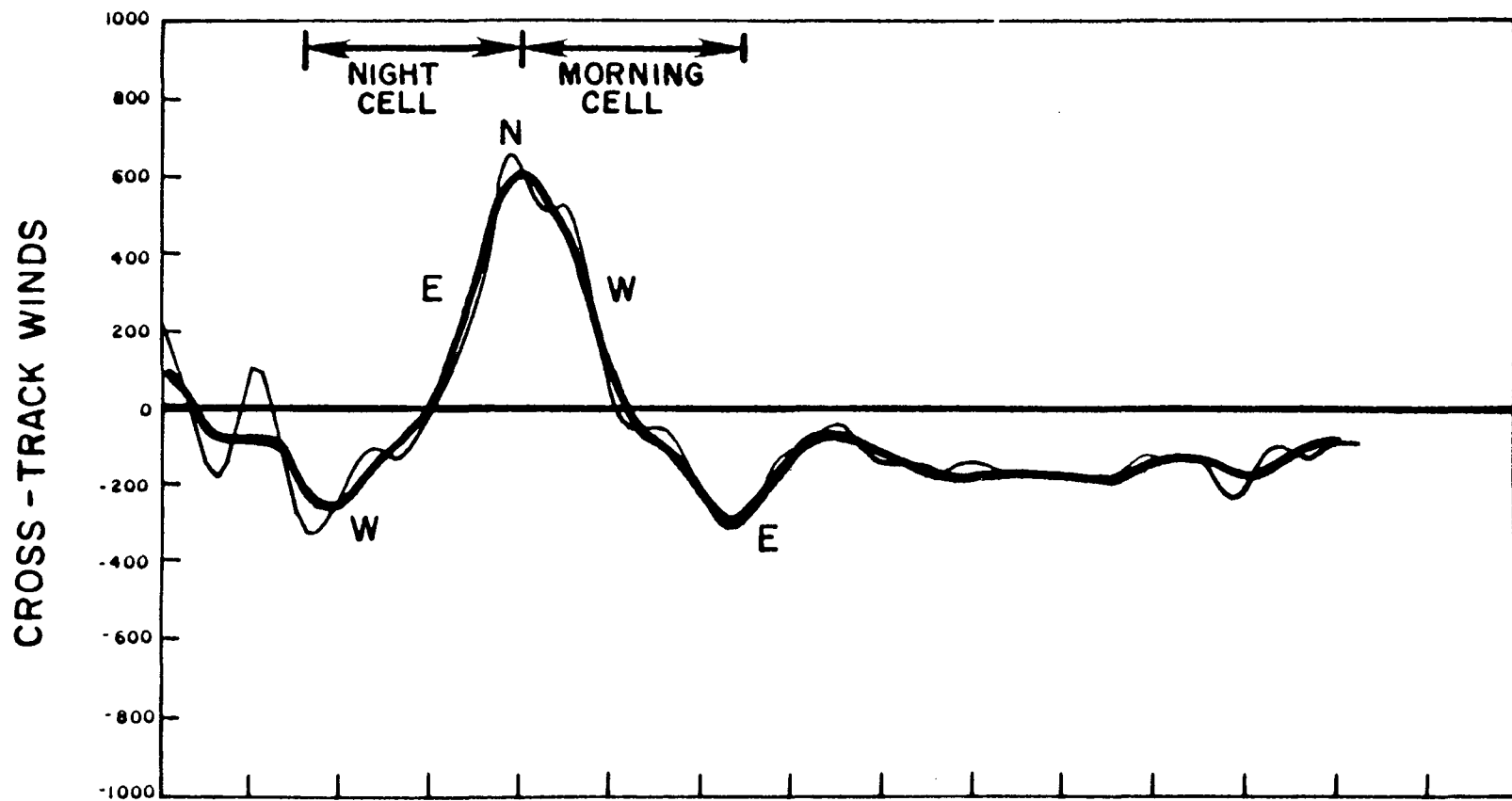
GMT	2400	2403	2407	2410	2413	2417	2420	2423	2427	2430	2433	2437	2440	2443	2447	2450
GGLAT	30	44	57	70	82	80	67	55	41	27	13	-1	-14	-27	-41	-55
GMLAT	39	53	67	79	87	73	59	46	32	18	4	-11	-23	-37	-51	-65
LT	2159	2150	2134	2105	1860	1244	1115	1060	1036	1027	1020	1014	1008	1001	952	938
ALT	220.2	213.5	206.6	200.0	192.5	185.7	179.4	174.4	170.7	169.8	172.6	179.5	189.0	202.3	217.1	232.2

SETA-1 CROSS-TRACK WIND DATA

Figure 5. Cross-axis winds, corresponding to geomagnetically disturbed conditions, plotted vs. GMT, geographic latitude (GGLAT), geomagnetic latitude (GMLAT), local time (LT), and altitude (ALT). Unsmoothed (light line) and smoothed (heavy line) data are shown. E, W, N refer, respectively to the fact that cross-track accelerations are due primarily to Eastward, Westward, and Northward flows.
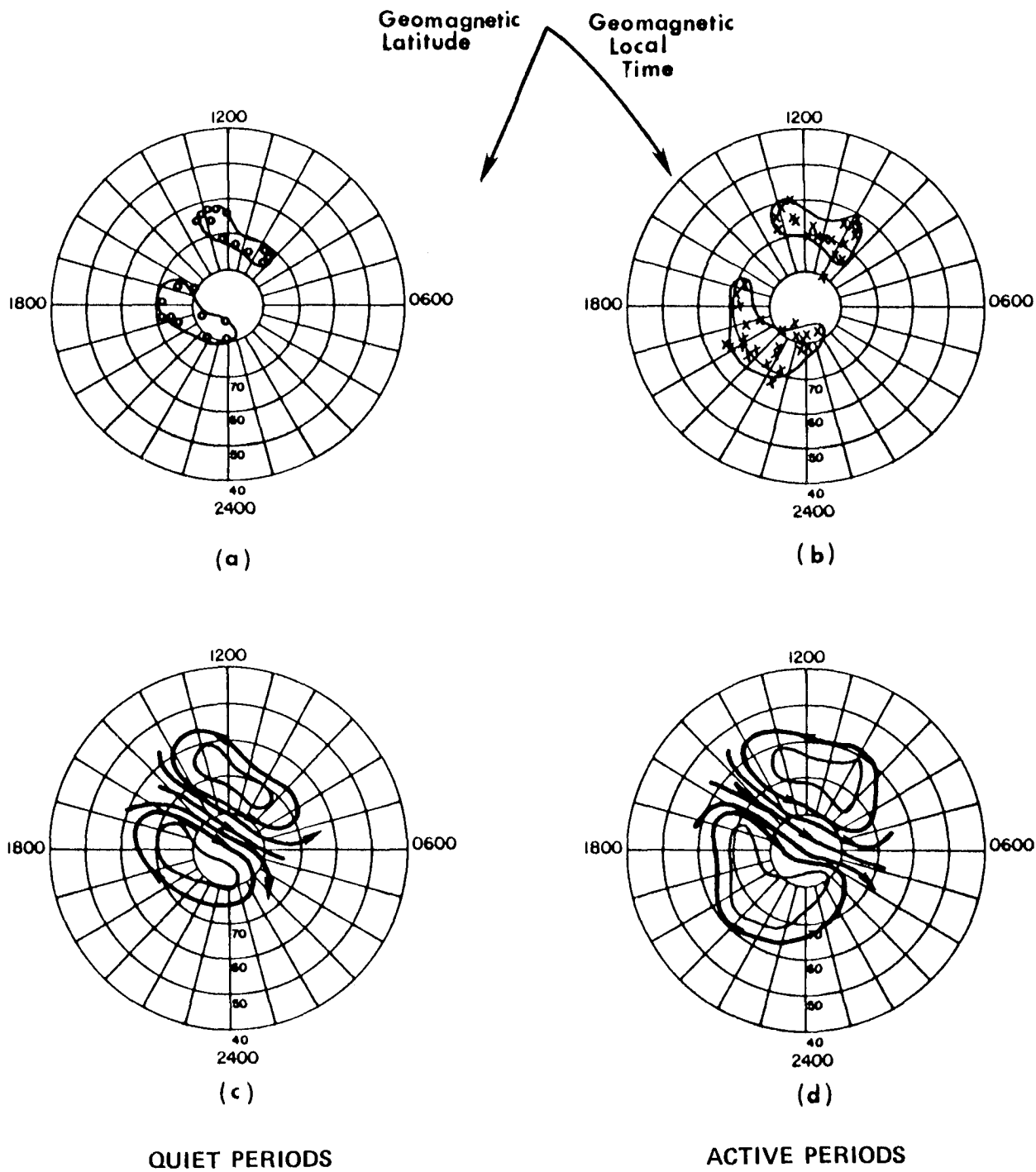
Figure 6. (a) and (b): "cell centers" of double-vortex circulation system for quiet and active geomagnetic conditions, respectively. (c) and (d): schematics of 2-cell circulation patterns consistent with the quiet and active period data, respectively.
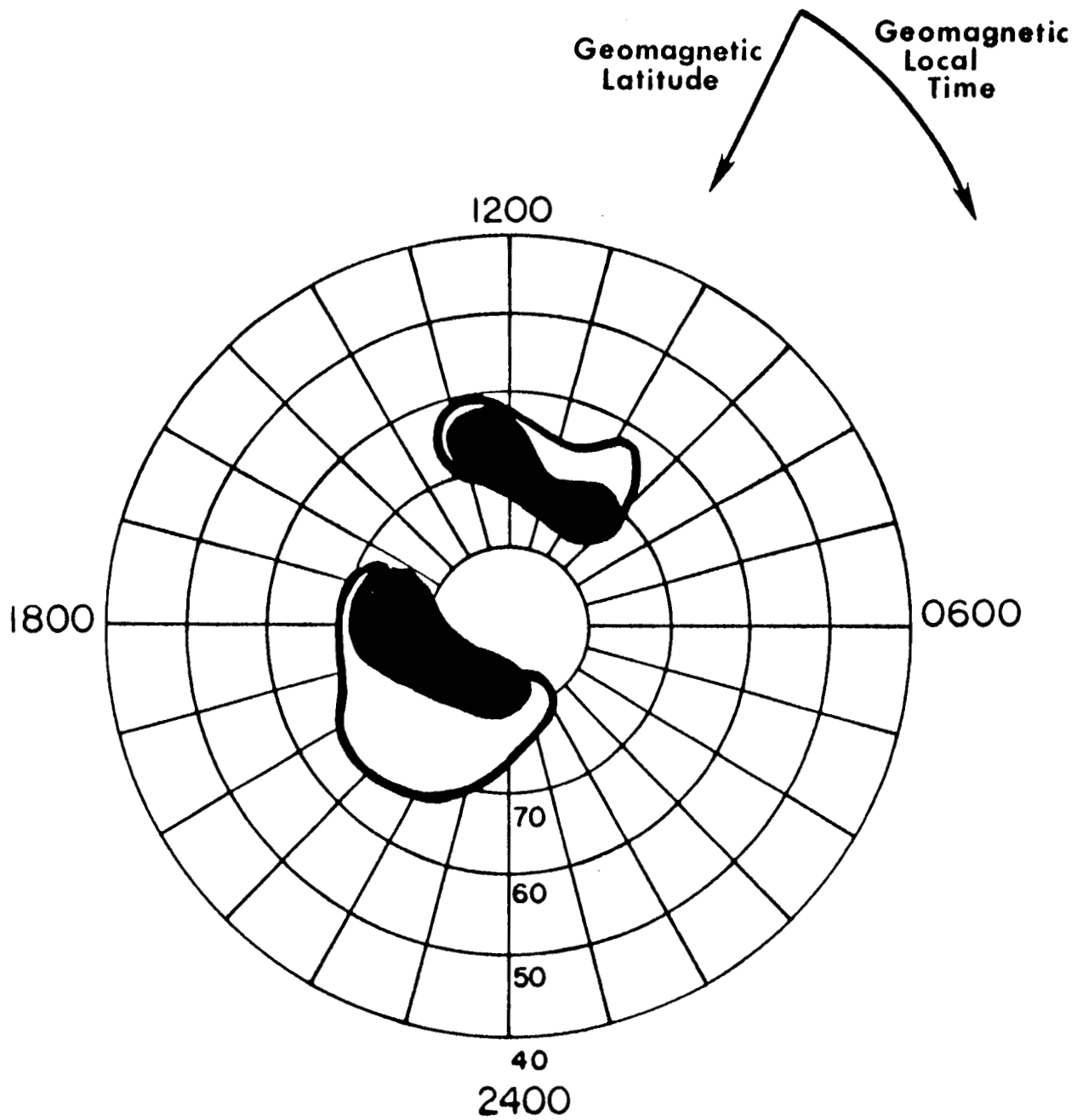
Figure 7. A comparison between areas including "cell centers" for quiet (black) and active (white) conditions.
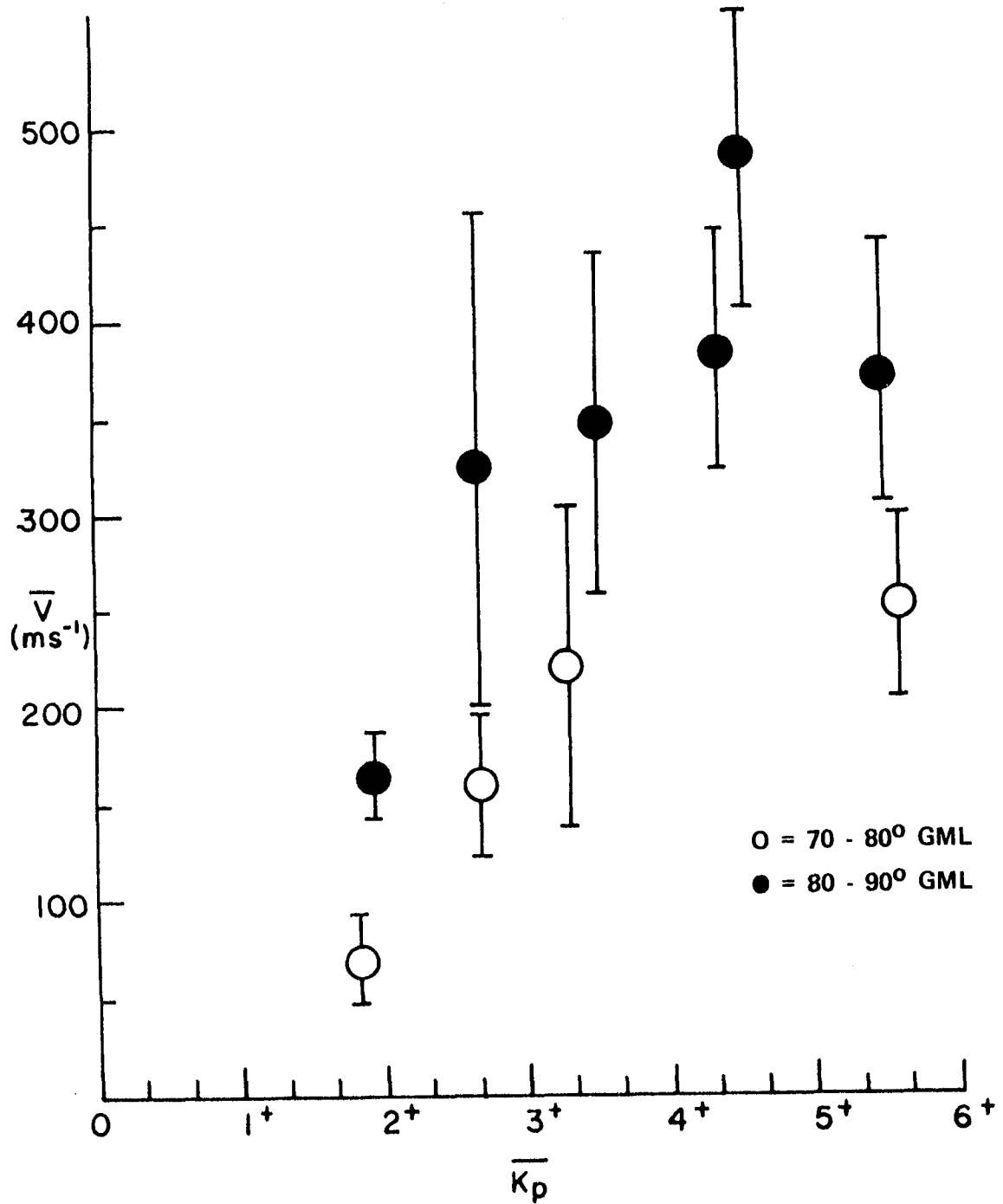
AVERAGE WIND VELOCITY VS. KP

Figure 8. Average wind data plotted vs. the corresponding average Kp values. Solid and open circles represent, respectively, measurements taken between 80-90° and 70-80° GMLAT. Standard deviations of the means are also indicated.

213

SUMMARY OF WINDS RESULTS FROM FIRST DATA SET

1. SATELLITE ACCELEROMETER CROSS-TRACK WIND DATA ARE
   USED TO INFER LOWER THERMOSPHERE CIRCULATION PATTERNS

2. MAIN FLOW IS ORIENTED PARALLEL TO 1600/0400 GLT MERIDIAN

3. TWO-CELL SYSTEM COVERS GREATER AREA OF POLAR CAP DURING
   ACTIVE CONDITIONS

4. WIND INTENSITY TENDS TO INCREASE WITH GEOMAGNETIC ACTIVITY

Figure 9. Summary of wind results from first data set.

Second Data Set:
isolated substorm
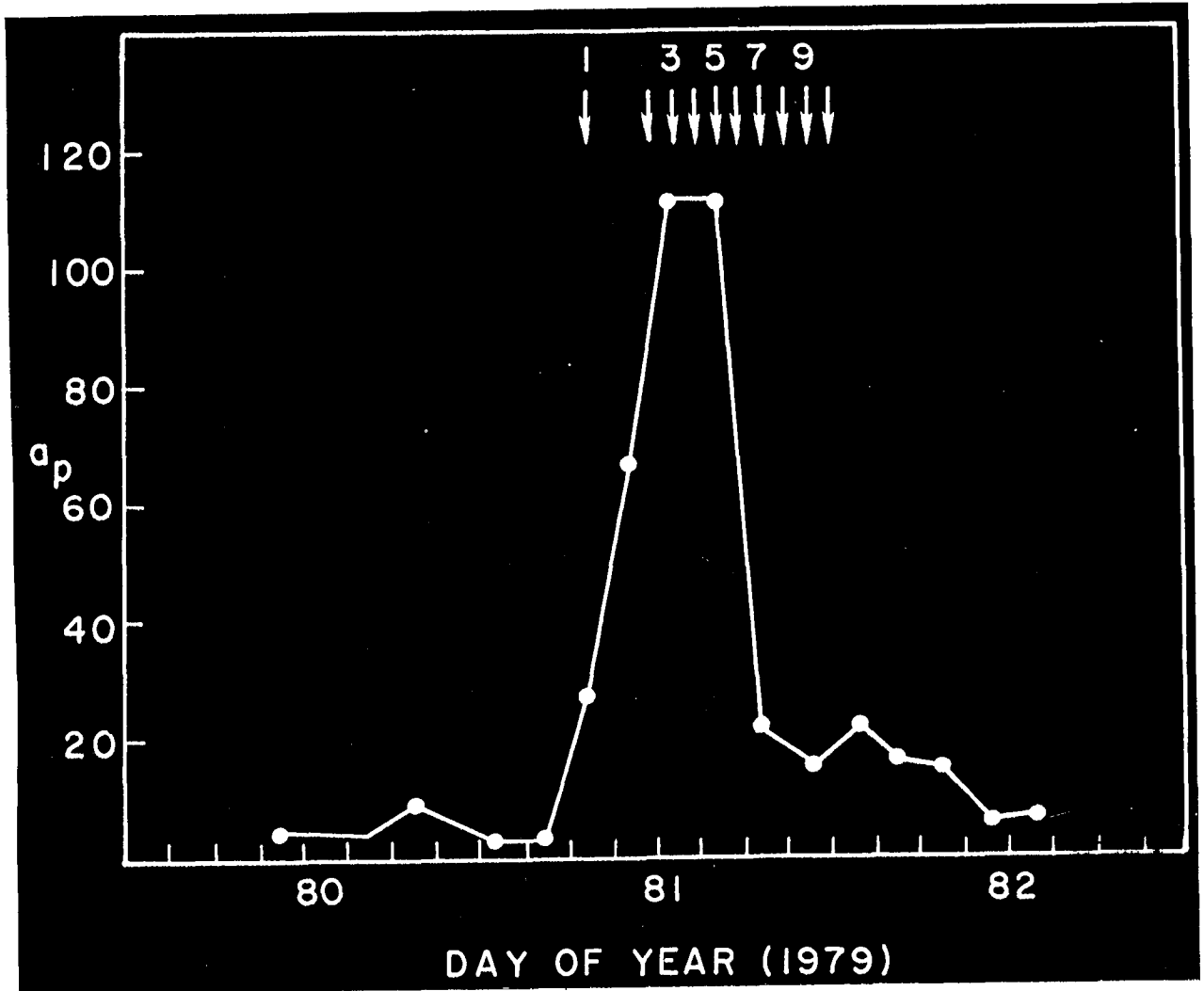
Figure 10. Variation of the 3-hourly planetary magnetic index a_p during the substorm under study. Vertical arrows indicate orbits (actually, times of polar crossings) which are explicitly included in the analysis of this paper.
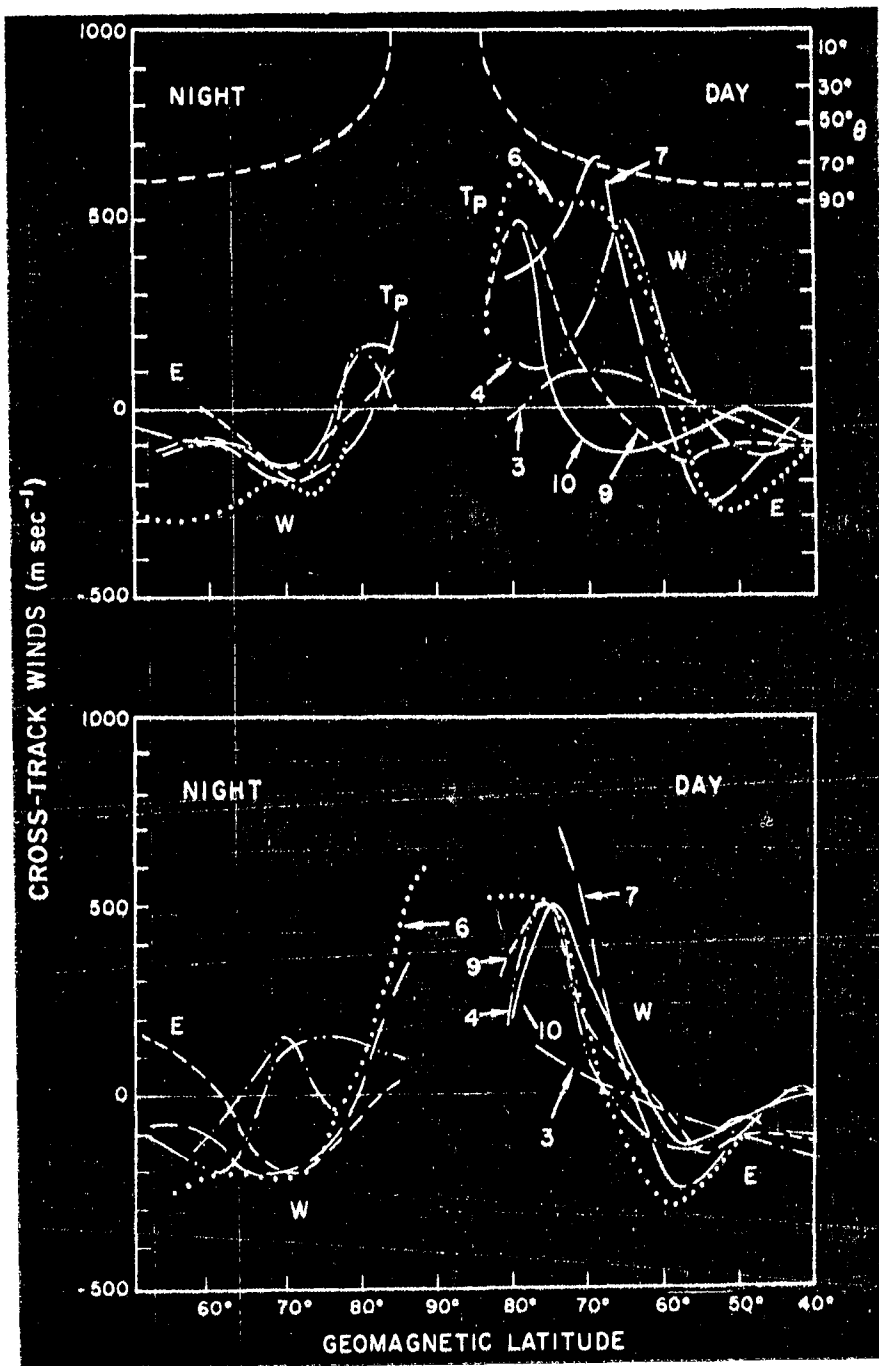
Figure 11. Cross-track winds from selected orbits (3, 4, 6, 7, 9, 10) as a function of geographic (top) and geomagnetic (bottom) latitudes. "E" denotes east-ward oriented winds, "W" denotes westward-oriented winds, and TP indicates trans-polar oriented winds. The angle 0 plotted as a dashed line in the top figure represents the relative orientation of the cross-track direction and the geographic meridian.

216
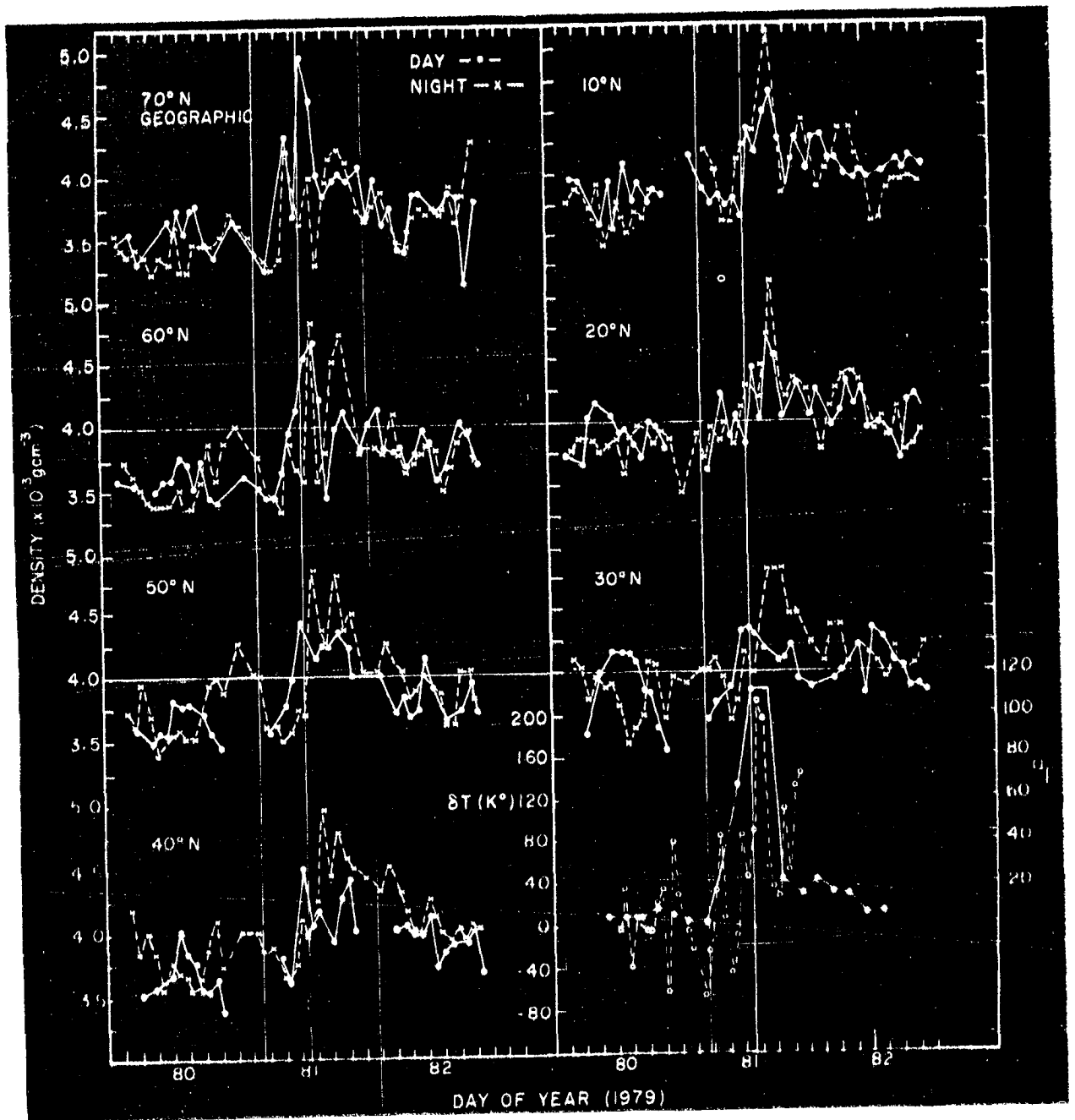
Figure 12. Temporal response of density at various geographic latitudes for day and night crossings. Exospheric temperatures from Millstone Hill and the a_p index are plotted in the bottom right hand frame of the figure. For reference, vertical lines are drawn through the "last quiet" and "first maximum" values of a_p.
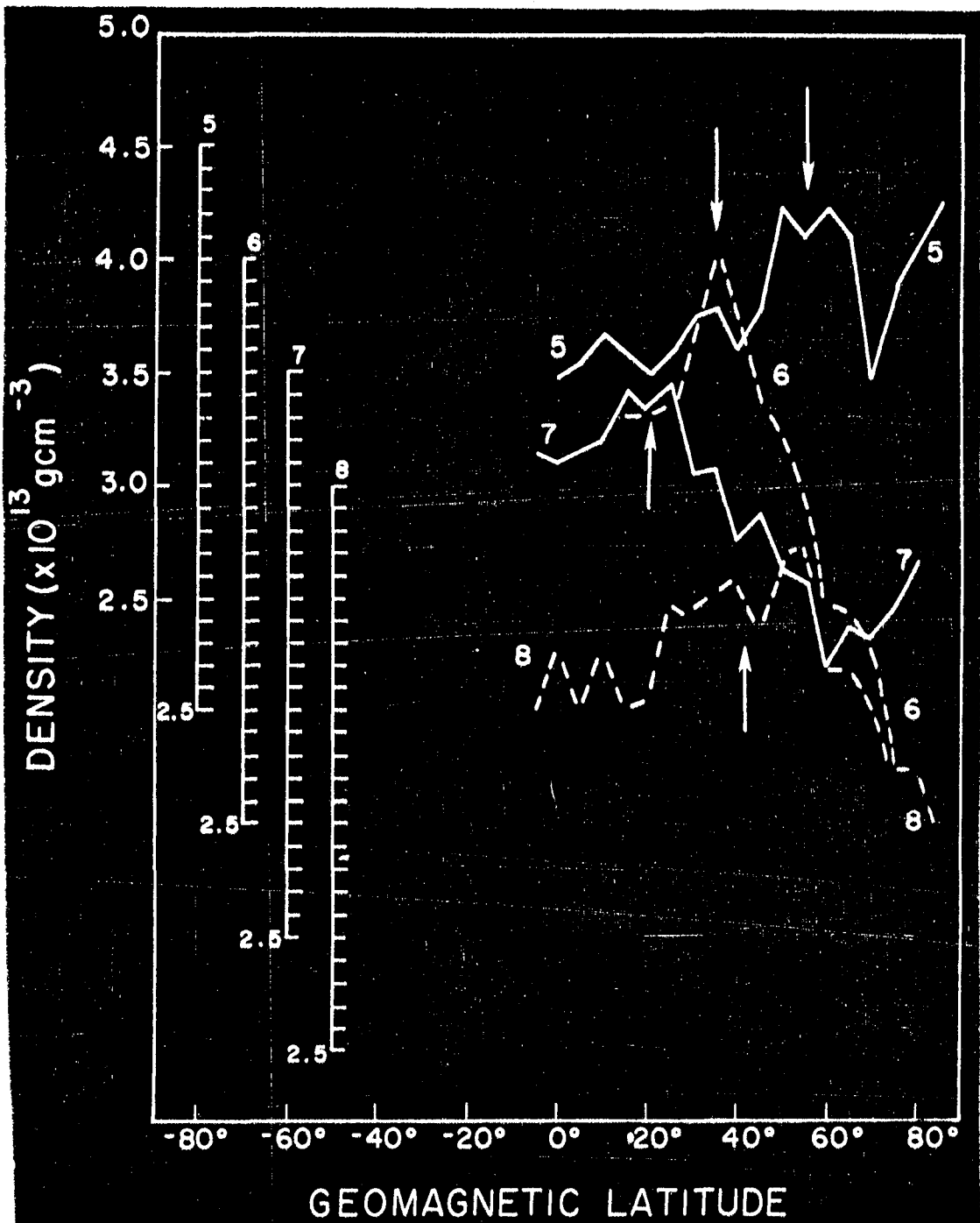
Figure 13. Nighttime density responses for orbits 5, 6, 7, 8 as a function of geomagnetic latitude. Vertical arrows indicate approximate latitudes corresponding to density bulge associated with propagating disturbance launched during the substorm.

CONCLUSIONS

1. SATELLITE ACCELEROMETER PROVIDES SIMULTANEOUS
   NEUTRAL DENSITY AND CROSS-TRACK WINDS

2. TRANS-POLAR WINDS IN LOWER THERMOSPHERE ARE
   PARALLEL TO 1600/0400 GLT MERIDIAN

3. WIND PATTERNS CAN PERSIST FOR SEVERAL HOURS
   AFTER STORM PERIOD

4. NEUTRAL DENSITY DATA SHOW EVIDENCE OF
   "MIDNIGHT SURGE" EFFECT

5. GRAVITY WAVE SIGNATURES ARE OBSERVED AT
   HIGH AND MIDDLE LATITUDES

Figure 14. Conclusions from analysis of both data sets described in this paper.

TRANSFER FUNCTION ANALYSIS OF THERMOSPHERIC PERTURBATIONS

H. G. Mayr, I. Harris, F. Varosi*, F. A. Herrero and N. W. Spencer
Laboratory for Atmospheres, NASA/Goddard Space Flight Center
Greenbelt, MD 20771

Applying perturbation theory, a spectral model (Mayr et al., JGR, 1984) in terms of vector spherical harmonics (Legendre polynomials, specifically) is used to describe the short term thermospheric perturbations originating in the auroral regions. The source may be Joule heating, particle precipitation or ExB ion drift-momentum coupling. A multiconstituent atmosphere is considered, allowing for the collisional momentum exchange between species including Ar, O_2, N_2, O, He and H. The coupled equations of energy, mass and momentum conservation are solved simultaneously for the major species N_2 and O. Applying homogeneous boundary conditions, the integration is carried out from the Earth's surface up to 700 km. In our analysis, the spherical harmonics are treated as eigenfunctions, assuming that the Earth's rotation (and prevailing circulation) do not significantly affect perturbations with periods which are typically much less than one day. Under these simplifying assumptions, and given a particular source distribution in the vertical, a two-dimensional transfer function is constructed to describe the three dimensional response of the atmosphere. In the order of increasing horizontal wave numbers (order of polynomials), this transfer function reveals five components: (A) The trapped component which is confined to the source region and decays slowly, with the time constant depending on the height of energy deposition and the magnitude of eddy diffusion for example. (B) The quasi-horizontally propagating gravity wave which is represented by the lower cut-off and the first resonance maximum in the transfer function. In the thermosphere, it is also the dominant maximum. The horizontal wave length (order of 1000 km) and propagation velocity (700 m/s) are large. (C) The obliquely propagating wave generated through partial reflection from the base of the thermosphere. This wave appears as a broad secondary maximum in the transfer function; its horizontal wave length and propagation velocity (about 350 m/s) is smaller; this wave is important near the source but cannot propagate very far horizontally. (D) The ducted wave which is produced in the non-dissipative lower atmosphere by total reflection from the Earth's surface and partial reflection from the mesopause temperature minimum. Leaking back into the thermosphere where it originates, this wave has a relatively short wavelength but can travel large distances away from the source region (pole to equator); the horizontal propagation velocity is about 250 m/s. (E) The waves reflected from the surface which appear in the transfer function as broad secondary maxima. In general, these waves have relatively short horizontal wavelengths and dissipate rapidly above the mesopause. Thus, they cannot propagate far away from the source. To compile the transfer function, the numerical computations are very time consuming (about 100 hours on a VAX for one particular vertical source distribution). However, given the transfer function, the atmospheric response in space and time (using Fourier integral representation) can be constructed with a few

*Science Applications Research, Riverdale, Maryland

seconds of CPU. This model is applied in a case study of wind and temperature measurements on the Dynamics Explorer B, which show features characteristic of a ringlike excitation source in the auroral oval. The data can be interpreted as gravity waves which are focused (and amplified) in the polar region and then are reflected to propagate toward lower latitudes.
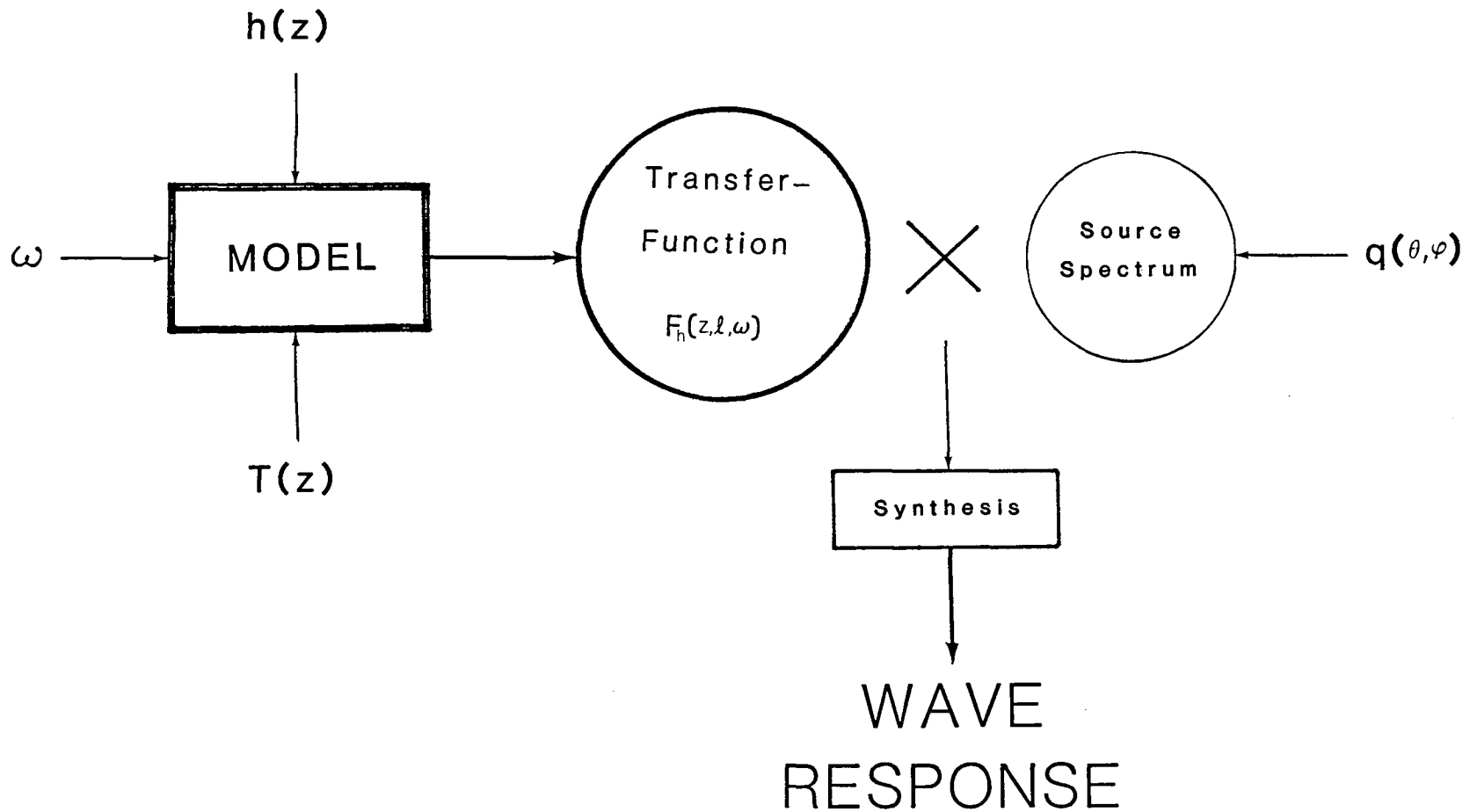
Figure 1. Block diagram illustrating the analysis. With a fixed height distribution of the excitation source h(z), and for frequencies ω, and horizontal wave numbers ℓ, the transfer function is constructed from a numerical integration of the perturbation equations (model). The model describes the perturbation amplitudes in a static background atmosphere with a height dependent temperature distribution, T(z), and corresponding density variations. The temporal and horizontal variations of the source are spectrally analyzed (source spectrum) and folded into the transfer function to construct (or synthesize) the wave response.
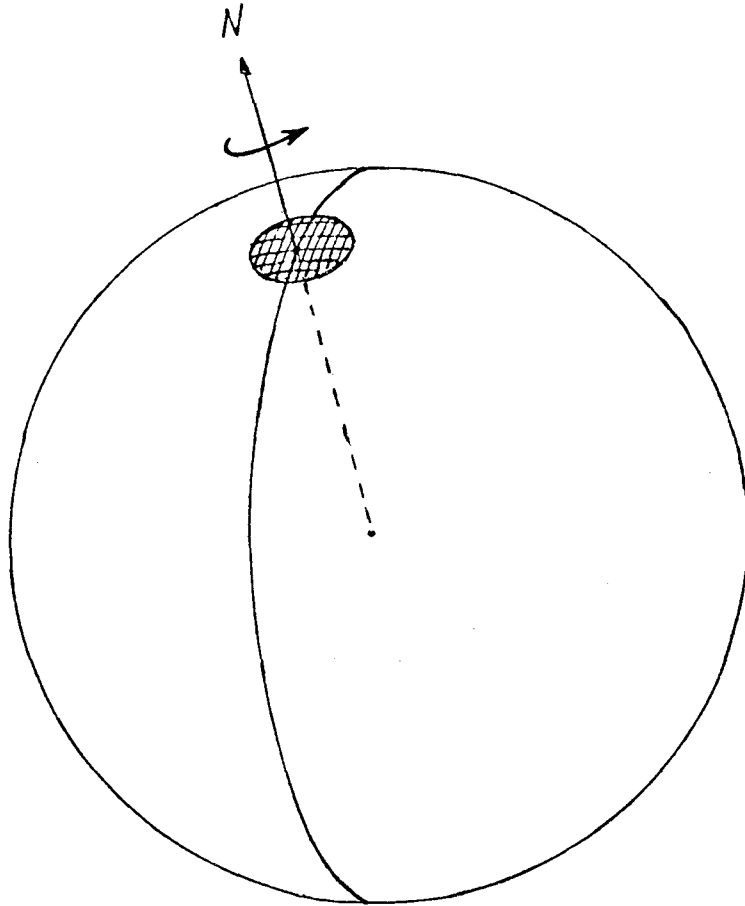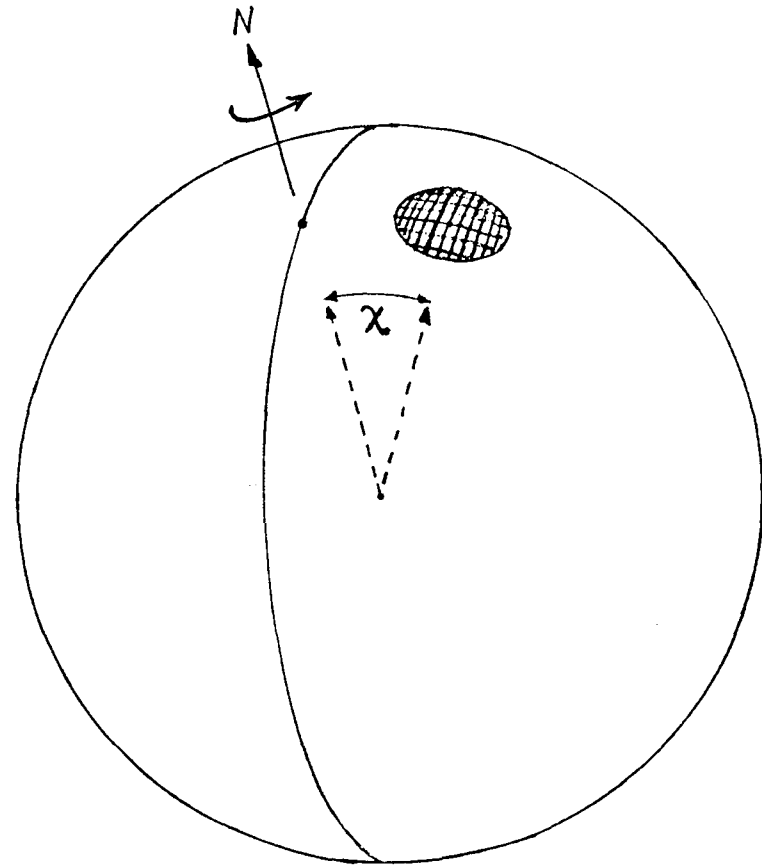
Figure 2. Assuming that the Earth's rotation and prevailing circulation do not significantly affect thermospheric perturbations with periods much less than one day, one should expect that gravity waves tend to propagate radially away from a "source pixel" as illustrated in the shading. To first order, the response is "source symmetric". Under this condition, spherical hamonics with zonal wave number m = 0 (Legendre polynomials) which normally describe axi-symmetric configurations, can be used to describe an arbitrary three dimensional configuration representing a conglomerate of individual source pixels. The two dimensional transfer function, F_h (z, ℓ, ω), can then be used to describe the three dimensional wave response.

TRANSFER FUNCTION

TEMPERATURE
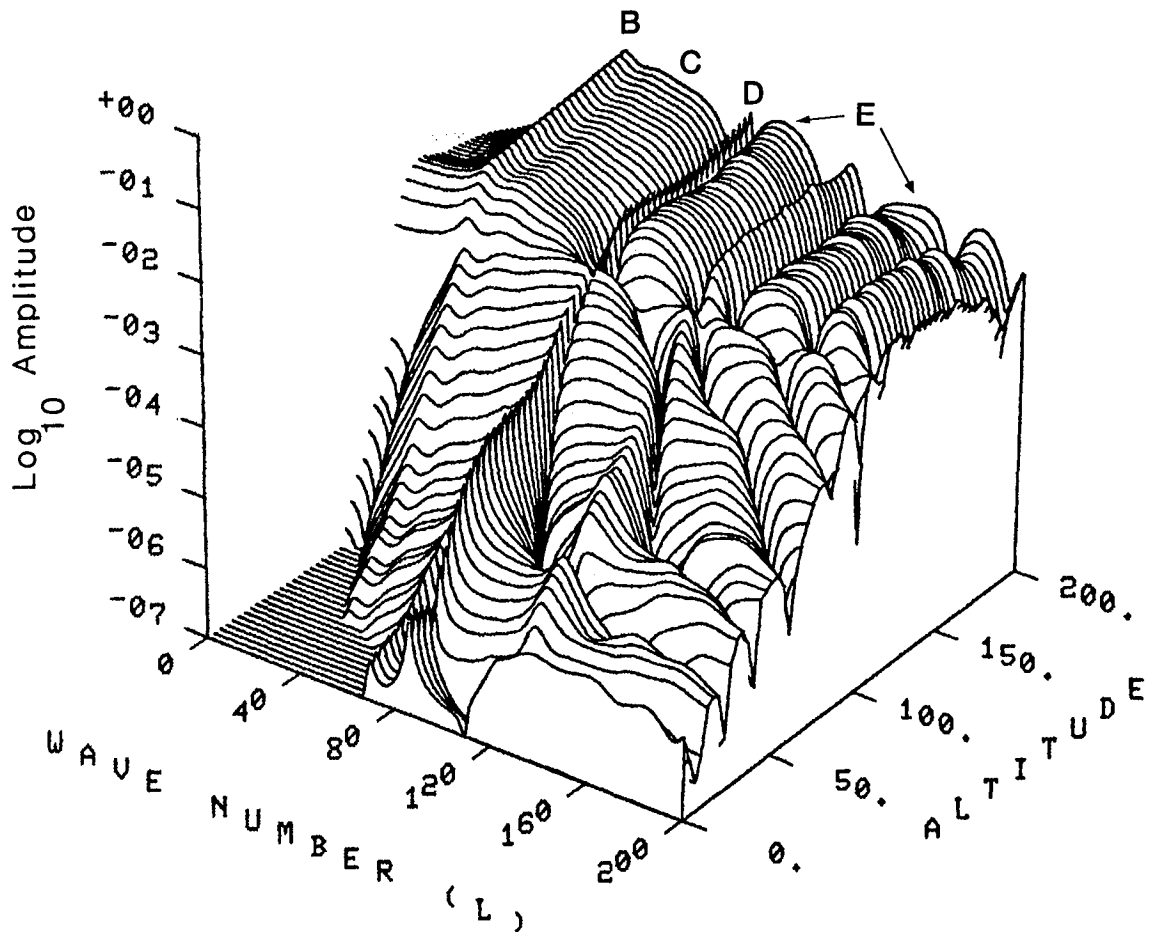
Figure 3. For a wave period of half an hour, we show the computed transfer function of the relative temperature amplitude. The perturbations are excited by a height distributed heat source due to Joule heating. Adhering to the order in the abstract, the four propagating wave modes are identified: (B) the dominant, quasi-horizontally propagating gravity wave near the lower cutoff at the horizontal wave number $\ell = 32$, consistant with the theory of Hines (1960). (C) The wave reflected from the temperature gradient at the base of the thermosphere (Richmond, 1978). (D) The ducted wave returning from the lower atmosphere, which is formed through total reflection at the surface and partial reflection from the mesopause temperature minimum at 80 km (Hines, 1960; Friedman, 1966); this wave appears in the transfer function as a narrow resonance maximum near $\ell = 90$ and persists throughout the atmosphere. (E) The broad secondary maxima at higher wave numbers which are due to reflection from the surface (Francis, 1974).
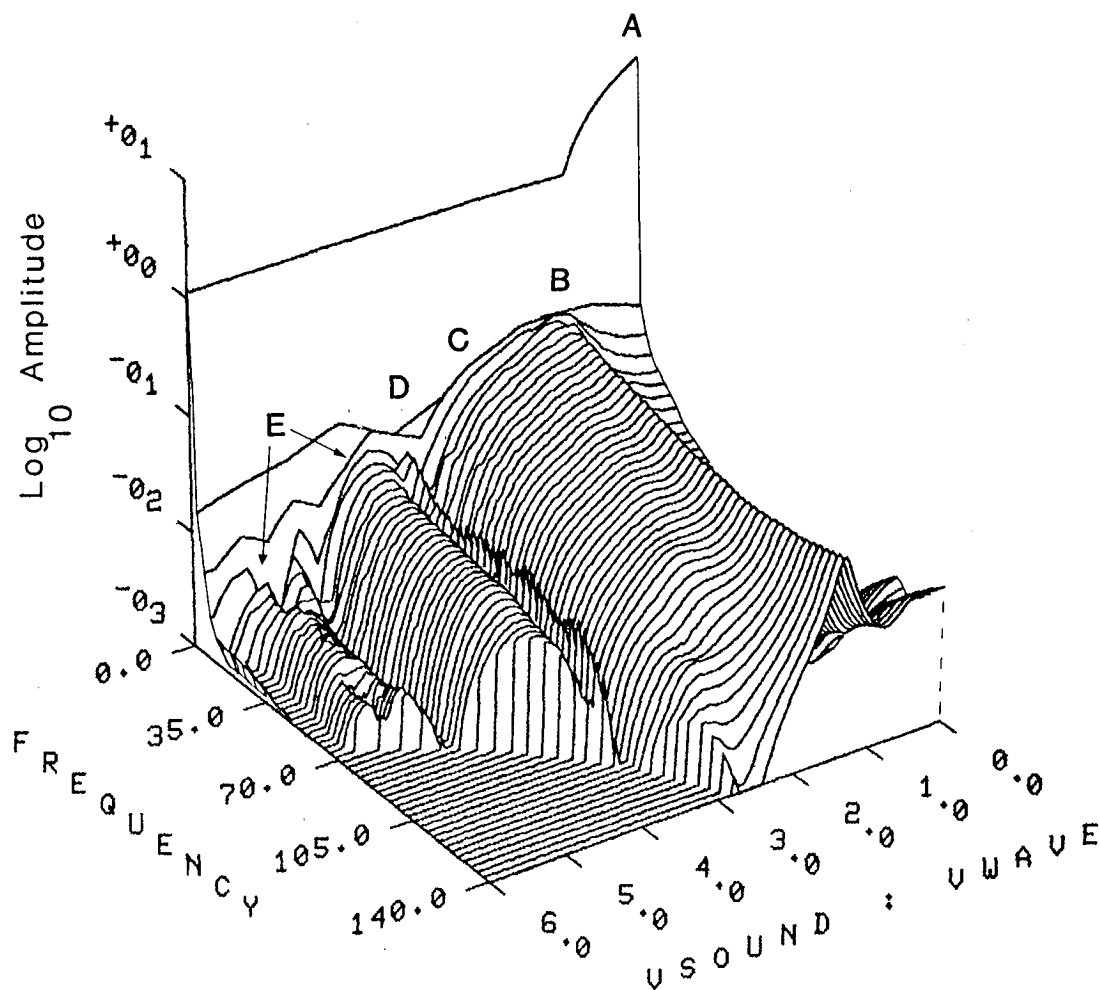
Figure 4. Computed transfer function for the temperature amplitude at 300 km, shown versus the frequency and the ratio between speed of sound and horizontal propagation velocity (proportional to ℓ/ω, for $\omega > 2$). The frequency range extends from 0 to 140 cycles per day, i.e., down to periods of 10 minutes. Note that the individual features of the transfer function line up along constant values of ℓ/ω, consistent with classical gravity wave theory (Hines, 1960). The labels B through E identify the wave modes discussed in Figure 3. At the lower end of the frequency spectrum, labelled A, the transfer function shows the property of the thermospheric low pass filter (Volland and Mayr, 1970); the global scale and long term variations in the temperature (and density) are preferentially excited. This property is determined by the long time constant for dissipative processes such as heat conduction and accounts for the slow decay of the "trapped" density and temperature perturbations in the source region.
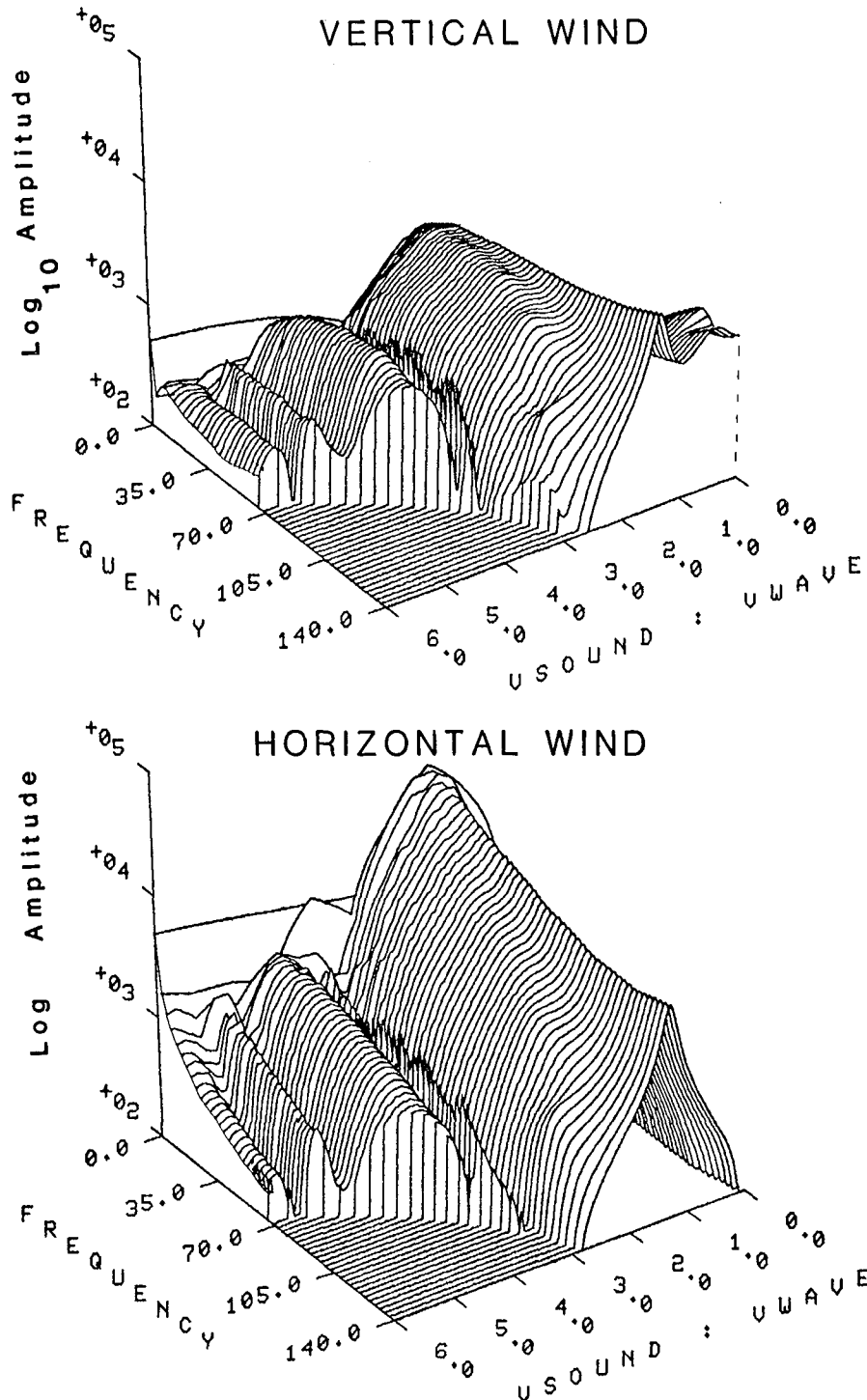
Figure 5. Analogous to Figure 4, we show the computed transfer functions for the vertical and horizontal velocities at 300 km. Note that the amplitudes are relatively small at lower frequencies; in contrast to the temperature (Figure 4), the low pass filter (labelled A) is not important. With increasing frequency, the amplitude of the vertical velocity grows and eventually becomes comparable to that of the horizontal velocity.
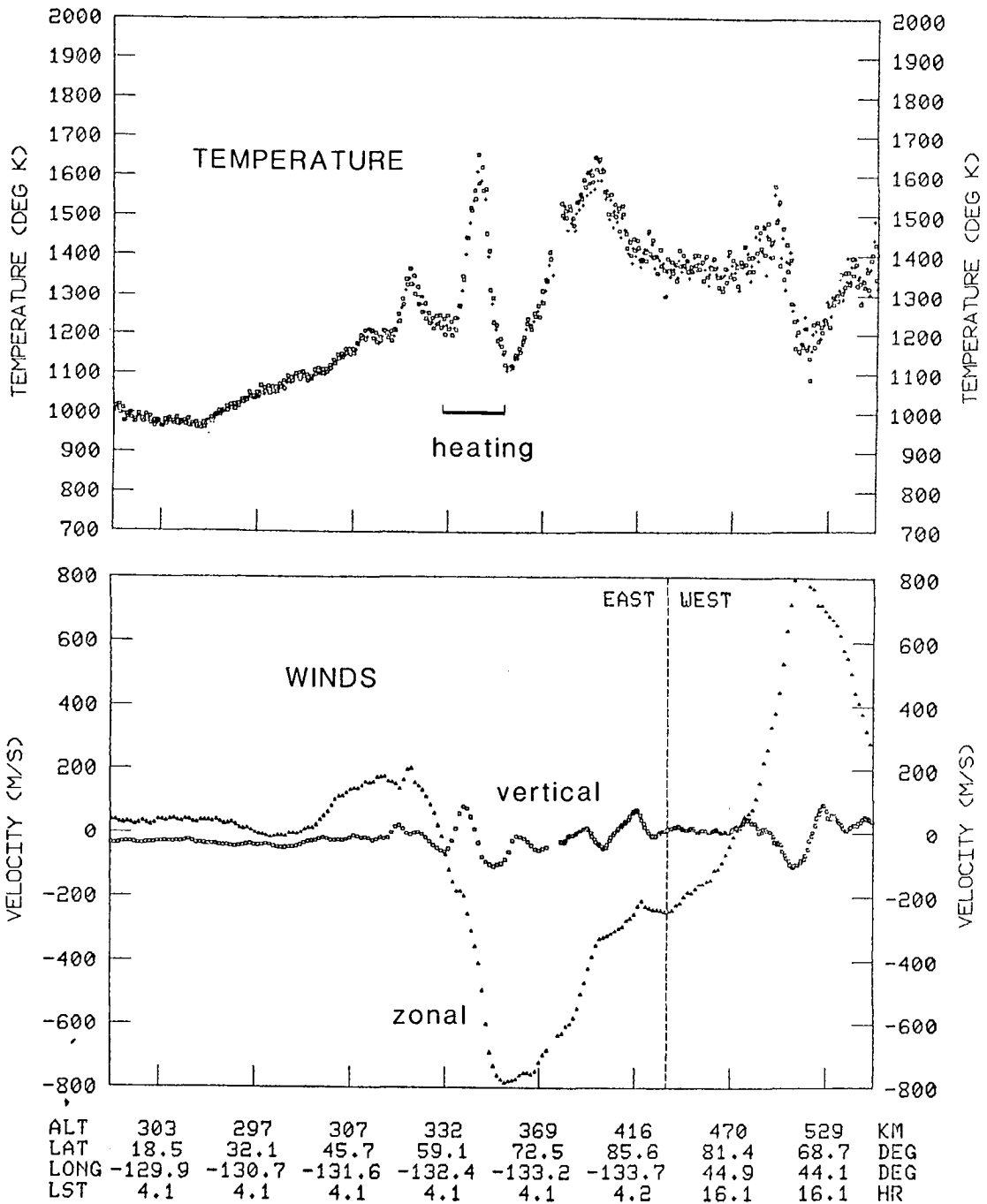
Figure 6. Temperature and wind measurements from the DE-2 WATS experiment (Spencer et al., 1982) during a magnetic substorm on December 25, 1981. (For quiet conditions, the temperatures are about 1100 K). Near 65° latitude, a region of energy deposition is indicated as inferred from the magnetic field and particle flux measurements on DE-2 (Farthing, Sugiura et al., 1981; Winningham et al., 1981). Airglow measurements of the 1500 A emission from DE-1 (Frank et al., 1981) made four hours earlier showed the auroral oval centered near the magnetic pole.

228
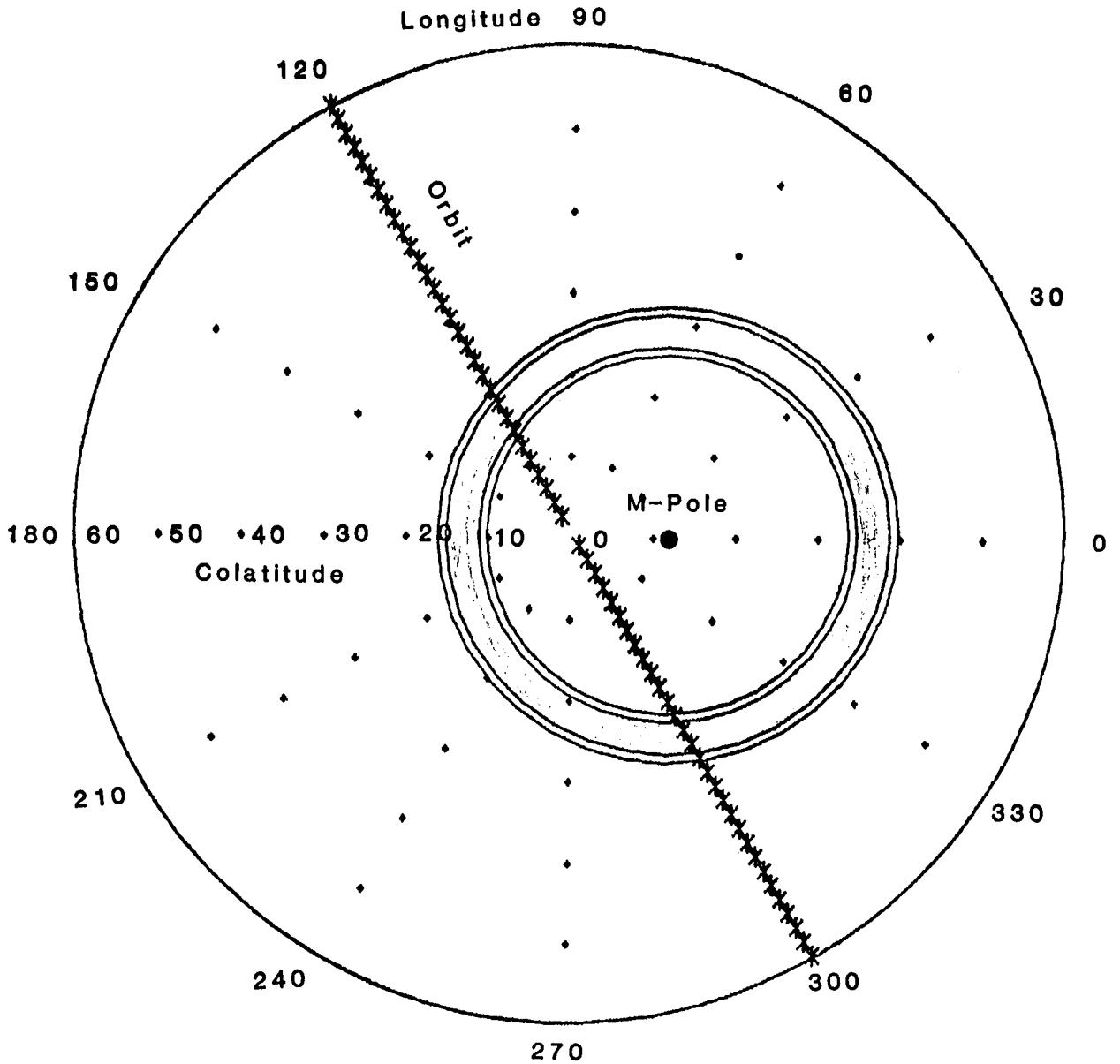
Figure 7. Based on the measurements from the Dynamics Explorers, we adopt the source geometry shown in this figure. The source, due to Joule heating, is turned on abruptly, then is kept constant for two hours when it is turned off again. The meridian is indicated along the satellite orbit for which the wave response is simulated.
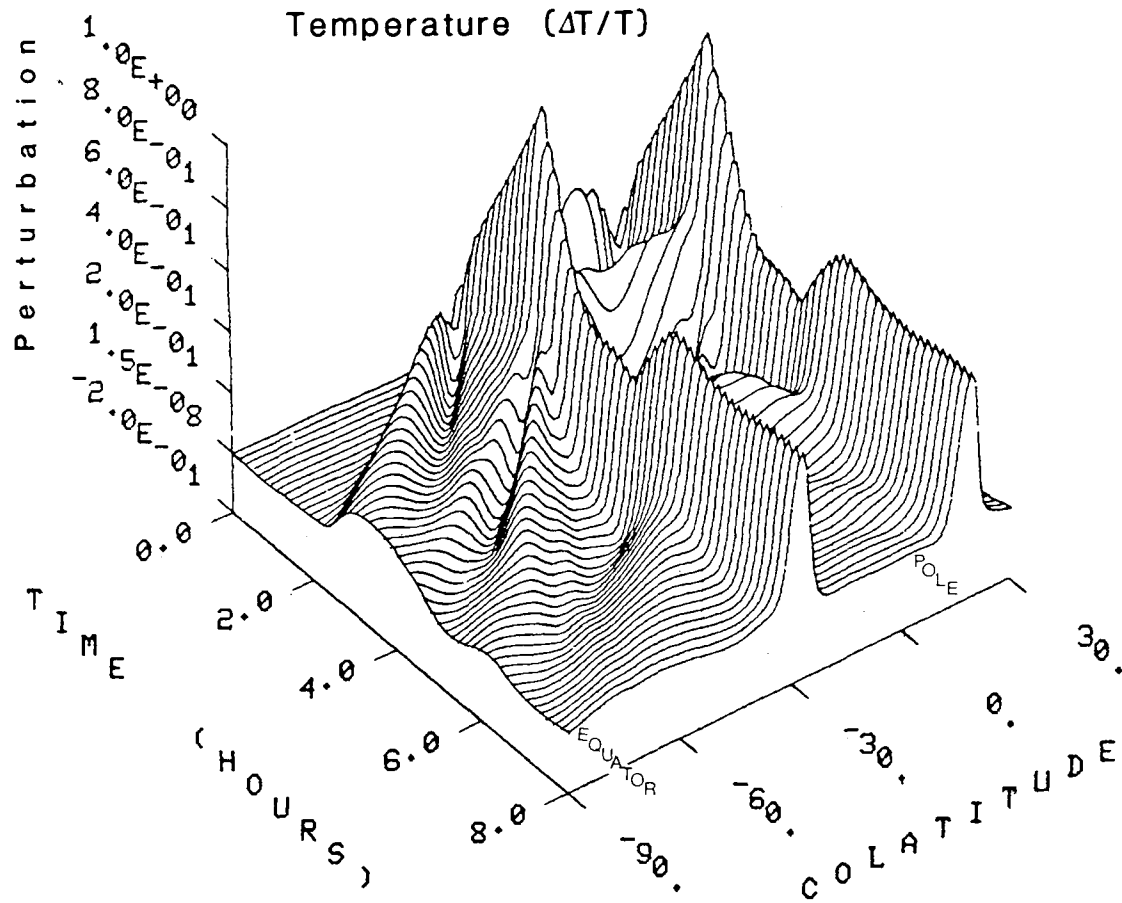
Figure 8. During the transient process of energization, a broad spectrum of frequencies is prominent in the source. The frequency spectrum of the resultant thermospheric disturbance is determined by the source spectrum and the transfer function. Thus, the frequencies preferentially excited are those which match, through the resonances in the transfer function, the characteristic horizontal dimension of the source. This in turn produces the local ringing and the wave disturbances which propagate away from the source region. Shown here is a three dimensional display of the computed temperature perturbation plotted versus colatitude and time (at t = 0 the source is turned on). One perturbation propagates toward the equator, while a second one propagates toward the center, i.e. the magnetic pole, where convergence leads to amplification. The latter wave is "reflected" from the center and then also propagates equatorwards. Both wave trains are launched when the source is turned on and off, thus producing a complicated disturbance.
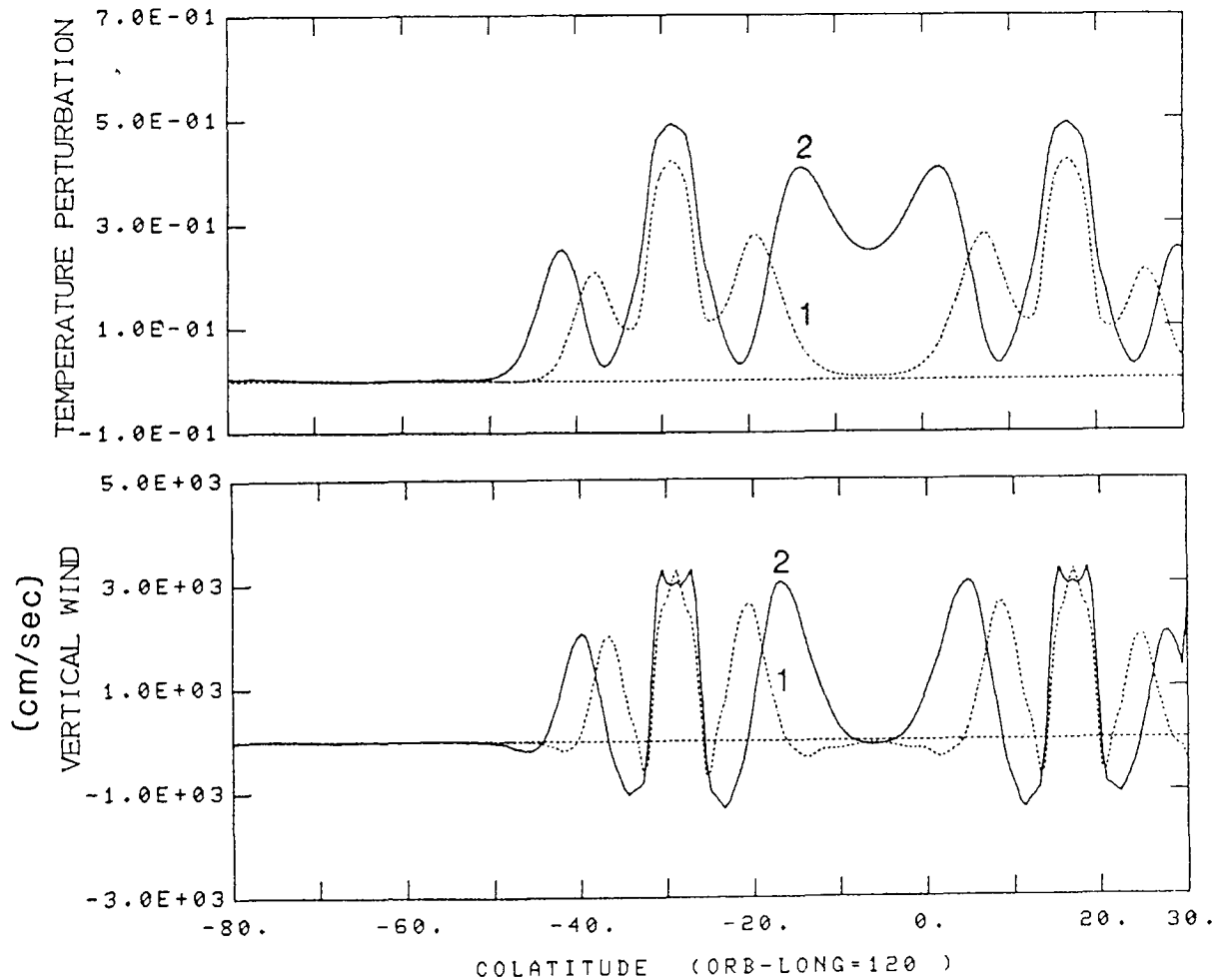
Figure 9. Along a satellite pass one would observe only a snapshot of this disturbance. Shown here are latitudinal cross sections of the computed vertical velocity and relative temperature perturbation about half an hour (24 minutes (1) and 36 minutes (2)) after the source is turned on. In this time interval, the numerical results can simulate the observations from DE-2 that are shown in Figure 6. The height integrated (localized) energy source required to produce this perturbation is 160 erg/cm²/sec and is very large when compared with the EUV input. During magnetically disturbed conditions, however, such heating rates can be supplied through joule heating (M. Sugiura, this workshop).

EQUATORIAL THERMOSPHERIC MEASUREMENTS OF TEMPERATURES AND WINDS AT AREQUIPA, PERU

John W. Meriwether, Jr.
Space Physics Research Laboratory
University of Michigan
Ann Arbor, MI 48103

Manfred A. Biondi
Department of Physics
University of Pittsburgh
Pittsburgh, PA

Arequipa FPI observatory: Facts

Field-widened 10 cm FPI Automatic operations. Located at Arequipa, Peru (16.5 S, 71.5 W) (at the NASA lidar satellite tracking station) 4.5 degrees south of magnetic equator FPI observed winds overhead of Jicamarca radar. Observing directions typically Z, N, S, W or N, S, E, W. Data selected from observations between new moon, April 1983, and new moon, August, 1983; 55 nights reduced. Some results from 1984 but not all reduced. Error bars typically 15-20 m/s for winds, 50 to 75 degrees for temperature.

Equatorial kinetic temperature: Results

Enhancement of FPI temperatures above quiet levels a few hours after the start of magnetic activity. Magnitude of this enhancement about 300 degrees. This is followed by relaxation to pre-storm levels. Apparent average offset of RPI temperatures from MSIS by 100-200 degrees for relatively quiet times. Definite suggestion of a midnight thermal enhancement for April and August data. Magnitude about 100 degrees. Seen in both 1983 and 1984 observations.

Conclusions

6300A surface brightnesses: Results

Definite enhancement of 6300A surface brightness in the south as compared with other directions. Probably connected to the tropical airglow arcs. Meridional winds small (<25 m/s) throughout night. Indication of northward migration of the observed 6300A enhancement in the evening hours as observations approach local winter solstice. This is probably related to the observed poleward (to the south) meridional wind (of magnitude 50 m/s) in this period.

Equatorial thermospheric winds: Results

Zonal component of winds always eastward, but speed approaches zero sooner near equinox than at summer solstice. Typical magnitude at peak is of order 100 to 150 m/s. Suggesstion of zonal wind increase after twilight and recovery of 6300A emission for April data. Origin not clear

but may be related to midnight thermal enhancement. Meridional wind virtually zero for equinox in 1983; shows evening flow towards winter hemisphere in early evening for solstice data. Suggestion of post-midnight surge in April 1984 data. No major effects associated with mag. storm activity. Suggestion of decrease in zonal component below nominal levels.
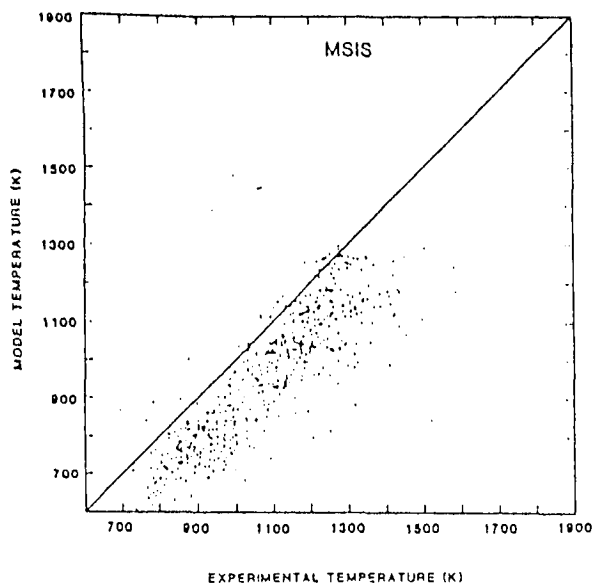
Fig. 3. Comparison of the experimental temperatures with the MSIS empirical model [*Hedin et al.*, 1977].
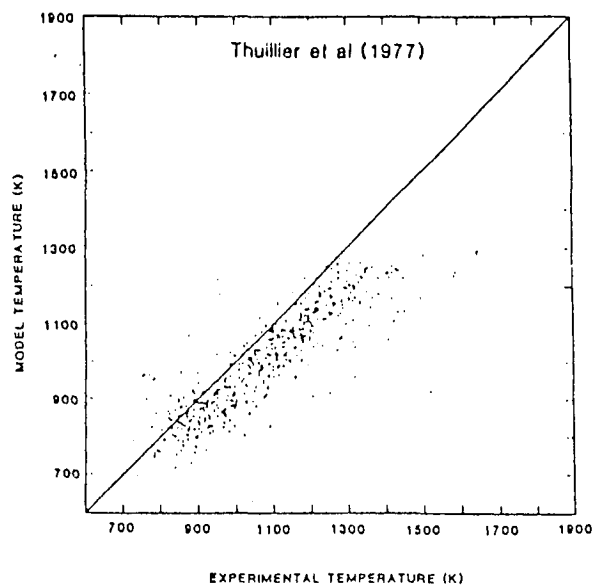
Fig. 4. Comparison of the experimental temperature with the empirical model of *Thuillier et al.* [1977a, b].
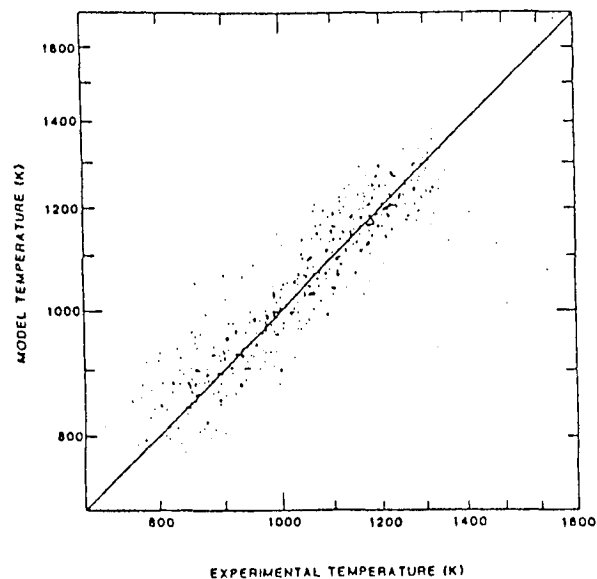
Fig. 11. Fit of the experimental data to four parameters: solar radio flux, geomagnetic activity, annual variation of the solar declination and a semi-annual variation. The correlation coefficient is 0.91.
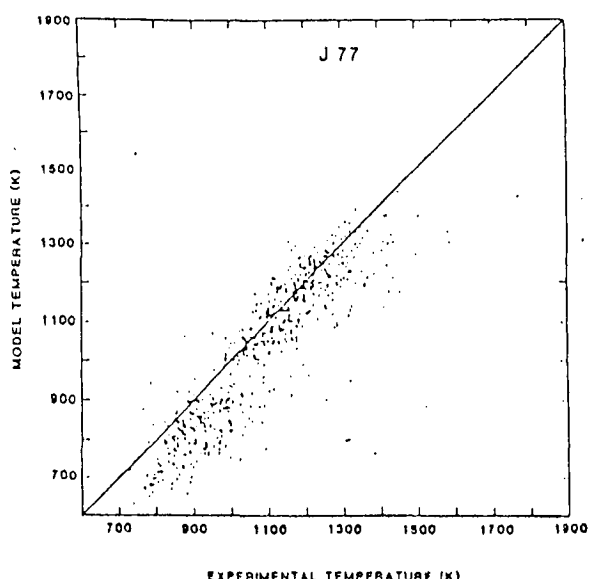
Fig. 5. Comparison of the experimental temperatures with the empirical model of *Jacchia* [1977].

235

237

15/16 APRIL 1983   5/6 JUNE 1983   23/24 JUNE 1983   30/31 JULY 1983

NORTH

WEST

SOUTH

INTENSITY

LOCAL TIME

239

16/17 APRIL 1984   19/20 APRIL 1984

MERIDIONAL WINDS (m/s)

INTENSITY   TEMPERATURE (°K)

LOCAL TIME

244

16/17 APRIL 1984   19/20 APRIL 1984

ZONAL WINDS (m/s)

3/4 JUNE 1983   4/5 JUNE 1983   6/7 JUNE 1983
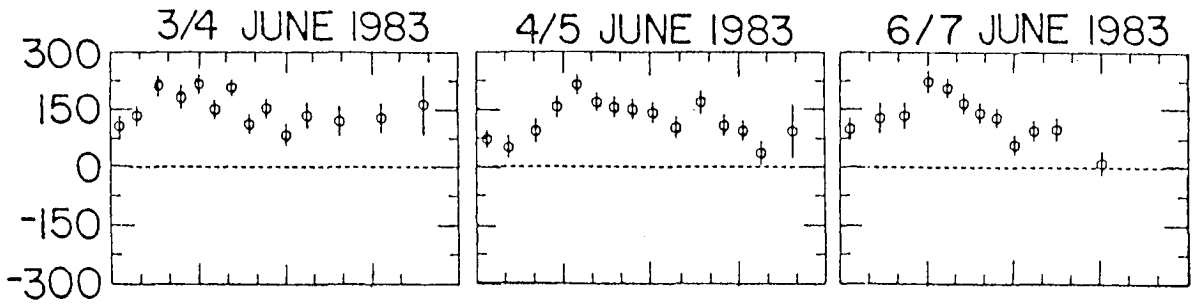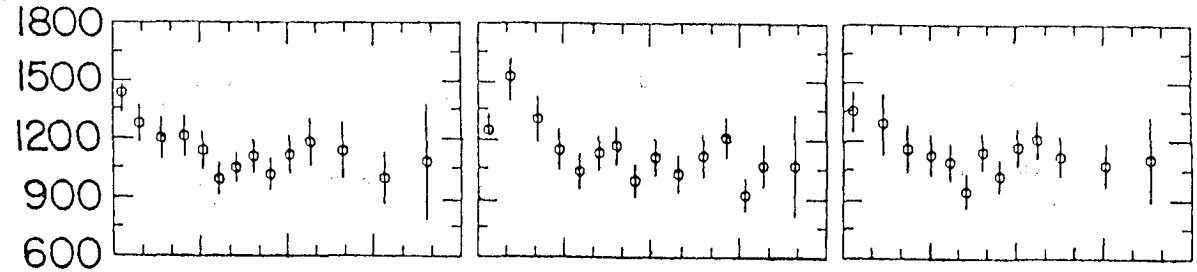
TEMPERATURE (°K)

INTENSITY
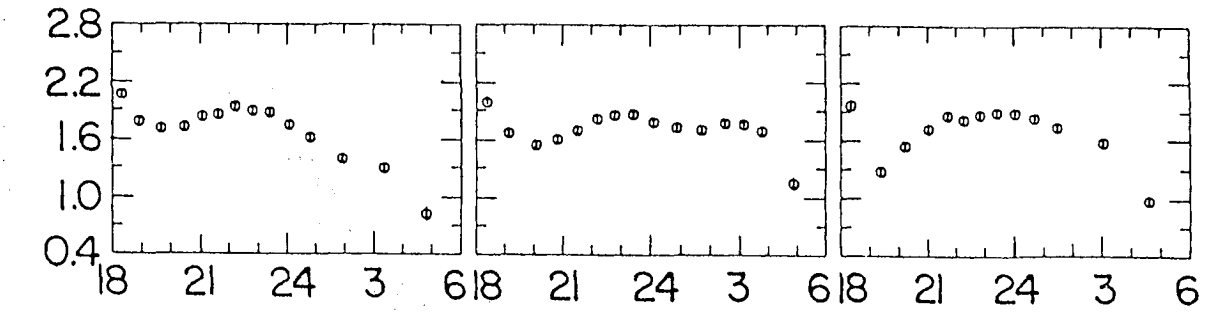
LOCAL TIME
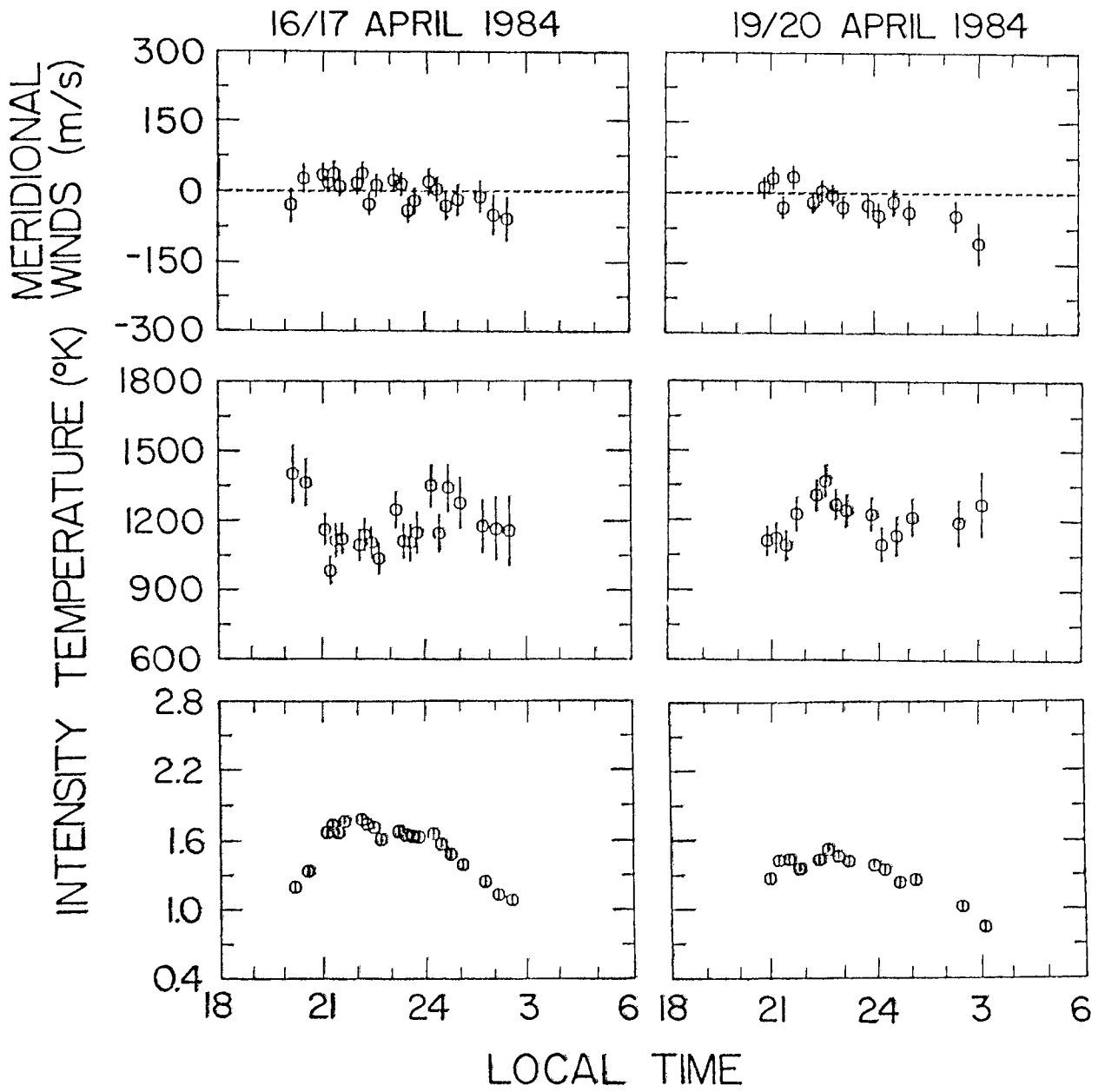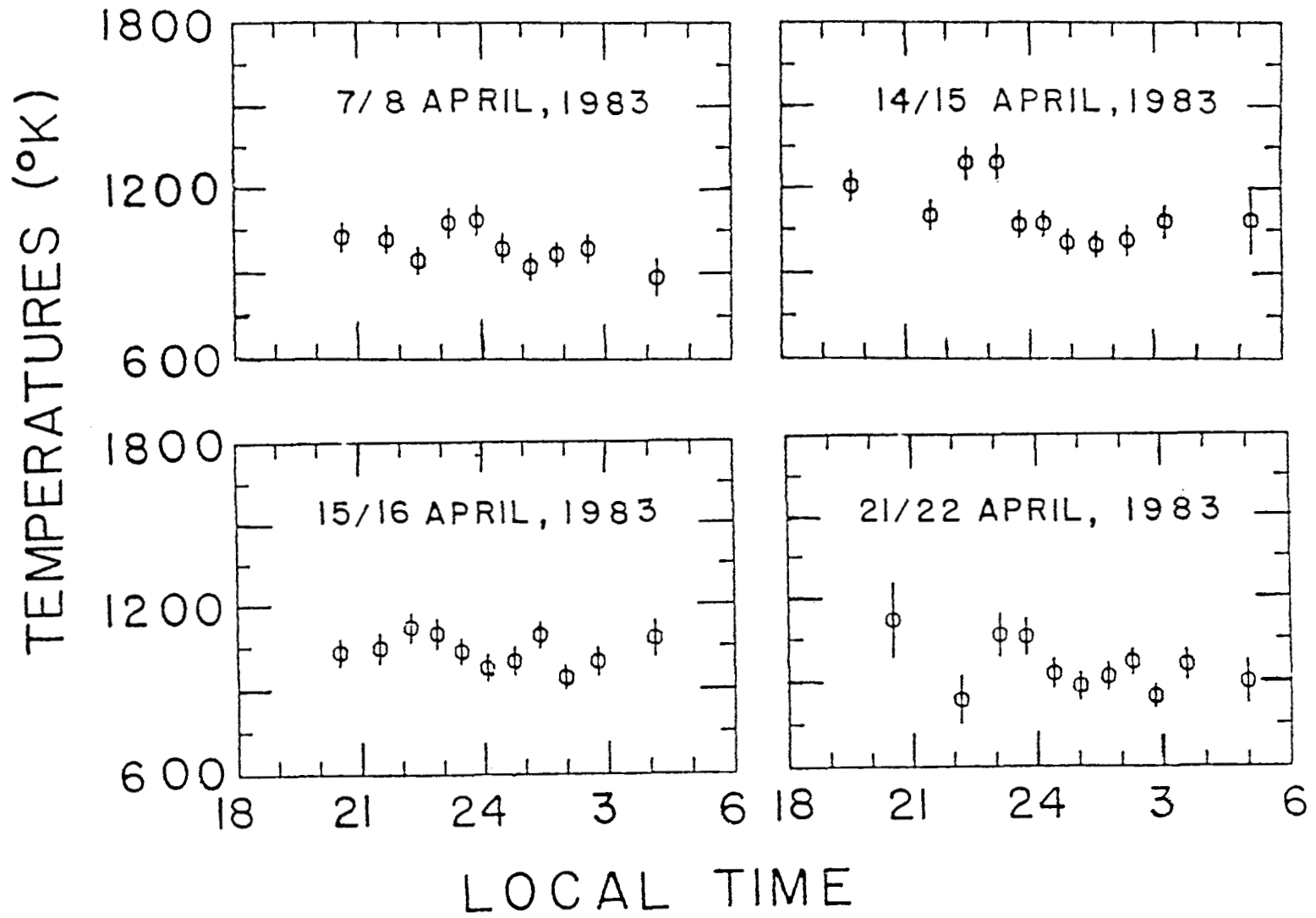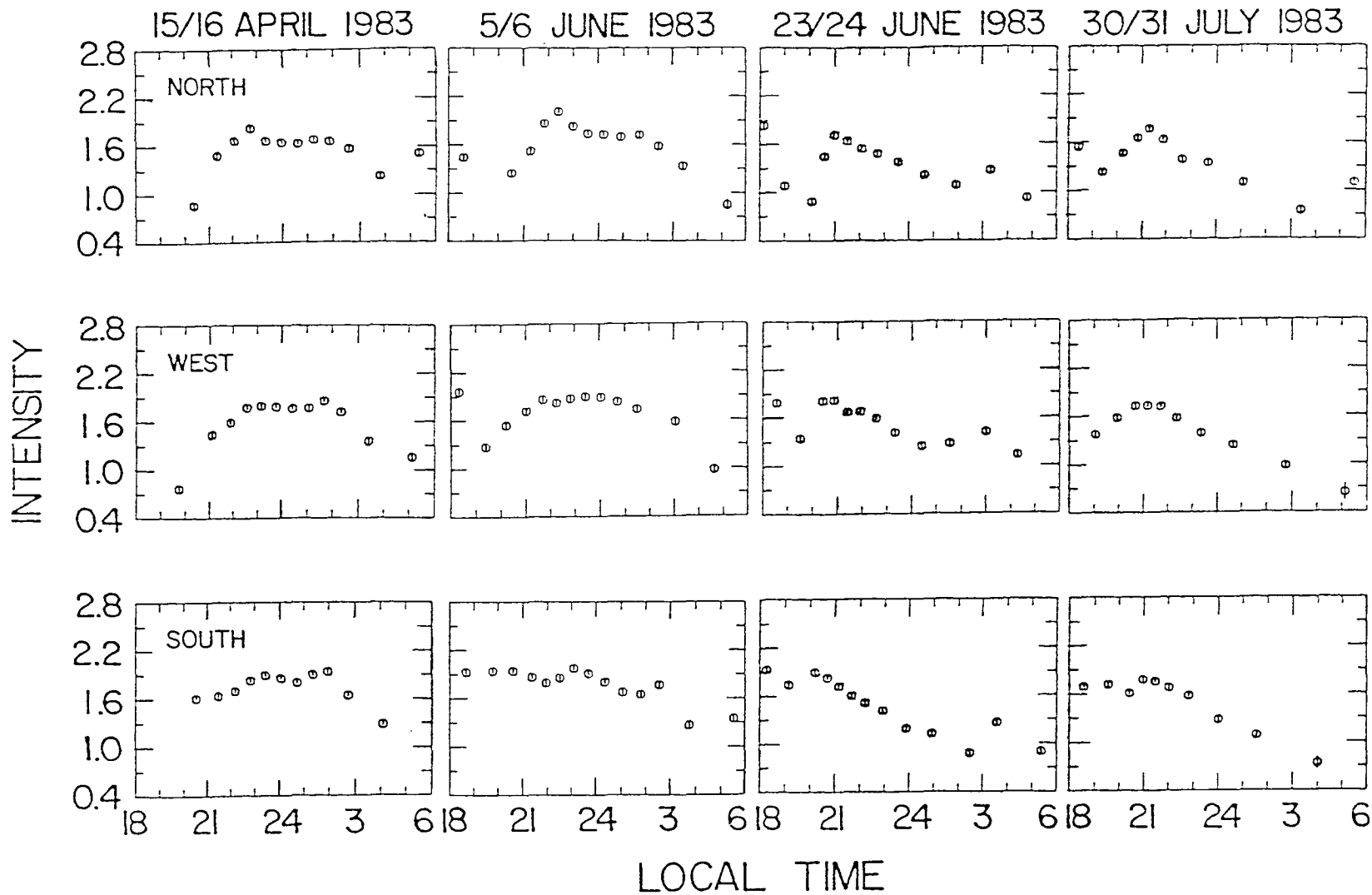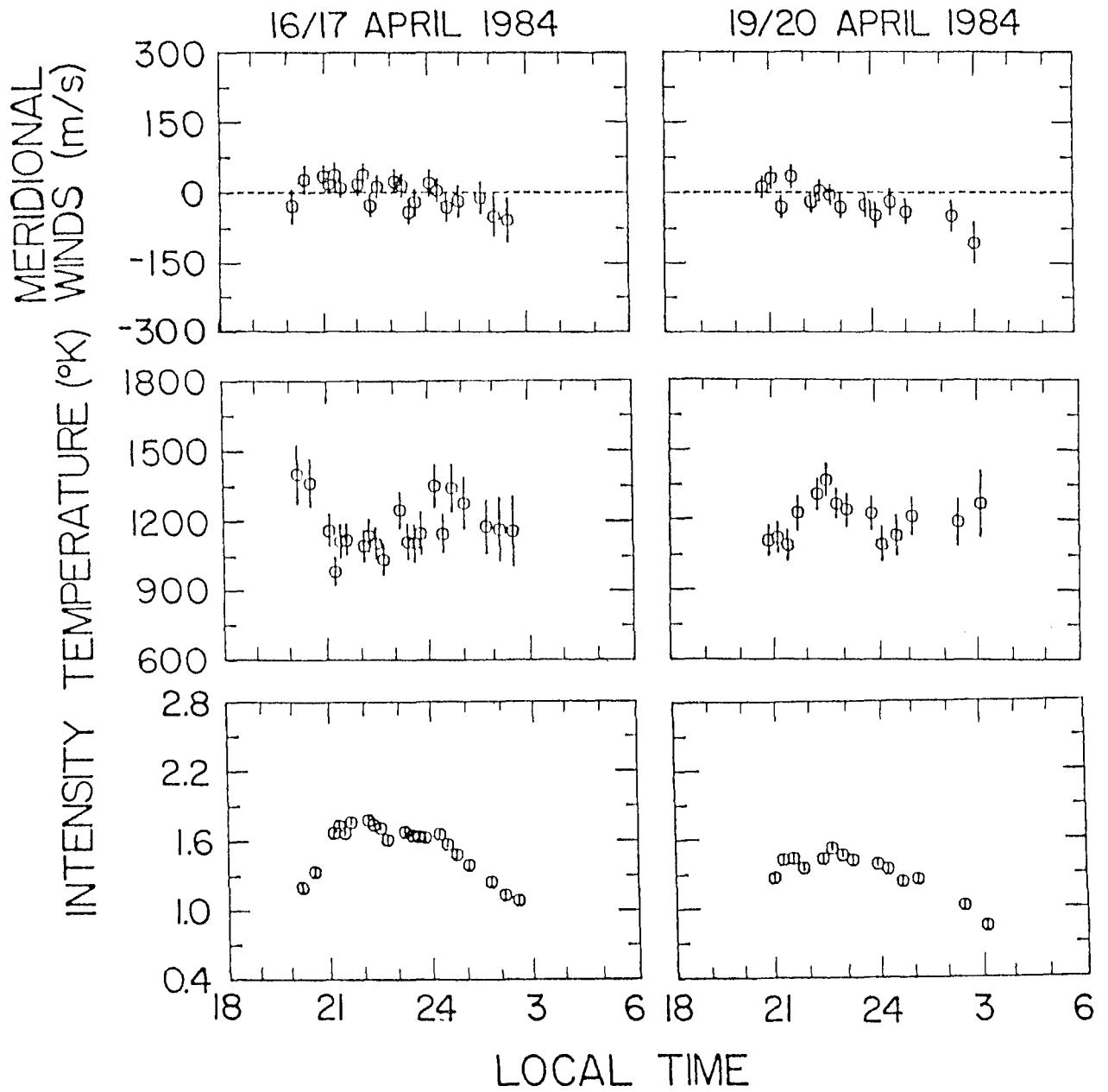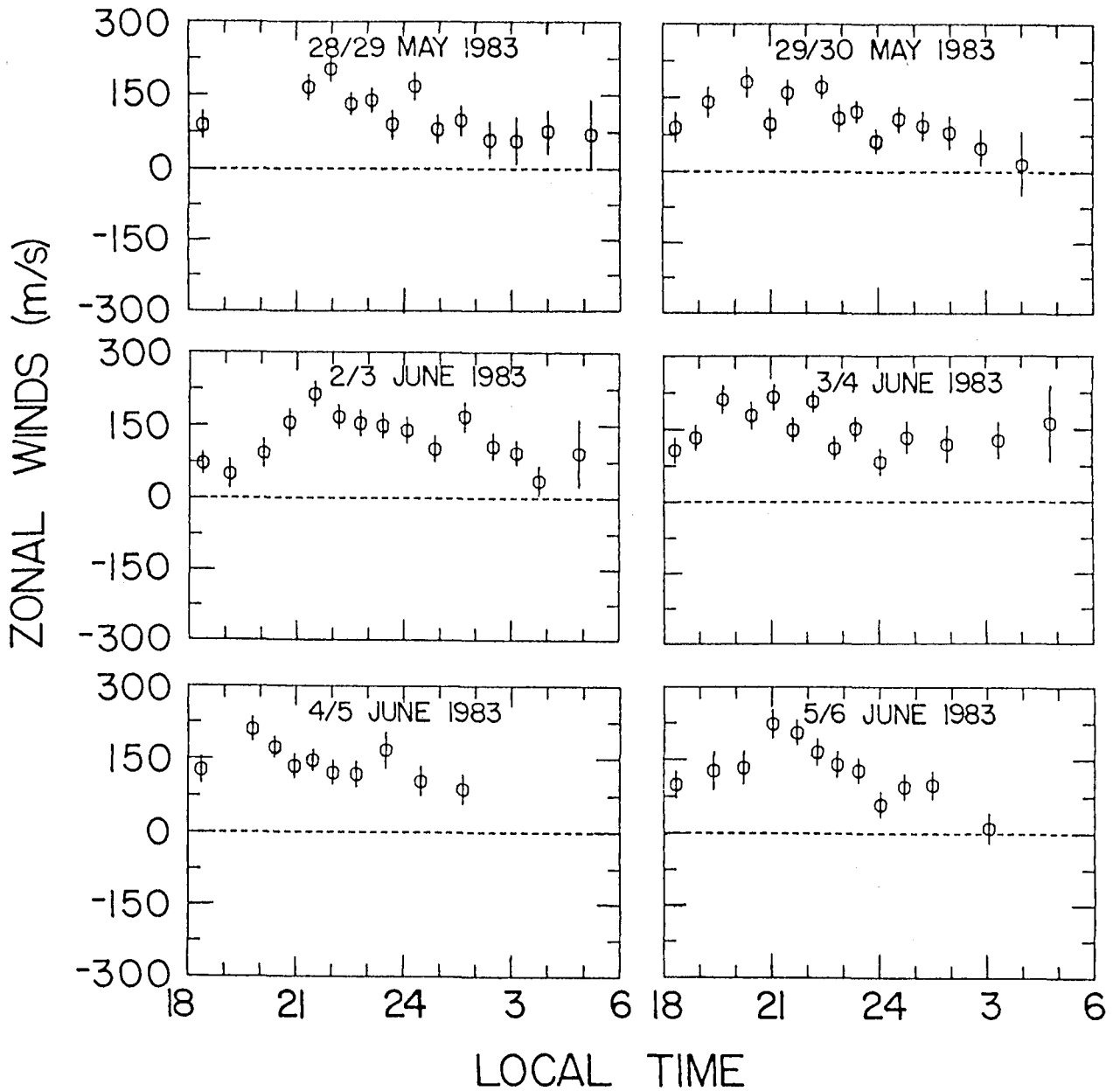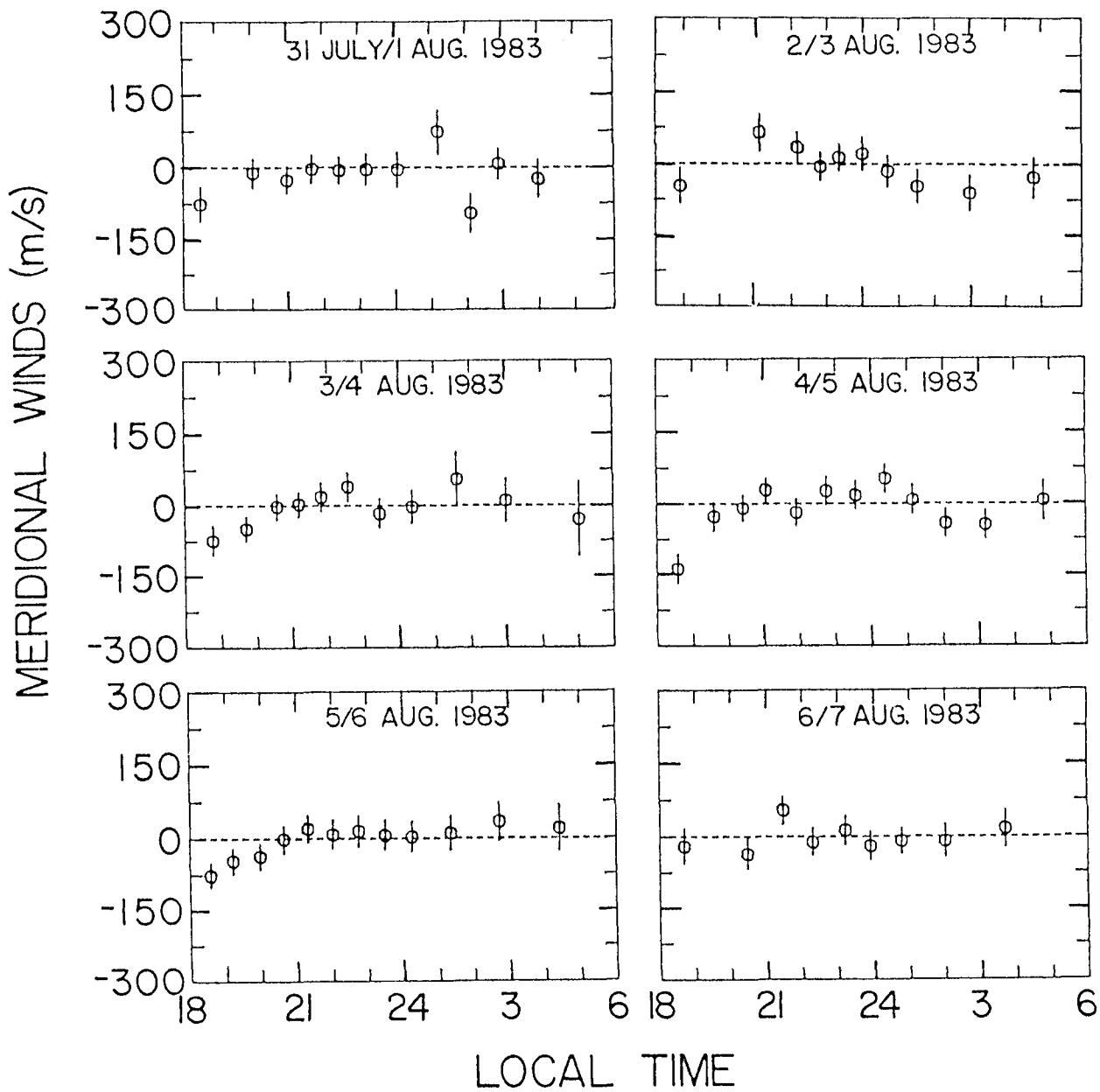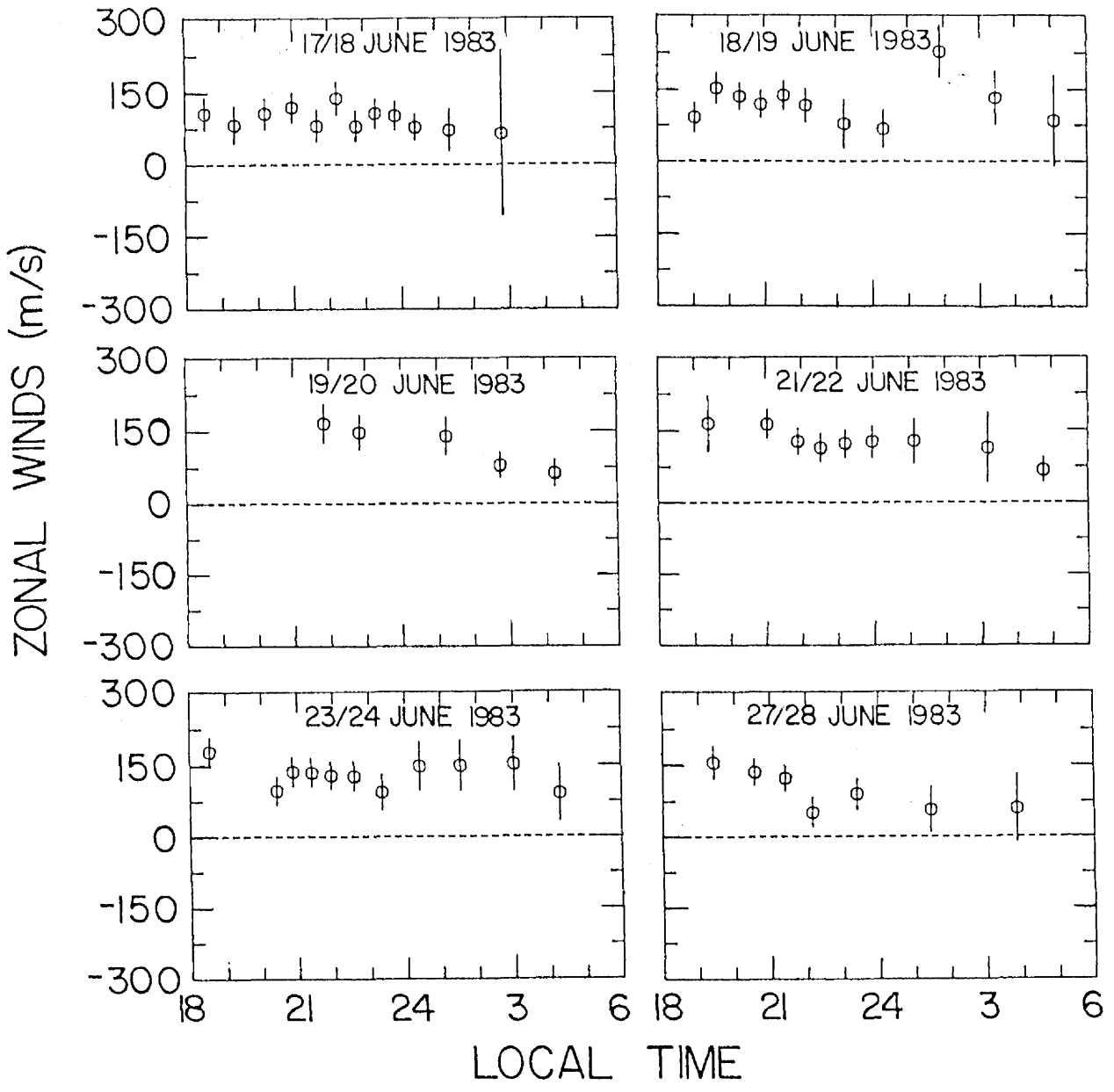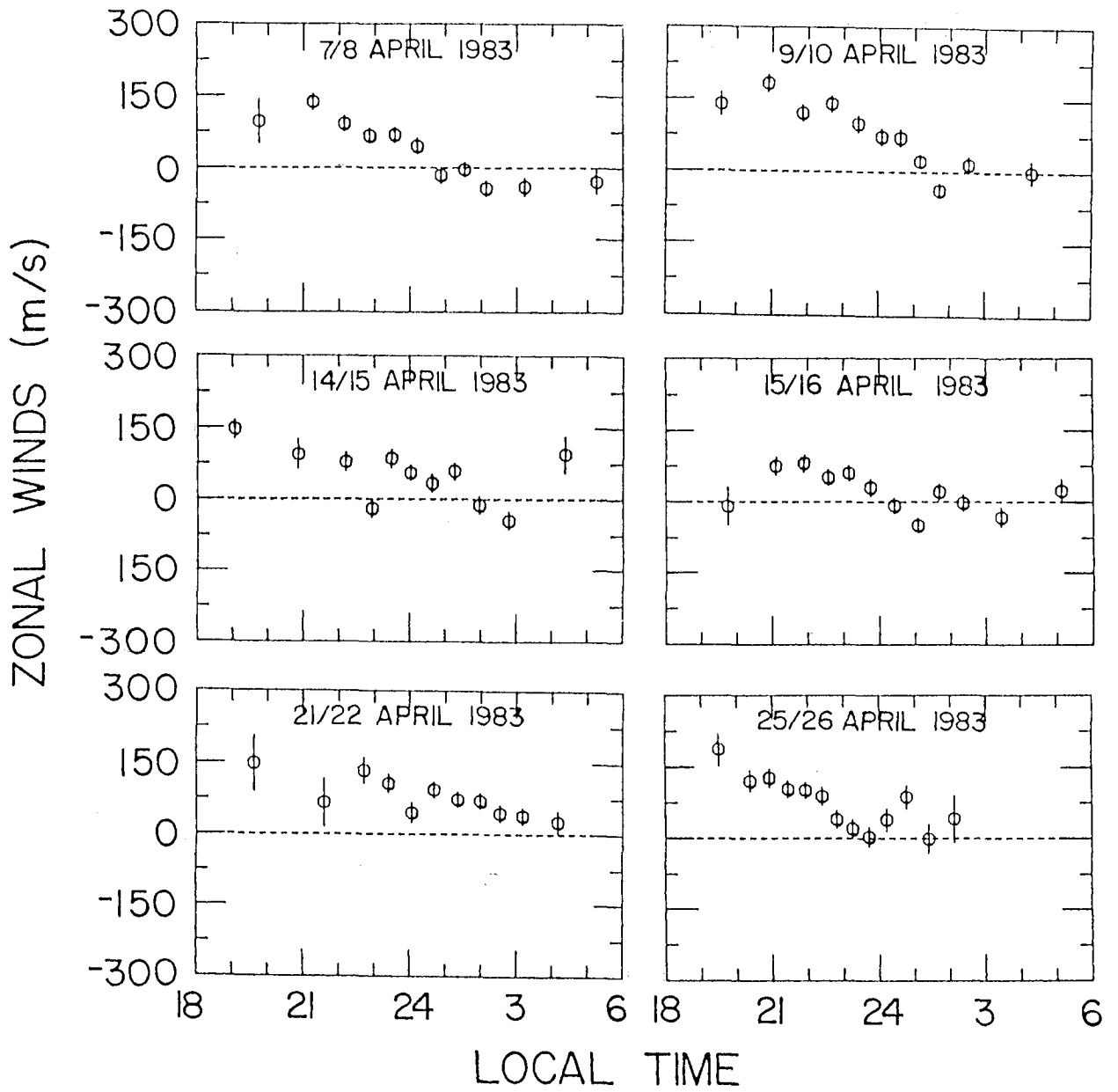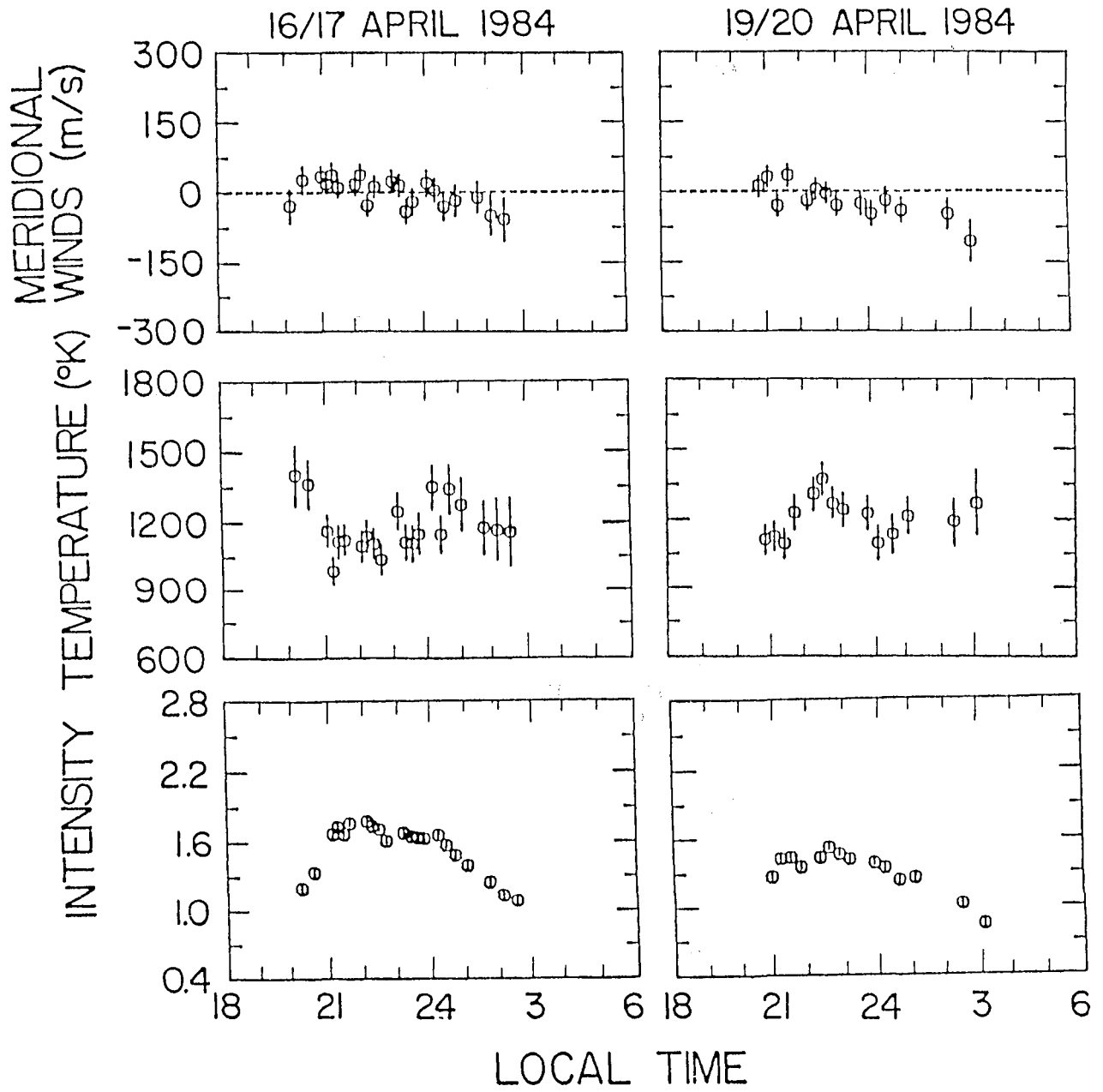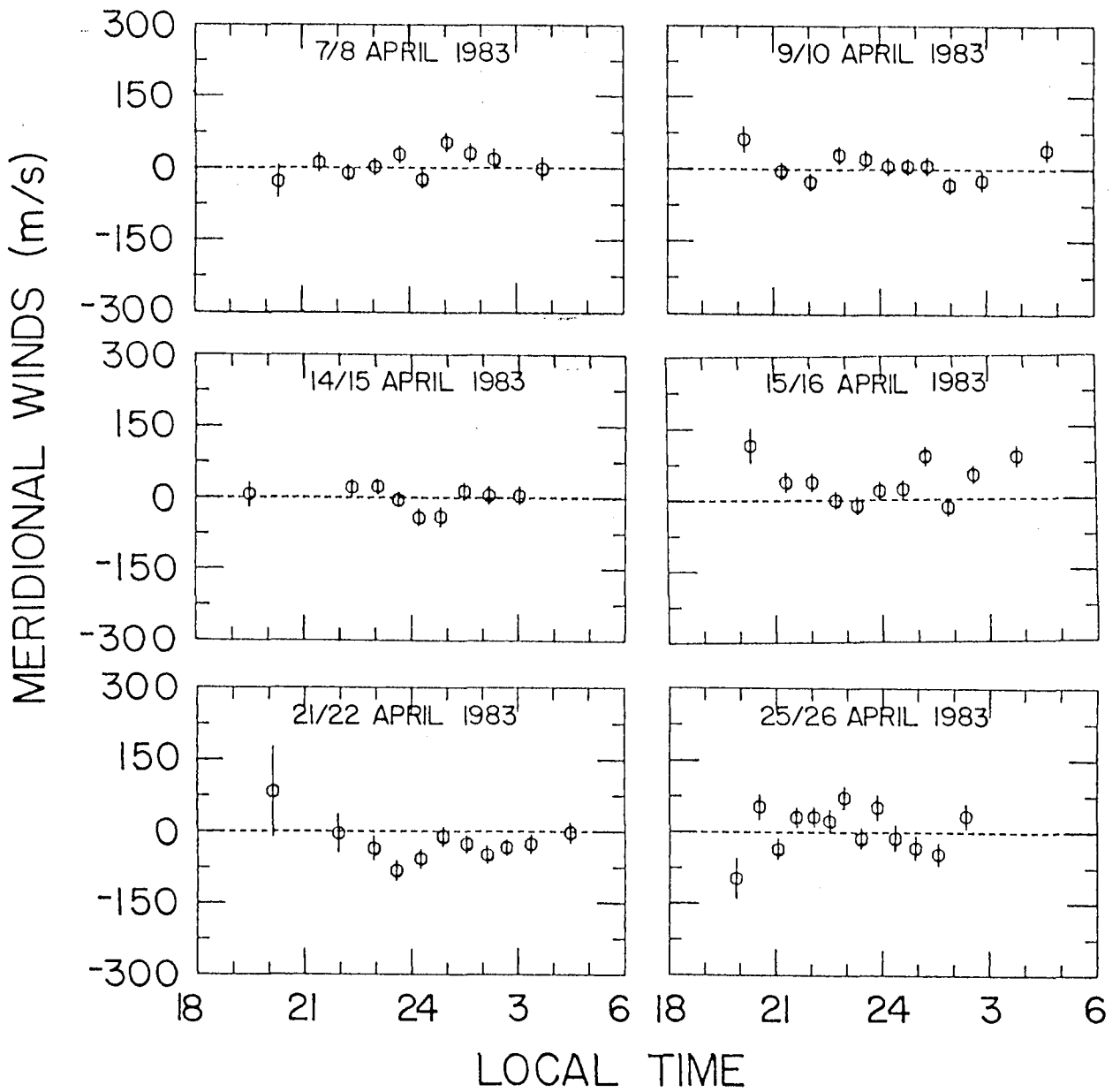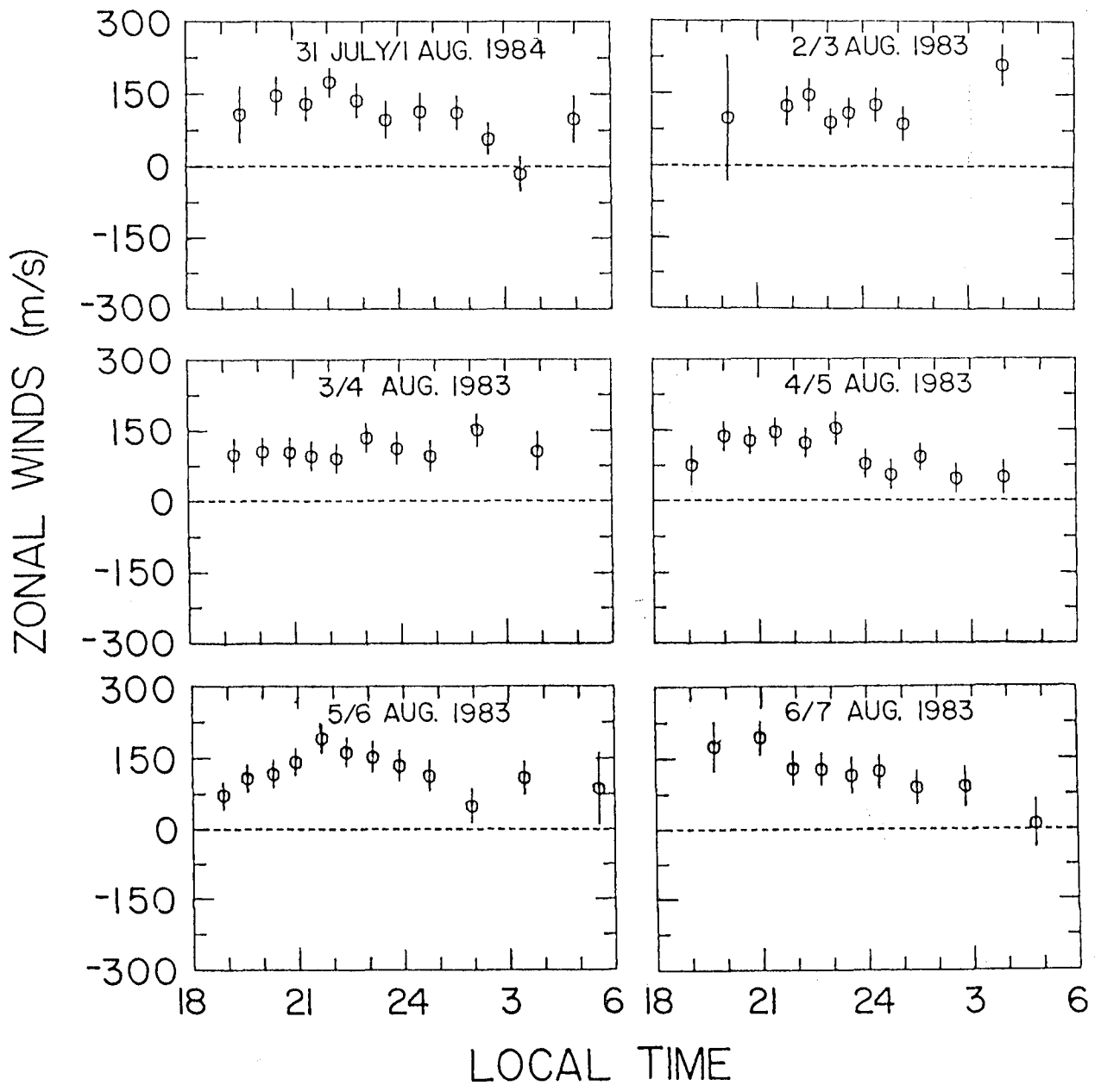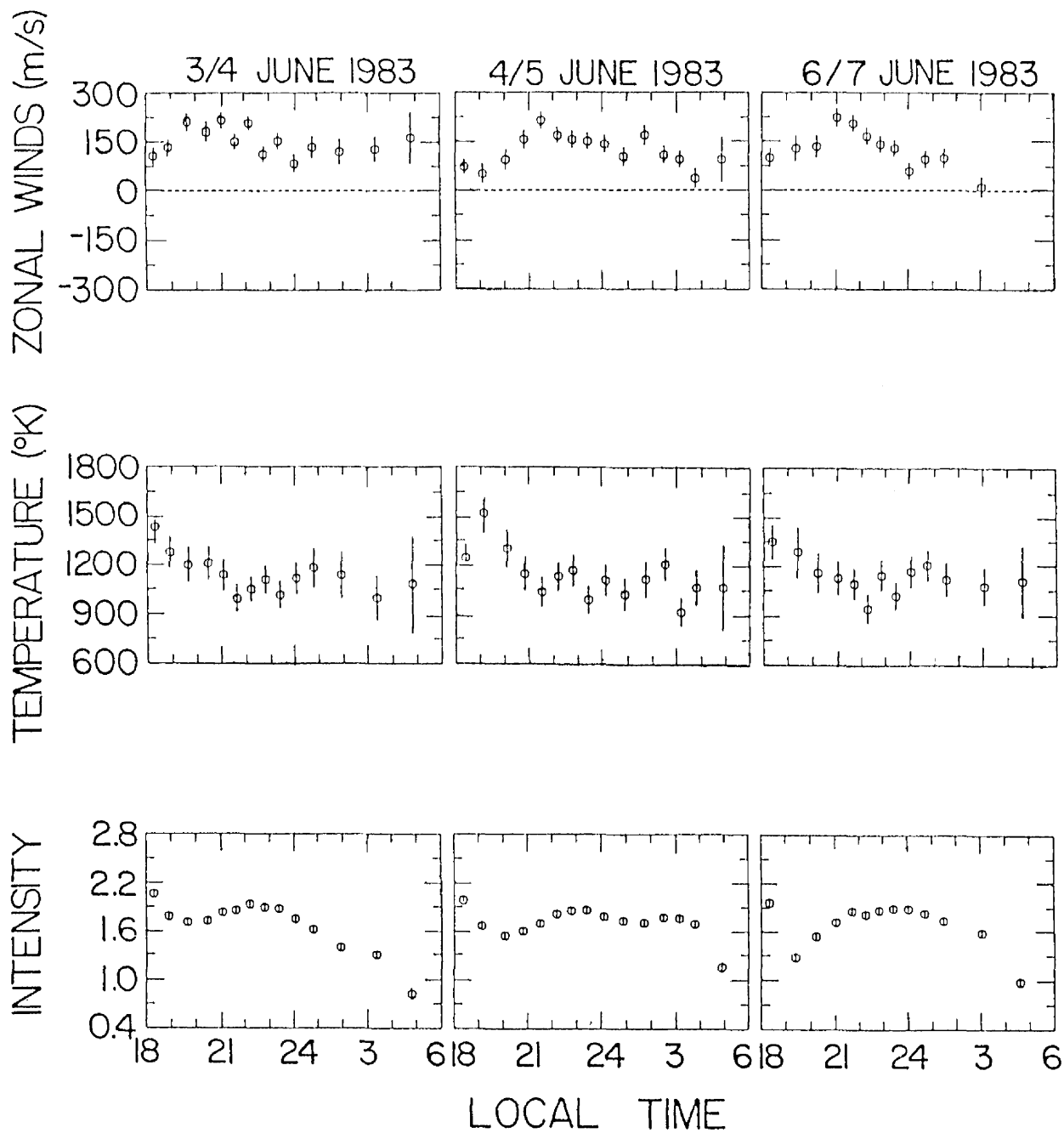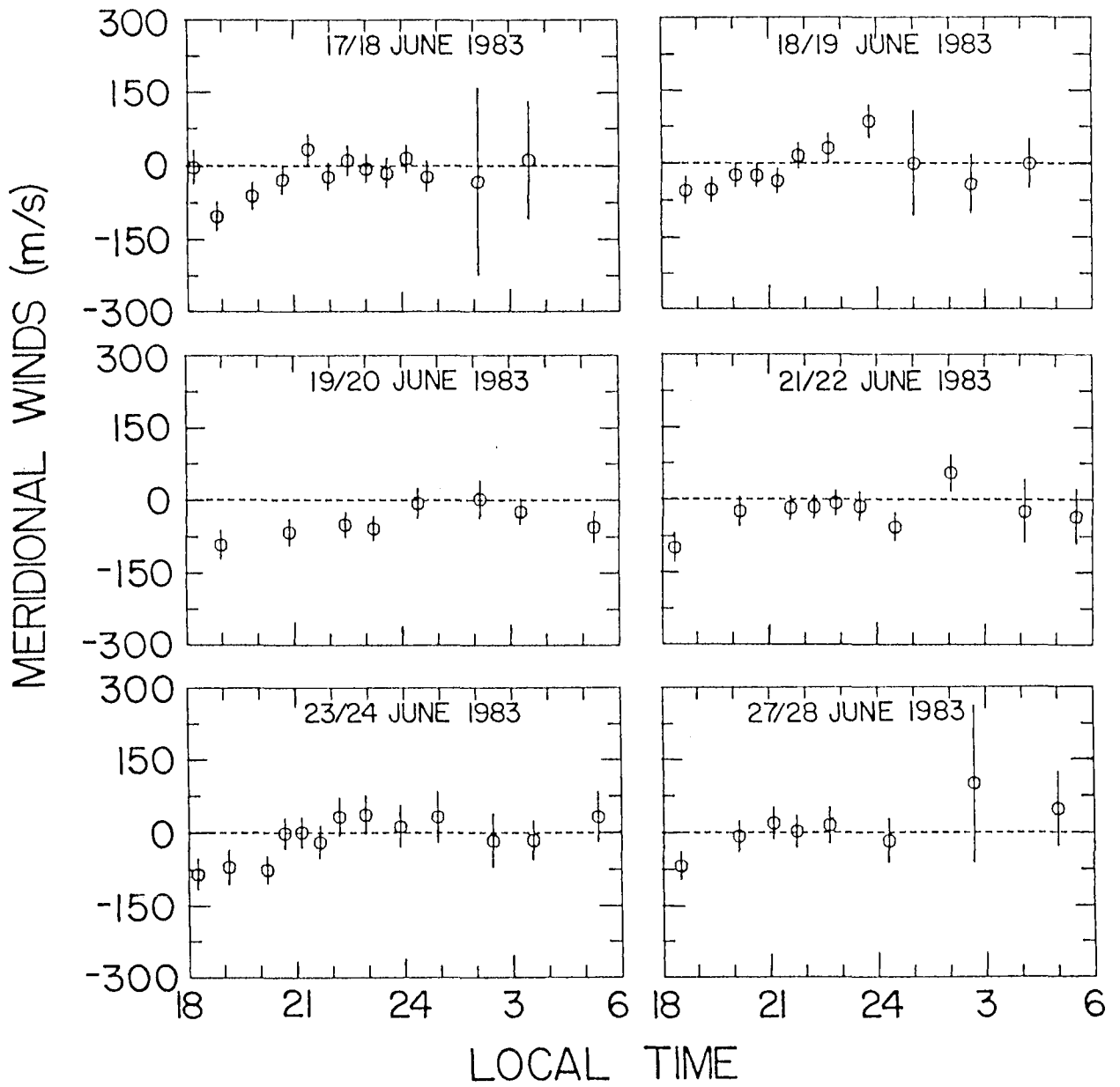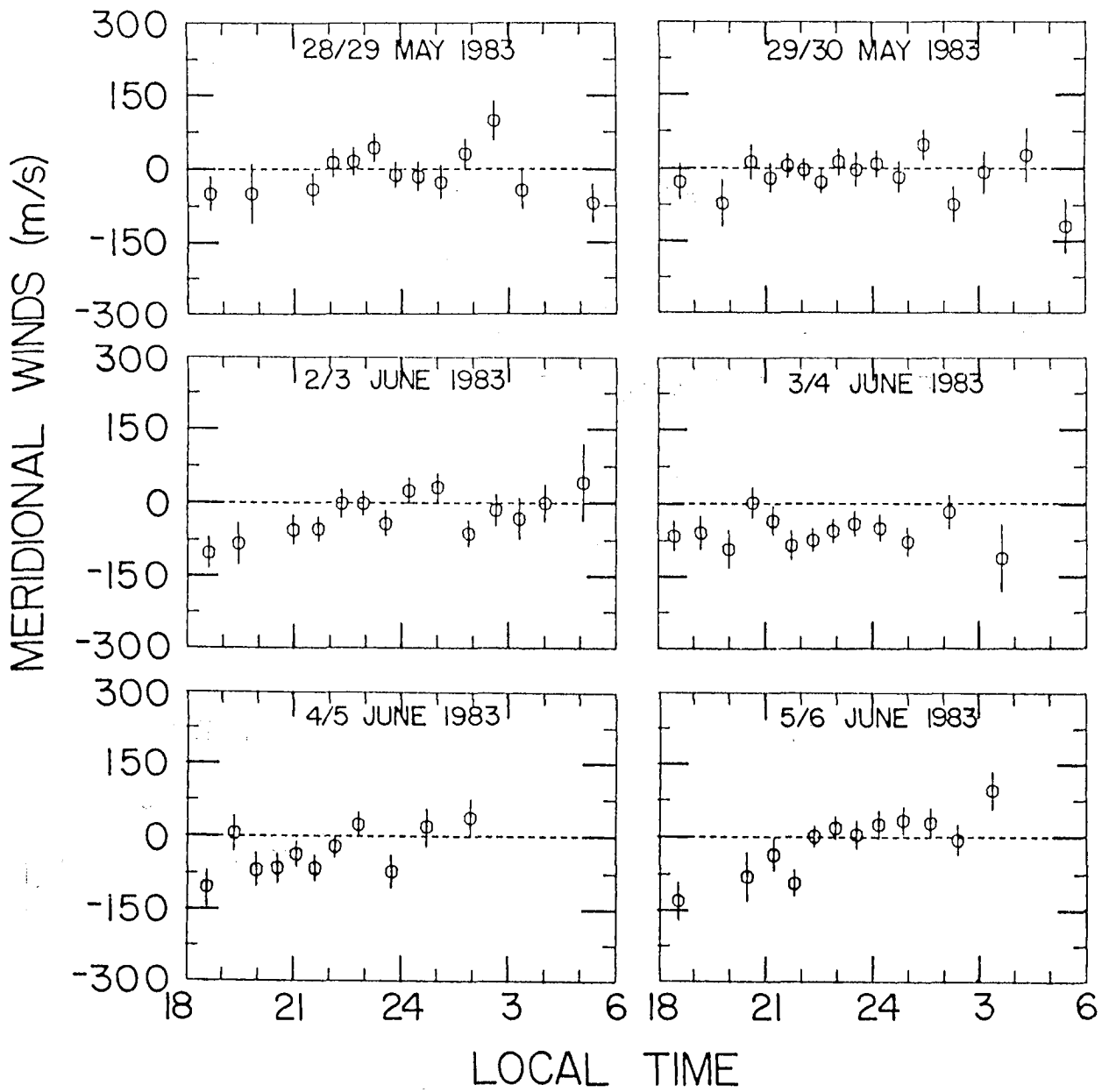
Horizontal wind, temperature, and intensity observations
DAY 271, 1984
Arequipa, Peru
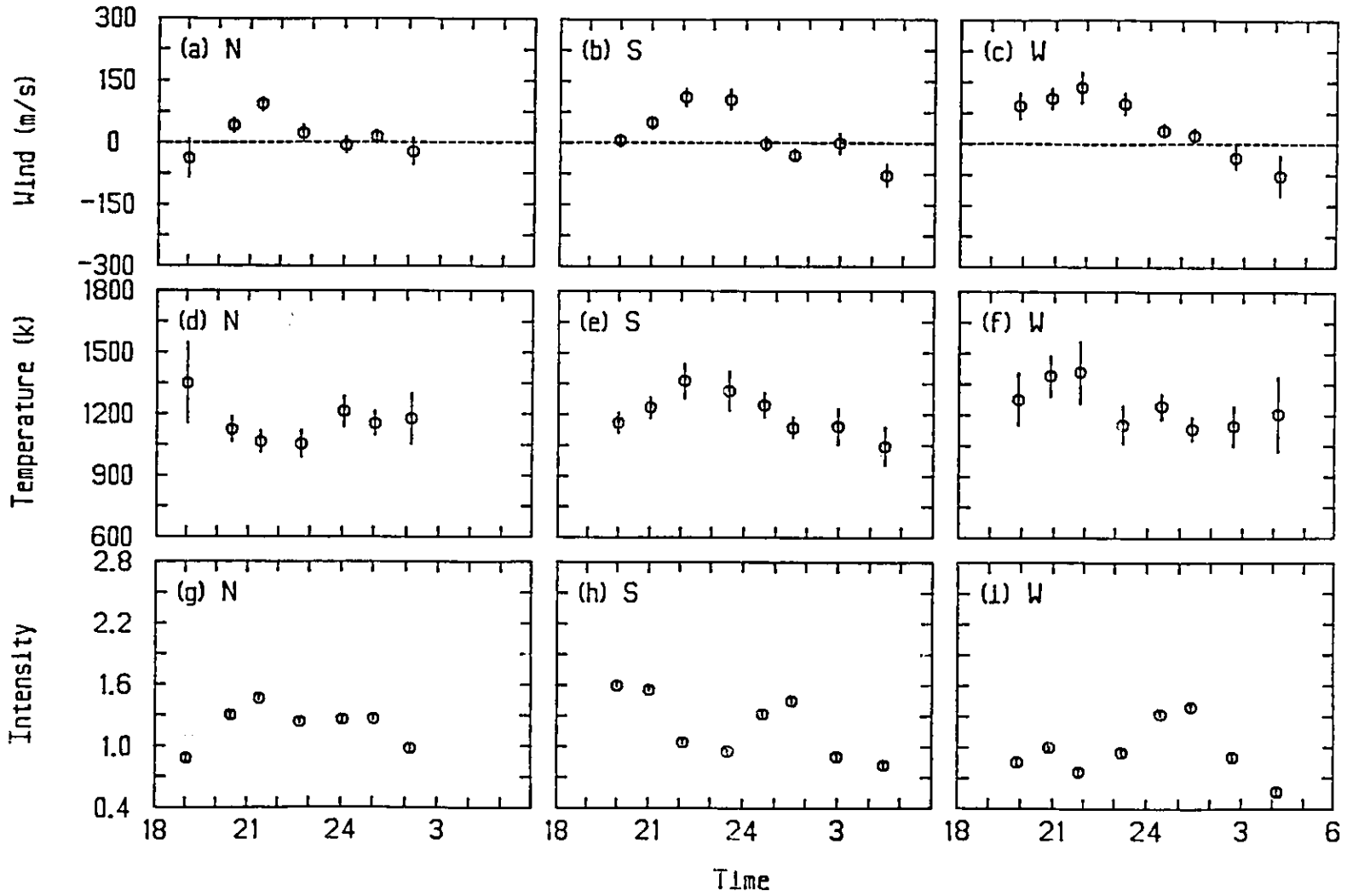
POLAR CAP OBSERVATIONS OF THERMOSPHERIC WINDS AND TEMPERATURES AT SONDRE STROMFJORD, GREENLAND

John W. Meriwether, Jr. and P. Shih
Space Physics Research Laboratory
University of Michigan
Ann Arbor, MI 48105

Conclusions

Temperatures:

Agreement of averaged temperatures with MSIS looked reasonable for several nights, but for many nights there are differences: 1) midnight period of cooling and 2) temperature increases associated with overhead crossings of the auroral belt. The observed rise of the temperature before dawn in conjunction with the high 6300A intensities suggests a connection between the two effects: soft particle precipitation most likely candidate but frictional heating perhaps also a possibility. Comparison with TGCM calculations also needed.

Thermospheric winds:

The technique for formulating neutral wind vectors performs well in most cases. The observed patterns show evidence for abatement in the midnight sector in the meridional wind component at the separatrix between the two cells with a frequency of the order of 20-25%. Also observed in radar observations at Sondre Stromfjord. The observed patterns for magnetically quiet conditions show flow characteristic of the auroral belt, westward in evening followed by the midnight surge. The observed patterns for active conditions show dominance either by the evening cell or the morning cell, but most often the former. We need to correlate our results with IMF measurements.
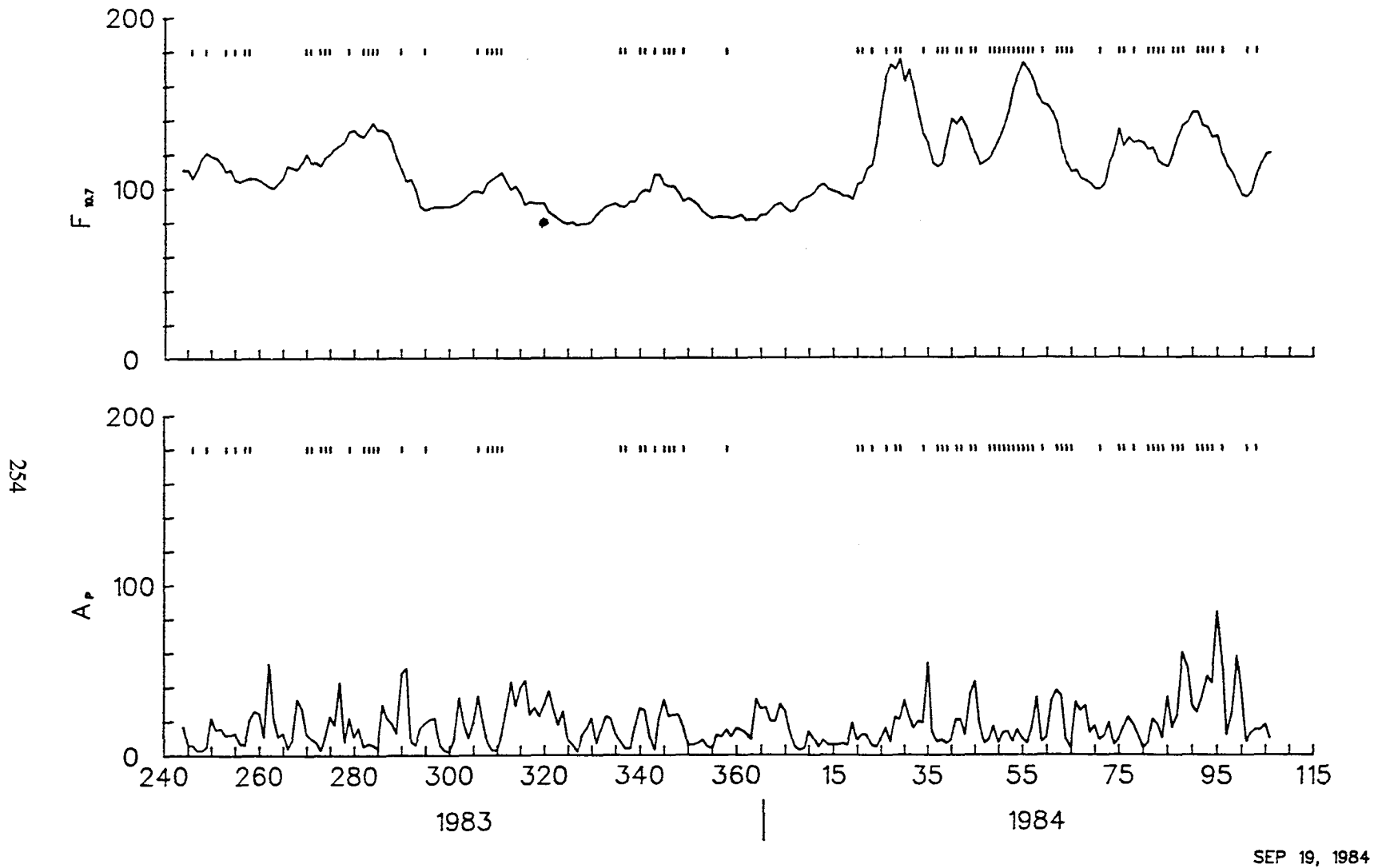
Figure 1. Solar and geomagnetic conditions of the Fabry-Perot observations conducted at Sondre Stromfjord, Greenland,September 1983 to April 1984

SEP 19, 1984

Neutral Wind Vector
October 21/22, 1983 day 295 (UT)
Sondre Stromfjord, Greenland
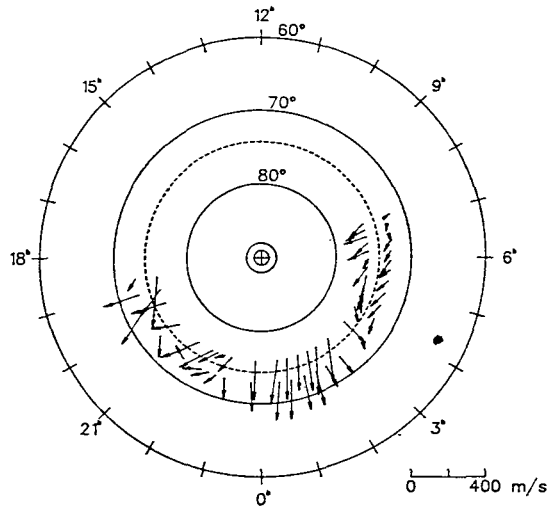
Neutral Wind Vector
December 5/6, 1983 day 340 (UT)
Sondre Stromfjord, Greenland
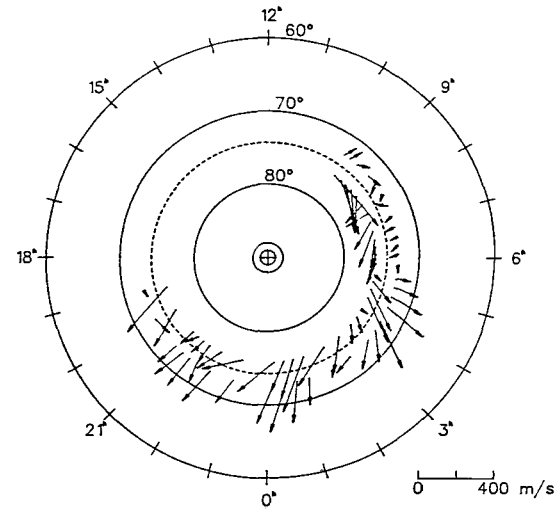
0   400 m/s

0   400 m/s

October 21/22, 1983 day 295 (UT)

December 5/6, 1983 day 340 (UT)

(a) North

(b) South

(a) North

(b) South

Meridional Wind (m/s)

Meridional Wind (m/s)

Magnetic Local Time

Magnetic Local Time
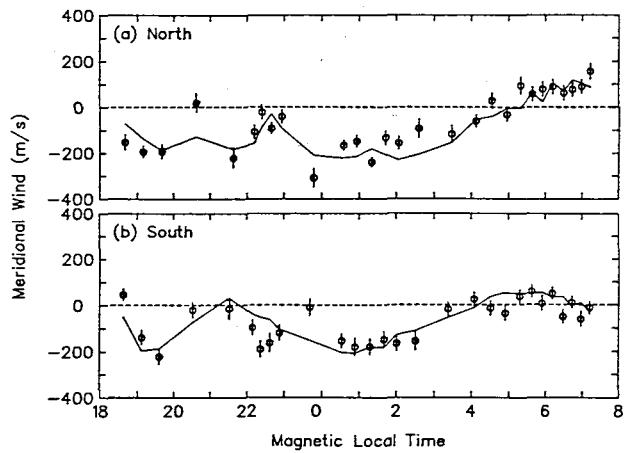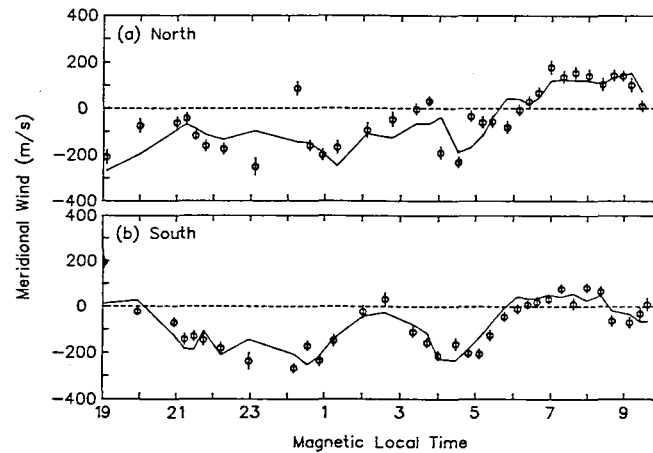
Figure 2

September 14/15, 1983 day 258 (UT)
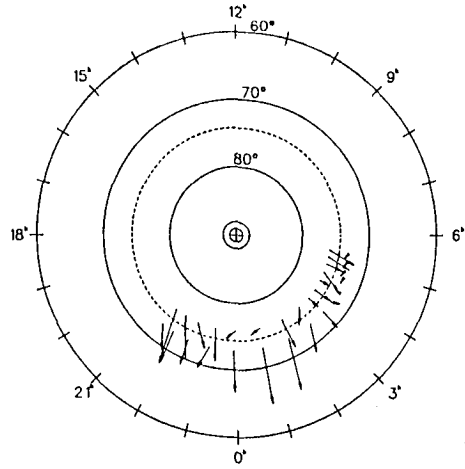
March 4/5, 1984 day 65 (UT)
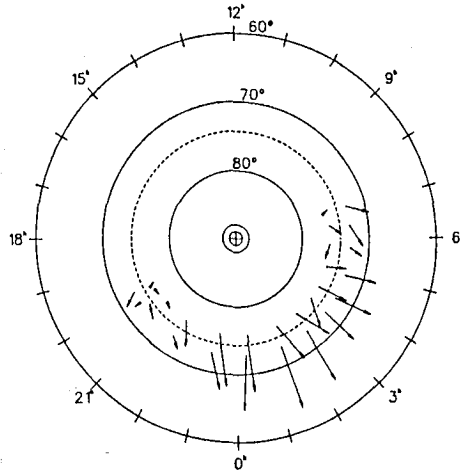
March 27/28, 1984 day 88 (UT)
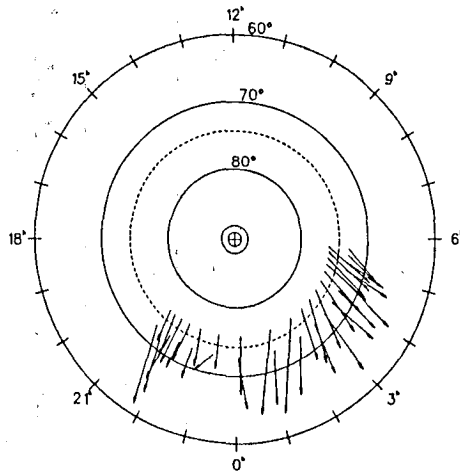
Figure 3
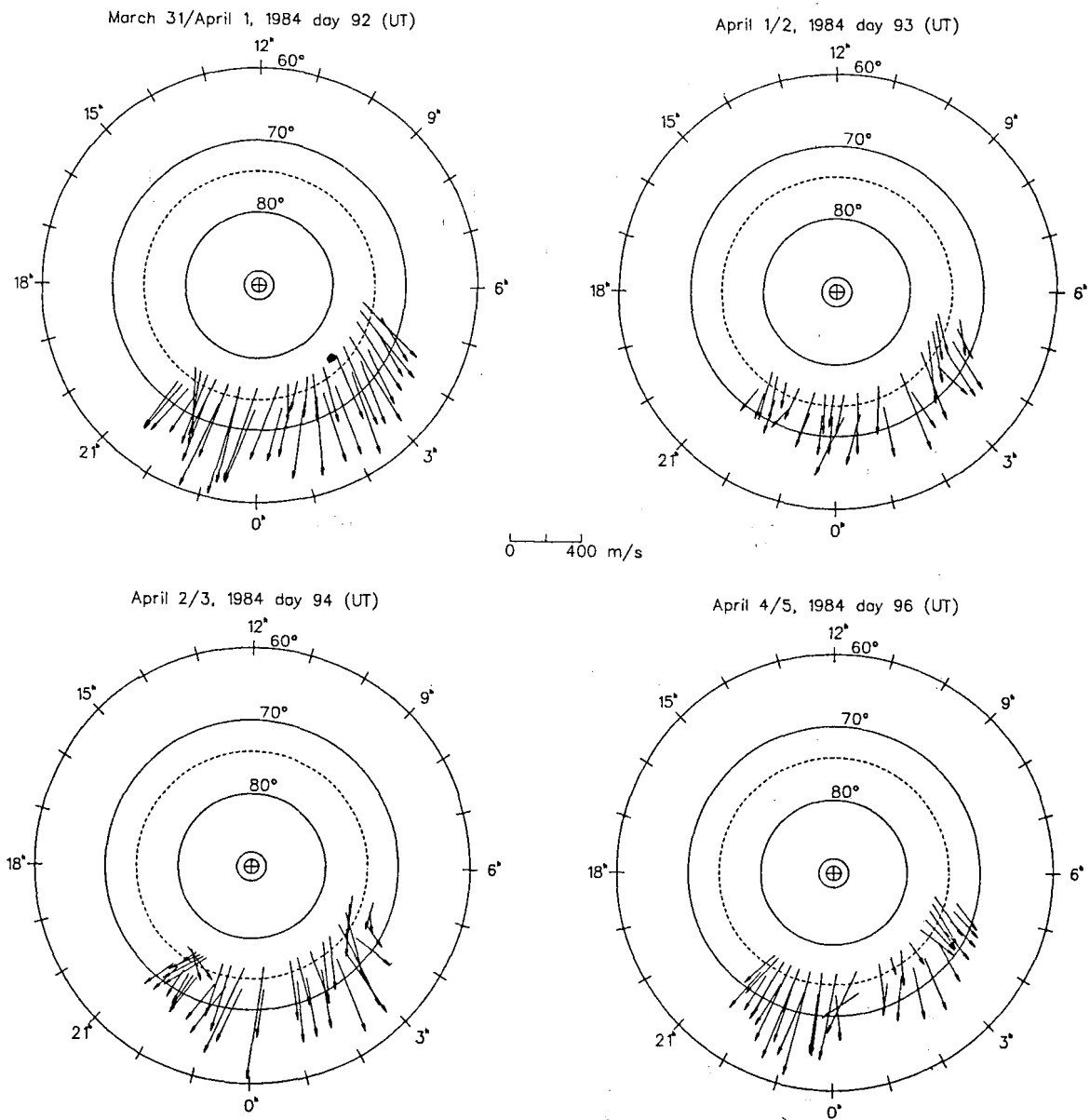
256

March 31/April 1, 1984 day 92 (UT)

April 1/2, 1984 day 93 (UT)

April 2/3, 1984 day 94 (UT)

April 4/5, 1984 day 96 (UT)

Figure 4

257

Figure 5

Figure 6

259
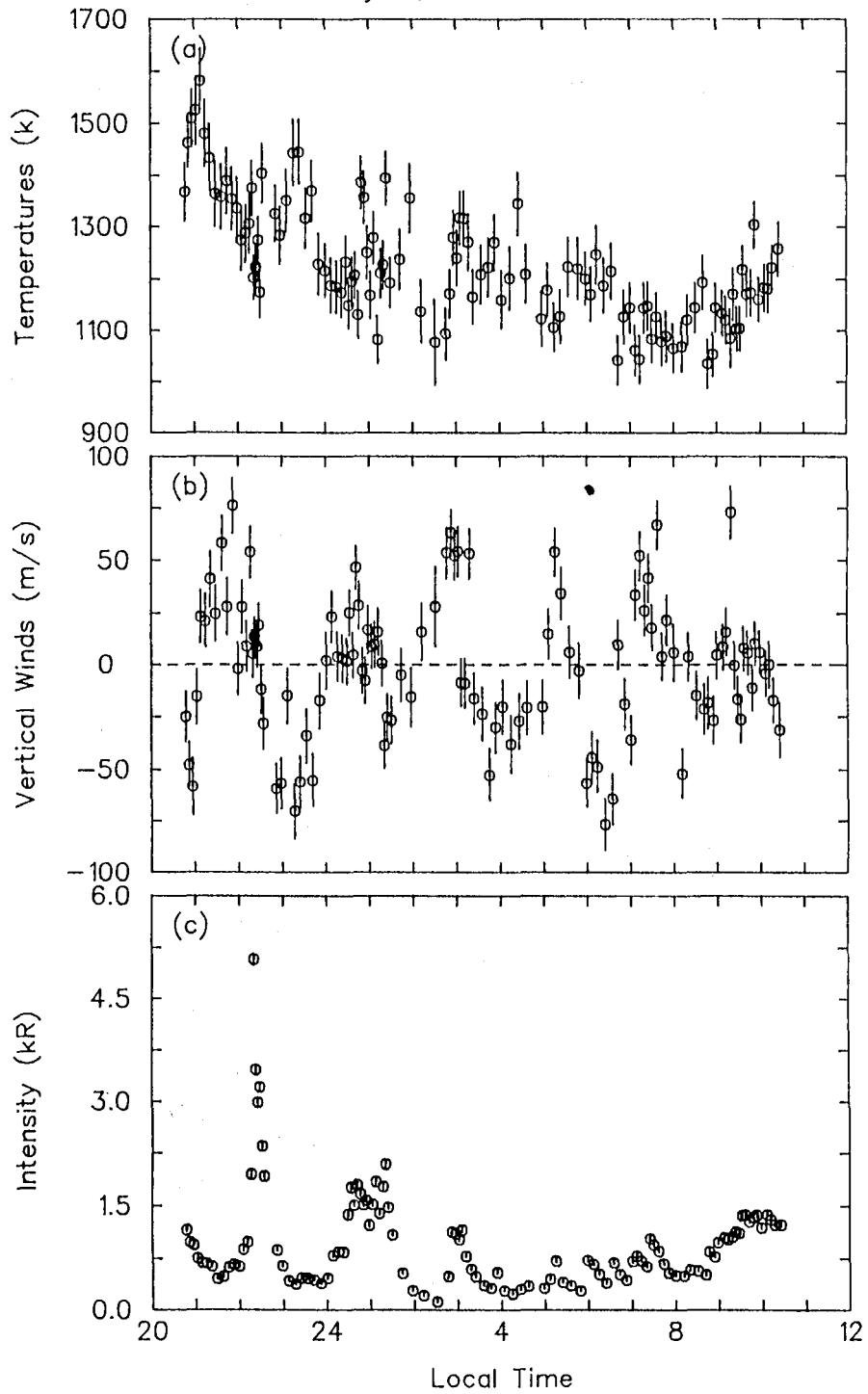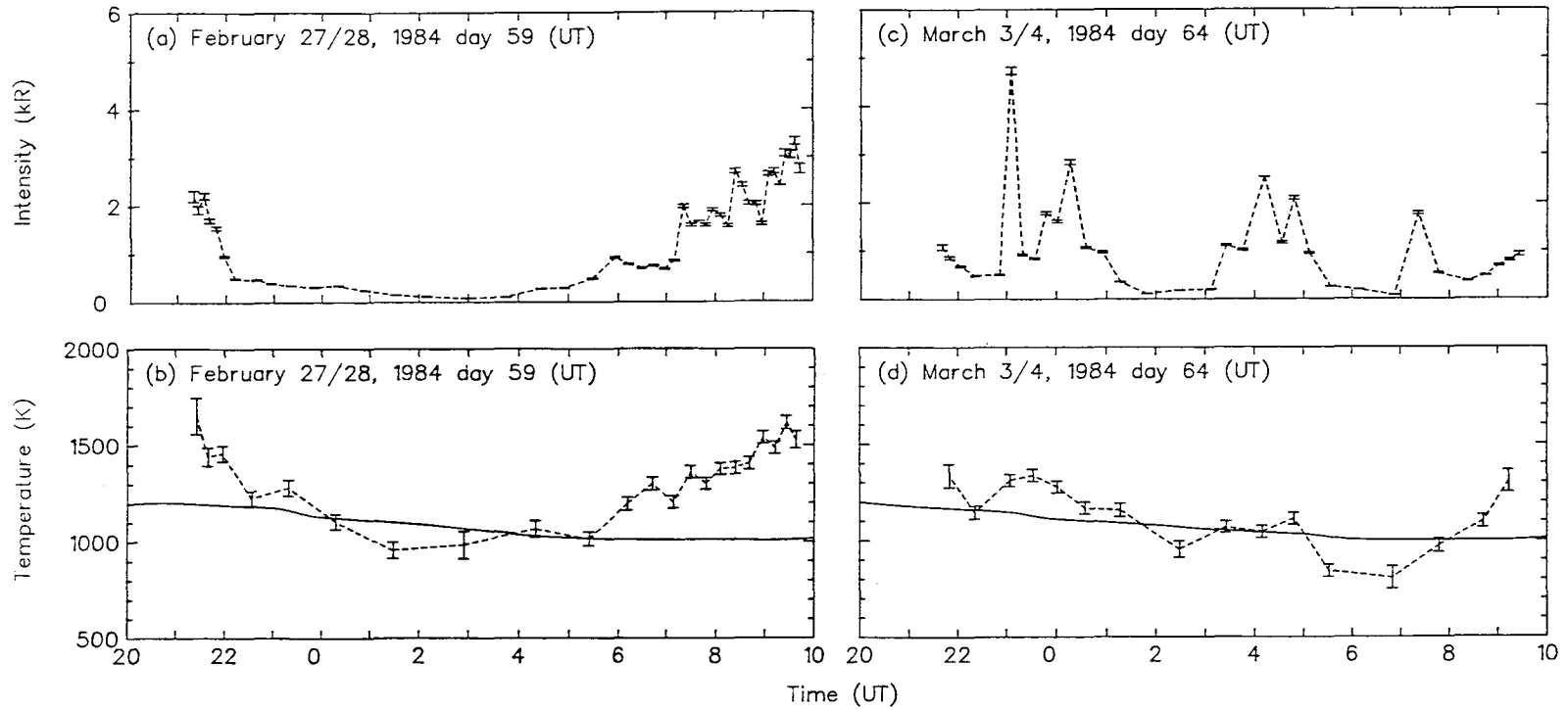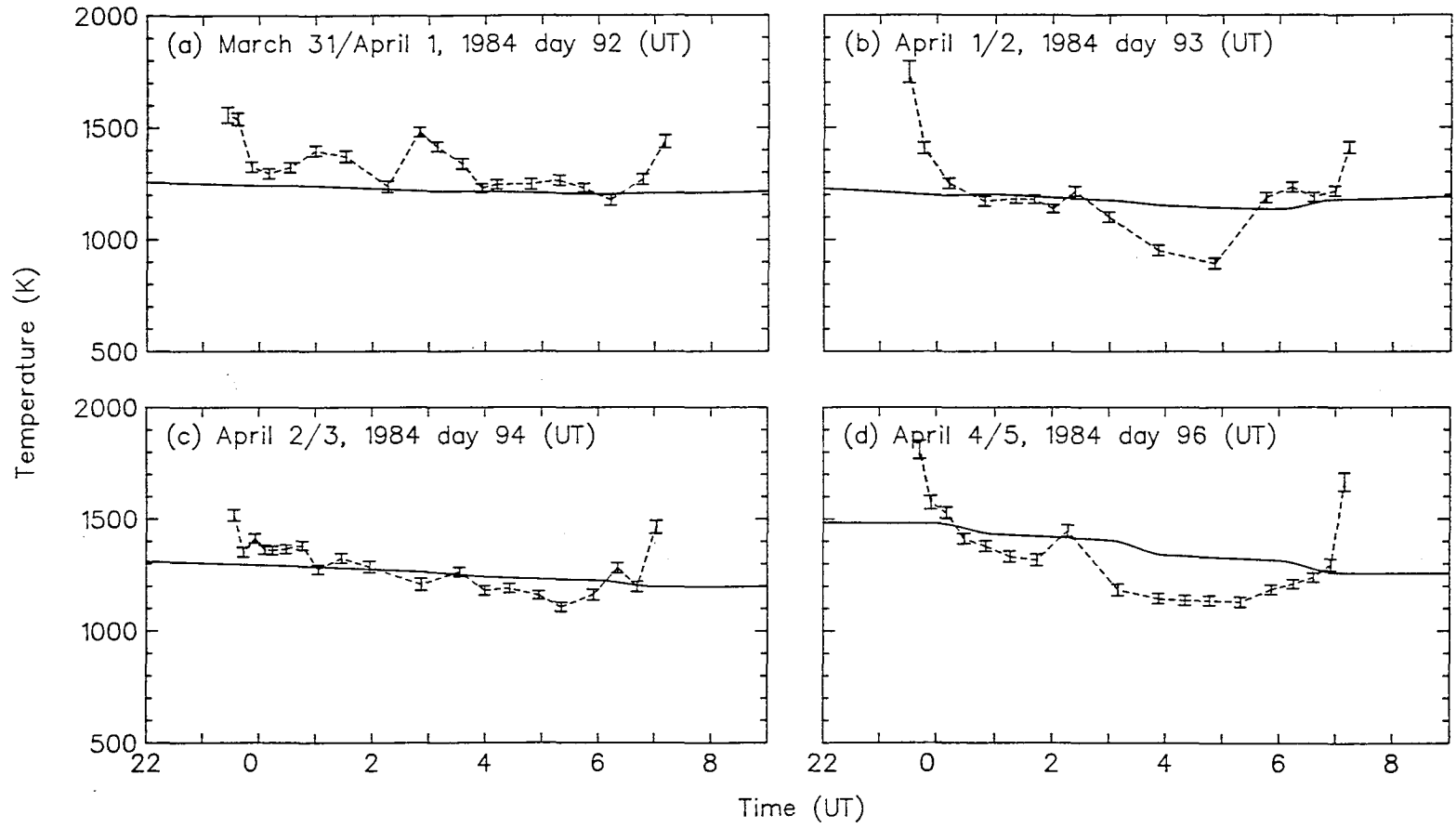
SEP 27, 1984

Figure 7
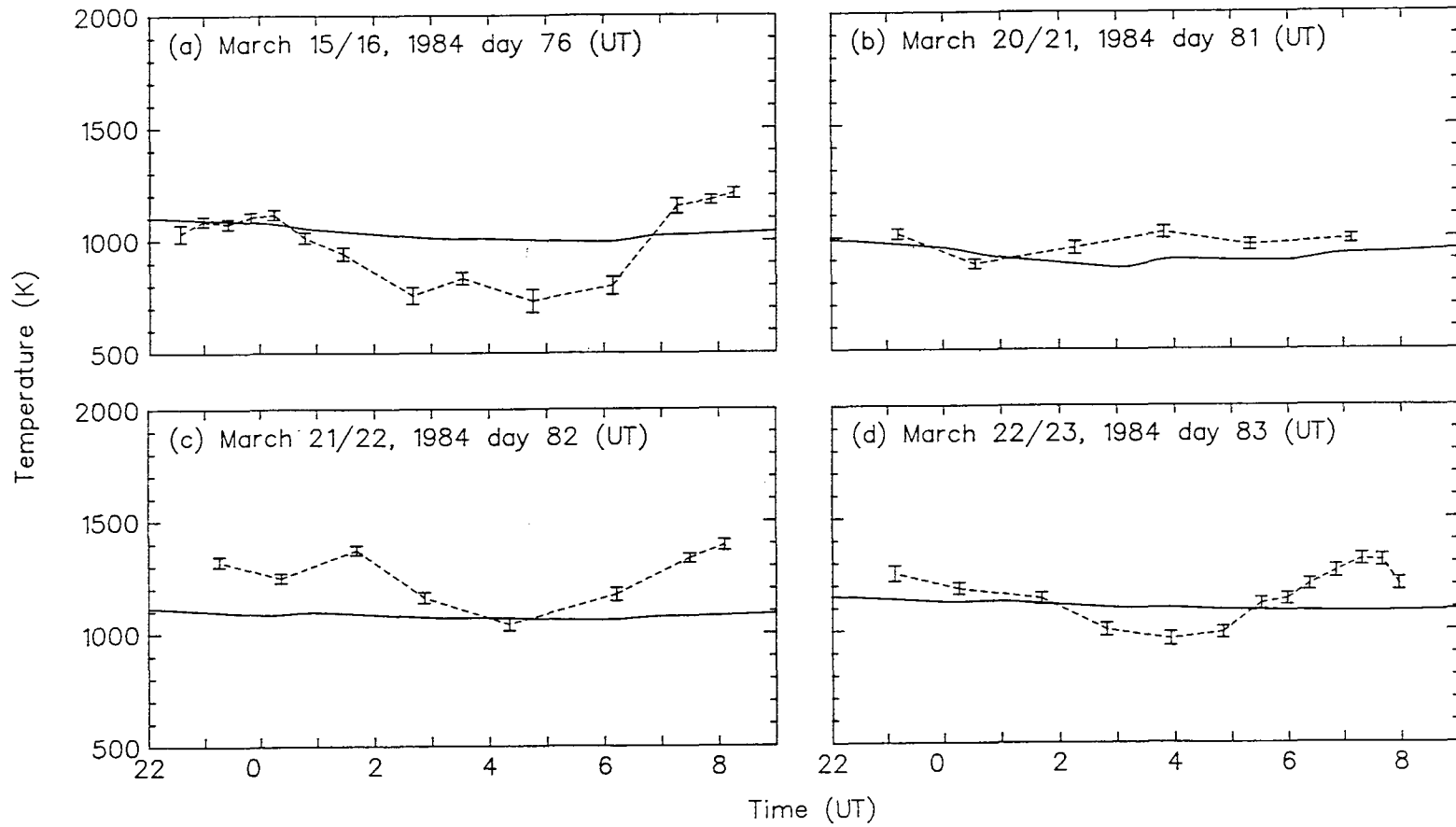
SEP 27, 1984

Figure 8

ZONAL WIND OBSERVATIONS DURING A GEOMAGNETIC STORM

N. J. Miller and N. W. Spencer
Laboratory for Atmospheres
NASA/Goddard Space Flight Center
Greenbelt, MD 20771

In situ measurements taken by the Wind and Temperature Spectrometer (WATS) onboard the Dynamics Explorer 2 spacecraft during a geomagnetic storm display zonal wind velocities that are reduced in the corotational direction as the storm intensifies. The data were taken during November 24-26, 1982 within the altitudes 275-475 km in the dusk local time sector equatorward of the auroral region. Characteristic variations in the value of the Dst index of horizontal geomagnetic field strength are used to monitor the storm evolution. The detected global rise in atmospheric gas temperatures indicates the development of thermospheric heating. Concurrent with that heating, reductions in corotational wind velocities were measured equatorward of the auroral region. Just after the sudden commencement, while thermospheric heating is intense in both hemispheres, eastward wind velocities in the northern hemisphere show reductions ranging from 500 m/s over high latitudes to 30 m/s over the geomagnetic equator. After 10 hours storm time, while northern thermospheric heating is diminishing, wind velocity reductions, distinct from those initially observed, begin to develop over southern latitudes. In the latter case, velocity reductions range from 300 m/s over the highest southern latitudes to 150 m/s over the geomagnetic equator and extend into the northern hemisphere. The observations highlight the interhemispheric asymmetry in the development of storm effects detected as enhanced gas temperatures and reduced eastward wind velocities. Zonal wind reductions over high latitudes can be attributed to the storm induced equatorward spread of westward polar cap plasma convection and the resulting plasma-neutral collisions. However, those collisions are less significant over low latitudes; so zonal wind reductions over low latitudes must be attributed to an equatorward extension of a thermospheric circulation pattern disrupted by high latitude collisions between neutrals transported via eastward winds and ions convecting westward.
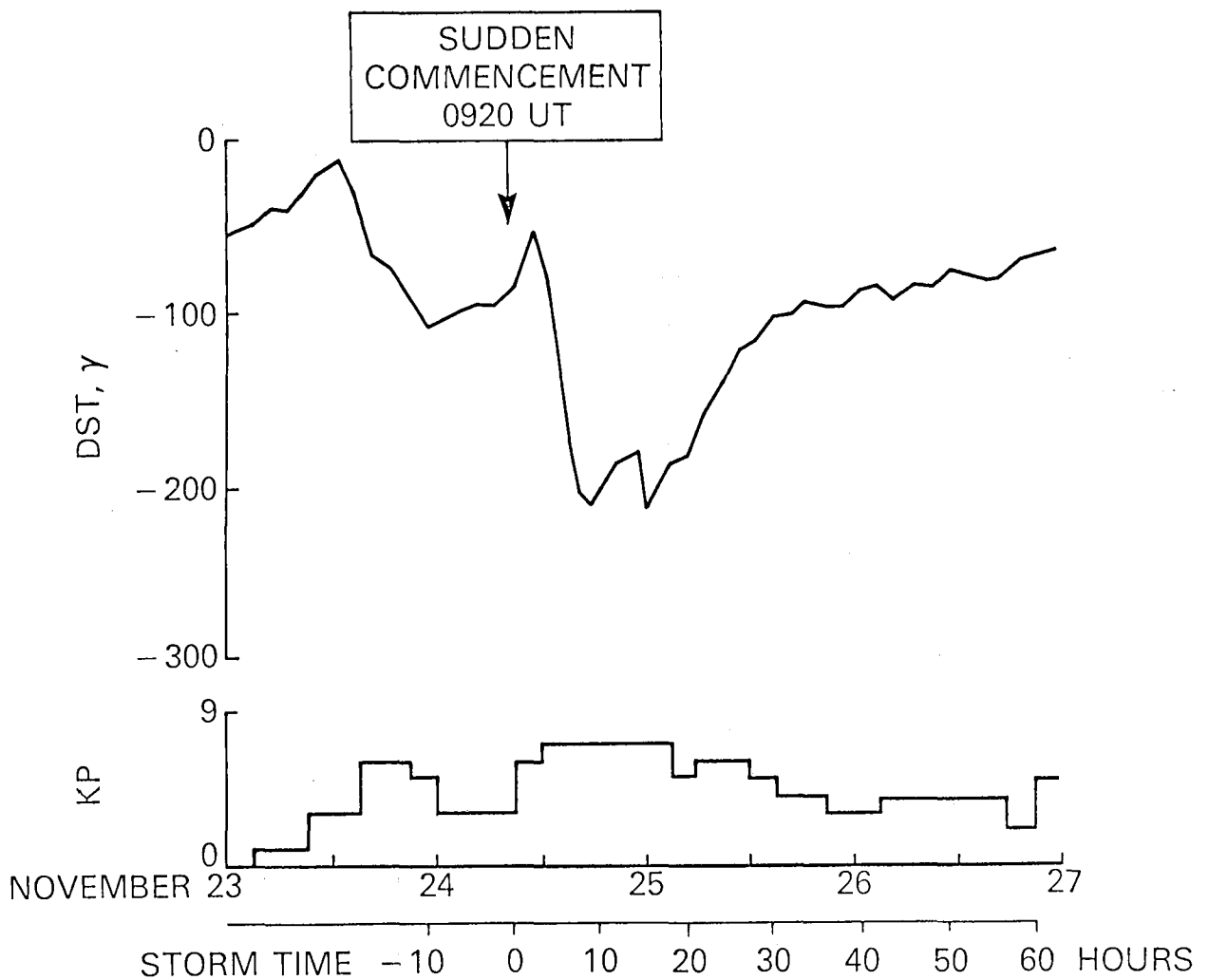
Figure 1. Magnetic characteristics of the period November 24-26, 1982. The Dst index decreases to −218γ at 1800 UT on the 24th; the three-hourly Kp index reaches 7 near 1400 UT on the 24th and remains there until after 0300 UT on the 25th. Storm time is measured from the time of the sudden commencement.
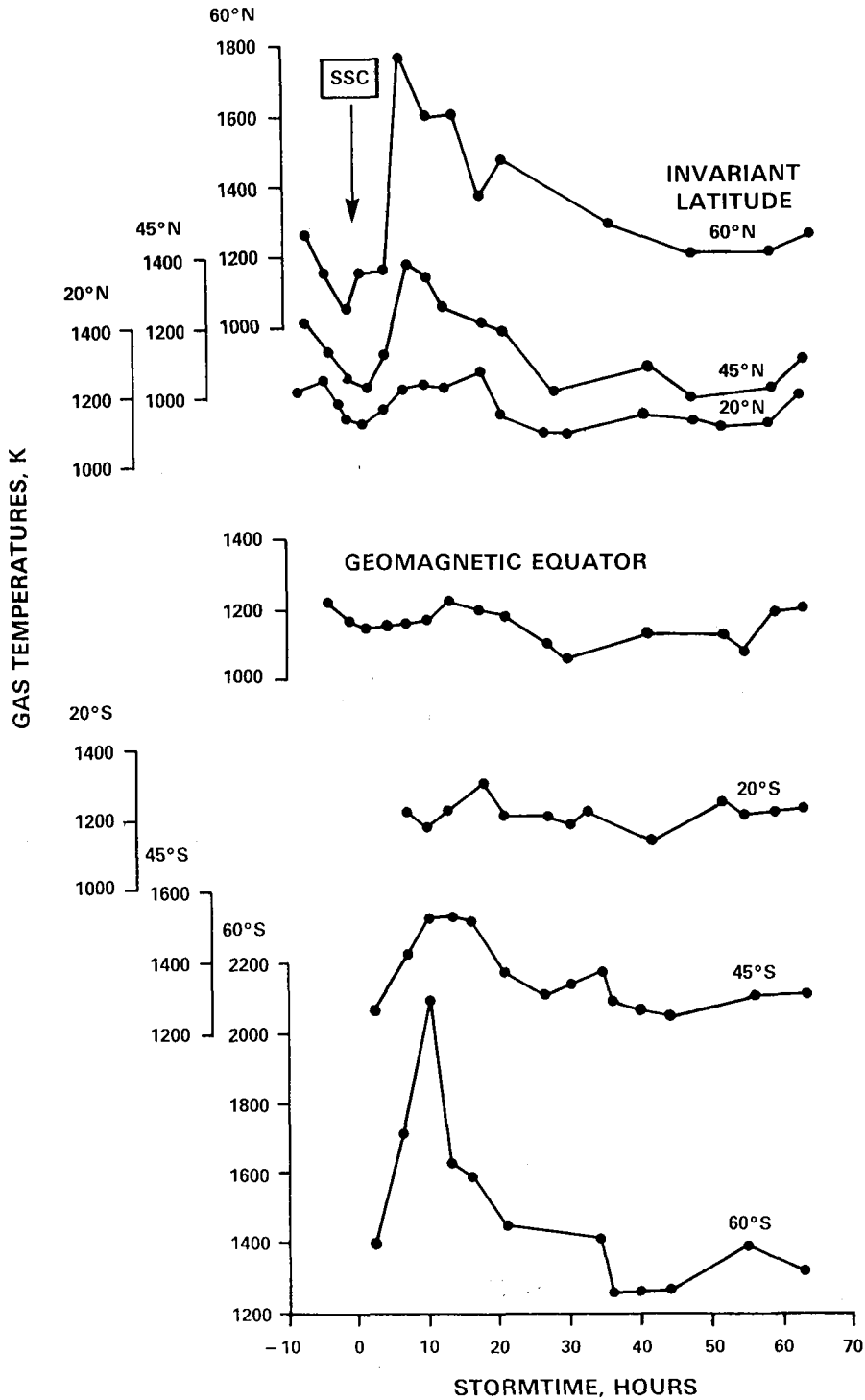
Figure 2. Gas temperatures measured by the WATS instrument in the dusk local time sector within the altitude range 275-475 km. The effects of thermospheric heating appear between 0-20 hours storm time over all dusk latitudes equatorward of 60° invariant latitude. The temperature rises 660° K over 60°N invariant latitude but only 70° K over ghe geomagnetic equator.

265
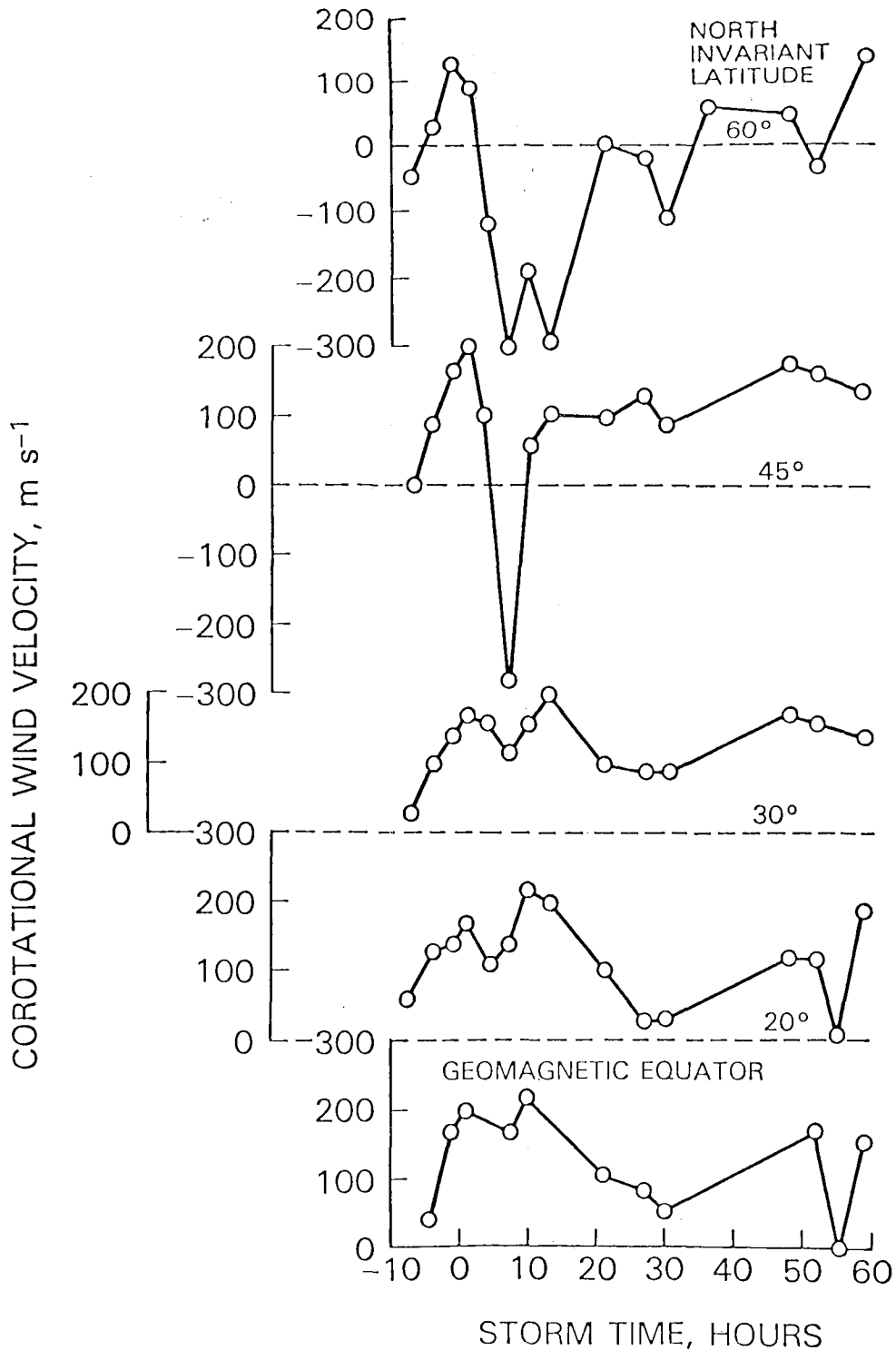
Figure 3. Zonal wind velocities measured over northern latitudes by the WATS instrument at the same time as the measurements represented in Figure 2. Velocities are relative to the corotation velocity, hence zero means corotation. Over all northern latitudes equatorward of 60° invariant latitude, velocities display a decrease in value immediately after the sudden commencement.
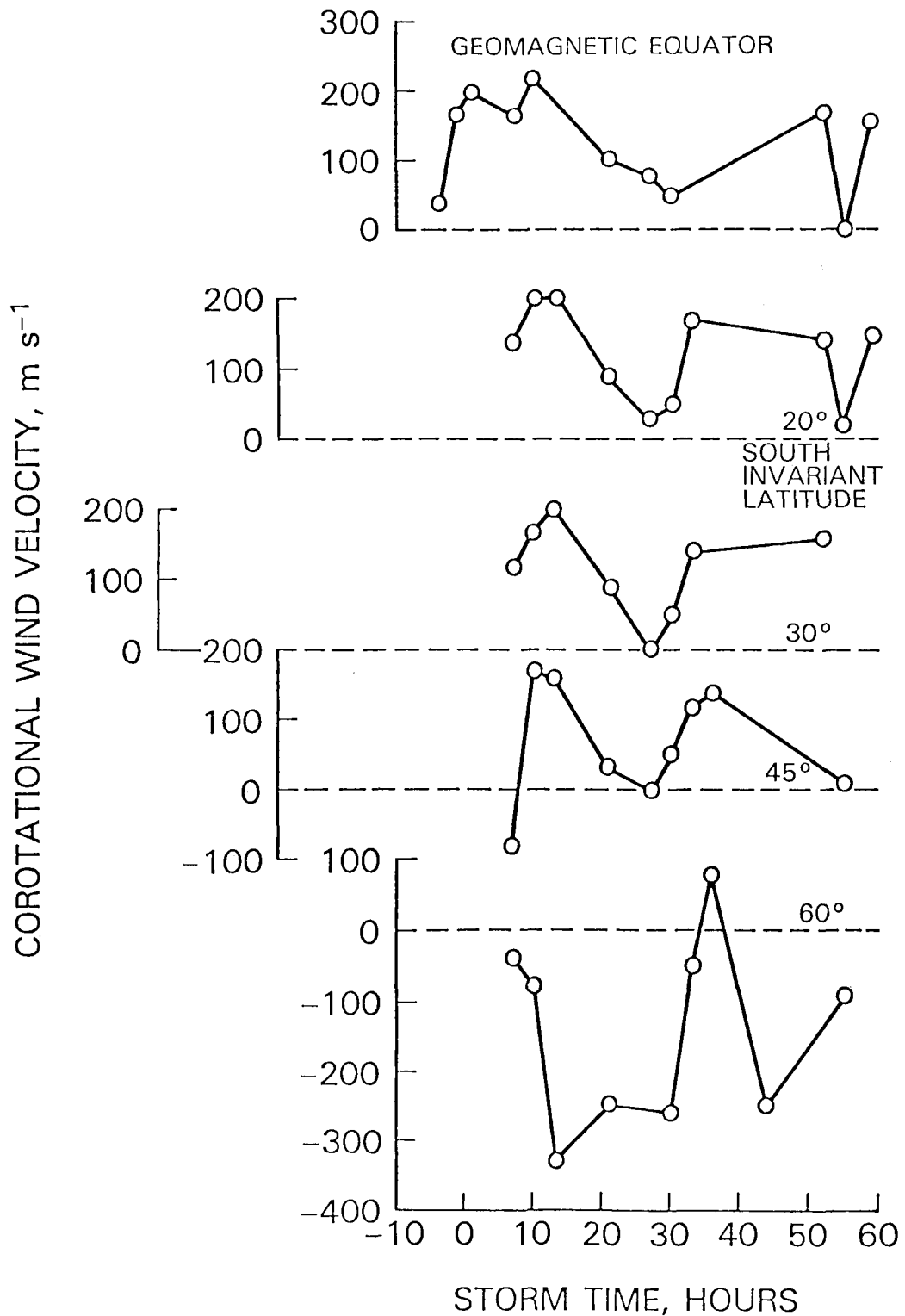
Figure 4. Zonal wind velocities measured as in Figure 3 but over southern latitudes. After 20 hours storm time the data display a velocity decrease that affects the zonal wind over latitudes from 60° south invariant latitude to 20° north invariant latitude.

MEASUREMENTS OF THERMOSPHERIC RESPONSE TO AURORAL ACTIVITIES

S. Okano* and J. S. Kim

Department of Atmospheric Science
State University of New York at Albany
1400 Washington Avenue
Albany, New York 12222

The Joule heating produced by auroral electrojets and its thermospheric response can be studied by monitoring the thermospheric temperatures by optical methods; simultaneously, the concurrent auroral electrojet activities can be investigated by using geomagnetic records obtained from stations along a meridian close to the observation site of optical measurements.

We report, in this paper, the measurements of thermospheric response to auroral activities which were made at Albany (42.68°N, 73.82°W), New York on September 2, 1978 (UT) when an isolated substorm occured. The thermospheric temperatures were measured by using a high-resolution Fabry-Perot interferometer that determines the line profiles of the [OI] 6300Å line emission. The intensities and latitudinal positions of auroral electrojets were obtained by the analysis of magnetograms from the IMS Fort Churchill meridian chain stations.

*Present Address: Upper Atmosphere and Space Research Laboratory, Tohoku University, Sendai, Japan
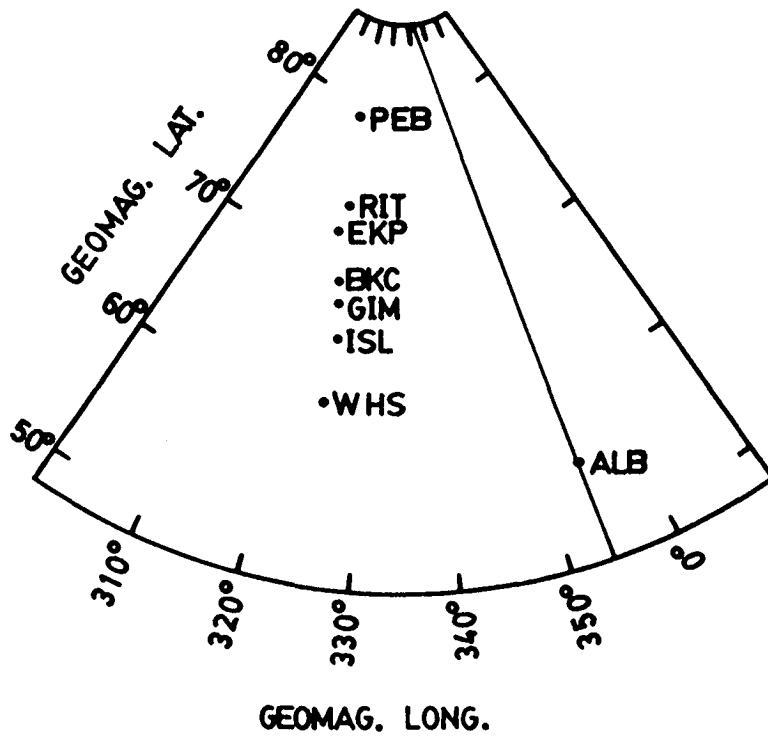
Figure 1. Locations of magnetic stations and Albany, New York in geomagnetic coordinates.
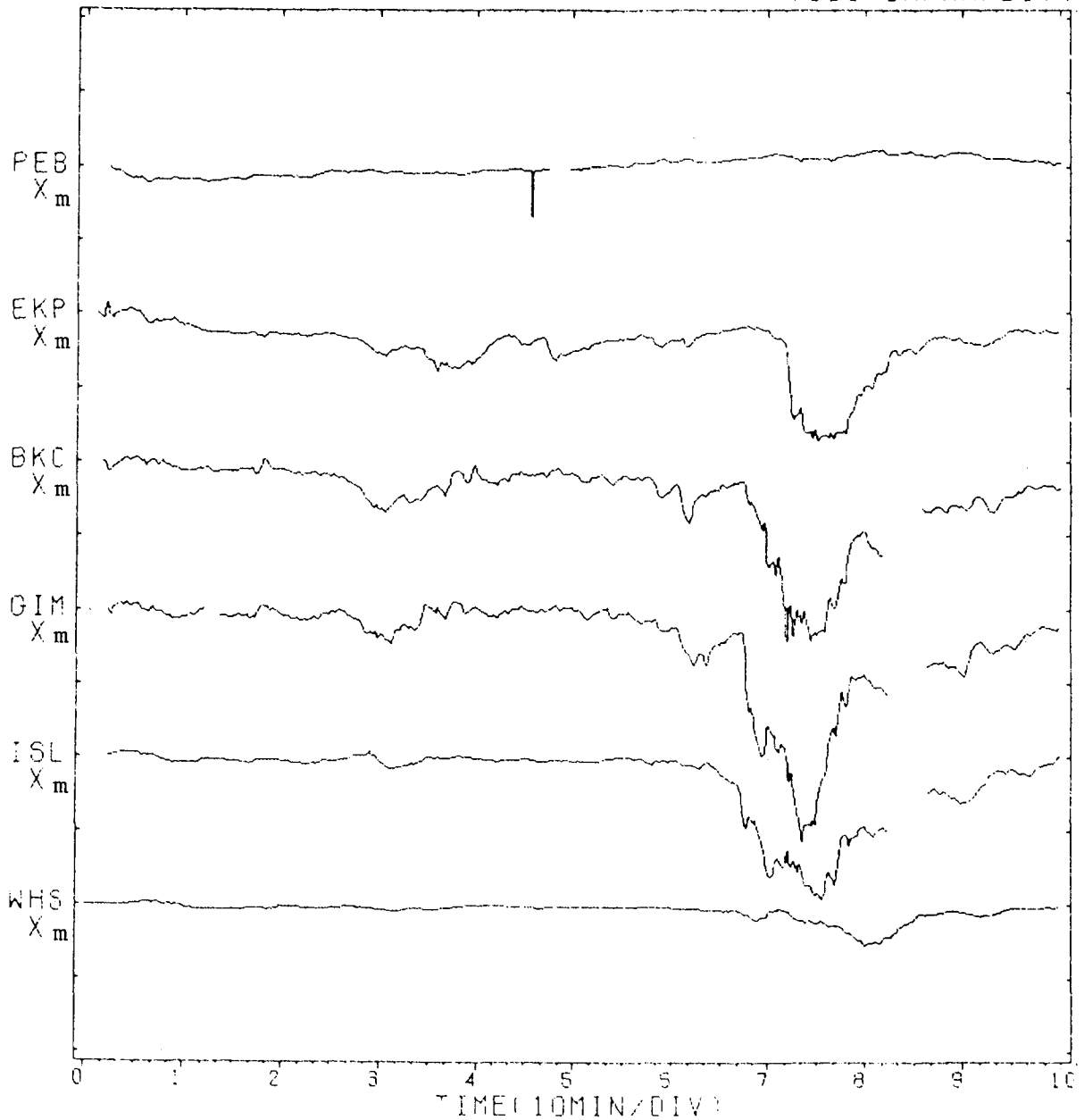
Figure 2a. The plots of the one-minute averages of X_m (magnetic north) components observed at stations in the Fort Churchill chain on September 2, 1978 (UT).
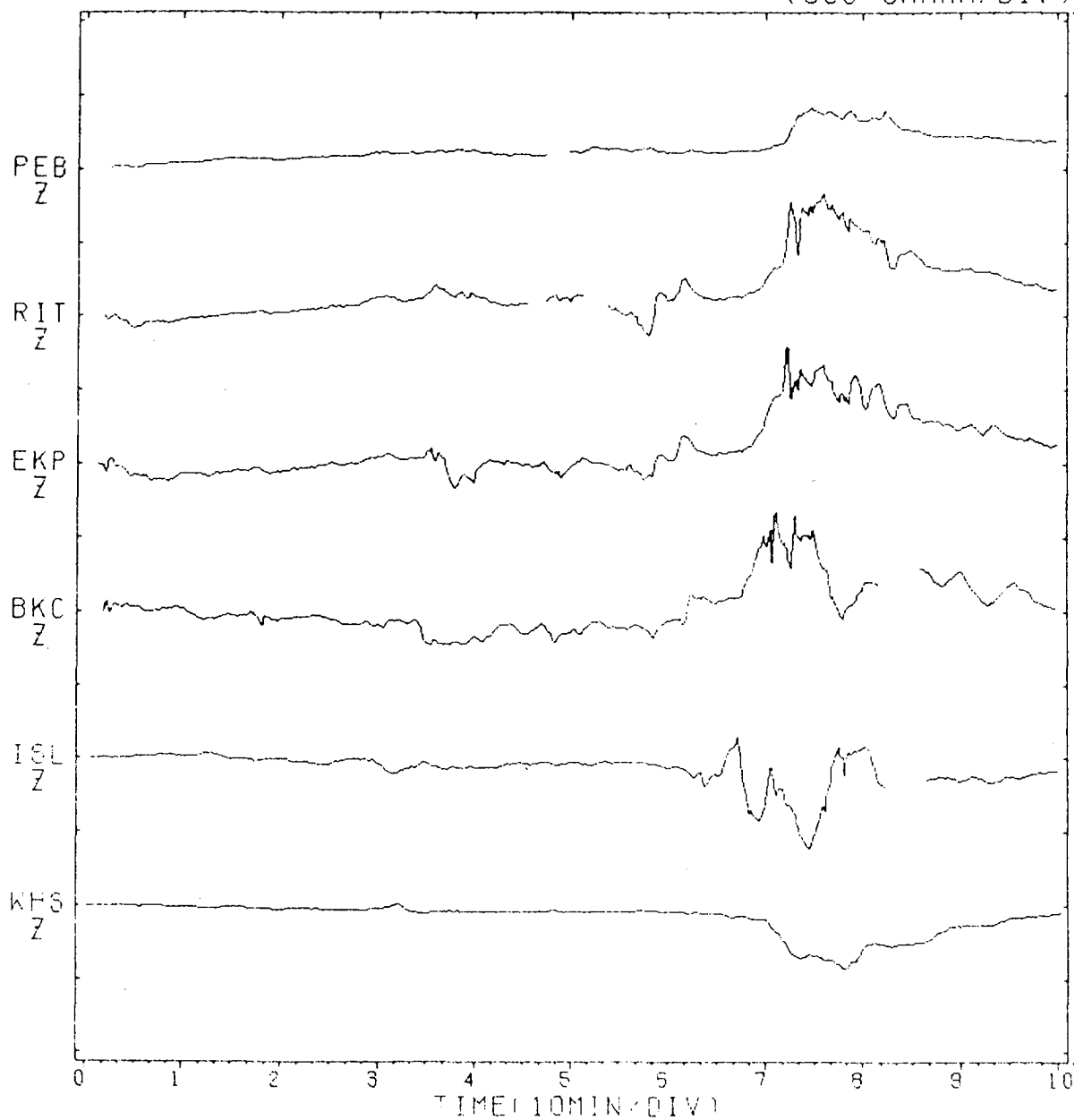
Figure 2b. The plots of the one-minute averages of Z (downward) components observed at stations in the Fort Churchill chain on September 2, 1978 (UT).
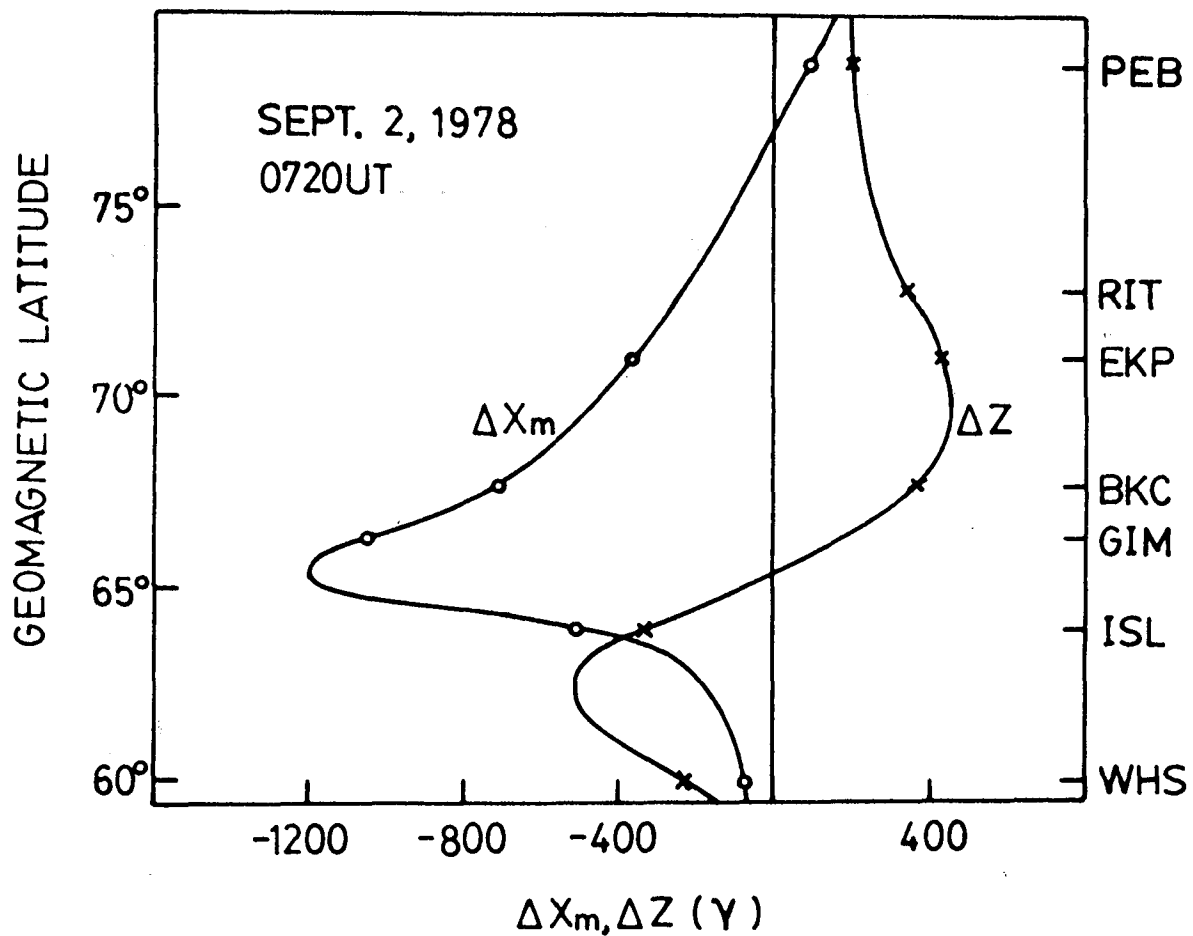
Figure 3. ΔX_m and ΔZ values at 0720 UT on September 2, 1978 from each station were plotted and the best-fitted curves were drawn through ΔX_m and ΔZ data, respectively, in order to determine the position and intensity of the westward electrojet.
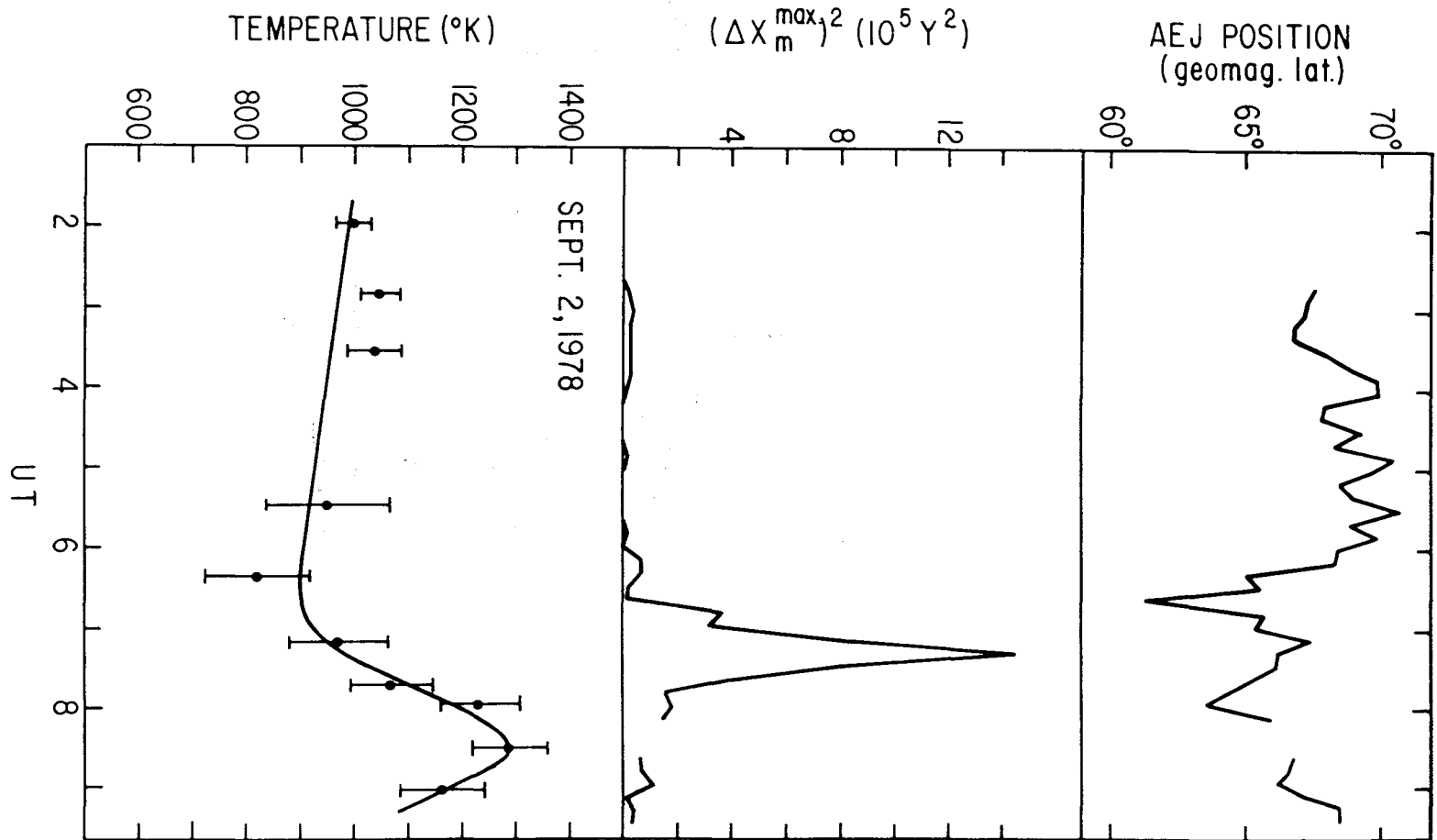
Figure 4. The position of electrojet and $(\Delta X_m^{max})^2$ value that were obtained by the analysis of magnetograms from the IMS Fort Churchill meridian chain stations and thermospheric temperature measured from Albany, New York are plotted as a function of universal time from top to bottom, respectively.

INITIAL RESULTS OF THE GLOBAL THERMOSPHERIC MAPPING STUDY (GTMS)

W. L. Oliver, J. E. Salah, R. G. Musgrove, and J. M. Holt
MIT Haystack Observatory, Westford, Massachusetts 01886 U.S.A.

V. B. Wickwar
SRI International, Menlo Park, California 94205 U.S.A.

G. J. Hernandez
NOAA, Boulder, Colorado 80303 U.S.A.

R. G. Roble
NCAR, Boulder, Colorado 80307 U.S.A.

The Global Thermospheric Mapping Study (GTMS) is a multi-technique experimental study of the thermosphere designed to map simultaneously its spatial and temporal morphology with a thoroughness and diversity of measurement techniques heretofore unachieved. Three-day campaigns at the summer and winter solstices are planned to study the seasonal variations in thermospheric structure. The GTMS is designed around the Incoherent Scatter Radar Chain in the western hemisphere. The European incoherent scatter radars and the worldwide communities of Fabry Perot interferometers, meteor wind radars, partial reflection drifts radars, MST radars, and satellite probes are included to extend the spatial coverage and types of measurements available. Theoretical and modeling support in the areas of thermospheric and ionospheric structure, tides, and electric fields are included to aid in program planning and data interpretation.

The initial GTMS campaign was conducted on 26-28 June 1984, during a period of sharply declining solar activity. Solar activity was low on the three observation days (F10.7 = 97, 98, 96) and magnetic conditions were unsettled to active (A = 10, 12, 20). All six incoherent scatter radar facilities collected data. Each collected F region data day and night while Saint Santin and Millstone Hill additionally collected E region data during daylight hours. Initial results from Sondrestrom and Millstone Hill are presented. Good quality Fabry Perot data were collected at Fritz Peak and San Jose dos Campos. Weather conditions produced poor results at Arequipa and Arecibo. Initial results from Fritz Peak are presented. Mesosphere/lower-thermosphere observations were conducted under the ATMAP organization. The magnetometer chains also were operational during this campaign. Initial TGCM predictions have been made for assumed solar-geophysical conditions, and selected results are presented.

Sondrestrom ionospheric results show a decrease in electron density from June 26 to 27 to 28, isolated periods of ion frictional heating during the nights throughout the field of view, and strong ionospheric convection velocity reversals well beyond midnight. Neutral wind results show a major period of enhanced northward velocity in response to strong heating to the south of the radar on June 28, the most disturbed of the three days.

Millstone Hill ionospheric results show lower densities on June 27 than on June 26 but higher densities on June 28. Frictional heating effects and velocity reversals are restricted to the most northerly observations. Millstone Hill neutral atmosphere results show a higher temperature and

atomic oxygen density over a wide latitude range on June 28 than on the previous two days, with particularly strong effects at lower latitudes. These are believed to be the first incoherent scatter radar determinations of the latitudinal variation of the neutral atomic oxygen density.

Fritz Peak Fabry Perot data show a strong latitudinal gradient in neutral temperature, with temperatures 5 degrees in latitude to the north of the station exceeding those to the south by 200 K. Early on the morning of June 28 the Fabry Perot winds showed a sudden and strong shift toward the equator with the winds to the north exceeding 300 m/s but the winds to the south attaining a speed of only 130 m/s.

TGCM simulations were made to predict the global steady-state behavior of thermospheric temperature, winds, density, and composition for pre-assumed values for solar flux (F10.7 = 120– somewhat high) and magnetic activity (Ap = 4 – somewhat low). A cross-tail magnetospheric potential and an auroral particle input of 2 ergs/cm**2/sec were included but tides were not. These simulations predict a strong summer-solstice neutral temperature gradient over North America with a temperature maximum over Greenland. Meridional wind predictions over Sondrestrom show a strong diurnal flow with poleward velocities of 170 m/s during the day and equatorward velocities of 300 m/s at night. A large quantity of such results are available from the simulations.

As more data are received and analyzed, composite maps of global upper atmospheric and ionospheric structure will be compiled and compared with models and simulations which will be updated as pertinent information on solar/geophysical inputs becomes available. Magnetometer data will be used to estimate global Joule heating rates to act as inputs to the models. The models will rely to various degrees on inputs from the measurements and on feedback from other models as thermospheric, ionospheric, and electrodynamic properties of the upper atmosphere all are interdependent.

A second GTMS campaign will be conducted on 15-17 January 1985. Optical coverage, especially at high northern latitudes near the Radar Chain, should be much improved during this period.

The GTMS data-taking campaigns will be followed by a Workshop at MIT on 17-19 July 1985. In addition to the GTMS solstice campaigns, the Workshop will include the Equinox Transition campaign, a radar/optical campaign coordinated by AFGL in September 1984, designed to observe the summer-winter thermosphere circulation transition and the competition between high-latitude and sub-solar forcing in controlling circulation structure. Consideration will be given to presenting these results at an AGU session in December 1985 or at an NCAR/URSI Radar Workshop on coordinated radar campaigns.

GTMS – EXPERIMENTAL ORGANIZATION

OVERALL COORDINATION – MILLSTONE HILL (W. OLIVER, J. SALAH)
TECHNIQUE COORDINATORS –
    INCOHERENT SCATTER RADARS   W. OLIVER
        SONDRE STROMFJORD   V. WICKWAR
        MILLSTONE HILL   W. OLIVER
        ARECIBO, JICAMARCA   W. SWARTZ
        EISCAT, SAINT SANTIN   D. ALCAYDE
    FABRY PEROT INTERFEROMETERS   J. MERIWETHER
    METEOR RADARS   R. ROPER (GLOBMET)
    PARTIAL REFLECTION RADARS   J. FORBES (ATMAP)
    MST RADARS   J. FORBES (ATMAP)
    SATELLITE PROBES   A. HEDIN

GTMS – THEORY/MODEL/SIMULATION ORGANIZATION

1	–	THERMOSPHERE SIMULATION (TGCM)	ROBLE ET AL.
2	–	THERMOSPHERE MODEL COMPARISON (E.G., MSIS)	HEDIN ET AL.
3	–	TIDES MODELING/COMPARISON	FORBES ET AL.
4	–	IONOSPHERE SIMULATION	SCHUNK ET AL.
5	–	ELECTRIC FIELD MODELING/COMPARISON	RICHMOND ET AL.
6	–	NE/TE MODEL COMPARISON	BRACE ET AL.
7	–	NE MODEL COMPARISON	CHIU ET AL.

SOLAR CYCLE 21 – 10.7cm FLUX
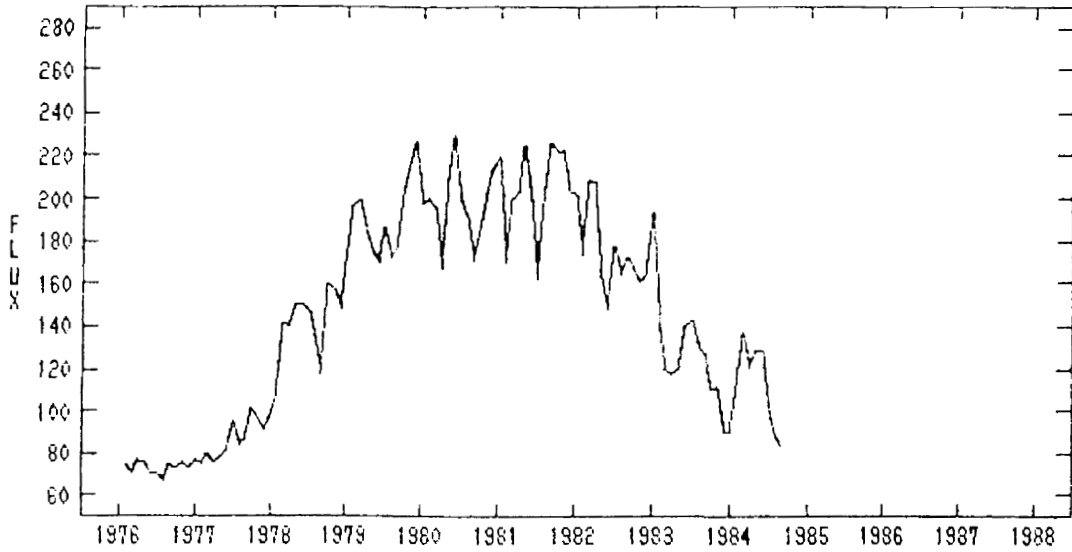
AFRED FOR JUN 1984
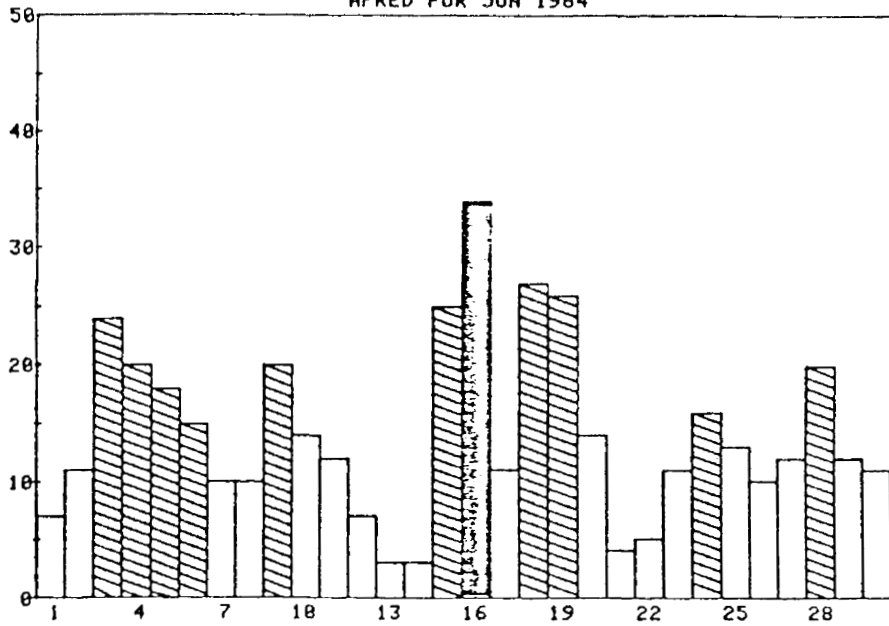
GTMS - 26-28 JUNE 1984 - SOLAR/GEOPHYSICAL INDICES

MONTHLY AVERAGES   DAILY VALUES
-------------------   --
MONTH   F10.7   DAY   F10.7   AFR   K-FREDERICKSBURG   K-ANCHORAGE
-----   -----   ---   -----   ---   ----------------   ----------------
MARCH   122.0   JUNE 24   100.3   16   5-4-2-2-2-2-2-3   5-6-3-3-2-3-2-3
APRIL   128.7   25   101.3   13   4-3-2-2-2-2-3-3   4-3-3-2-3-3-3-2
MAY   128.3   26   96.8   10   3-3-3-2-1-1-2-3   3-3-2-3-2-3-2-3
JUNE   100.3   27   98.2   12   4-4-3-2-1-0-2-2   5-4-4-4-3-2-3-2
JULY   89.3   28   96.2   20   3-3-4-3-3-3-4-4   4-4-5-4-4-6-4-3
AUGUST   83.7   29   97.0   12   3-2-2-3-1-3-3-3   4-3-3-3-1-3-3-3
SEPT.   (78.1)   30   97.8   11   3-3-2-2-2-2-3-3   3-4-3-3-4-4-2-3

            SITES INVOLVED IN THE GLOBAL THERMOSPHERIC MAPPING STUDY

         SITE   STATE/COUNTRY   LAT   LON   EXPERIMENT TYPE
         ----   -------------   ---   ---   ---------------
         Saint Santin   France   44   2   IS
         SOUCY   West Germany   52   10   MST
         Bologna   Italy   44   11   MR
         EISCAT   Scandanavia   69   19   IS
         Kiruna   Sweden   68   20   FP
         Kyoto   Japan   35   135   MR
         Adelaide   South Australia   -35   138   FP   PR
         Christchurch   New Zealand   -43   172   PR
         Fairbanks   Alaska   64   212   FP
         Poker Flat   Alaska   64   212   MST
         Calgary   Alberta   51   246   FP
         Saskatoon   Saskachewan   52   254   PR
         Fritz Peak   Colorado   40   255   FP
         Sunset   Colorado   40   255   MST
         Urbana   Illinois   40   272   MR   MST
         Atlanta   Georgia   33   276   MR
         Ann Arbor   Michigan   42   277   FP
         Laurel Ridge   Pennsylvania   40   281   FP
         Jicamarca   Peru   -12   283   IS   MST
         Millstone Hill   Massachusetts   43   289   IS   FP
         Arequipa   Peru   -16   289   FP
         Durham   New Hampshire   43   289   MR
         Arecibo   Puerto Rico   18   294   IS   FP   MST
         Sondrestrom   Greenland   67   309   IS   FP
         San Jose dos Campos   Brazil   -23   314   FP

         LAT: LATitude, + in northern hemisphere, - in southern
         LON: east LONgitude
         IS: Incoherent Scatter
         FP: Fabry Perot interferometer
         MR: Meteor wind Radar
         PR: Partial Reflection drifts radar
         MST: Mesosphere-Stratosphere-Troposphere radar

GTMS   -   26-28 JUNE 1984   -   IS   -   EISCAT

DAYS OF OBSERVATION: 26-28 JUNE

OBSERVING SCHEME: CP-3 - WIDE LATITUDE SCAN

CYCLE TIME: 30 MINUTES

MEASURED QUANTITIES - IONOSPHERIC (F REGION)
        NE, TE, TI, E FIELD - VS LATITUDE

MEASURED QUANTITIES - NEUTRAL (UPPER THERMOSPHERE)
        TEMPERATURE   - VS LATITUDE
        MERIDIONAL WIND - VS LATITUDE
        OXYGEN DENSITY - VS LATITUDE

DATA QUALITY: PRESUMED GOOD

GTMS   -   26-28 JUNE 1984   -   IS   -   SAINT SANTIN

DAYS OF OBSERVATION: 26-28 JUNE

OBSERVING SCHEME: VERTICAL TRANSMITTED BEAM (SAINT SANTIN)
                  3 RECEIVERS SCANNING TRANSMITTED BEAM
                     (NANCAY, MENDE, MONPAZIER)
                     (MONPAZIER RESTRICTED TO F REGION ON 28-TH)

CYCLE TIME: DAY   - 60 MINUTES
            NIGHT - 30 MINUTES

MEASURED QUANTITIES - IONOSPHERIC (LOCAL)
      F REGION - NE, TE, TI, E FIELD
      E REGION - NE, TE, TI, COLL. FREQ., ION DRIFT

MEASURED QUANTITIES - NEUTRAL (LOCAL)
      F REGION - TEMPERATURE
                 MERIDIONAL WIND
                 OXYGEN DENSITY (DAY)
      E REGION - TEMPERATURE   (DAY)
                 WIND VECTOR   (DAY)
                 N2 DENSITY   (DAY)

DATA QUALITY: GOOD

280

GTMS – 26–28 JUNE 1984 – IS – ARECIBO

DAYS OF OBSERVATION – 26–28 JUNE

OBSERVING SCHEME – CONICAL BEAM SWING
                   INTERLACED POWER AND SPECTRAL MEASUREMENTS

CYCLE TIME: 16 MINUTES FOR ANTENNA SWING
             1–2 MINUTES FOR LINE-OF-SIGHT MEASUREMENTS

MEASURED QUANTITIES – IONOSPHERIC (LOCAL F REGION)
     NE, TE, TI, E FIELD

MEASURED QUANTITIES – NEUTRAL (LOCAL UPPER THERMOSPHERE)
     TEMPERATURE
     MERIDIONAL WIND
     OXYGEN DENSITY (DAYTIME)

DATA QUALITY – GOOD

GTMS – 26–28 JUNE 1984 – IS – JICAMARCA

DAYS OF OBSERVATION: FARADAY ROTATION (NE) – 26–28 JUNE
                     IS SPECTRAL DATA   – 27–28 JUNE

OBSERVING SCHEME –
     SPLIT BEAM, EAST AND WEST

CYCLE TIME: 5 MINUTES

MEASURED QUANTITIES – IONOSPHERIC (LOCAL F REGION)
     NE, TE, TI, E FIELD

MEASURED QUANTITIES – NEUTRAL (LOCAL UPPER THERMOSPHERE)
     TEMPERATURE
  ?? OXYGEN DENSITY (DAYTIME)

DATA QUALITY: FARADAY ROTATION – GOOD
              IS SPECTRAL   – UNCERTAIN

281

```
             GTMS   -   26-28 JUNE 1984   -   IS   -   SONDRESTROM


DAYS OF OBSERVATION - 26-28 JUNE

OBSERVING SCHEME -
       11-POSITION MEASUREMENT: 5 PAIRS STRADDLING FIELD LINE
                                      (FOR E FIELD VS LATITUDE)
                            1 POSITION UP B FIELD
                                      (FOR LOCAL WINDS)
       N-S ELEVATION SCAN (SCALAR QUANTITIES VS LATITUDE)
       UP B FIELD AFTER 11-POSITION AND ELEVATION SCAN

CYCLE TIME:  22.5 MINUTES (6 MINUTES UP B)

MEASURED QUANTITIES - IONOSPHERIC (F REGION)
     NE, TE, TI, E FIELD - VS LATITUDE

MEASURED QUANTITIES - NEUTRAL (UPPER THERMSOPHERE)
       TEMPERATURE       - VS LATITUDE
       MERIDIONAL WIND - LOCAL
   ?? OXYGEN DENSITY

DATA QUALITY - GOOD
```

```
          GTMS   -   26-28 JUNE 1984   -   IS   -   MILLSTONE HILL


DAYS OF OBSERVATION - 26-28 JUNE

OBSERVING SCHEME -
       DOUBLE ELEVATION SCAN: ONE ALONG MILLSTONE MERIDIAN
                              ONE CANTED 30 DEGREES TO WEST
       ZENITH MEASUREMENTS
       DAYTIME: ADDED 3-POSITION E REGION MEASUREMENT

CYCLE TIME:  NIGHT - 30 MINUTES
             DAY   - 60 MINUTES

MEASURED QUANTITIES - IONOSPHERIC
     F REGION - NE, TE, TI, E FIELD - VS LATITUDE
     E REGION - NE, TE, TI, COLL. FREQ., ION DRIFT - LOCAL

MEASURED QUANTITIES - NEUTRAL
     F REGION - TEMPERATURE       - VS LATITUDE
                MERIDIONAL WIND - VS LATITUDE
                OXYGEN DENSITY  - VS LATITUDE (DAY)
     E REGION - TEMPERATURE      - LOCAL     (DAY)
                WIND VECTOR      - LOCAL     (DAY)
                N2 DENSITY       - LOCAL     (DAY)

DATA QUALITY - GOOD
```

GTMS   -   26-28 JUNE 1984   -   FABRY PEROT OBSERVATIONS

6300-A NIGHTTIME OBSERVATIONS

1 - SAO JOSE DOS CAMPOS:
          JUNE 25   - 1850-2330 LT
          JUNE 26/27 - 1900-0430 LT (VERY LOW INTENSITY AFTER OO LT)
          JUNE 27   - NO OBSERAVTIONS (BAD WEATHER)
          JUNE 28   - NO OBSERVATIONS (BAD WEATHER)
          JULY 01/02 - 1950-0200 LT
          JULY 02/03 - 1830-0400 LT (LOW INTENSITY)
          JULY 03/04 - 1830-0300 LT

2 - AREQUIPA - DATA TAKEN, WEATHER WAS CLOUDY

3 - ARECIBO - DATA TAKEN, SKY WAS HAZY, POOR QUALITY

4 - FRITZ PEAK:
          JUNE 27   - 0300-1100 UT (TEMPERATURE ONLY)
          JUNE 28   - 0300-1100 UT (TEMPERATURE + HORIZONTAL WIND)

5 - LAUREL RIDGE - TAPE RECORDER MALFUNCTION

6 - ANN ARBOR - NO DATA

7 - CALGARY - NO DATA

8 - FAIRBANKS - NO DATA, INOPERATIVE IN SUMMER

9 - SONDRESTROM - NO DATA, INOPERATIVE IN SUMMER

          OTHERS ??

GTMS   -   26-28 JUNE 1984   -   D&E-REGION/MESOSPHERE OBSERVATIONS

1 - ENTIRE ATMAP NETWORK - REPORTS INCOMPLETE
          METEOR RADARS
          PARTIAL REFLECTION DRIFTS RADARS
          MST RADARS

2 - INCOHERENT SCATTER RADARS - DAYTIME ONLY
          MILLSTONE HILL
          SAINT SANTIN

3 - FABRY PEROT INTERFEROMETERS (GREEN LINE) - NO OBSERVATIONS
          (ONLY F REGION RED LINE DATA WERE TAKEN)

GTMS - 26-28 JUNE 1984 - SATELLITE DATA

???

GTMS - 26-28 JUNE 1984 - MAGNETOMETER DATA

MAGNETOMETER CHAINS WERE OPERATING

KAMIDE AND AKASOFU PLAN TO CALCULATE GLOBAL MAPS OF
    JOULE HEAT PRODUCTION AND IONOSPHERIC CURRENTS

GTMS/EQUINOX-CIRCULATION WORKSHOP

WORKSHOP TO STUDY GLOBAL FEATURES OF
THERMOSPHERE STRUCTURE AS OBSERVED DURING:

    (1) GTMS SUMMER (JUNE 1984) AND WINTER (JANUARY 1985)
       SOLSTICE CAMPAIGNS

    (2) EQUINOX-CIRCULATION (SEPTEMBER 1984) CAMPAIGN

WORKSHOP DATES/PLACE: 17-19 JULY 1985 AT MIT

GTMS/EQUINOX-CIRCULATION AGU SESSION

DECEMBER 1985 MEETING IN SAN FRANCISCO

SESSION TO BE PLANNED AT JULY 1985 WORKSHOP

ABSTRACTS DUE IN TO AGU IN SEPTEMBER 1985

Illustration of the latitude-altitude coverage attained by a
north-south elevation scan down to about 5 degrees at Millstone
Hill. Plotted is the logarithm (base 10) of the electron density
(cm**-3).

MILLSTONE HILL RADAR - 27,JUN,1984
START UT = 0:24:44   AZ =   0.1   EL =   5.3
END UT   = 0:41: 3   AZ = 180.1   EL =   5.7

LOG (NE) TI (deg K) TE (deg K) VO (m/s)

MILLSTONE HILL RADAR 26-29 JUNE 1984
LOG(NE), TI, TE, VO vs LT and GEODETIC LATITUDE at 350 km
Elevation scan at 180, 360 deg AZ

OLIVER, page 287

MILLSTONE HILL   26-29 JUNE 1984

EXOSPHERIC TEMPERATURE VERSUS UT AND GEODETIC LATITUDE

288

MILLSTONE HILL   26-29 JUNE 1984

ATOMIC OXYGEN DENSITY VERSUS UT AND GEODETIC LATITUDE

Kp

CMжк-3

OLIVER, page 289
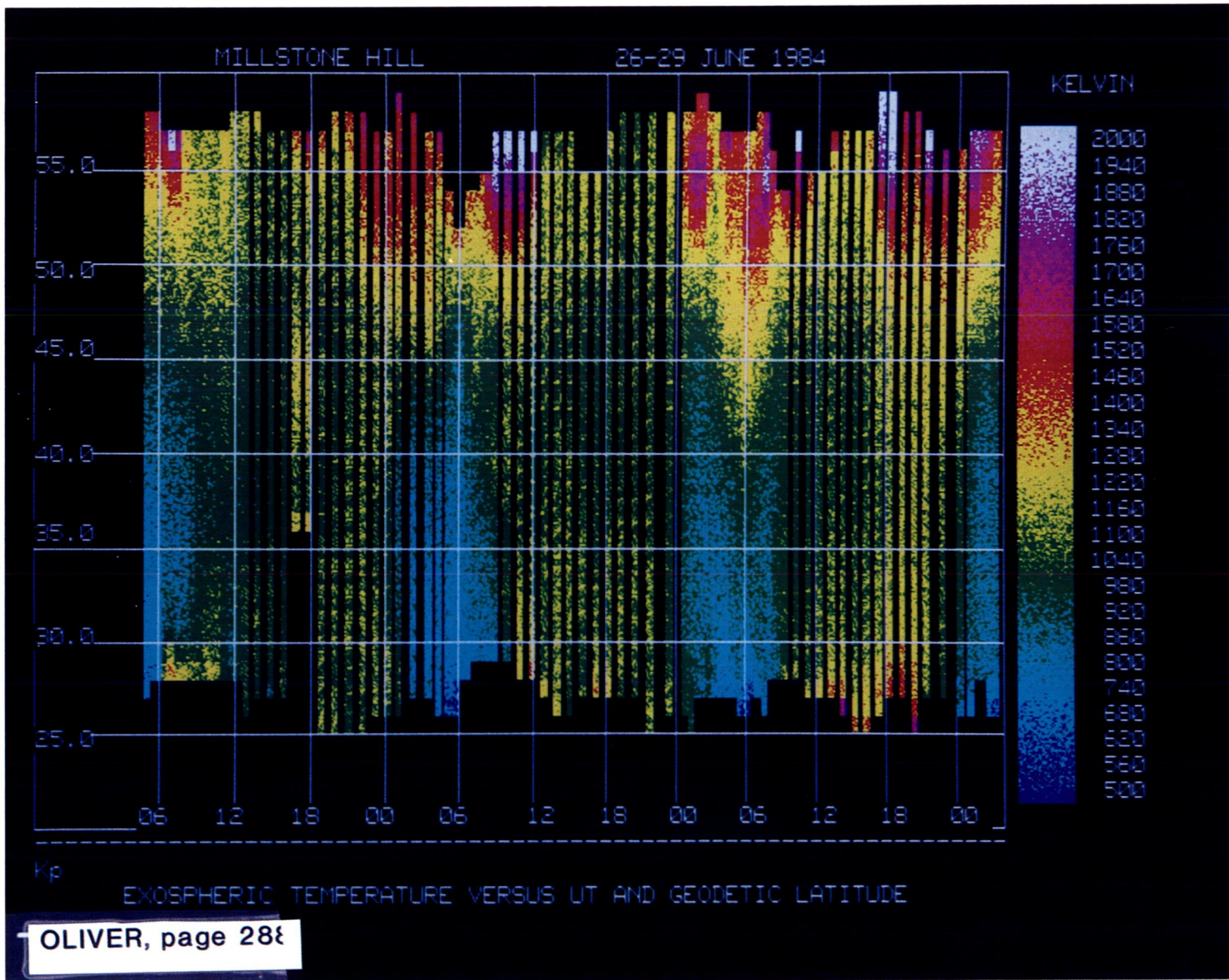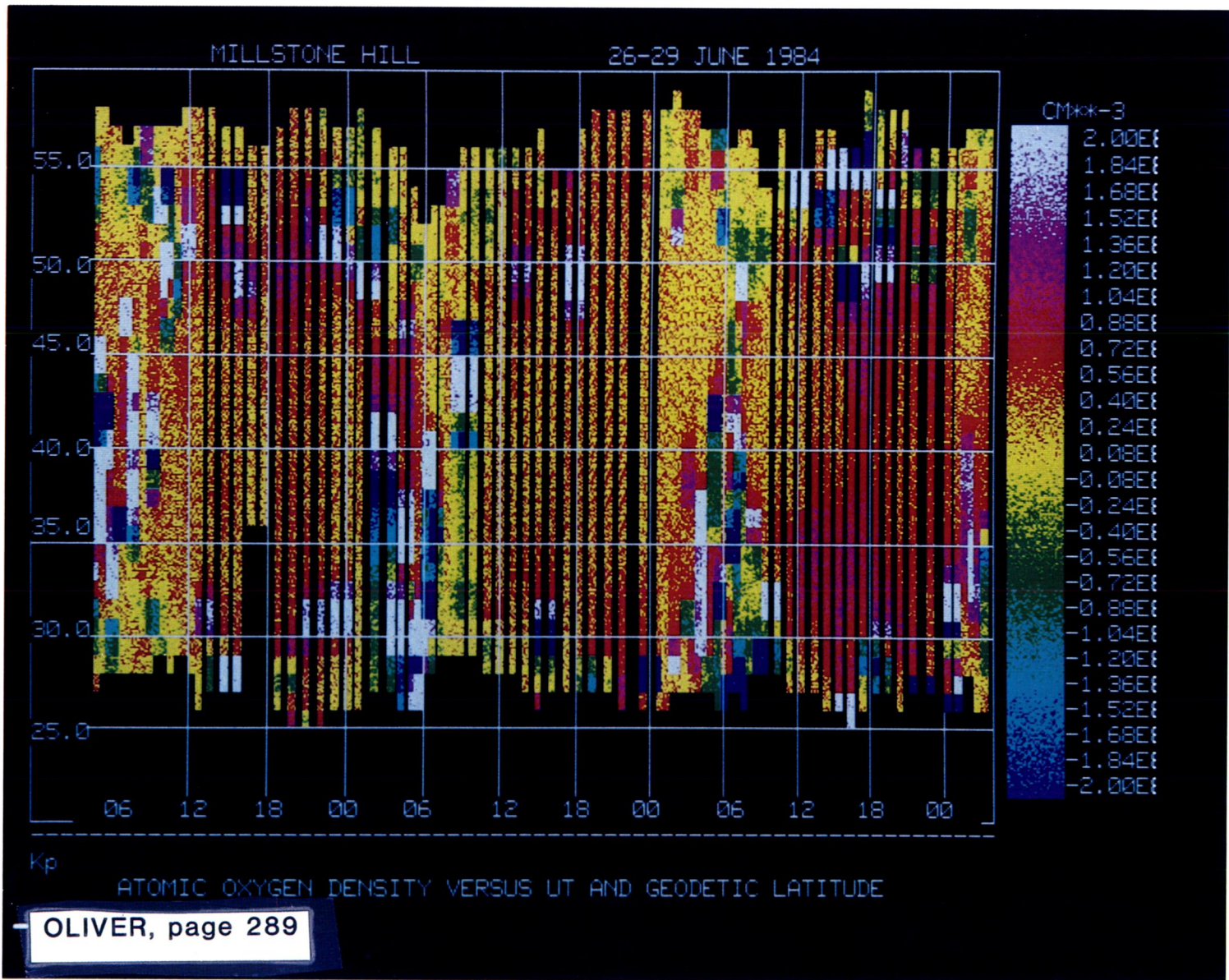
LOG (NE)
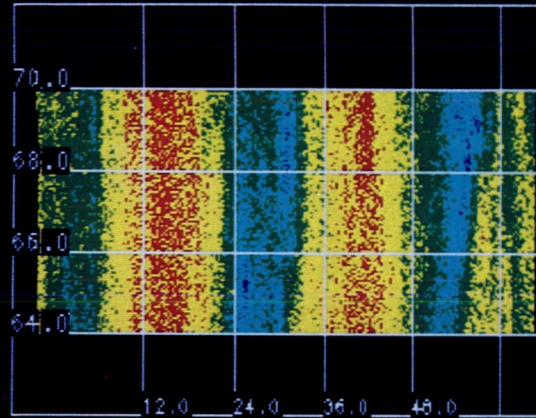
TI (deg K)
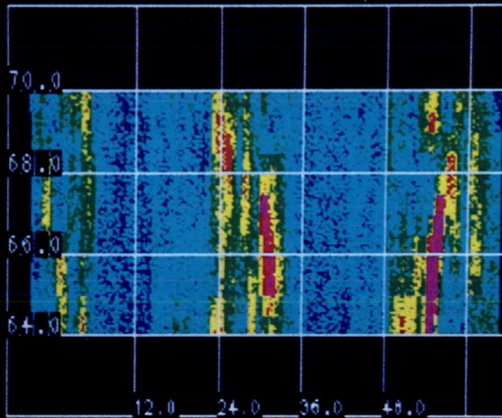
TE (deg K)

VO (m/s)

NE	TI
5.8	2100.
5.7	2000.
5.6	1900.
5.5	1800.
5.4	1700.
5.3	1600.
5.2	1500.
5.1	1400.
5.0	1300.
4.9	1200.
4.8	1100.
4.7	1000.
4.6	900.
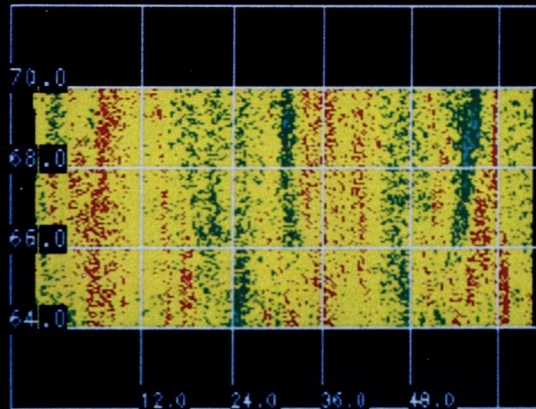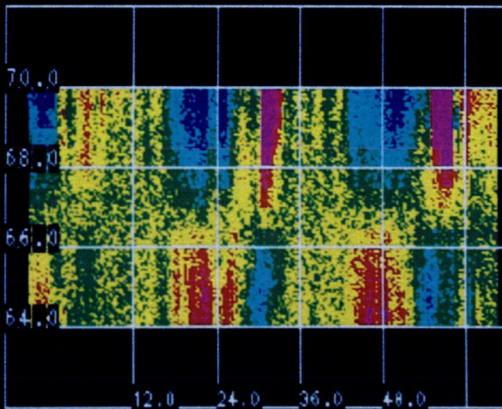
TE	VO
3750.	400.0
3500.	333.3
3250.	266.7
3000.	200.0
2750.	133.3
2500.	66.7
2250.	0.0
2000.	-66.7
1750.	-133.3
1500.	-200.0
1250.	-266.7
1000.	-333.3
750.	-400.0

SONDRESTROM RADAR   26-28 JUNE 1984
LOG(NE), TI, TE, VO vs LT and GEODETIC LATITUDE at 300 km
Elevation scan at 153, 333 deg AZ

OLIVER, page 290

Thermospheric temperatures measured in four directions from Fritz
Peak during the night of 26/27 June 1984.
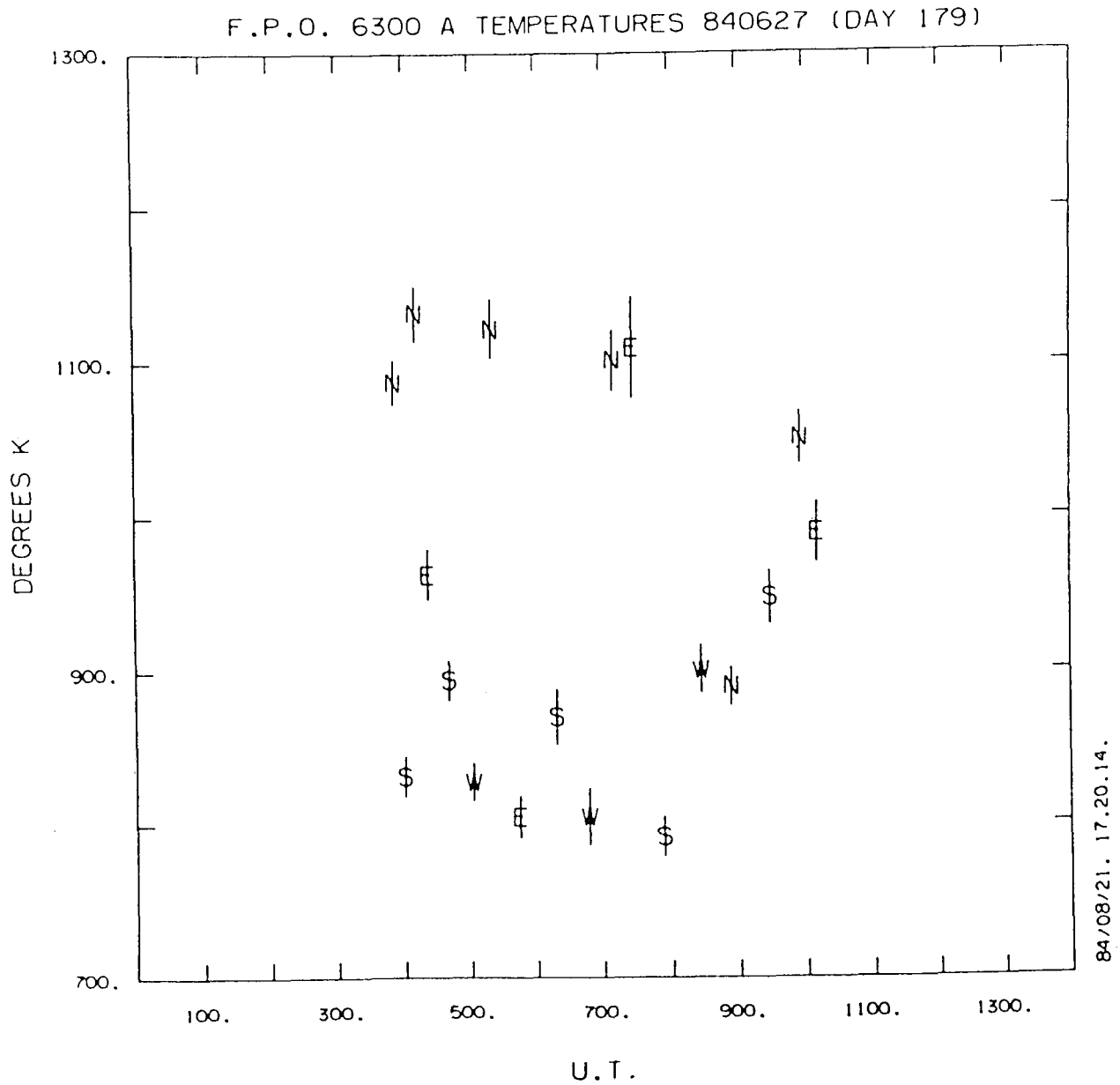
F.P.O. 6300 A TEMPERATURES 840627 (DAY 179)

84/08/21. 17.20.14.

Thermospheric temperatures measured in four directions from Fritz
Peak during the night of 27/28 June 1984.

F.P.O. 6300 A TEMPERATURES 840628 (DAY 180)

Thermospheric meridional winds measured in four directions from
Fritz Peak during the night of 27/28 June 1984.

F.P.O. 6300 A WINDS 840628 (DAY 180)
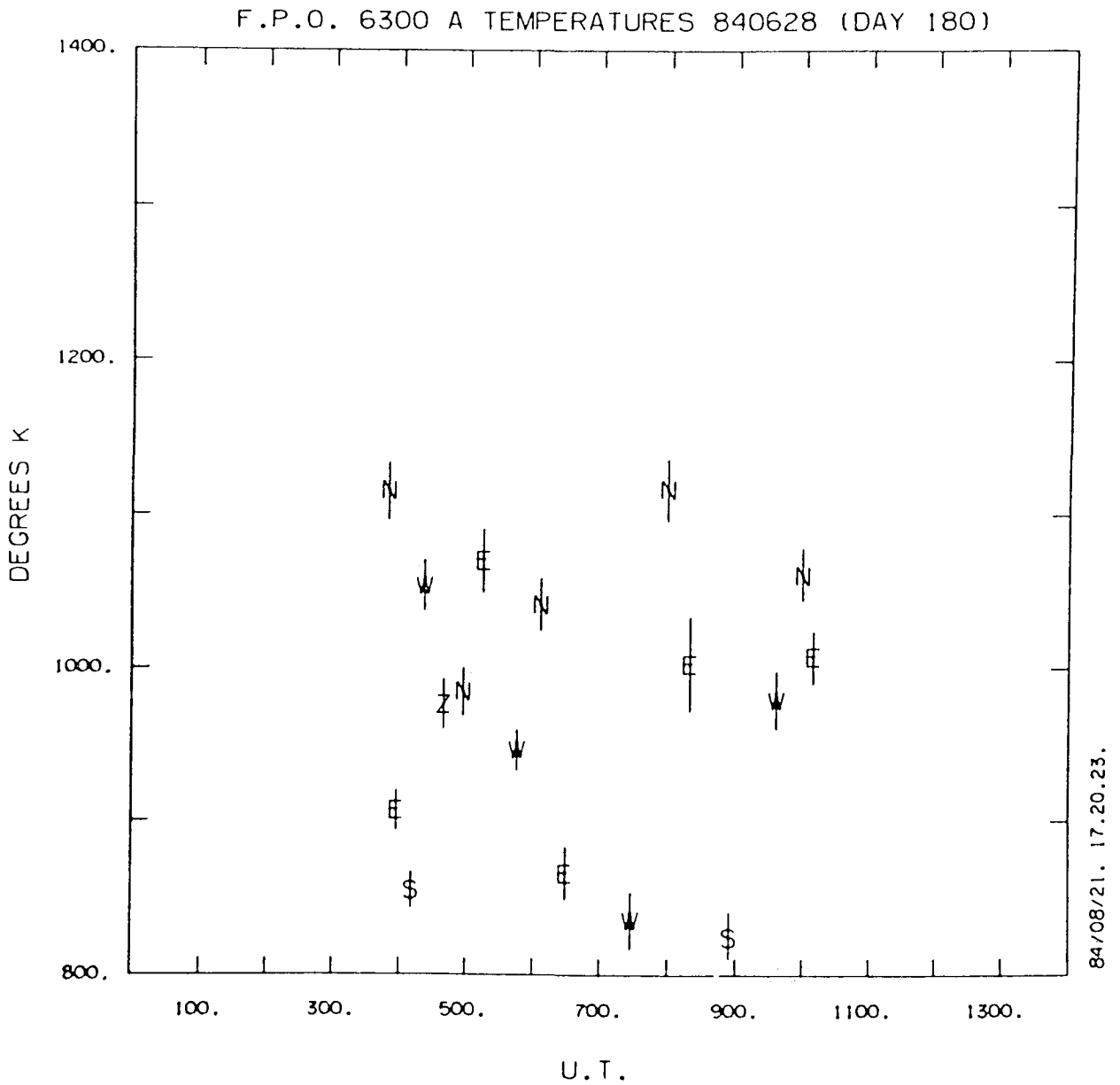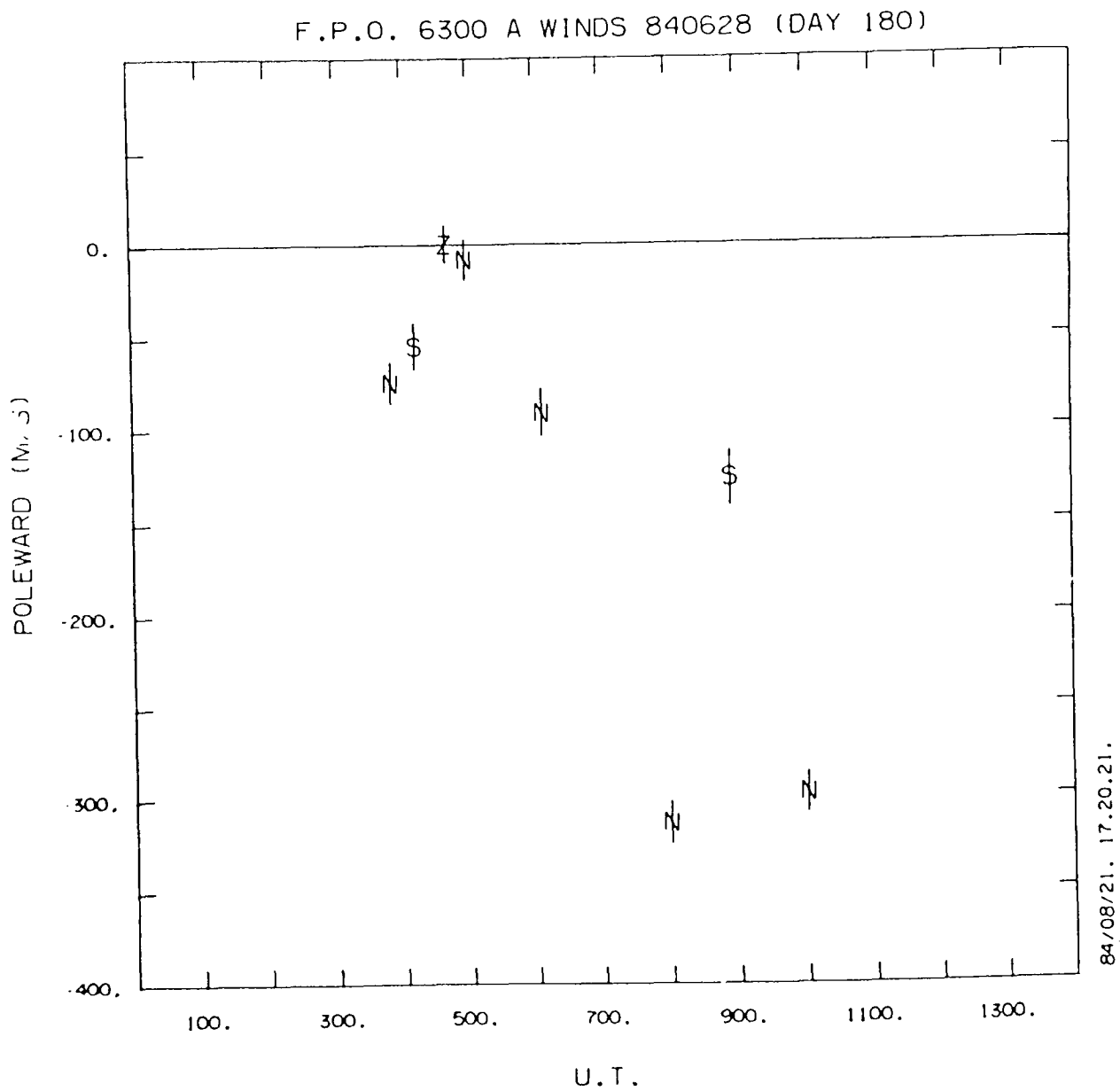
Thermospheric zonal winds measured in four directions from Fritz
Peak during the evening of 27/28 June 1984.

F.P.O. 6300 A WINDS 840628 (DAY 180)

84/08/21. 17.20.22.
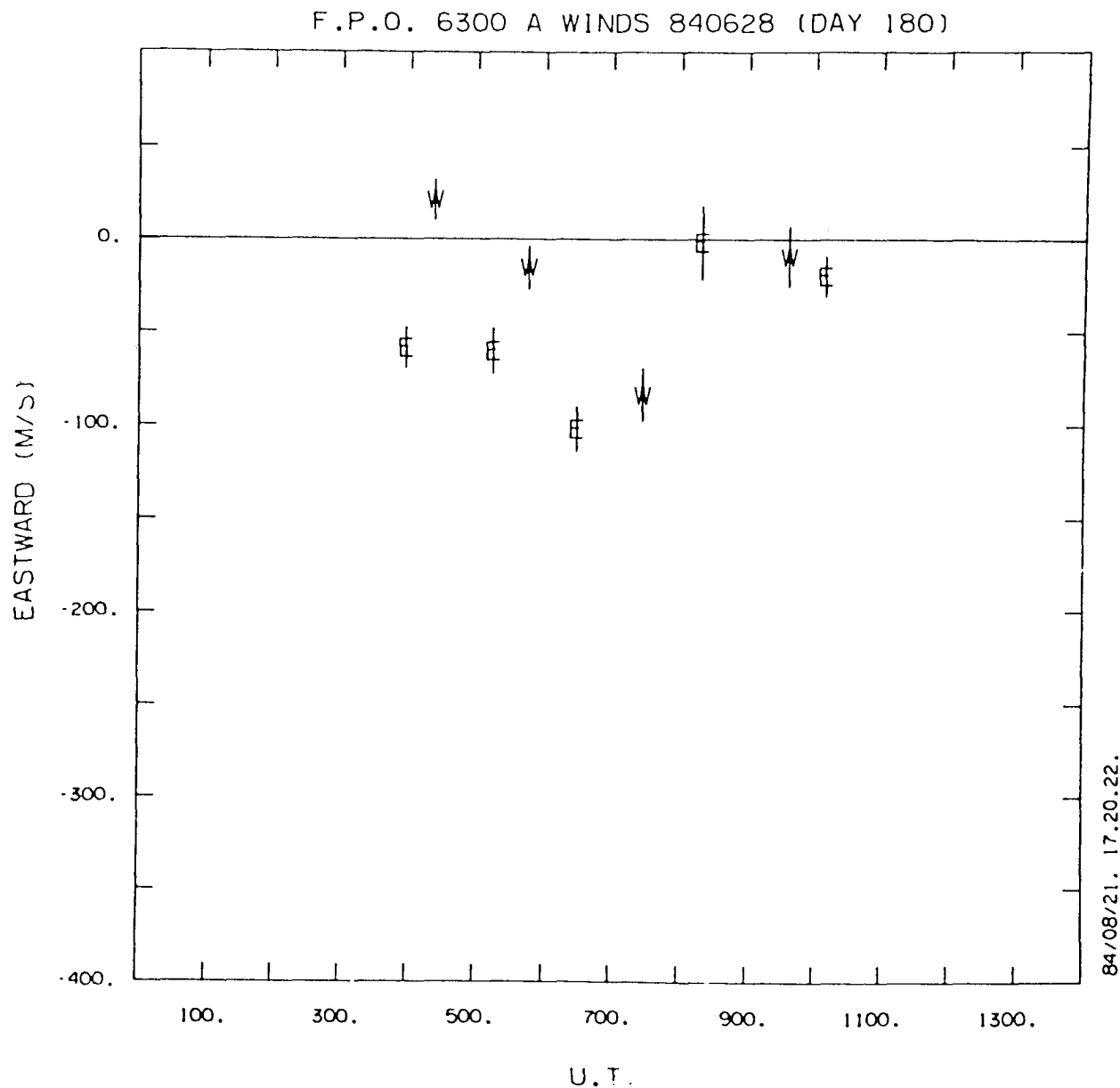
UTIME=12. 0   FIELD=T   Z= 1.0
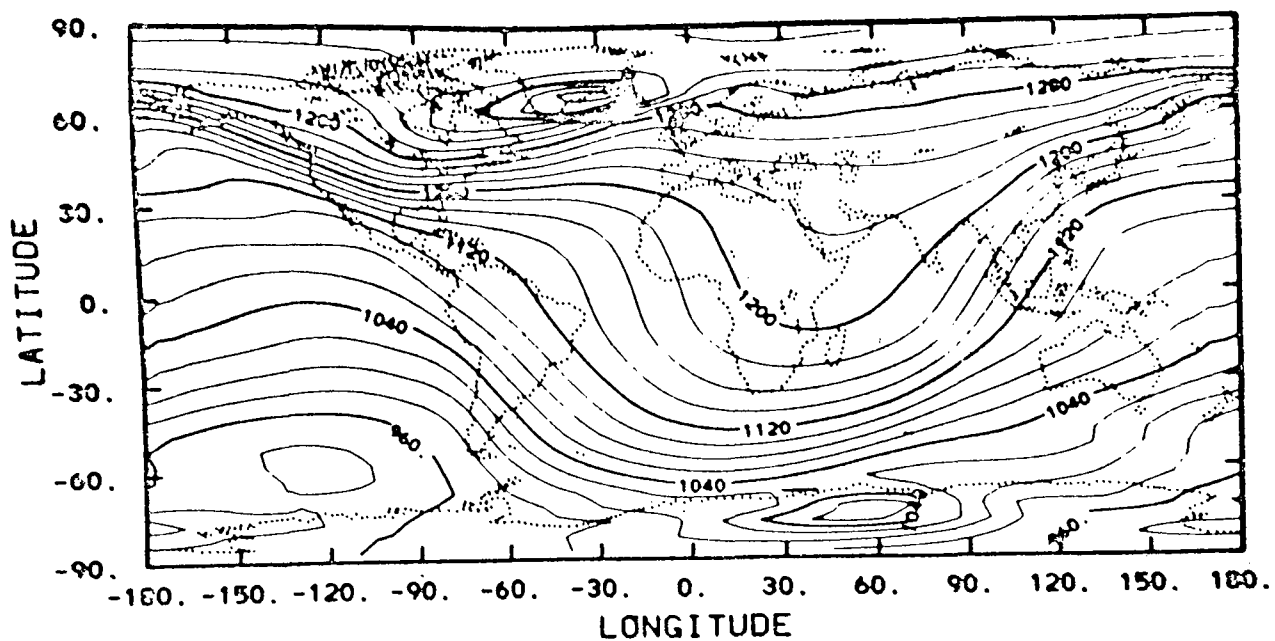
TGCM simulation of the global temperature field at UT=12 hours at
an altitude of about 300 km.

MERIDIONAL WIND (M/SEC)   (62.5, -50.0)
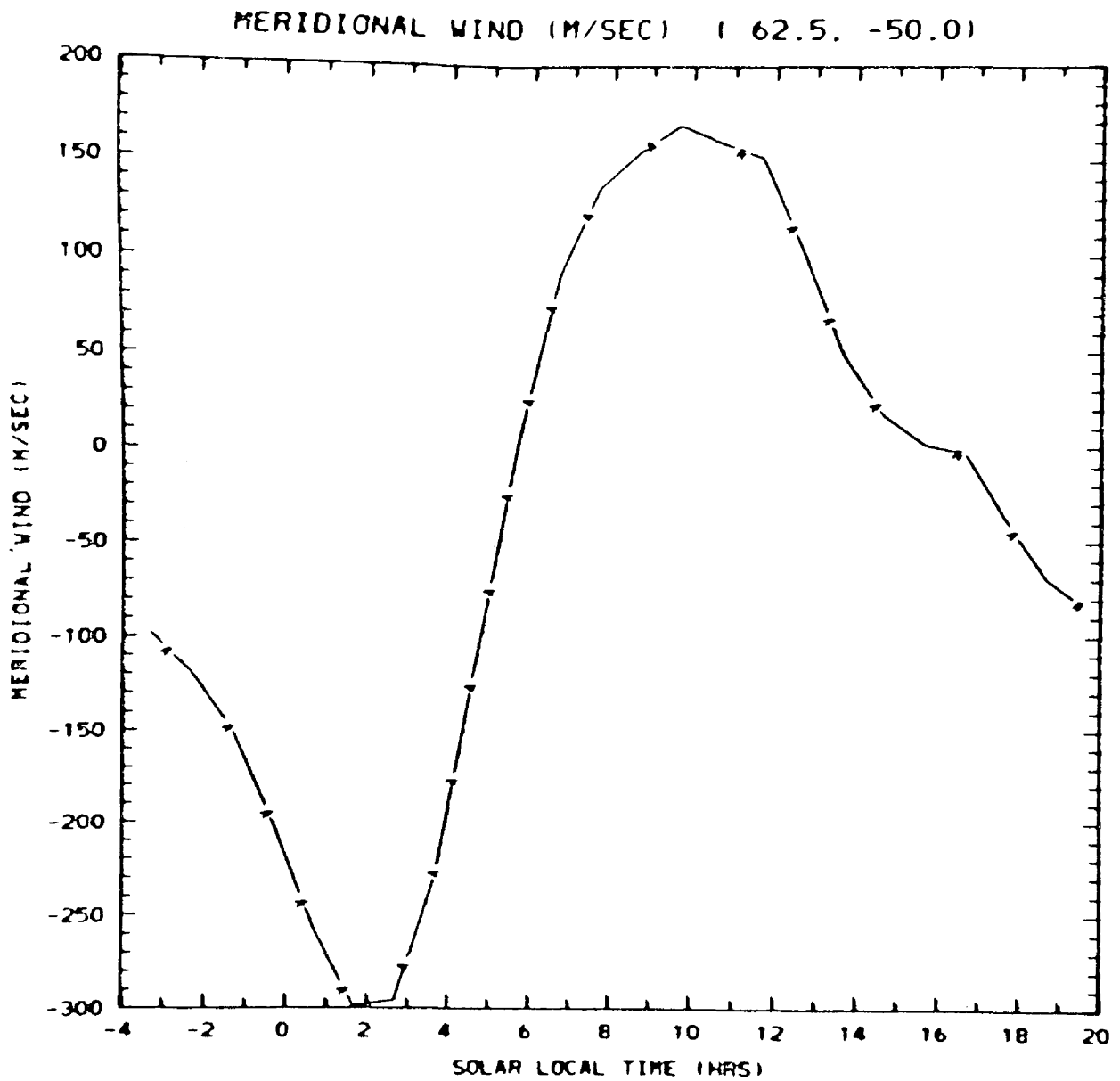
TGCM simulation of the steady-state meridional wind flow at F
region altitudes above Sondre Stromfjord during 26-28 June 1984.

OBSERVATIONS OF VERTICAL WINDS AND
THE ORIGIN OF THERMOSPHERIC GRAVITY WAVES
LAUNCHED BY AURORAL SUBSTORMS AND WESTWARD TRAVELLING SURGES

David Rees
Department of Physics and Astronomy
University College London
Gower Street, London WC1E 6BT, UK

Several sequences of observations of strong vertical winds in the upper thermosphere will be discussed in this paper, in conjunction with models of the generation of such winds. In the auroral oval, the strongest upward winds are observed in or close to regions of intense auroral precipitation and strong ionospheric currents. The strongest winds, of the order of 100 to 200 m/sec are usually upward, and are both localized and of relatively short duration (10 to 20 min). In regions adjacent to those displaying strong upward winds, and following periods of upward winds, downward winds of rather lower magnitude (40 to about 80 m/sec) may be observed. Strong and rapid changes of horizontal winds are correlated with these rapid vertical wind variations. Considered from a large scale viewpoint, this class of strongly time-dependent winds propagate globally, and may be considered to be gravity waves launched from an auroral source. During periods of very disturbed geomagnetic activity, there may be regions within and close to the auroral oval where systematic vertical winds (upward or downward) of the order of 50 m/sec will occur for periods of several hours. Such persistent winds are part of a very strong large scale horizontal wind circulation set up in the polar regions during a major geomagnetic disturbance. This second class of strong horizontal and vertical winds corresponds more to a standing wave than to a gravity wave, and it is not as effective as the first class in generating large scale propagating gravity waves and correlated horizontal and vertical oscillations. A third class of significant (10 to 30 m/sec) vertical winds can be associated with systematic features of the average geomagnetic energy and momentum input to the polar thermosphere, and appear in statistical studies of the average vertical wind as a function of Universal Time at a given location.

INTRODUCTION

Recent papers by Hernandez[1], Meriwether et al[2], and Rees et al[3, 4] have described the observation of significant (20 to 150 m/sec) vertical winds from mid-latitude[1] and from high (auroral) latitude stations[2, 3, 4], using ground-based Fabry-perot interferometers to observe the thermospheric OI 630 nm emission line. Spencer et al[5, 6] have observed similar vertical wind magnitudes in-situ from their satellite-borne WATS (Wind and Temperature Sensor) instruments on Atmospheric Explorer and on Dynamics Explorer.

Such wind magnitudes are at least one order of magnitude larger than the systematic vertical winds (3 -5 m/sec) which can be associated with the diurnal 'breathing' of the thermosphere[7, 8] at upper thermospheric levels (300 to 400 km) in response to solar UV and EUV heating at middle and low latitudes. Generally, the observations of strong vertical winds indicate that there is a rapid

time-variation of such winds, and that the horizontal scale of the regions of strongest upward and downward flow is also relatively limited, of the order of 100 to a few hundred km.

The observations indicate that the strong vertical winds are the result of intense excitation of the middle and upper thermosphere. The source is strong, localized and may vary rapidly with time. Correlated horizontal and vertical wind changes[1,3] suggest that, after the initial excitation, the propagation of the wind disturbance follows the natural thermospheric response to strong excitation, a form of gravity wave propagation, where the disturbances may propagate throughout the entire global thermosphere.

RESUME OF OBSERVATIONS

The most frequently observed class of strong (> 50 m/sec) vertical wind disturbance[3] is associated with auroral substorms and westward-travelling-surges, and similar energetic auroral phenomena. On examining the data from several hundred nights when observations of thermospheric winds are available from Kiruna Geophysical Institute (67 N, 22 E geographic), a location within the auroral oval, it would appear that such disturbances are observed, on average, about one in two or three nights of clear sky observations, for the geomagnetic activity conditions of the period late 1980 to late 1983.

The observations indicate that when any substorm or westward travelling surge occurs equatorward of the observing station, or propagates from equatorward to overhead, strong upward vertical winds will be observed immediately prior to the arrival of the surge or substorm, as seen in the auroral emissions (particularly in OI 630 nm). Associated with the strong upward winds is an outward explosion of the horizontal winds.

There is a high degree of correlation between the vertical and horizontal wind changes, which will be described in reference to three particular examples. Events which occur poleward of the observing station create similar changes of the horizontal wind, and although the vertical wind changes are not usually observed as clearly for such events, this has to be purely a result of less favourable observing geometry.

I. Nov 23/24 1982

Figure 1 shows the combined horizontal and vertical wind observations from KGI during the night of Nov 23/24 1982. There was a major substorm and westward travelling surge about 19 UT, which propagated toward and overhead Kiruna from the southeast. This propagation can be inferred from the OI 630 nm intensity observations. Following a general increase in the magnitude of westward and equatorward winds between 18.00 UT and about 18:40 UT, there was an short-lived period of extremely strong upward winds (up to 165 m/sec) starting about 18.50 UT, which coincided with a sudden reversal in the meridional wind as observed to the north of Kiruna.

Note: all of the observations of the 'horizontal' winds were made at a zenith distance of 60 degrees. For a mean emission altitude of 240 km, this observing region is some 400 km away from Kiruna along the specific viewing direction.

After 19.20, the strong upward vertical winds subsided, and the meridional wind, to the north of Kiruna, reverted to a strong equatorward value (400 m/sec). The degree of correlation between changes in the various wind components, and the nature of the 'outward explosion' of the winds during the disturbance is illustrated further in Figure 2. There were at least two surges of the equatorward wind observed to the south of Kiruna, during the period 19.00 to 20.30 UT, which could be associated with this period of intense auroral activity.

Later in the night, up to midnight UT, there were several significant fluctuations of the vertical wind, of the order of 50 m/sec. These fluctuations are difficult to relate to local auroral activity, and may reflect the propagation of waves from more distant auroral disturbances.

II. Feb. 4/5 1983

Wind observations during a second disturbed night (Feb 4/5 1983) are shown in Figure 3. There were several fluctuations of the vertical wind up to about 20 UT, and then there was a short period of violent (150 m/sec) upward wind centered about 21 UT. Immediately before and after the period of strongest upward winds, there was a short period of 50 m/sec downward winds. As with the wind observations of the Nov 23/24 period, there was again a strong reduction of the equatorward wind observed to the north of Kiruna during the period around that when the strongest upward winds occurred.

A significant feature of the auroral activity of both these periods was that the auroral activity was mainly equatorward of Kiruna.

III. Dec. 7/8 1982

To contrast with observations which are typical of strong events where the main auroral and electrojet activity occurs equatorward of Kiruna, the data obtained on Dec. 7/8 1982 will be shown. Between 19.00 and 20.00 UT, the wind component observed in the northwest direction changed by about 600 m/sec, with rather smaller changes in all other directions. The vertical wind during this event was, however, strongly downward (50 m/sec). The main auroral activity and the centre of the auroral electrojet were north of Kiruna.

This difference in location of the main auroral activity relative to Kiruna explains the different vertical wind behaviour which was observed caused by the two rather similar geomagnetic events. The comparison of the two events also defines the spatial extent of the region of strong upward winds rather well.

When the major region of heating is overhead or to the north (poleward) of Kiruna, by perhaps 200 km, the equatorward and poleward wind explosion is observed. This is associated with a region of downward winds overhead Kiruna, as the atmosphere relaxes on leaving the region of intense heating. When the strong heating is about 200 km equatorward of Kiruna, rather than directly overhead or poleward, the effects of the heating in driving upward and poleward winds are directly observable.

Part of the explanation is due to the combination of the observing geometry and the geometry of the earth's magnetic field. OI 630 nm is generated from regions (200 to 300 km) which are significantly higher than those where the particle and frictional heating maximises during auroral substorms (120 to 160 km). The region of maximum heating would thus be expected to be somewhat poleward (~ 50 km) of the region of maximum OI 630 nm emission, assuming that they were related. In practice, it might appear from some of the time-variations observed in OI 630 nm and the wind variations that the regions of highest heating were rather further poleward (100-200 km) of the maximum OI 630 nm emissions.

From the auroral intensity data obtained during these rather representative events, the latitudinal extent of the regions generating the strongest upward winds appeared to be about 200 km. The longitudinal extent is probably of the order of 1000 km, but will be related to the specific morphology of a given auroral event.

PERIODS OF SYSTEMATIC LARGE VERTICAL WINDS DURING MAJOR GEOMAGNETIC DISTURBANCES

In Figure 5, some of the wind observations made from Kiruna during the afternoon of Dec. 17 1982 are shown. Very fast westward winds occurred during the early part of the afternoon, peaking in excess of 900 m/sec, mainly westward and northwestward in direction. Throughout the period from 13:30 UT to 17:00 UT (3.5 hours), there was a mean downward vertical wind of the order of 50 m/sec. Kiruna was located on the poleward side of the main part of the greatly expanded auroral oval during this extremely disturbed period. The combination of extremely rapid westward winds, driven[9] by ion drag in the auroral oval, and downward winds appear to be part of a form of standing wave, with the atmosphere relaxing as it leaves a region of intense acceleration and heating (the dusk auroral oval).

Systematic mean vertical winds of the order of 10 to 20 m/sec have also been found[3] in statistical analyses of many days of thermospheric wind observations from both Skibotn (Norway) and Svalbard (Spitzbergen, 16 E 79 N). These mean vertical winds appear to be consistent and reproducible signatures of the geomagnetic forcing of the auroral and polar thermosphere, and are distinct from the strong time-dependent winds discussed above.

THEORETICAL EXPLANATION AND SIMULATION OF INTENSE VERTICAL WINDS

Figure 6 displays the simulated horizontal (vector) and vertical (scalar) wind component distributions over the northern, winter, polar region during a period of relatively quiet geomagnetic conditions. This is a quasi-steady state simulation, the only time-dependence being due to the rotation of the earth, carrying the offset geomagnetic polar regions around the geographic poles, and thus varying the location, and solar photo-ionisation and insolation, of the geomagnetic polar regions as a function of UT.

There is weak upwelling at low and middle latitudes on the dayside, and weak downwelling on the nightside at middle latitudes, except for a small, post-midnight, region of weak upwelling associated with the 'post-midnight bulge', and its temperature/thermospheric wind anomaly. The geomagnetic polar region contains regions of significant upwelling (3 to 10 m/sec) around the boundaries of the auroral oval, and over the central polar cap. There are also regions of weak downwelling in the poleward boundaries of the dusk and dawn parts of the auroral oval.

In Figure 7, the horizontal and vertical wind distribution is shown for a second quasi-steady state simulation which uses a geomagnetic input within the polar regions[4] corresponding to moderately disturbed conditions ($Kp \sim 4$). Upward wind velocities are considerably enhanced, with peak values of the order of 40 m/sec in the dayside cusp. Regions of moderate downward winds (10 m/sec) border the regions of upwelling. The peak upward winds of 40 m/sec in the dayside cusp are generated by a combination of convergence from the dusk and dawn auroral oval, frictional heating within the dayside auroral oval, and a soft 'cusp' electron source of the order of 4 ergs/cm^{2}.

Figures 8, 9 and 10 show, with the same presentation as Figures 6 and 7, the circulation changes which develop during a simulated geomagnetic (auroral) substorm[4] in the region near magnetic midnight.

The simulated disturbance is started at 20.4 UT (Figure 8), with a large input of energy into a limited region of the auroral oval close to magnetic midnight. There is an immediate response in the vertical wind, with upward velocities of the order of 200 m/sec throughout the region where the peak energy input (100 ergs/cm^{2}) has been dumped. Horizontal wind changes occur with a

300

slight delay, but within 30 min (at 20.9 UT, Figure 9), there is a major expansion of the atmosphere horizontally, as well as vertically, away from the region of intense energy input. The equatorward and poleward wind surges generated by the large input can be easily seen propagating away from the vicinity of the simulated substorm. Large equatorward winds have reached a latitude of 50 degrees in the midnight region, from their source latitude of 70 degrees, withinn 30 min of the substorm onset.

The major 'substorm' source of energy is cut off at 20.9 UT, allowing a recovery from the disturbance. By 21.6 UT (Figure 10), the wind distribution within the polar cap and auroral oval has returned to a state close to the initial state. However, at lower geomagnetic latitudes, large wind disturbances continue to propagate equatorward for several more hours. By 21.6 UT, the disturbances have reached 30 degrees latitude, and within a further hour (2.2 hours after onset), the propagating waves from the northern polar region meet with those generated in the southern hemisphere near the equator.

Figures 9 and 10 display the extent to which these propagating waves have correlated vertical and horizontal wind oscillations. At a particular mid-latitude ground-based station, the vertical and horizontal winds will both oscillate quasi-periodically as the series of gravity waves propagate past the station.

The wind disturbances set up by a single geomagnetic pulse, with a simple geometrical and time-dependent variation of the geomagnetic energy inputs, are quite complex, and there is also a complicated local time/longitudinal structure. The simulated disturbances correspond quite well to the time-dependent observations reported[1, 3], and have many of the features of the theoretical gravity waves which have been generated in previous linear two-dimensional models.

During extremely disturbed periods, the auroral oval expands equatorward, there is a considerable increase in the cross-polar cap electric potential, and the total deposition of geomagnetic energy in both polar regions may exceed 10^{12} watts. The effects of such conditions on the thermosphere can be estimated from Figure 11, which is taken from a simulation generated to correspond to an event observed on Dec 12 1981. This event was qualitatively similar to the one observed on Dec 17 1982, described previously.

Extremely large sunward horizontal winds occur in the dusk and dawn parts of the auroral oval, particularly in the dusk oval (near 1 km/sec), and there are also strong anti-sunward winds of close to 800 m/sec over much of the polar cap. The vertical winds generated under such conditions are qualitatively similar to those shown in Figure 7, but with a factor of 2 to 4 increase in magnitude. For example, the downward winds of 10 m/sec which occur on the poleward boundary of the dusk auroral oval are increased to about 40 to 60 m/sec. It would appear that this is the simplest mechanism which can account for the persistent 50 m/sec downward winds observed from Kiruna during the disturbance of Dec 17 1982. The persistent downward winds exist as a 'standing wave', where the atmosphere is relaxing after intense acceleration and heating in the dusk auroral oval.

Under less disturbed conditions, the persistent diurnal variation of vertical wind behavior observed at polar and auroral locations can also be explained in a similar way. There is considerable day to day variation in this behaviour, which can be related to the complex time-dependent variations of individual geomagnetic disturbances.

SUMMARY

Vertical winds of the order of 5 to 10 m/sec or larger are a persistent feature of the polar upper thermosphere. The signature of geomagnetic heating of the upper thermosphere under relatively quite geomagnetic conditions can explain average upward and downward winds of such

magnitudes which are observed in systematic studies. Such magnitudes exceed the average diurnal variations associated with the thermospheric 'breathing' in response to solar UV and EUV heating at low and middle latitudes.

Violent excursions of the vertical wind, of short duration, typically 10 to 20 min, where upward velocities of 200 m/sec may be observed at times, and with large correlated changes of the horizontal wind, can be associated with intense auroral substorms and similar energetic events (Westward Travelling Surges, etc). Such events generate a localized explosion of the upper themosphere. Away from the source region, the propagating waves from such events are essentially the thermospheric gravity waves launched from an auroral source. These waves propagate globally, and leave the mid-latitude thermosphere 'ringing' for many hours, as the gravity waves propagating form both hemispheres interact. During periods of moderate to intense geomagnetic activity, the wave patterns may become so complex that it is impossible to identify individual disturbances by their correlated horizontal and vertical wind changes (10 to 30 m/sec at mid-latitudes, rather than the 100 m/sec observed at auroral latitudes).

During extremely disturbed periods, standing waves may be generated, with embedded regions of large (upward and downward) vertical winds (50 m/sec), associated with, or adjacent to, regions of horizontal winds of the order of 500 m/sec. Although these may be the signature of the deposition of intense geomagnetic heating of the thermosphere, their long duration, sometimes exceeding 4 to 6 hours, implies that they are less efficient generators of gravity waves than the source associated with auroral substorms in the magnetic midnight region.

It is not possible to identify from the FPI observations alone the combination of heating sources which contribute to generating the strong vertical winds. The 3-D T-D model allows various mixes of heat sources to be tested. If the source were kilo-volt auroral electrons, a deposition rate in excess of 100 erg/cm^2/sec would be required to explain 100 m/sec upward winds (with the 10 min observed duration). Satellite observations of precipitation include such values, but probably too rarely to explain the frequency of strong upward vertical winds.

A significant or large contribution from supra-thermal or low energy electrons would decrease the demand on total energy input considerably, since these electrons heat the thermosphere at levels where the generation of large vertical winds is more efficient (per unit energy deposition rate).

There are objections to this source as a sole generator of strong vertical winds. Firstly, even modest (10 − 20 ergs/cm^2/sec) of 5 to 10 ev electrons require very large number fluxes of electrons, which may not be consistent with potential source regions. Secondly, there is little supporting data from satellite or ground-based auroral morphology studies. In particular, the FPI itself tends to observe the largest vertical winds in regions which are poleward, but immediately adjacent, to regions where the substorm- or surge-associated enhancement of OI 630 nm emission occurs.

A third contributor to the energy requirements could be intense frictional and Joule heating in the region of, and immediately adjacent to, the substorm- and surge activity. Intense field-aligned currents are known, from recent satellite observations, to complete the magnetospheric circuit associated with substorm and surge current systems in adjacent regions which are not strongly excited by auroral precipitation. The strong horizontal currents required to complete the circuit of upward and downward field-aligned currents have to flow through regions where the ionospheric conductivity is not particularly enhanced. This implies that the Joule and frictional heating rates might be quite intense, and a valuable contributor to the total heating demanded by the observed strong vertical winds. Measurements of the state of the ionosphere, and its current and electric field systems, in regions adjacent to substorms and surges have, as yet, provided rather inadequate

results to fully test and complete the menu of geomagnetic heat sources contributing to these violent and rather fascinating wind disturbances.

Acknowledgements

REFERENCES

1. HERNANDEZ, G. (1982) Vertical motions of the neutral thermosphere at midlatitude. Geophys. Res. Lett. 9, 555.
2. MERIWETHER, J. (1983) Private Communication.
3. REES, D., SMITH, R. W., CHARLTON, P. J., MCCORMAD, F. G., LLOYD, N., and AKE STEEN. The generation of vertical thermospheric winds and gravity waves at auroral latitudes-I. Observations of vertical winds. Planet. and Sp. Sci. 32, 667-684.
4. REES, D., SMITH, M. F., and GORDON, R. The generation of vertical thermospheric winds and gravity waves at auroral latitudes-II. Theory and numerical modelling of vertical winds. Planet and Sp. Sci. 32, 685-705.
5. SPENCER, N. W., THEIS, R. F., WHARTON, L. E. and CARIGNAN, G. (1976) Local vertical motions and kinetic temperature from AE—C as evidence for aurora-induced gravity waves. Geophys. Res. Lett. 3,313.
6. SPENCER, N. W., WHARTON, L. E., CARIGNAN, G. and MAURER, J., (1982) Thermosphere zonal winds, vertical motions and temperature as measured for Dynamics Explorer. Geophys. Res. Lett. 9, 953.
7. GEISLER, J. E. and DICKINSON, R. E. (1968) Vertical motions and nitric oxide in the upper mesosphere. J. atmos. terr. Phys. 30, 1505.
8. HERNANDEZ, G. and ROBLE, R. G., (1979) On divergences of the thermospheric meridional winds at midlatitudes. Geophys. Res. Lett. 6, 294.
9. REES, D., FULLER-ROWELL, T. J., SMITH, M. F., GORDON, R., KILLEEN, T. L., HAYS, P. B., SPENCER, N. W., WHARTON, L. and MAYNARD, N. C. (1985). The Westward jetstream of the evening auroral oval (accepted by Planet. and Sp. Sci.)
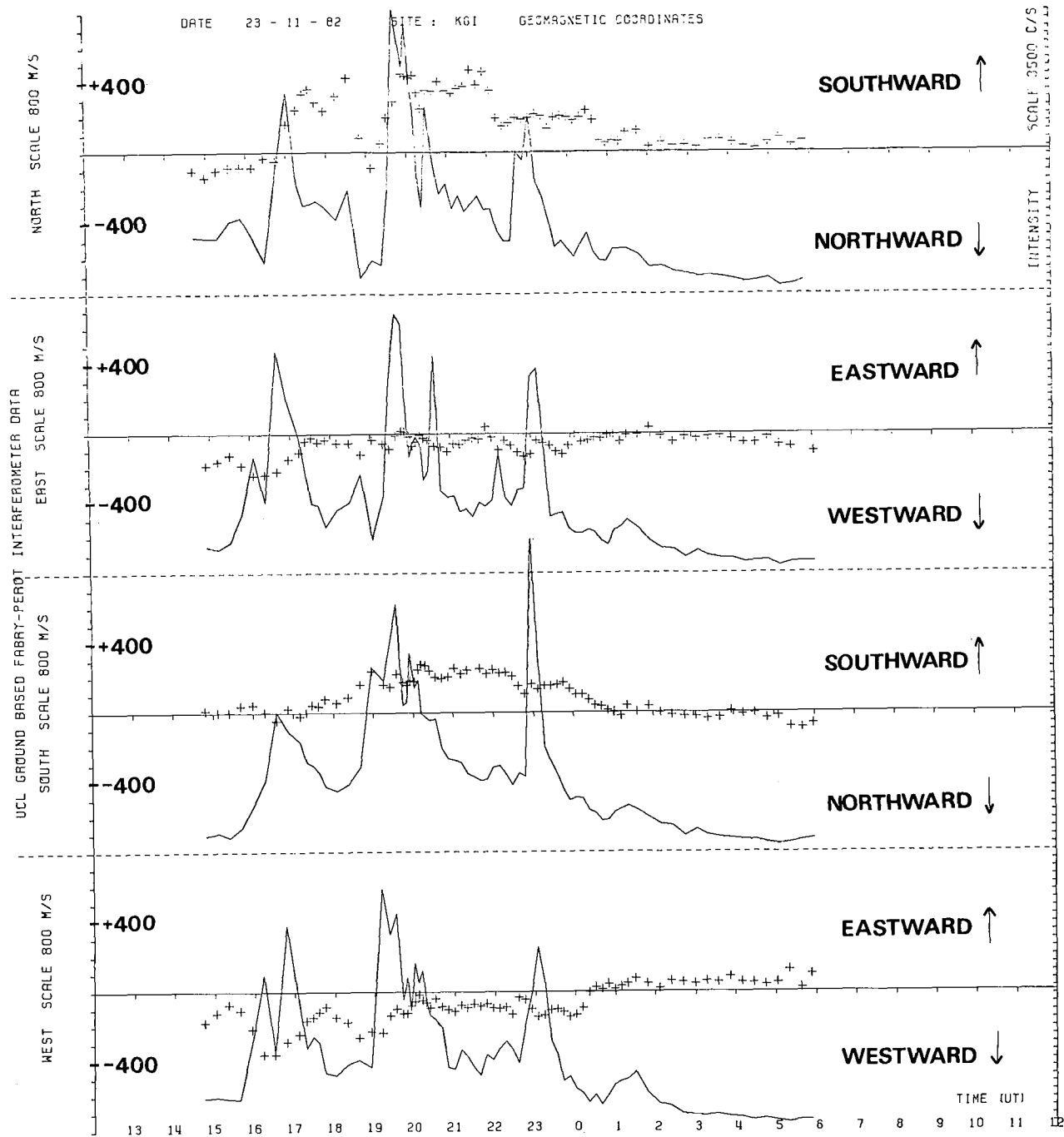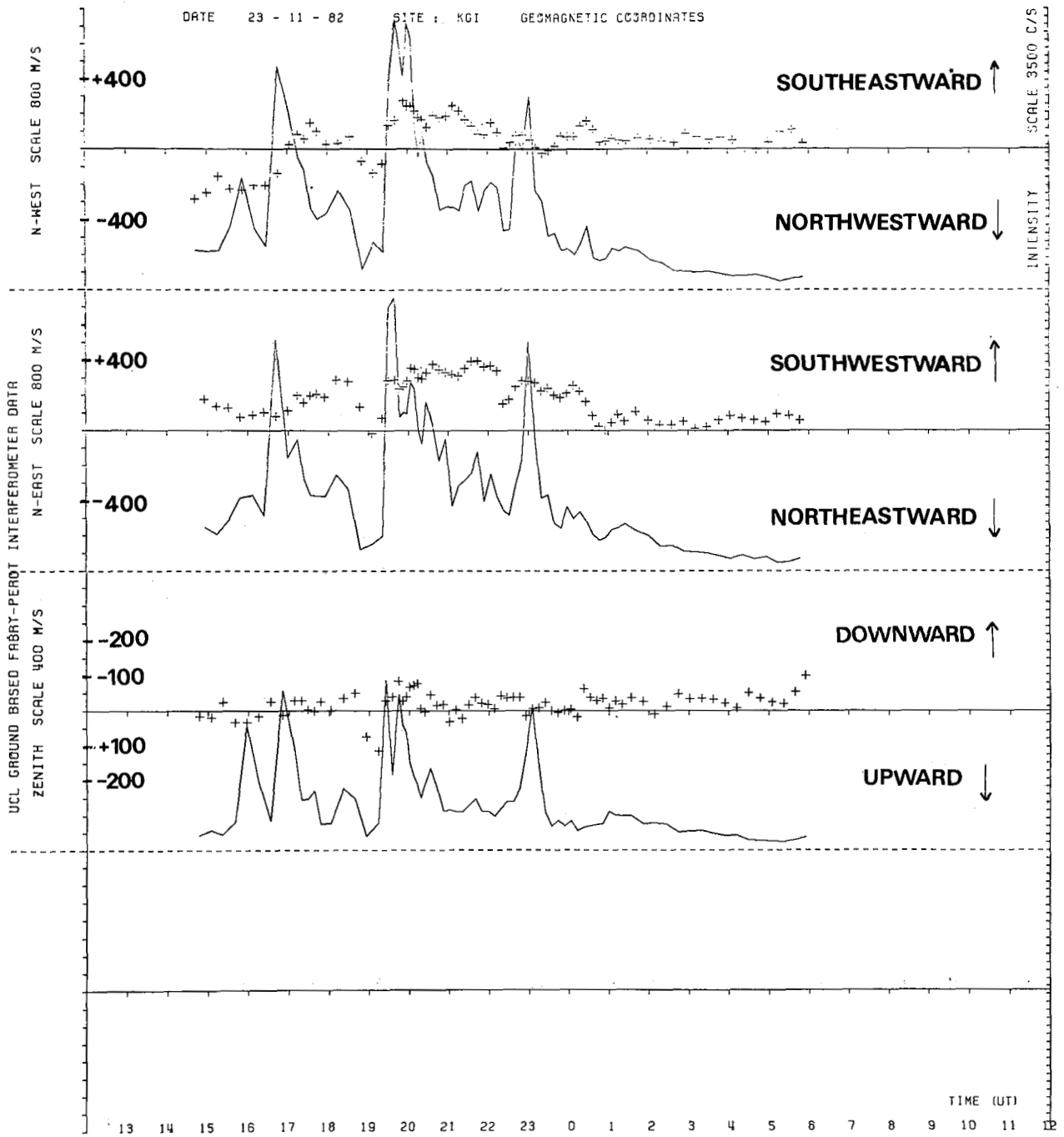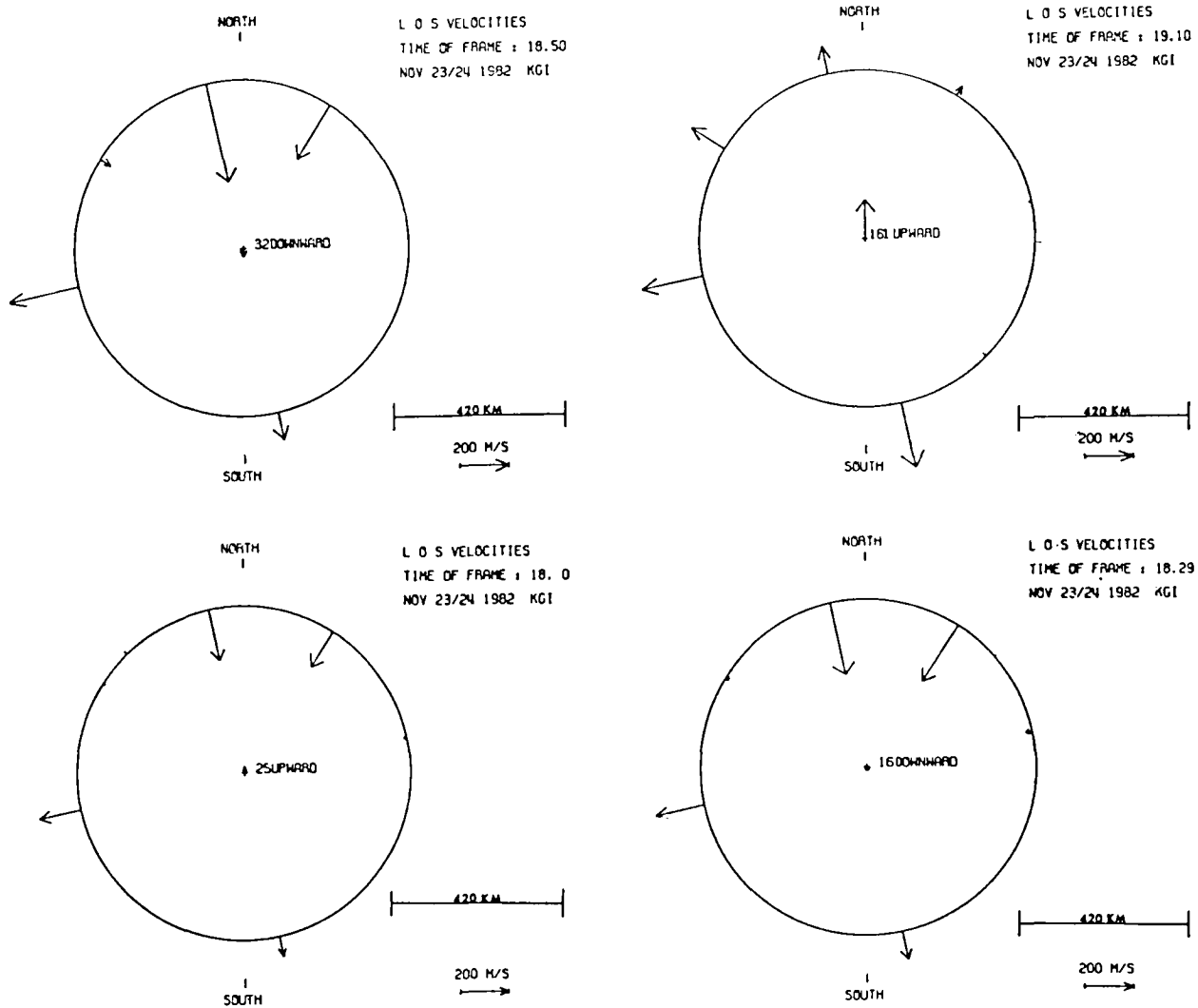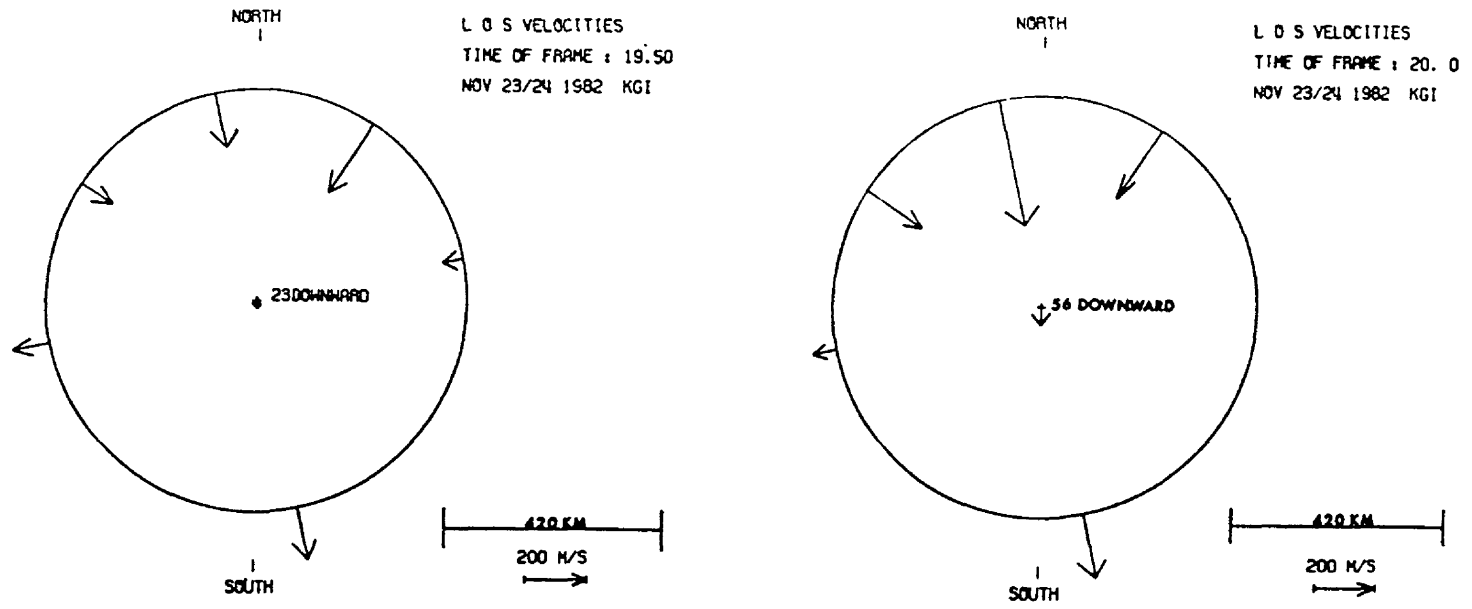
Figure 1a. Thermospheric wind observations in the N, NE, E, S, W, NW and Vertical Directions from the FPI at Kiruna Geophysical Institute on the night of 23/24 Nov 1982. The major focus of interest is the correspondence between changes observed in each of the viewing directions in the period 18.00 to 20.00 UT before, during and after the strong geomagnetic disturbances around 19.00 UT. Observed winds are indicated by the crosses (+), and the OI 630 nm emission intensity by the continuous line.

305

Figure 1b. Continuation of Figure 1.

NORTH

L O S VELOCITIES
TIME OF FRAME : 18.50
NOV 23/24 1982 KGI

3200HNWARD

420 KM

200 M/S

SOUTH

NORTH

L O S VELOCITIES
TIME OF FRAME : 19.10
NOV 23/24 1982 KGI

161 UPWARD

420 KM

200 M/S

SOUTH

NORTH

L O S VELOCITIES
TIME OF FRAME : 18. 0
NOV 23/24 1982 KGI

25UPWARD

420 KM

200 M/S

SOUTH

NORTH

L O S VELOCITIES
TIME OF FRAME : 18.29
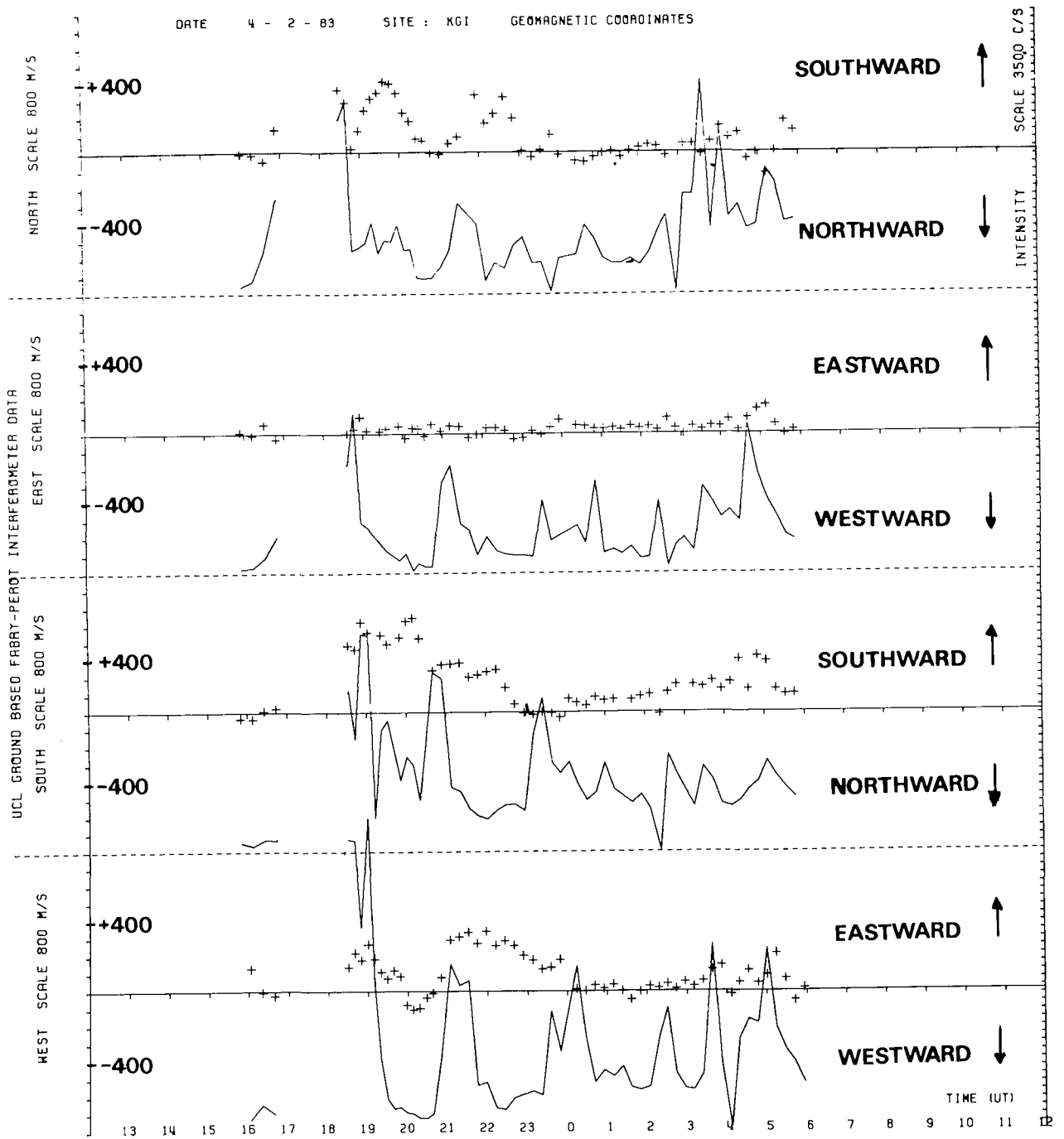NOV 23/24 1982 KGI

1600HNWARD

420 KM

200 M/S

SOUTH

Figure 2a. Thermospheric wind observations in the N, NE, E, S, W, NW and Vertical Directions from the FPI at Kiruna Geophysical Institute on the night of 23/24 Nov 1982. The period 18.00 to 20.00 UT before, during and after the strong geomagnetic disturbances around 19.00 UT is examined in detail, with the instantaneous wind distribution being shown at times between 18.00 and 20.00 UT, to place the vertical winds in the context of the horizontal circulation.

NORTH

L O S VELOCITIES
TIME OF FRAME : 19.50
NOV 23/24 1982 KGI

2300WNWARD

SOUTH

420 KM

200 M/S

NORTH

L O S VELOCITIES
TIME OF FRAME : 20. 0
NOV 23/24 1982 KGI

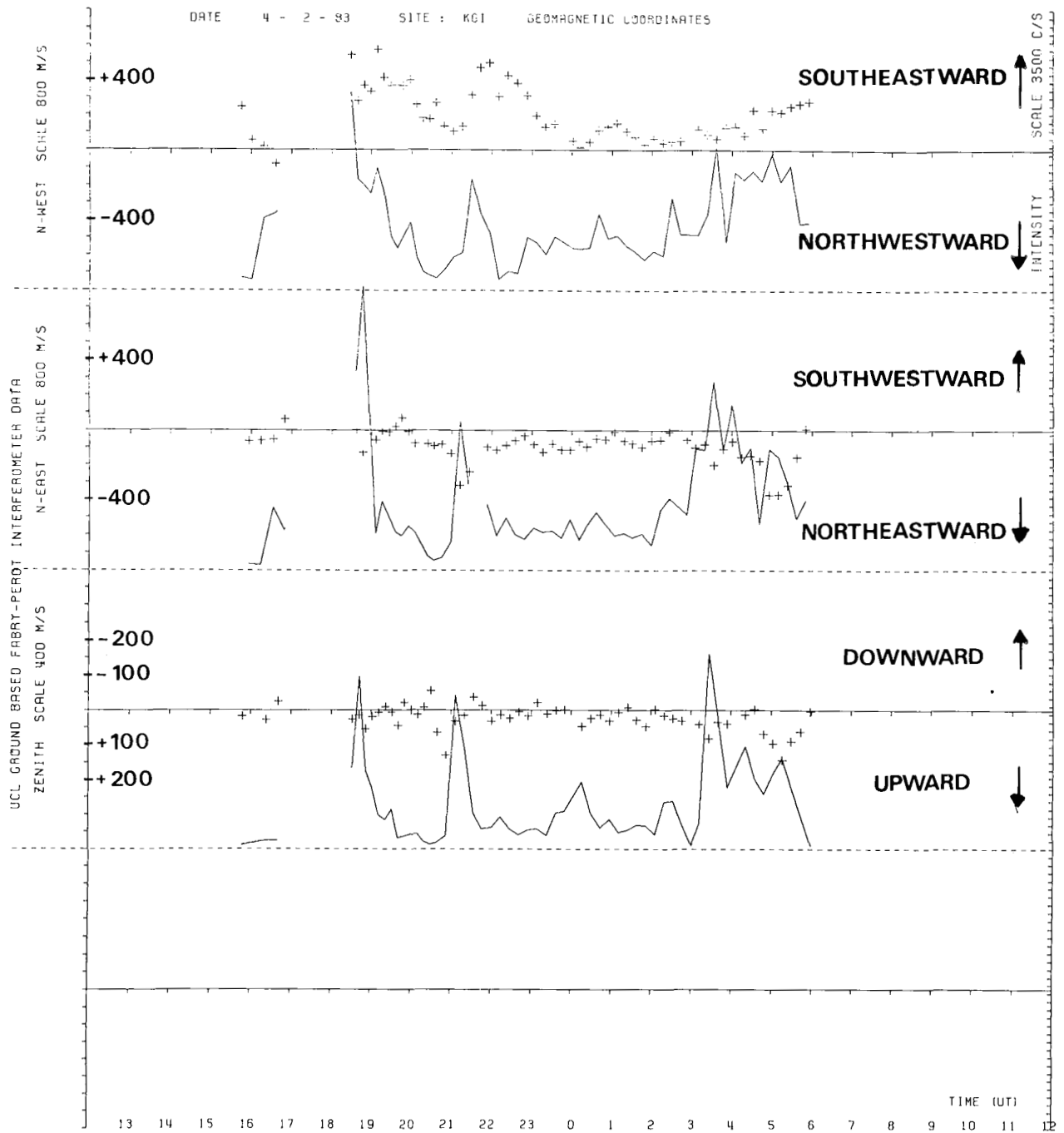56 DOWNWARD

SOUTH

420 KM

200 M/S
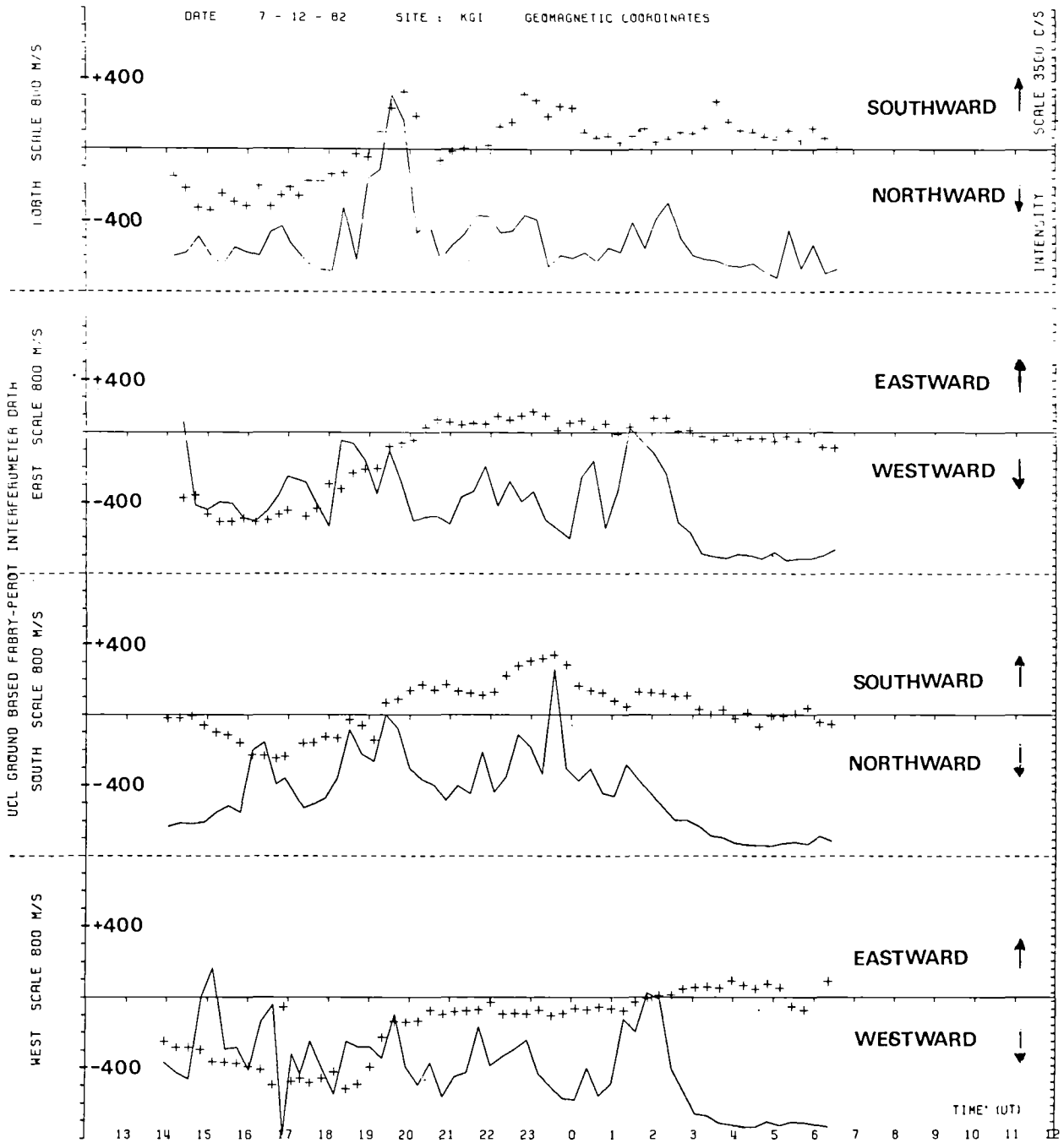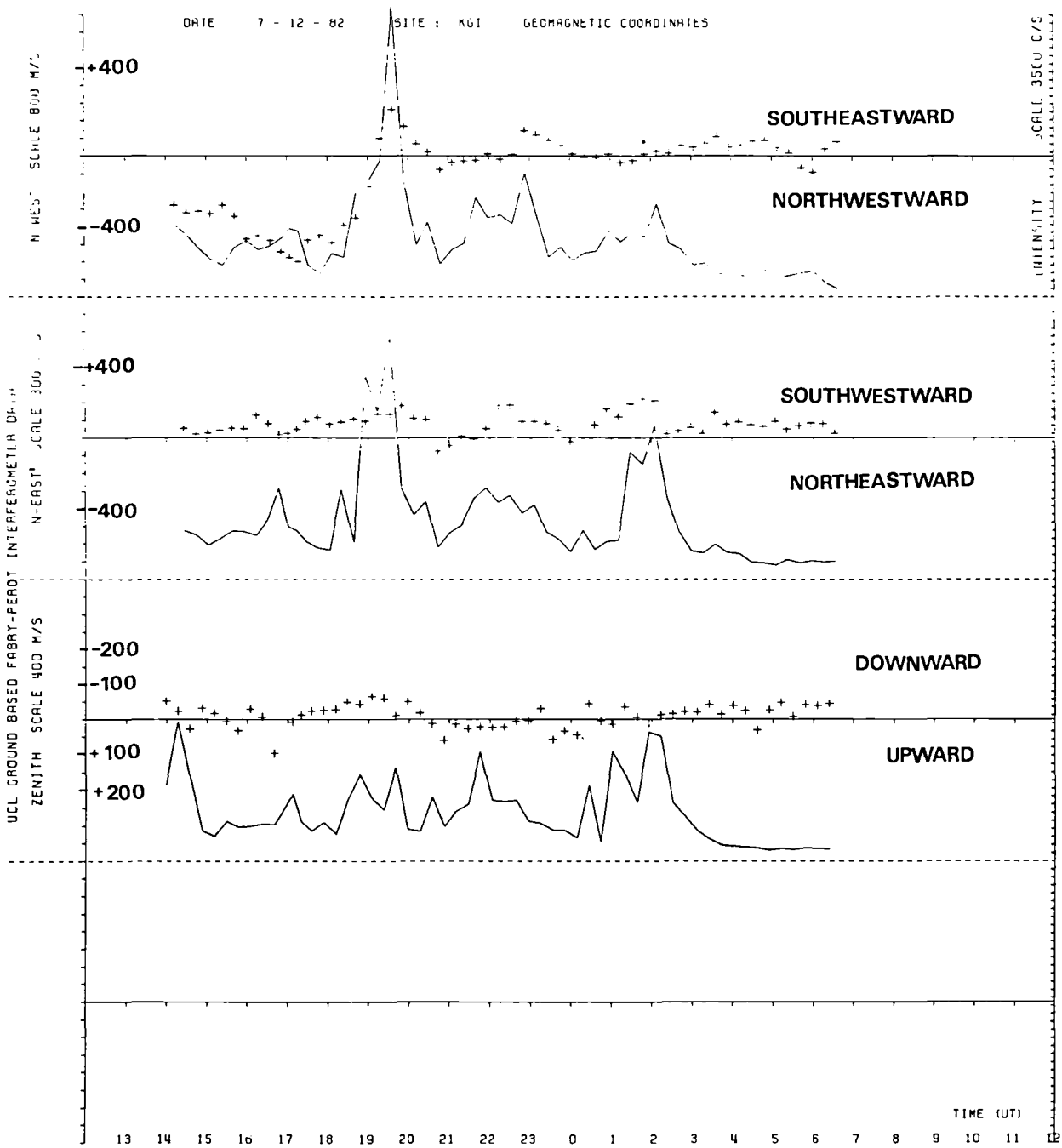
Figure 2b. Continuation of Figure 2.

Figure 3a. Thermospheric wind observations in the N, NE, E, S, W, NW and Vertical Directions from the FPI at Kiruna Geophysical Institute on the night of 4/5 Feb 1983. The major focus of interest is the correspondence between changes observed in each of the viewing directions near the strong geomagnetic disturbance around 21.00 UT. There was a 'great red' aurora between 17.00 and 18.00 UT. Observed winds are indicated by the crosses (+), and the OI 630 nm emission intensity by the continuous line.
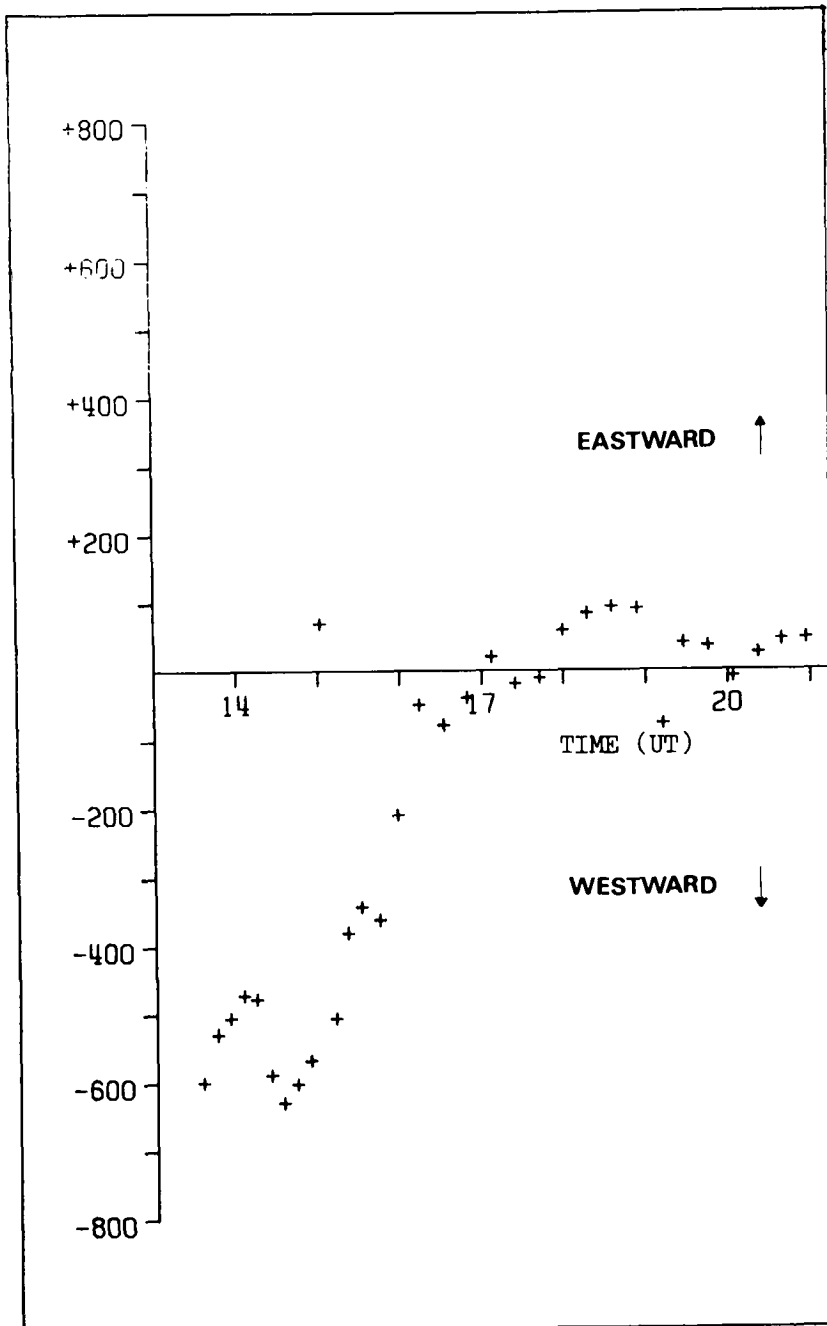
Figure 3b. Continuation of Figure 3.

310

Figure 4a. Thermospheric wind observations in the N, NE, E, S, W, NW and Vertical Directions from the FPI at Kiruna Geophysical Institute on the night of 7/8 Dec 1983. The major focus of interest is the correspondence between changes observed in each of the viewing directions in the period 18.00 to 20.00 UT before, during and after the strong geomagnetic disturbances around 19.00 UT. Observed winds are indicated by the crosses (+), and the OI 630 nm emission intensity by the continuous line.

311

Figure 4b. Continuation of Figure 4.

312

Figure 5a. Thermospheric wind observations in the West, North,
Northwest and Vertical Directions from the FPI at Kiruna
Geophysical Institute on the night of 17 Dec. 1982. The major focus
of interest is the correspondence between the strong westward winds
in the period 13.30 to 16.00 UT during the major geomagnetic
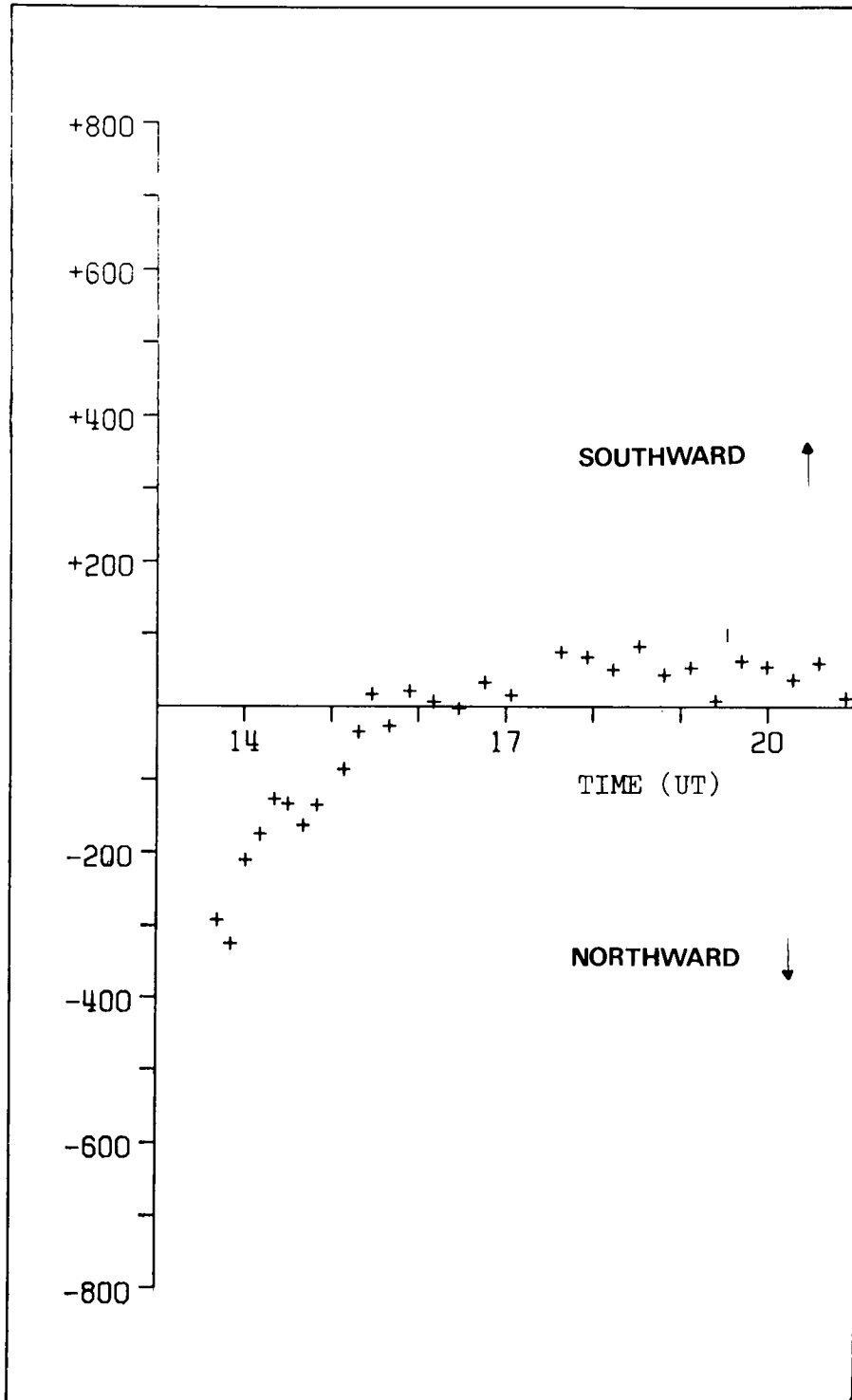disturbances which started at 08.00 UT. Observed winds are indicated
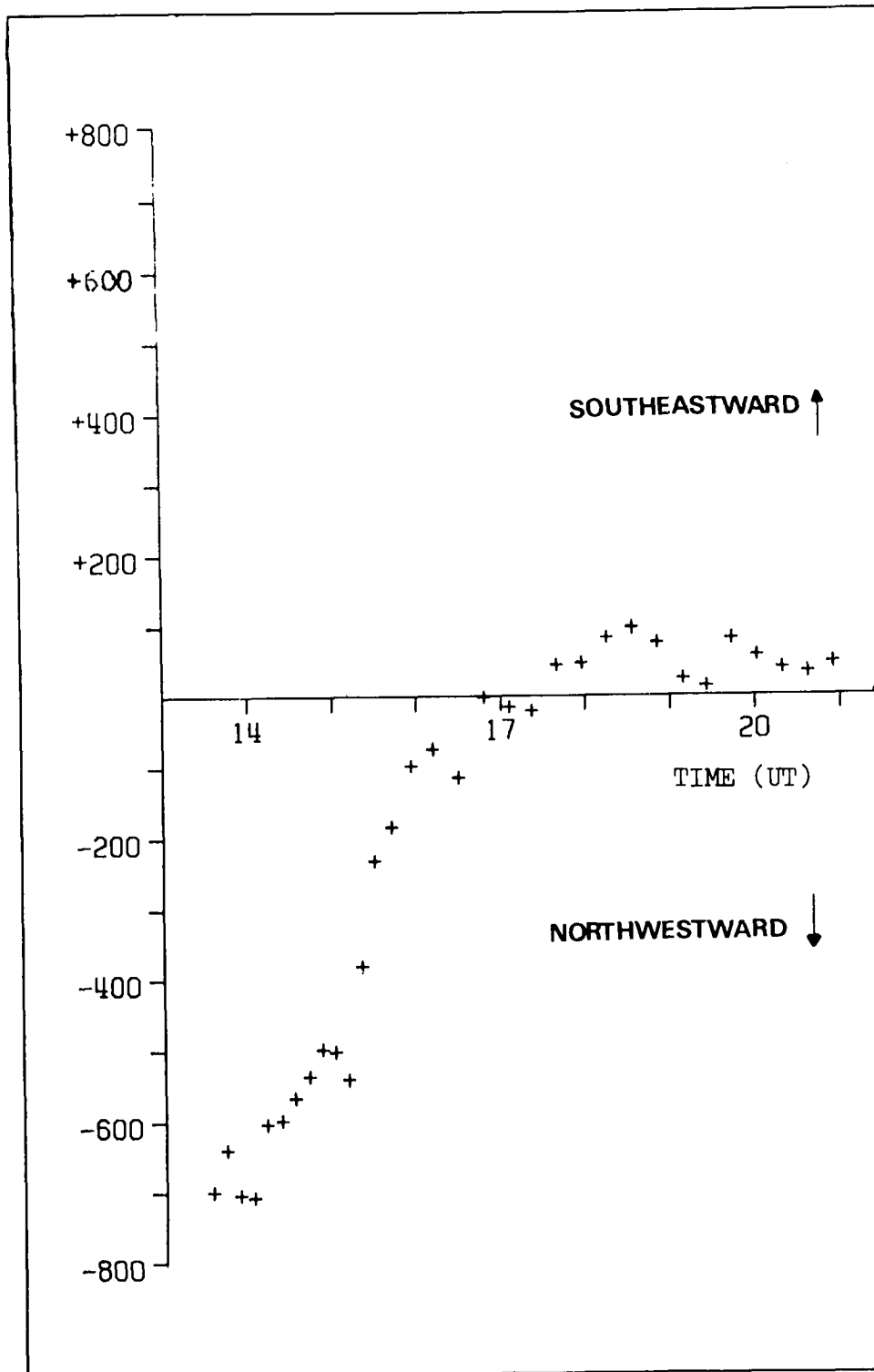by the crosses (+).

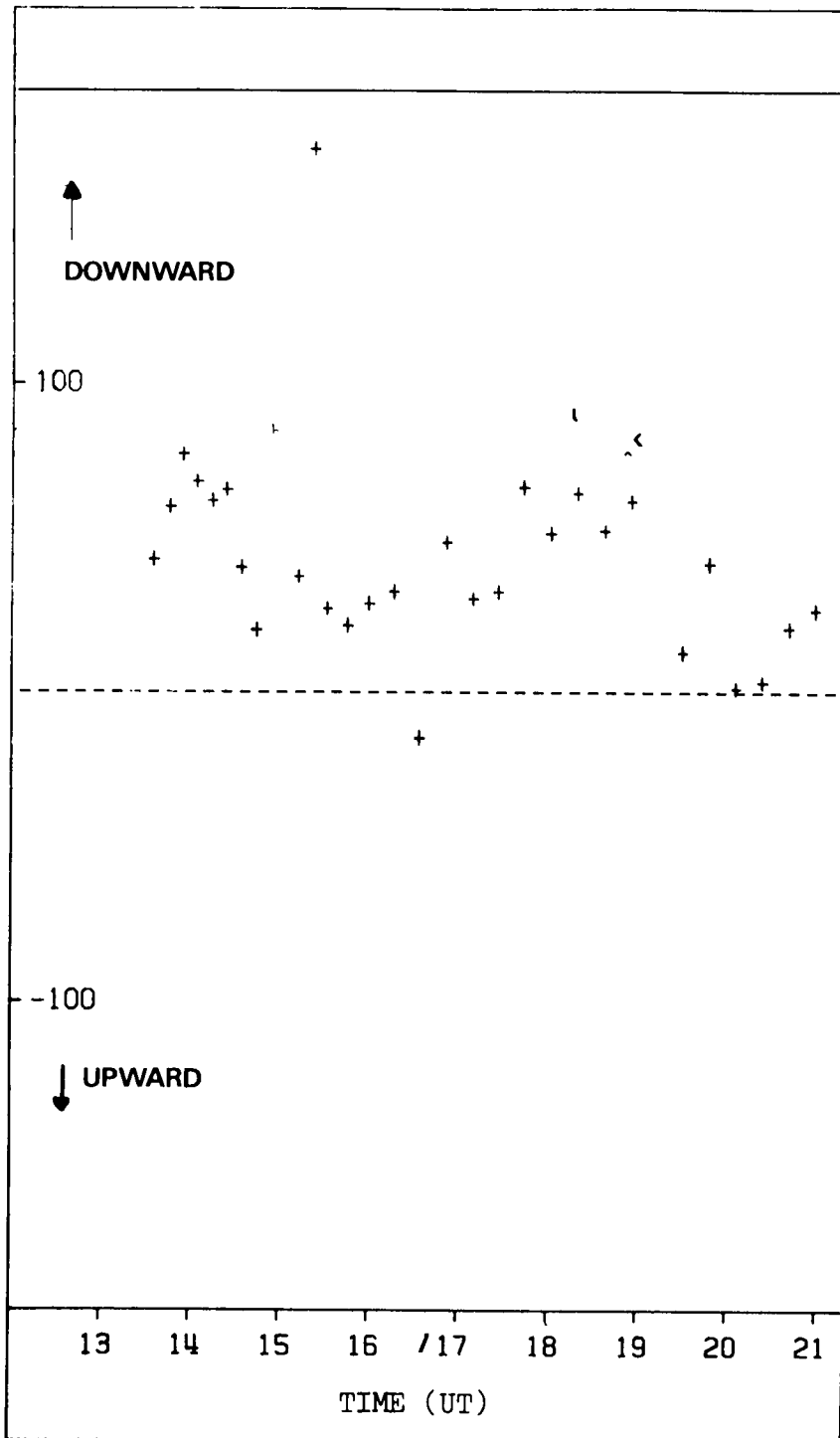Figure 5b. Figure 5 continued.

314

Figure 5c. Figure 5 continued.

Figure 5d. Figure 5 continued.
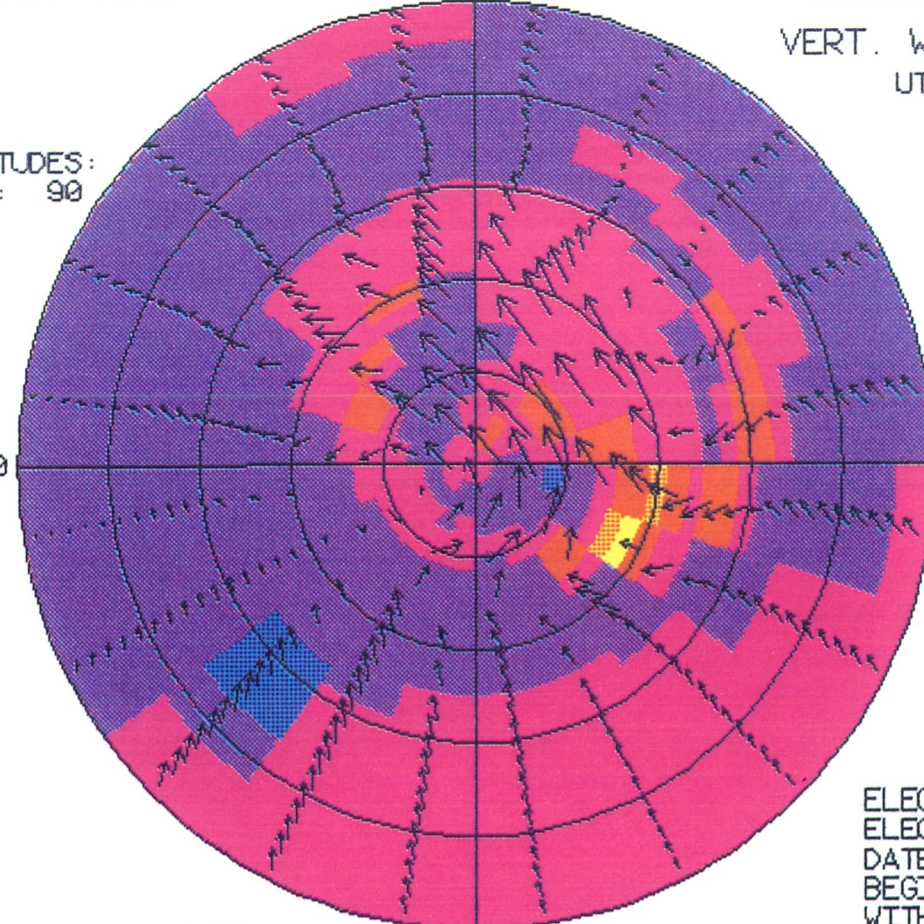
Figure 6. Vertical and Horizontal wind distributions over the Northern Polar region for relatively quiet geomagnetic conditions. Even at a low level of geomagnetic energy and momentum input, there are upward winds over much of the winter auroral oval and polar cap regions. At lower latitudes, the upward winds of the dayside, and the downward winds of the nightside, can be observed. The magnitudes of these mid-latitude winds are less than 5 m/sec at 320 km.
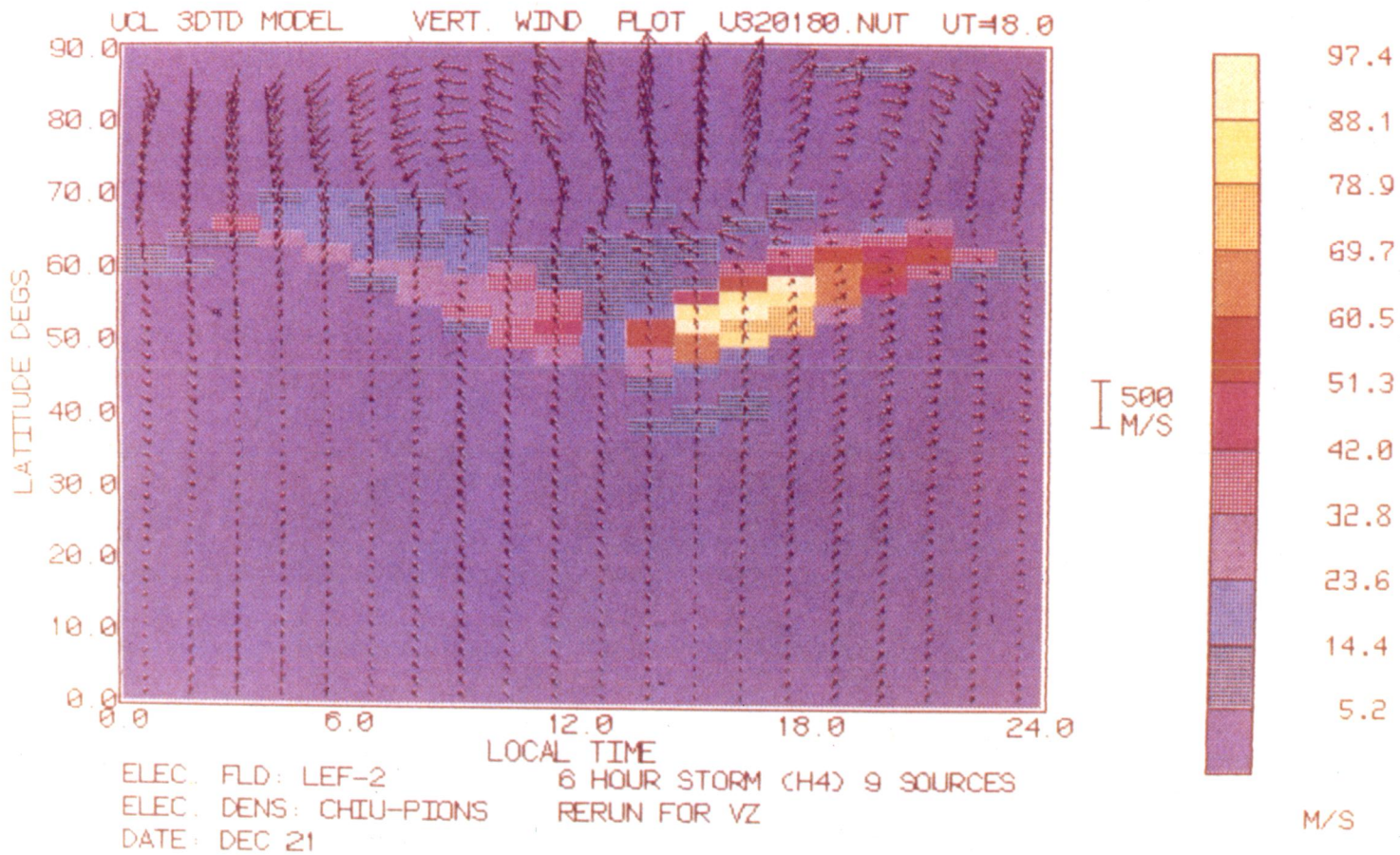
Figure 7. Vertical and Horizontal wind distributions over the Northern Polar region for rather disturbed geomagnetic conditions. Upward winds of 40 m/sec occur in the dayside polar cusp region, where there is strong convergence and 'soft' particle heating. There are upward winds of 5 to 20 m/sec around much of the auroral oval.

Figure 8. Vertical and Horizontal wind distributions over the Northern Polar region during a geomagnetic substorm. The intense heating from particle and Joule heating effects in the midnight region of the auroral oval generate strong localized upward winds, and force an outward explosion of the thermosphere away from the region of the substorm and westward travelling surge. This Figure shows the onset phase, when the rapid upward vertical winds have been generated, but before the outward expansion has had time to develop.
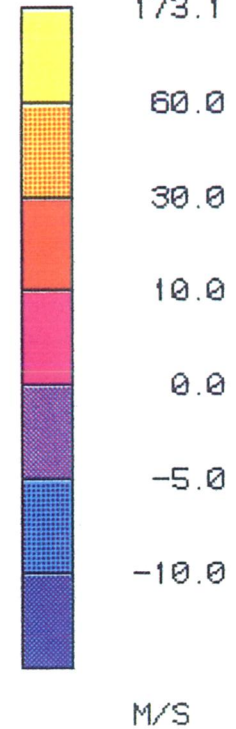
REES, page 319

Figure 9. Vertical and Horizontal wind distributions over the Northern Polar region for geomagnetic substorm conditions. The situation, simulated in Figure 8, has developed for a further 40 min, and now the outward explosion from the region of the substorm is clearly defined. At this stage, the gravity waves expanding from the auroral source region are well defined.
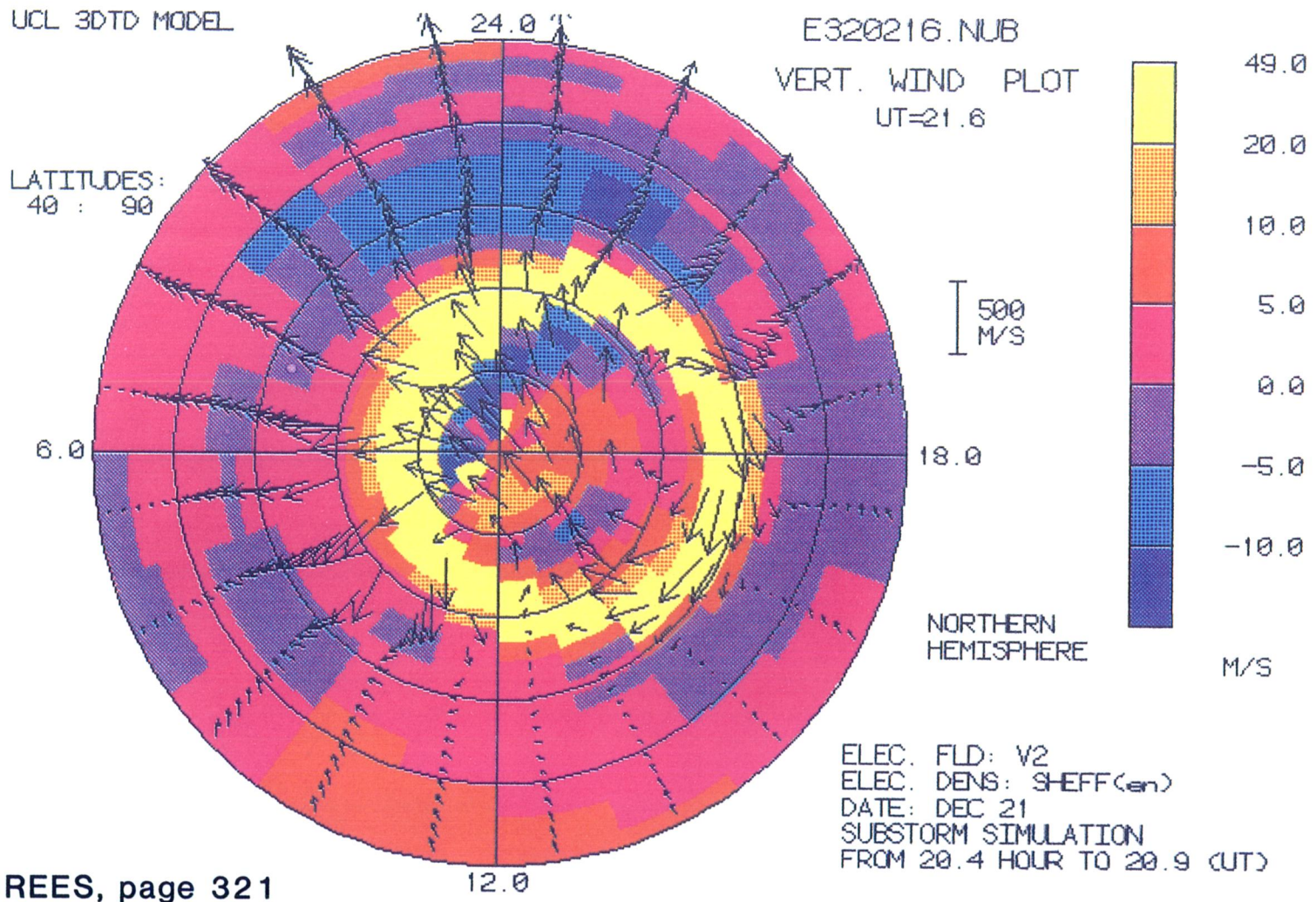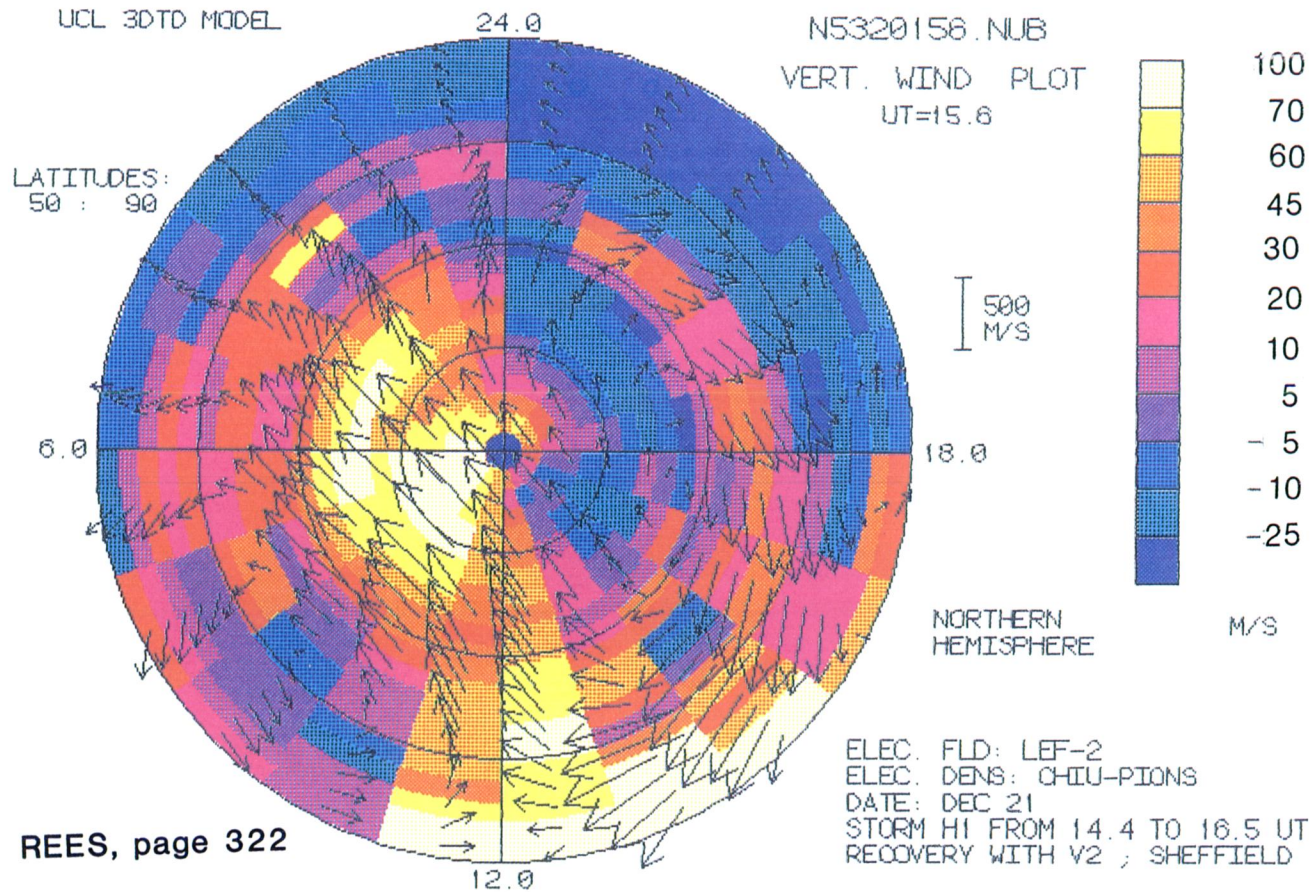
Figure 10. Vertical and Horizontal wind distributions over the Northern Polar region for geomagnetic substorm conditions. This Figure shows the initial recovery phase after the disturbance. The outward explosion is no longer evident, and the peak upward winds have subsided. At lower latitudes, in the nightside part of the thermosphere, the rapid equatorward propagation of the gravity waves launched by the intense auroral disturbance can be seen.

REES, page 321

Figure 11. Vertical and horizontal wind distributions over the northern polar region for very disturbed geomagnetic conditions. This simulates the wind disturbances during a period when the IMF is extremely strong (20 nT), and with a large southward component. At such times, the auroral oval expands, and there may be a cross-cap potential of 120 – 150 kV. Km/sec winds are driven in the auroral oval and over the polar cap, and regions of systematic upward and downward wind flows exist within, and around the boundaries of the regions of intense geomagnetic energy and momentum inputs.

THE TIME-DEPENDENT DYNAMICAL RESPONSE OF THE THERMOSPHERE TO MAJOR GEOMAGNETIC DISTURBANCES

David Rees
Department of Physics and Astronomy
University College London
Gower Street, London WC1E 6BT, UK

Several recent observations of thermospheric dynamics, made in the polar regions during extremely disturbed geomagnetic periods are reviewed. In general, the magnitude and the variability of winds in the thermospheric polar regions increases with magnetic activity, as measured by any of the conventional indices. However, none of the conventional indices is a particularly good aid to predicting wind magnitudes. In very general terms, two major factors may be considered in describing the wind system. The magnitude of the IMF and, in particular, its southward component, determine the size of the auroral oval, and the strength of the cross-polar cap potential. This determines the size of the auroral oval, the magnitude of the sunward winds in the auroral oval and of those blowing anti-sunward over the polar cap, and is probably the major factor in determining the rate of geomagnetic energy deposition in the thermosphere. Superimposed on this enhanced polar circulation system will be the effects of discrete auroral substorms. From a global view-point, the effect of substorms is to generate a series of strong disturbances which propagate from their source region, usually near magnetic midnight in the auroral oval. The energy associated with discrete substorms is, however, usually a rather small proportion of the total global geomagnetic input during disturbed periods. Some of these substorm-related effects are discussed in more detail in an accompanying paper. A very large asymmetry in the development of polar wind disturbances can be related to the direction and magnitude of the 'Y' component of the IMF. The location of very fast anti-sunward wind jets in the polar cap follows the ion drift asymmetries generated by positive (dusk side maximum) or negative (dawn side maximum) values of the IMF Y component. In the dawn auroral oval and during moderately to very disturbed conditions, strong sunward winds are only observed when the IMF Y component is zero or negative. When the IMF Y component is positive, the winds of the dawn auroral oval are relatively small, or purely equatorward, even during extremely disturbed conditions. These observations of thermospheric wind disturbances will be evaluated by comparison with global simulations of the thermospheric response to theoretical and semi-empirical models of the polar electric field, and of the effects of magnetospheric particle precipitation.

WIND COMPONENT WEST (+tve EASTWARD)

WIND COMPONENT EAST (+tve EASTWARD)
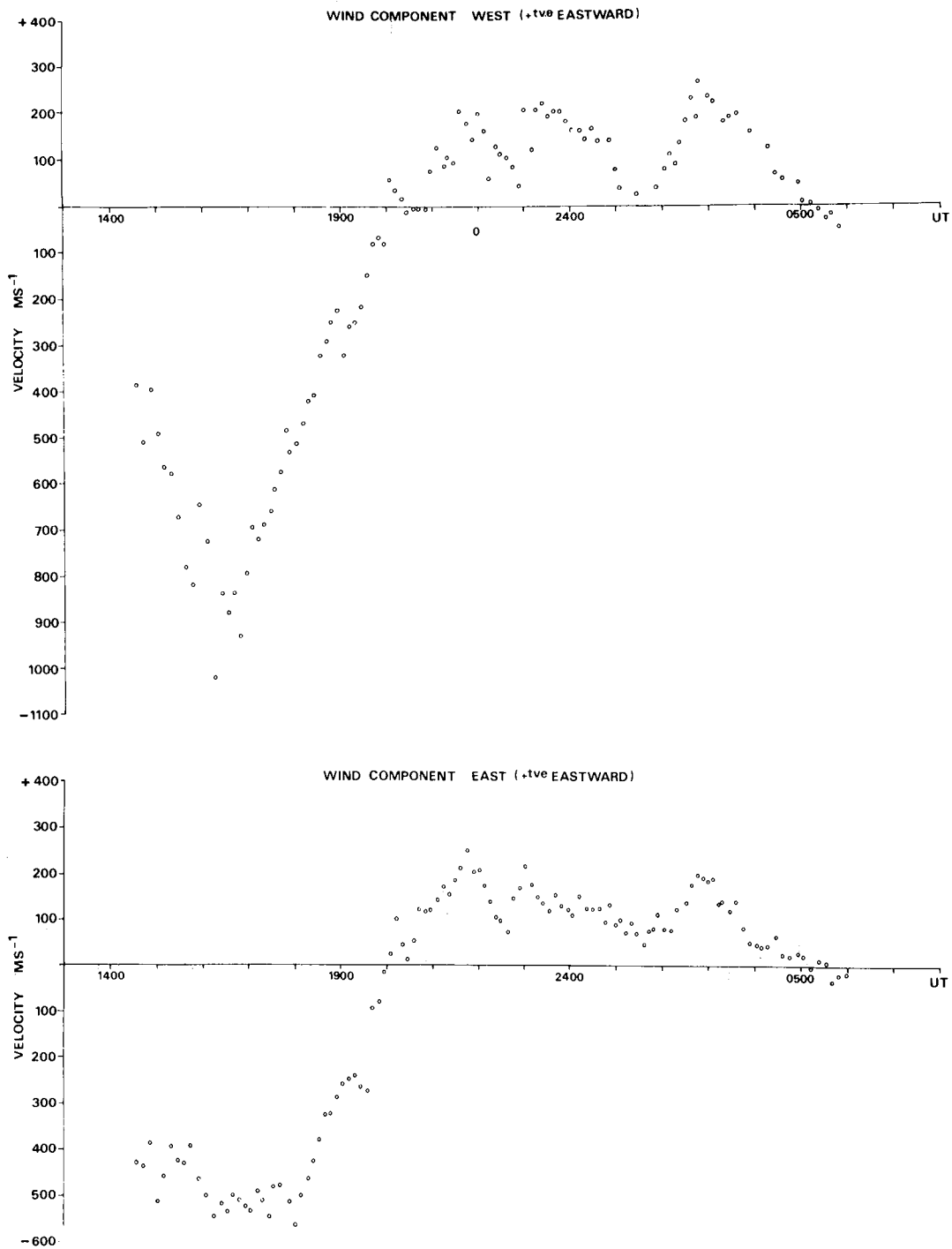
DEC 12/13 1981

Figure 1. Neutral wind response observed at Kiruna on Dec 12, 1981, by a ground-based fabry-Perot interferometer. Zonal Wind velocity component. Winds are measured in locations 400 km to the east and to the west of Kiruna. Altitude of OI 630 nm emission is about 240 km.

324
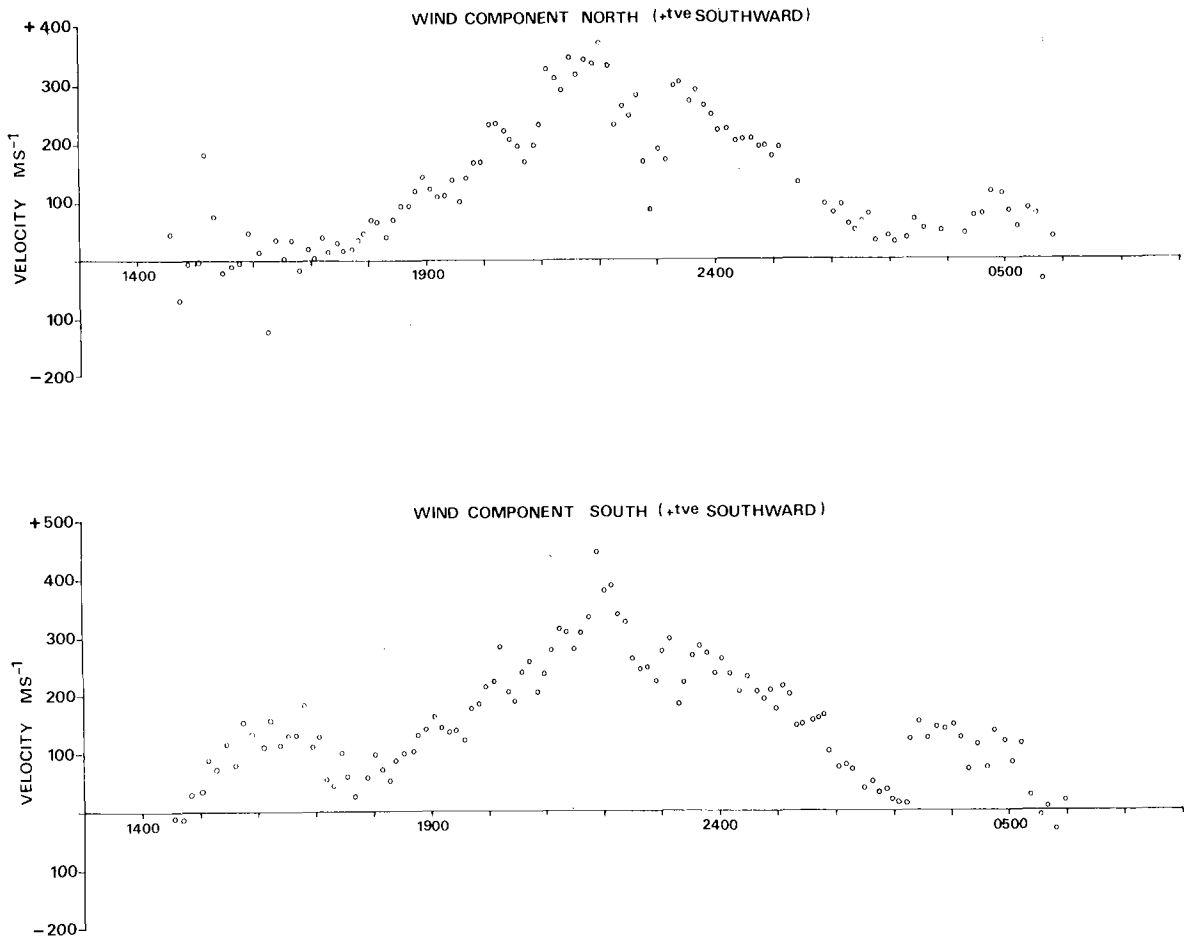
Figure 2. As Figure 1, but for the meridional wind component. Meridional components are measured about 400 km to the north and to the south of Kiruna.
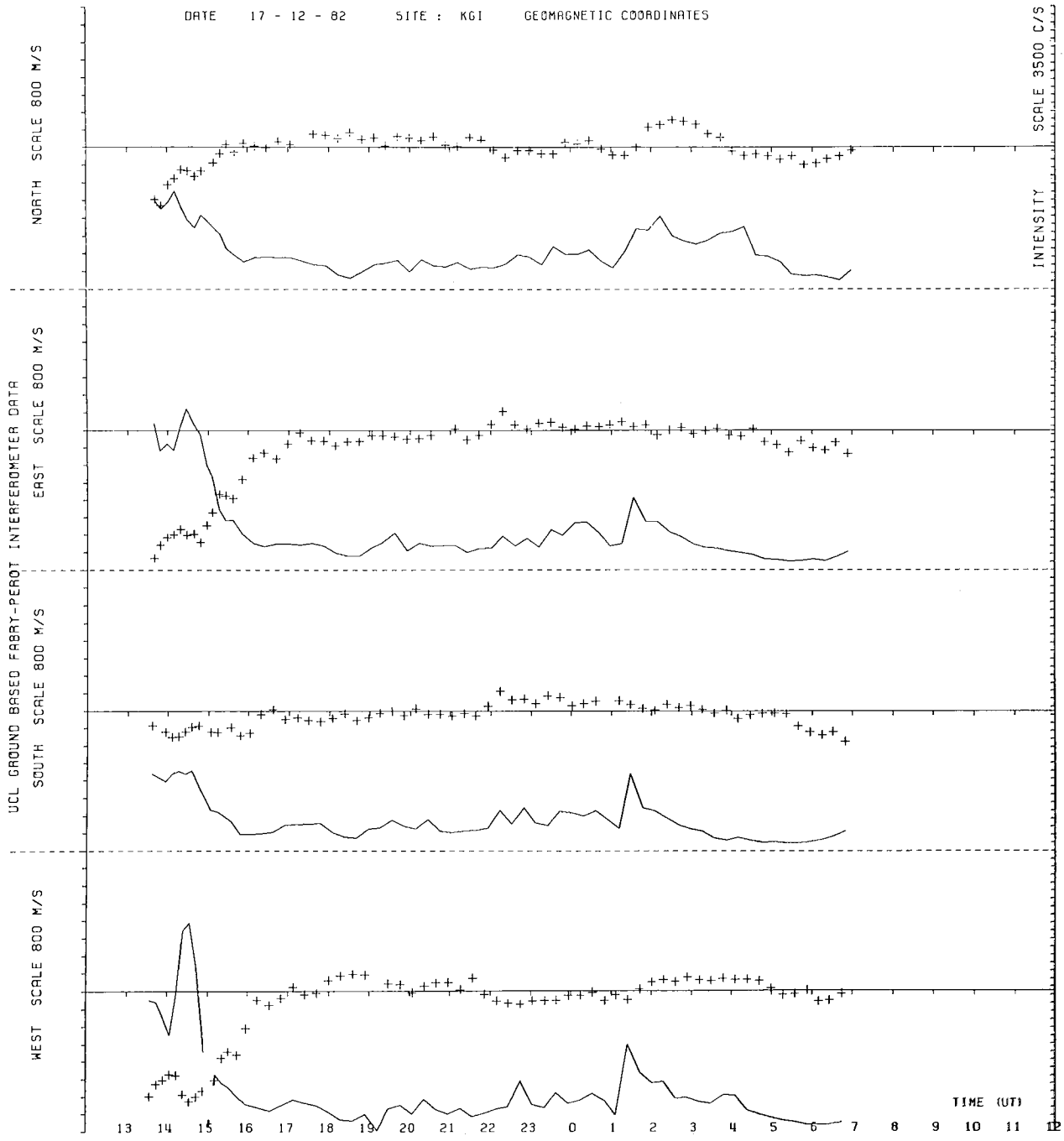
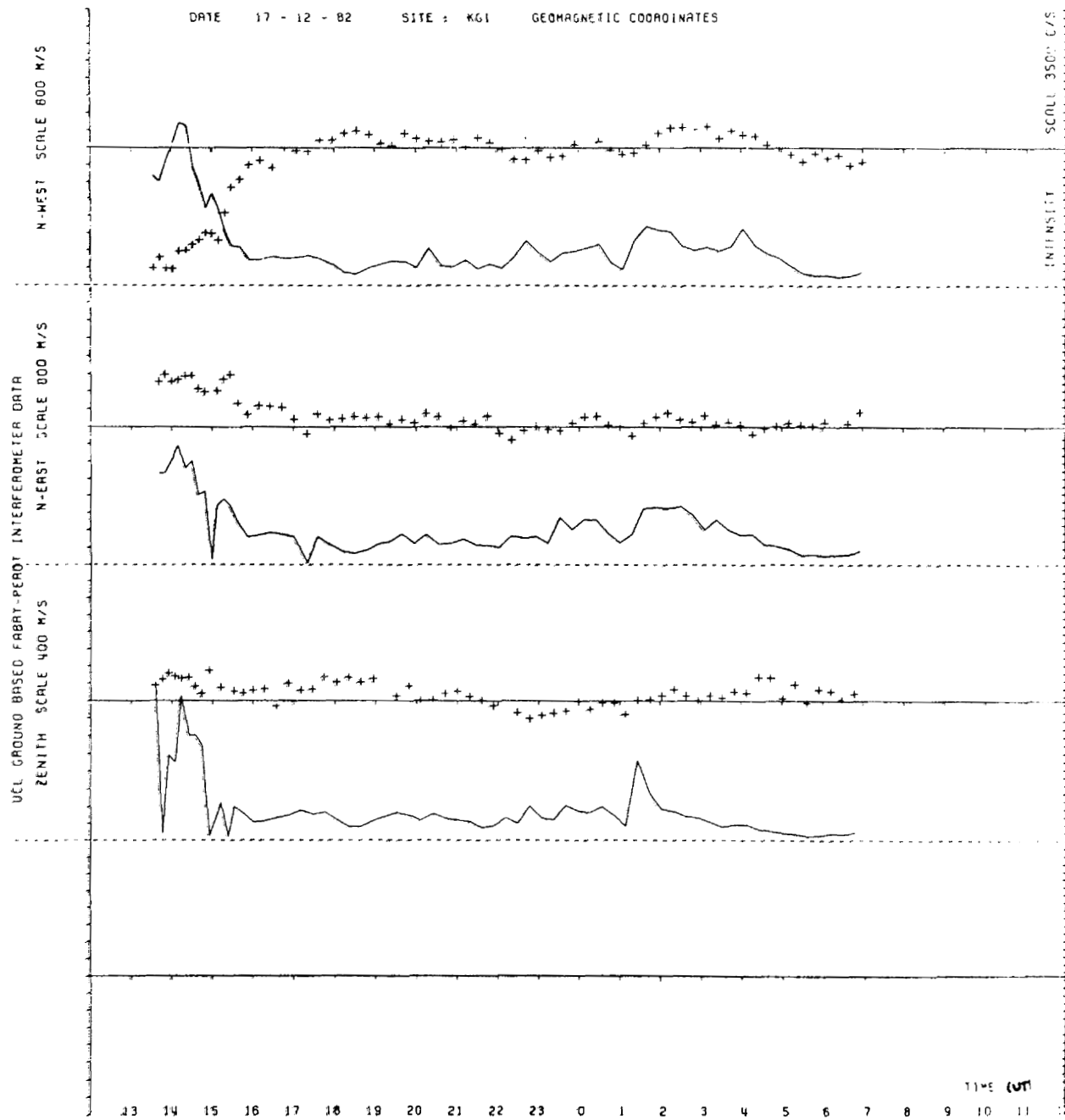Figure 3. As Figure 1, but for Dec 17, 1982, zonal wind.

Figure 4. As Figure 3, but for the meridional wind component.

327

DIRECTION: WEST   DATE: 12- 2-82   SITE: K.G.I.   SC AGL:45 OG   HT: 240 KM
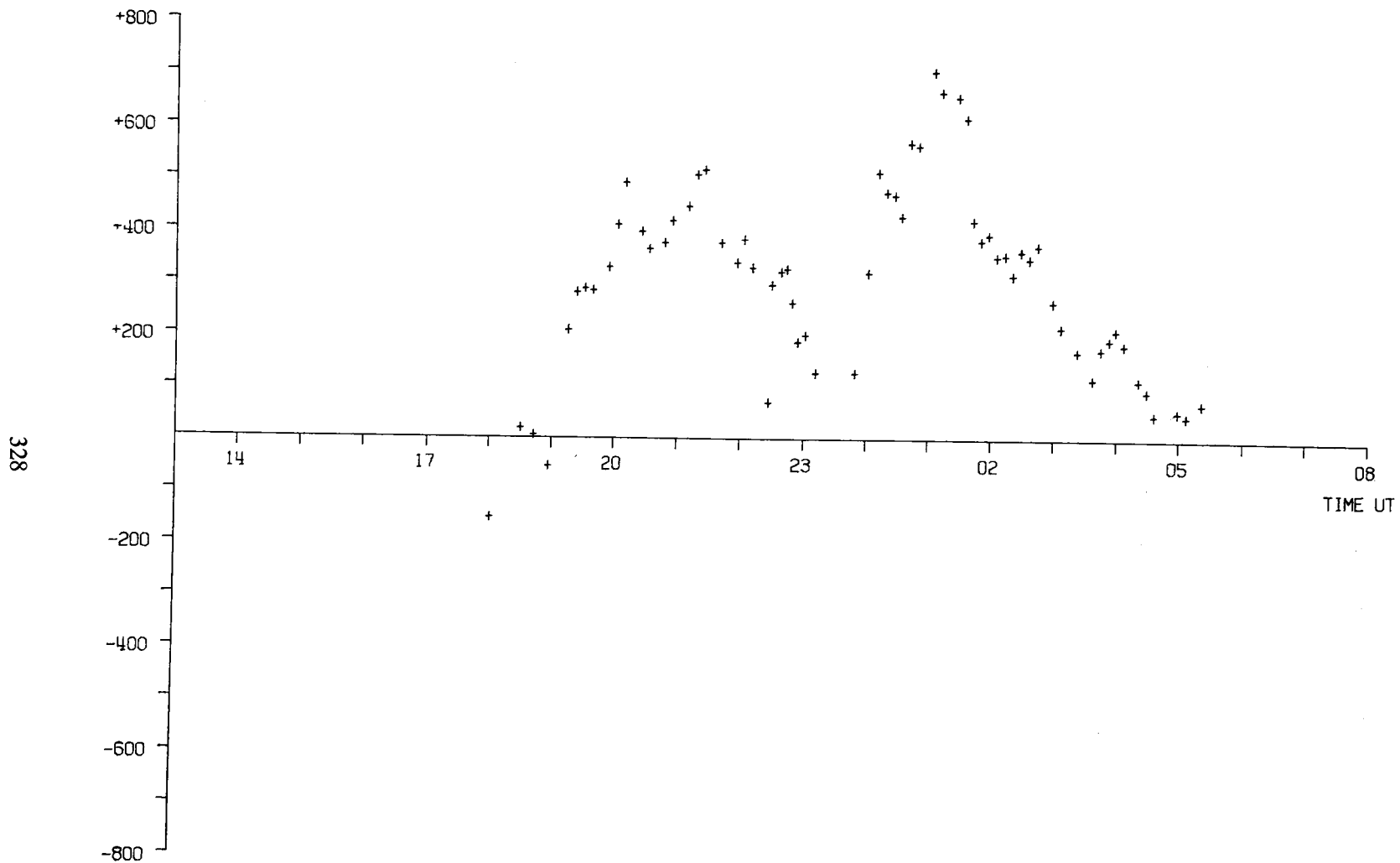

Figure 5. As Figure 1, but for Feb 12/13, 1982, zonal wind.

DIRECTION: NORTH   DATE: 12- 2-82   SITE: K.G.I.   SC AGL:45 DG   HT: 240 KM
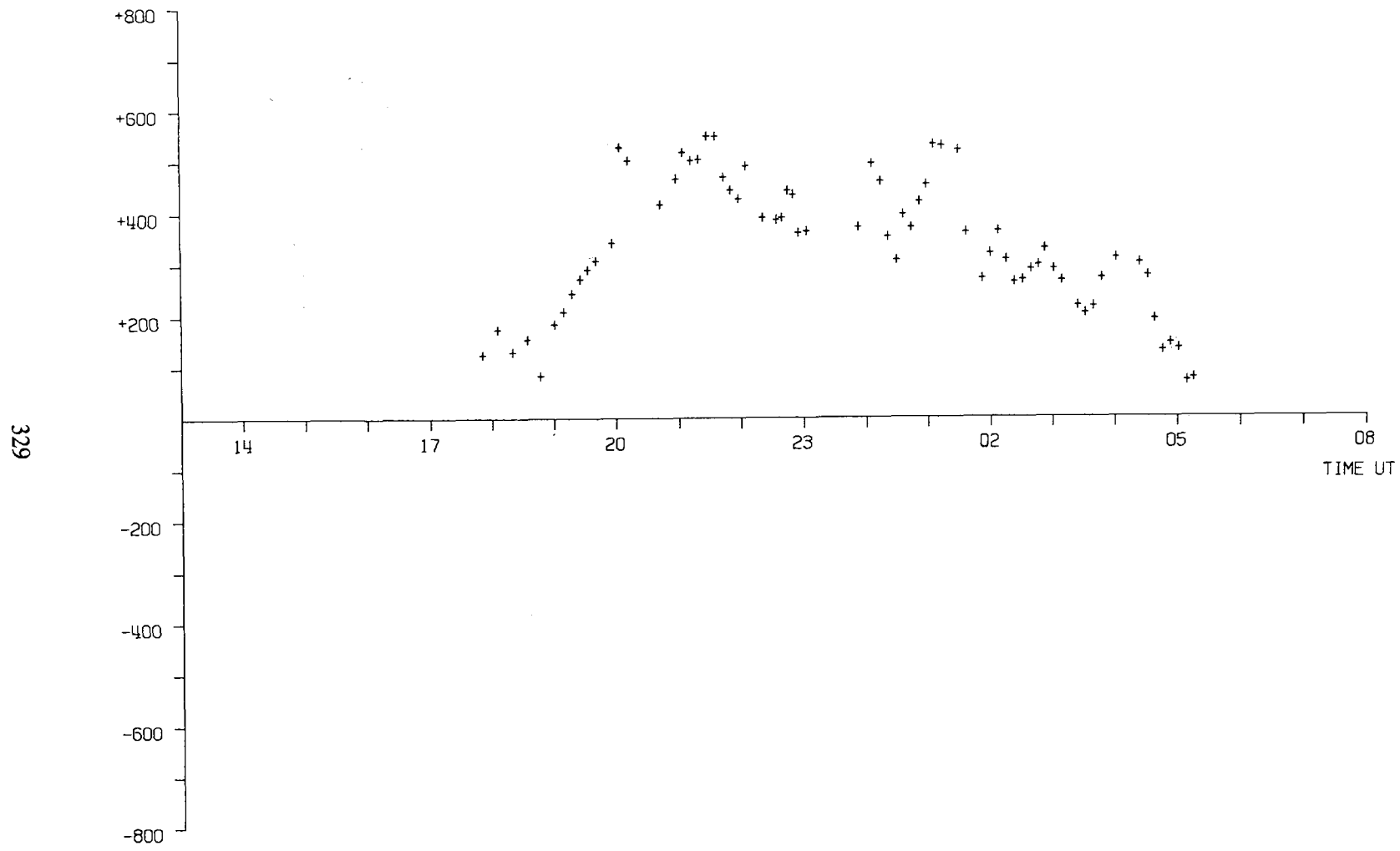
Figure 6. As Figure 5, but for the meridional wind component.
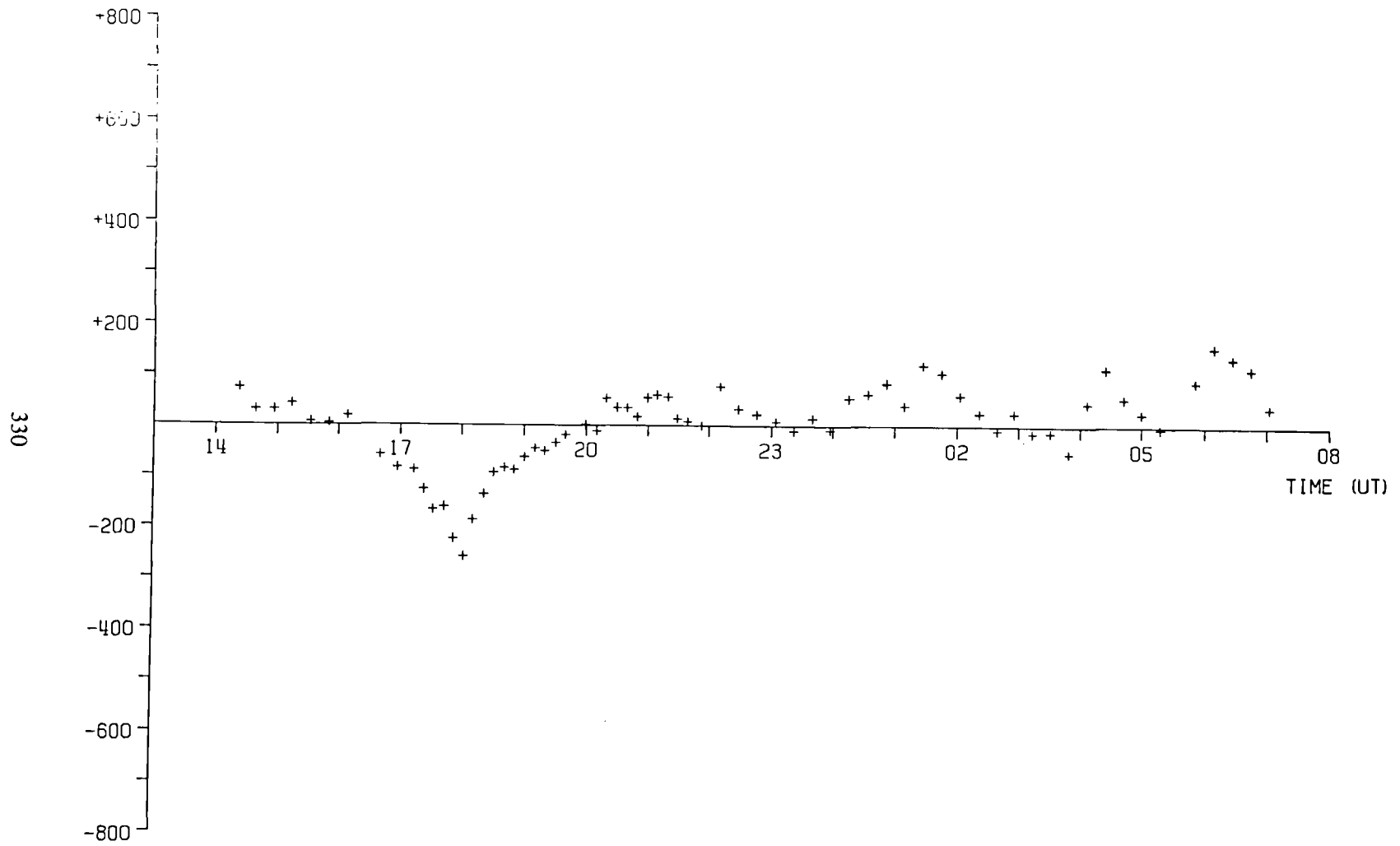
Figure 7. As Figure 1, but for January 9/10 1983, zonal wind.
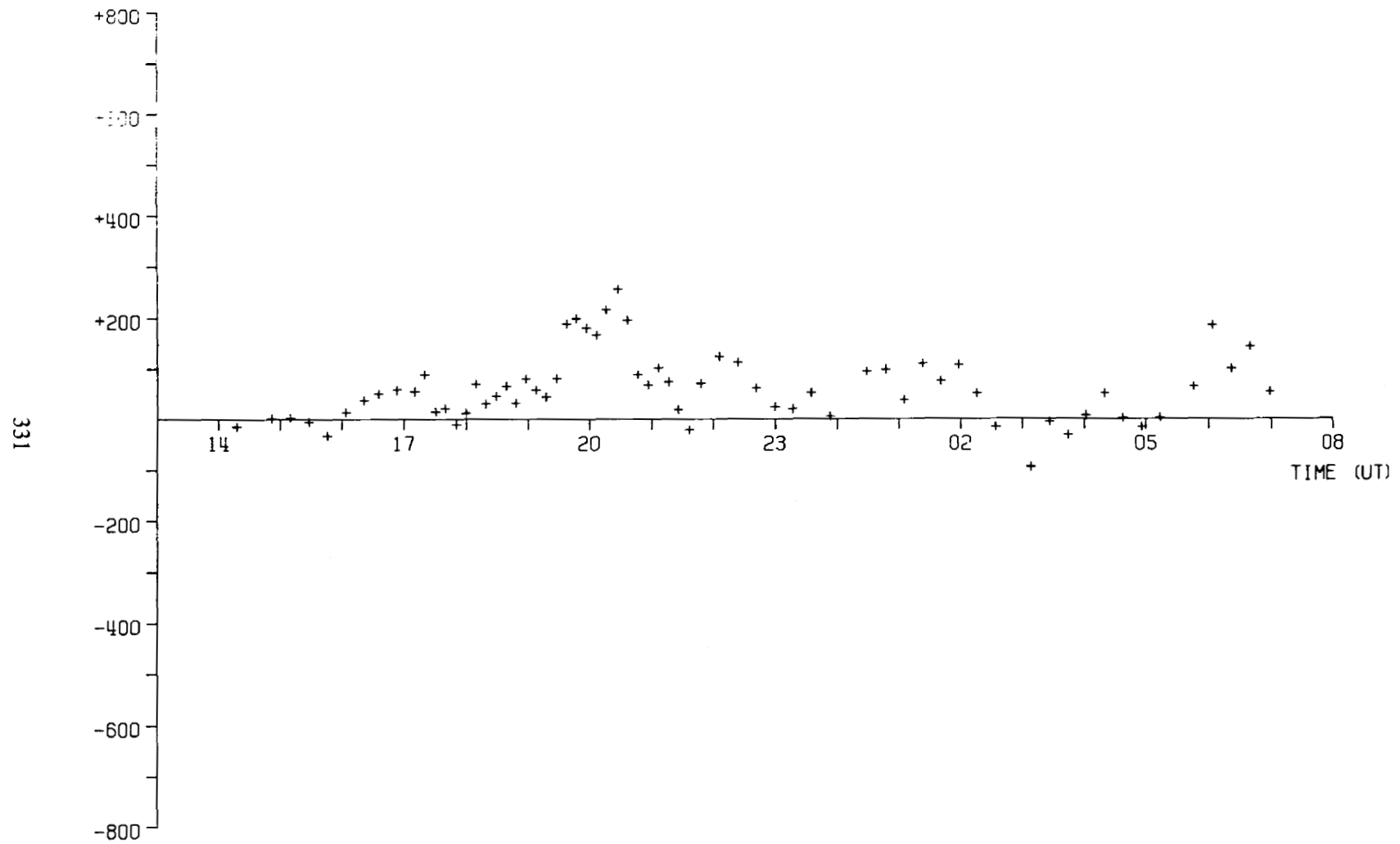
Figure 8. As Figure 7, but for the meridional wind component.

Figure 9. Thermospheric winds (320 km altitude) from the UCL 3-D T-D model for relatively quiet geomagnetic conditions. (J2 320, 180, NUB, polar)

REES, page 332

Figure 10. Thermospheric winds (320 km altitude) from the UCL 3-D T-D model for relatively disturbed geomagnetic conditions. (JQ 320 180, NUB, polar)
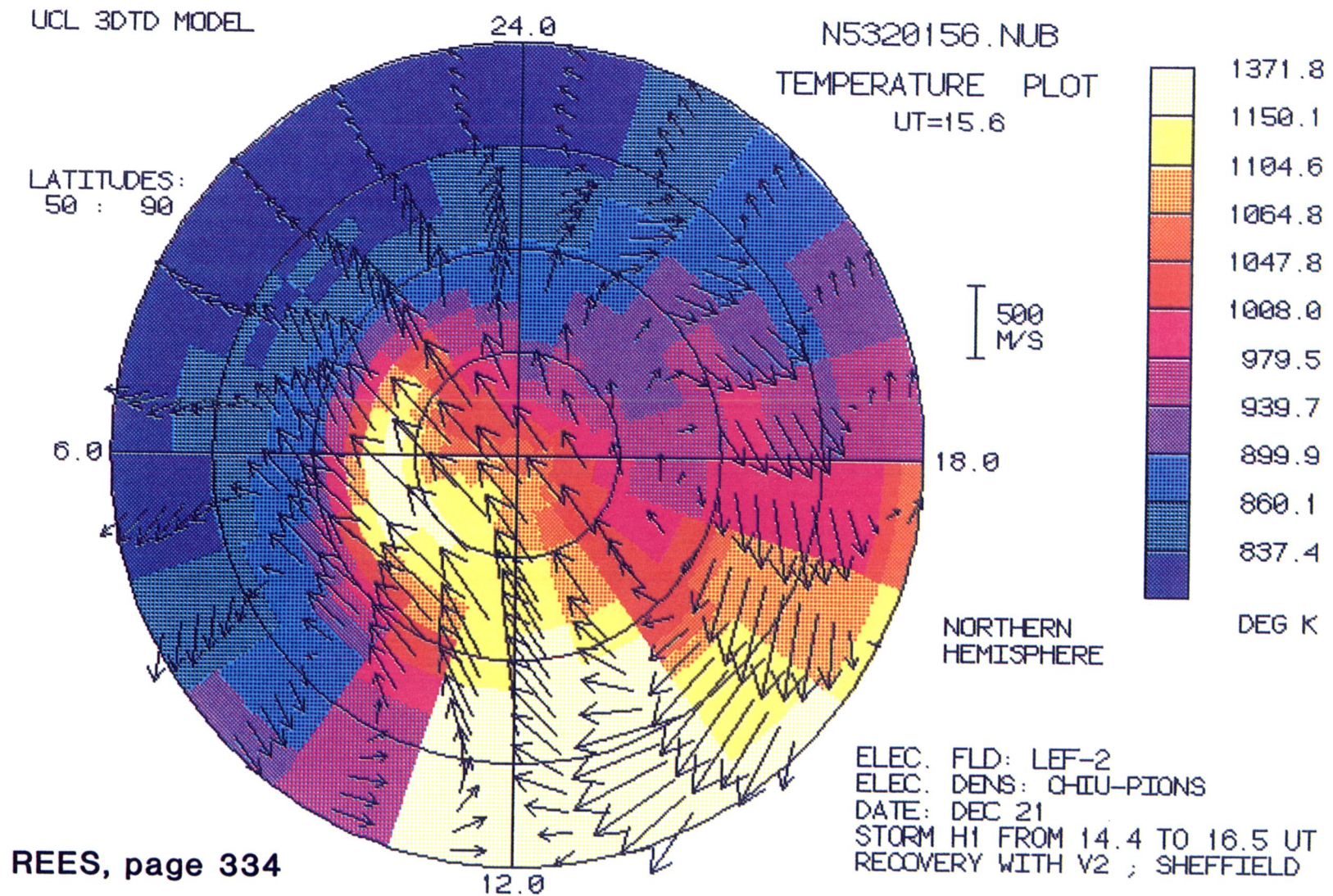
REES, page 333

Figure 11. Thermospheric winds (320 km altitude) from the UCL 3-D T-D model for geomagnetic storm conditions. (N4, 320, 156, NUB, polar)
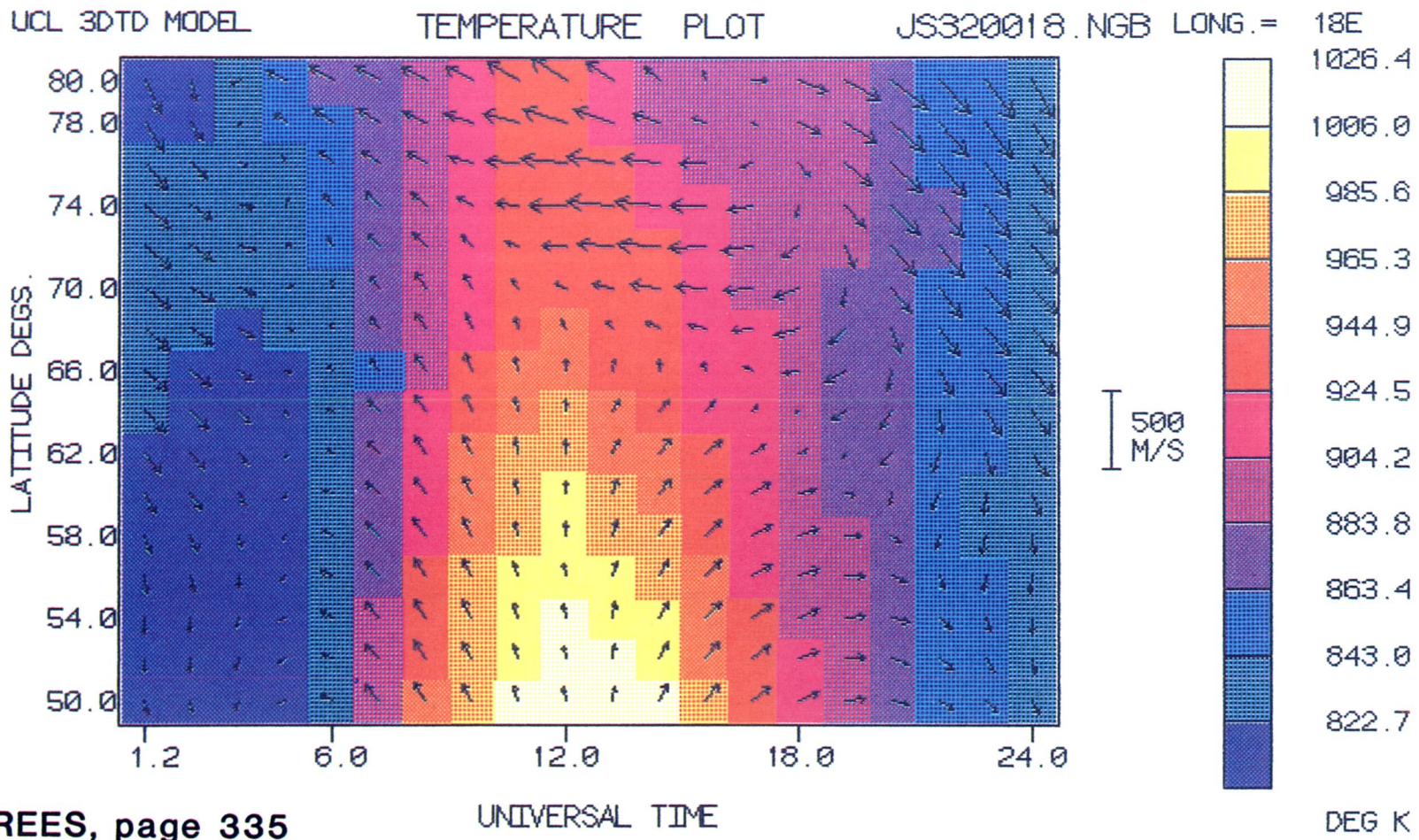
Figure 12. Thermospheric winds (320 km altitude) from the UCL 3-D T-D model for relatively quiet geomagnetic conditions. (J2 320, 018, NGB, CART, 50-80)
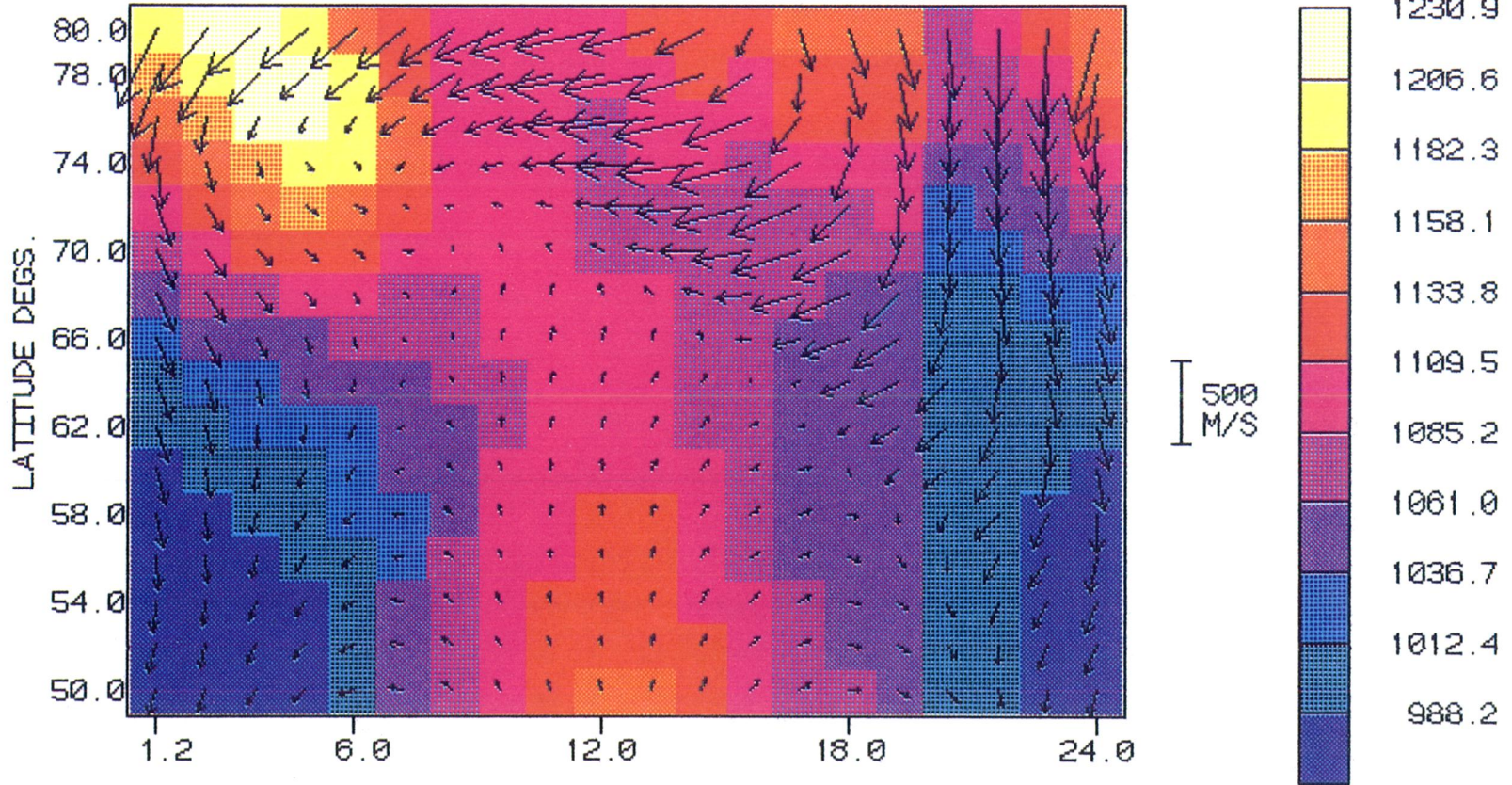
Figure 13. Thermospheric winds (320 km altitude) from the UCL 3-D T-D model for relatively disturbed geomagnetic conditions. (JQ 320, 018, NGB, CART 50-80)
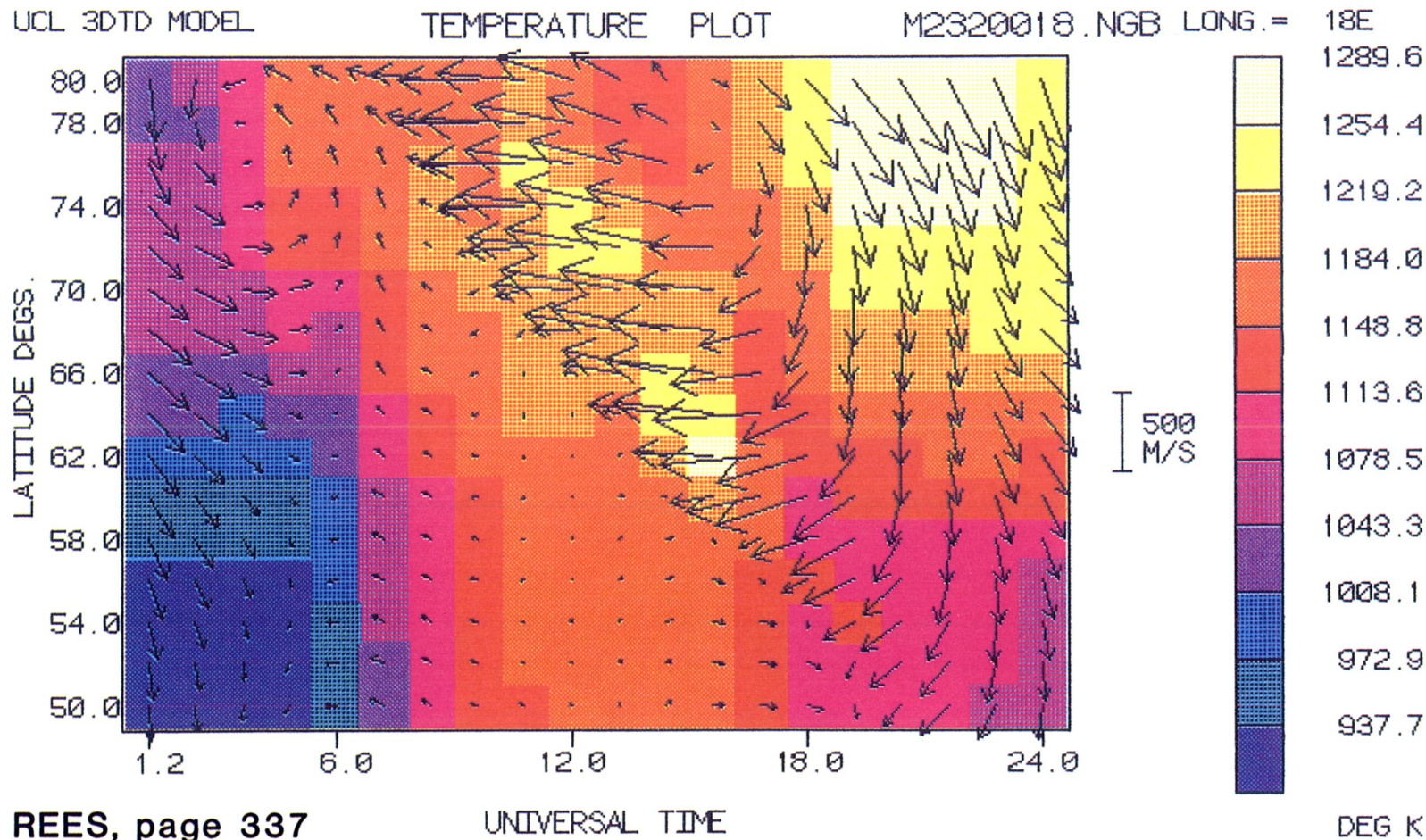
REES, page 337

Figure 14. Thermospheric winds (320 km altitude) from the UCL 3-D T-D model for relatively quiet geomagnetic conditions. (M2 320, 018, NGB, CART, 50-80)
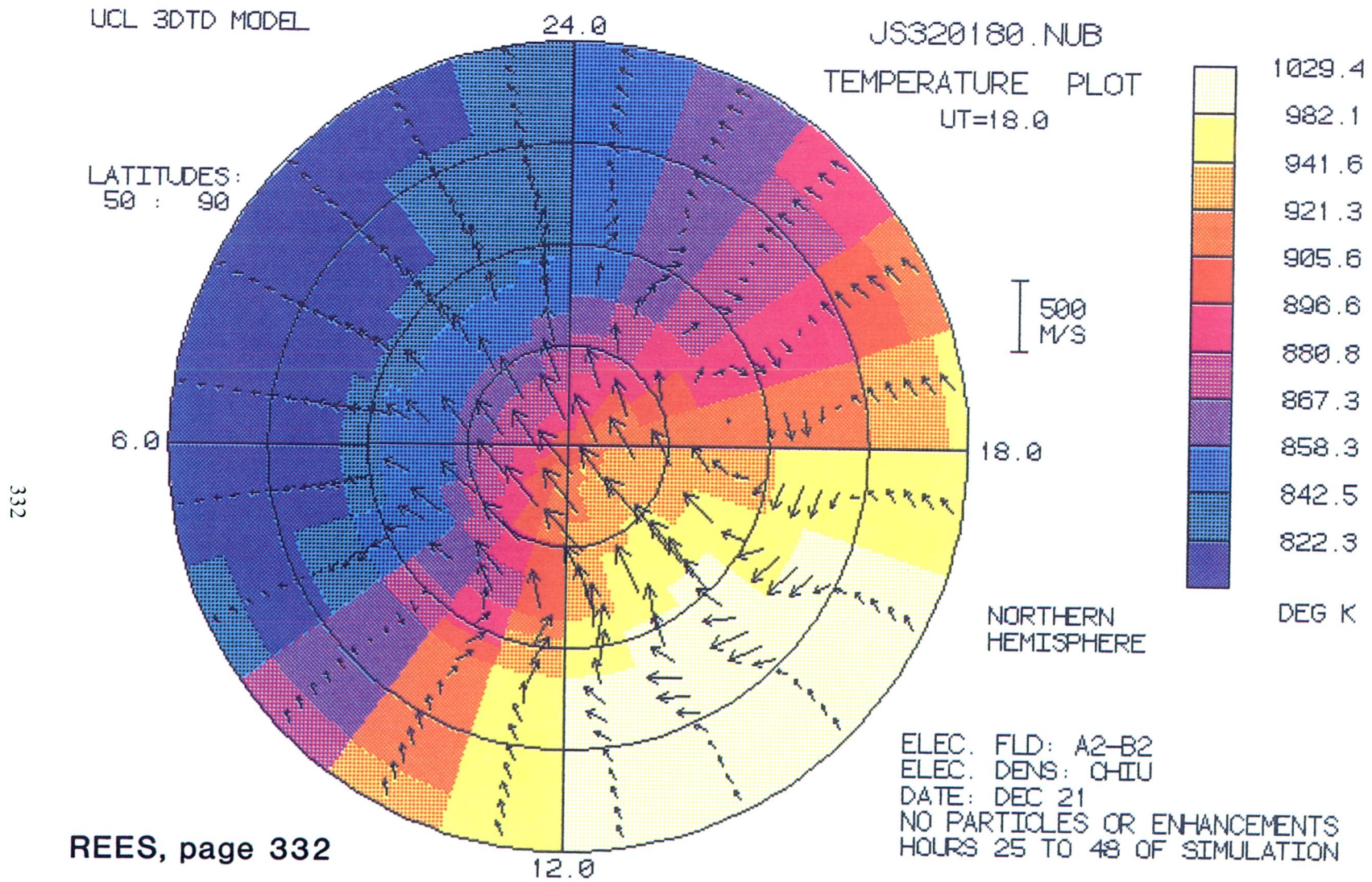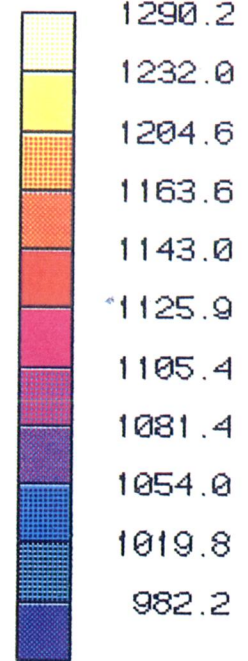
Figure 15. Thermospheric winds (320 km altitude) from the UCL 3-D T-D model for relatively disturbed geomagnetic conditions. (JQ 320, 000 NUB, polar). Simulation for a positive Y component of the IMF.
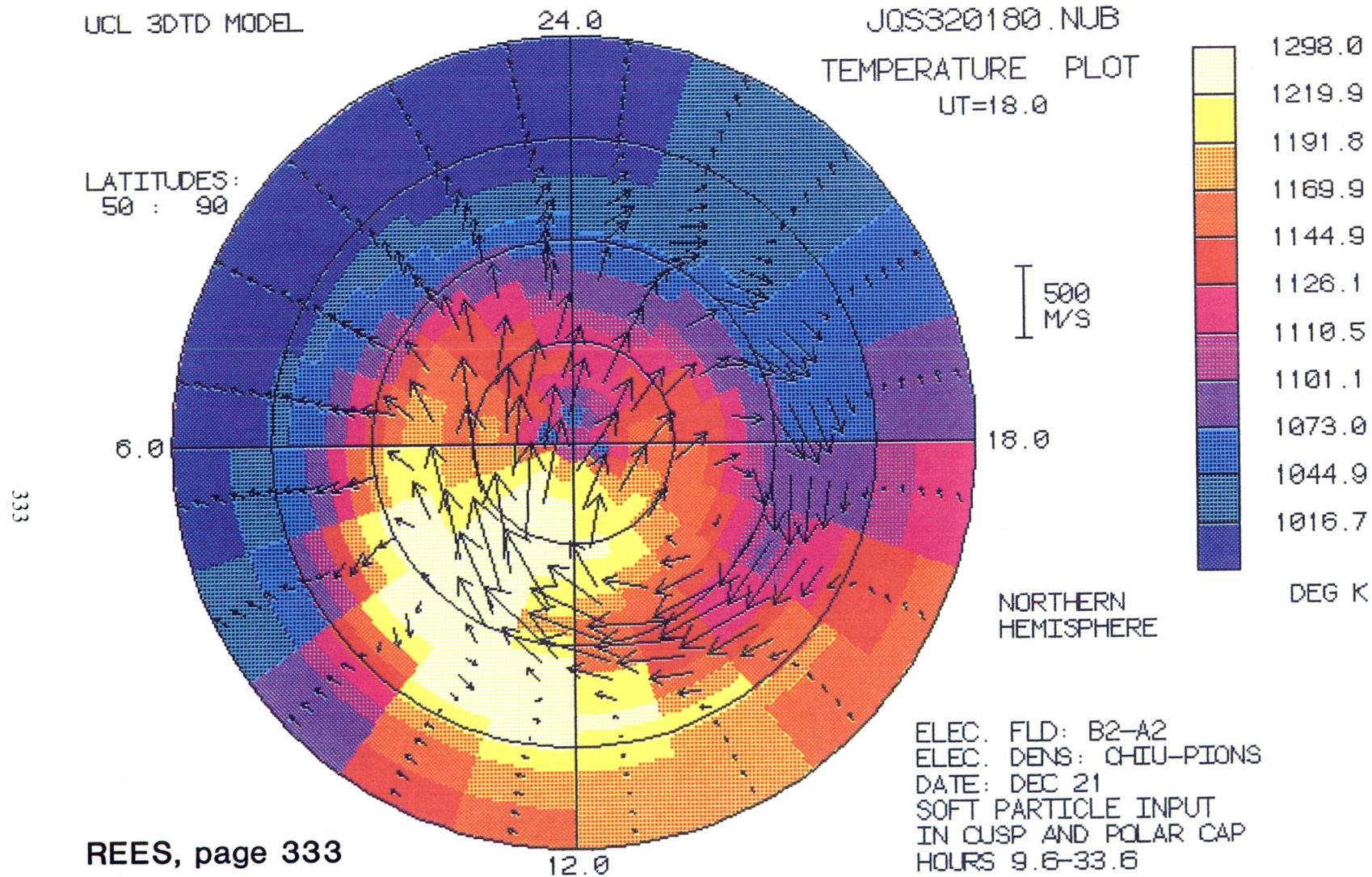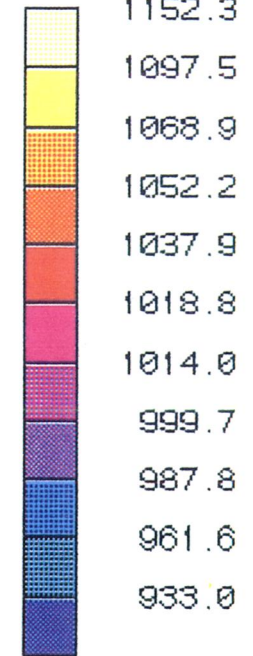
Figure 16. Thermospheric winds (320 km altitude) from the UCL 3-D T-D model for relatively disturbed geomagnetic conditions. (KB2 320, 000, NUB, polar). simulation for a negative Y component of the IMF.

SELF-CONSISTENT MODELLING OF THE
POLAR THERMOSPHERE AND IONOSPHERE
TO MAGNETOSPHERIC CONVECTION AND PRECIPITATION
(Invited Review)

David Rees, Tim Fuller-Rowell,
Department of Physics and Astronomy,
University College London,
Gower Street, London WC1E 6BT, UK

Shaun Quegan
Marconi Space and Defense Systems, Chelmsford UK
Roy Moffett
Applied Maths. Dept., Sheffield University, Sheffield, UK

It has recently been demonstrated that the dramatic effects of plasma precipitation and convection on the composition and dynamics of the polar thermosphere and ionoshpere include a number of strong interactive, or feed-back, processes. To aid the evaluation of these feed-back processes, a joint three dimensional time-dependent global model of the earth's thermosphere and ionosphere has been developed in a collaboration between University College London and Sheffield University. This model includes self-consistent coupling between the thermosphere and the ionosphere in the polar regions. Some of the major features in the polar ionosphere, which the initial simulations indicate are due to the strong coupling of ions and neutrals in the presence of strong electric fields and energetic electron precipitation will be reviewed. The model is also able to simulate seasonal and UT variations in the polar thermosphere and ionoshperic regions which are due to the variations of solar photoionization in specific geomagnetic regions such as the cusp and polar cap.

INTRODUCTION

Two three-dimensional time-dependent models of the global thermosphere have been developed as diagnostic tools to aid the evaluation of empirical thermospheric data[1, 2]. These models have included descriptions of the major energy and momentum inputs to the thermosphere, such as solar UV and EUV heating, and the geomagnetic polar inputs caused by the combined effects of energetic particle precipitation and the magnetospheric convective electric field imprinted on the polar regions[3, 4, 5].

The descriptions of the geomagnetic inputs have been somewhat improved by iterative ionospheric/thermospheric modelling[6, 7]. It has been possible to model the polar ionosphere as influenced by magnetospheric precipitation and solar illumination, and as modified by ionospheric convection and thermospheric winds which have themselves been driven by ion drag resulting from the combination of enhanced plasma densities and strong convection. This ionosphere, plus the particle precipitation energy and convection electric field has then been used to generate the

resulting patterns of thermospheric winds, and the consequent changes of thermospheric density, composition and temperature.

The precipitation and convection models used in these initial attempts were, however, very idealized, and it was only possible to iterate between the ionoshperic and thermospheric models by a laborious data base exchange once per 24 hours UT. Fully time-dependent, and UT-dependent computations could not be carried out by this method, although the results represented, for the polar ionosphere and thermosphere, a major advance over the use of the global 'Chiu' ionosphere[8], which has no contribution which can be recognized as due to the influence of the magnetospheric processes. The compositional effects of the geomagnetic input were not passed back to the ionospheric model, rather the MSIS empirical model was used to predice thermospheric composition under representative solar, seasonal and geomagnetic conditions.

More complex precipitation patterns[9] and convection patterns[10], using a one-dimensional solution to the ionospheric effects of the precipitation, based on Roble and Rees (1977), have been used in an interim attempt to study the response of the polar thermosphere to severe geomagnetic disturbances. These attempts have been a useful means of representing the enhancement of ionospheric conductivity, ion drag and frictional heating both in the simulation of average geomagnetic input conditions[12, 13] and for storm-time simulations[14, 15]. Plasma transport effects due to convection and winds are, however, crucial at F-region altitudes. Additionally, the feedback of induced changes of thermospheric composition, which changes rapidly and locally during intense geomagnetic distrubances, is an important omission in previous ionospheric modelling studies.

To overcome these limitations, a strategy has been developed which permits the combination of 3-D T-D global thermospheric model and a polar/auroral ionosphere model to be run with the frequent interchange of the inter-dependent parameters. Firstly, however, the description of the geophysical processes which occur within the ionosphere have had to be updated, compared with the descriptions used in previous work[6, 7].

The computational and data base strategy, permitting the frequent interchange of essential parameters, and the detailed physical content of the new ionospheric code will be described in detail in a series of papers now in preparation, however, it is appropriate to cover the major elements which have been changed since the prior work (i.e.[6, 7, 12]).

DESCRIPTION OF THE JOINT MODEL

I. THE IONOSPHERIC CODE

The polar ionospheric code developed at Sheffield University for simulating structures of the polar ionosphere, the plasmasphere, and the causes of complex phenomena such as the mid-latitude trough, has been described in a series of papers[6, 7, 16]. The earlier model dealt primarily with the problems of the upper F region, and its extension either into the plasmasphere, or into the high-altitude polar ionosphere. The light atomic ions, essentially O^+, He^+, and H^+, were thus the most important components of the ionospheric code.

In dealing with the lower parts of the ionosphere, below about 200 km, many aspects of the original code have had to be modified. Molecular ions, which have much more rapid recombination rates than atomic ions, tend to dominate over the atomic ions in the increased presence of molecular nitrogen and molecular oxygen. As a result, residence times are thus much shorter, so that transport effects, particularly due to horizontal transport, become less important. However, strong vertical movements of ionization, resulting from fast horizontal convection, and also from rapid horizontal and vertical wind motions, must be considered.

Next, the strategy of data interchange between two vastly different styles of models has to be optimised:

The thermosphere model exists on a regular global grid, using spherical coordinates in the horizontal dimension, and with pressure coordinates in the vertical dimension. The global grid rotates with the earth.

The ionosphere model exists as a series of one-dimensional, time-dependent solutions to the conditions within a hypothetical flux tube. The contents of these flux tubes are influenced by precipitation, solar photoionization, and recombination and charge exchange processes (etc), as the flux tubes are convected through regions where the geophysical conditions vary greatly.

A typical flux tube in the polar regions is convected throughout the dayside and nightside parts of the polar cap and auroral oval, experiencing highly variable solar photo-ionization, particle precipitation and convection velocity. The flux tube will also be convected through regions where the temperature and composition of the thermosphere, in addition to the wind velocity, will be highly variable. For convenience, the convection paths followed by individual flux tubes are used as the fundamental grid of the ionospheric model.

Even when the only time-dependence in the model is that induced by the UT-dependent location of the geomagnetic polar regions with respect to solar illumination, each flux tube has to be followed for many hours. As the flux tube convects throughout the high latitude regions, the solution will eventually become convergent and stable to the input conditions, which can vary over extreme ranges as flux tubes convect into and out of sunlight, or regions of strong convection and/or precipitation.

A sequence of points thus have to be followed along each convection path, so that at any specific Universal Time, there is a reasonably uniform distribution of populated flux tubes along each of the convection paths which are used in the computations.

II. THE THERMOSPHERIC CODE

The UCL three dimensional time-dependent global thermospheric model has been described in detail in a number of recent papers[12-15]. The only significant change created in the interactive and self-consistent modelling approach is that, in the high latitude regions, the earlier computation of the ionosphere from either the CHIU global model (applicable to quiet geomagnetic conditions only), or by the PIONS ionospheric model[14-15], is now replaced by the ionospheric computations described conceptually above. For the gain of realism, the additional computation involved in this procedure uses only marginally greater computer resources than the previous ionospheric computation from the CHIU model, or from implementing the PIONS routine.

PRESENT STATUS

The present status of this work is that early diagnostic tests of the joint code have been run, to test the numerical method and code, and to examine the sensitivity of the resulting ionosphere to the range of geomagnetic and solar/seasonal conditions.

Several of the early interesting results from these tests will be discussed, with their significance for the future adaption of the joint code to the routine computation of self-consistent global models of the thermosphere and ionosphere.

SIMULATIONS WITH STEADY-STATE GEOMAGNETIC INPUTS

Some major results of the work of Quegan et al[6], and Fuller-Rowell et al[7] will be summarized. The 'Sheffield' model, used a geometry of co-incident geographic and geomagnetic poles (UT-independent), and were carried out for the northern polar region at winter solstice. Separately, the polar ionosphere and the global thermosphere models were run to stability, and the relevant data sets were interchanged (ionospheric density distribution transferred to the thermosphere model, and thermospheric winds etc transferred to the ionospheric model). This data set interchange was iterated once (after 24 hours). The resulting thermospheric and ionospheric data were convergent after this single iteration.

The polar ionosphere and thermosphere wind system resulting from these early computations[6] are shown at 320 km altitude in Figure 1. For comparison, Figure 2 shows the polar ionosphere and the thermospheric wind system produced by the CHIU ionosphere model.

In the polar ionosphere, the auroral enhancement of plasma density is very pronounced, and a 'hole' has appeared in the polar cap as a result of plasma stagnation with this particular polar electric field. Around the boundaries of the auroral oval, features similar to the trough associated with the plasmapause have appeared[6, 16].

In comparison with empirical data, two major factors must be considered. Firstly, although the values used to describe the magnetospheric precipitation are by no means extreme, individual flux tubes are exposed to this precipitation for many hours within both the dusk and the dawn parts of the auroral oval. Secondly, there is no feed-back into the thermospheric composition in this early simulation, so that one important consequence of intense enhancement of ion-neutral momentum coupling, namely the strong enhancement of molecular nitrogen density in thermospheric regions which are strongly heated by frictional or particle heating, does not occur due to use of the MSIS global model.

The very long exposure to persistent (if moderate) particle fluxes, and the lack of thermospheric compositional response, generates ionospheric plasma densities within the auroral oval which are probably higher than would really occur. Naturally time-dependent ionospheric convection, where individual flux tubes are carried into and out of regions of auroral precipitation, and the enhancement of nitrogen density in regions of strong thermospheric heating, causing a major increase in the effective ionospheric recombination rate, are likely to suppress the high modelled auroral electron density values.

Features such as the ionospheric 'polar hole', which have been observed in satellite data, are due, in the model simulations, to stagnation regions, where plasma remains caught up in polar cap regions on the night-side where there is no precipitation and where there is no solar photo-ionization.

In reality, such conditions may rarely occur, and Killeen et al[17] have recently shown that regions of major polar cap plasma depletions may be the signature of intense ion-neutral coupling in regions of very fast anti-sunward ion flow.

TIME-DEPENDENT JOINT SIMULATIONS

The structure of both thermospheric and ionospheric parts of the model has been created so that there is an easy interchange of data sets between the two models. At present, one or other model is being run independently, in virtually the same mode used in the original study[6]. The exception is that thermospheric composition can be passed between the models, and a sequence of simulations are in progress to examine the effects of closing feedback loops such as the geomagnetic effects on thermospheric composition.

344

The structure of the models is organized in such a way that, with a minimum time constant of 15 minutes, the geomagnetic inputs to the polar ionosphere and thermosphere can be varied. Ultimately, this will allow the realistic simulation of strongly time-dependent events. At this stage, the major limitation to exploitation of the joint ionospheric/thermospheric model will then be the limited availability of truly global data sets describing the geomagnetic input to the polar ionosphere and thermosphere.

SIMULATIONS OF THE POLAR IONOSPHERE

The first simulations using the new ionospheric code have used, as part of the input, the thermospheric wind system derived from 3D TD model simulations for approximately equivalent seasonal, solar activity and geomagnetic activity. Simulations have been carried out for the summer and winter solstices and for the equinox. As a result of these simulations, it is possible to see the effects of variable solar photo-ionization, and of seasonally-variable thermospheric composition in the polar regions.

Although the simulations have been carried out for a full range of Universal Times, the results will only be displayed at a single UT for each of the four simulations to be described. Two of the simulations use the 'A2' polar convection field (Figure 3[10]) to describe the northern hemisphere polar convection when the IMF Y component is negative. The last simulation, for northern winter solstice, uses the 'B2' polar convection field (Figure 4), corresponding to a condition when the IMF Y component is positive. The convections paths, followed by individual flux tubes, responding to these convection patterns, as seen from the sun, are shown in Figures 5 and 6 respectively.

For all of these simulations, a background thermospheric wind model, which is approximately that corresponding to the situation for which we are now generating the ionospheric model, has been used. The neutral gas composition and temperature for these initial simulations have been taken from MSIS[17], preparatory to running the full interactive model.

A. THE POLAR IONOSPHERE AT WINTER SOLSTICE:

Northern Hemisphere, A2 convection, IMF BY negative

Figures 7 and 8 show the polar plasma densities at 18 UT at altitudes of 160 and 320 km respectively. At each altitude, the auroral enhancement of plasma density is pronounced, as is the mid-latitude peak of plasma density in the early afternoon hours on co-rotating flux tubes below the latitude of the auroral oval.

B. THE POLAR IONOSPHERE AT SUMMER SOLSTICE:

Northern Hemisphere, A2 convection field (IMF BY negative)

In Figures 9 and 10, the ionospheric structure for the same UT is shown for the summer solstice (N. Hemi.). In this simulation, the peak electron densities in the auroral oval are considerably lower than in the winter simulation. This is due to the greater amount of molecular nitrogen, at the equivalent altitude and pressure level, in the upper thermosphere at the summer solstice, causing an increase in the effective ionospheric recombination rate, which more than offsets the increased solar photo-ionization in this summer period. As a result, the electron densities fall to about 50% of the peak values obtained in the winter solstice simulation.

In Figure 11, the corresponding plasma density distribution from the Chiu model is shown for the northern summer polar region. The peak number densities are not too different, however, the entire distribution has changed, so that the effects of plasma precipitation are most marked, while the mid-latitude densities of the theoretical model are significantly below those of the Chiu model.

DISCUSSION

IONOSPHERIC STRUCTURES IN THE POLAR REGIONS

The dominating structure seen in the polar plasma densities is the enhancement of electron density in the vicinity of the auroral oval, at all altitudes, and during summer and winter solstice conditions. The plasma density enhancements are due to the prolonged exposure of individual flux tubes to magnetospheric precipitation as these flux tubes convect sunward within both the dusk and the dawn parts of the auroral oval. Although the precipitating fluxes are modest, the duration of exposure is prolonged (several hours). The peak plasma densities appear to be rather higher than occur in the real world, and we anticipate that this is due to the prolonged exposure of individual flux tubes to magnetospheric precipitation, with inadequate feed-back due to compositional change.

In the real world, under quiet and moderately disturbed geomagnetic conditions, the flux tubes may exprience much more variable convection and precipitation, which reduce the average ion generation. Also, thermospheric feed-back mechanisms, not yet allowed to operate fully (compositional changes), may act to deplete plasma densities on flux tubes which spend long periods within the auroral oval.

SEASONAL VARIATIONS

The seasonal variations of plasma density are in the sense which has been reported by Foster[19] from observations with the Millstone Hill Incoherent Scatter Radar. That is, the dayside electron densities are higher in winter than in summer, and the peak auroral oval plasma densities are likewise higher in winter than in summer. In the present simulations, this is due to the higher concentration of molecular species in the MSIS summer polar thermosphere. Since this is also a feature of the UCL 3-D T-D model[13, 15, 20], this seasonal anomaly in polar plasma density will, undoubtedly, also be a feature of the fully coupled ionosphere and thermosphere model.

VARIATIONS WITH THE Y COMPONENT OF THE IMF

The major variations which are induced by changing the polar convection field are only seen at the higher altitudes, where recombination is slower, and where the transport of plasma causes a strong modification of the plasma distribution. Figures 8 and 10 (BY negative) illustrate the pattern created when the highest anti-sunward ion flow regions is the dusk side of the polar cap.

A tongue of enhanced plasma density reaches back across the polar cap on the dusk side when BY is negative. This is very reminiscent of the structures described by Weber et al[21]. They have reported anti-sunward convecting patches of enhanced ionospheric plasma density and related features of polar cap airglow features.

When the region of highest anti-sunward flow moves to the dawn side of the polar cap (BY positive), the plume of enhanced plasma density follows this change in the polar convection, and creates a quite asymmetrical plasma distribution compared with Figures 8 and 10.

In the joint modelling studies which have been carried out so far, the wind structures (3-D T-D model) and the thermospheric composition and temperature structures (MSIS for comparable conditions) which have been imposed as input conditions to the ionospheric model are moderately close to the conditions we would expect to develop. This does not, however, allow the full feed-back processes to develop, particularly in thermospheric temperature and composition. The major effects which would be anticipated as a result of closing the feed-back loop are associated with the enhancement of recombination coefficients in regions where there is strong ion-neutral coupling and frictional heating, or where there is strong particle heating. These fully-coupled simulations will be carried out in the near future, and it will then be possible to examine the conclusions mentioned earlier relating to the regions of strong depletion of polar cap plasma densities.

A significant problem which has to be solved in the near future is how to introduce a better method of preventing the plasma densities within the auroral oval from reaching unrealistically large values. Possibly, the explanation lies in the feed-back coupling of enhancement of molecular neutral and thus ionic species in those regions where there is intense heating for long periods, as plasma is forced to remain on convection paths which remain for long periods in regions such as the dusk auroral oval. Another possibility is that the temporal variations of precipitation and convection ensure that, in the real world and under slightly to moderately disturbed conditions, specific flux tubes are continuously moving into and out of regions of significant precipitation. In this way, the enhancement of plasma density would be rather more modest.

Accounting for this latter mechanism in a theoretical model is not a trivial process, but represents one of the outstanding goals of simulating in a realistic way the structure of the polar ionosphere under a range of realistic seasonal, solar and geomagnetic conditions, where the major feed-back mechanisms between the ionosphere and polar thermosphere are taken into account.

REFERENCES

1. FULLER-ROWELL T. J. and REES D. (1980). A three-dimensional time-dependent global model of the thermosphere J. Atmos. Sci. *37*, 2545-2567.
2. ROBLE R. G., DICKINSON, R. E., and RIDLEY E. C. (1982). Global Circulation and Temperature Structure of the Thermosphere with High-latitude Plasma Convection J. Geophys. Res. *87*, 1599-1614.
3. HINTEREGGER H. E. (1981). Representation of solar EUV fluxes for aeronomical applications. Adv. Space Res. *1*, 39-52.
4. KNUDSEN W. C., BANKS P. M., WINNINGHAM J. D. and KLUMPAR D. M. (1977). Numerical model of the convecting F2 ionosphere at high latitudes. J. Geophys. Res. *82*, 4784-4792.
5. HEPPNER J. P. (1977). Empirical models of high latitude electric fields. J. Geophys. Res. *82*, 1115-1125.
6. QUEGAN S., BAILEY G. J., MOFFETT R. J., HEELIS R. A., FULLER-ROWELL T. J., REES, D., and SPIRO R. W. (1982). A Theoretical Study of the distribution of Ionization in the High Latitude Ionosphere and the Plasmasphere: first results on the Mid-latitude Trough and Light-ion trough. J. Atmos. Terr. Phys. *44*, 619-640.
7. FULLER-ROWELL T. J., REES D., QUEGAN S., BAILEY G. J., and MOFFETT R. J. (1984). The effect of realistic conductivities on the high-latitude neutral thermospheric circulation. Planet. Space Sci. *32*, 469-480.
8. CHIU Y. T. (1975). An improved phenomenological model of ionospheric density. J. Atmos. Terr. Phys. *37*, 1563-1570.
9. SPIRO R. W., REIFF P. F. and MAHER L. J. (1982). Precipitating electron energy flux and auroral zone conductances—an empirical model. J. Geophys. Res. *87*, 8215-8227.
10. HEPPNER J. P. and MAYNARD N. M. (1983). Paper presented at Chapman Conference at Irvington Virginia. March, 1983.
11. ROBLE R. G. and REES M. H. (1977). Time dependent studies of the aurora: Effects of particle precipitation on the dynamic morphology of ionospheric and atmospheric properties. Planet. Space Sci. *25*, 991.
12. REES D., FULLER-ROWELL T. J., GORDON R., KILLEEN T. L., HAYS P. B., WHARTON L. E. and SPENCER N. W. (1983). A Comparison of Wind Observations of the Upper Thermosphere from the Dynamics Explorer Satellite with the Predictions of a Global Time-dependent Model. Planet. Space Sci. *31*, 1299-1314.
13. REES D. (1985). Theoretical Thermosphere Models. Paper presented at COSPAR, Graz (1984). To be published Adv. Space Res.
14. REES D., FULLER-ROWELL T. J., SMITH M. F., GORDON R., KILLEEN T. L., HAYS P. B., SPENCER N. W., WHARTON L., MAYNARD N. C. (1985). The Westward Thermospheric Jet-Stream of the Evening Auroral Oval. Accepted by Planet. Space Sci.
15. REES D., SMITH M. F. and GORDON R. (1984). The Generation of Vertical Thermospheric Winds and Gravty Waves at Auroral Latitudes - II. Theory and Numerical Modelling of Vertical Winds. Planet. Space Sci. *32*, 685-705.
16. MOFFETT R. J. and QUEGAN S. (1983). The Mid-Latitude Trough in the Electron Concentration of the Ionospheric F-Layer: a review of observations and modelling. J. Atmos. Terr. Phys. *45*, 315-343.

17. KILLEEN T. L., HAYS P. B. CARIGNAN G. R., HEELIS R. A., HANSON W. B., SPENCER N. W. and BRACE L. H. (1984). Ion-Neutral Coupling in the High-Latitude F Region: Evaluation of Ion Heating Terms From Dynamics Explorer 2. J. Geophys. Res. *89*, 7495-7508.

18. HEDIN A. E., REBER, C. A., NEWTON G. P., SPENCER N. W., BRINTON H. C., MAYR H. G., and POTTER W. E. (1977). A global thermospheric model based on mass spectrometer and incoherent scatter data. MSIS 2. Composition. J. Geophys. Res. *82*, 2148-2156.

19. FOSTER J. C. (1984). Ionospheric Signatures of Magnetospheric Convection. J. Geophys. Res. *89*, 855-865.

20. HEDIN A. E., REES D. and FULLER-ROWELL T. J. (1985). In preparation.

21. WEBER E. J., BUCHAU J., MOORE J. G., SHARBER J. R., LIVINGSTON R. C., WIN-NINGHAM J. D. and REINISCH B. W. (1984). F Layer Ionization Patches in the Polar Cap. J. Geophys. Res. *89*, 1683-1694.
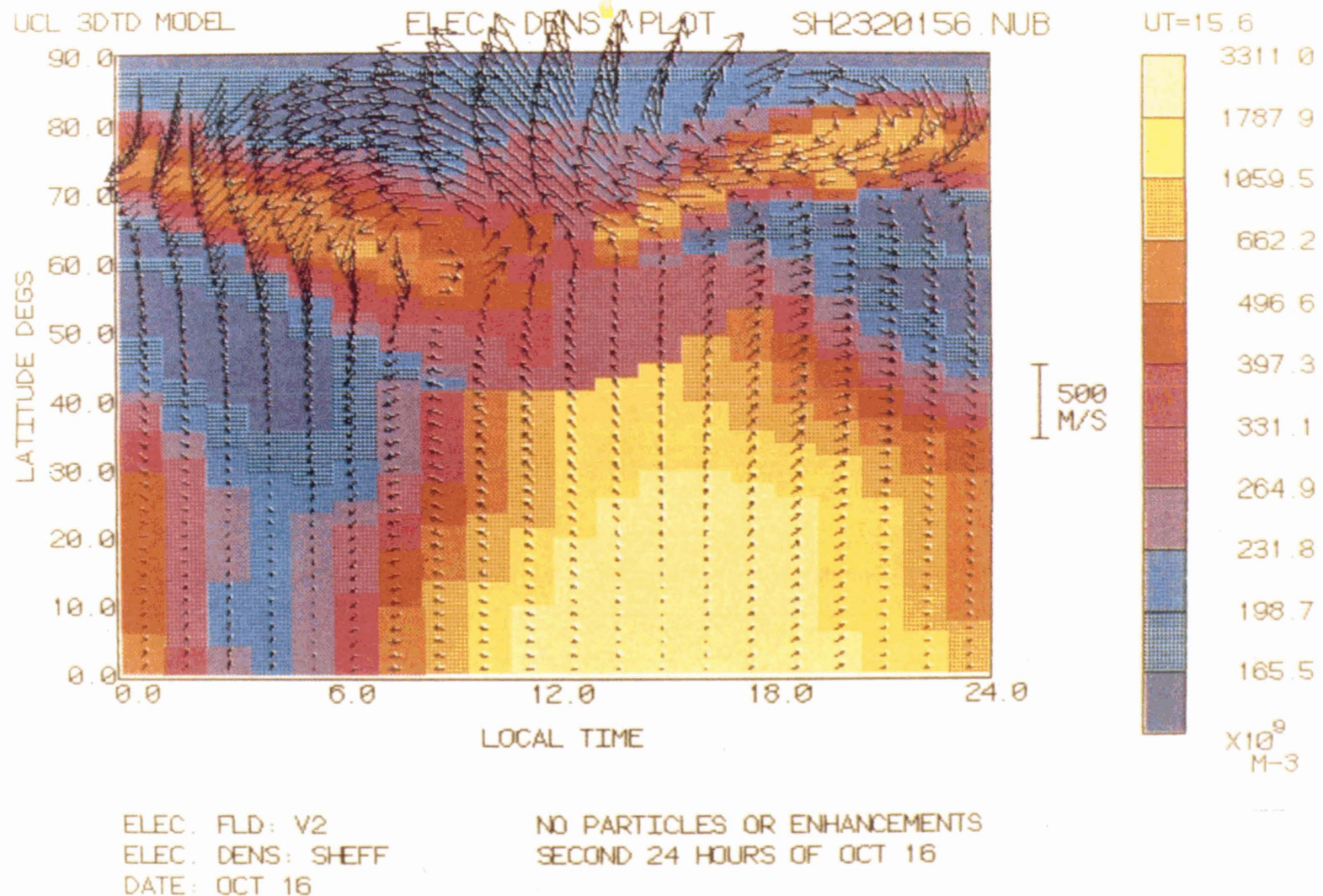
Figure 1. Thermospheric wind system at 320 km produced by the 'Sheffield' polar electron density model, in combination with the Heppner model B2 polar electric field. The polar presentation is in geographic coordinates, and the contours of the electron density distribution are also shown. The enhancement of electron density around the dusk and dawn parts of the auroral oval is distinct.
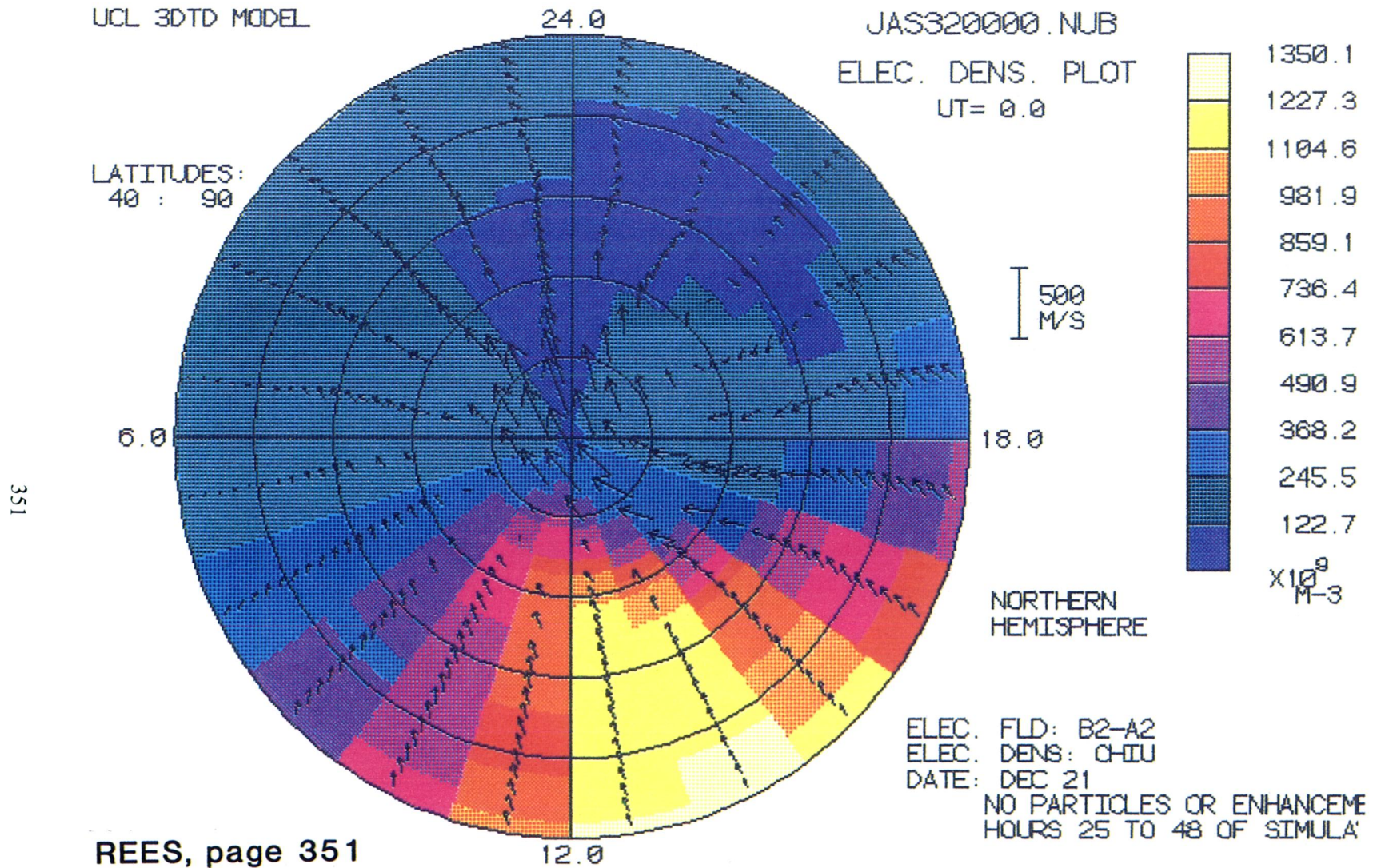
Figure 2. Thermospheric wind system at 320 km produced by the 'Chiu' global ionospheric model, with the same polar electric field as used to produce Figure 1. The much lower electron densities can be seen from the scalar background values. The winds in the auroral oval are significantly lower, approximately half the value of those produced by the 'Sheffield' ionosphere.

MODEL A-2
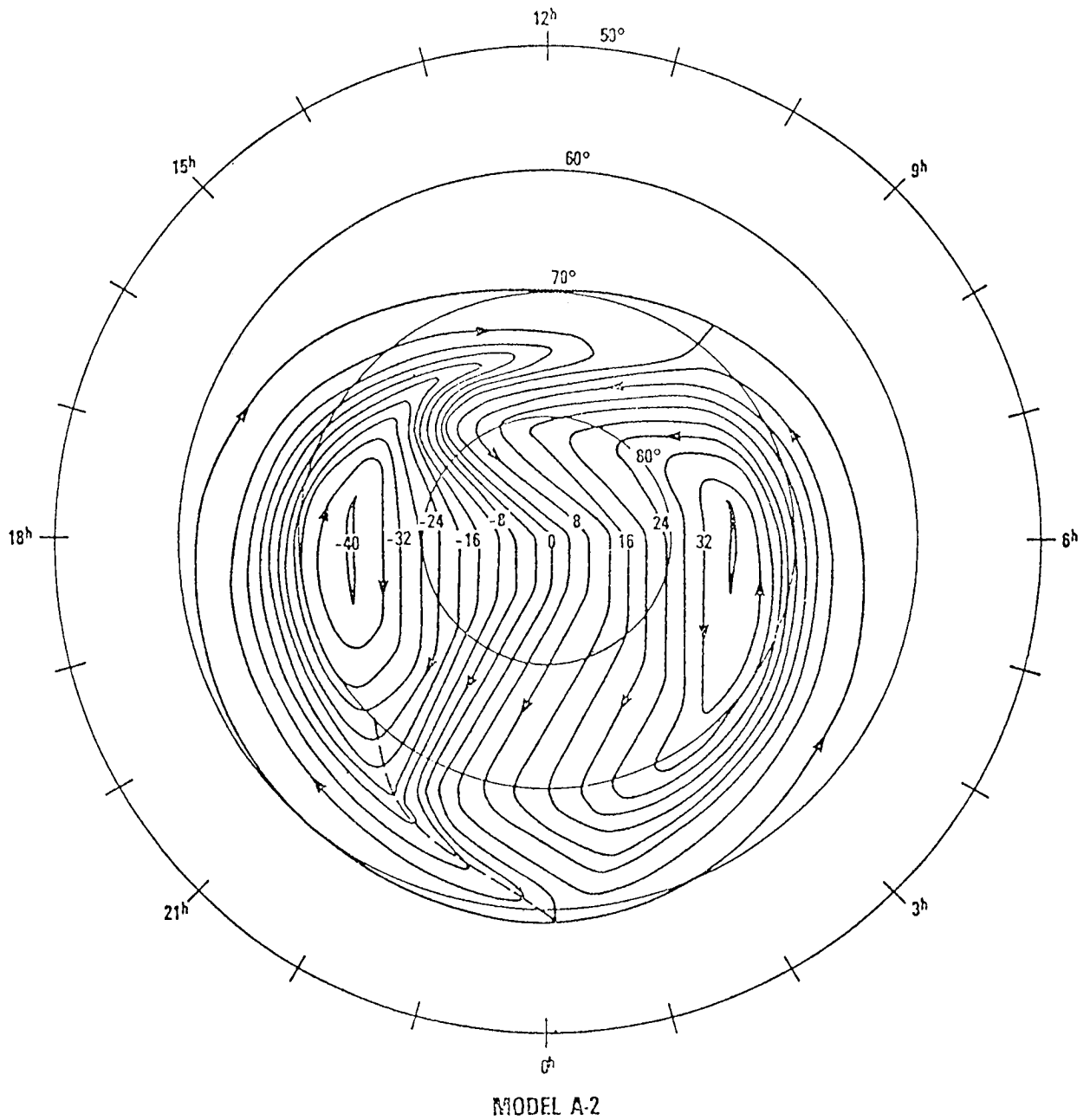
Figure 3. The A2 model of the polar electric field, from Heppner and Maynard 1983. This field is applied to the northern hemisphere when the IMF BY component is negative, and to the southern polar region when the IMF BY component is positive. It applied to moderately disturbed geomagnetic conditions 3 < kp < 4 (approx).
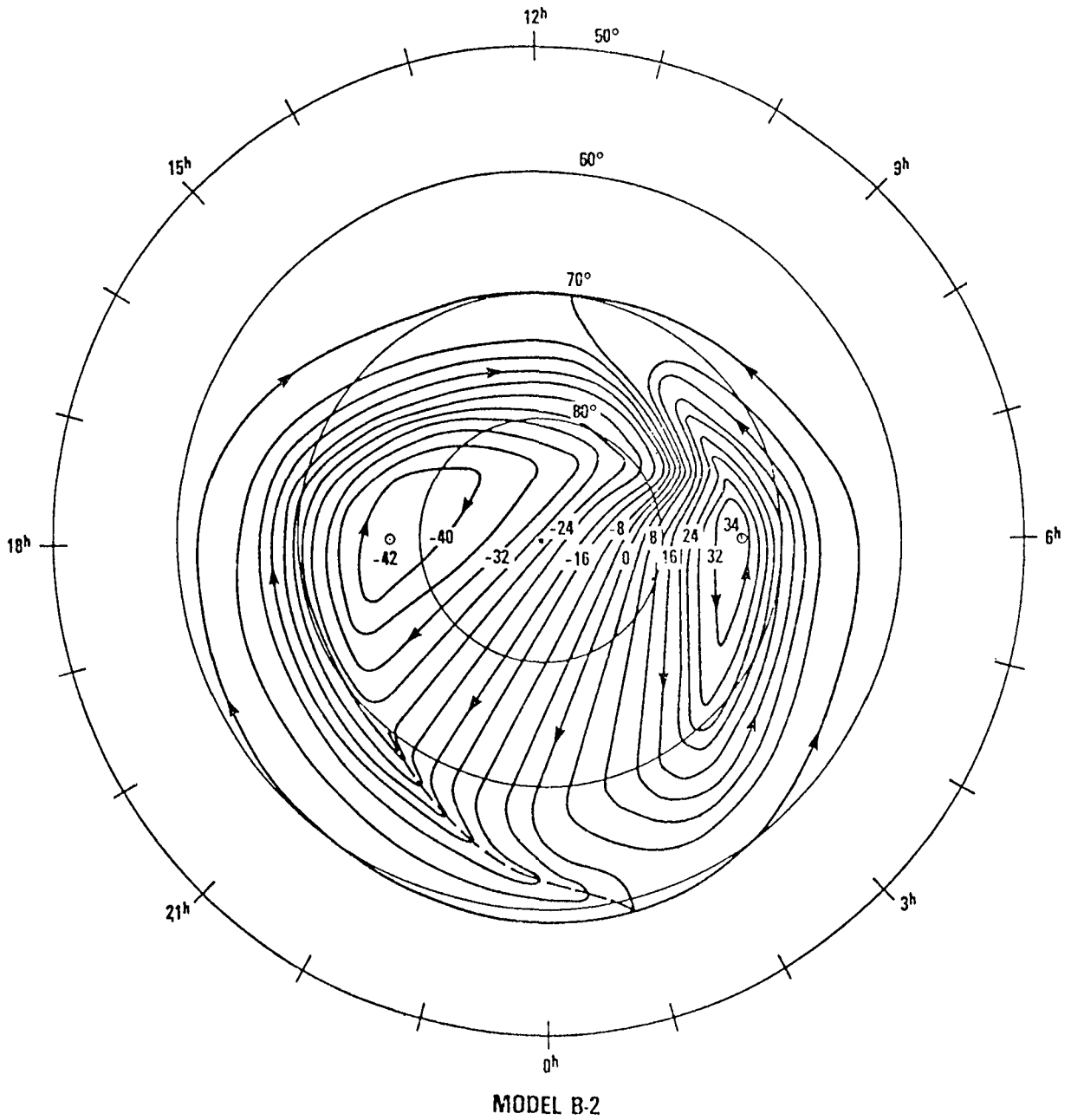
Figure 4. The B2 model of the polar electric field, from Heppner and Maynard 1983. This field is complementary to the A2 field, i.e. is applied to the northern hemisphere when the IMF BY component is positive.

Figure 5. Convention paths traced by ionospheric flux tubes following the A2 polar electric field, as seen in solar and geomagnetic coordinates.

*** Const. Potential ***
****** GRID PATHS ******

180.0

ELEC. FIELD: B2

06 MLT

-90.0

18 MLT

0.0

12 MLT
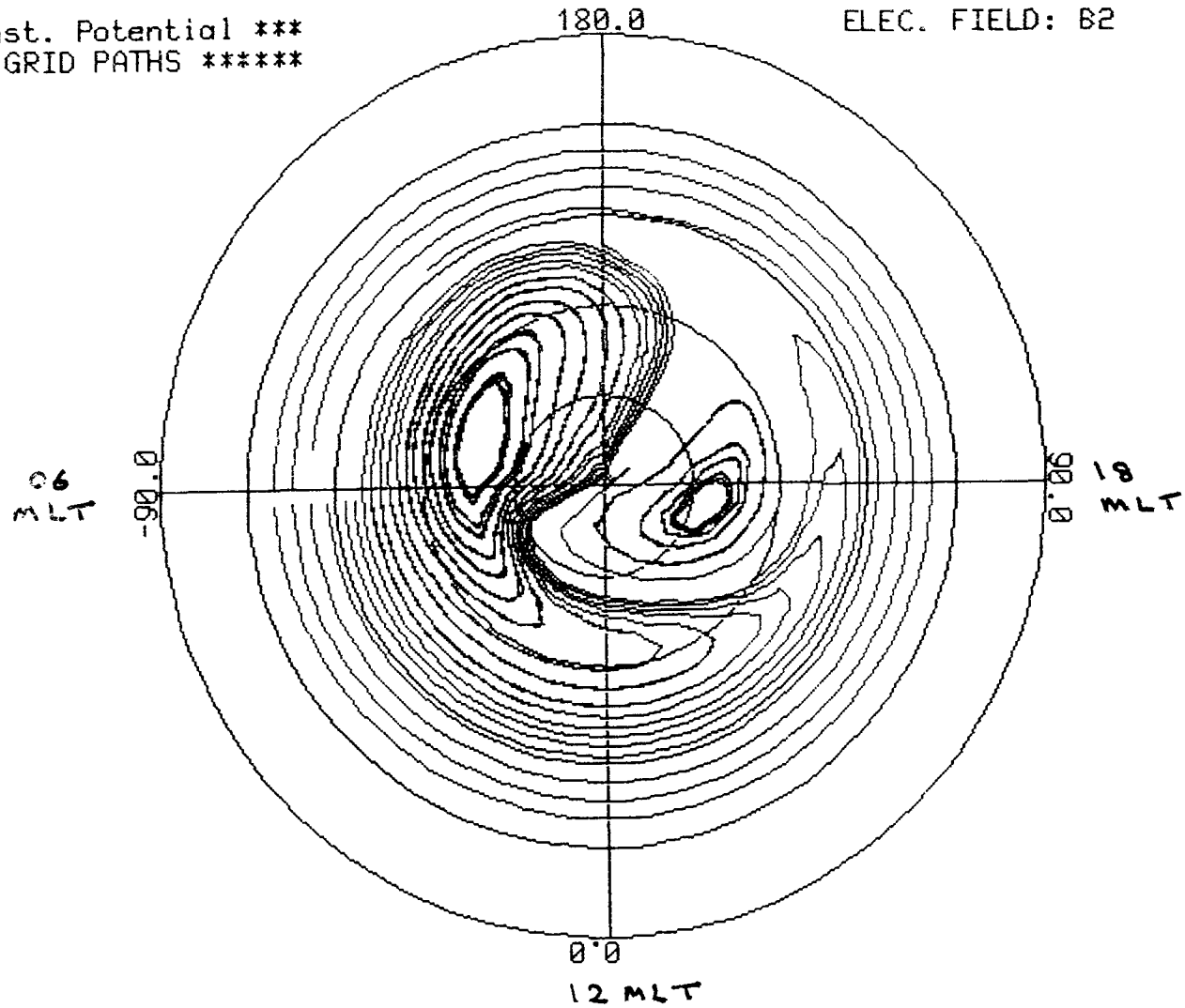
Figure 6. Convection paths traced by ionospheric flux tubes following the B2 polar electric field, as seen in solar and geomagnetic coordinates. The contrast between the concentration of paths over the dusk (A2) and dawn (B2) sides of the polar cap is the most striking feature.

Figure 7. Polar plasma densities at 160 km altitude produced by the winds and electric fields (convection) due to the A2 electric field and the same precipitation used in the original 'Sheffield' study. This study has been carried out for conditions of (northern) winter solstice, so that there is little solar photo-ionization within the auroral oval and polar cap regions. It can be seen that the plasma density enhancement is strictly limited to the vicinity of the auroral oval and its associated precipitation.

Figure 8. Same as Figure 7, but at 320 km. Transport effects are now very important, and there is an intense plume of ionisation carried anti-sunward over the polar cap, away from the polar cusp region, by the strong anti-sunward ion convection velocities in the dusk region of the polar cap.

HEIGHT: 160Km *** ELECTRON DENSITY PLOT *** DATA-FILE:D020000.ELD
UT: 0.00
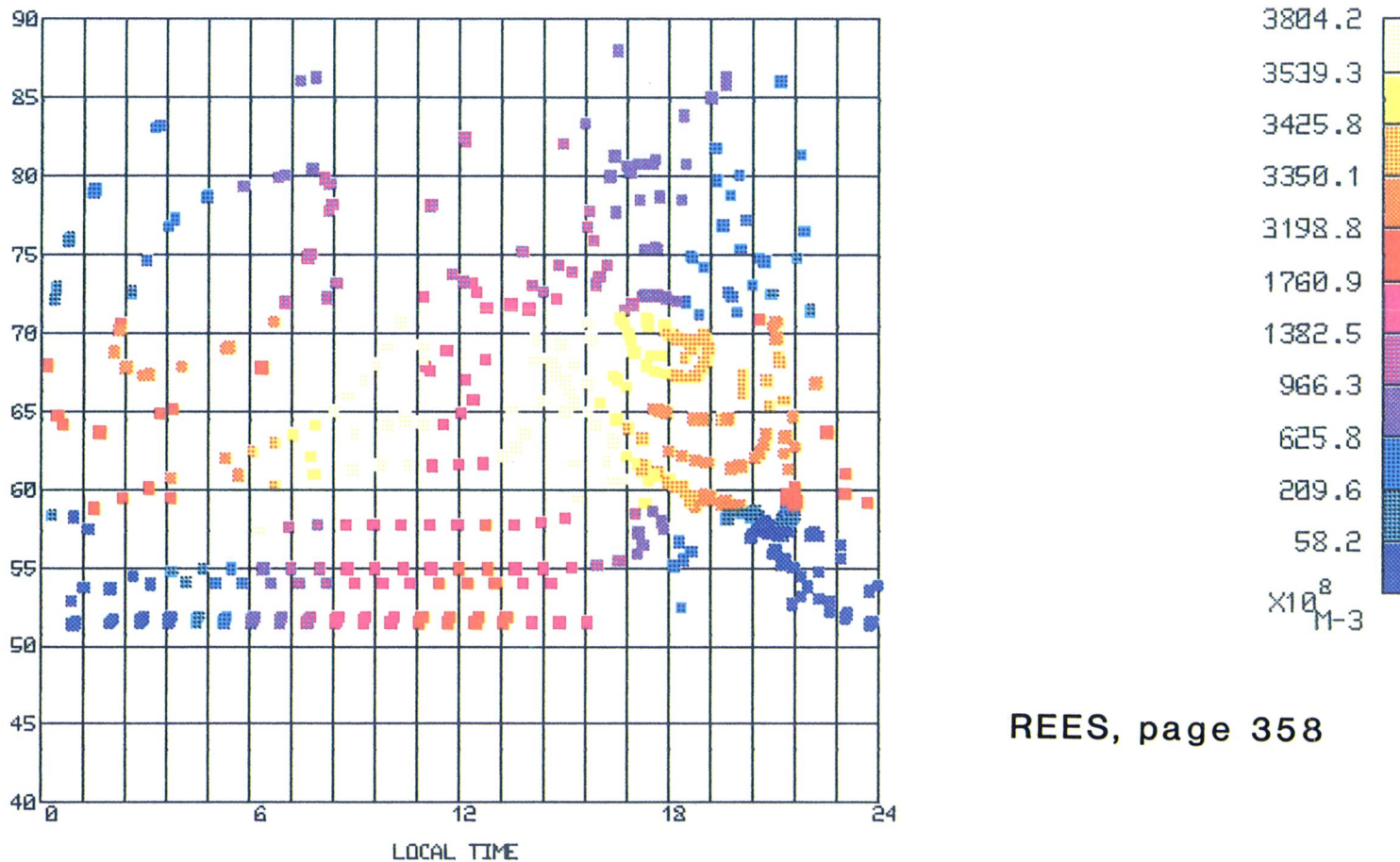
358

Figure 9. Same as Figure 7, at 160 km altitude, but for (northern) summer solstice conditions. Despite the much higher solar photo-ionisation source, the actual electron densities, within the auroral oval, and on the dayside, at sub-auroral latitudes, are lower than those generated in the winter solstice model.
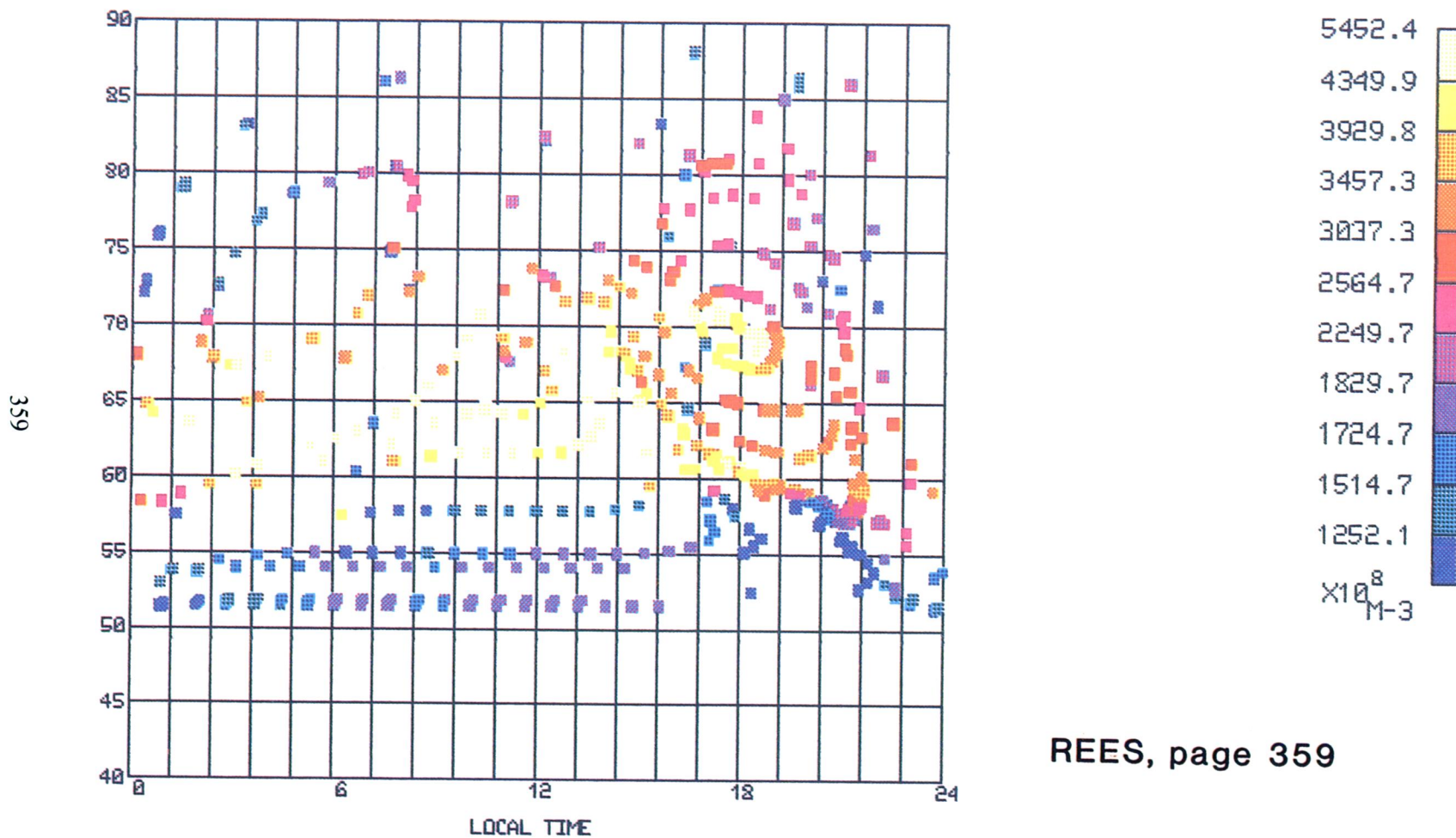
Figure 10. Same as Figure 9, but at 320 km altitude.
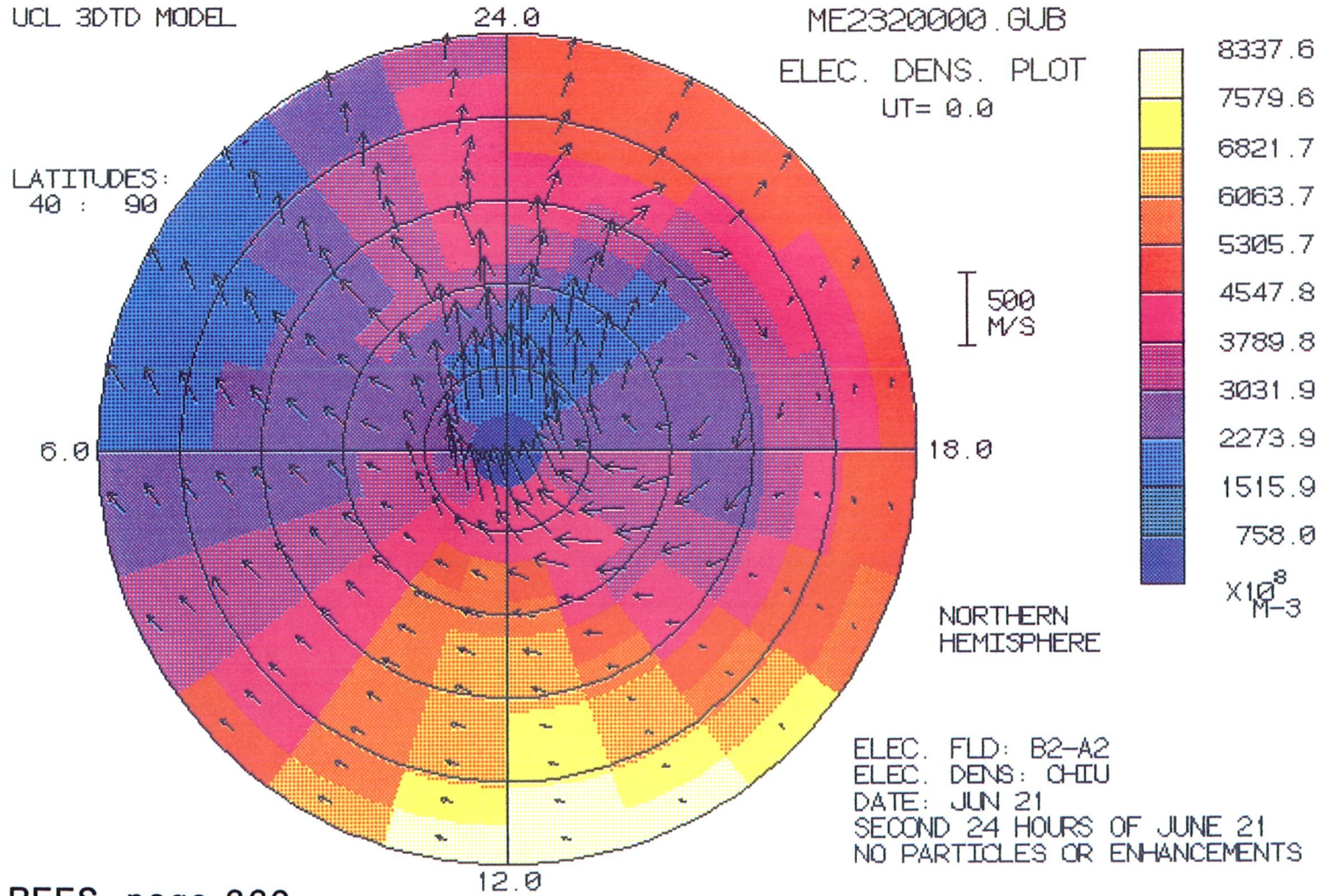
Figure 11. Thermospheric wind system at 320 km produced by the 'Chiu' global ionospheric model, with the same polar electric field as used to produce Figure 2, but for the June solstice. The electron densities are rather lower, at mid-latitudes than for the Dec. solstice.

PARTICLE PRECIPITATION INTO THE THERMOSPHERE
(Invited Review)

Patricia H. Reiff
Department of Space Physics and Astronomy
Rice University, Houston, TX 77251-1892

Particle precipitation plays an important role in thermospheric dynamics, often being both the most important ionization source and the most important heat source, comparable to Joule heating rates in the auroral zones [Harel et al., 1981; Rees, et al., 1983; see Reiff, 1983a] and typically exceeding solar ultraviolet as an ionization mechanism in the nightside auroral zones and winter polar caps (Figure 1, from Wallis and Budzinski, [1981]). Rees [1963] has shown that, roughly speaking, one electron-ion pair is produced by each 35 eV of incident electron energy flux; thus, over half of the incident electron energy flux goes into heating rather than into ionization. Precipitating ions also can produce ionization, also requiring roughly 35 eV per pair [Rees, 1982]; however, since ion energy fluxes are typically much weaker than electron fluxes, they have often been neglected.

The altitude at which the electrons and ions deposit their energy is strongly dependent on particle energy, with ionization occurring at progressively lower altitudes for increasingly more energetic electrons. For 300 keV electrons, the altitude of maximum ionization occurs at 72 km; 95 km for 40 keV; ~ 107 km for 10 keV, ~ 170 km for 1 keV, and > 216 km for 0.4 keV [Figure 2, from Rees, 1963]. Ions deposit their energy at altitudes higher than electrons of comparable energy [Rees, 1982]. The altitude of ionization becomes important in determining resultant conductivity profiles, with lower altitudes favoring a higher ratio of Hall to Pedersen conductance; this in turn affects the height distribution of Joule heating rates.

The bulk of the particle precipitation occurs on field lines which map to the plasma sheet and ring current regions. The auroral zone precipitation is greatly enhanced over its typical loss cone fluxes by the existence of electric fields parallel to the magnetic field line [Knight, 1973]. The auroral electric fields are associated with upward field-aligned (Birkeland) currents. The lower-latitude ring current precipitation is caused principally by pitch-angle scattering in the equatorial plane. (See review by Reiff, [1983b]).

It is not currently possible (nor is it likely in the near future) to have a complete, detailed, global distribution of particle precipitation on a nearly-continuous basis, although progress is being made using several complementary techniques. In-situ spacecraft and rocket particle observations are extremely useful and yield results on very good spatial scales along the flight track (km to m, for rocket flights); global models, however, must be constructed statistically, and as such lose much small-scale detail (Figure 3, from Spiro et al. [1982]). Using a number of spacecraft (Tiros and DMSP), separated in local time, one can construct a global energy flux estimate with roughly 15-minute time resolution [David Evans, personal communication, 1984]; however, obtaining a two-dimensional pattern from combining different in-situ data sets is a cumbersome technique and cannot at present be done accurately with less than a two-hour time resolution [Simons et al.,

1985]. Some of the statistical models have become very detailed, however, with complete spectra (not just energy flux and average energy) available at each local time-latitude bin (Figure 4 from Hardy et al., [1985]). Incoherent radar studies can also be used to infer precipitating electron fluxes [Vondrak and Baron, 1977], but they also are limited in field of view.

Optical techniques show perhaps the most promise for developing an accurate two-dimensional pattern on reasonable time scales. Images from high altitude (such as Dynamics Explorer and the proposed International Solar Terrestrial Research Program) have the advantage of global coverage at ten-minute time resolution, at the expense of spatial resolution (~ 50 km) [Frank et al., 1982]. Lower-orbiting spacecraft, such as Hilat and DMSP (which will add ultraviolet imaging to its optical data starting in 1989), have much better spatial resolution (~ km); however, a single pass generally cannot image the entire auroral zone, and is repeated only with 45-minute time resolution (e.g., Meng and Huffman, 1984). Ultraviolet and X-ray imaging are particularly helpful, since they are responsive to the more energetic particles, and, combined with optical data, can yield a reasonable estimate of the energy distribution of the precipitating particles. [e.g., Luhmann, 1977; Imhof et al., 1982]. Calibration of the optical images by "ground truth" (images which include radar facilities) or "space truth" (in situ particle detectors) is vital and is currently underway.

In summary, the particle precipitation into the thermosphere is both an important ionization source and an important heat source; since the globally-integrated value can vary over more than a factor of ten, and the instantaneous local rate can vary over nearly three orders of magnitude (Figure 5, from Spiro et al., [1982]) global maps of precipiation rates are extremely important for predicting thermospheric "weather."

REFERENCES

Frank, L. A., J. D. Craven, J. C. Burch and J. D. Winningham, Polar views of the earth's aurora with Dynamics Explorer, *Geophys. Res. Lett., 9,* 1001-1004, 1982.

Hardy, D. A., M. S. Gussenhoven, and E. Holeman, A statistical model of auroral electron precipitation, *J. Geophys. Res.,* (in press), 1985.

Harel, M., R. A. Wolf, R. W. Spiro, P. H. Reiff, C. K. Chen, W. J. Burke, F. J. Rich and M. Smiddy, Quantitative simulation of a magnetospheric substorm. 2. Comparison with observations, *J. Geophys. Res., 86,* 2242-2260, 1981

Imhof, W. L., J. Stadsnes, J. R. Kilner, D. W. Datlowe, G. H. Nakano, J. B. Reagan, and P. Stauning, Mappings of energetic electron precipitation following substorms using the satellite bremsstrahlung technique, *J. Geophys. Res., 87,* 671-680, 1982.

Knight, S., Parallel electric fields, *Planet. Space Sci., 21,* 741-750, 1973.

Luhmann, J. G., Auroral bremsstrahlung spectra in the atmosphere, *J. Atmos. Terr. Phys., 39,* 595, 1977.

Meng, C. -I., and R. E. Huffman, Ultraviolet imaging from space of the aurora under full sunlight, *J. Geophys. Res., 11,* 315-318, 1984.

Rees, M. H., Auroral ionization and excitation by incident energetic electrons, *Planet Space Sci., 11,* 1209-1218, 1963.

Rees, M. H., On the interaction of auroral protons with the earth's atmosphere, *Planet. Space Sci., 30,* 463-472, 1982.

Rees, M. H., B. A. Emery, R. G. Roble, and K. Stamnes, Neutral and ion gas heating by auroral electron precipitation, *J. Geophys. Res., 88,* 6289-6300, 1983.

Reiff, P. H., Models of auroral zone conductances, in *Magnetospheric Currents,* ed. T. A. Potemra, p. 180-191, AGU Press, Washington, 1983a.

Reiff, P. H., Polar and auroral phenomena: A review of U.S. progress during 1979-1982, *Rev. Geophys. space Phys., 21,* 418-433, 1983b.

Simons, S. L., P. H. Reiff, R. W. Spiro, D. A. Hardy, and H. W. Kroehl, A comparison of precipitating electron energy flux on March 22, 1979 with an empirical model, *J. Geophys. Res.,* (in press), 1985.

Spiro, R. W., P. H. Reiff, and L. J. Maher, Jr., Precipitating electron energy flux and auroral zone conductances - an empirical model, *J. Geophys. Res., 87,* 8215-8227, 1982.

Vondrak, R. R. and M. J. Baron, A. method of obtaining the energy distribution of auroral electrons from incoherent scatter radar measurements, in *Radar Probings of the Auroral Plasma,* Proceedings of the EISCAT summer school, Tromso, Norway, 1975, ed. A. Brekke (Universitetforlaget, Tromso-Oslo-Bergen, 1977), p. 315-330.

Wallis, D. D., and E. E. Budzinski, Empirical models of height integrated conductivities. *J. Geophys Res., 86,* 125-137, 1981.
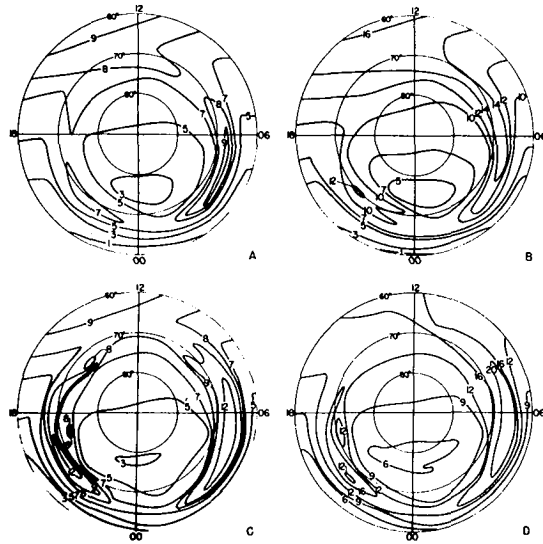
Figure 1. Contour plots of Σ_p and Σ_H (mhos) for the two K_p cases produced by particle, background, and solar sources for 1700 UT on April 1. (a) Σ_p for $0 \leq K_p \leq 3_0$, (b) Σ_H for $0 \leq K_p \leq 3_0$, (c) Σ_p for $3_0 < K_p$, (d) Σ_H for $3_0 < K_p$ [from Wallis and Budzinski, 1981].
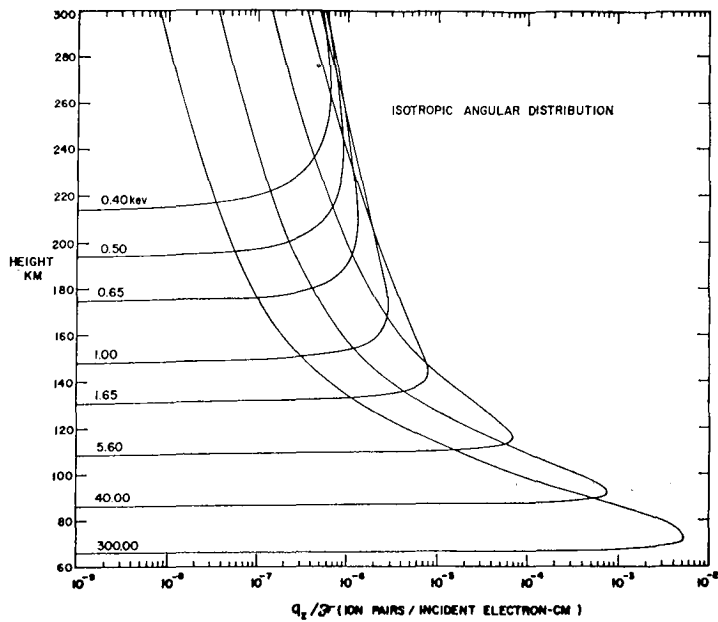

Figure 2. Ionization profiles for incident isotropic monoenergetic electrons of energies between 0.40 and 300 keV, respectively [from Rees, 1963].
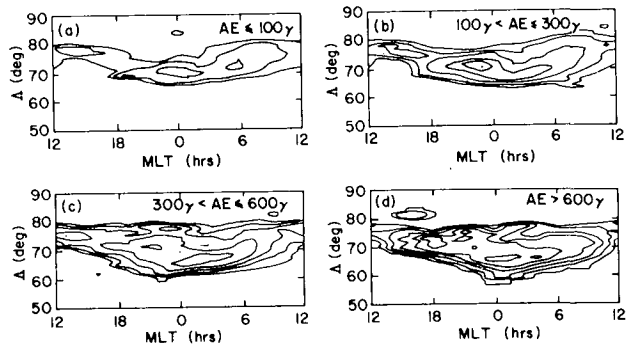
PRECIPITATING ENERGY FLUX

Figure 3. Contours of constant precipitating electron energy flux sorted according to auroral electrojet (AE) index. The outermost contours correspond to a bin-average energy flux of 2.5 x 10^{-1} erg cm^{-2} s^{-1}, with adjacent contours representing factor of 2 increases in energy flux [from Spiro et al., 1982].
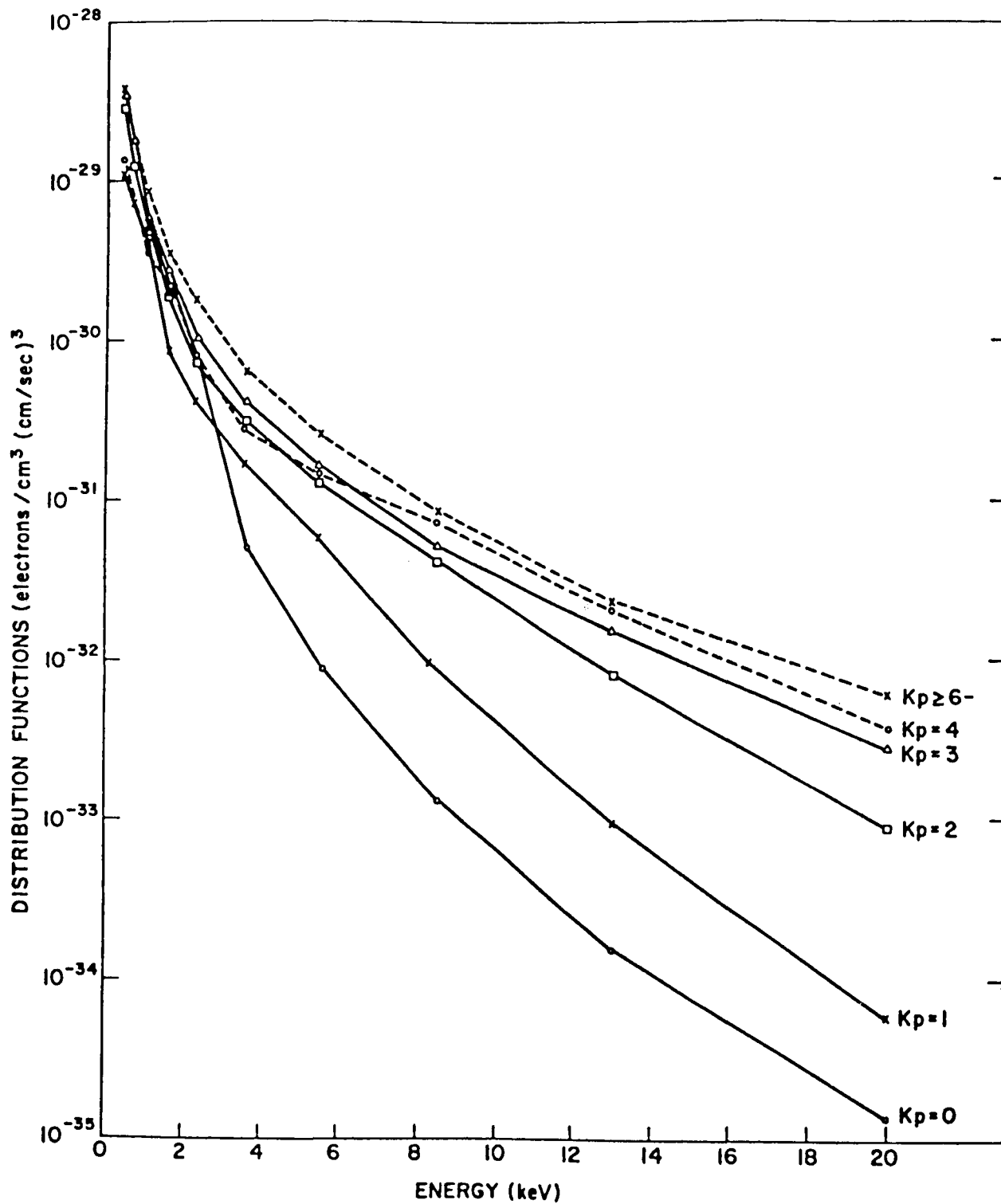
Figure 4. The average distribution function at the pre-noon average energy maximum for each K_p level. The logarithm of the distribution function is plotted versus energy on a linear scale. Only points at energies above 440 eV are included [from Hardy et al., 1985].
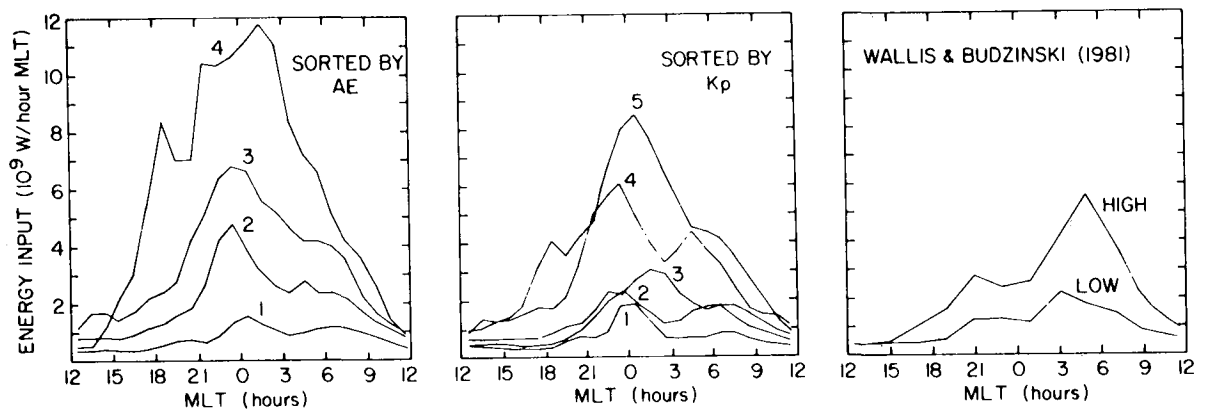
Figure 5. Total precipitating electron energy input (both hemispheres) per hour magnetic local time.(a) Data sorted according to AE index, (b) data sorted according to Kp index, and (c) results calculated from data given in Tables A1 and A2 of Wallis and Budzinski [1981].

A METHOD FOR EXTRACTING MERIDIONAL WINDS FROM IONOSONDE MEASUREMENTS BY USING IONOSPHERIC MODELS

P. G. Richards and D. G. Torr
Center for Atmospheric and Space Sciences
Utah State University, UMC 34
Logan, UT 84322

There has been great progress in modelling and measuring the dynamics of the neutral upper atmosphere in recent years [Hernandez and Roble, 1984a, b]. However, future progress will depend on the availability of global measurements of neutral winds.

At present, neutral winds can be deduced from the ion velocities measured by incoherent scatter radar and also by Fabry-Perot monitoring of the doppler shifted red line of atomic oxygen. Neither of the above methods can be relied on to provide adequate global coverage because radars are expensive to build and operate and Fabry-Perot measurements are restricted to clear skies and nighttime.

The purpose of this paper is to draw attention to a relatively cheap means of supplementing the data base of neutral winds provided by the radar and optical measurements with data obtained by ionosondes.

Rishbeth [1972] in his review of F-region dynamics, derived the relationship between the height of the F2 layer and the component of the neutral wind parallel to the magnetic field of the Earth. In this paper, we examine the sensitivity of the height and density of the F2 layer over Boulder, Colorado on 30 July 1982 to changes in meridional wind speed using a comprehensive interhemispheric numerical model [Richards and Torr, 1985] that solves the continuity and momentum equations for H^+ and O^+, the energy equations for Te and Ti, and the 2-stream photoelectron equations to obtain electron heating rates. For the neutral atmosphere temperature and densities, we have used MSIS-83 model of Hedin [1983].

REFERENCES

Hedin, A. E., A revised thermospheric model based on mass spectrometer and incoherent scatter data: MSIS-83, *J. Geophys. Res., 88,* 10170-10188, 1983.

Hernandez, G., and R. G. Roble, The geomagnetic quiet nighttime thermospheric wind pattern over Fritz Peak Observatory during solar cycle minimum and maximum., *J. Geophys. Res., 89,* 327-337, 1984a.

Hernandez, G., and R. G. Roble, Nighttime variation of thermospheric winds and temperatures over Fritz Peak Observatory during the geomagnetic storm of March 2, 1983, *J. Geophys. Res., 89,* 9049-9056, 1984b.

Rishbeth, H., Thermospheric winds and the F-region: A review, *J. Atmos. Terr. Phys., 34,* 1-47, 1972.
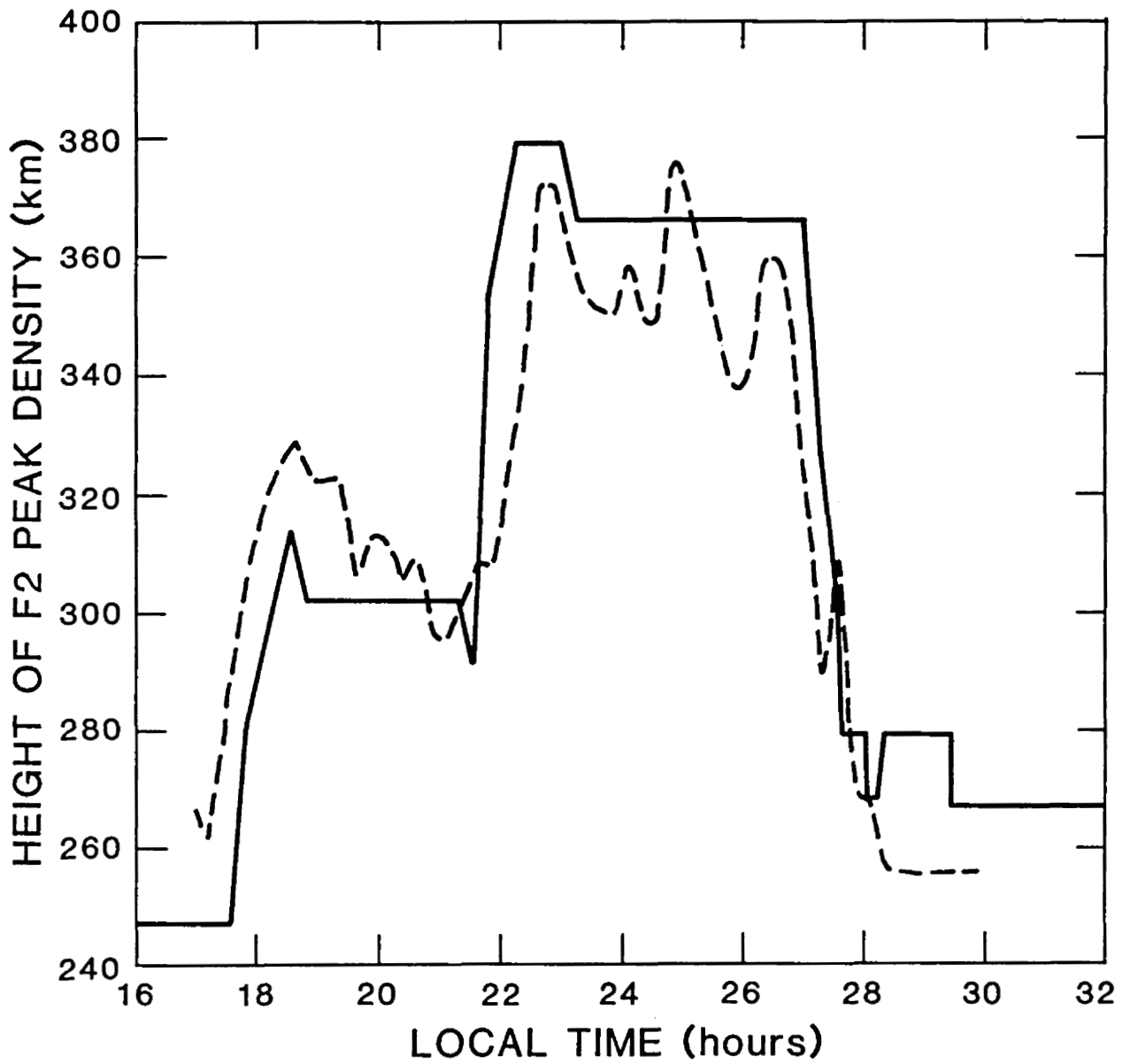
Figure 1. Variation in the height of the F2 layer over Boulder Colorado on 30 July 1982 (broken line) compared with the model calculation (full line).
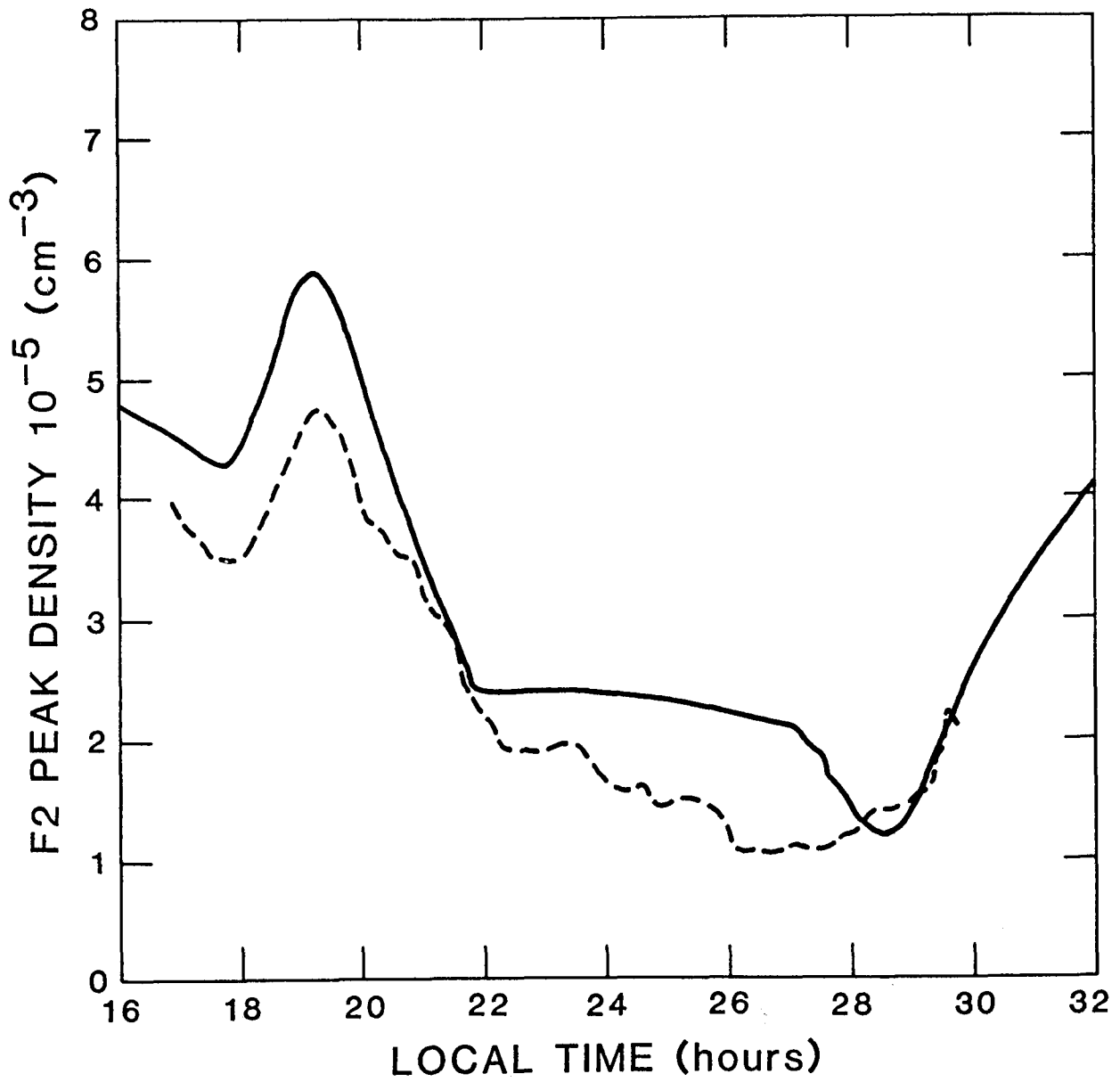
Figure 2. Observed (broken line) and calculated (full line) electron density variations corresponding to the conditions of Figure 1.
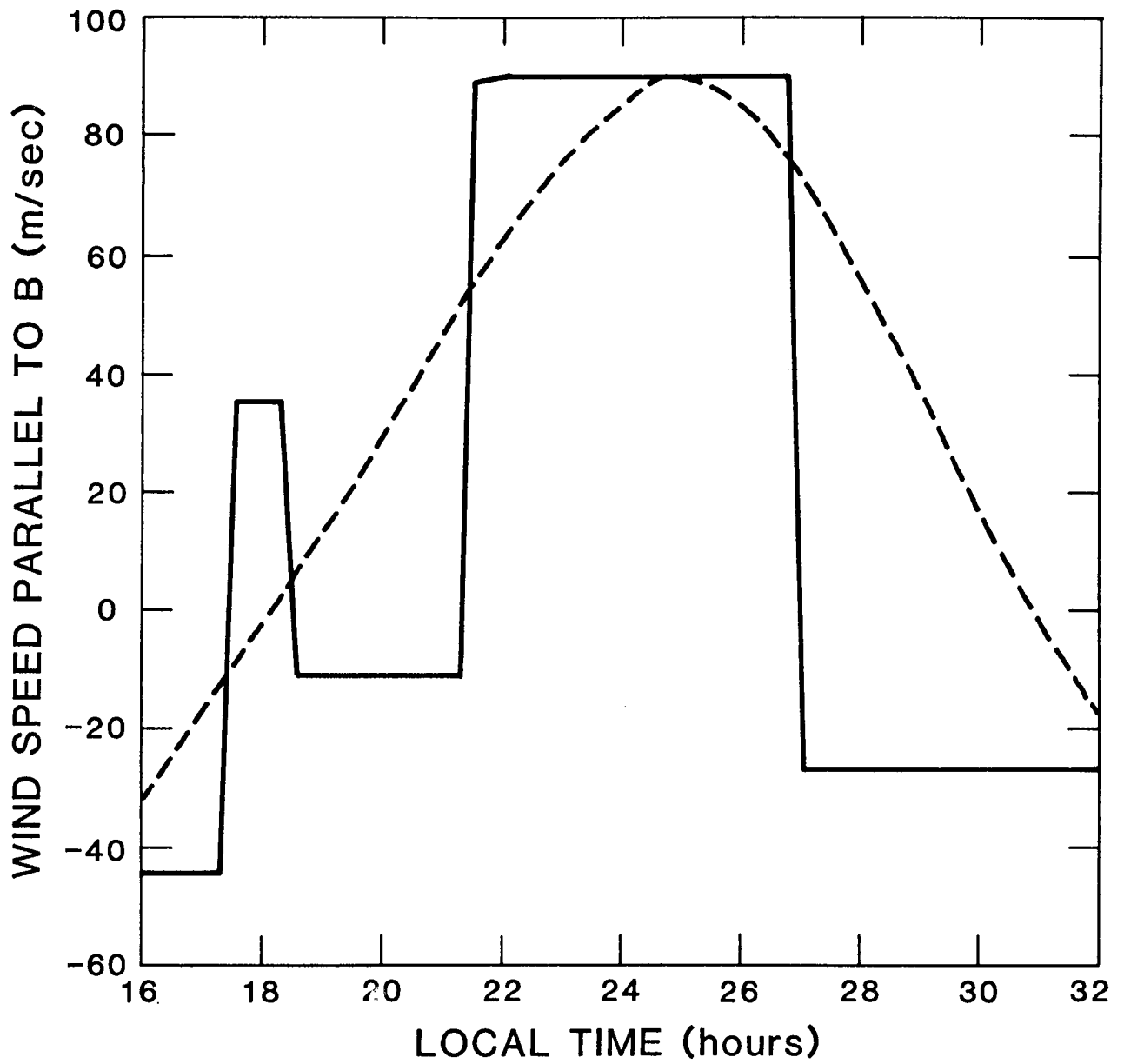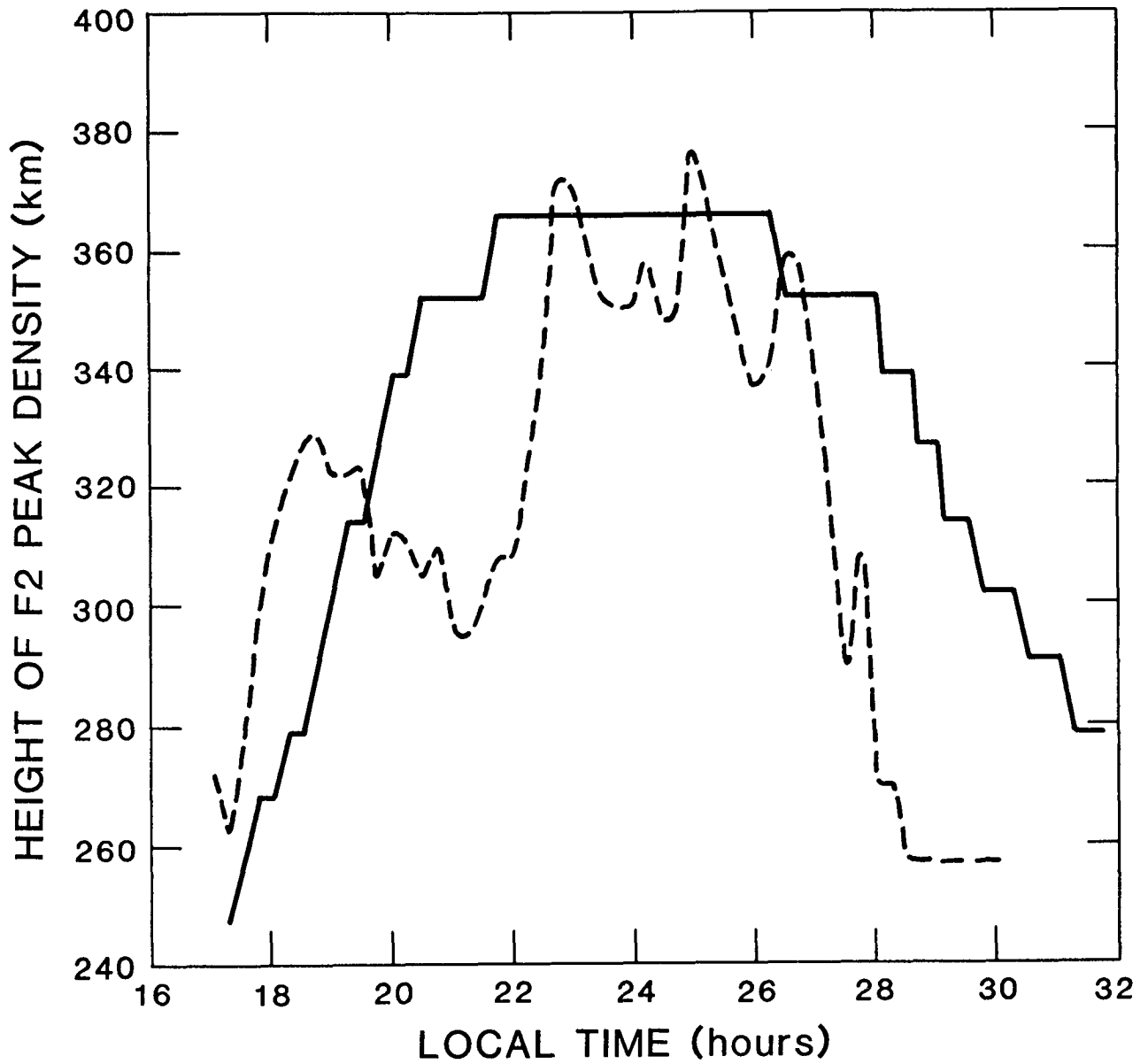
Figure 3. The full line represents the wind variation used to obtain the model results of Figures 1 and 2. The broken curve is the wind variation used to obtain the model results in Figures 4 and 5.

Figure 4. Variation in the height of the F2 layer over Boulder Colorado on 30 July 1982 (broken line) compared with the model calculation (full line) using the wind variation depicted by the broken line in Figure 3.
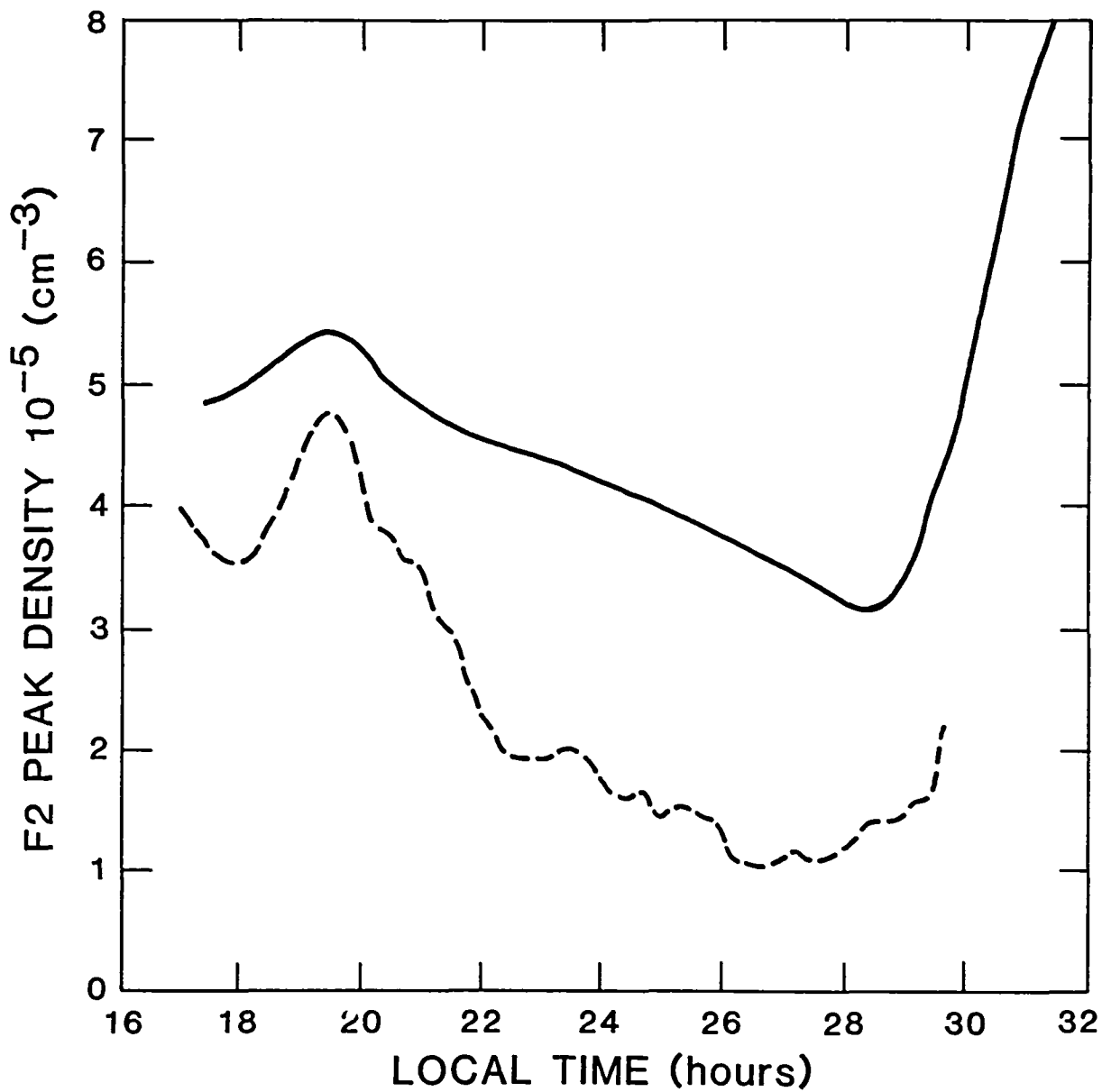
Figure 5. Observed (broken line) and calculated (full line) electron density variations using the wind variation depicted by the broken line in Figure 3.

THE QUADRUPOLE IONOSPHERE

H. Rishbeth
Department of Physics, University,
Southampton SO9 5NH England

The paper discusses the principal features that might exist in the terrestrial ionosphere if the geomagnetic field were to assume a quadrupole form during a magnetic polarity reversal. Two possible configurations are considered, the "axial quadrupole" (Fig. 1) and the "lateral quadrupole" (Fig. 2). Interesting phenomena are anticipated in "magnetic equatorial" regions where the field is horizontal, and fast magnetospherically-driven plasma convection might occur at latitudes where the field is steeply inclined.

The general effect of changes of field strength on conductivity is considered; a weaker field raises the ionospheric conducting layer and enhances the conductivity; a stronger field lowers the height of the conducting layer and decreases the conductivity.

Figure 1.

SUN

⊙ Neutral axis

* Plasmapause

—— Field line

◁—— Thermospheric wind

◄—≪ Plasma convection

—·—·— Auroral zone
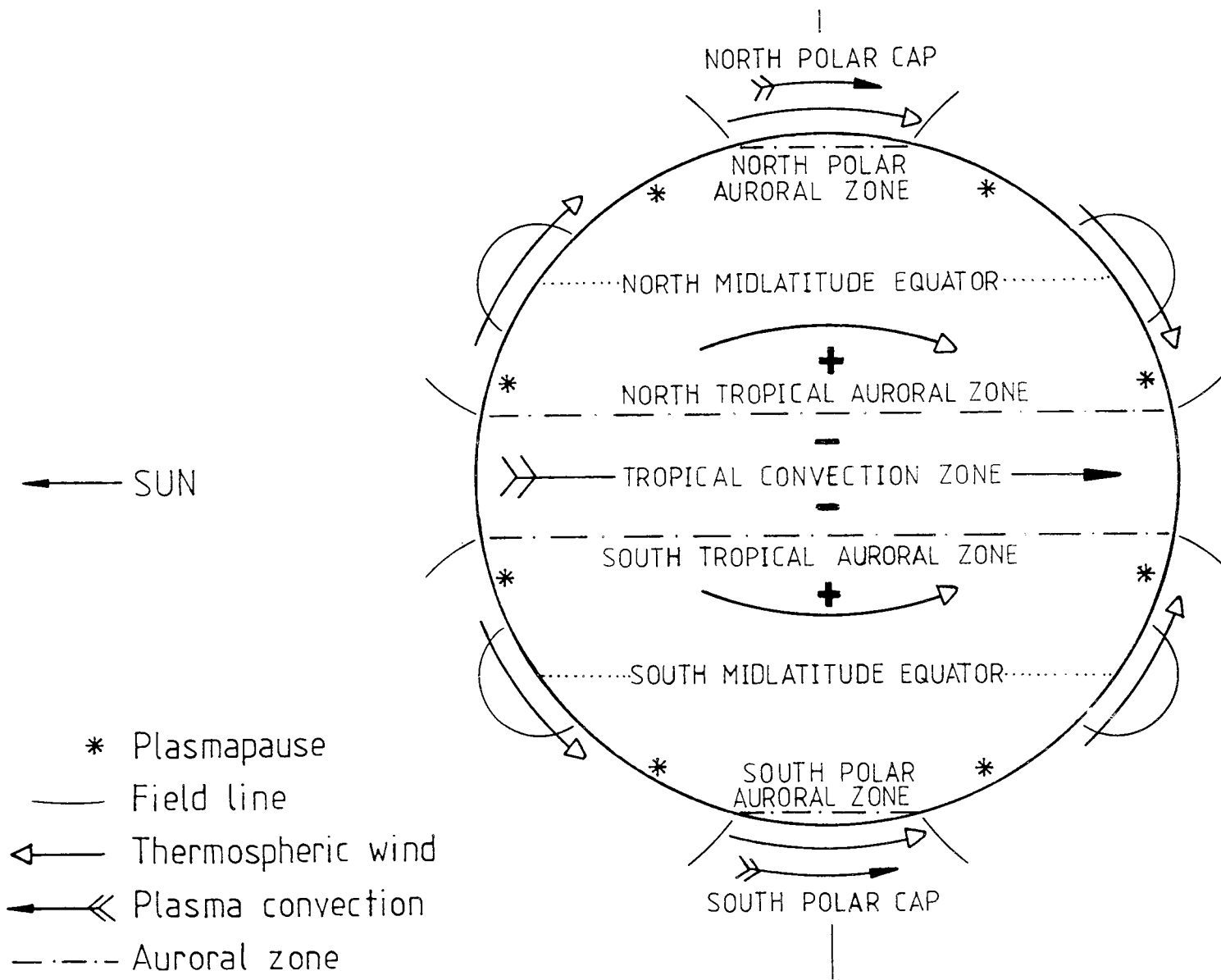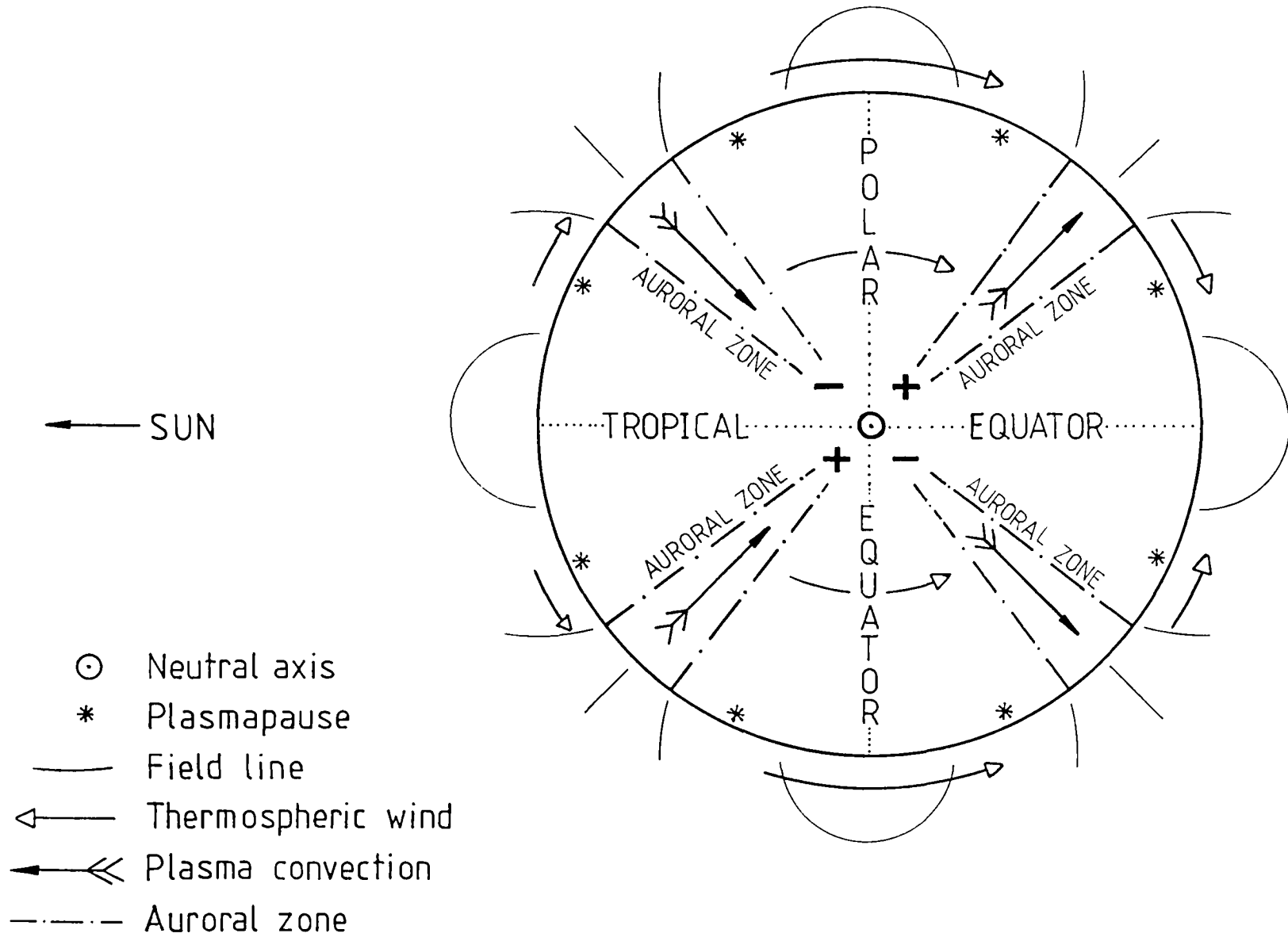
Figure 2.

EISCAT VELOCITY PATTERNS
FOR THEORETICAL PLASMA CONVECTION MODELS

H. Rishbeth
Rutherford Appleton Laboratory
Chilton, Didcot, Oxon OX11 OQX

J. J. Sojka
Centre for Atmospheric & Space Sciences Utah State University
Logan, Utah 84322

Theoretical line-of-sight velocities, as would be observed by the EISCAT radar, are computed for idealized models of plasma convection in the polar ionosphere. The calculations give the velocity as a function of range and Universal Time. For several variants of the Volland and Heelis convection models (Fig. 1, Fig. 2), the paper examines how the maxima, minima and reversals of velocity depend on beam azimuth. The analysis is designed to be applied to data from the UK-POLAR experiment, an example of which is shown in Fig. 3.
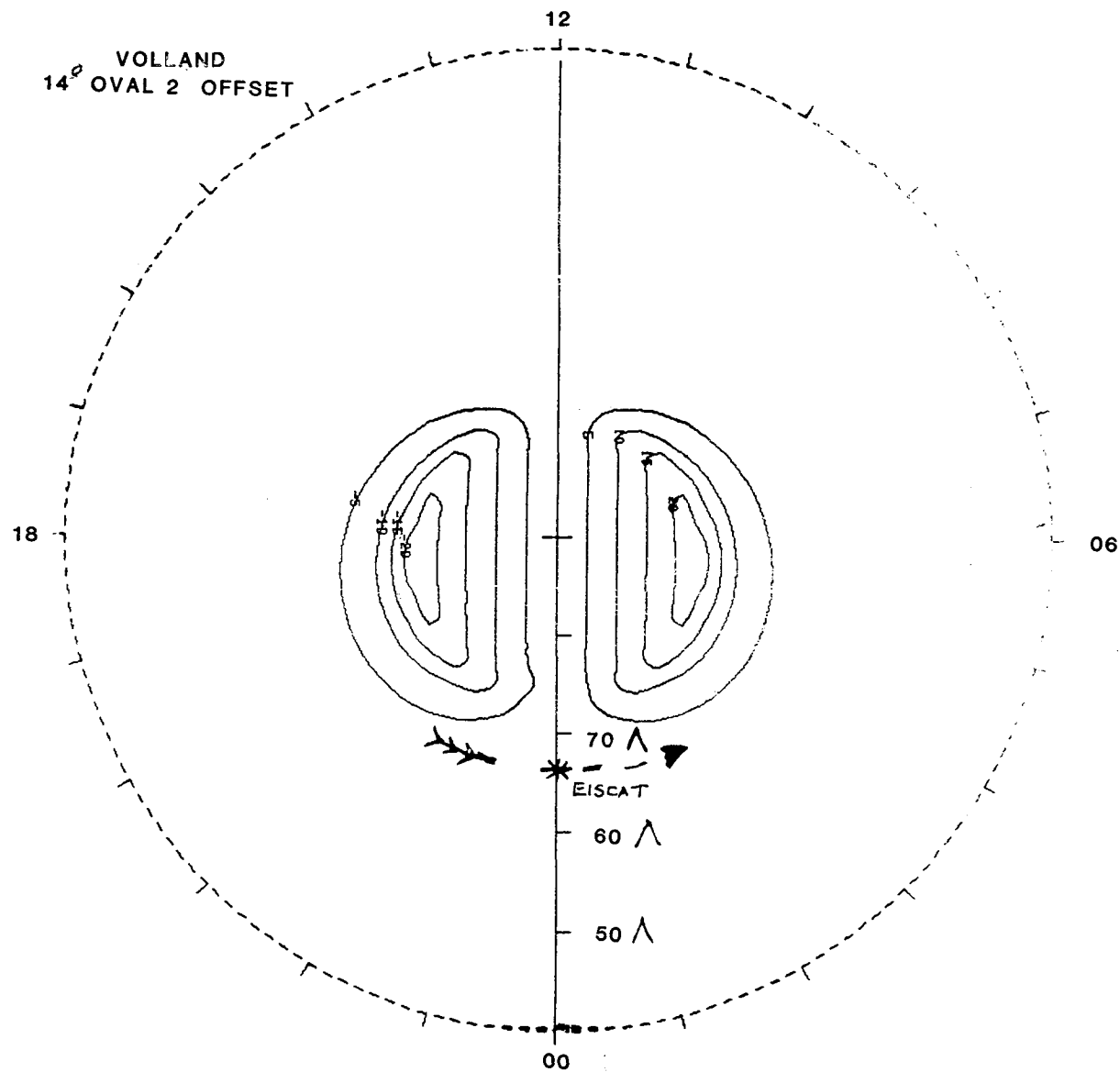
Figure 1.
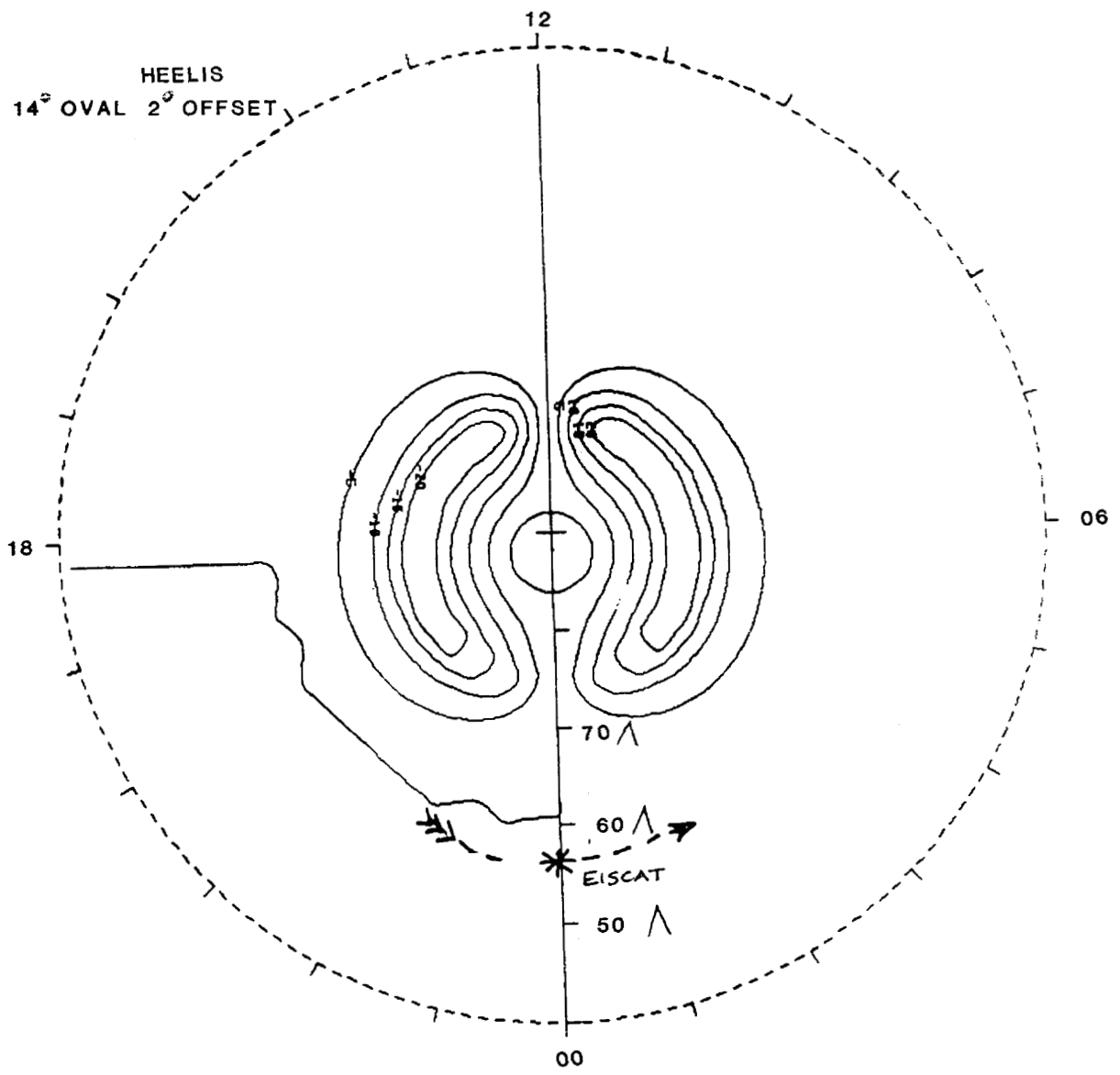
Figure 2.
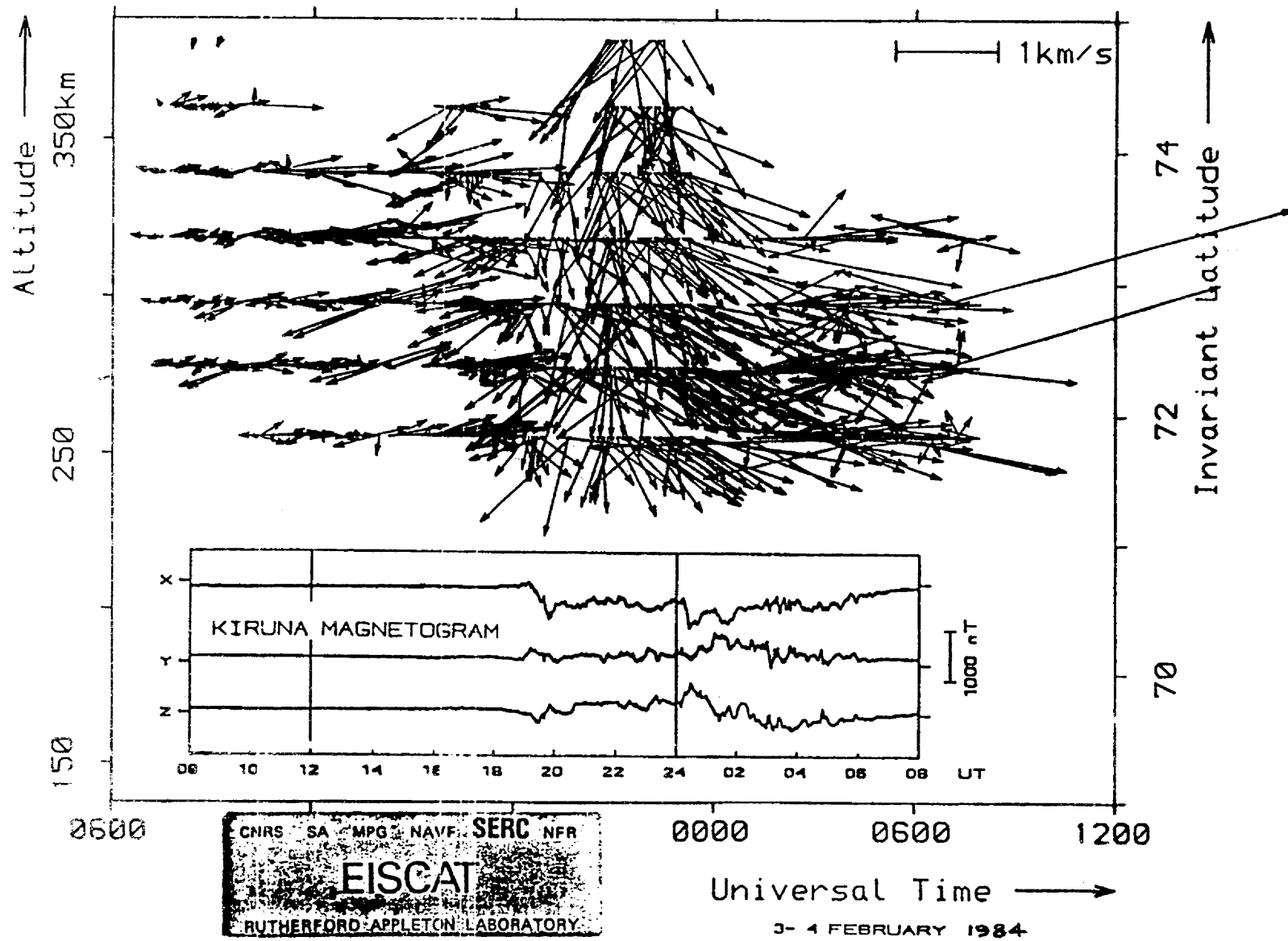
Figure 3.

RESULTS OF VARIOUS STUDIES MADE WITH THE NCAR
THERMOSPHERIC GENERAL CIRCULATION MODEL (TGCM)
(Invited Review)

R. G. Roble
High Altitude Observatory
National Center for Atmospheric Research
Boulder, CO 80307

The NCAR thermospheric general circulation model has been used for a variety of thermospheric dynamic studies. It has also been used to compare model predictions with measurements made from various ground-based Fabry-Perot interferometer stations, incoherent scatter radar stations and the Dynamics Explorer satellites. In this report the various input and output features of the model are described. These include the specification of solar EUV fluxes, and descriptions of empirical models to specify auroral particle precipitation, ion drag, and magnetospheric convection. Results are presented for solstice conditions giving the model perturbation temperature and circulation response to solar heating forcing alone and also with the inclusion of magnetospheric convections for two different dawn-dusk potential drops, 20 and 60 kV respectively. Results at two constant pressure levels $Z = +1$ at 300 km and $Z = -4$ at 120 km are presented for both the winter and summer polar cap regions. The circulation over the northern hemisphere polar cap in both the upper and lower thermosphere are presented along with a figure showing that the circulation is mainly a non-divergent irrotational flow responding to ion drag.

The results of a study made on the southern hemisphere polar cap during October 1981 where Dynamics Explorer satellite measurements of winds, temperature and composition are compared to TGCM predictions are also presented. A diagnostic package that has been developed to analyze the balance of forces operating in the TGCM is presented next illustrating that in the F-region ion drag and pressure provide the main force balance and in the E-region ion drag, pressure and the coriolis forces provide the main balance. The TGCM prediction for the June 10, 1983 total solar eclipse are next presented showing a thermospheric disturbance following the path of totality. Finally, results are presented giving the global circulation, temperature and composition structure of the thermosphere for solar minimum conditions at equinox with 60 kV magnetospheric convection forcing at high latitudes.

THERMOSPHERIC GENERAL CIRCULATION MODELS (TGCM)

OUTPUT

- NEUTRAL TEMPERATURE, T_n

- NEUTRAL WINDS u, v, w

- HEIGHT OF CONSTANT PRESSURE SURFACE, h

- NEUTRAL COMPOSITION, $n(O)$, $n(O_2)$, $n(N_2)$

INPUT

- EMPIRICAL ELECTRON DENSITY MODEL

- EMPIRICAL MAGNETIC FIELD

- EMPIRICAL ION DRIFT – MAGNETOSPHERIC CONVECTION
  - WIND DYNAMO
  - COROTATION

- EMPIRICAL AURORAL IONIZATION SOURCE

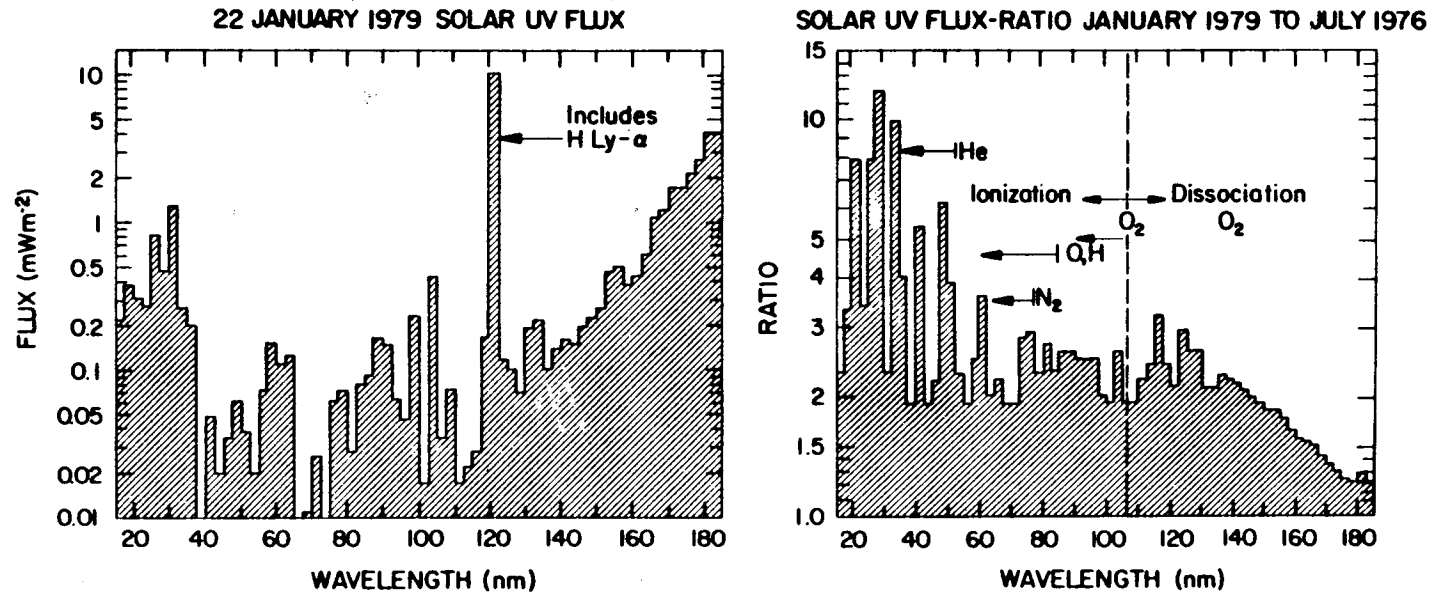- OTHER HEAT AND MOMENTUM SOURCES (i.e., PLASMA PAUSE HEATING, EQUATORIAL HEATING, ETC.)

Figure 1. Solar EUV spectrum measured by H. E. Hinteregger from the Atmospheric Explorer satellite on 22 January 1979 and ratio of the Solar EUV flux measured in January 1979 to that on July 1976.
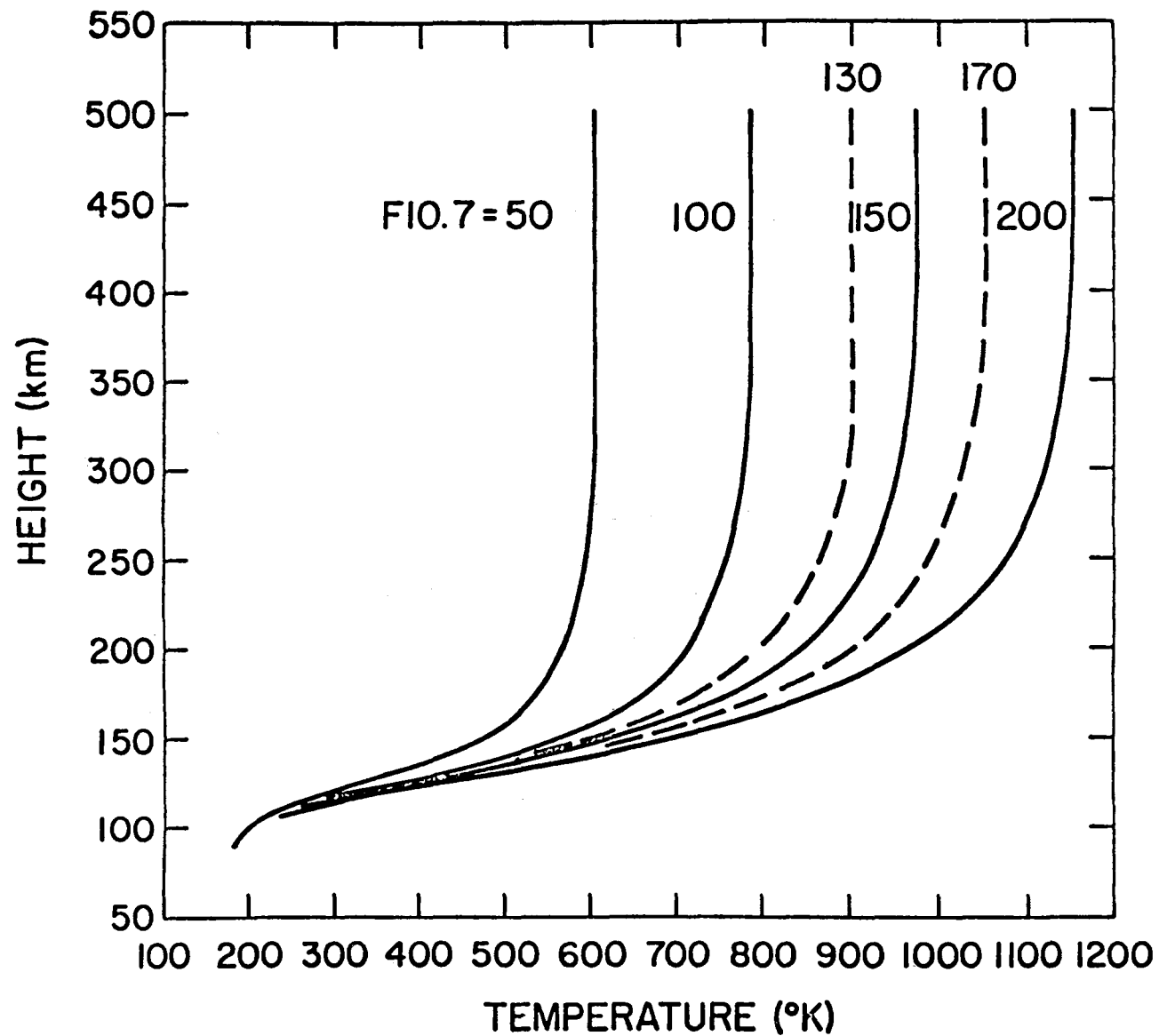
Figure 2. Calculated global mean exospheric temperature profiles for various solar F10.7 values. The dashed
lines are predictions from the MSIS model.
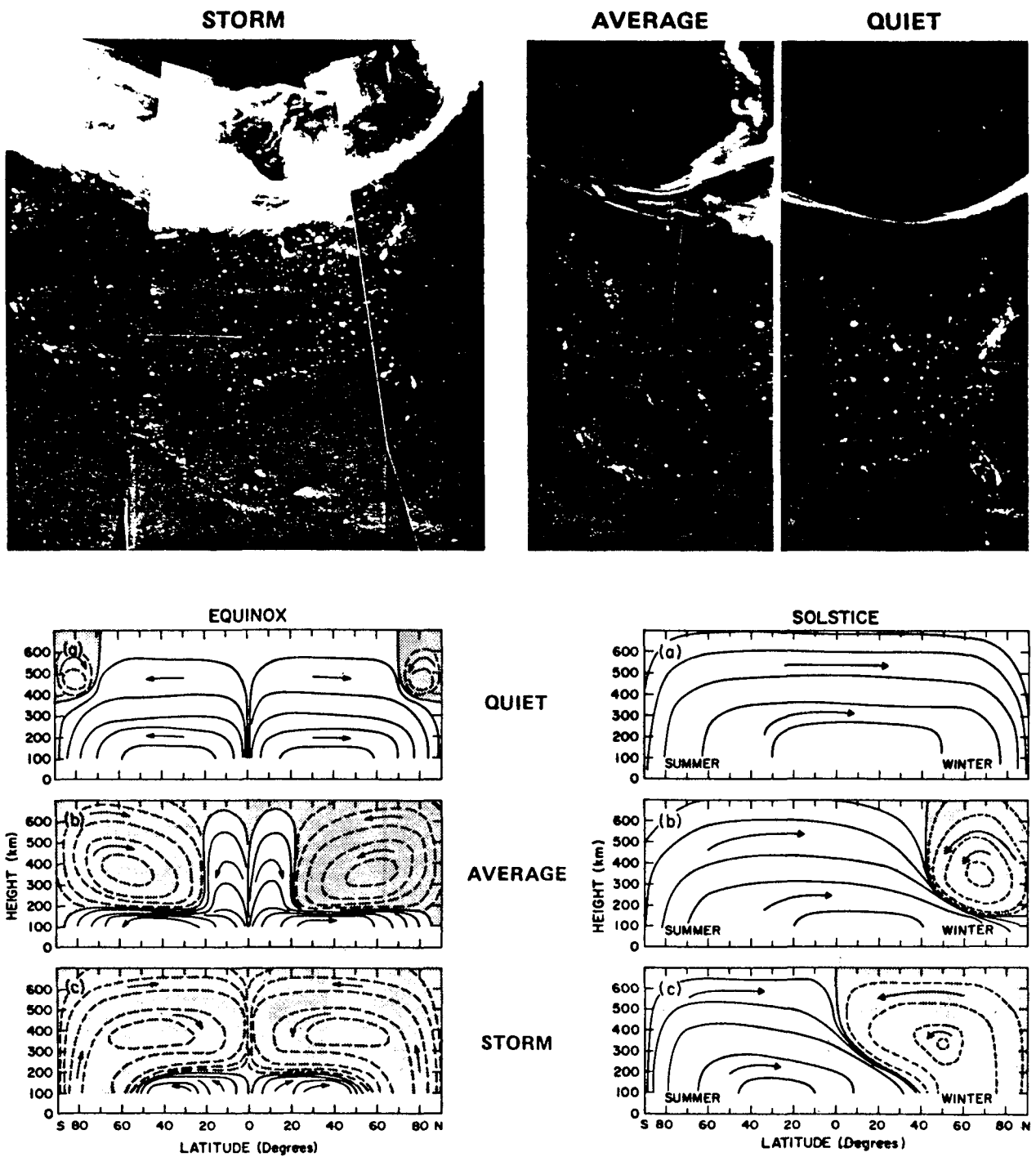
Figure 3. Mean thermospheric circulation for equinox and solstice conditions for various levels of geomagnetic activity.
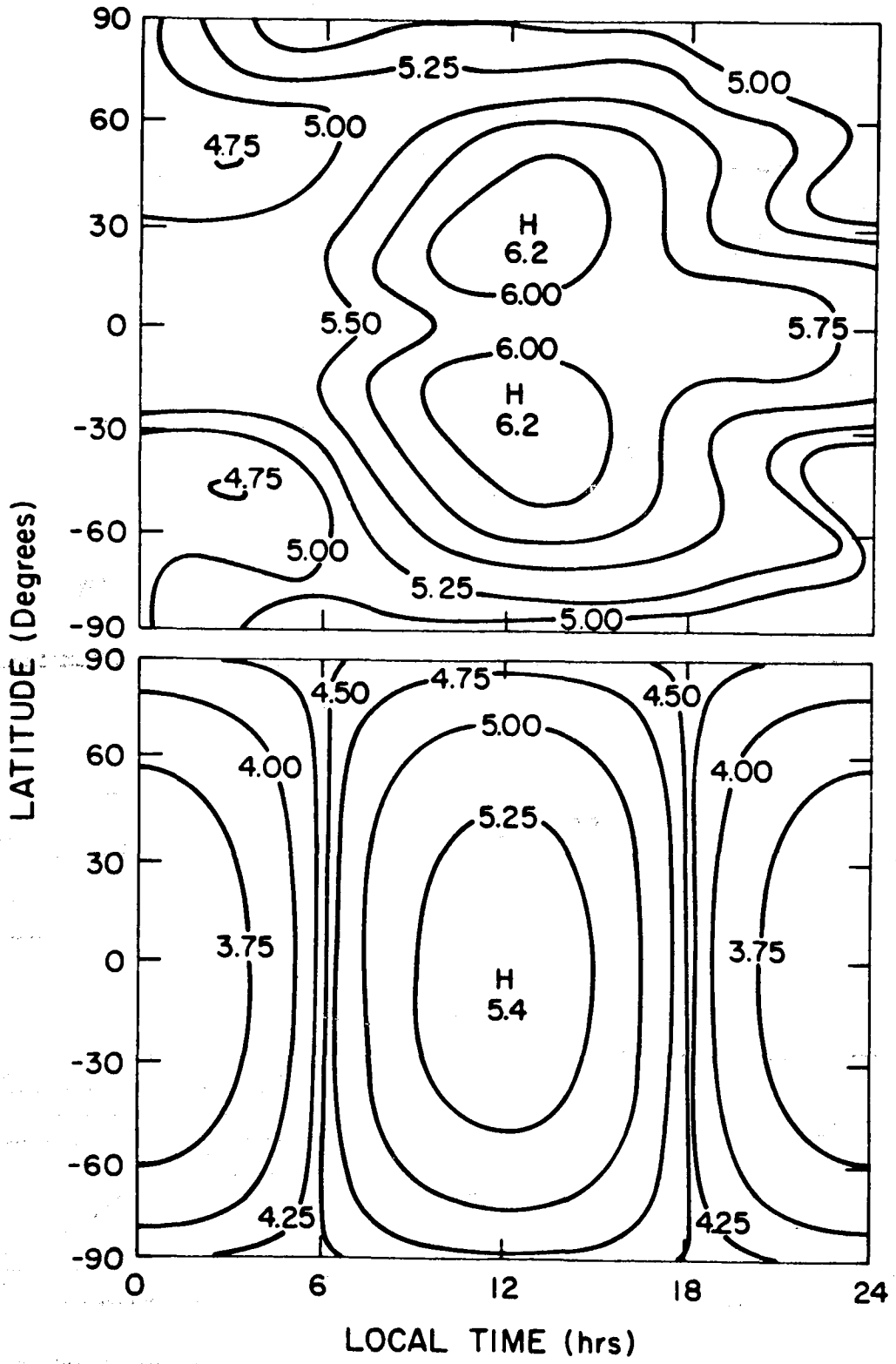
Figure 4. Contours of $\log_{10}$ (n_e, cm^{-3}) the electron densities obtained form the Chiu (1975) model for low solar activity, upper panel at 300 km, lower panel at 120 km.
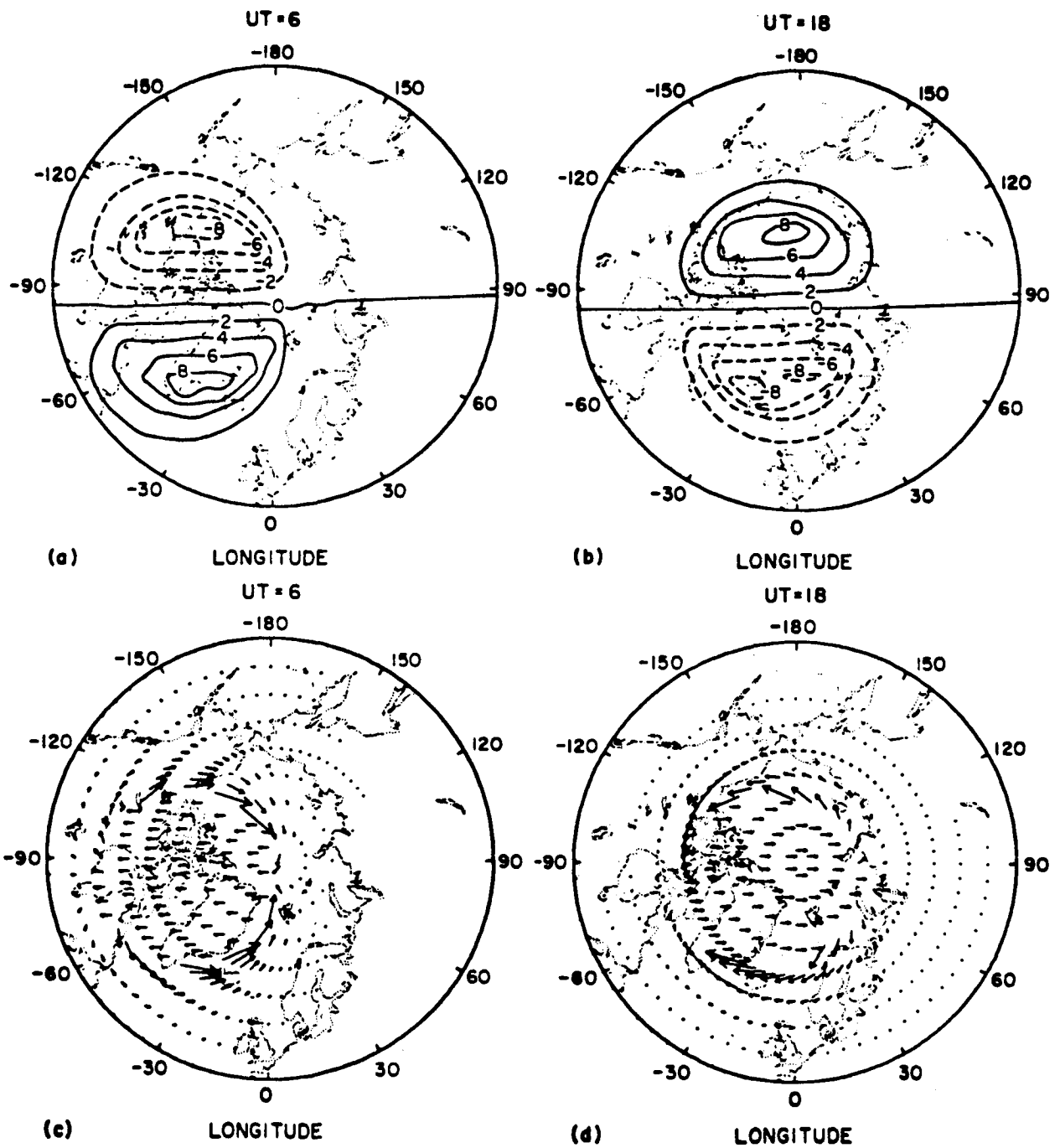
Figure 5. Upper figures, the magnetospheric convection potential pattern in kV for quiet geomagnetic activity over the northern hemisphere polar cap for two UT's. The lower figures represent the direction of the ion drift (E x B) associated with the potential pattern. Max. arrow represents a speed of 375 m s^{-1}.

PRECIPITATING ENERGY FLUX
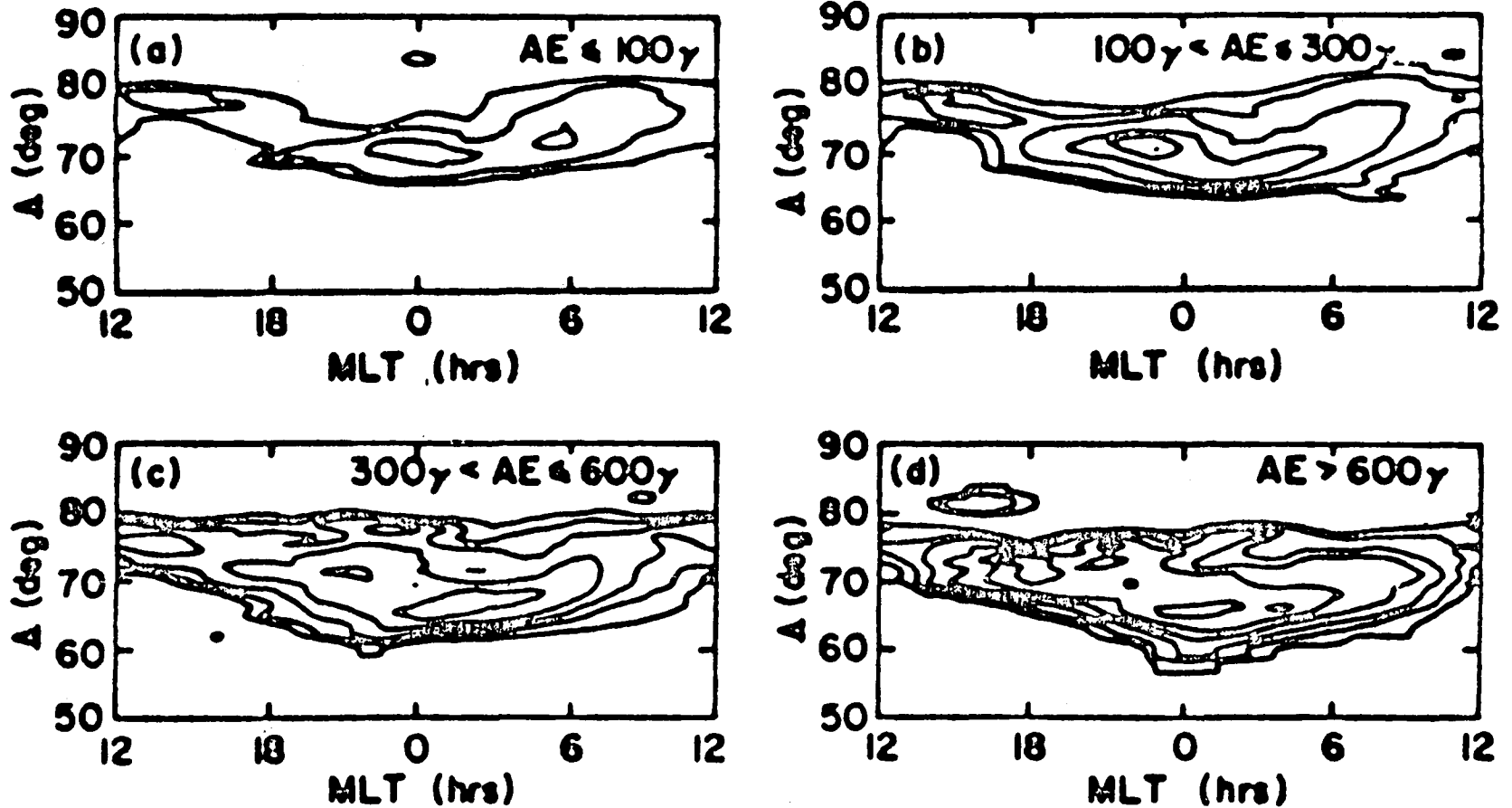
Figure 6. Contours of constant precipitating electron energy flux measured by the Atmospheric Explorer satellite and sorted according to auroral electrojet (AE) index. The outermost contours correspond to a line-average energy flux of 2.5 x 10^{-1} erg cm^{-2} s^{-1}, with adjacent contours representing factor of two increases in energy flux (Spiro et al., 1982)
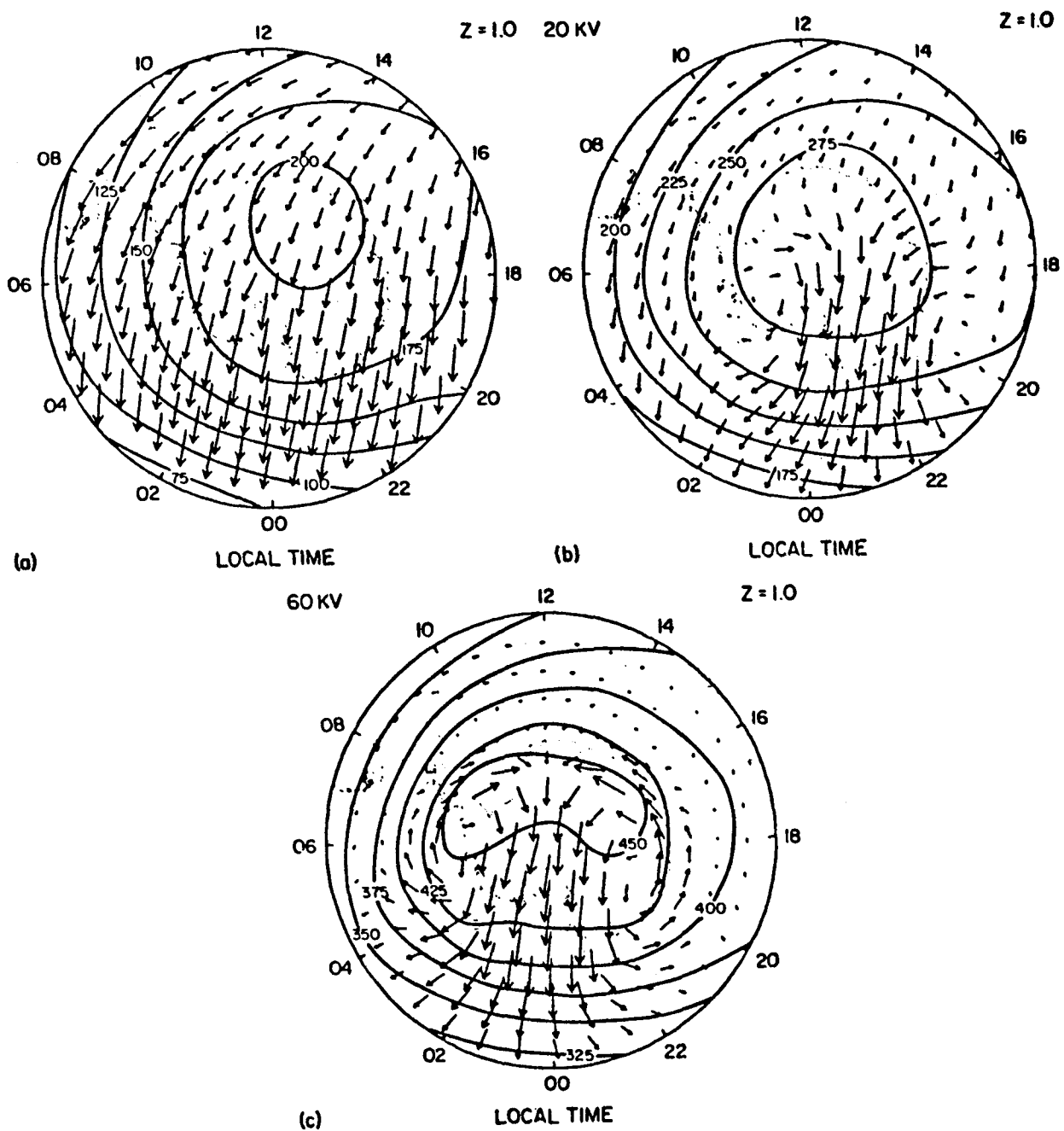
Figure 7. Polar plots giving the direction and magnitude of the calculated southern hemisphere (summer) high-latitude circulation and contours of perturbation temperature (K) along the Z = +1 (300 km) constant-pressure surface at December solstice for (a) solar heating only; (b) solar heating plus magnetospheric convection with a crosstail potential of 20 kV; and (c) solar heating plus magnetospheric convection with a cross-tail potential of 60 kV. The wind speed associated with the maximum arrow is 10 m/s in (a), 200 m/s in (b), and 380 m/s in (c) (Roble et al., 1983).
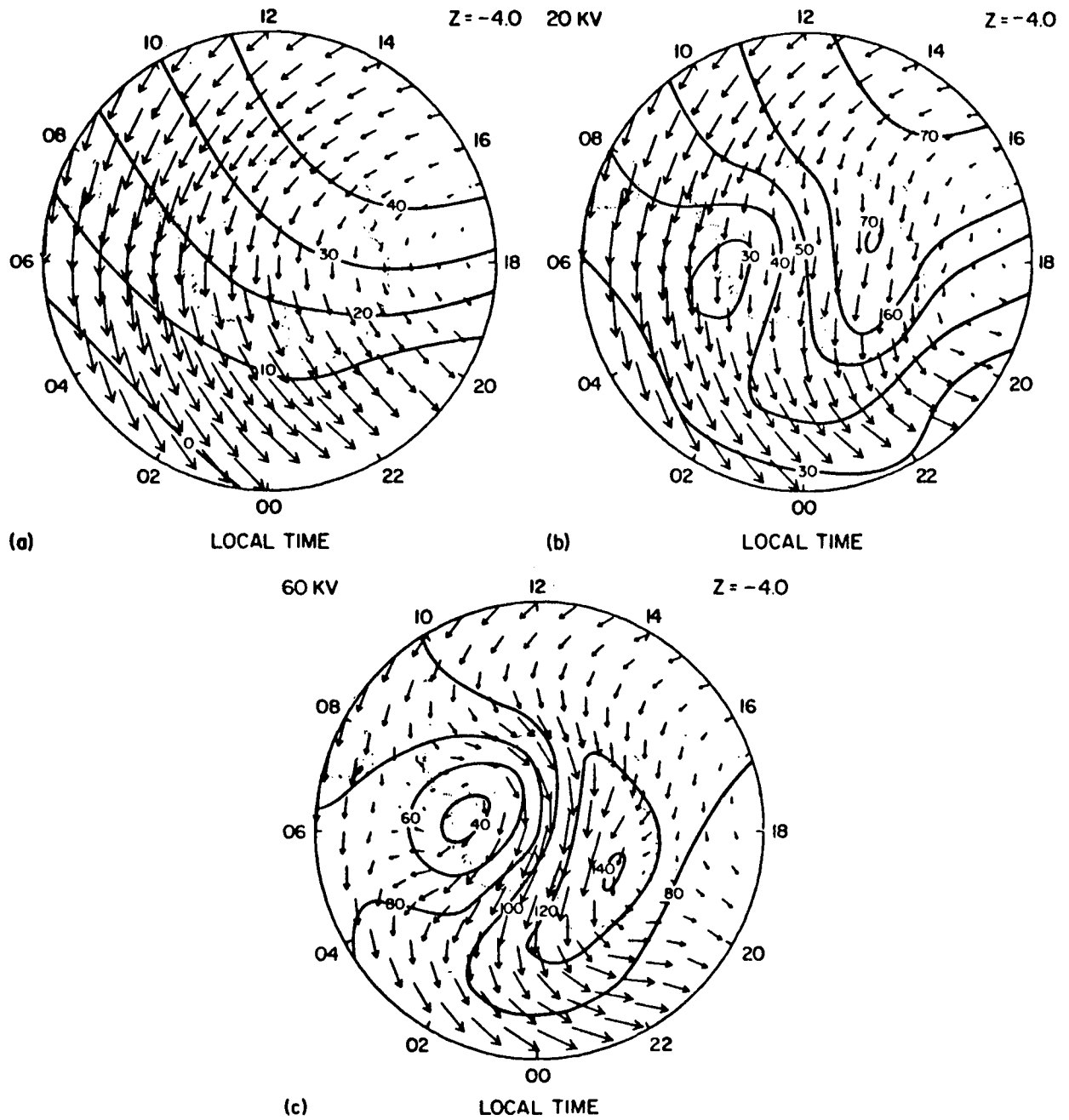
Figure 8. Same as Figure 7, except along the Z = -4 (130 km) constant-pressure surface. The wind speed associated with the maximum arrow is 75 m/s in (a), 77 m/s in (b), and 89 m/s in (c) (Roble et al., 1983)
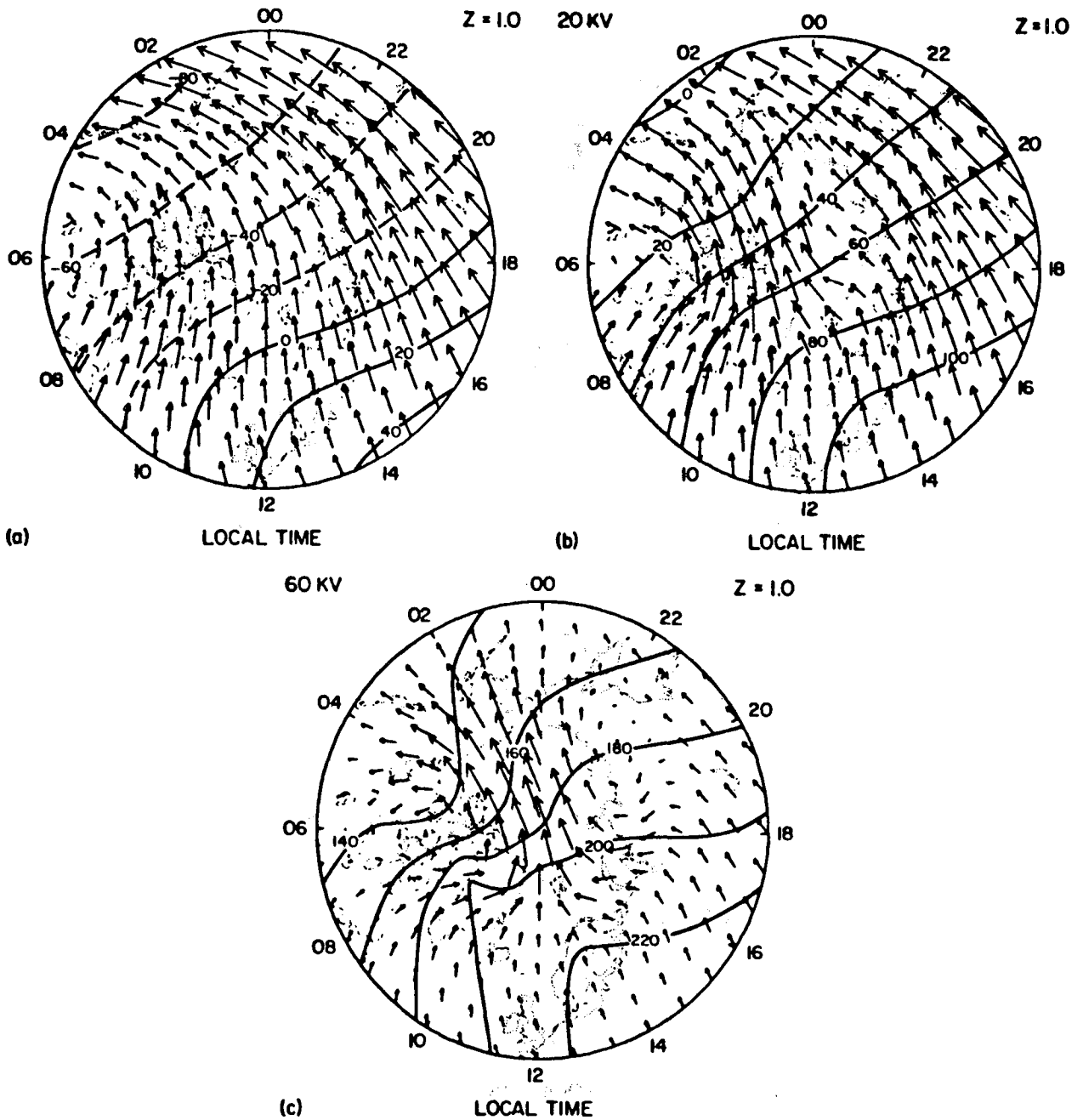
Figure 9. Same caption as in Figure 7 except for northern hemisphere (winter). The wind speed associated with the maximum arrow in 181 m s^{-1} in (a), 200 m s^{-1} in (b), and 339 m s^{-1} in (c) respectively.
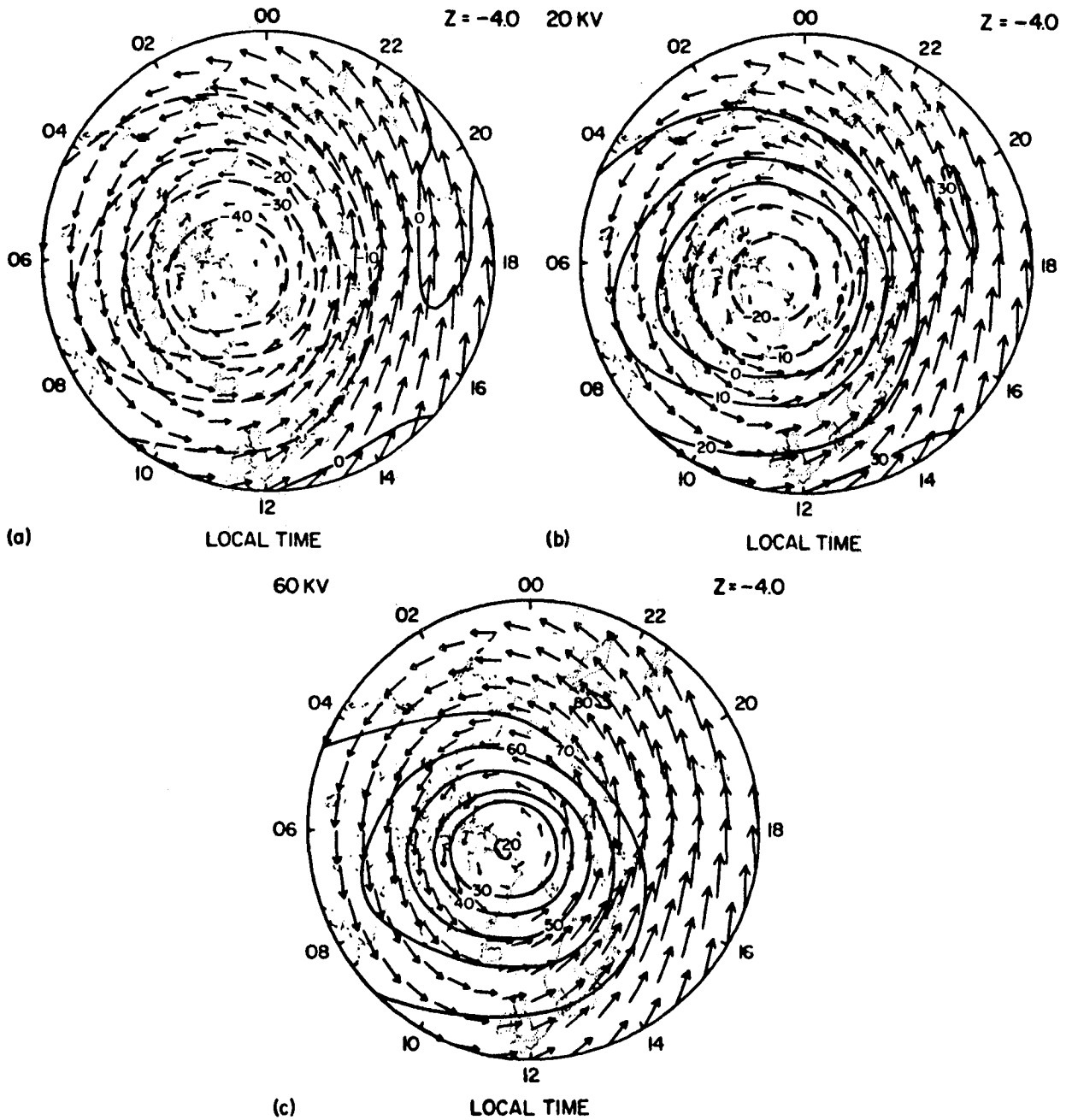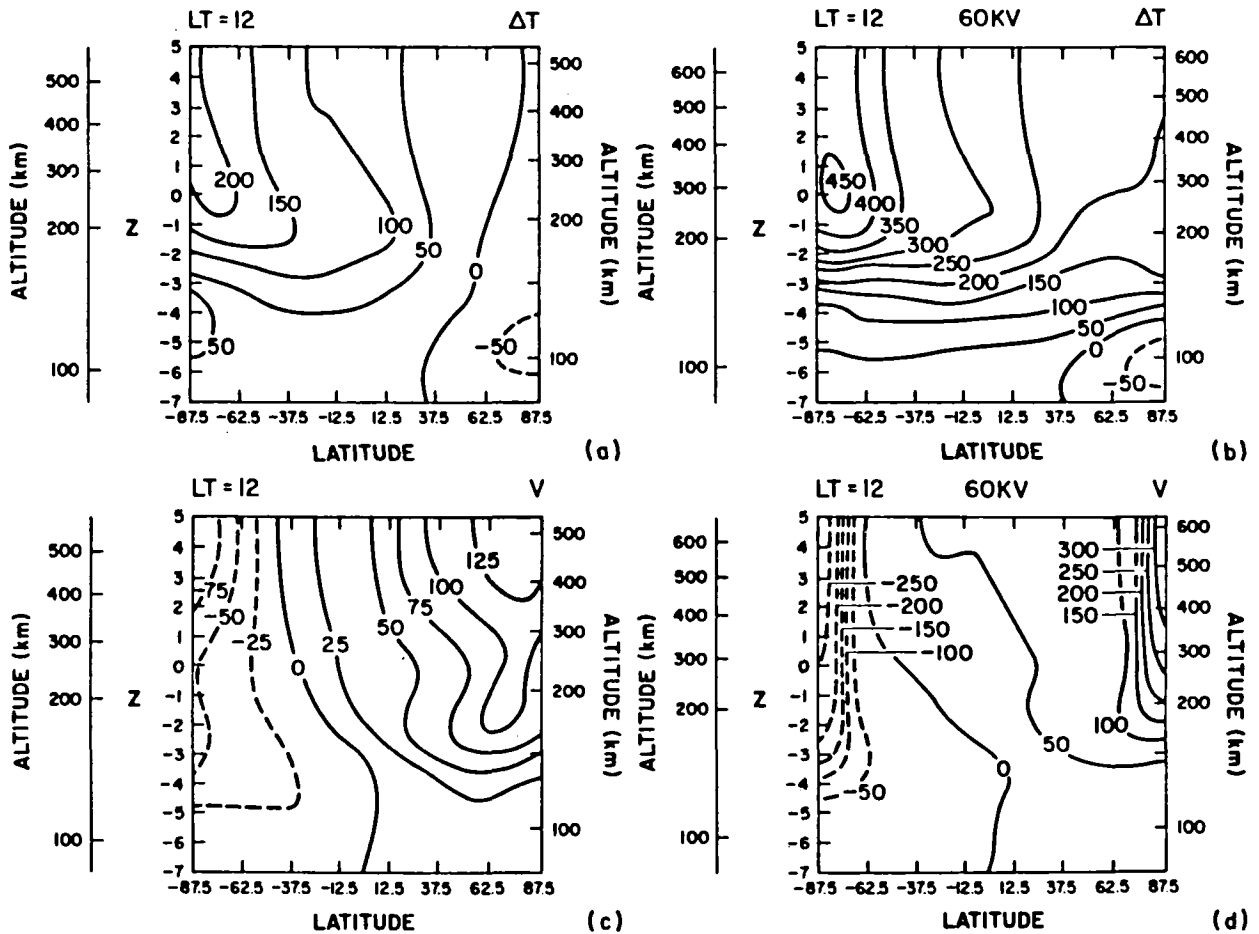
Figure 10. Same caption as in Figure 7 except along the Z = -4 (130 km) constant pressure surface in the Northern Hemisphere (winter). The wind speed associated with the maximum arrow is 108 m s⁻¹ in (a), 117 m s⁻¹ in (b) and 120 m s⁻¹ in (c), respectively.

394

Figure 11. Meridonal cross sections giving contours of the calculated perturbation temperature (K)
{ (a) and (b) } and meridional wind speed (m s⁻¹, positive northward) { (c) and (d) } ,
respectively. The local time of the meridional slice is 12.00 L.T. (a) and (c) are the perturbation
temperature and meridional wind for the case of solar heating only, and (b) and (d) are the
perturbation temperature and meridional wind for the case of solar heating plus magnetospheric
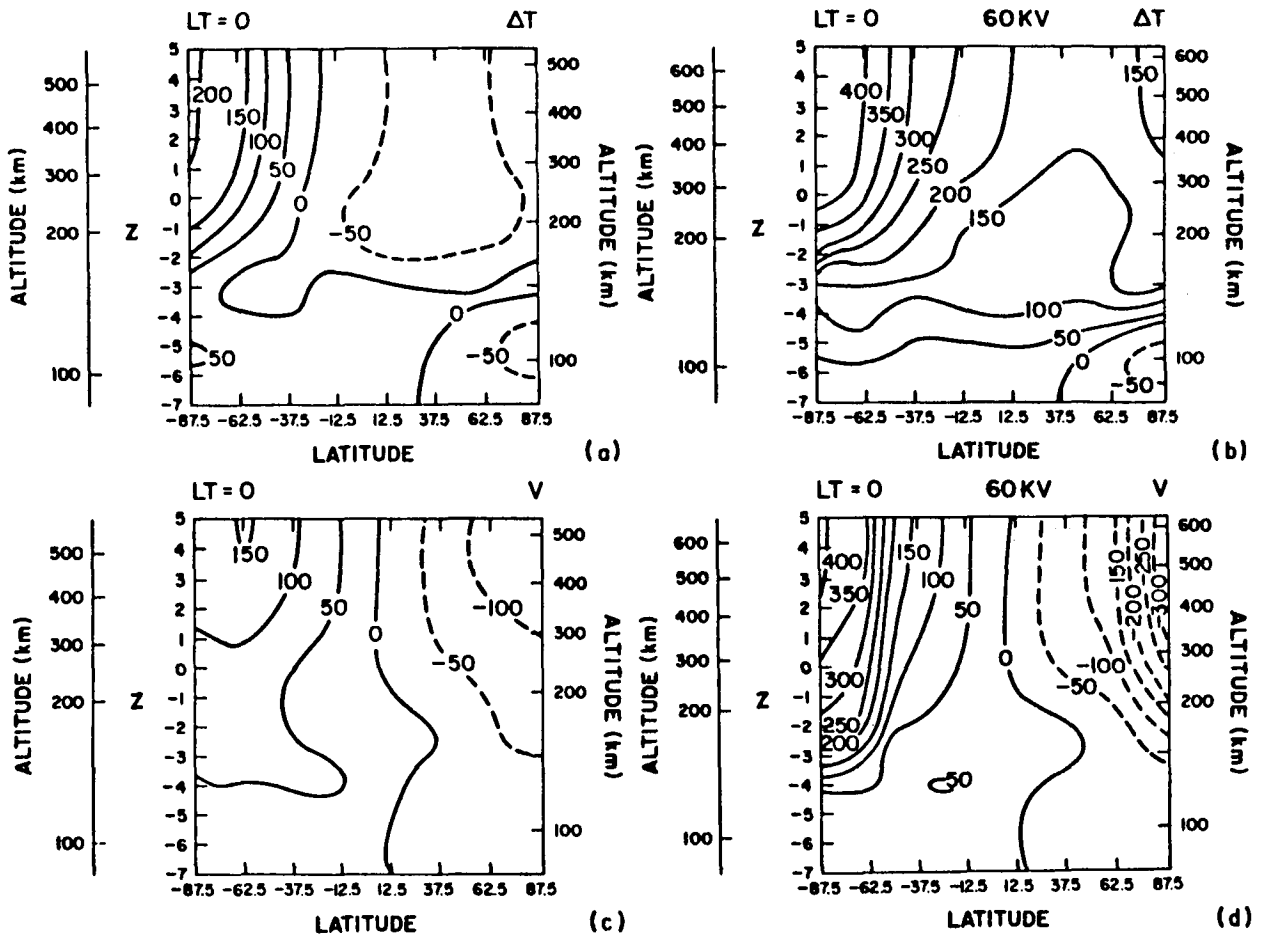convection with a cross-tail potential of 60 kV.

395

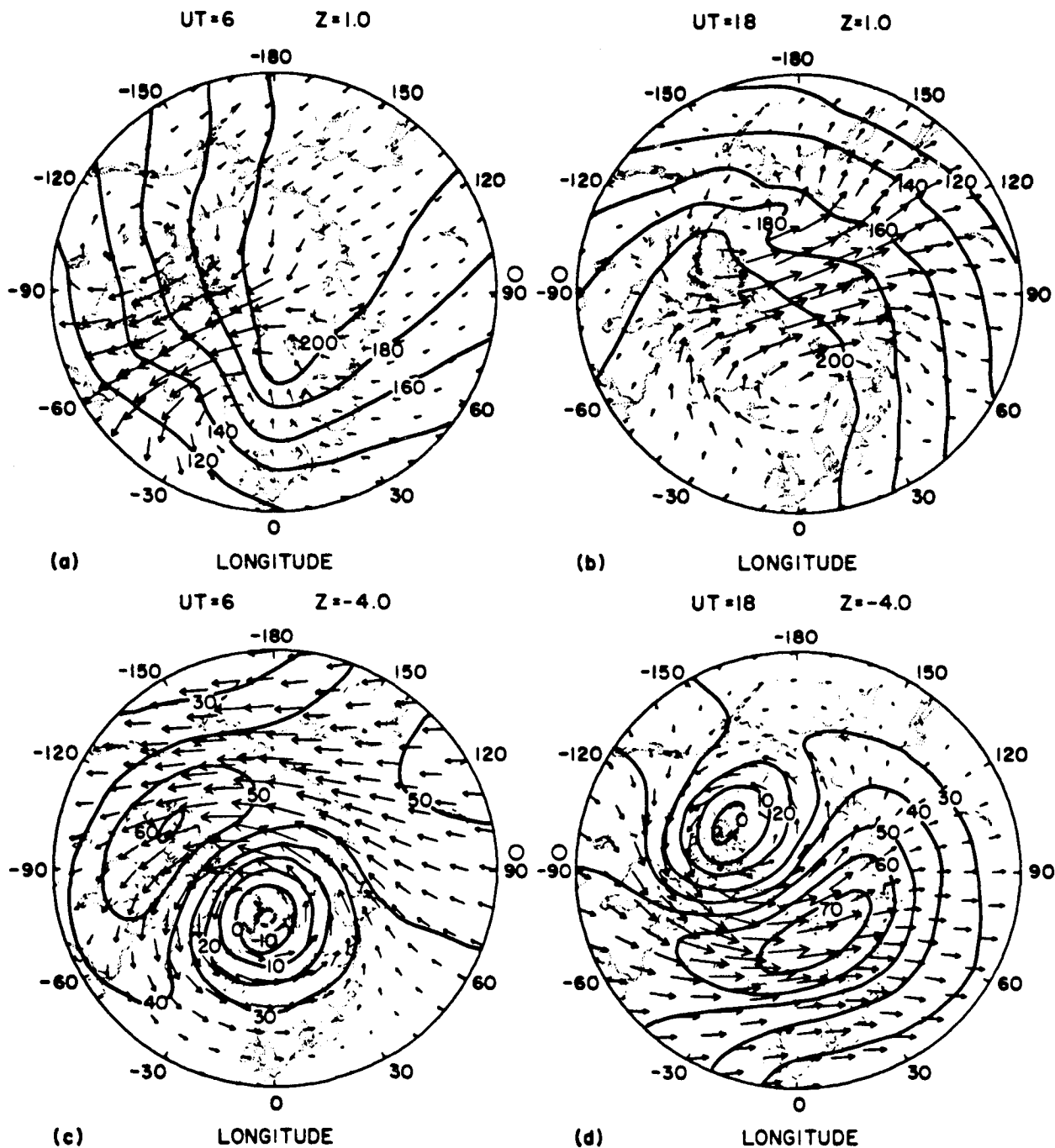Figure 12. Same caption as Figure 11 except along the 0.00LT meridian.

Figure 13. Contours of perturbation temperature (K) along the Z = + 1 (300 km) surface for two universal times, Figure 6a, 0600 UT, and Figure 6b, 1800 UT, and along the Z = -4 (130 km) surface at 0600 UT (Figure 6c) and 1800 UT (Figure 6d) for the case where the geographic and geomagnetic poles are displaced, and the crosstail potential for the magnetospheric convection model is 60 kV. The circulation is indicated by the arrows giving direction, and the length is the magnitude of the winds. The length of the maximum arrow represents 395 m s^{-1} (Figure 6a), 373 m s^{-1} (Figure 6b) 100 m s^{-1} (Figure 6c), and 109 m s^{-1} (Figure 6d), respectively. Local noon is indicated by an open circle on the boundary.
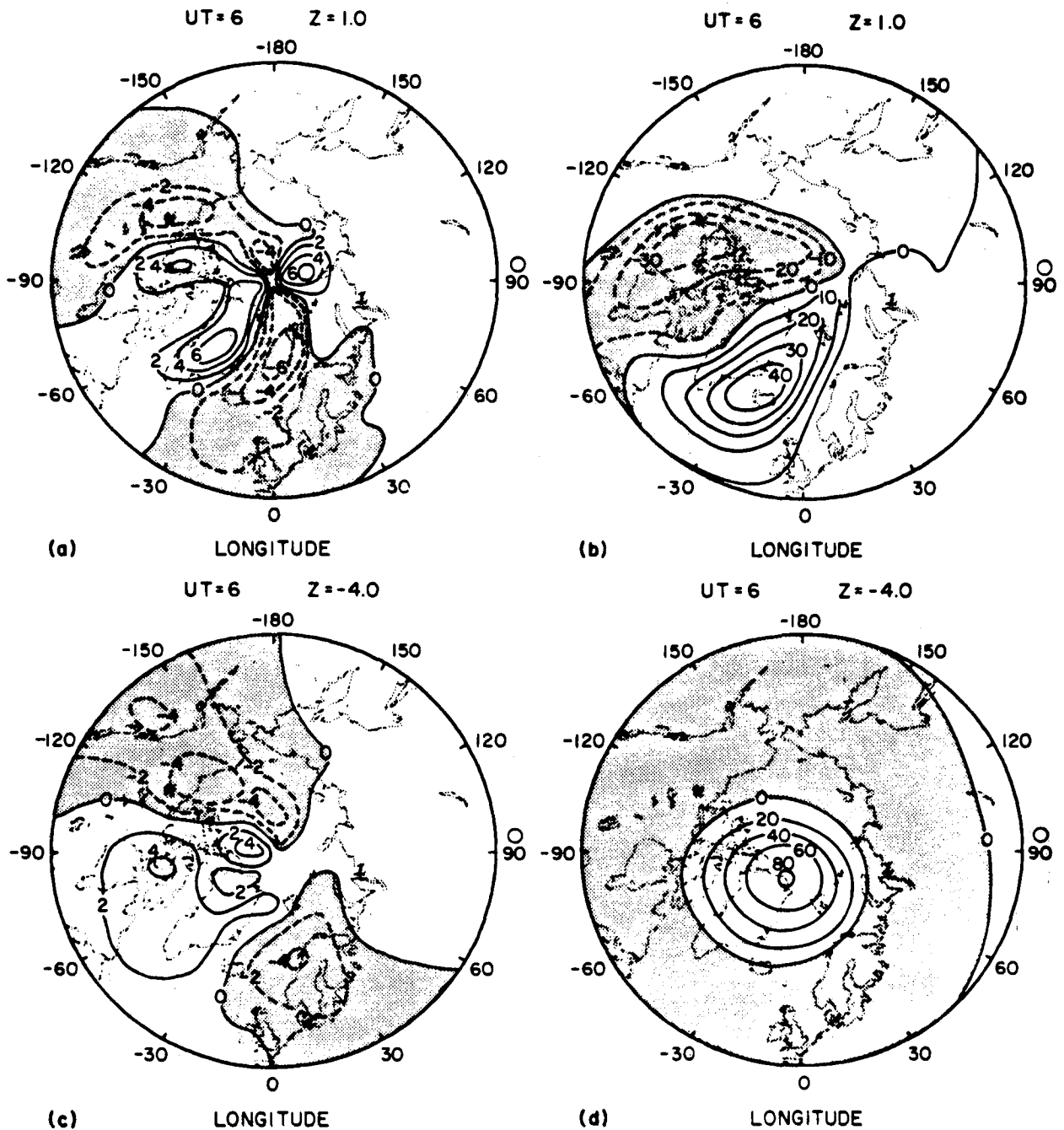
397

Figure 14. Contours of the calculated divergence and curl of the wind difference field shown in Figures 9b and 9d respectively. Positive contours represent divergence and counterclockwise rotation for the divergent and curl fields, respectively. Units are s⁻¹ when these fields are multiplied by 10^{-5} for Figures 10a and 10b and 10^{-6} for Figures 10c and 10d. Local noon is indicated by an open circle on the boundary.
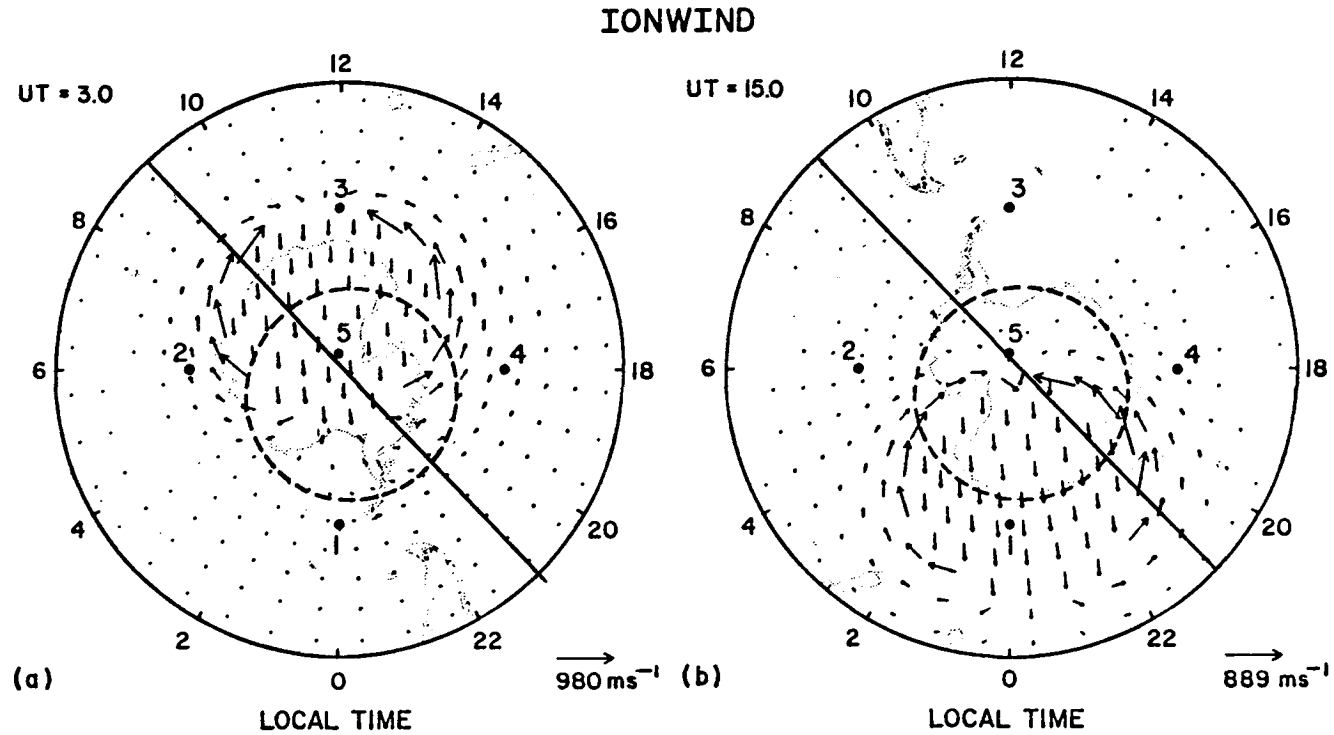
398

Figure 15. Vectors indicating the magnitude and direction of the ion drift, in the absence of neutral collisions, associated with magnetospheric convection over the southern hemisphere polar cap. The vectors are applied at the upper boundary of the model, and the TGCM calculates the ion drift at different altitudes, considering collisons with neutrals. Displaced geographic and geomagnetic poles are considered. The solid line through the geographic pole shows the geographic position of the satellite track at various universal times.
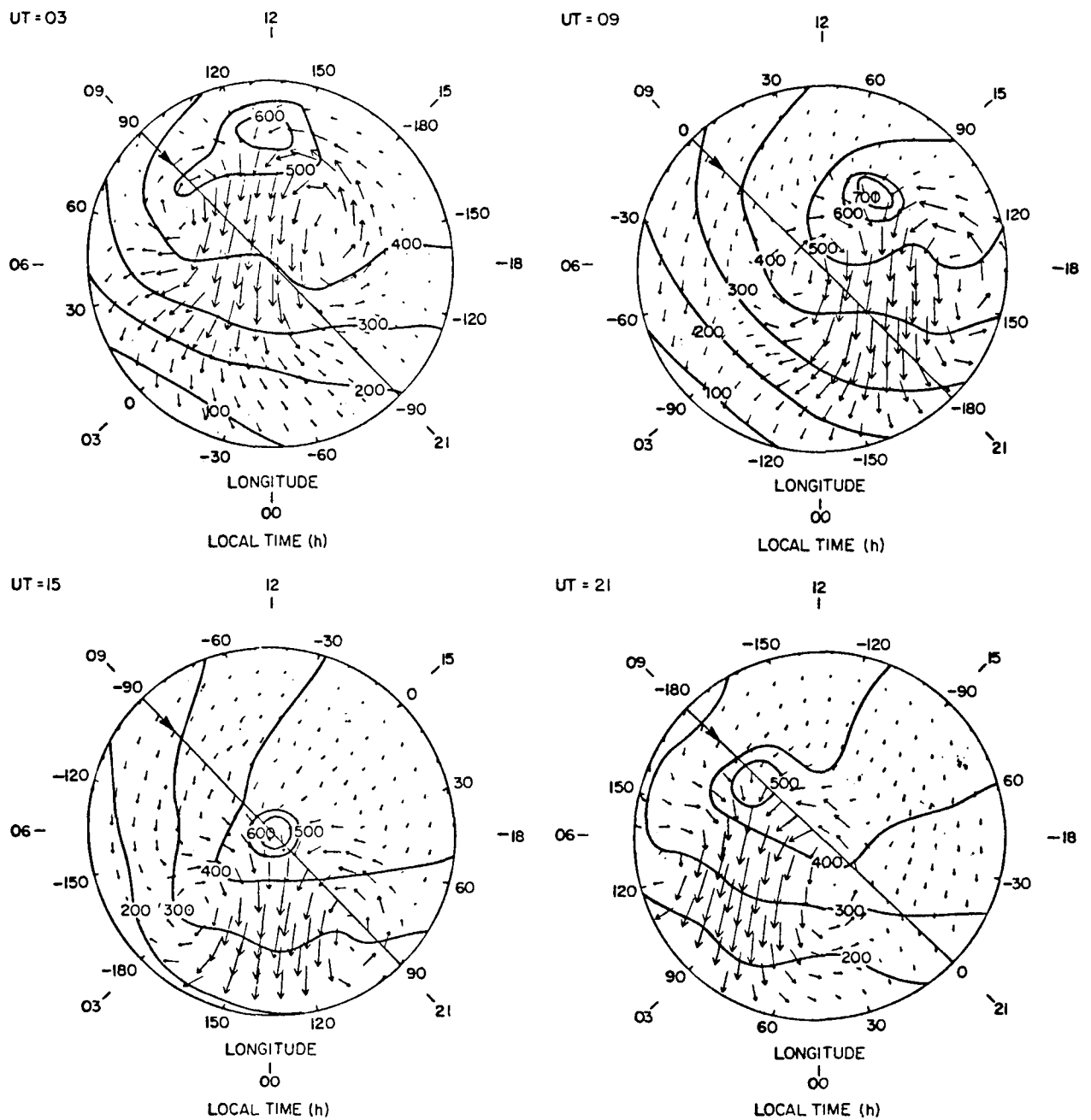
Figure 16. Contours of the TGCM-calculated perturbation temperature (degrees Kelvin) and wind vectors over the southern hemisphere polar cap at four different universal times: (a) 0300 UT, (b) 0900 UT, (c) 1500 UT, and (d) 2100 UT. The winds and perturbation temperature are values along the $Z = +1$ constant-pressure surface (5.4 x 10⁻⁵ μbar or 50 Pa) in the TGCM, that is at an altitude of approximately 300 km. The DE 2 satellite track is shown as the solid line in the figure on a 0900-2100 LT pass over the geographic pole. The maximum arrows represent wind velocities of (a) 375 m s⁻¹, (b) 368 m s⁻¹, (c) 404 m s⁻¹, and (d) 409 m s⁻¹, respectively.
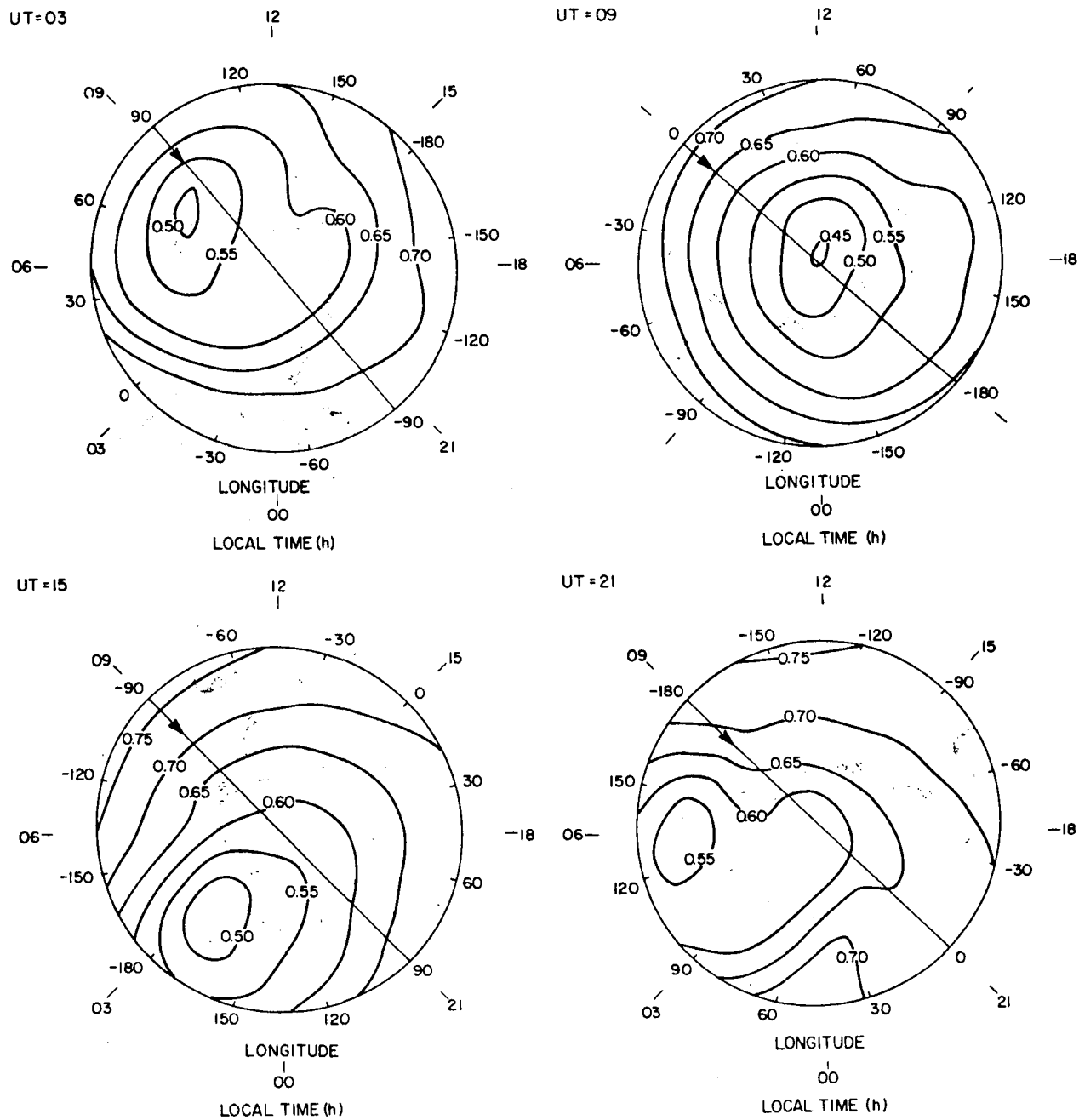
400

Figure 17. Contours of the TGCM-calculated atomic oxygen mass mixing ratio $\psi(0)$ along the Z = + 1 (300 km) constant-pressure surface over the southern hemisphere polar cap for four different universal times: (a) 0300 UT, (b) 0900 UT, (c) 1500 UT, and (d) 2100 UT.
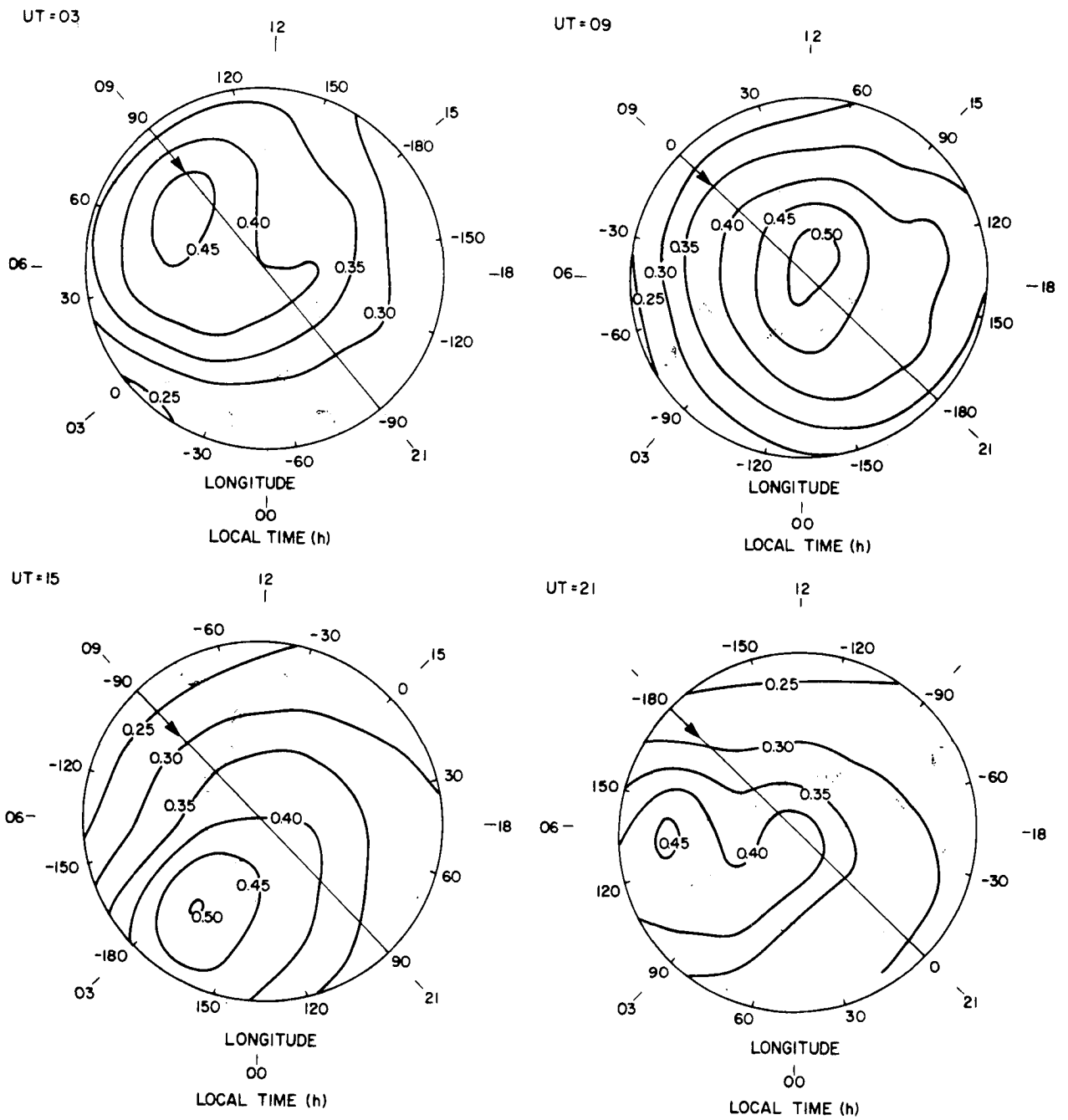
401

Figure 18. Same as Figure 17, except for the molecular nitrogen mass mixing ration ψ (N_2).
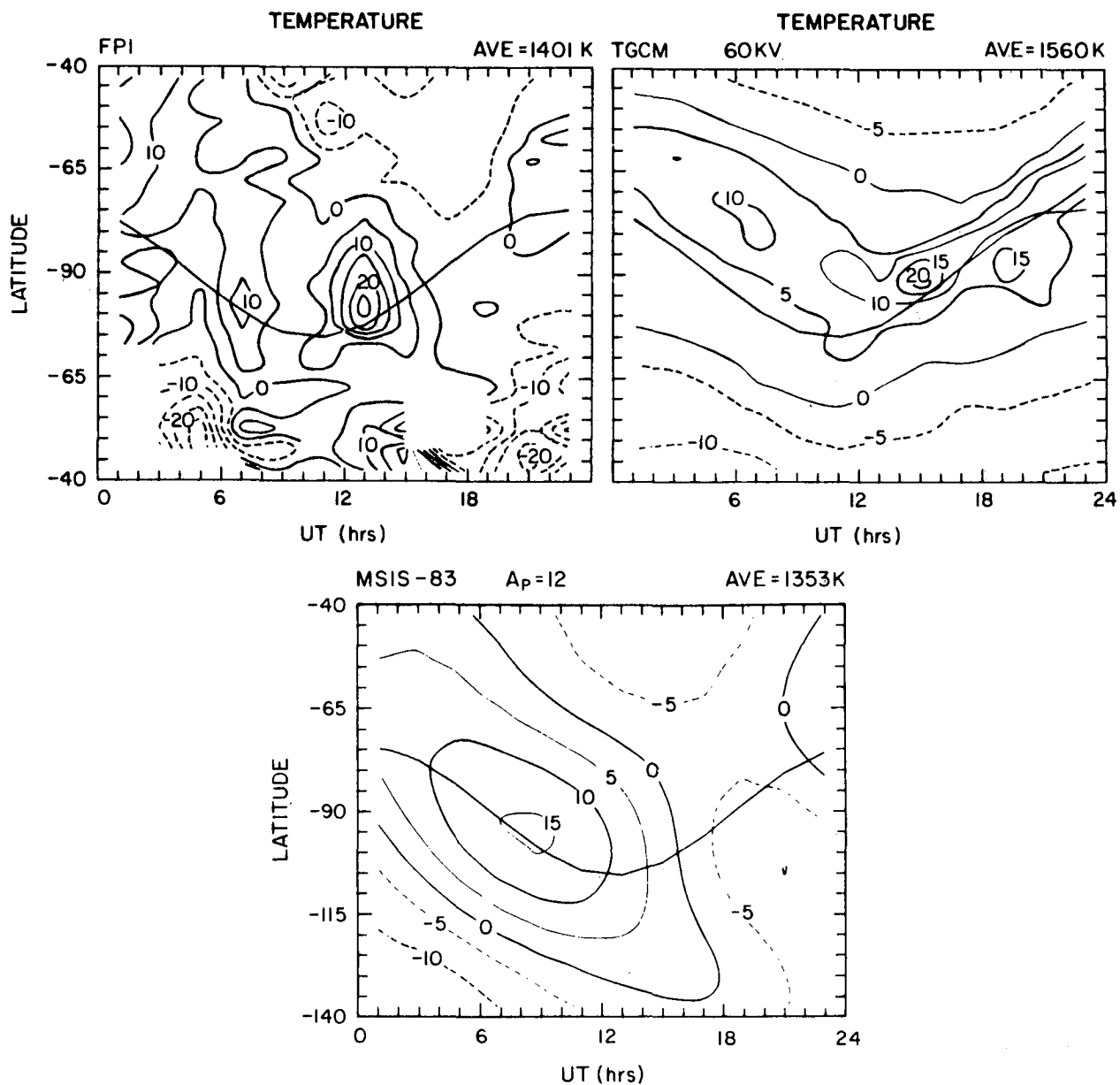
Figure 19. Contours of temperature variation (in percent) from an average value as a function of universal time over the southern hemisphere polar cap. (a) Average of DE 2 FPI measurements during October-November 1981. (b) TGCM model predictions. (c) MSIS-83 model predictions along the satellite track. The average temperature over the latitude-UT grid is indicated in the upper right corner. The solid curve is the geographic position of the south geomagnetic pole as a function of UT. The TGCM model predictions include heating by a magnetospheric cusp and magnetospheric convection with a cross-tail potential of 60 keV. In this figure and all succeeding figures with a similar presentation, data in the top portion of the figure have been obtained at a local solar time of 0900 hours, while data in the bottom part of the figure have been obtained at a local solar time of 2100 hours. This corresponds to the 12-hour local time change as the DE 2 spacecraft crosses the geographic pole in each continuous perigee pass.

403

OXYGEN
NACS   Ap<20   AVE=5.6×10⁸
TGCM   60KV   AVE=6.4×10⁸
MSIS-83 Ap=12   AVE=6.1×10⁸

NITROGEN
NACS   Ap<20   AVE=2.7×10⁸
TGCM   60KV   AVE=1.4×10⁸
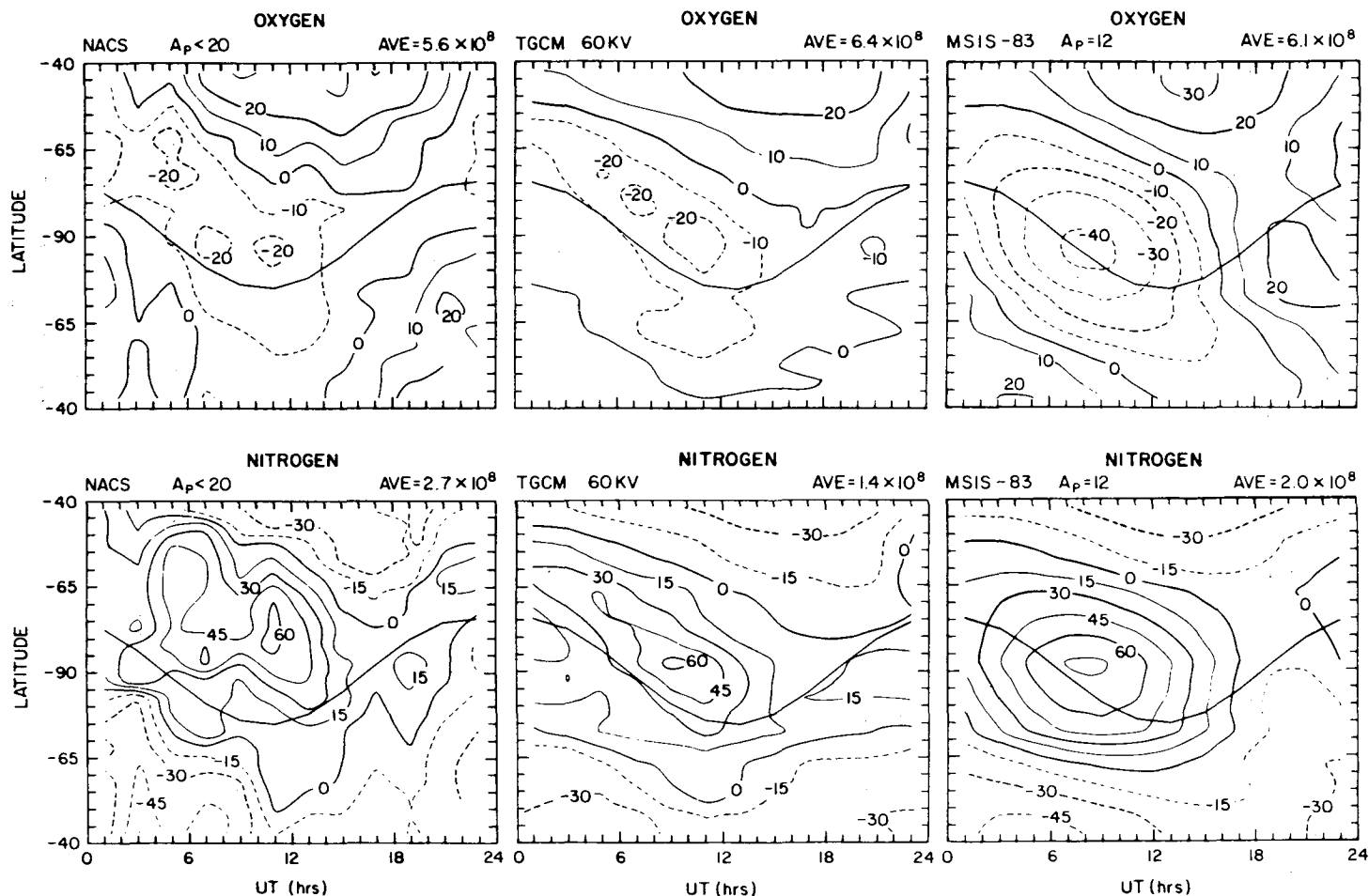MSIS-83 Ap=12   AVE=2.0×10⁸

Figure 20. Contours of the percent by which composition departs from an average value as a function of universal time over the southern hemisphere polar cap. (a) Average variation of atomic oxygen and (d) average variation of molecular nitrogen observed by the NACS instrument on board the DE 2 satellite during October-November 1981 for geomagnetic quiet conditions (Ap<20); (b) TGCM-calculated variation of atomic oxygen; (e) molecular nitrogen; (c) MSIS-83 predicted variation of atomic oxygen; and (f) molecular nitrogen for similar geophysical conditions. The solid curve indicates the projection of the diurnal locus of the south geomagnetic pole on the local time plane of the orbit. The TGCM model includes heating by a magnetospheric cusp and magnetospheric convection with a cross-tail potential of 60 eV.
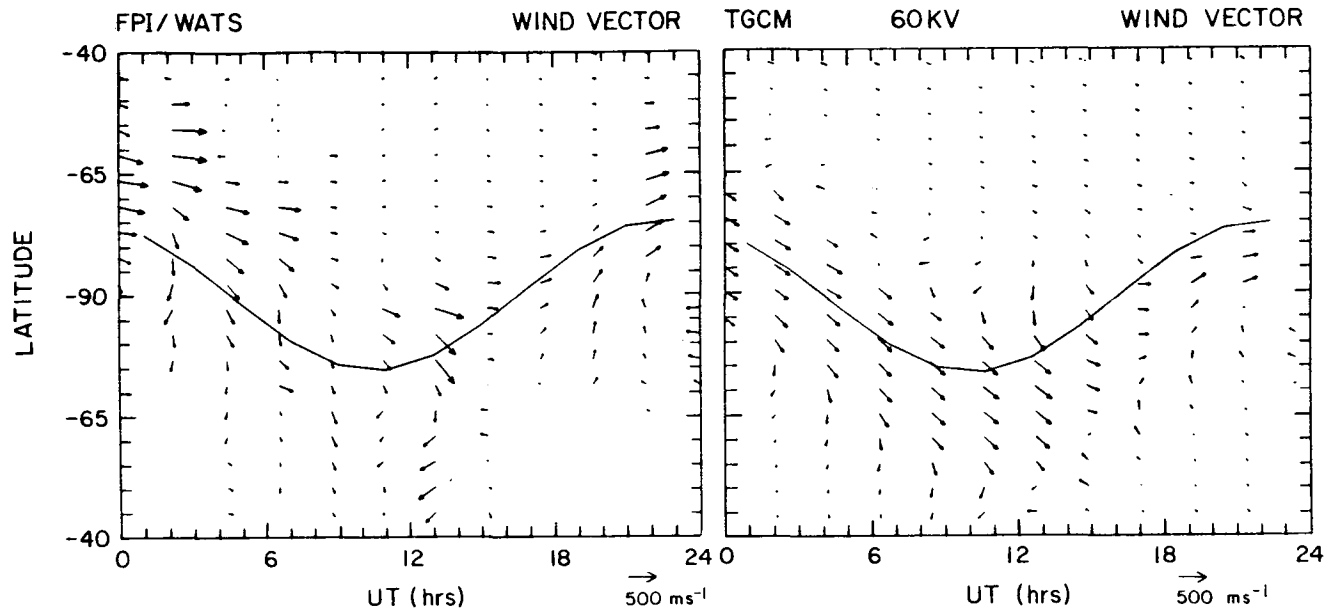
Figure 21. Neutral wind vectors as a function of universal time over the southern hemisphere polar cap. (a) Average of DE 2 FPI/WATS measurements during October-November 1981. (b) TGCM model predictions along the satellite track. The satellite track is from 2100 to 0900 LT (bottom to top of the figure), and the bulk of the arrows indicate a wind directed to the right of the satellite track. The reference arrow for each figure is 500 m s [-1]. The solid curve indicates the projection of the diurnal locus of the south geomagnetic pole on the local time plane of the orbit. The TGCM model includes heating by a magnetospheric cusp and magnetospheric convection with a cross-tail potential of 60 keV.
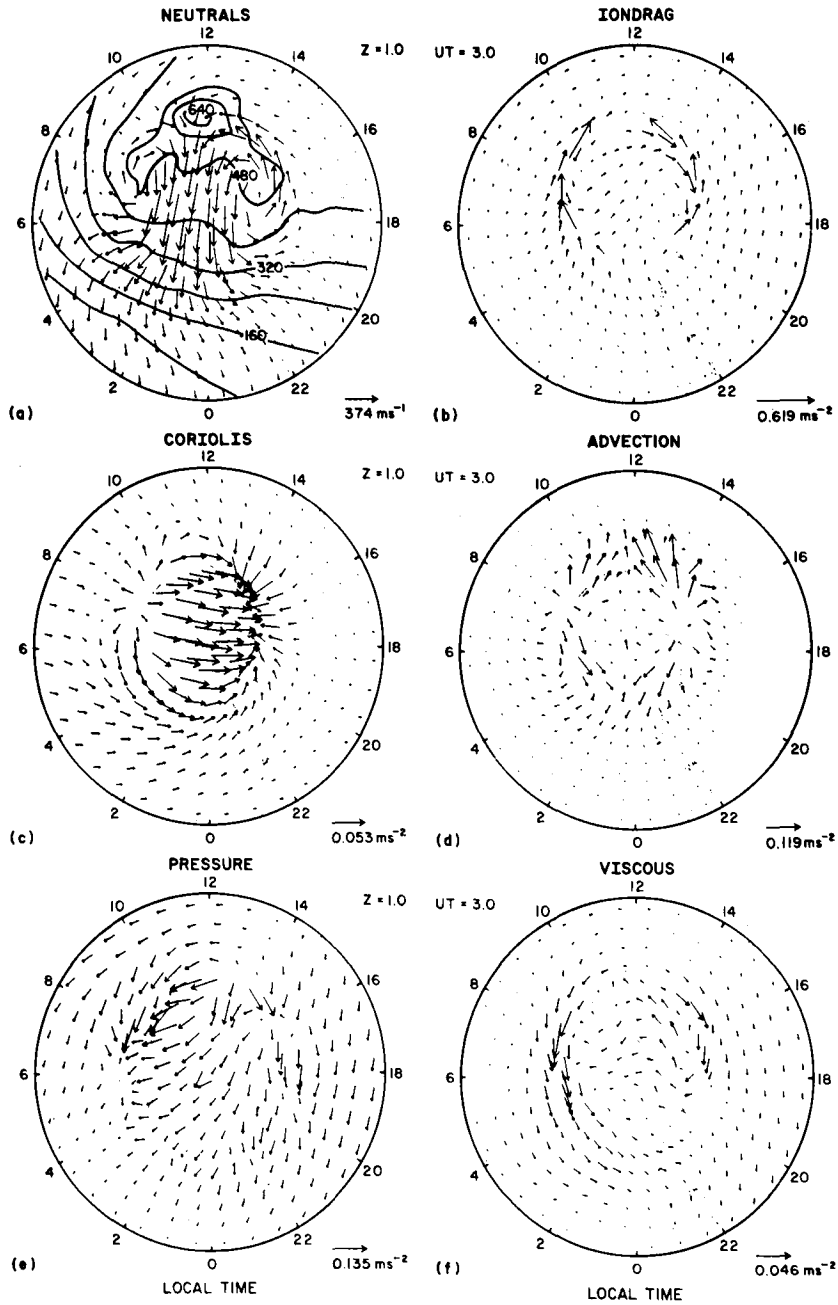
Figure 22. The calculated (a) wind vectors and perturbation temperature contours along the Z = +1 constant-pressure surface over the southern hemisphere polar cap at 0300 UT on October 21, 1981. The maximum arrow in (a) represents a wind velocity of 375 m s⁻¹. The Figures 3b through 3f give vectors of various forces acting on the neutral wind: (b) the ion-drag, (c) Coriolis, (d) advection, (e) pressure, and (f) viscous forces. Note that the length of the maximum arrow represents a different magnitude in each of the figures: (b) 0.62, (c) 0.05, (d) 0.12, (e) 0.14, and (f) 0.05 m s⁻².

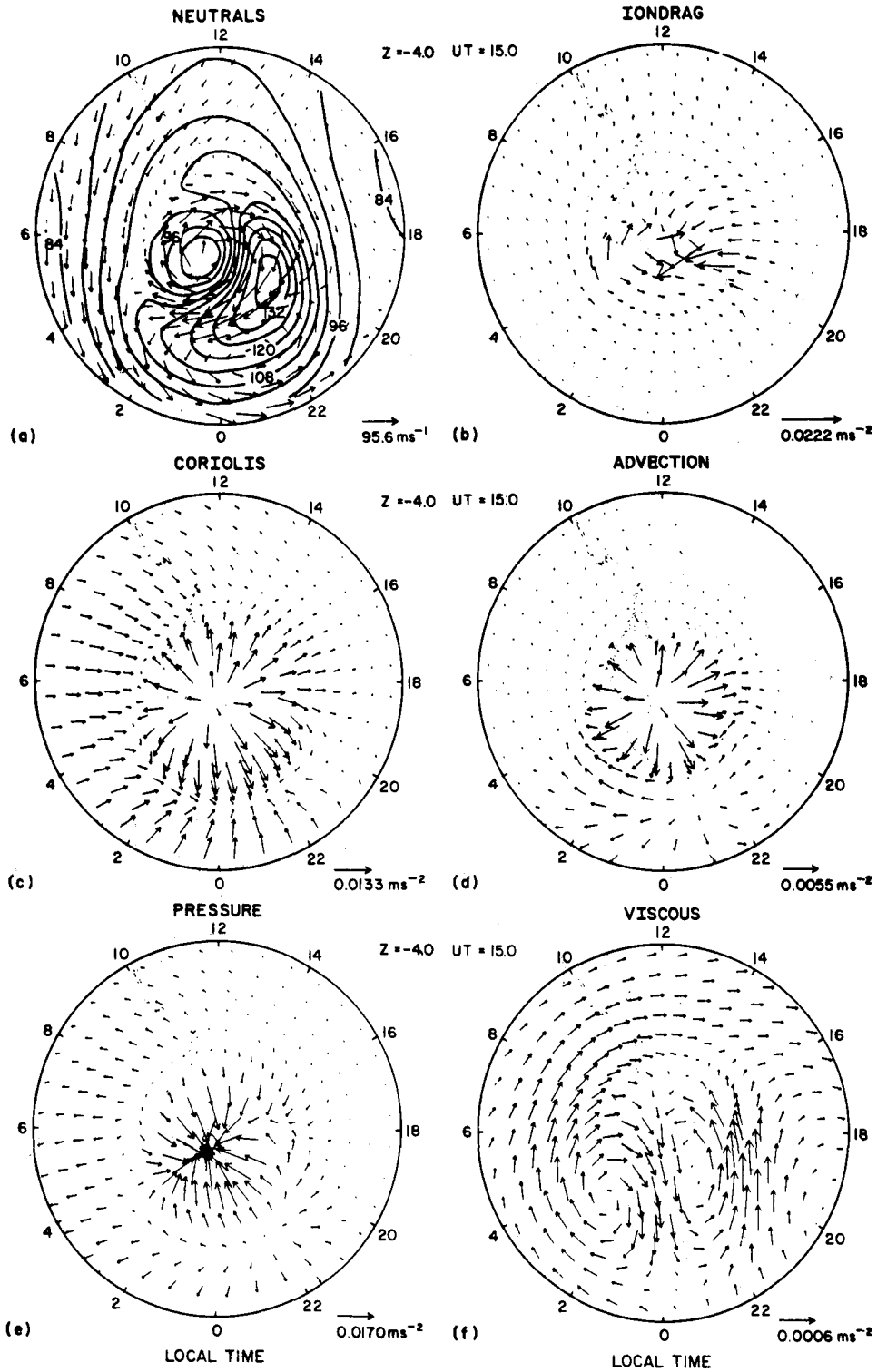Figure 23. Same as Figure 22, except for the Z = -4.0 constant-pressure surface at 1500 UT. The magnitude of the largest vector in (a) is 98.6 m s⁻¹, (b) 0.022, (c) 0.013, (d) 0.0055, (e) 0.017, and (f) 0.00041 m s⁻².
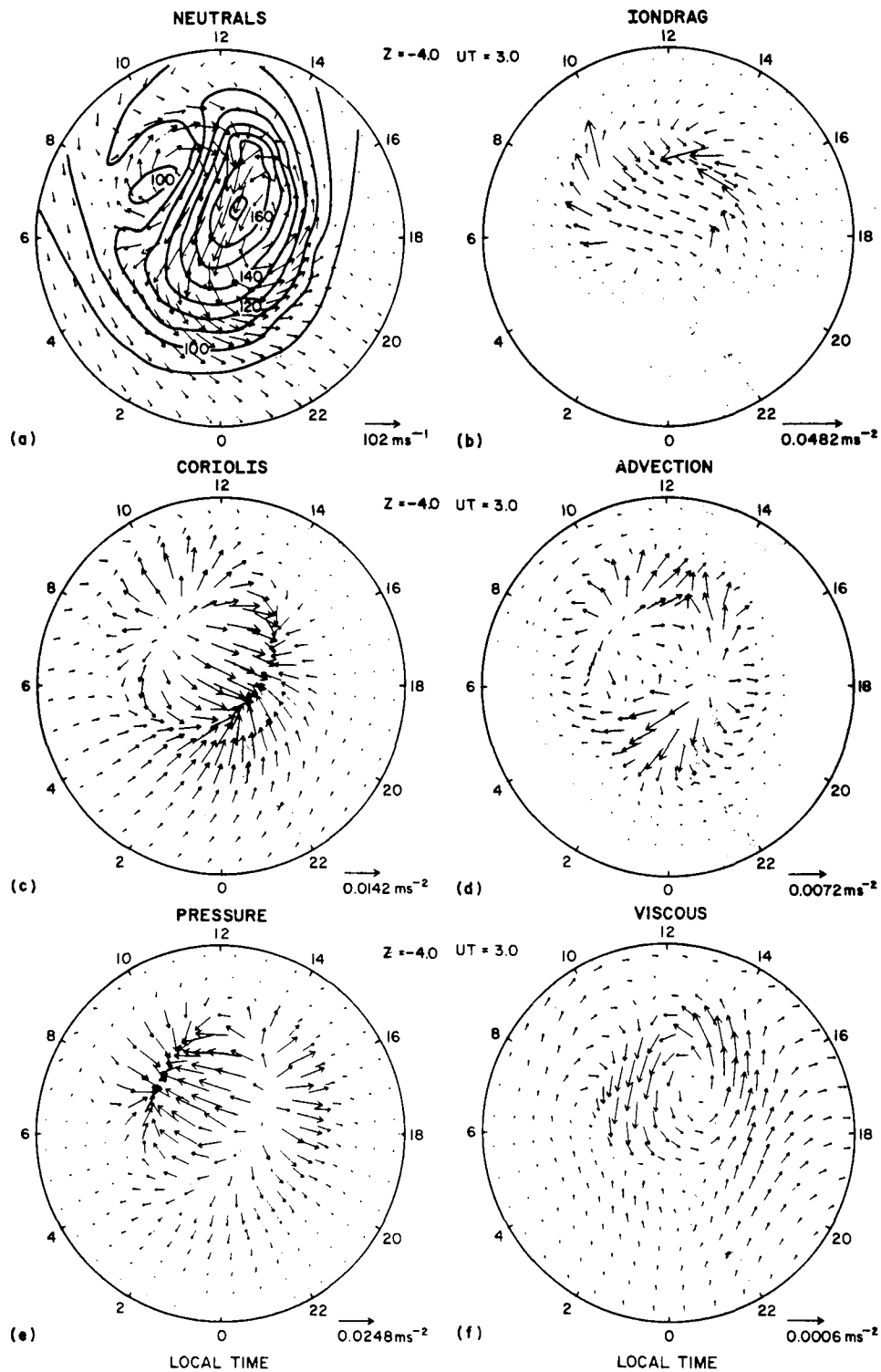
407

Figure 24. Same as Figure 22, except for the Z = -4.0 constant-pressure surface at 0300 UT. The magnitude of the largest vector in (a) is 102 m s⁻¹, (b) 0.048, (c) 0.014, (d) 0.0072, (e) 0.025, and (f) 0.00057 m s⁻².
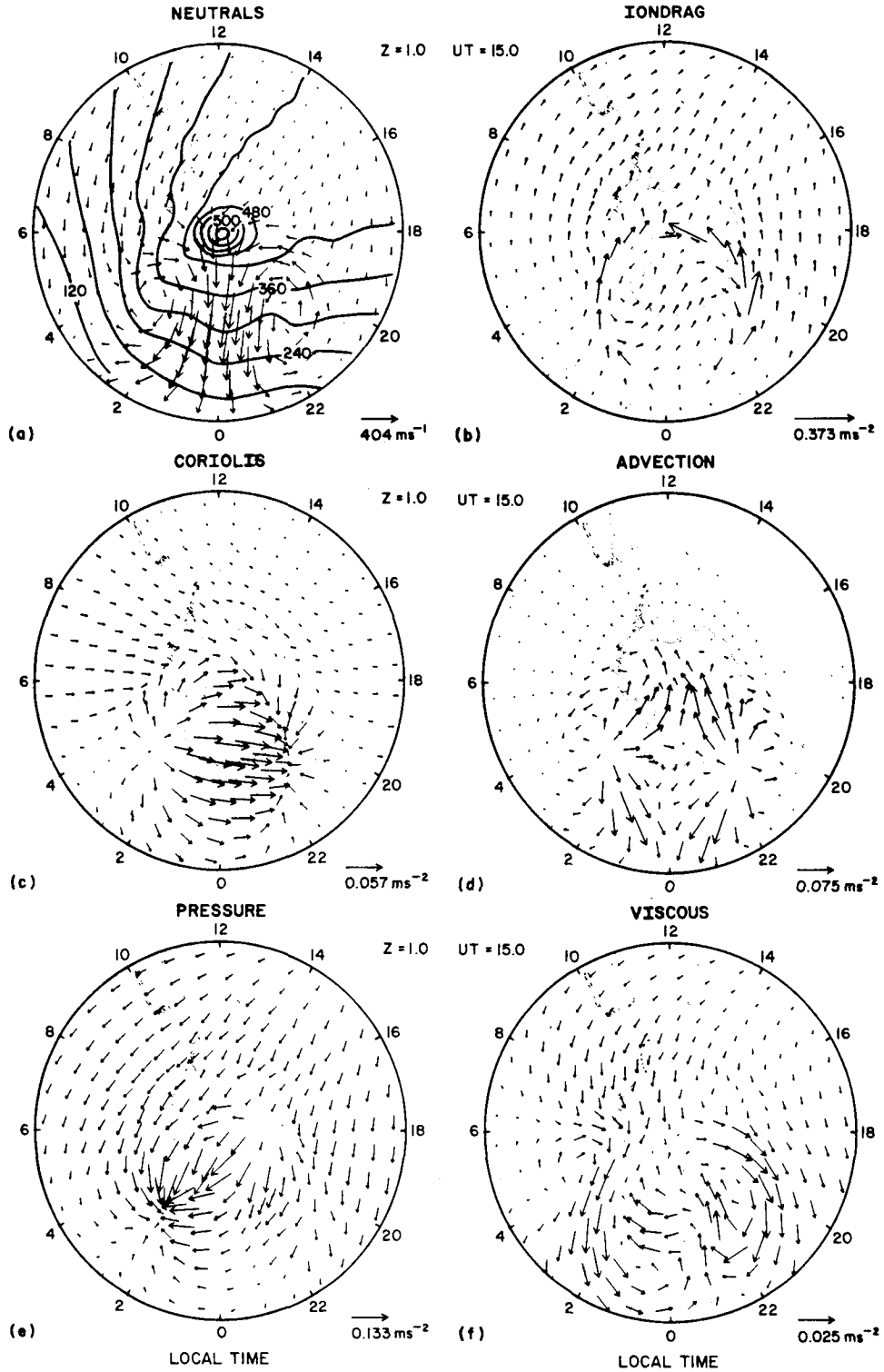
408

Figure 25. Same as Figure 22, except for 1500 UT. The magnitude of the largest vector in (a) is 405 m s⁻¹, (b) 0.37, (c), 0.06, (d) 0.07, (e) 0.13, and (f) 0.02 m s⁻².
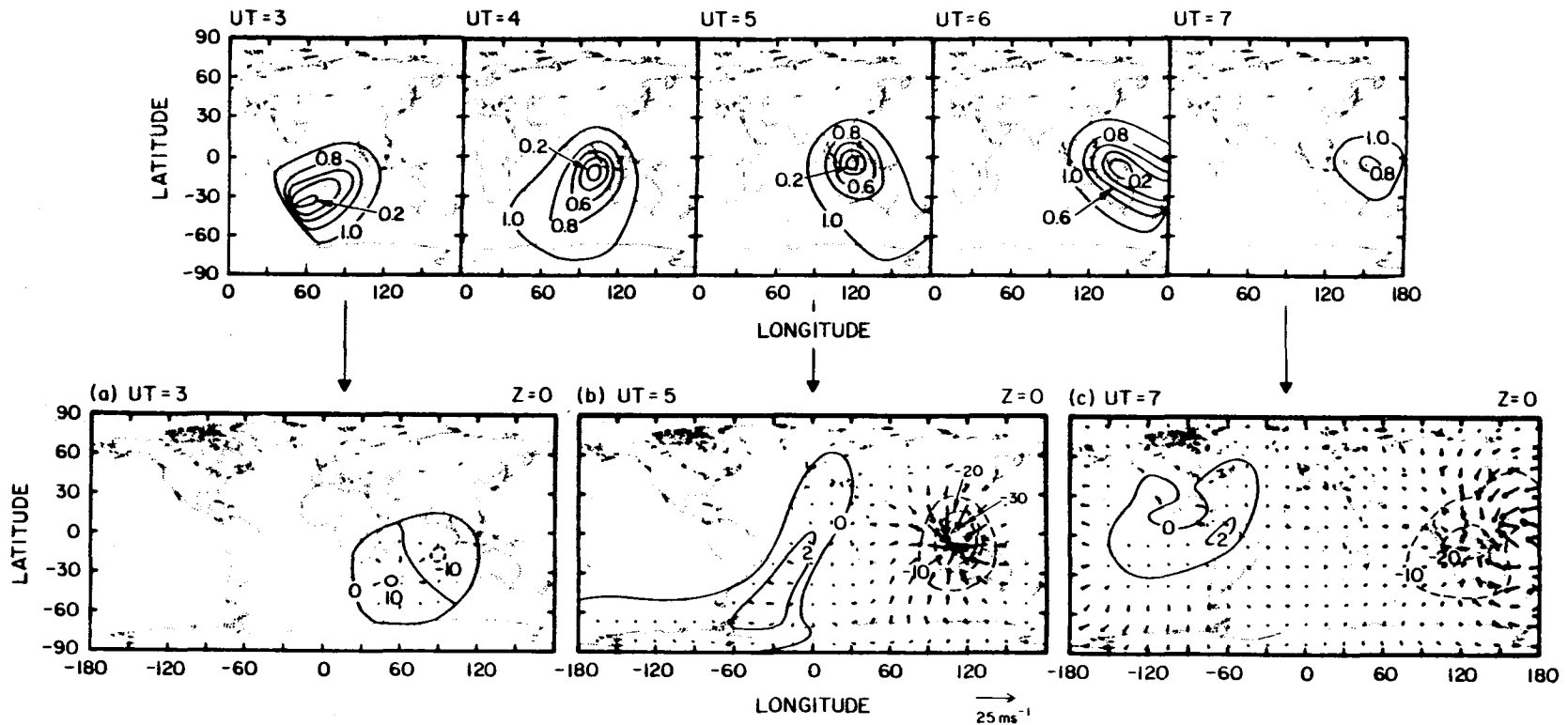
409

Figure 26. (a) Contours of the calculated eclipse function at 0300, 0400, 0500, 0600, and 0700 UT at 300 km indicating the temporal progression of the eclipse shadow on June 11, 1983. (b) Calculated temperature (degrees Kelvin) and wind (meters per second) difference fields caused by the eclipse shadow at 0300, 0500, and 0700 UT and along the model Z = 0 constant pressure surface at approximately 300 km.
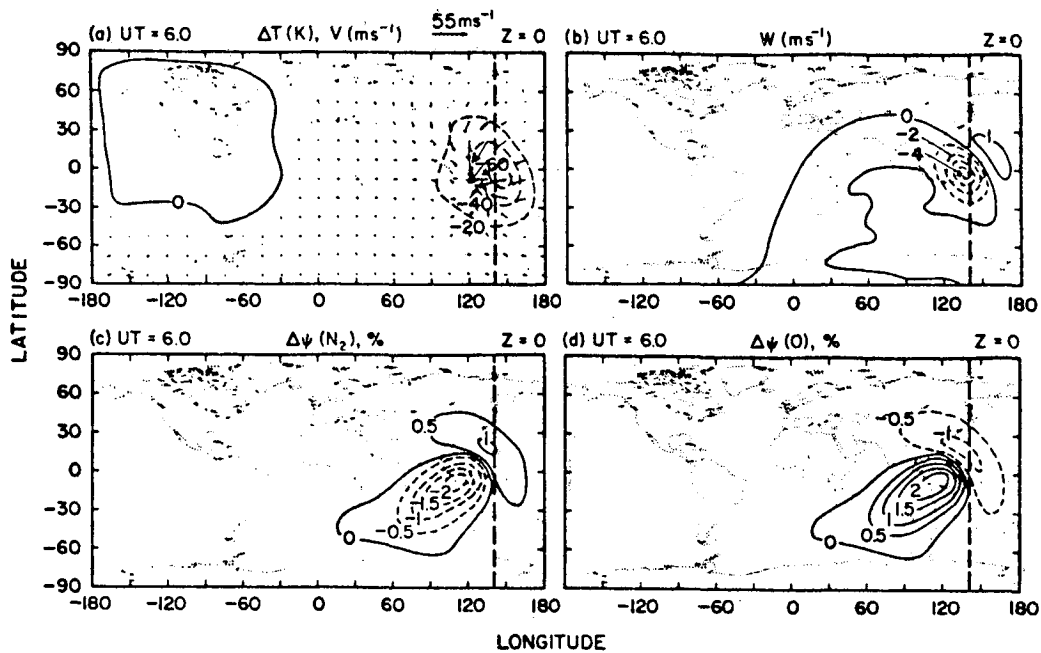
Figure 27. Contours of (a) calculated temperature (degrees Kelvin) and wind
(meters per second) difference fields, (b) vertical velocity (meters per second),
positive upward, (c) percent deviation of molecular nitrogen mixing ratio, and (d)
percent deviation of atomic oxygen mixing ratio at 0600 UT and along the model Z
= 0 constant pressure surface near 300 km during June 11, 1983 solar eclipse.
The heavy dashed line along the 140 °E longitude indicated the cross section of the
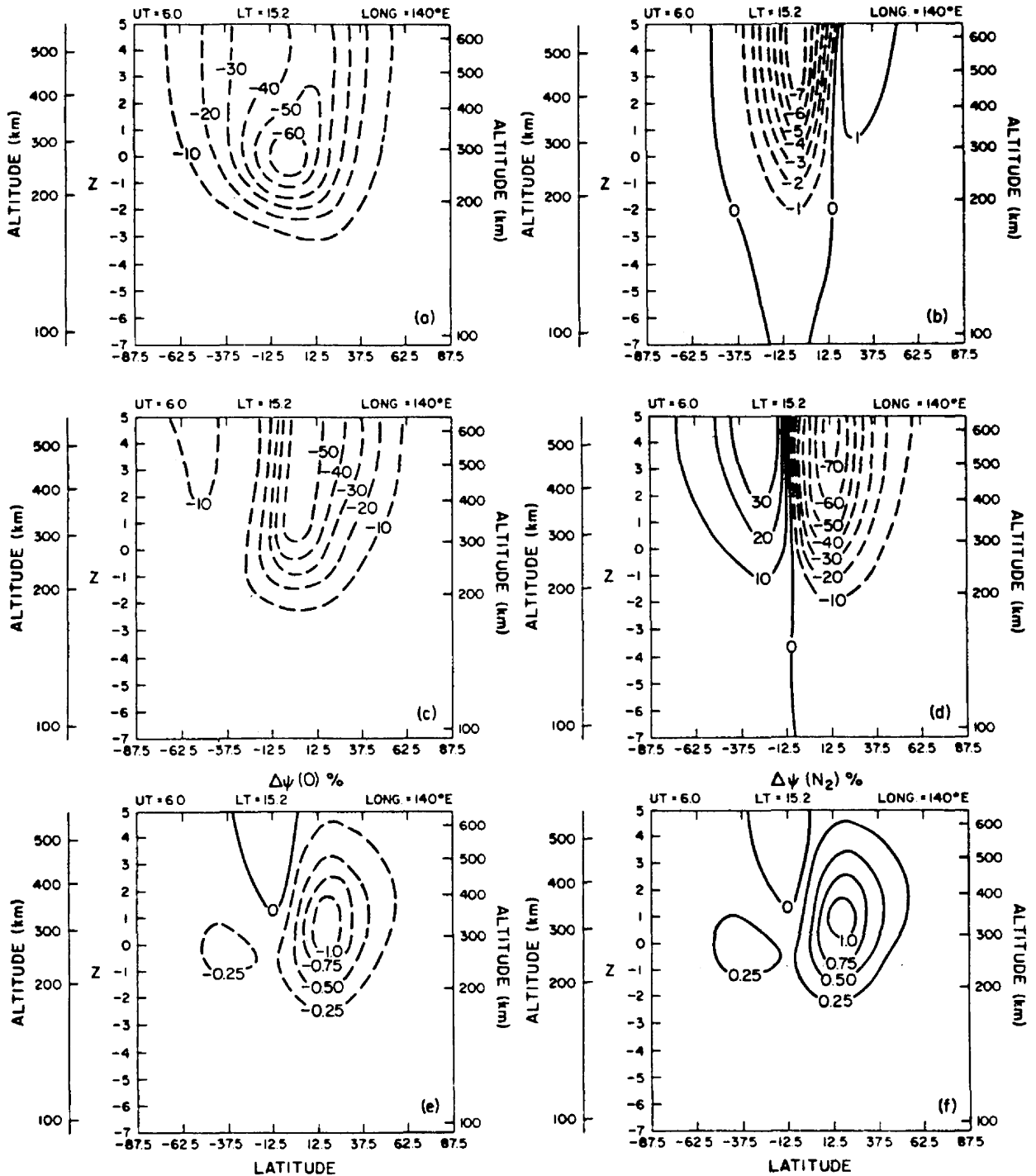contours presented in Figure 28.

411

Figure 28. Contours of calculated (a) temperature difference (degrees Kelvin), (b) vertical wind (meters per second), positive upward, (c) zonal wind (meters per second), positive eastward, (d) meridional wind (meters per second), positive northward, (e) percent change of atomic oxygen mixing ratio, and (f) percent change of molecular nitrogen mixing ratio along the 140 °E longitudinal slice at 0600 UT during the June 11, 1983 solar eclipse.
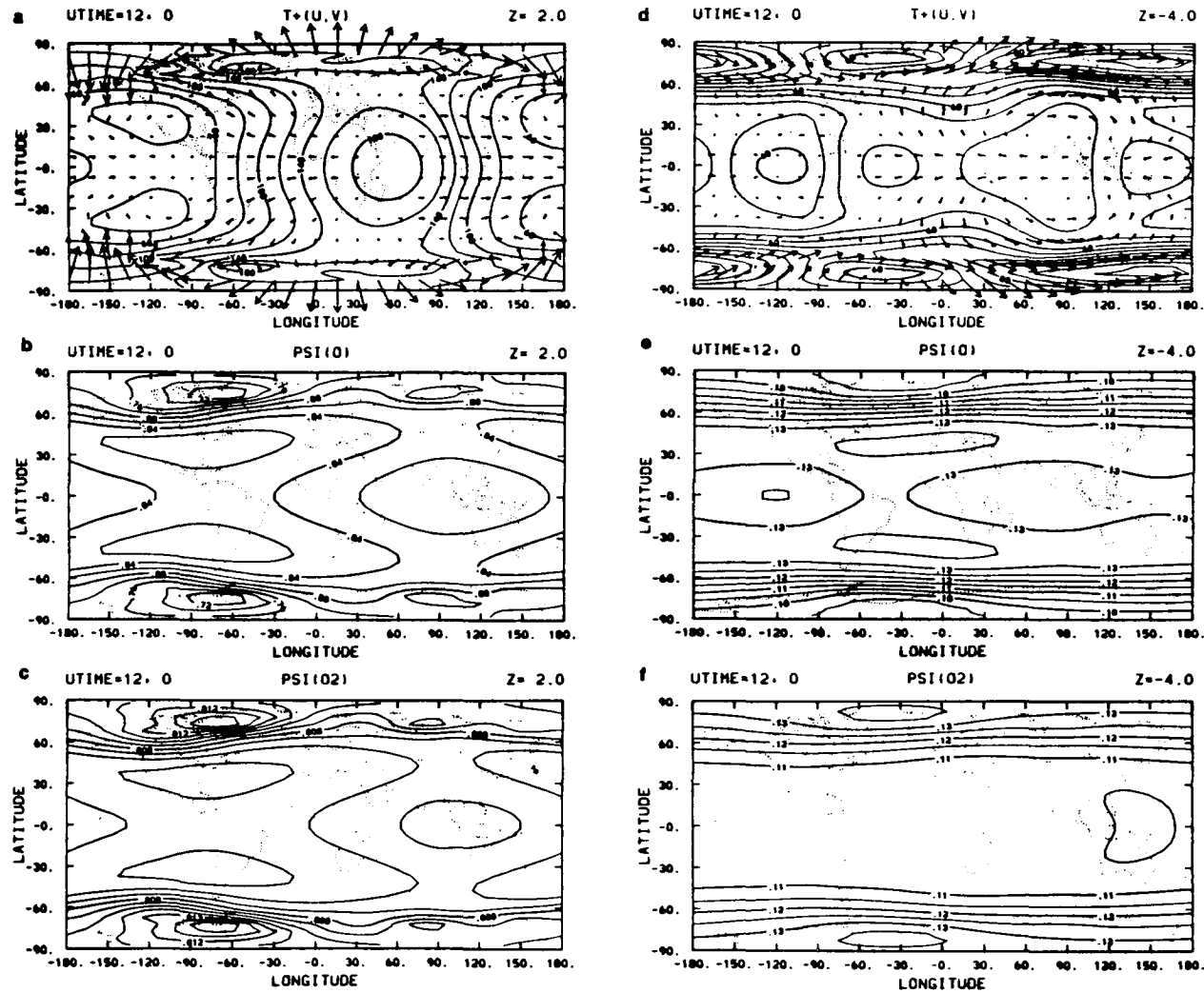
412

Figure 29. The calculated global circulation, temperature and compositional structure along the Z = +2 (300 km) constant-pressure surface for the case of solar heating plus magnetospheric convection with a cross-tail potential of 60 kV: (a) contours of perturbation temperature (K) and arrows giving wind direction and the length of the wind speed with the maximum arrow representing 336 m s⁻¹; (b) contours of ψ_0; (c) contours of ψ_{02}. The same fields along the Z = -4 (120 km) constant-pressure surface are represented in (d), (e) and (f), respectively. The maximum arrow in (d) represents a wind speed of 79 m/sec.

MILLSTONE HILL MEASUREMENTS AND TGCM SIMULATION
FOR THE 30 MAY 1984 ANNULAR SOLAR ECLIPSE

J. E. Salah, W. L. Oliver - MIT Haystack Observatory, Westford, MA 01886
B. A. Emery, R. G. Roble, E. C. Ridley - NCAR, Boulder, CO 80307
H. C. Carlson - AFGL, Hanscomb Air Force Base, Bedford, MA 01731

On 30 May 1984, the Millstone Hill incoherent scatter radar was operated to gather data on the effects of the annular solar eclipse on the structure and dynamics of the ionosphere and thermosphere. The eclipse path was about 3 deg. south of Millstone which experienced a maximum obscuration of 86% at about 1705 UT. Both the zenith and steerable antennas at Millstone were used in the experiment to collect data on the temporal evolution of the eclipse effects. This experiment represented the first opportunity at Millstone to collect data during an eclipse in the absence of a major magnetospheric disturbance which had previously made the unravelling of eclipse effects difficult. In addition, the configuration of the experiment and analysis of the data included a detailed examination of the effects on the neutral atmosphere. A major catalyst for this study was the opportunity to compare the results with the predictions made from the Thermospheric General Circulation Model (TGCM) at NCAR, as a calibration point for the model. The plans for the experiment were formulated at the February 1984 Incoherent Scatter Data Users Workshop; the Arecibo and Sondrestrom radars also participated as part of a radar chain experiment. The analysis of the data from these stations is in progress; this paper presents the initial results from Millstone Hill.

The observations, confirming the TGCM predictions, indicate a drop in electron density by 60% at the peak obscuration time in the altitude range 130 – 250 km. At higher altitudes, a smaller decrease (14%) is observed, in contrast to the model predictions and the difference is due to assumed flux boundary conditions. Although a difference in mean electron temperature exists between model and temperature, a good agreement is found in the relative drop ($\sim 25\%$) during the eclipse. Within somewhat large fluctuations it is possible to discern a 50° K drop in the exospheric temperature measurements as predicted from the TGCM.

From three dimensional ion drift measurements across the eclipse path a neutral wind velocity, governed primarily by the meridional component, of about 50 m/sec at eclipse time is observed. Within the uncertainties of the measurements, little change in the winds is observed prior to and following the eclipse, and the results are similar to previous summer day observations where a reversal occurs near 1400 EST. Electric fields derived from the data indicate magnitudes of the order of 1 mV/m or less, primarily north-westward except between 1530 and 1730 U.T. where the field is south-eastward. While the TGCM predicted similar overall wind magnitudes and directions as observed, it has been difficult to verify the convergence of wind perturbations onto the eclipse

path as would be expected and as indicated by the model. This is because of geometric considerations of the ion drift vectors relative to the eclipse path, and because of the sensitivity of the radar measurements in the F-region to both the meridional and zonal components. It is nonetheless possible to state that the overall dynamic behavior predicted by the TGCM is consistent with the observations.
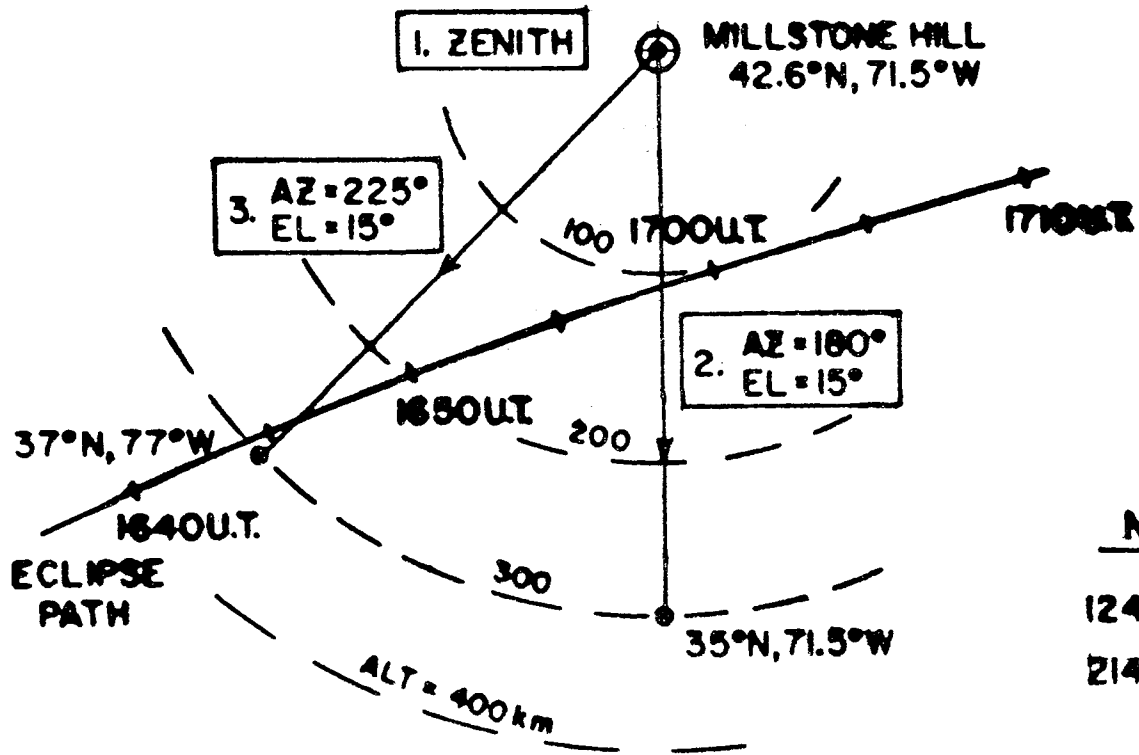
ANNULAR SOLAR ECLIPSE OF 1984 MAY 30
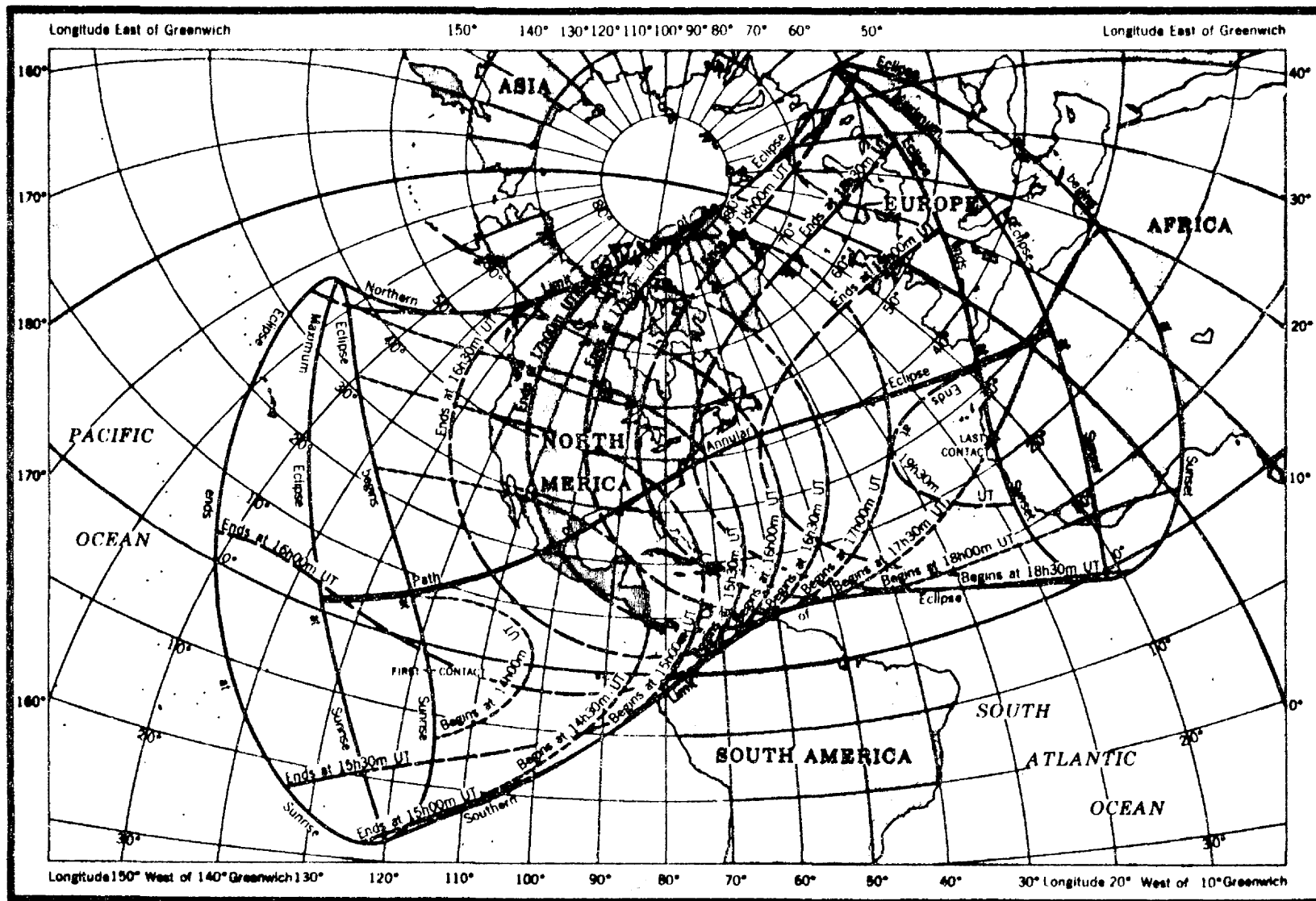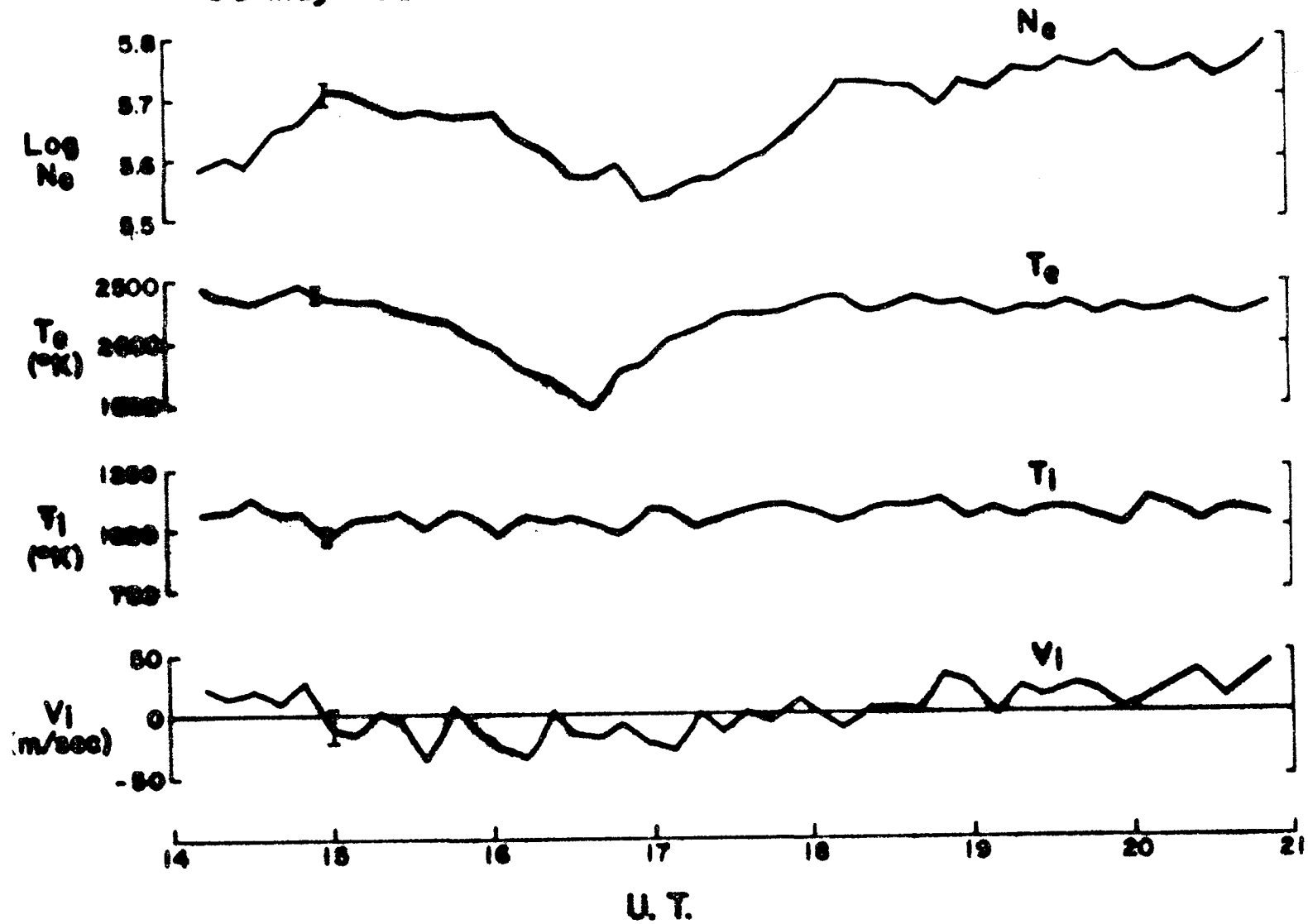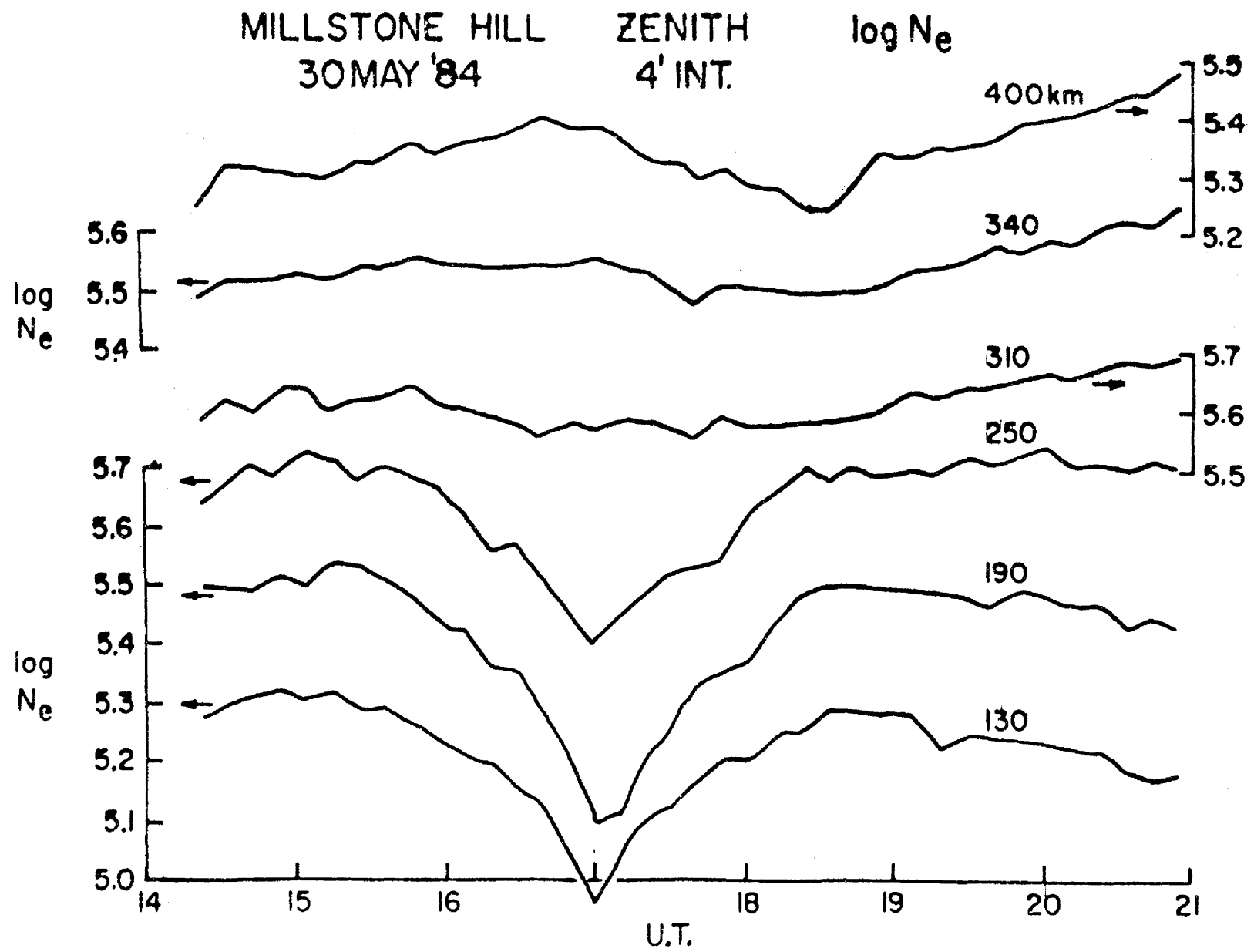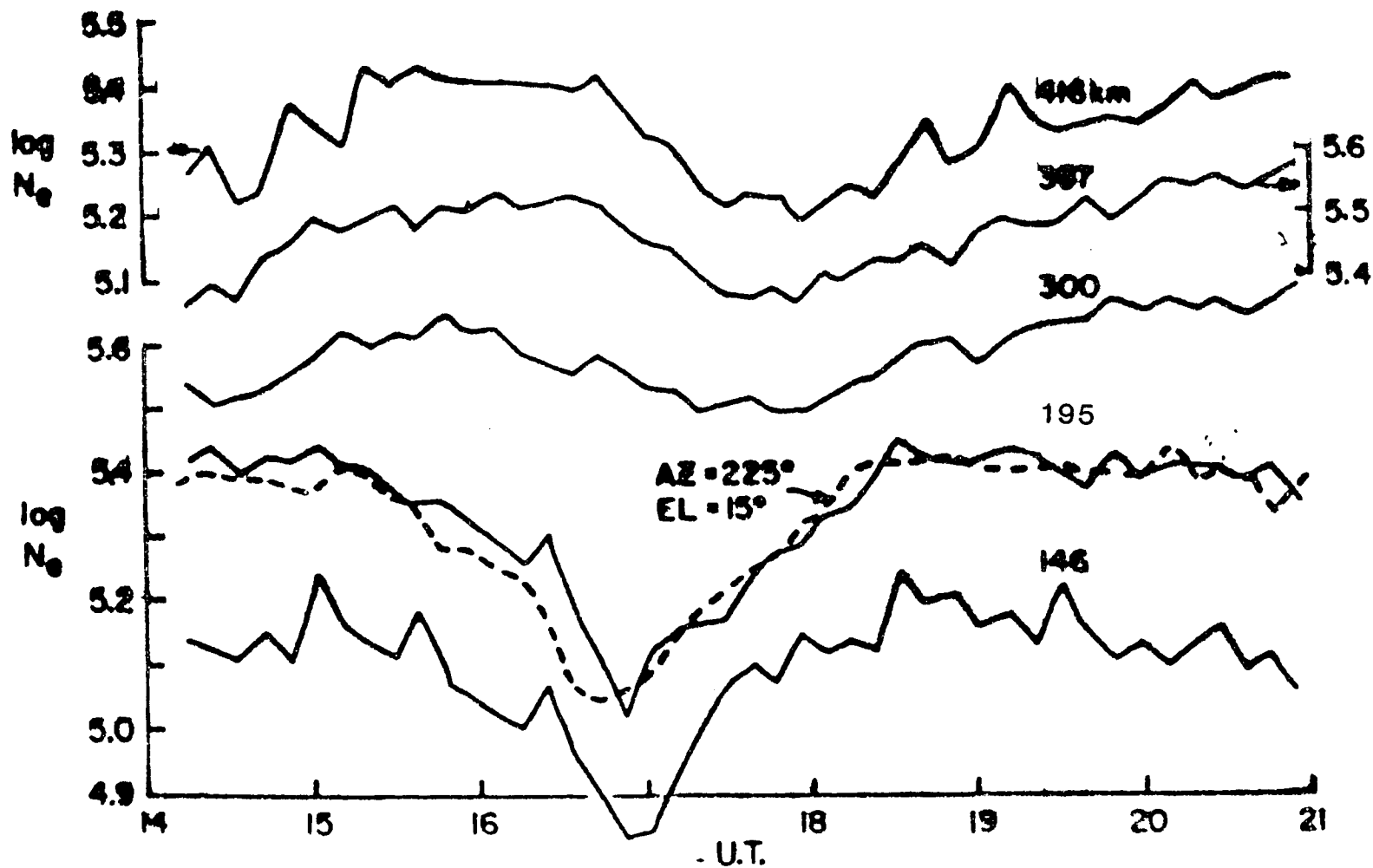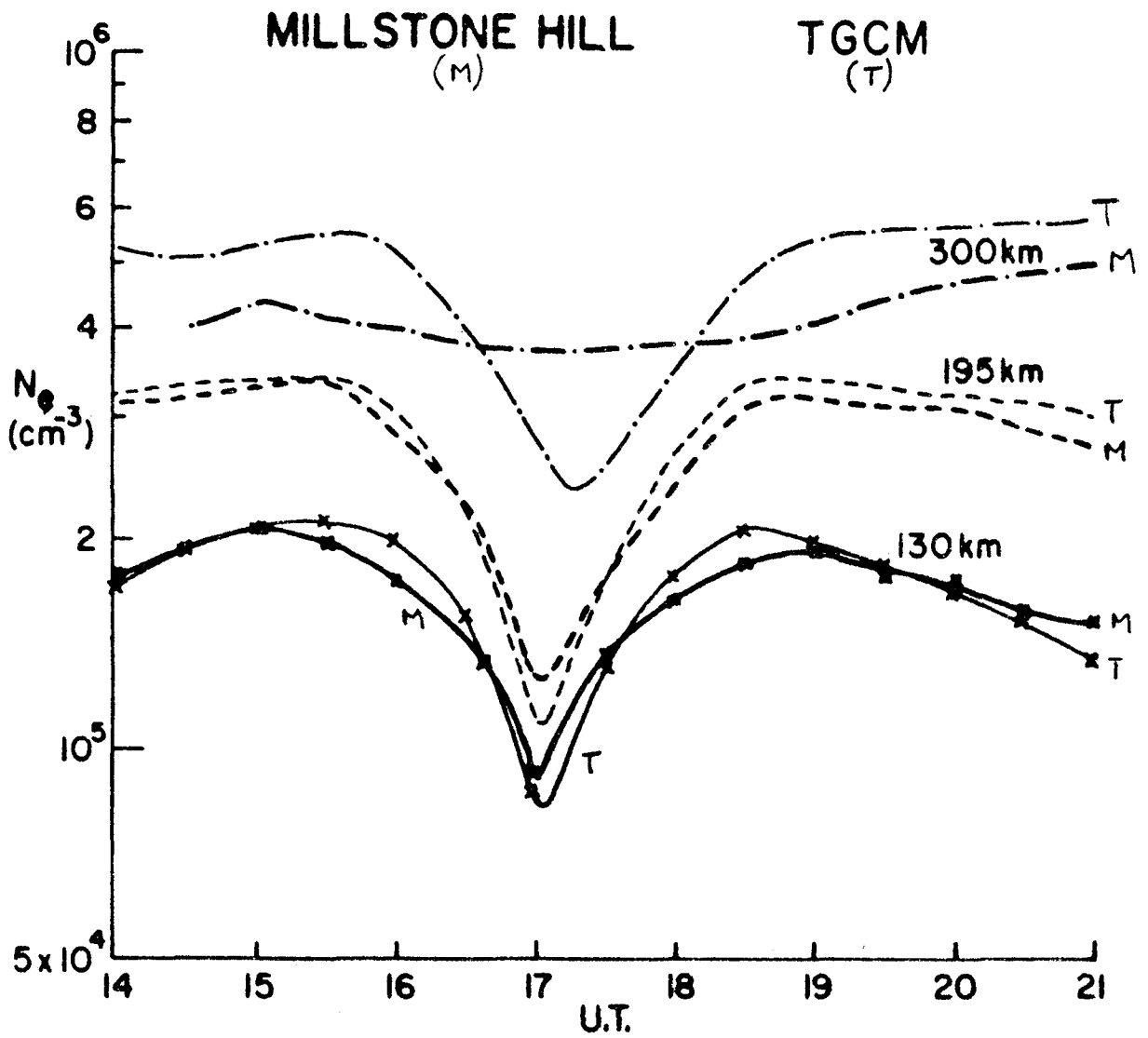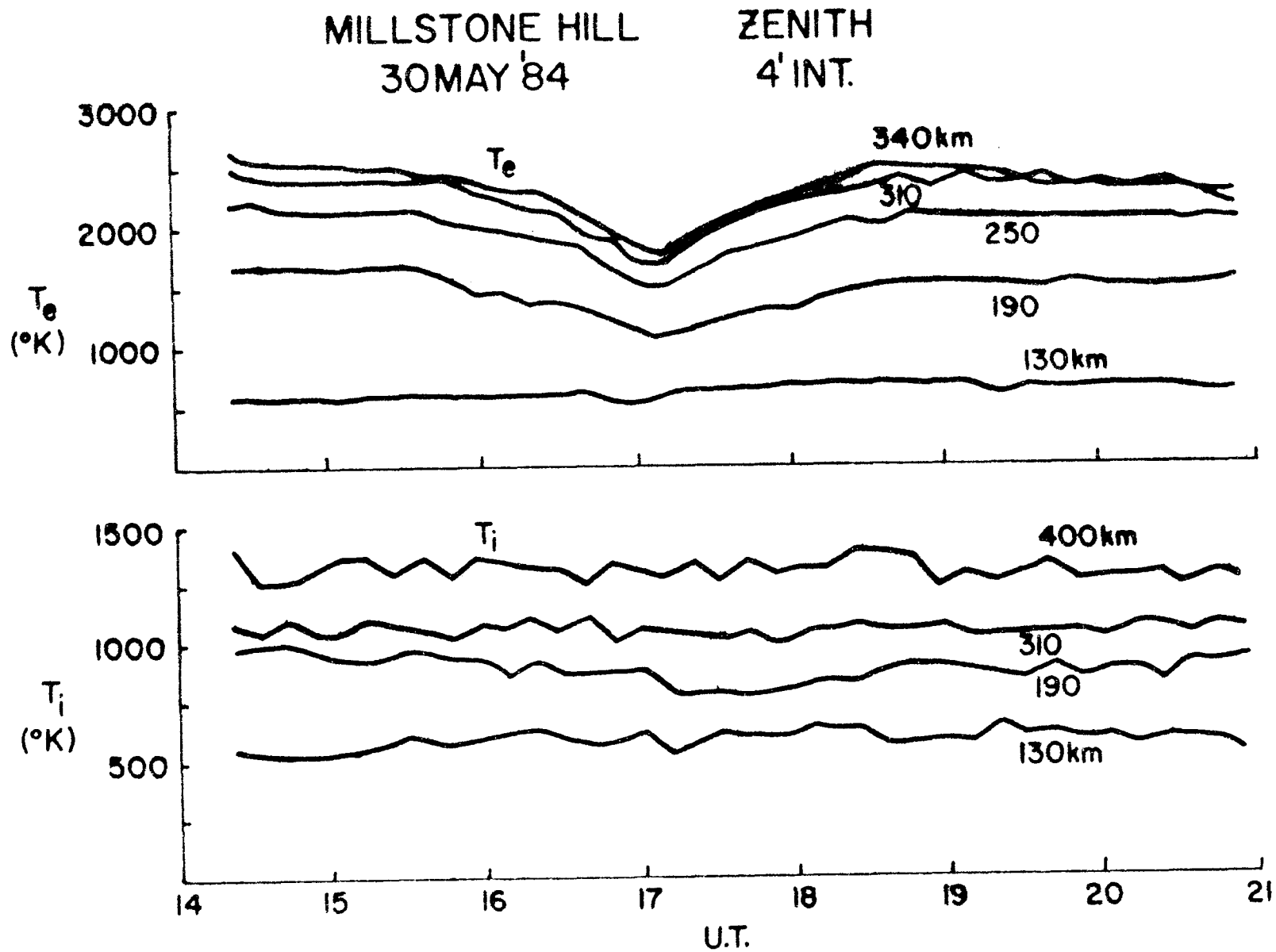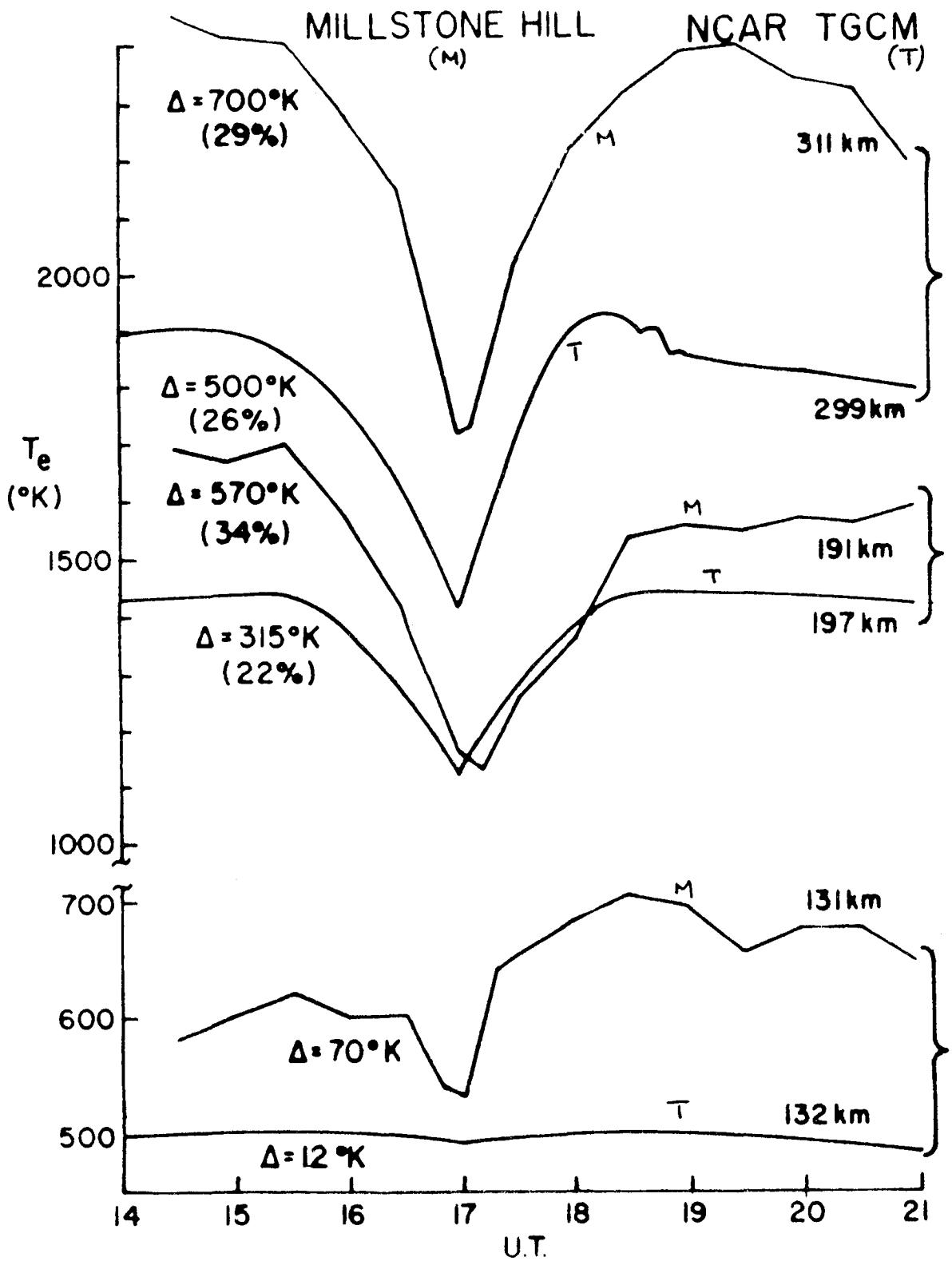
Figure 1.

Figure 2.

Figure 3.

Figure 4.

Figure 5.

Figure 6.
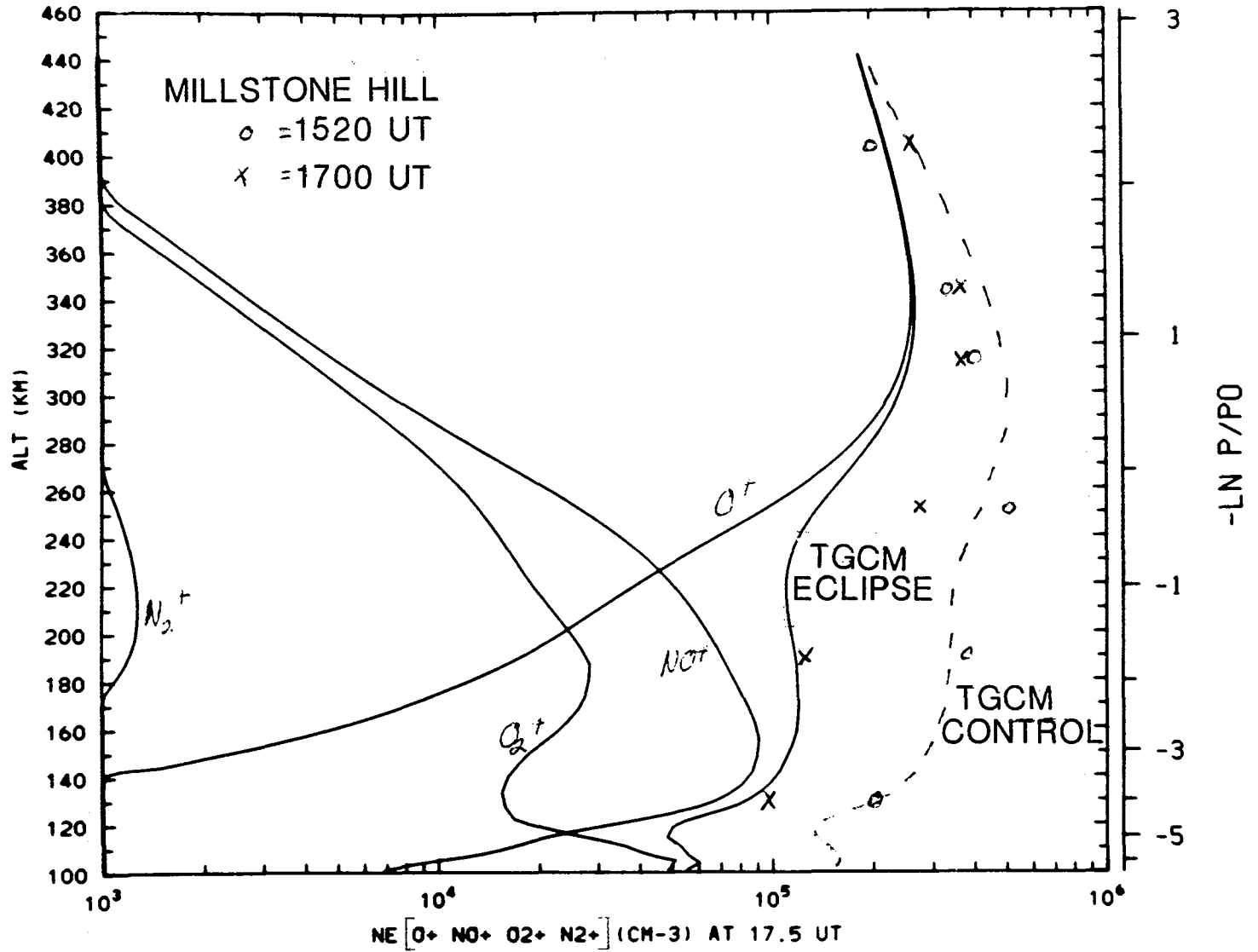
Figure 7.

Figure 8.

Figure 8a. NCAR TGCM update.
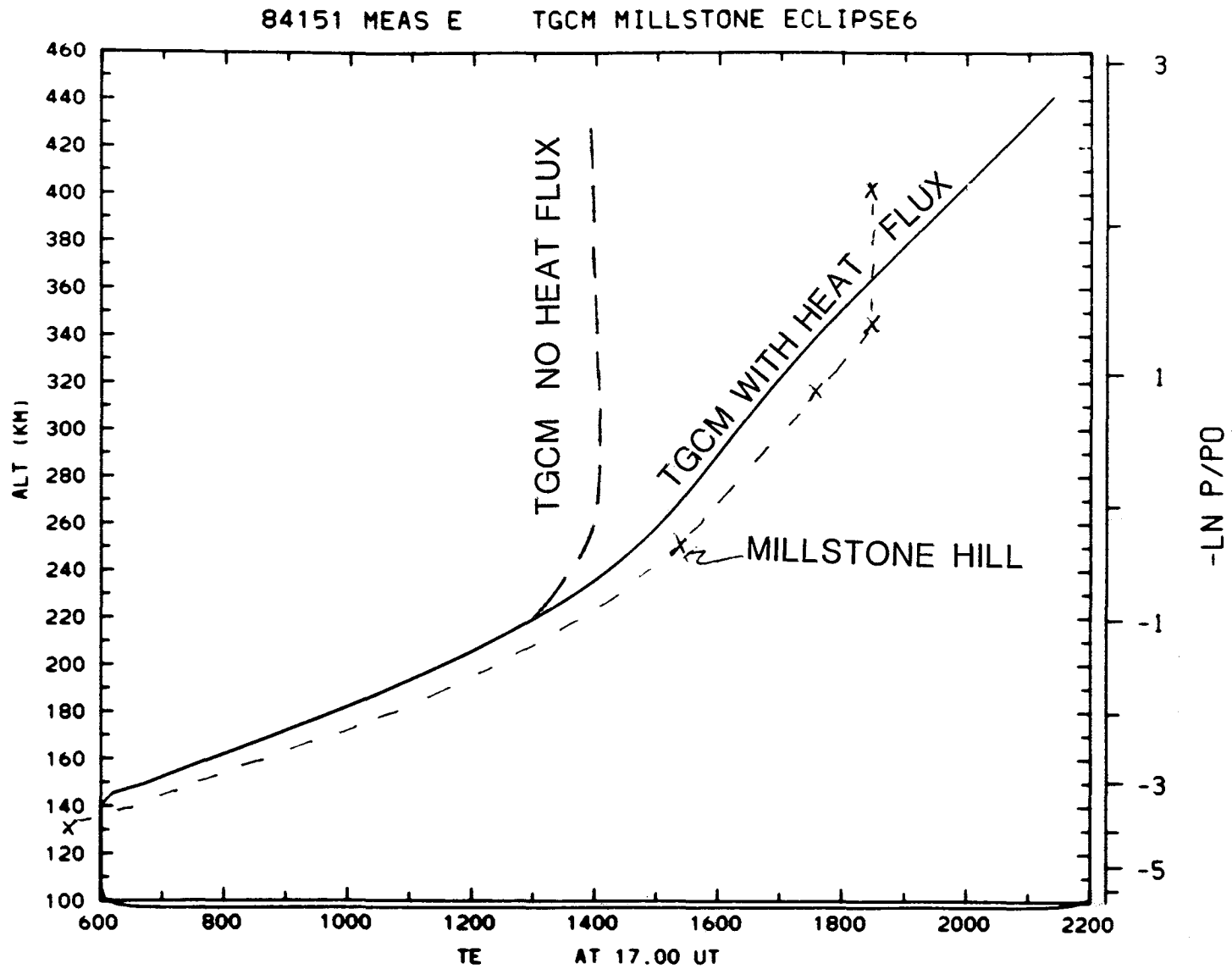
Figure 8b. NCAR TGCM update.
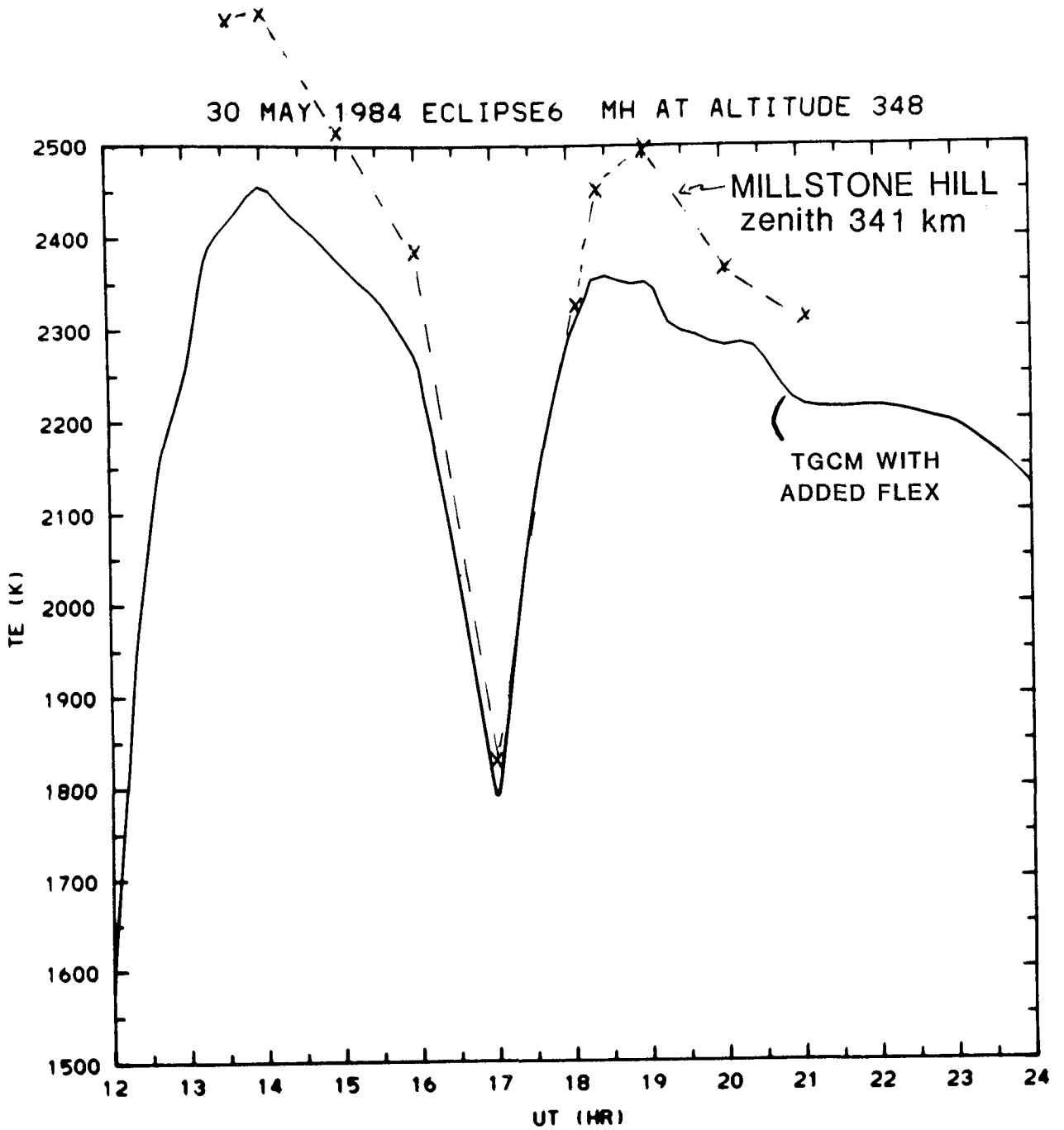
Figure 8c. NCAR TGCM update.
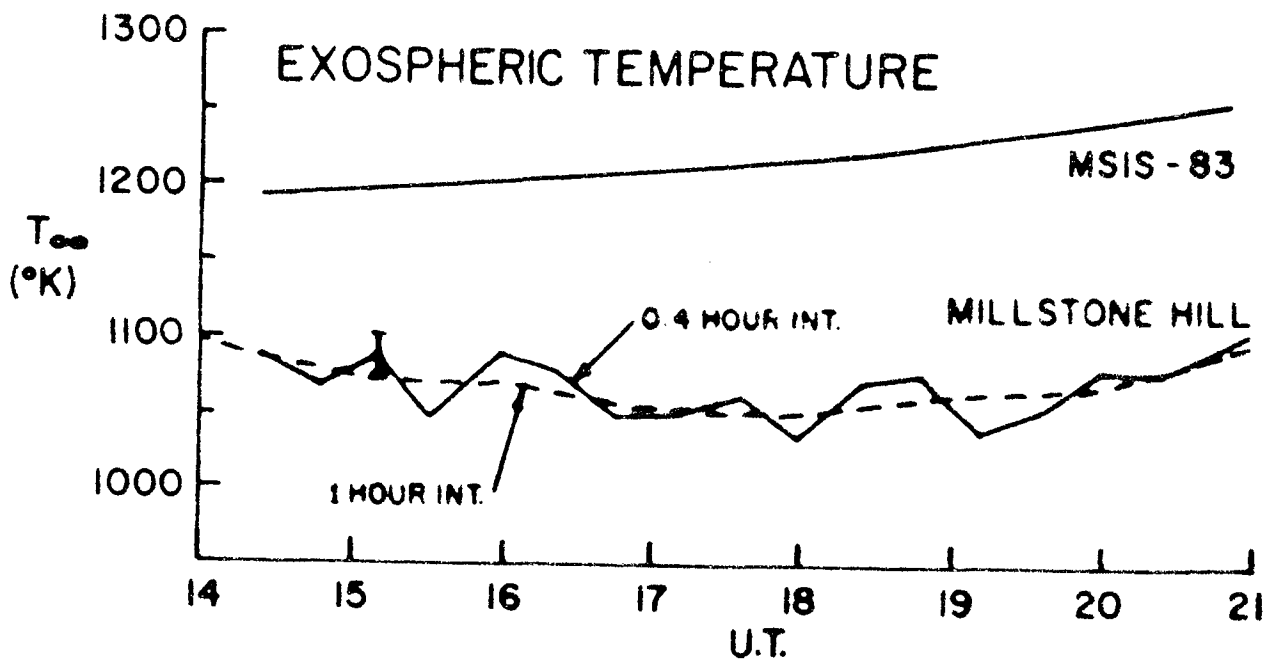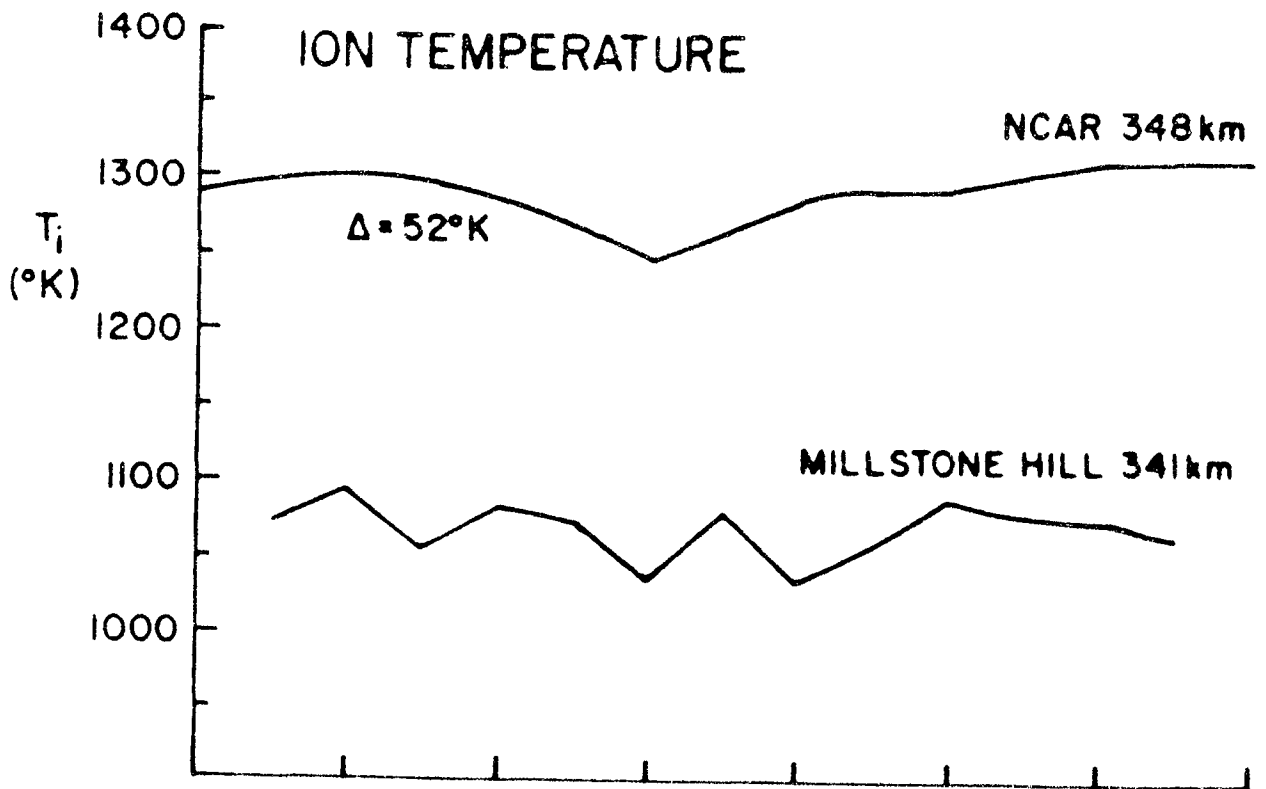
Figure 9.
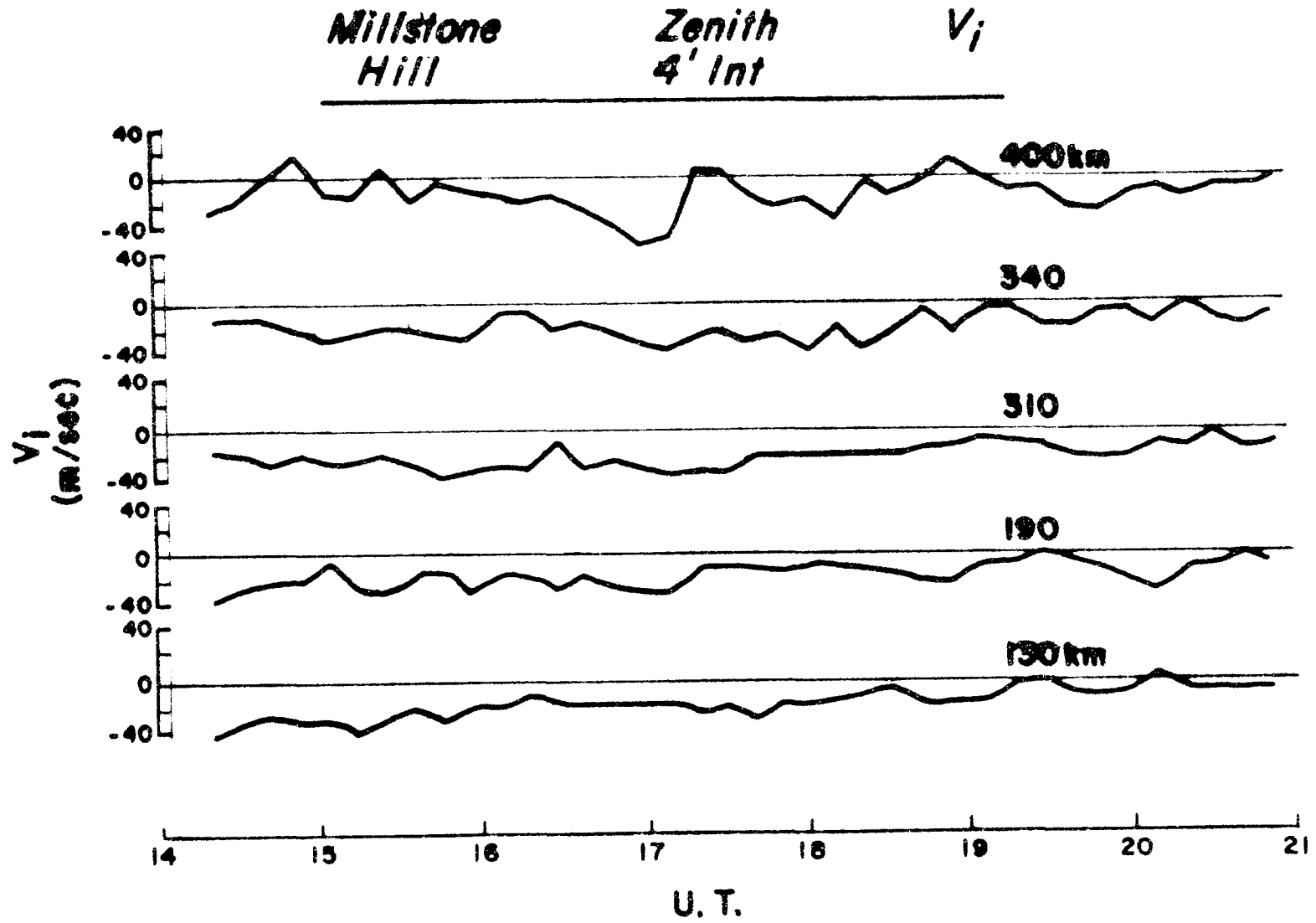
Figure 10.

429
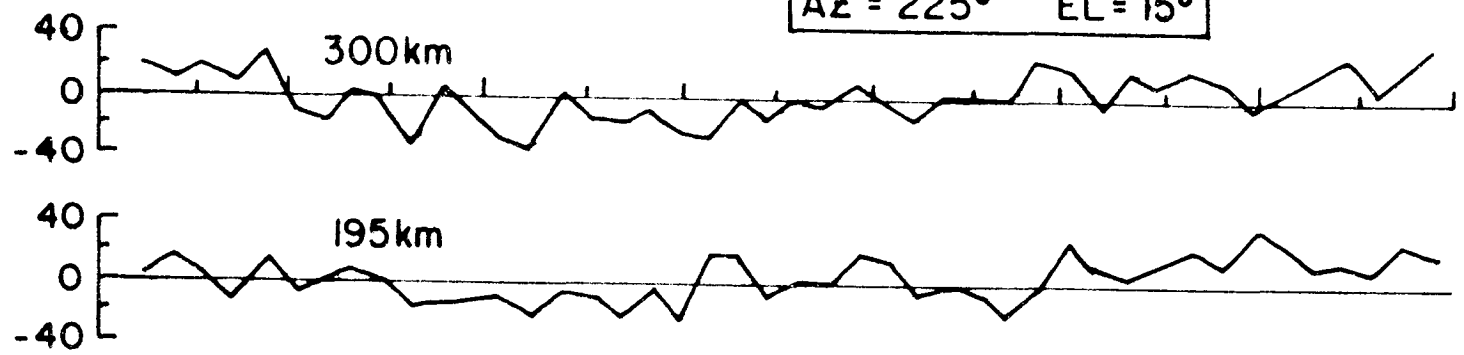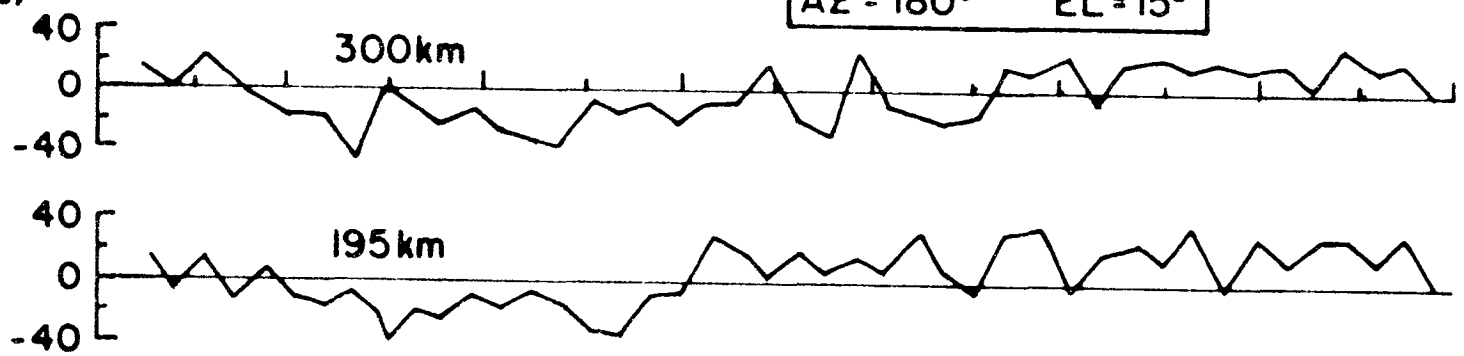
Figure 11.

DERIVATION OF NEUTRAL WINDS

V_I (ZENITH) $-0.95\ V_{DIFF}$ $=$ $-0.29\ V_N' + 6\ E_X + 1.5\ E_Y$

V_I (S, 15°E) $-0.54\ V_{DIFF}$ $=$ $-0.16\ V_N' - 17\ E_X + 0.8\ E_Y$

V_I (SW, 15°E) $-0.4\ V_{DIFF}$ $=$ $-0.12\ V_N' - 12\ E_X + 15\ E_Y$

WHERE $V_N' = V_N - 0.25\ U_N$

U_N, E_X: EASTWARD POSITIVE

$\mathbf{V}_N, E_Y$: NORTHWARD POSITIVE

U, V = M/SEC E: MV/M

Figure 12.

MILLSTONE HILL 30 MAY '84

— 0.5 HOUR AVERAGE
--- SMOOTHED DRIFTS

NEUTRAL WINDS
$V' = V - 0.25U$

ELECTRIC FIELD (EAST)

ELECTRIC FIELD (NORTH)
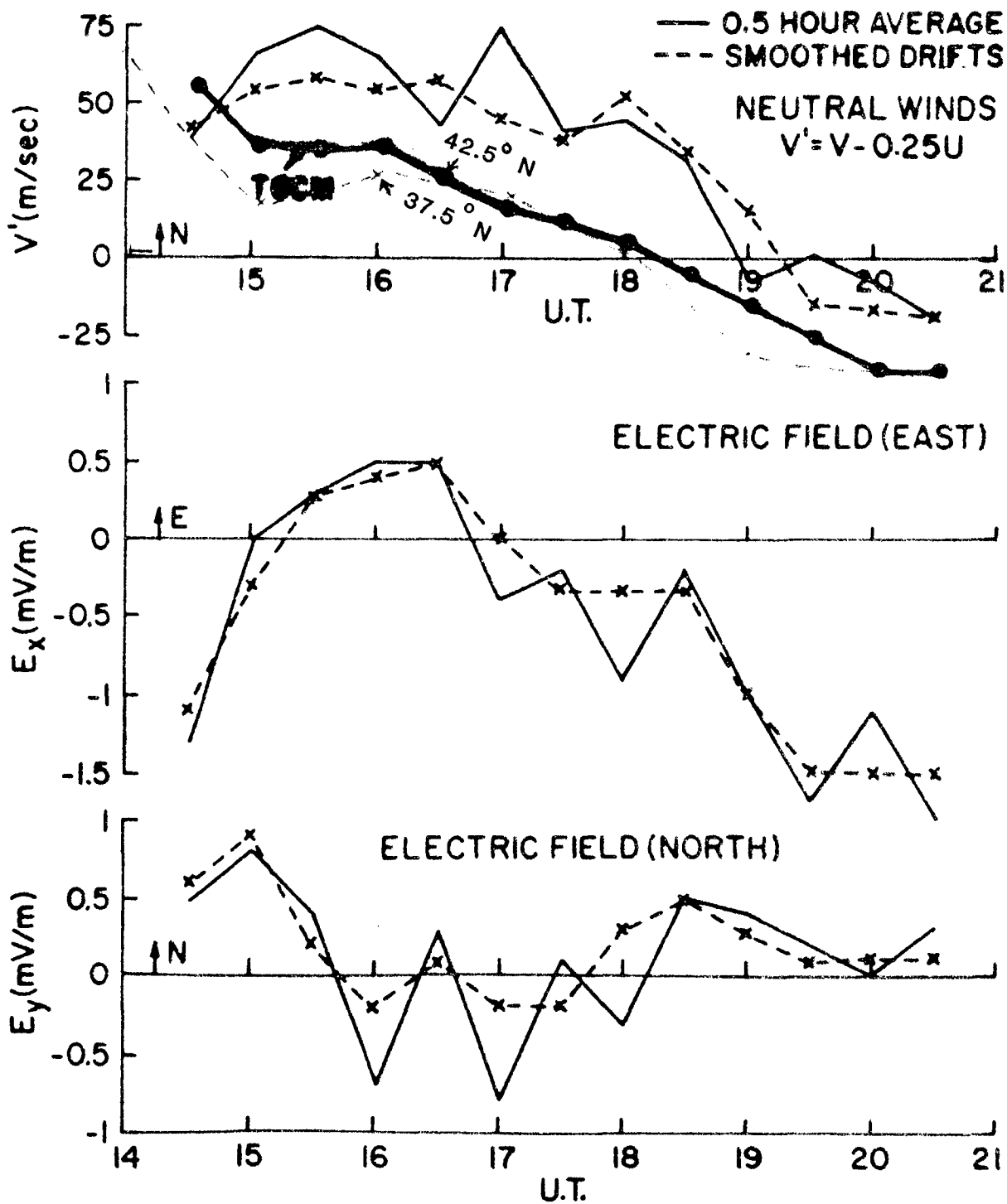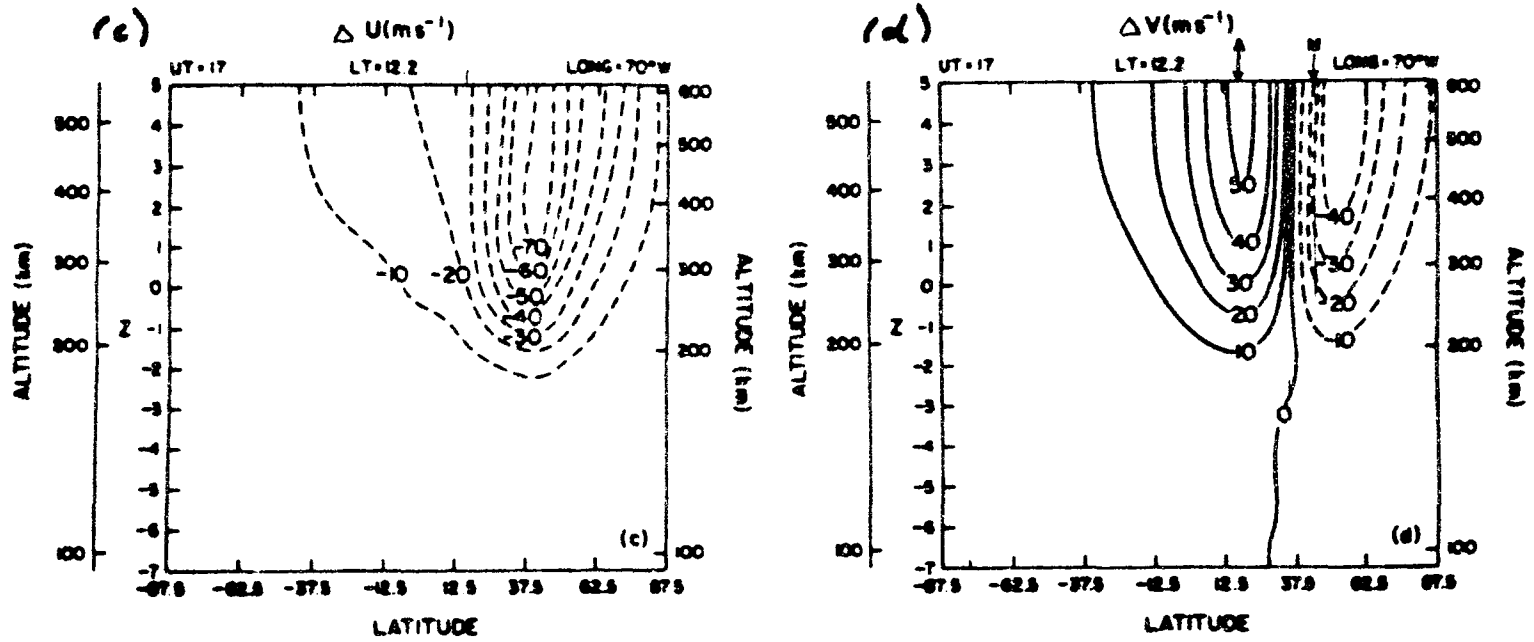
Figure 13.

Figure 14. NCAR TGCM predictions of Neutral Wind Perturbations for Eclipse - 17 U.T.
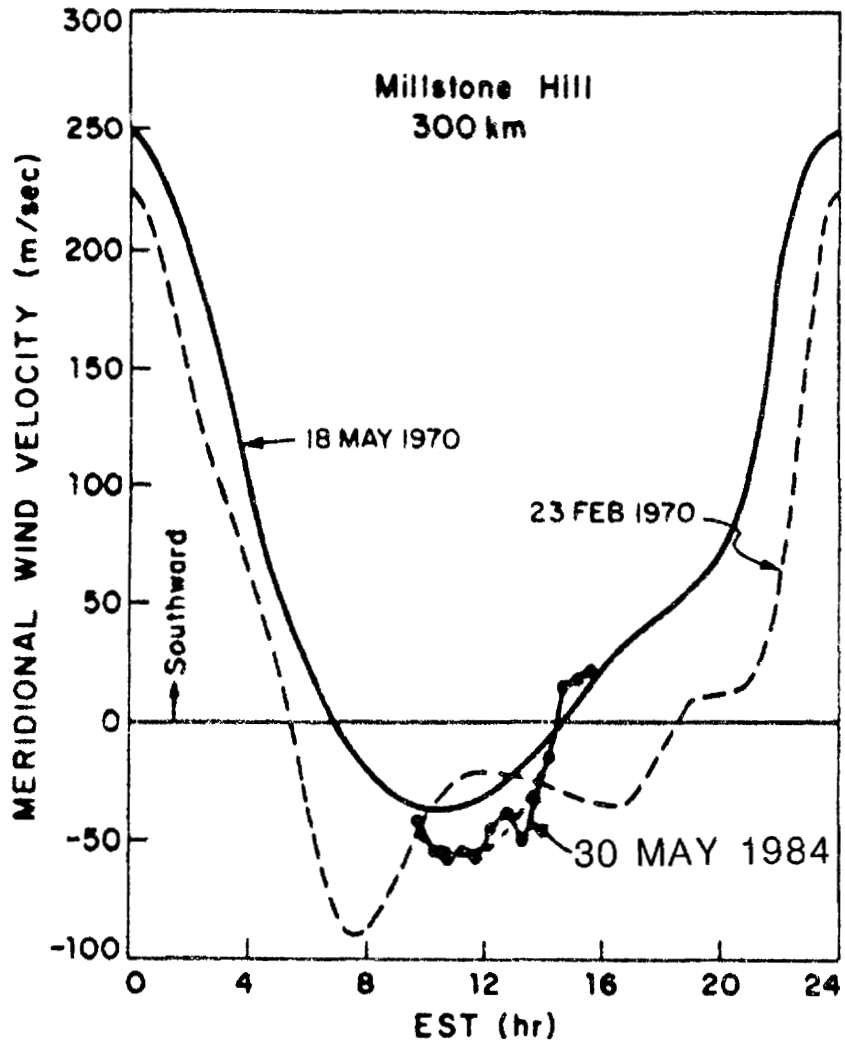
Figure 15.
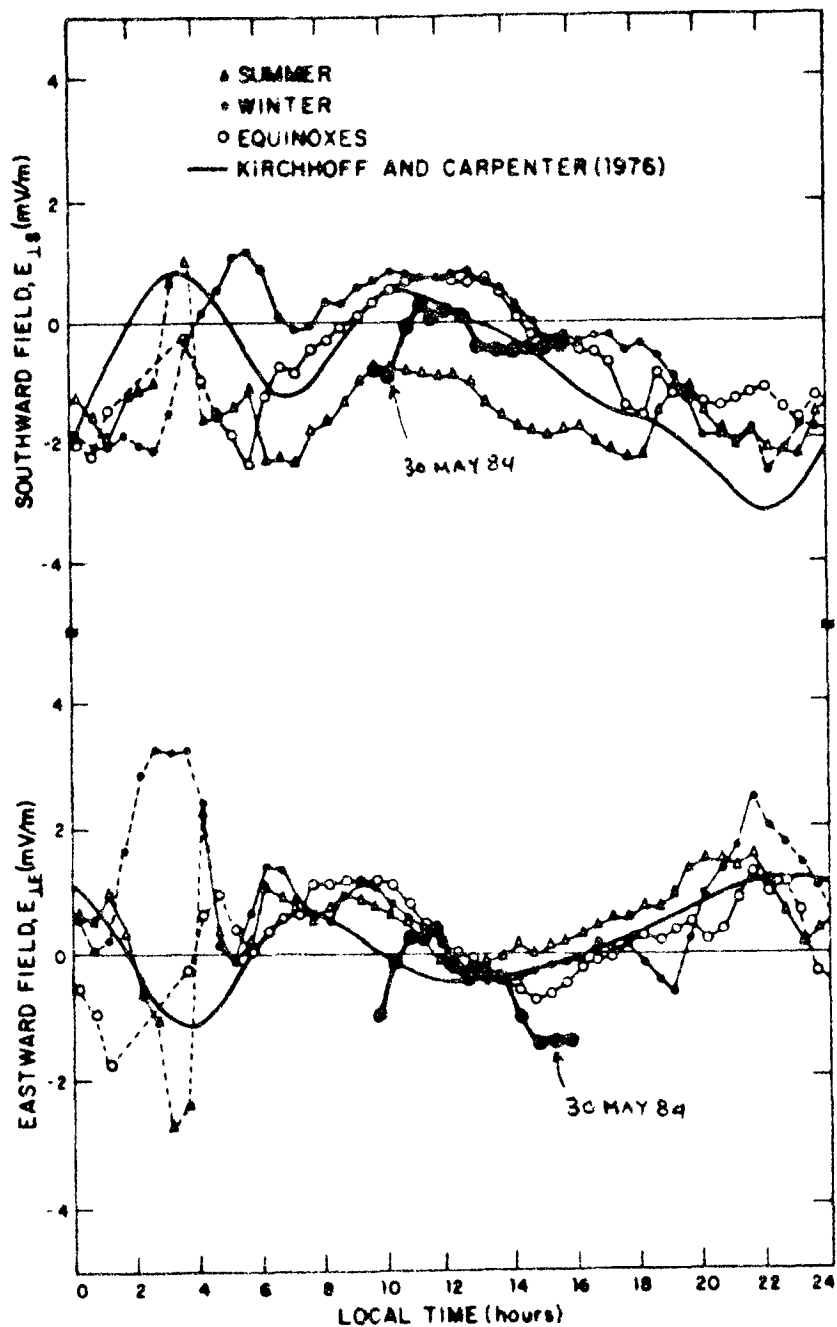
Figure 16.

		NCAR TGCM	MILLSTONE HILL
$\dfrac{\Delta N_E}{N_E}$	130 KM	61%	55%
	200 KM	68%	62%
	300 KM	56%	14%
$\dfrac{\Delta T_E}{T_E}$	130 KM	2%	12%
	200 KM	22%	34%
	300 KM	26%	29%
$\dfrac{\Delta T_\infty}{T_\infty}$		~5%	~4%
V-0.25U	300 KM 17 UT	+ 20 M/SEC (N) (42.6°N)	+45 M/SEC (N) (42.6-35°N)
	E-FIELD		< 1MV/M EASTWARD 15-17 UT SOUTHWARD 16-18 UT

Figure 17.
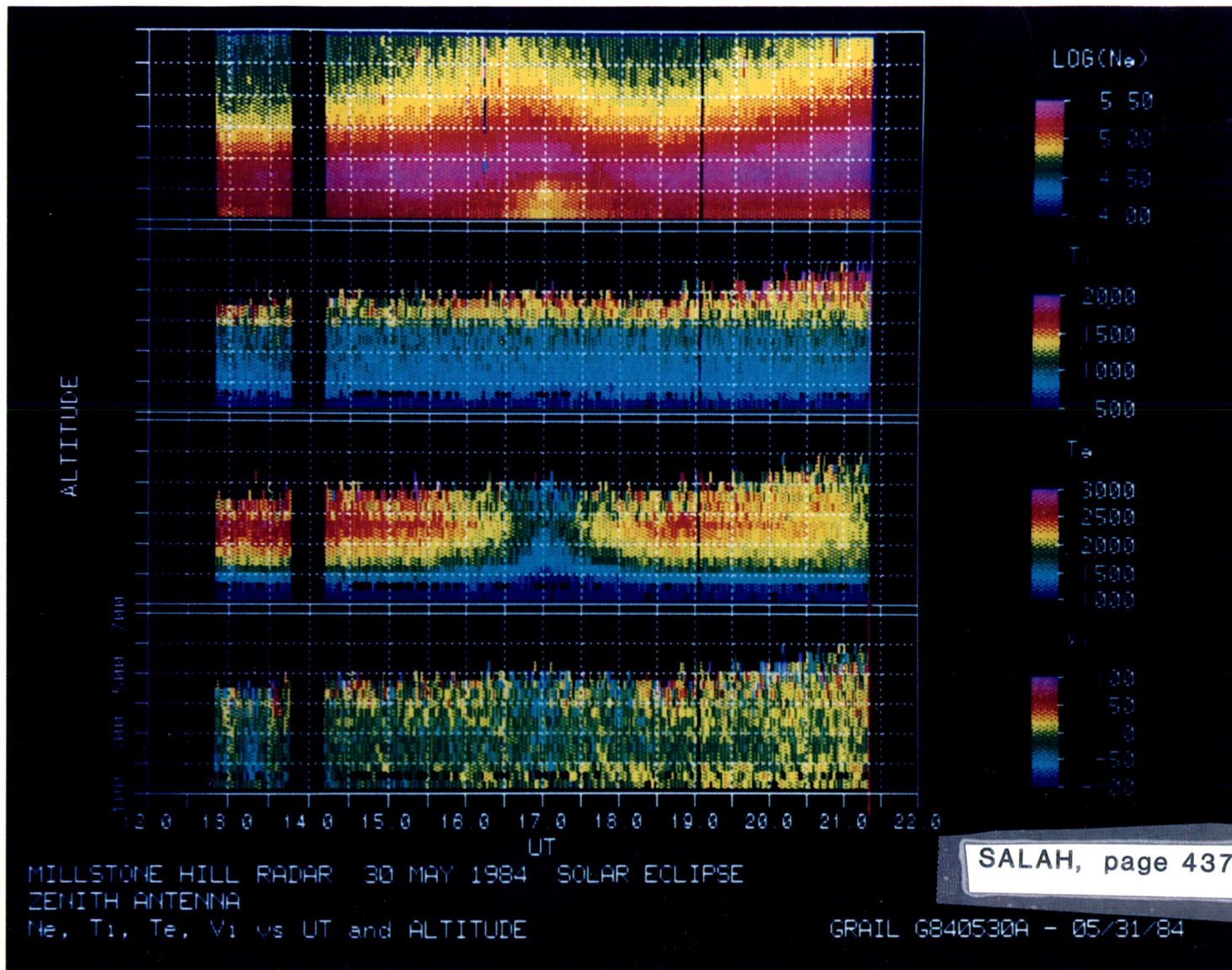
Figure 18.
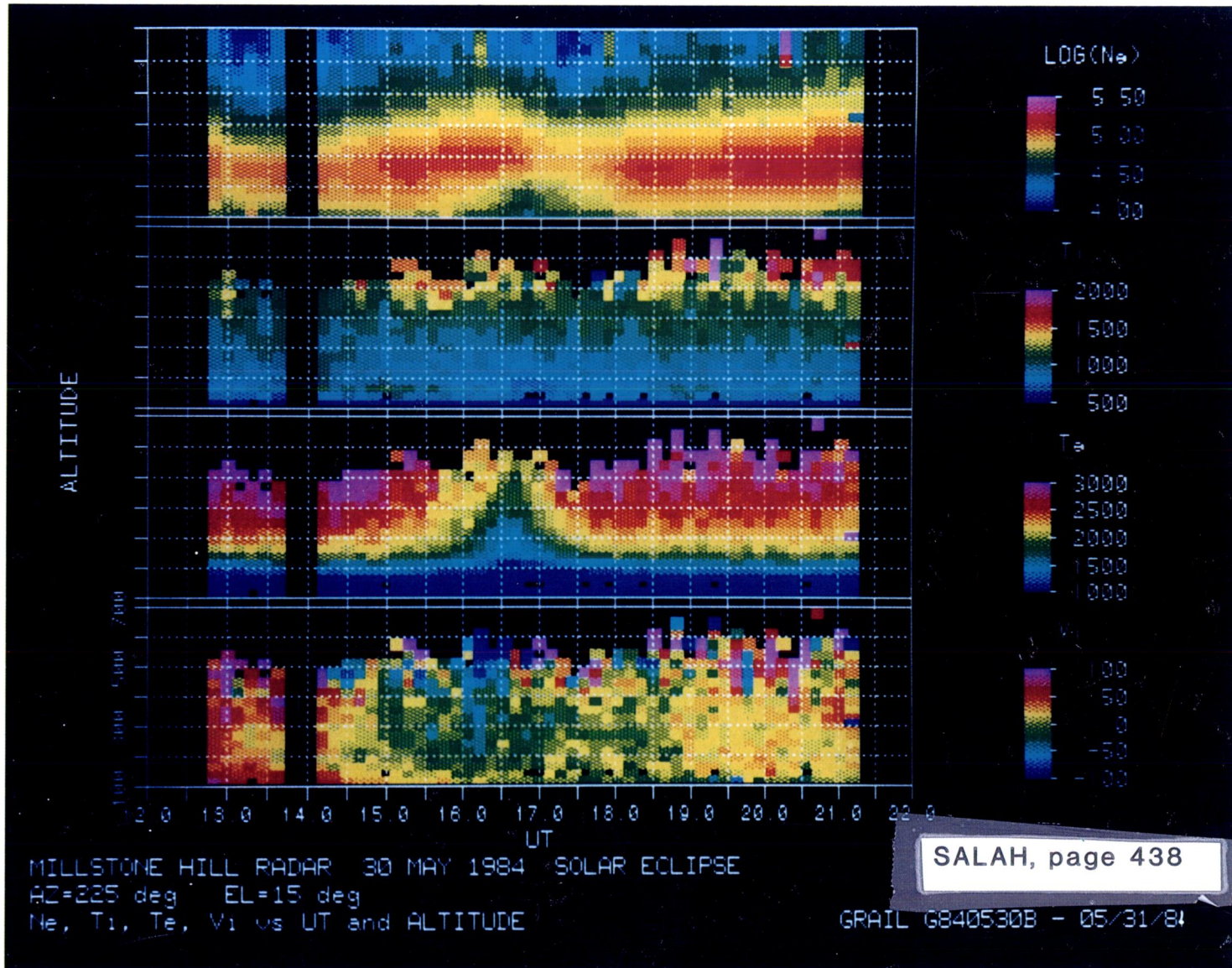
Figure 19.

A DYNAMO THEORY PREDICTION FOR SOLAR CYCLE 22: SUNSPOT NUMBER, RADIO FLUX, EXOSPHERIC TEMPERATURE, AND TOTAL DENSITY AT 400 KM

K. H. Schatten and A. E. Hedin
Laboratory for Atmospheres
NASA/Goddard Space Flight Center
Greenbelt, MD 20771

Using the "dynamo theory" method to predict solar activity, a value for the smoothed sunspot number of 109 ± 20 is obtained for solar cycle 22. The predicted cycle is expected to peak near December, 1990 ± 1 year. Concommitantly, $F_{10.7}$ radio flux is expected to reach a smoothed value of 158 ± 18 flux units. Global mean exospheric temperature is expected to reach 1060 ± 50K and global total average total thermospheric density at 400 km is expected to reach 4.3×10^{-15} gm cm^{-3} ± 25%.
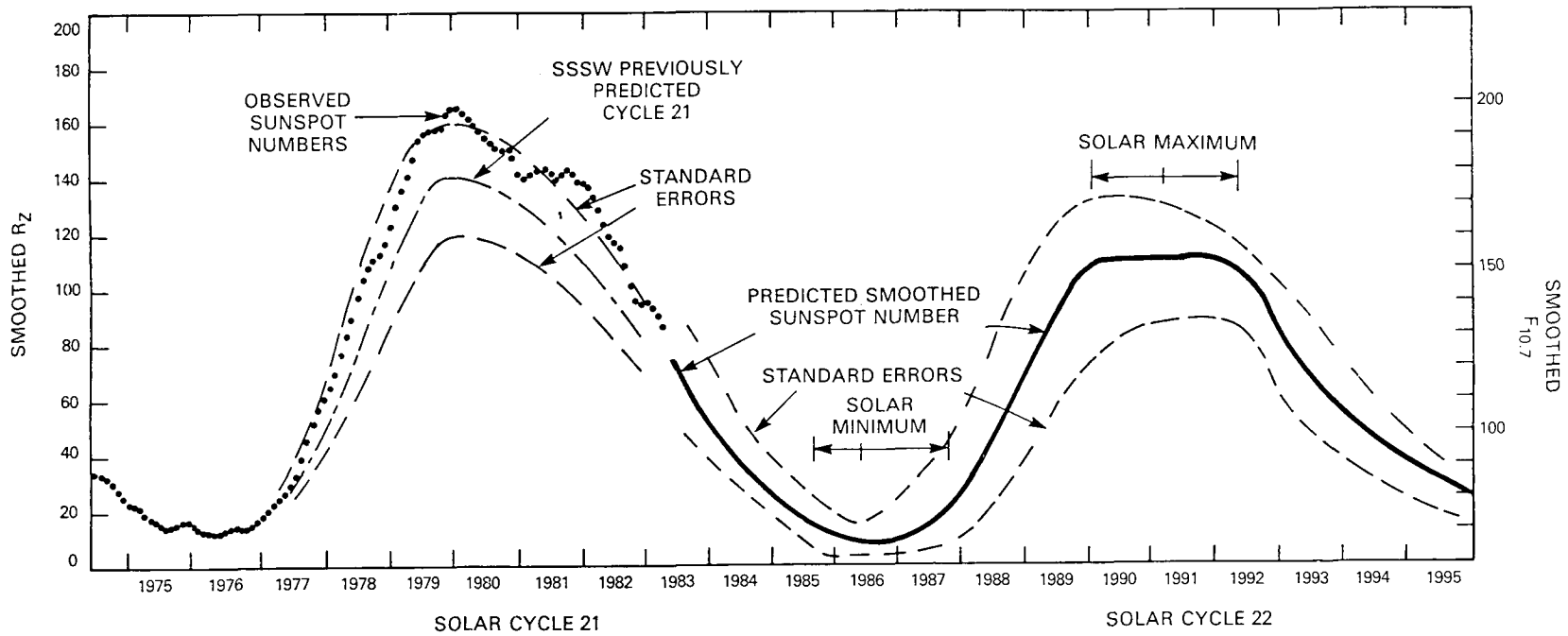
Figure 1. Predicted smoothed sunspot number and radio flux from 1984 to 1995 (solid curve). Estimated early average uncertainties (dashed curves) are smaller than in many other predictions. The previous prediction for solar cycle 21 (shown) compares well with the observed sunspot numbers (dots).
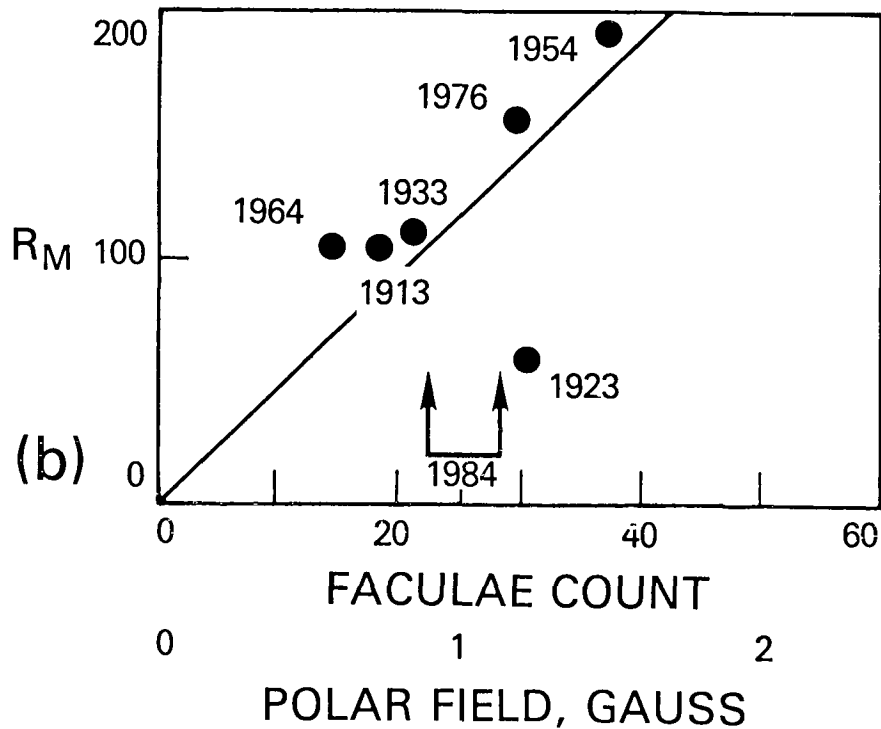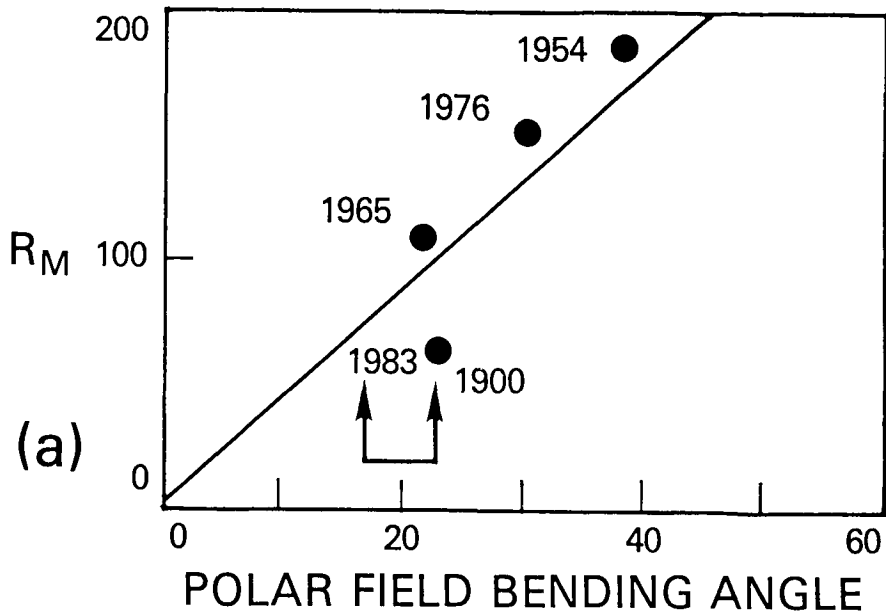
Figure 2. Smoothed maximum sunspot numbers versus polar field bending angle (a) and field strength and faculae count (b) at or near the previous sunspot minimum. The dots are labeled by the year that the polar field value was obtained. The arrows show the 1983 (top) value for the polar field bending and the 1984 (bottom) polar field strength.
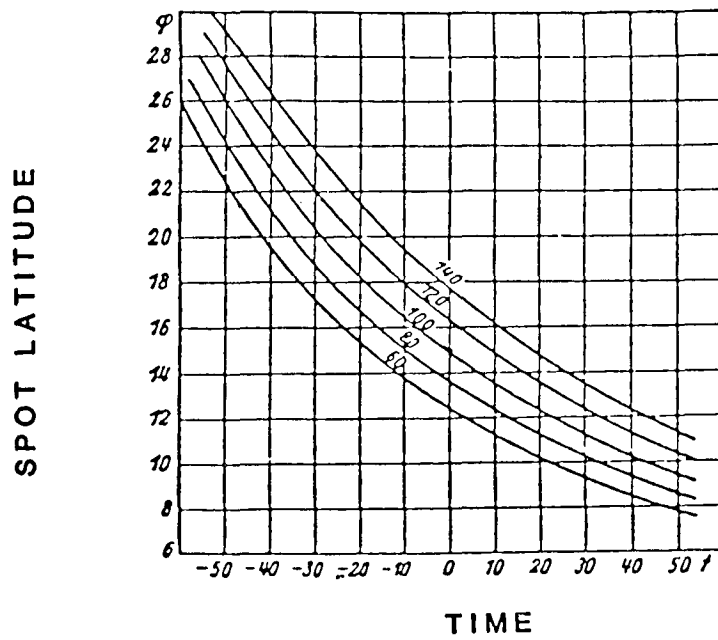
Figure 3. Migration of spot zone for different R_m (heights of sunspot maximum). *Abcissae:* time measured in solar rotation from sunspot maximum; *ordinates:* latitude (Waldmeier, 1939).
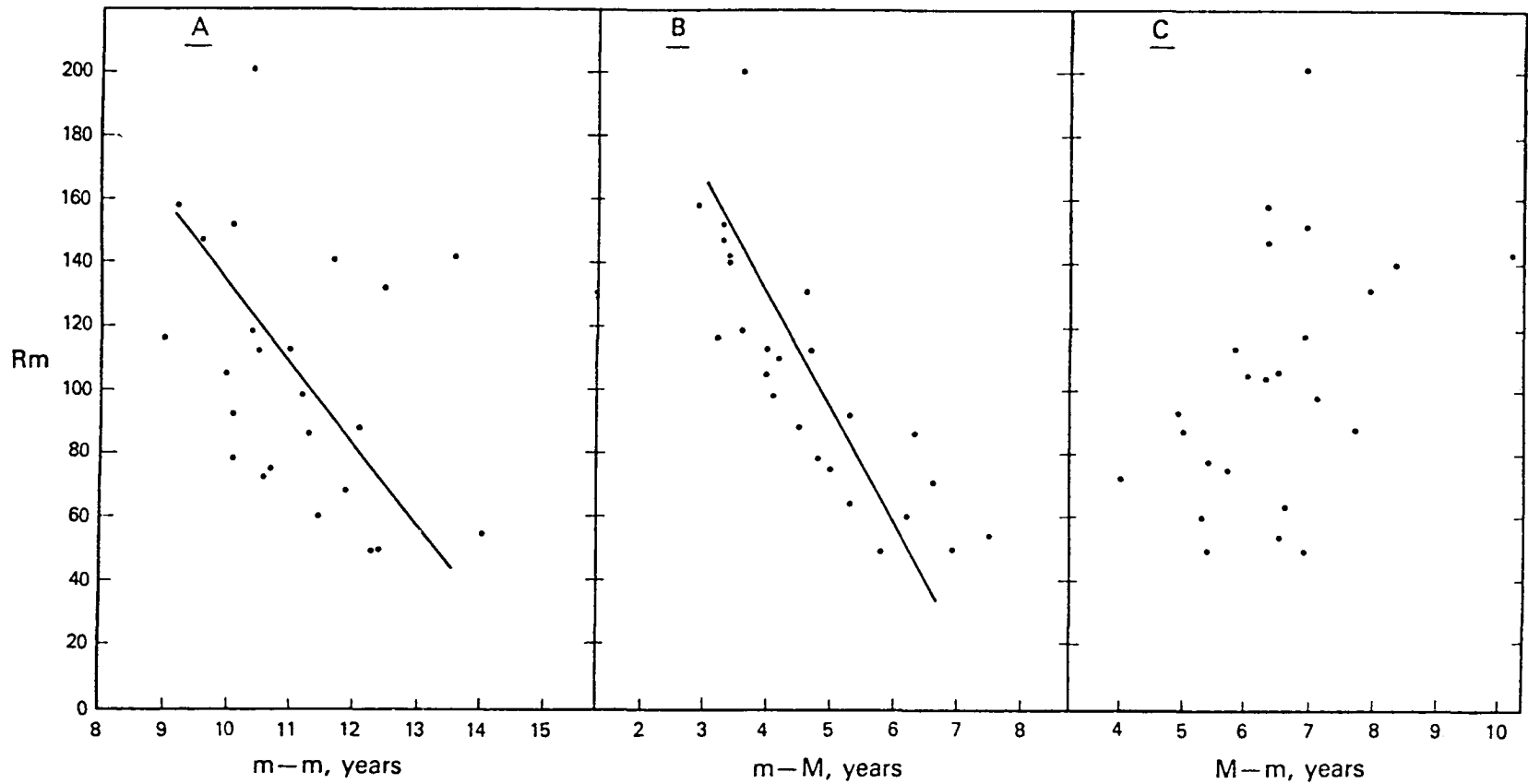
Figure 4(a). Left-The solar activity minimum to minimum duration (m-m), is graphed vs. solar maximum sunspot number. (b) Middle-The rising portion of the cycles' duration (m-M) is graphed. (c) Right-The trailing end of the sunspot cycles' duration (M-m).
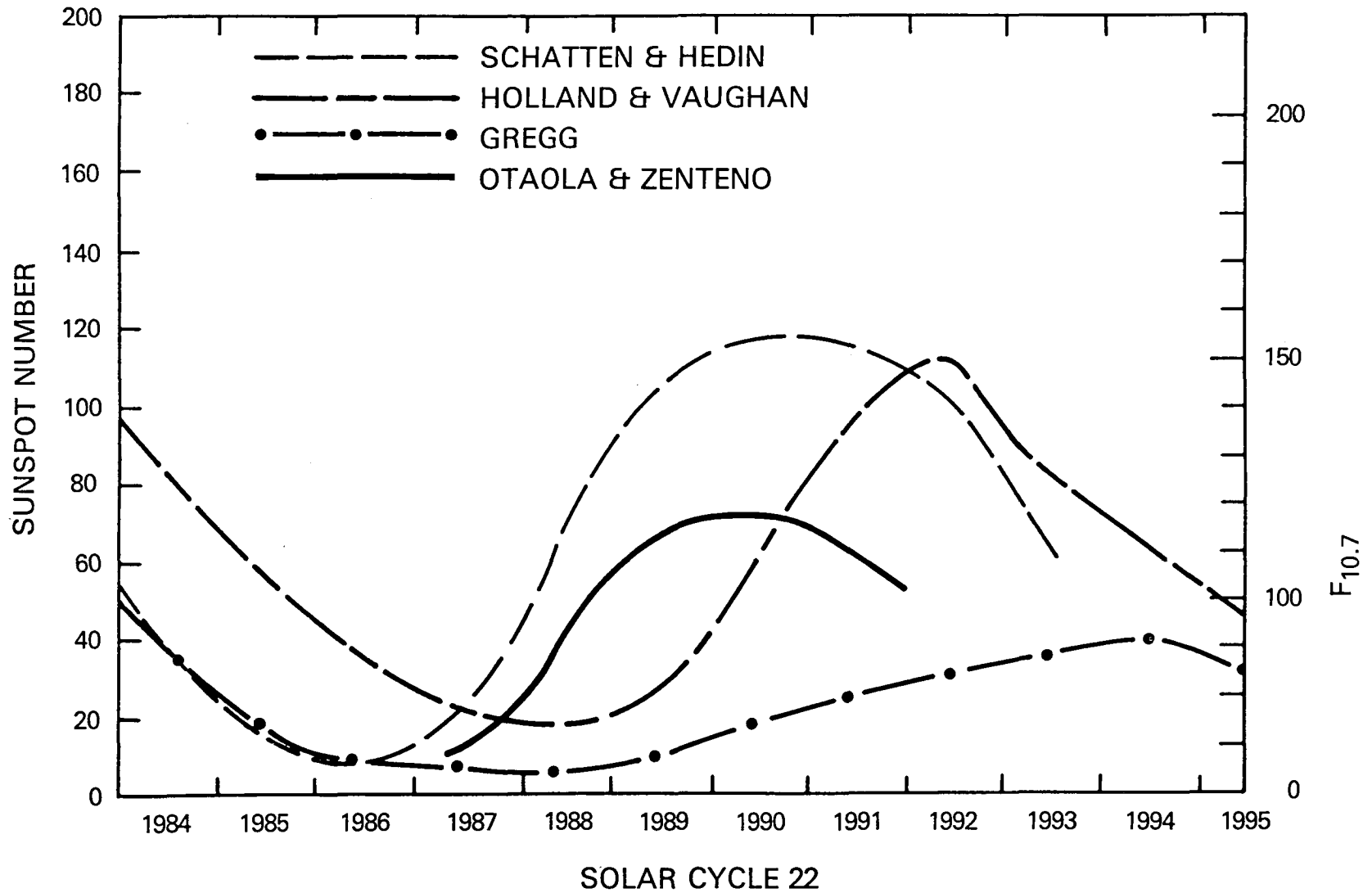
Figure 5. Shown are the predicted sunspot numbers from 1984 to 1995 with various authors' methods.

A THREE DIMENSIONAL MODEL OF THE VENUSIAN
THERMOSPHERE WITH SUPERROTATION

D. R. Stevens-Rayburn
Applied Research Corporation
Landover, Md. 20785

H. G. Mayr and I. Harris
Planetary Atmospheres Branch
Goddard Space Flight Center
Greenbelt, Md. 20771

An improved three-dimensional spectral model of the thermosphere of Venus is described. The model solves the Navier-Stokes equations and includes nonlinear effects for an arbitrary number of atmospheric species. A two-dimensional axisymmetric model of the superrotation of the thermosphere is also presented. This model addresses the Pioneer-Venus mission finding, which suggested the thermospheric rotation rate to be much higher than that of the planet as seen from the asymmetric distribution of hydrogen and helium. Both models include the effects of an anisotropic eddy diffusion that is consistent with atmospheric mixing length theory.
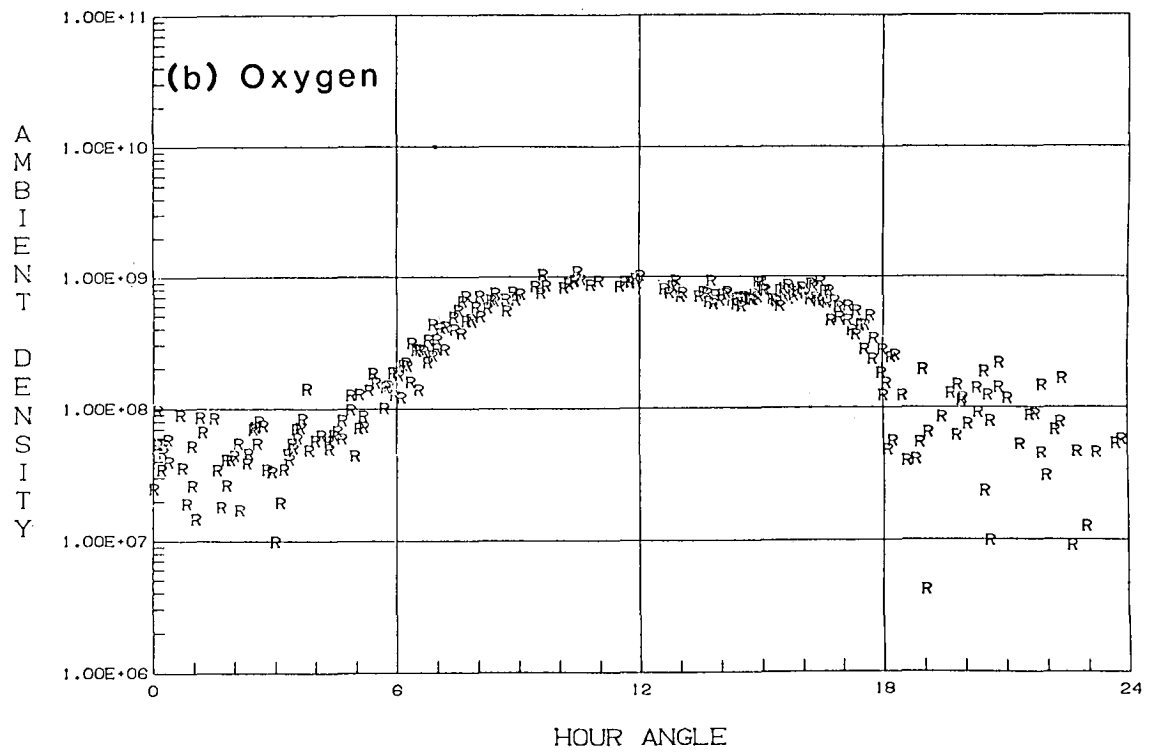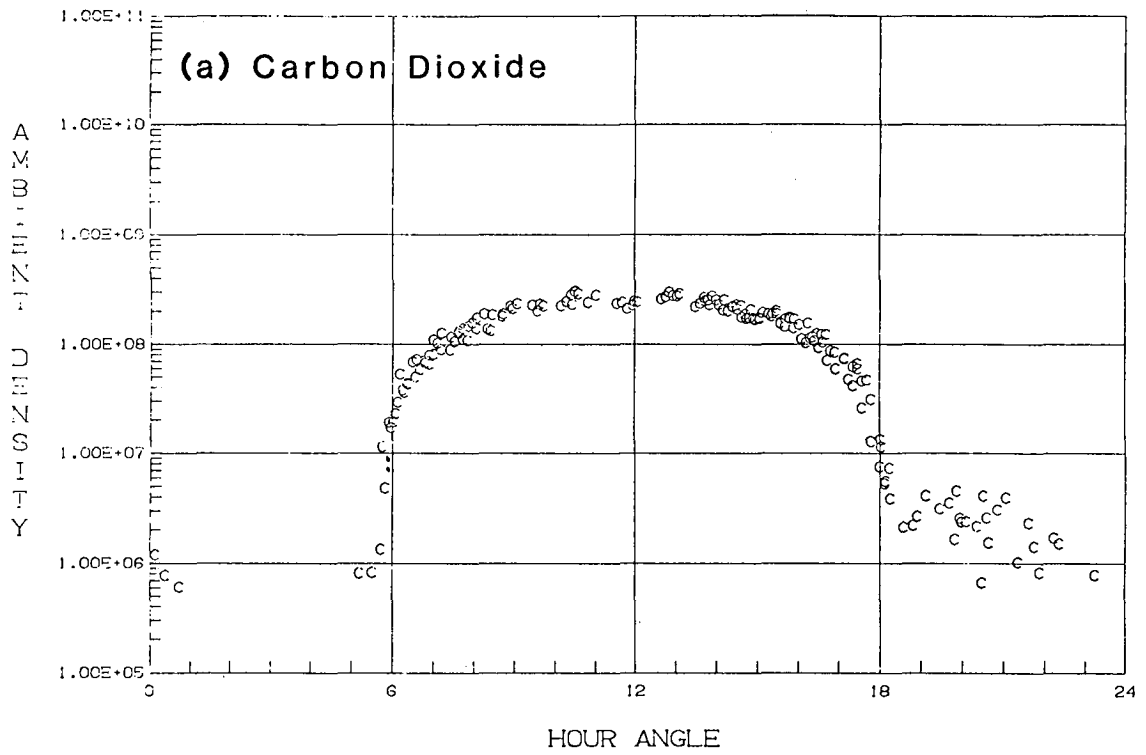
Figure 1. Pioneer Venus density profiles for carbon dioxide and oxygen (W. T. Kasprzak and A. E. Hedin, private communication).

446
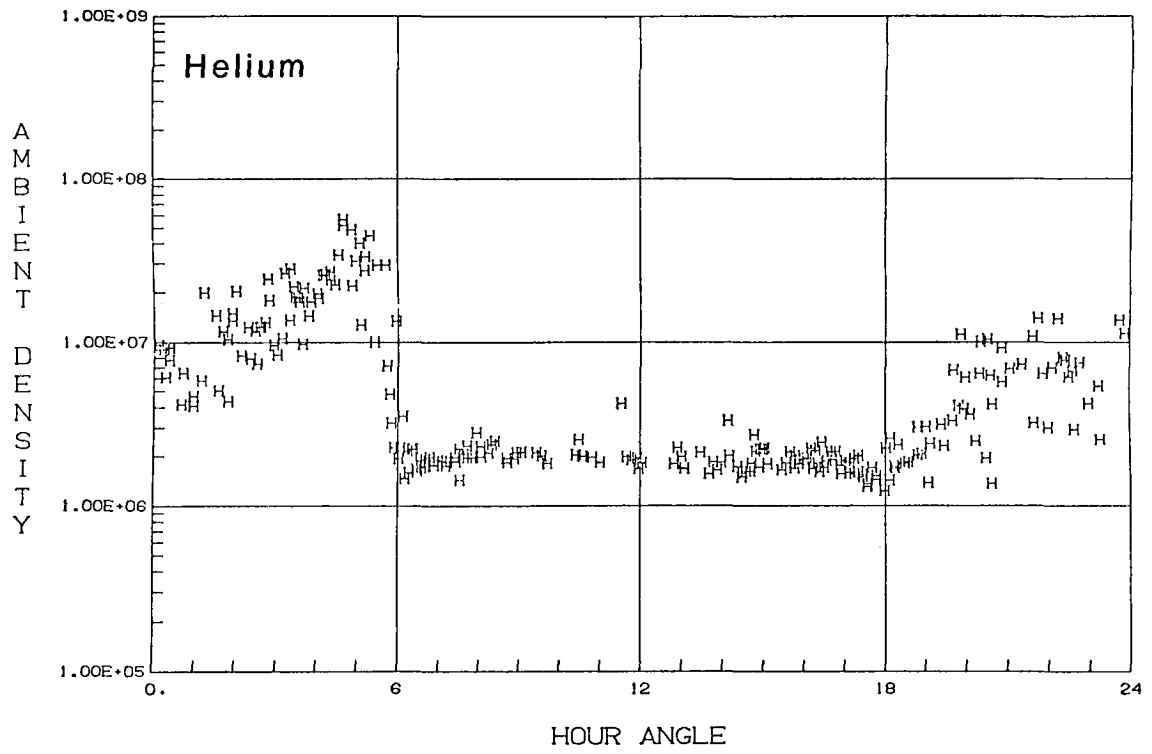
Figure 2. Pioneer Venus density profile for helium (ibid.).

EQUATORIAL CROSS-SECTION

Altitude   170 km.
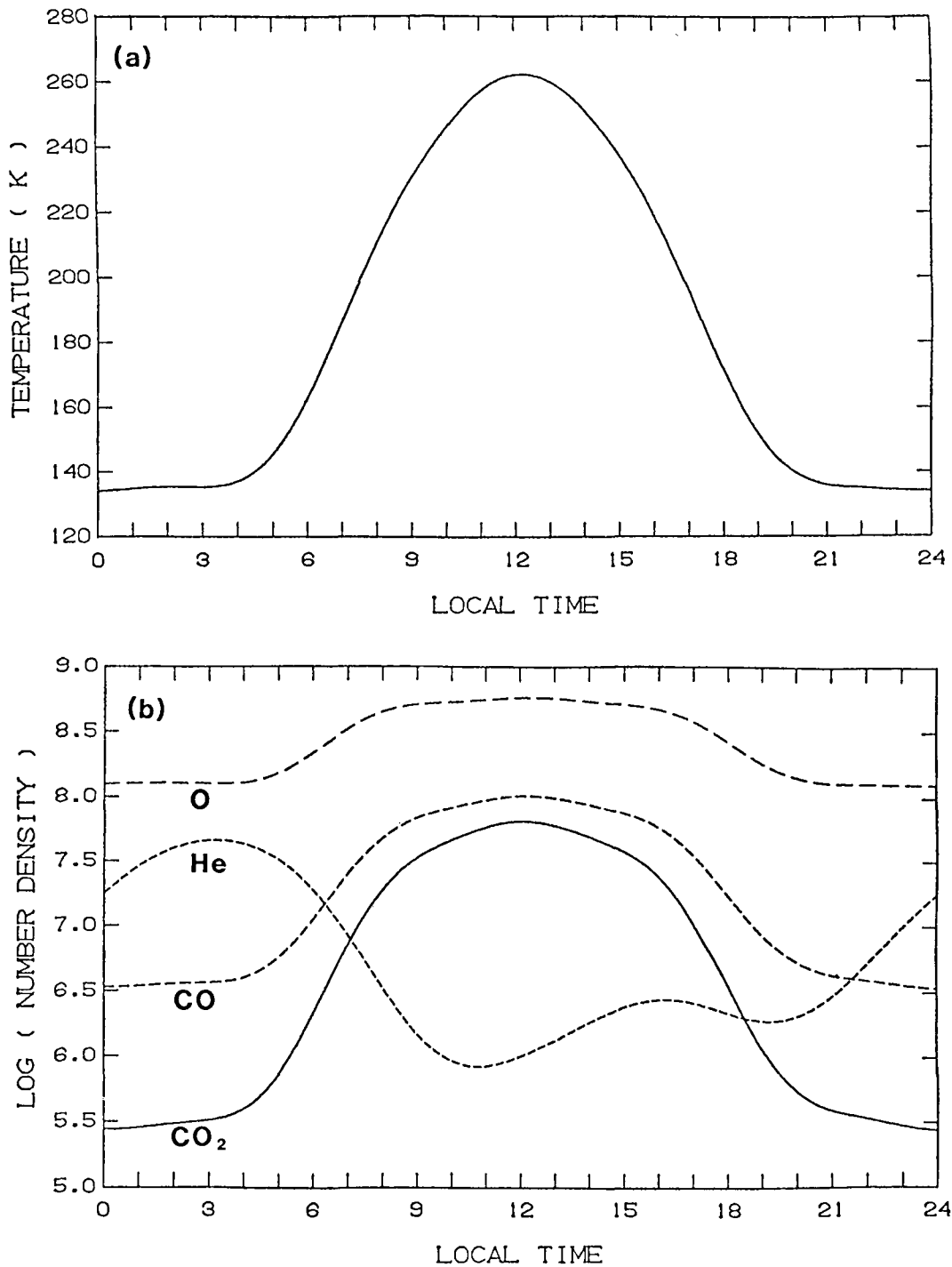
Figure 3. Thermospheric dynamics model results:
(a) Equatorial cross-section of temperature versus local time at 170 km.
(b) Equatorial cross-section of densities versus local time at 170 km.

Altitude 170 km.

(a) HORIZONTAL WIND VELOCITY VECTOR MAP

SPECIES   OXYGEN

VELOCITY SCALE (100 M/S)   →

(b)   VERTICAL VELOCITY (CM / S)

Figure 4. Thermospheric dynamics model results:
(a) Horizontal wind velocity vector map at 170 km.
(b) Contour map of vertical velocity for oxygen at 170 km.

449
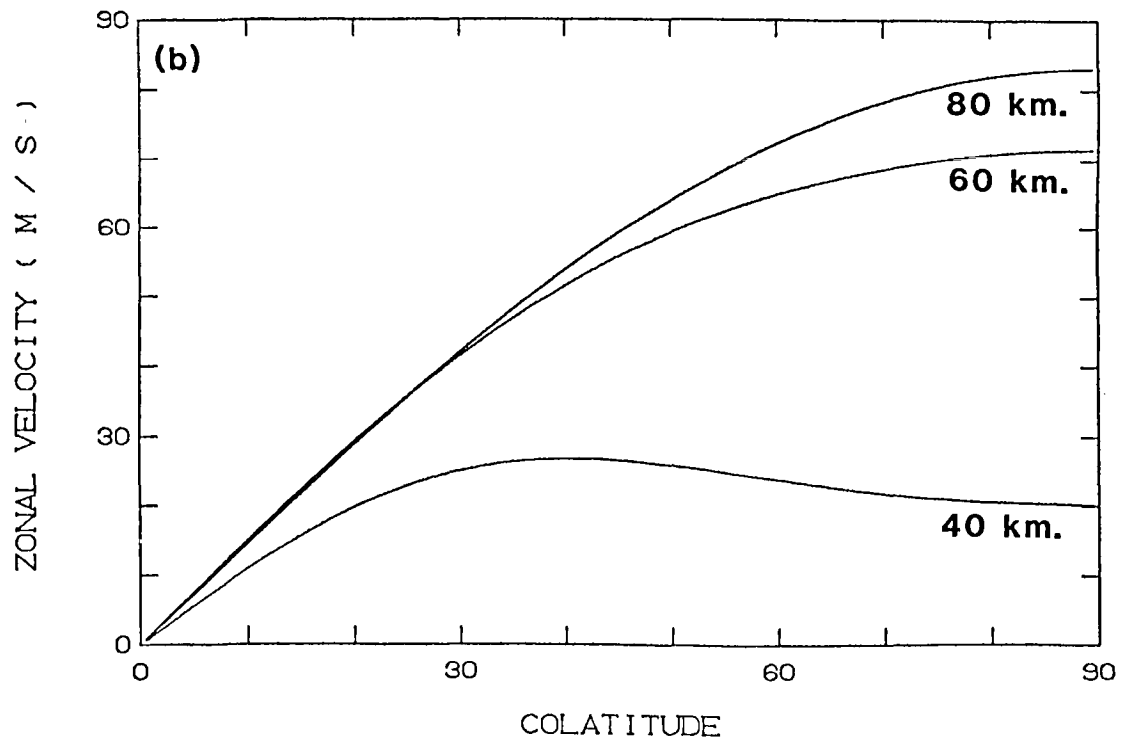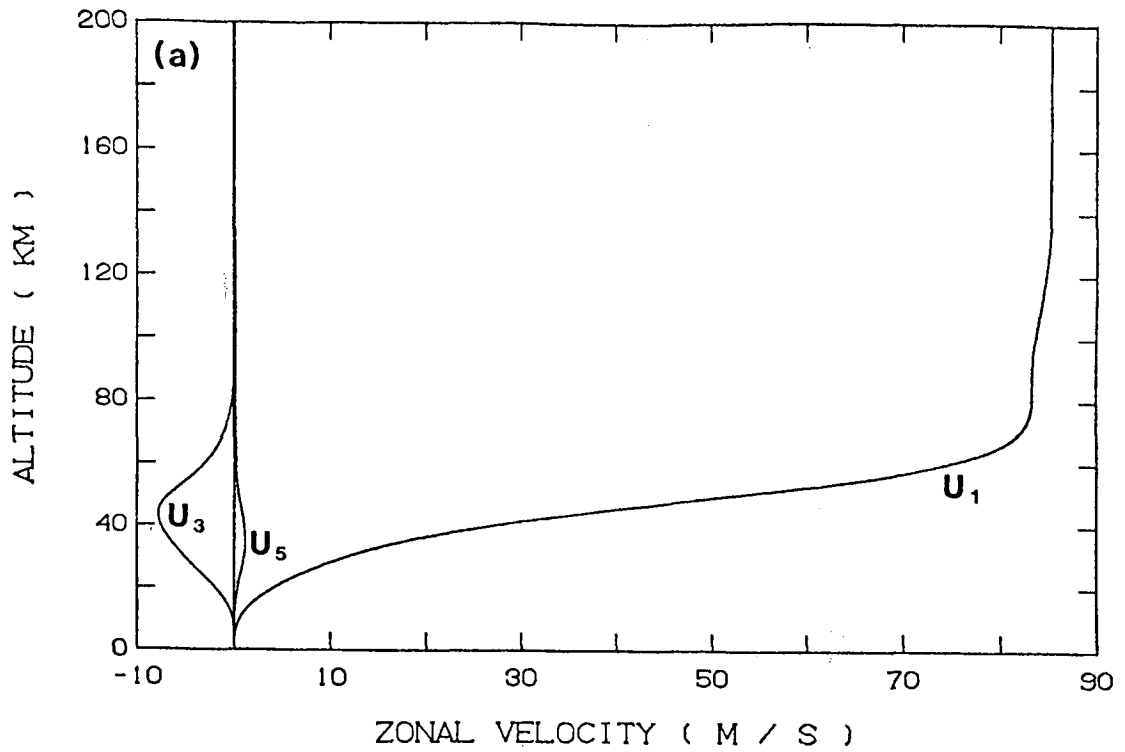
Figure 5. Superrotation model results:
(a) Zonal velocity components versus altitude.
(b) Zonal velocity versus latitude.

JOULE HEATING AND FIELD-ALIGNED CURRENTS:
PRELIMINARY RESULTS FROM DE-2

M. Sugiura
Laboratory for Extraterrestrial Physics
NASA/Goddard Space Flight Center
Greenbelt, MD 20771

There are three main processes by which energy is transferred from the magnetosphere to the thermosphere. These are, not necessarily in the order of importance: (a) charge exchange of the ring current particles; (b) precipitation of charged particles; and (c) joule dissipation by the magnetosphere-ionosphere current systems. The importance of this last process has been recognized and the rate of joule heating has been estimated by many workers (references given in Table 1).

Observations of the electric ($\underline{E}$) and magnetic ($\underline{B}$) fields from DE-2 are providing a new set of data on field-aligned currents. One of the remarkable features found in these observations is the high correlation between an orthogonal pair of the $\underline{E}$ and $\underline{B}$ field components (Siguira et al., 1982, 1984; Sugiura, 1984; general references on field-aligned currents are given in these papers). Figure 1 shows an example, where $\Delta\underline{B}$ is the perturbation magnetic field obtained by substracting a model internal field from the observed field. The north-south component of the electric field is well correlated with the east-west component of the magnetic field. The correlation is 0.94, using ½ second averages. Figure 2, which gives high-pass filtered data of the same set as Figure 1, shows that the correlation between the orthogonal $\underline{E}$ and $\underline{B}$ components is equally good for the fluctuating components; the correlation coefficient is 0.93.

Figure 3 demonstrates this reasoning. Figure 3 shows the spacecraft X, Y, and Z components of $\Delta\underline{B}$ and the spacecraft X component of $\underline{E}$ during a northern polar pass. The interplanetary magnetic field was northward ($B_z > 0$), and hence the size of the polar cap was small. Figure 4 shows how the angle, α, between the orbit plane and the dipole meridian plane changes along the pass; the definition of the angle α is illustrated in Figure 5. The interval between 1417 and 1423 UT was further divided into 1-minute intervals and the correlation coefficient between ΔB_z and E_x was calculated for each of these 1-minute intervals. The results are shown in Table 2. We conclude that the proportionality between the orthogonal $\underline{B}$ and $\underline{E}$ components is invariant with respect to rotation of the coordinate system. Hence the missing E_z must be proportional to ΔB_x to the same extent that E_x is correlated to ΔB_z.
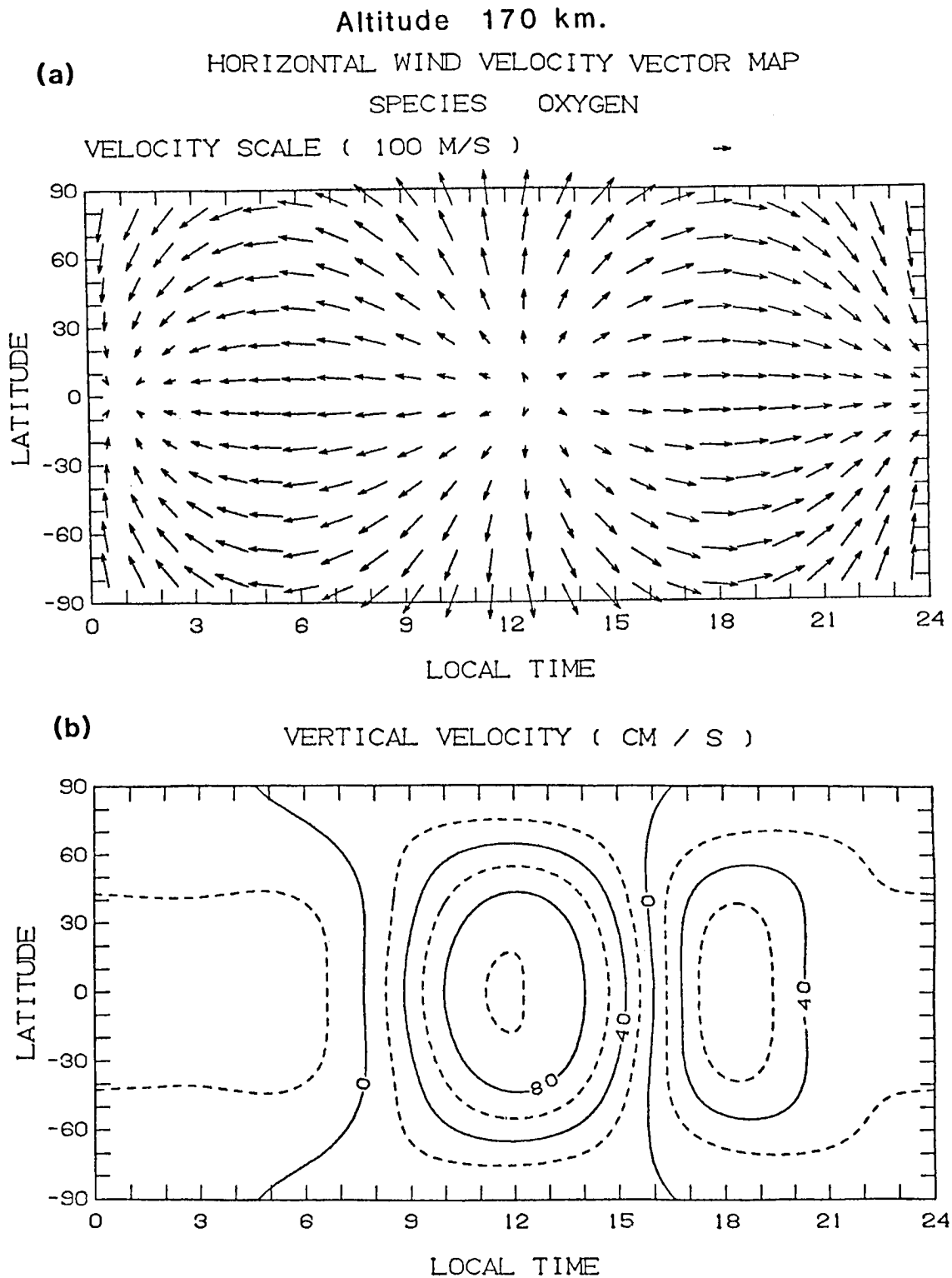
Comparing ΔB_z with E_x for the evening auroral oval pass in Figure 3, ΔB_z changes are very small, but are correlated with E_x as seen in the correlation coefficient, r, for intervals D and E. The ΔB_z amplitudes are small in these intervals because the ionosphere was not illuminated and hence the conductivity was low. The precipitating electrons did not have energies large enough to produce appreciable ionization in the E region of the ionosphere (according to the LAPI plasma observations); hence field-aligned currents could now flow, and the electric field was large, being not short-circuited. The solar elevation angle along the pass is indicated in Figure 3.

Figure 6 shows a pass on the following day when IMF B_z became southward. Now the size of the polar cap has expanded, and there are appreciable field-aligned currents in the auroral oval in darkness (near midnight) because of enough ionization from auroral electrons. Note the good correlation in interval C where α changed rapidly.

From the DE-2 observations of $\underline{E}$ and $\Delta\underline{B}$, we conclude that the electric field and the perturbation magnetic field are orthogonal and that their magnitudes are proportional. Their directional relation is such that $\underline{E} \times \Delta\underline{B}$ is downward. This relation between $\underline{E}$ and $\Delta\underline{B}$ is frequently observed, especially on the dayside.

It can be shown that when the above relation between the electric and magnetic fields holds, the following equations constitute a particular solution of the current continuity equation.

$$\Sigma_p - k/\mu_o = 0 \tag{1}$$

$$\nabla \cdot \underline{J}_H = 0 \tag{2}$$

where Σ_p is the ionospheric Pedersen conductance, k the constant of proportionality between the orthogonal perturbation magnetic field and electric field components, μ_o the permeability of free space, and $\underline{J}_H$ the height-integrated Hall current. If (1) holds, then with the proportionality between the electric and perturbation magnetic fields, we obtain a relation that the vertical component of Poynting's vector equals joule dissipation, namely that the vertically downward energy flow equals joule dissipation; that is, the divergence of the horizontal energy flux is zero. The energy flux from below the ionosphere is expected to be negligible because the perturbation magnetic vector is parallel to the electric field; this is because the magnetic field below the ionisphere is mainly from the Hall current. It seems reasonable that the divergence of the Hall current is zero to the same extent as the plasma convection flow is horizontally divergence free. If this is true, then the field-aligned current sheets are parallel to the convective flow pattern or the equipotential surfaces.

If we accept the above solution, then the Polynting vector $\underline{E} \times \Delta\underline{B}/\mu_o$ provides the energy flux from the magnetosphere that is expended in the ionosphere by joule dissipation. During the magnetic storm of September 6, 1982 the peak energy flux reached 200 mW/m^2 in the cusp region. In an auroral oval pass the peak energy flux is typically a few tens of mW/m^2 under moderately dislturbed conditions.

In recent years, observational data have accrued concerning the relationship between the interplanetary magnetic field and the size of the polar cap and also about the evolution of a substorm or a magnetic storm. It is suggested that these findings be incorporated in future model calculations.

REFERENCES

Maynard, N. C., J. P. Heppner, and A. Egeland, Intense, variable electric fields at ionospheric altitudes in the high latitude regions as observed by DE-2, *Geophys. Res. Lett., 9,* 981-984, 1982.

Sugiura, M., A fundamental magnetosphere-ionosphere coupling mode involving field-aligned currents ad deduced from DE-2 observations, *Geophys. Res. Lett., 11,* 877-880, 1984.

Sugiura, M., N. C. Maynard, W. H. Farthing, J. P. Heppner, B. G. Ledley, and L. J. Cahill, Jr., Initial results on the correlation between the magnetic and electric fields observed from the DE-2 satellite in the field-aligned current regions, *Geophys. Res. Lett., 9,* 985-988, 1982.

Sugiura, M., T. Iyemori, R. A. Hoffman, N. C. Maynard, J. L. Burch, and J. D. Winningham, Relationships between field-aligned currents, electric fields, and particle precipitation as observed by Dynamics Explorer-2, in *Magnetospheric Currents,* T. A. Potemra, ed., Geophys. Monograph 28, Am. Gephys. Union, pp. 96-103, 1984.

JOULE DISSIPATION BY ELECTRIC CURRENTS

COLE	1962	Austr. J. Phys., 15, 223
	1971	Planet. Space Sci., 19, 59
	1975	J. Atmos. Terr. Phys., 37, 939
KATO	1962	Planet. Space Sci., 9, 939
REES and WALKER	1968	Annls. Geophys., 24, 193
MAYR and VOLLAND	1972	Planet. Space Sci., 20, 379
	1974	J. Atmos. Terr. Phys., 36, 2025
BATES	1973	Planet. Space Sci., 21, 2073
HAYS et al.	1973	Planet. Space Sci., 21, 559
CHANG et al.	1974	J. Atmos. Terr. Phys., 36, 889
BANKS and SIREN	1974	EOS, 56, 1157
WICKWAR et al.	1975	J. Geophys. Res., 81, 4364
RICHMOND and MATSUSHITA	1975	J. Geophys. Res., 80, 2839
TAEUSCH and HINTON	1975	J. Geophys. Res., 80, 4346
STRAUSS and SCHULTS	1976	J. Geophys. Res., 81, 5822
BANKS	1977	J. Atmos. Terr. Phys., 39, 179
BANKS et al.	1981	J. Geophys. Res., 86, 6869
THIELE et al.	1981	Planet Space Sci., 29, 455
VICKREY et al.	1982	J. Geophys. Res., 87, 5184
NISBET	1982	J. Atmos. Terr. Phys., 44, 797
KAMIDE et al.	1982	J. Geophys. Res., 87, 8228
BAUMJOHANN and KAMIDE	1984	J. Geophys. Res., 89, 383

Table 1

INTERVAL UT	ANGLE α DEGREES	MLT HRS	CORR. COEFF.	Σp MHOS
1417-1418	151-137	13.4-14.4	0.99	11.3
1418-1419	137-109	14.4-16.5	0.98	7.4
1419-1420	109-68	16.5-19.3	0.99	6.0
1420-1421	68-40	19.3-21.0	0.90	2.8
1421-1422	40-27	21.0-21.8	0.97	4.1
1422-1423	27-20	21.8-22.2	0.97	2.7

Table 2
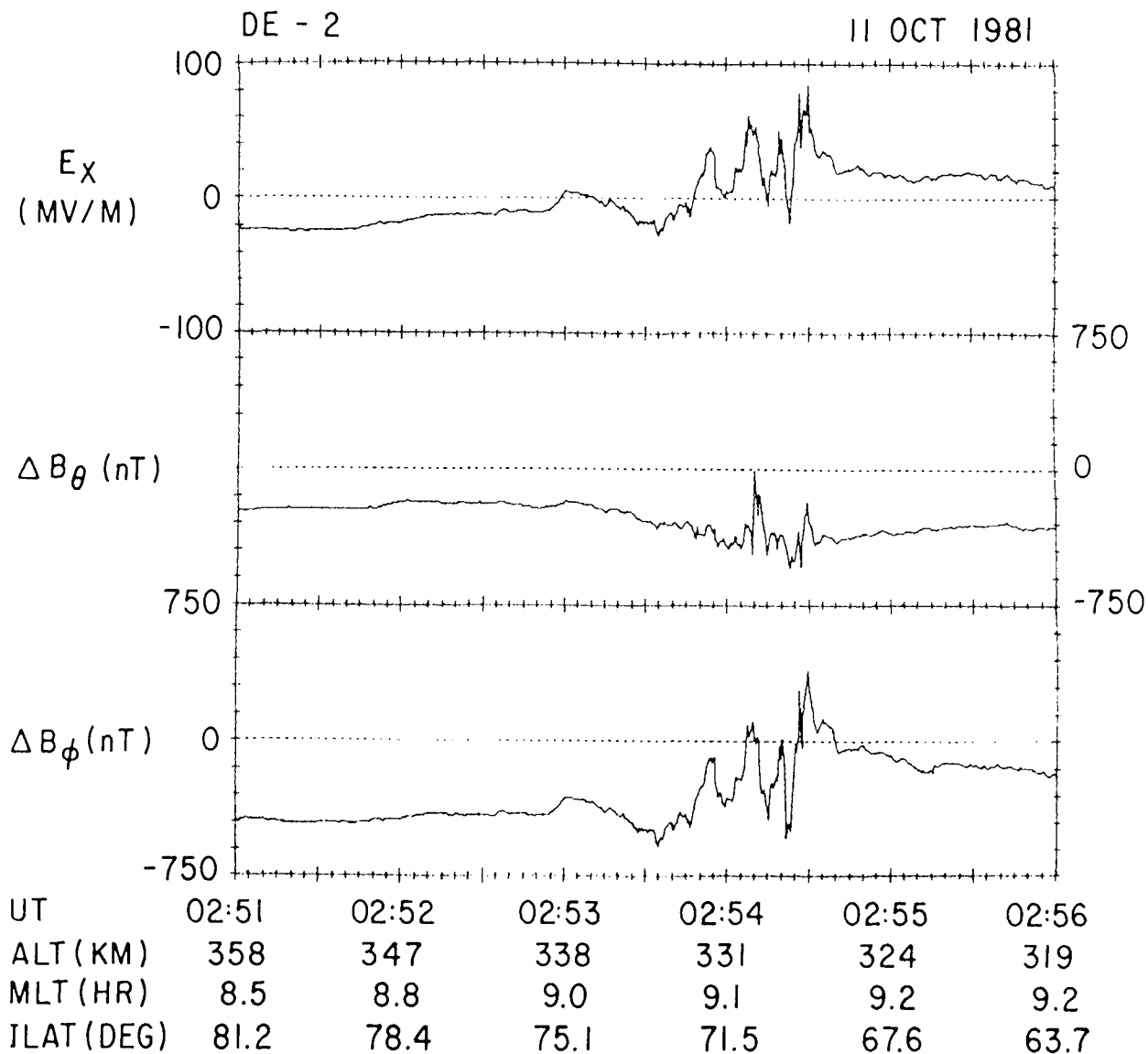
Figure 1. The north-south component of E, the north-south and east-west components (in dipole coordinates) of the peturbation B field.
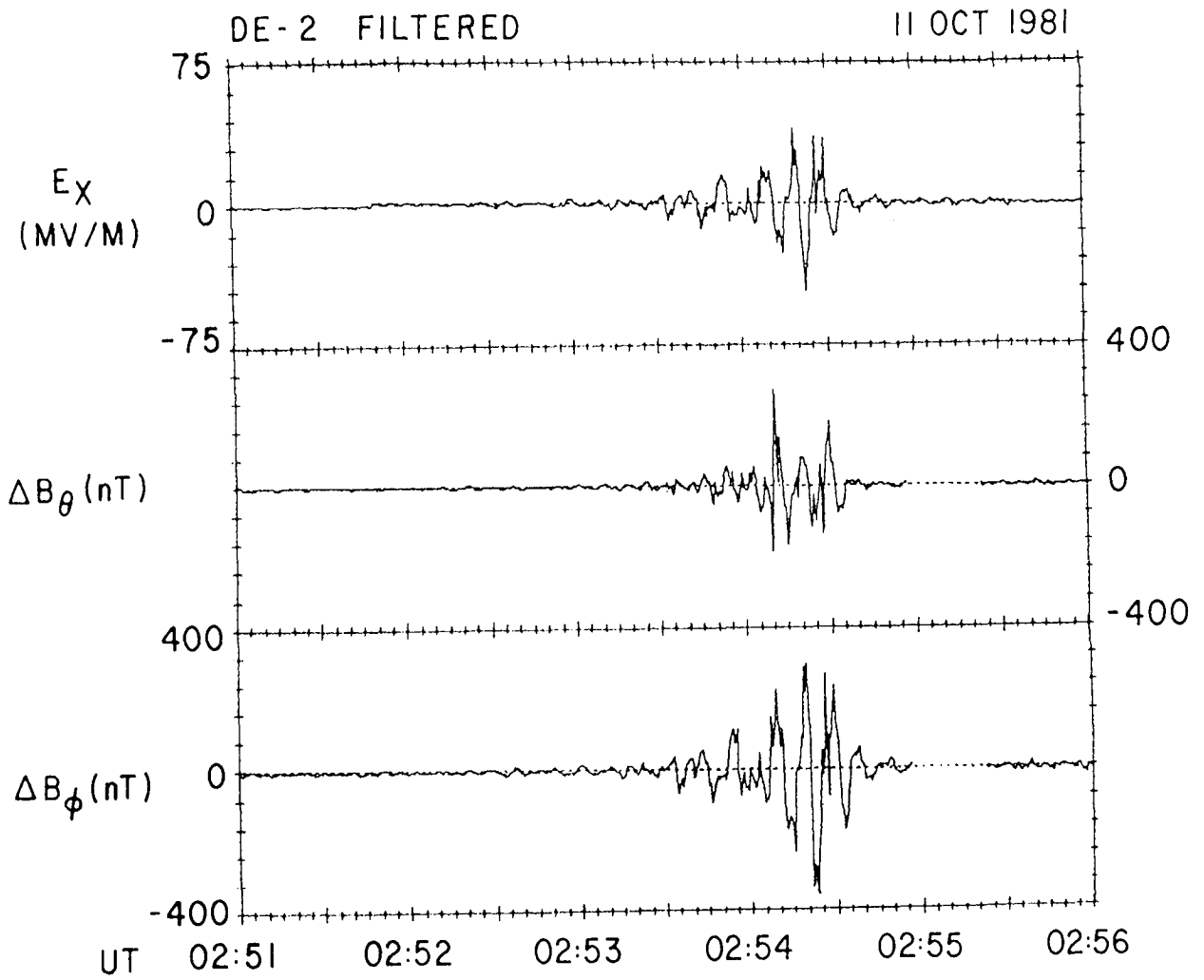
Figure 2. Data in Figure 1 were passed through a high-pass filter to extract fluctuating components. The orthogonal components of E and B are still well correlated.
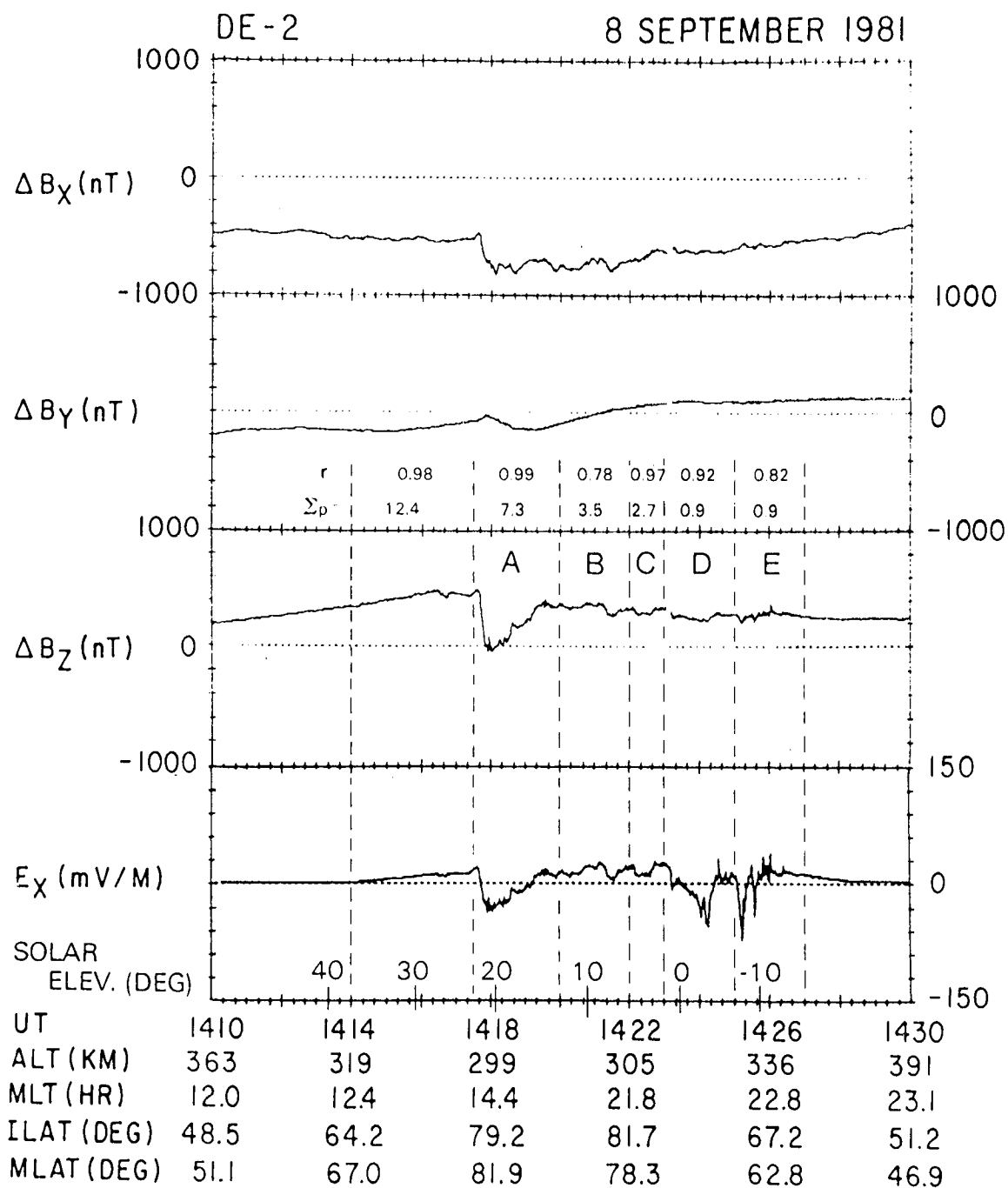
Figure 3. A northern polar pass of DE-2 on 8 September 1981 during IMF $B_z > 0$. The correlation between the orthogonal pair of B and E components (i.e., ΔB_z vs. E_x) is high even when the angle α (Fig. 4) changes rapidly as in intervals A and B.

458
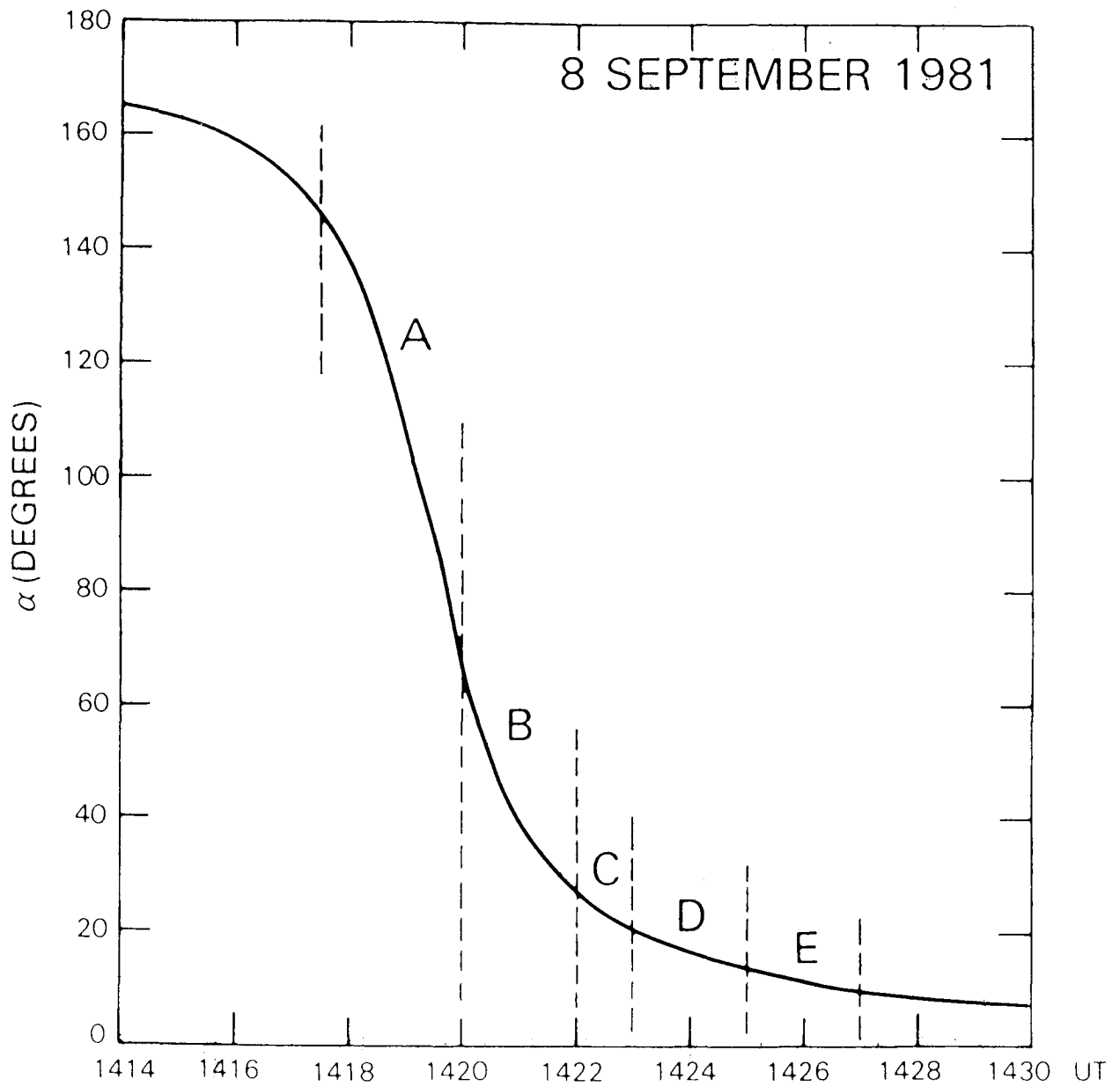
Figure 4. Angle α along the pass in Fig. 3.
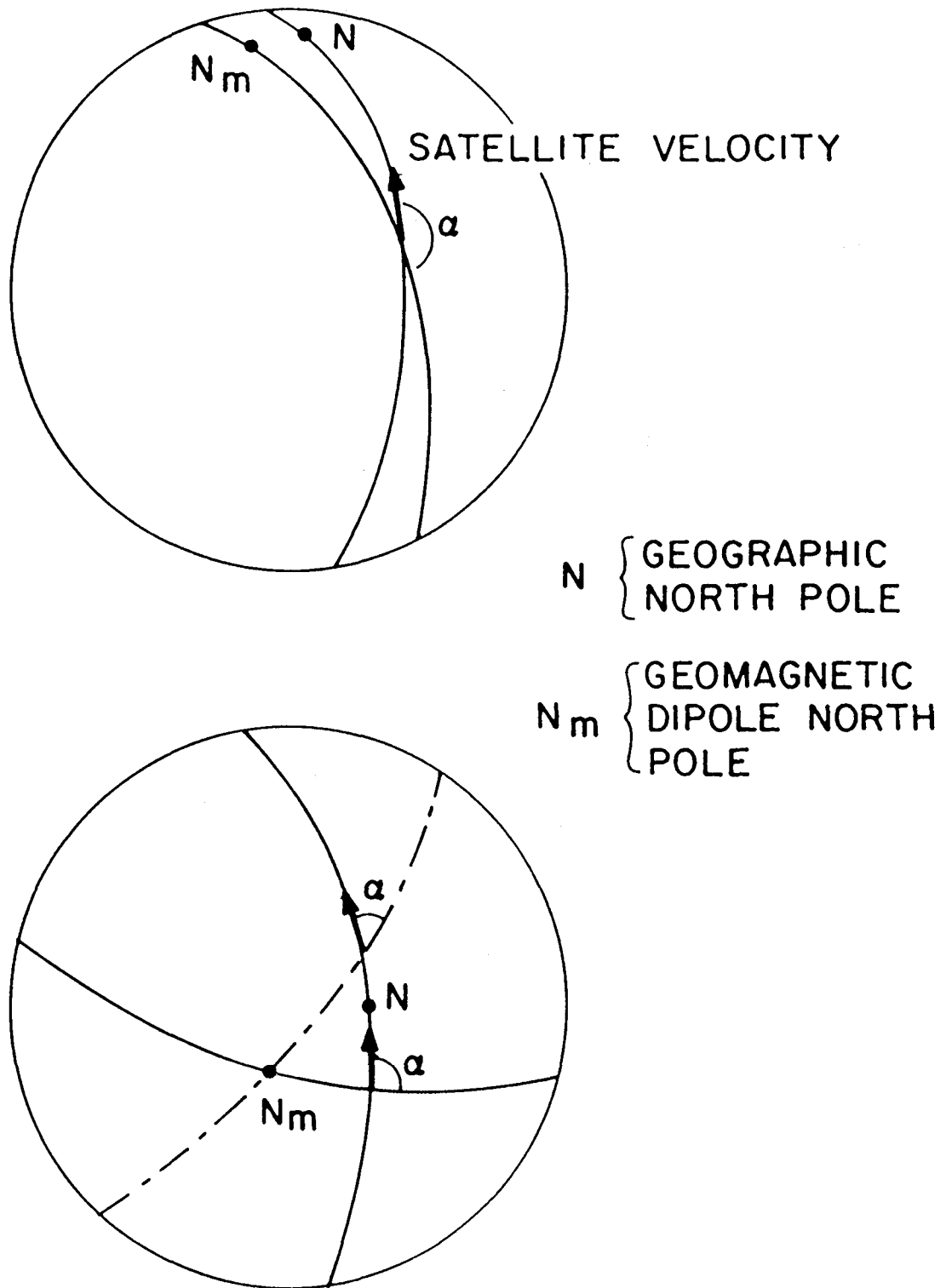
Figure 5. Angle, α, between the orbit plane and the dipole meridian plane; α is measured from the dipole south direction to the direction of the spacecraft velocity.
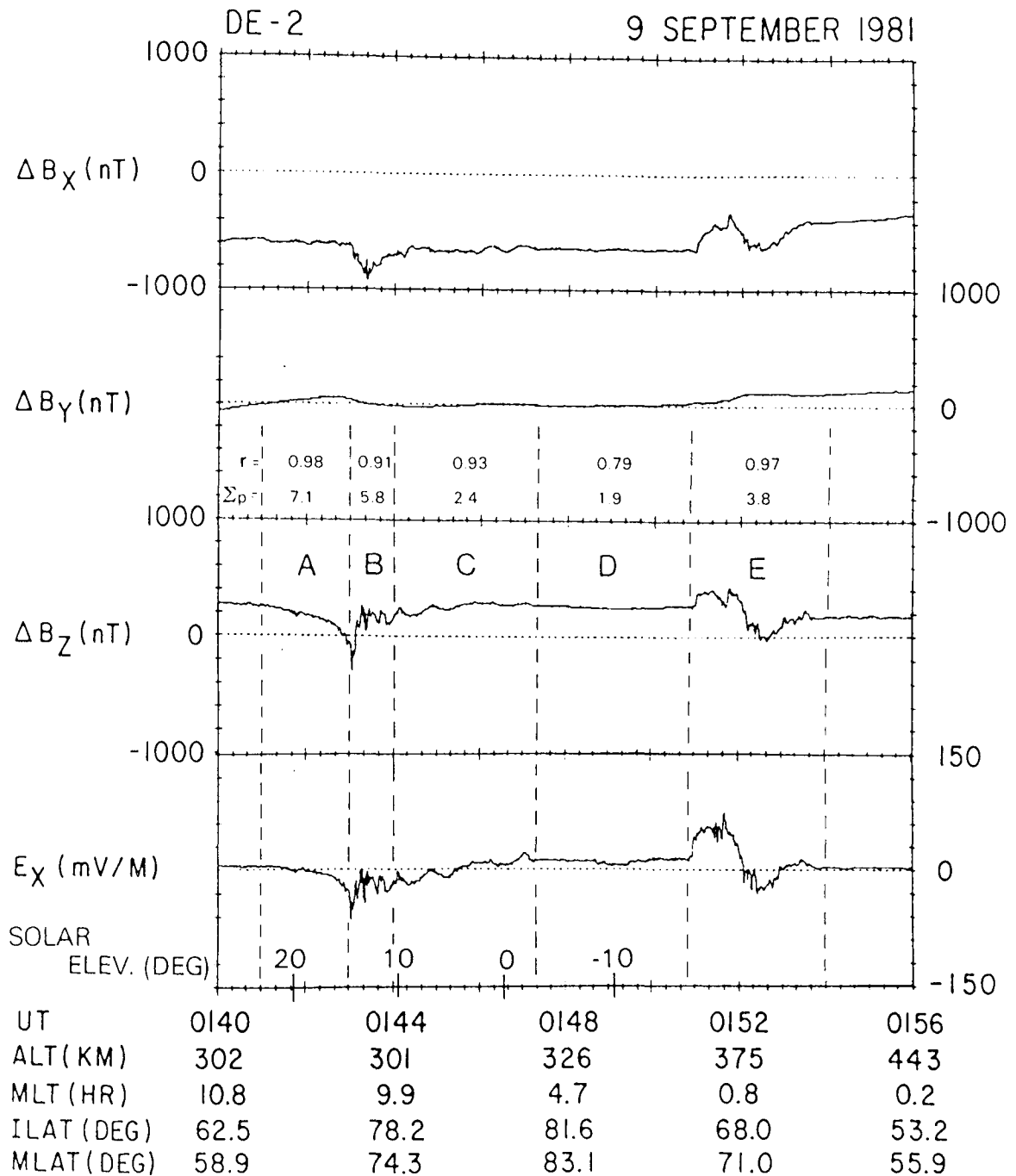
Figure 6. A northern pass when IMF $B_z <$ on September 1981. The angle α changed rapidly from intervals B to C. The field-aligned current was appreciable on the nightside because of auroral electrons.

OBSERVATIONS OF COMPOSITION FROM PIONEER VENUS

H. A. Taylor, Jr.
NASA/Goddard Space Flight Center
Laboratory for Atmospheres
Greenbelt, Maryland 20771

Low latitude distributions of atmospheric neutral hydrogen have been derived at Venus for the period 1979-1980. In-situ measurements of H^+, O^+, O, and CO_2 obtained from the ion and neutral mass spectrometers on the Pioneer Venus orbiter are combined with the appropriate chemical equilibrium relationship to determine the abundance of neutral hydrogen which is very difficult to measure directly. The measurements are all obtained below 165 km on the nightside and below 200 km on the dayside, based on evidence for chemical equilibrium prevailing up to those altitudes. During the period examined nearly three complete diurnal cycles were available and a comparison of the year-to-year variation in hydrogen content is made across the dawn region where the distributions of light gases are most pronounced. The dawn bulge in H (and also in He) which was reported from the first diurnal cycle by Brinton et al. (1979) is found to persist. The hydrogen concentrations peak near $2\text{-}5 \times 10^7/cm^3$, which is about 400 times greater than dayside concentrations. Superimposed upon the diurnal variation are strong day-to-day variations in which n(H) changes by as much as a factor of five. Such variations are linked to pronounced changes in the ion and neutral composition which sometimes occur in association with solar wind disturbances passing the planet. The interaction of the solar wind and the planetary environment somehow results in large changes in the relative abundances and scale heights of the ion and neutral species, thus modifying the derived values of n(H). These variations in the ion distributions are not surprising owing to the strong dependence of the nightside ionization upon convection from the dayside and associated sensitivity of this convection to changes in solar wind pressure and interplanetary magnetic field variations. The variation exhibited by the neutrals, however, appears to require some other explanation owing to the limited momemtum transfer between the ions and neutrals. Allowing for these short term perturbations, there appears to be no clear evidence for interannual variation in n(H) during the period examined, apparently consistent with the very small change in solar EUV flux over the same interval.
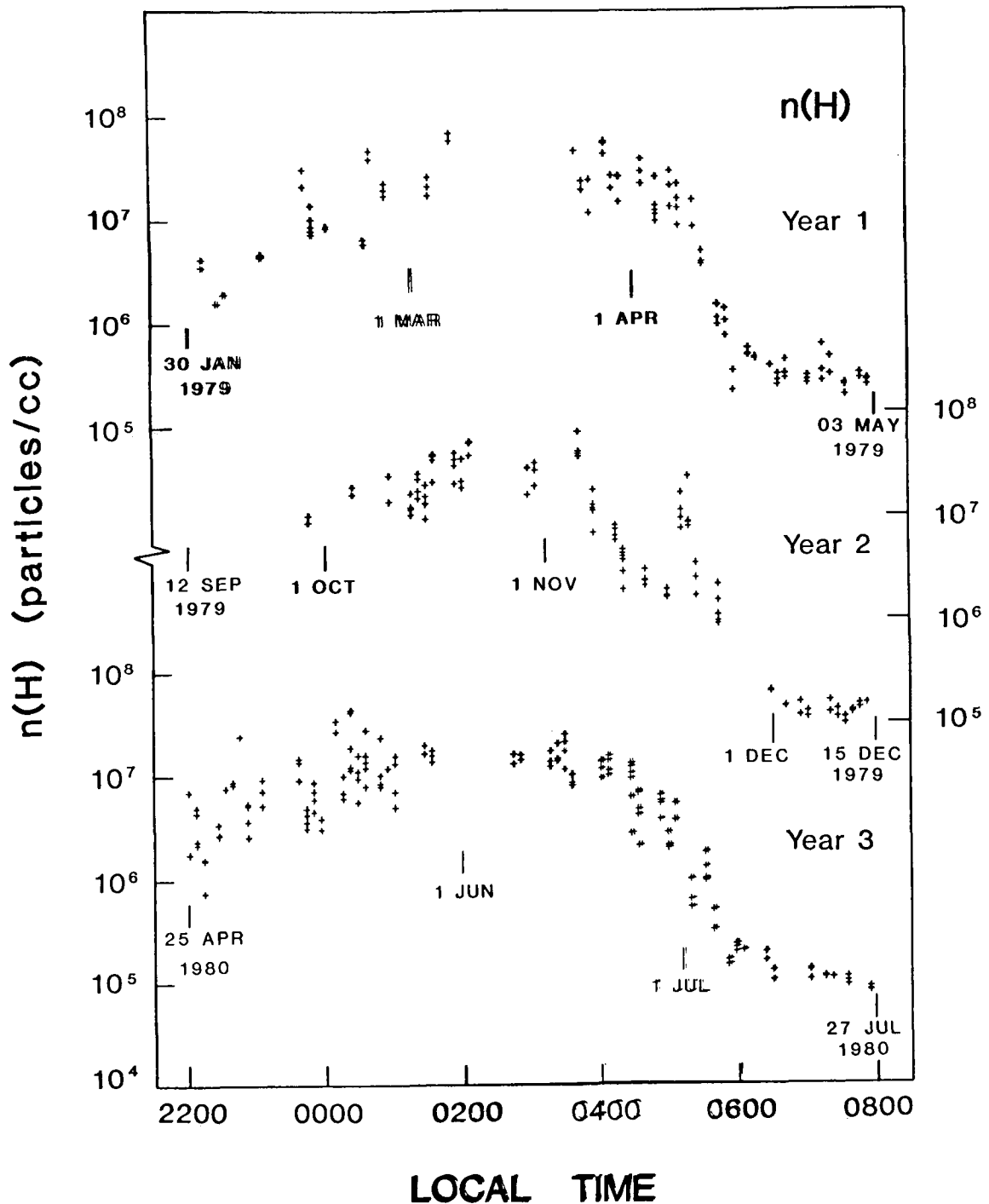
Figure 1. Local time distributions of n(H) derived from in-situ ion and neutral composition measurements at Venus during 1979-1980. Clusters of points are for individual orbits at specific local times. Gaps occur due to data interruptions and mode incompatibilities. The dawn bulge in hydrogen is evident featuring a sharp night-to-day gradient near 0500-0600. Sharp day-to-day variations in n(H) are attributed to solar wind perturbations and associated interaction with the ion and neutral constituents used in the derivation of hydrogen.
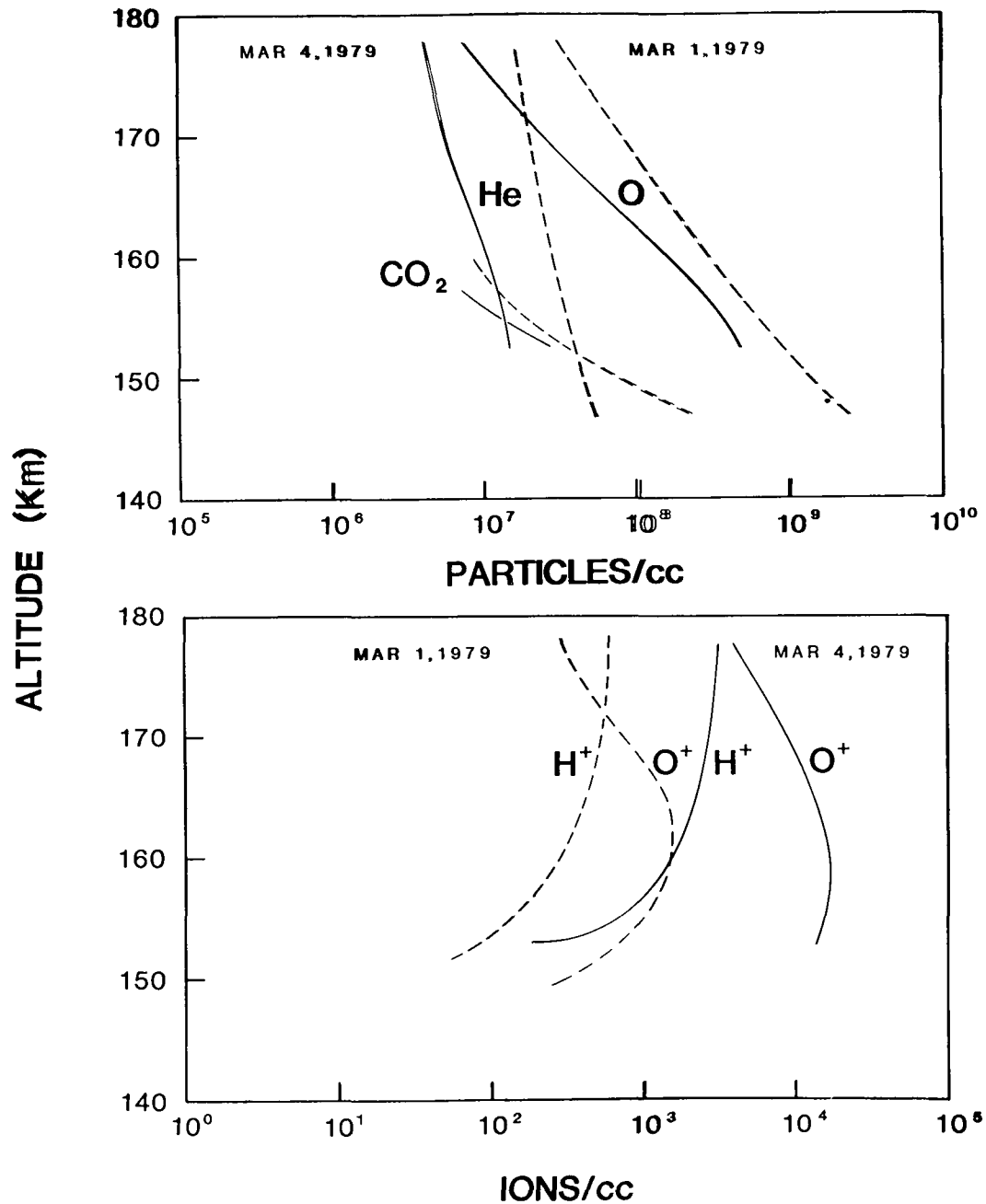
Figure 2. A comparison of the individual neutral and ion species variations observed in association with the passage of a strong solar wind disturbance on March 1 relative to a quiet day on March 4. Note for the neutrals in the upper panel that each of the species is more abundant on the disturbed day while in the lower panel the ion abundances are lower on the disturbed day. The reduction in nightside ion abundances with increased solar wind pressure occurring on March 1 is understandable on the basis of the day-to-night convection necessary for maintenance of the nightside ionosphere. The response of the neutrals is unexplained but apparently reflects compound results of energetic and dynamic perturbations from undetermined sources included in the overall solar wind disturbance event.

WAMDII OBSERVATION OF AN AURORAL ATMOSPHERIC WAVE EVENT

R. H. Wiens and G. G. Shepherd
C.R.E.S.S. York University, Toronto, Canada M3J 1P3

K. V. Paulson
Dept. of Physics, University of Saskatchewan, Saskatoon, Canada S7N OWO

Field tests of WAMDII[1] (Wide Angle Michelson Doppler Imaging Interferometer) on February 23/24, 1984 in Saskatoon produced wind images of the aurora that show well-defined wave structures in λ5577. Wavelengths and velocities of these structures suggest an acoustic-gravity wave interpretation, but their short duration warrants their being termed an event. The dopplergrams are presented with emphasis on the interpretation of the waves and a discussion of possible sources.

[1]G. G. Shepherd and WAMDII Coinvestigators, submitted to Geophys. Res. Let., 1984

ATTENDANCE LIST
THERMOSPHERE DYNAMICS WORKSHOP
OCTOBER 3-5, 1984

PARTICIPANT   AFFILIATION

Charles A. Barth   University of Colorado
Steven W. Bougher   NCAR
Roger G. Burnside   University of Michigan
George R. Carignan   University of Michigan
Herbert C. Carlson, Jr.   AFGL
K. S. W. Champion   AFGL
David Cleary   University of Colorado
William A. Coley   University of Texas
Robert Dickinson   NCAR
Mark Engebretson   Augsburg College
L. A. Frank   University of Iowa
Cassandra Fesen   NCAR
Jeffrey M. Forbes   Boston University
Rolando R. Garcia   NCAR
Marvin R. Geller   NASA/GSFC
J. C. Gerard   Universite de Liege
Stan Gross   Polytechnic Institute of New York
William B. Hanson   University of Texas
Isadore Harris   NASA/GSFC
Paul B. Hays   University of Michigan
Alan E. Hedin   NASA/GSFC
R. A. Heelis   University of Texas
G. Hernandez   NCAR
Bruce C. Herniter
Federico A. Herrero   NASA/GSFC
Colin O. Hines   Canada
Walter Hoegy   NASA/GSFC
Robert A. Hoffman   NASA/GSFC
Wayne Kasprzak   NASA/GSFC
T. L. Killeen   University of Michigan
J. S. Kim   State University of New York

469

PARTICIPANT	AFFILIATION
M. F. Larsen	Clemson University
Simon Lee	
John Lynch	NASA Headquarters
Kaichi Maeda	NASA/GSFC
Hans Mayr	NASA/GSFC
F. G. McCormac	University of Michigan
Robert Meier	Naval Research Laboratory
Ibsteen Mikkelson	Danish Meteorology Institute
Nathan J. Miller	NASA/GSFC
Daniel Morrison	Naval Research Laboratory
John Nisbet	Pennsylvania State University
William L. Oliver	MIT Haystack Observatory
David Rees	University College London
Patricia Reiff	University of Texas
Philip G. Richards	Utah State University
Arthur D. Richmond	NCAR
Henry Rishbeth	University of Southampton
R. G. Roble	NCAR
Joseph E. Salah	MIT Haystack Observatory
Salvatore L. Salamone	MIT Lincoln Labs
Kenneth H. Schatten	NASA/GSFC
Erwin Schmerling	NASA/GSFC
Peifu I. Shih	University of Michigan
Tatsuo Shimazaki	NASA/ARC
Roger W. Smith	University of Alaska
Nelson W. Spencer	NASA/GSFC
Donald Stevens-Rayburn	Applies Research Corporation
Jeff Stein	
Masahira Sugiura	NASA/GSFC
Harry Taylor, Jr.	NASA/GSFC
Brian A. Tinsley	University of Texas
Frank Varosi	Systems and Applied Research
R. L. Walterscheid	Aerospace Corporation
Vincent Wickwar	SRI International
Rudolph Wiens	CRESS-York University
Chih-Chung Yung	

1. Report No. NASA CP-2389	2. Government Accession No.	3. Recipient's Catalog No.
4. Title and Subtitle THERMOSPHERE DYNAMICS WORKSHOP II		5. Report Date June 1986
		6. Performing Organization Code 614
7. Author(s) Hans G. Mayr and Nathan J. Miller, Editors		8. Performing Organization Report No. 85B0268
9. Performing Organization Name and Address Goddard Space Flight Center Greenbelt, Maryland 20771		10. Work Unit No.
		11. Contract or Grant No.
12. Sponsoring Agency Name and Address National Aeronautics and Space Administration Washington, D.C. 20546		13. Type of Report and Period Covered Conference Publication
		14. Sponsoring Agency Code

15. Supplementary Notes

16. Abstract

This volume contains figures used in talks presented during Thermosphere
Dynamics Workshop II hosted by Goddard Space Flight Center. The abstracts
provide details given in each talk but the figures represent the fundamental
information exchanged within the Workshop. Atmospheric observations re-
ported on included recent measurements of thermospheric composition, gas
temperatures, auroral emissions, ion-neutral collisional coupling, electric
fields, and plasma convection. Theoretical studies reported on included
model calculations of thermospheric general circulation, thermospheric tides
thermospheric tidal coupling to the lower atmosphere, interactions between
thermospheric chemistry and dynamics and thermosphere-ionosphere coupling
processes

17. Key Words (Selected by Author(s)) Thermospheric composition Auroral emissions Electric fields Plasma convection	18. Distribution Statement Unclassified - Unlimited Subject Category 42		
19. Security Classif. (of this report) Unclassified	20. Security Classif. (of this page) Unclassified	21. No. of Pages 472	22. Price A20

National Aeronautics and
Space Administration
Code NIT-4

Washington, D.C.
20546-0001

Official Business
Penalty for Private Use, $300

TOC
LIBRARY
MS/185

NASA

DO NOT REMOVE SLIP FROM MATERIAL

Delete your name from this slip when returning material
to the library.

NAME	MS
Jay Italiano	149

NASA Langley (Rev. May 1988)   RIAD N-75